Studies on Advanced Solid Electrolytes for Solid-State Metal Batteries

Thesis submitted for the Degree of

Doctor of Philosophy (Science)

of

Department of Physics

Jadavpur University, Kolkata

By

Kuntal Ghosh

Registration no. SOPHY15092022

Index no. 90/22/Phys./27

Energy Materials and Devices Division
CSIR-Central Glass and Ceramic Research Institute
196 Raja S C Mullick Road
Kolkata 700 032, India

September 2025

CERTIFICATE FROM THE SUPERVISORS

This is to certify that the thesis entitled **"Studies on Advanced Solid Electrolytes for Solid-State Metal Batteries"** submitted by Shri **Kuntal Ghosh** (Registration no. **SOPHY15092022**, and **Index no. 90/22/Phys./27**), who got his name registered on **09.03.2022** for the award of Ph.D. (Science) degree of Jadavpur University, is absolutely based upon his own work under the supervision of Dr. Mir Wasim Raja, Principal Scientist, Energy Materials and Devices Division (EMDD), CSIR-Central Glass and Ceramic Research Institute (CSIR-CGCRI), Kolkata, West Bengal -700032, India, and that neither this thesis nor any part of it has been submitted for either any degree /diploma or any other academic award anywhere before.

15.09.2022

Dr. Mir Wasim Raja
Principal Scientist
Energy Materials and Devices Division
CSIR-Central Glass and Ceramic Research Institute
Jadavpur, Kolkata-700032, India

डॉ. मीर वसीम राजा / Dr. Mir Wasim Raja
प्रमुख वैज्ञानिक / Principal Scientist
ऊर्जा सामग्री और उपकरण विभाग / Energy Materials & Devices Division
सीएसआईआर-केन्द्रीय काँच एवं सिरामिक अनुसंधान संस्थान
CSIR-Central Glass & Ceramic Research Institute
विज्ञान एवं प्रौद्योगिकी मंत्रालय, भारत सरकार
Ministry of Science & Technology, Govt. of India
196, राजा एस. सी. मल्लिक रोड / 196, Raja S.C. Mullick Road
कोलकाता / Kolkata-700 032

DECLARATION

I hereby declare that the matter embodied in this thesis entitled **"Studies on Advanced Solid Electrolytes for Solid-State Metal Batteries"** is the result of investigations carried out by me in Energy Materials and Devices Division, CSIR-Central Glass and Ceramic Research Institute, Kolkata under the supervision of Dr. Mir Wasim Raja and it or its any part has not been submitted for any degree or diploma or any other academic award elsewhere.

Kuntal Ghosh
15/09/2025

Kuntal Ghosh
Energy Materials and Devices Division
CSIR-Central Glass and Ceramic Research Institute
Jadavpur, Kolkata-700032, India

Dedicated to

my beloved family members, my best friend, and my teachers

Acknowledgements

The process of a research journey is, in many ways, enjoyable — but "enjoyable" here does not simply mean happy or easy. It is filled with struggles, failures, frustrations, and, at the same time, small victories that make the journey meaningful. If I look at the bigger picture, the roadmap is often similar for all researchers — first comes the trial and failure, then the inevitable frustration, and then, slowly, a new beginning. Along the way, there are always those "what if" moments: *what if I had studied the fundamentals more deeply, what if I had learned DRT earlier…* Perhaps these "what ifs" are what keep the researcher in us alive and moving forward. Yet, no two journeys are identical — each one is deeply personal, and that uniqueness is what makes every research journey special.

The initial phase of my journey was the most crucial. That stage determines how one progresses, and at that time, I did not yet have the maturity, confidence, or patience that research demands. It is in this stage that the role of a supervisor becomes indispensable. Their knowledge, spirit, and guidance leave an impression that lasts for years. I am deeply thankful to my supervisor, **Dr. Mir Wasim Raja**. He was the one with whom I began my solid-state research journey, at a time when I had no idea about anything. His experience and knowledge-sharing were absolutely crucial in those days. For that initial phase, I would give him 100 out of 100. It always felt like we were a team. What I valued most was the freedom he gave me — the freedom to try something new, to explore uncharted paths, and even the freedom to fail and start again. For this, my foremost gratitude will always be reserved for him.

I would also like to express my heartfelt gratitude to my research advisory committee members, **Dr. Nimai Chand Pramanik** and **Dr. Nabin Baran Manik**. Manik Sir, who also heads the Department of Physics at Jadavpur University, has always been a source of encouragement and steady support.

When I first joined CSIR-CGCRI, I was completely new to this world, and everything felt overwhelming. In those early days, the presence of **Dr. Abhijit Das Sharma**, then the Head of our Department, gave me the assurance that I was in safe hands. His gentle guidance during my formative stage helped me to find my footing. Though he has now superannuated, his impact remains deeply etched in my memory. Today, our division is led by **Dr. Jayanta Mukhopadhyay**, who has always shown faith not just in me but in every student struggling and growing in the labs. To both of them, I remain sincerely thankful.

Even though I did not work closely with most scientists in our division, I observed and admired them quietly. Among them, I want to especially thank **Dr. Srabanti Ghosh**. Without the ZIVE SP1 instrument that was procured under her efforts, many of my experiments and much of my learning would have been impossible. I also extend my gratitude to **Dr. Allu Amarnath Reddy, Dr. Barnasree Chandra, Dr. Goutam Kishore Gupta, Dr. Soupitak Pal, Prof. Chittaranjan Sinha, and Dr. Pratyay Basak** for their unwavering support throughout this journey.

There are also people I hardly interacted with personally, yet their influence has been profound. The most important among them is **Dr. Sourindra Mahanty**. His immense contribution in building the battery research infrastructure of our institute has given me, and countless others, the opportunity to dream bigger.

But this journey has never been only about experiments, results, or instruments. It has always been about people. The ones who stood by me when nothing seemed to work, when experiments failed week after week, and when the pressure felt unbearable. My almost five years at CSIR-CGCRI would have been

impossible without the kindness and support of **Sudip da, Pradip da, Nabanita di, Debabrata da, Suman da, Ashok da, Nitai da, Mahadeb da, Hirak, Bimal da, Ratikanta da, Sunil da, Goutam da, Pratik da, Pushpam, Mousumi di, Prosenjit da**, and many others who became part of my everyday life in the institute. Whether it was helping me with small but crucial tasks in the lab, or simply offering a smile or a word of encouragement in the corridor, you reminded me that I was never alone in this struggle.

This journey would not have been possible without her — my girlfriend, best friend, lab partner, biggest enemy, research partner, teammate, and listener, **Mononita**. She has always stood beside me no matter what. She has been my strength. Her love for nature and animals has always fascinated me. I cannot imagine learning something new without first telling her. I probably irritated her the most, disturbed her often, but the journey with her has been one of the most precious parts of my life. Thank you for everything.

I would also like to thank all of my seniors, friends, and juniors for their knowledge, effort, and support. First and foremost, my senior **Susmita di (now Dr. Susmita)**. For a long time, only the two of us worked in the lab, and any doubt I had, I could simply ask her — and the problem was solved. I am also thankful to **Shoroshi di (now Dr. Shoroshi), Priyajit da (Dr. Priyajit Jash)**, and all my friends **Saibal, Samanta, Subhajit (now Dr. Subhajit), Koyel, Kabir**, and many others. I would also like to thank **Tandrima and Alok**, who worked with me for shorter periods. My lovable juniors — **Indrojit, Sinorul, Suman, Supriya, Riya, Sourabh, Dipendu, Soumita, Rajasekhar**, and many more — kept me on my toes with their questions, pushing me to learn more and share more.

I would like to thank my teachers — **Kartik kaka, Syakat Sir, Manoj Sir**, and many others. Without their support, I would not have been able to reach here.

I am equally grateful to my childhood friends — **Rajib, Soujannya, Subhankar, Subhash, Liton**, and many more. My B.Sc. and M.Sc. friends also hold a special place in my journey — **Supriyo, Amit, Pritam, Sourav**, and many others from my B.Sc. batch, and **Netrapal, Ashutosh, Shivam, Mukul, Ram, Aakash, Sourav, Jyoti, Debyendu, Mal**, and many more from my M.Sc. days. Even when we did not talk for years, I always felt their support.

Whatever I am today, I owe entirely to my family — **Maa, Baba, Dada, Boudi, and Vaijee**. From childhood to this day, they have protected me from all odds, guided me towards the right direction, and helped me whenever I needed them. If I receive this highest academic honor, the doctorate degree, it will be because of their hard work, dedication, and belief in the imperfect me. Maa, thank you for always being with me. This thesis is dedicated to you and to your spirit of never giving up. I also thank my extended family and relatives.

There are two people I missed the most during this journey — who left this world too early. **Sidhu**, you collected water hyacinth with me for my research back in 2021. Thank you for the precious moments you shared with me. And **Dida**, I hope you are happy with this achievement. I am sorry… I was late.

I also want to express my love and gratitude to **Mishtu, Chotu, Simba, Sundori, Lalu, Kalu, Barfi, Kulfi, Sandesh**, and many others — they loved and supported me like no one else.

And last but not least, I would like to thank **Time** — the greatest teacher of all. Finally, I thank **God and the Universe** for everything that I have achieved and not achieved, for every success and failure, for every triumph and every disaster.

CONTENTS

List of Figures

List of Tables

Abbreviations and Symbols

LLZO	$Li_7La_3Zr_2O_{12}$
c-LLZO	Cubic LLZO
t-LLZO	Tetragonal LLZO
LLGZO	$Li_{6.25}La_3Ga_{0.25}Zr_2O_{12}$
NZSP	$Na_3Zr_2Si_2PO_{12}$
LMO	$LiMn_2O_4$
LFP	$LiFePO_4$
NMC111	$Li(Ni_{1/3}Mn_{1/3}Co_{1/3})O_2$
NVP	$Na_3V_2(PO_4)_3$
SSE	Solid-State Electrolyte
CSPE	Composite Solid Polymer Electrolyte
HSE	Hybrid Solid Electrolyte
SIL	Solvated Ionic Liquid
LT	Liquid Therapy
ST	Solid Therapy
LiTFSI	Lithium bis(trifluoromethanesulfonyl)imide
$LiPF_6$	Lithium hexafluorophosphate
$NaPF_6$	Sodium hexafluorophosphate
NH_4F	Ammonium fluoride
NiO	Nickel oxide
LIB	Lithium-ion Battery
SMB	Sodium Metal Battery
SSLMB	Solid-State Lithium Metal Battery
ASSLB	All-Solid-State Lithium Battery
SS	Stainless Steel

σ	Ionic conductivity
σ_e	Electronic conductivity
t_+	Cation transference number
E_a	Activation energy
η	Overpotential
R_b	Bulk resistance
R_{gb}	Grain boundary resistance
R_{int}	Interfacial resistance
R_{ct}	Charge transfer resistance
Z'	Real impedance
Z''	Imaginary impedance
J	Current density
E	Potential / Voltage
t	Time
Q	Capacity
C_{sp}	Specific capacity
CE	Coulombic efficiency
CCD	Critical Current Density
SOC	State of Charge
DOD	Depth of Discharge
A	Electrode area
d	Electrolyte thickness
T	Temperature

Highlights of the Thesis

The rapid rise in demand for electric vehicles (EVs) is transforming the whole energy landscape across the globe, with a projection to exceed 200 million EVs by 2030. This surge evolves the whole energy storage segment for better batteries with higher energy density, longer driving range, and the highest safety. Conventional lithium-ion batteries heavily rely on flammable liquid electrolytes that cannot fully meet these requirements due to the instability with Li metal and uncontrolled dendritic growth. As a result, solid-state lithium metal batteries (SSLMBs), which combine lithium metal as anodes and a robust solid electrolyte, have emerged as a promising configuration for next-generation EVs.

Among the various solid electrolytes, garnet-type $Li_7La_3Zr_2O_{12}$ (LLZO) has received significant attention due to its wide electrochemical window, high conductivity at room temperature, and excellent compatibility with lithium metal. Yet, its practical use was hindered by high interfacial and grain boundary resistance due to the presence of various surface impurities and poor Li wettability that promotes point contact and uncontrolled dendrite penetration. The mechanical brittleness of garnet electrolyte also complicated the device integration for a practical battery cell.

This thesis addresses these challenges through a progressive and multi-scale engineering strategy. It started from advancing the synthesis and interfacial chemistry to microstructural control, dual-therapy interventions, and an innovative composite design with unconventional exploration for future studies. The key highlights of all the chapters are described below,

Introduction & Motivation in Chapter 1: A thorough literature survey is carried out to provide a critical overview of limitations in Li-ion technology, the promise of solid-state systems, classifications of electrolytes, and the synthesis barriers that shape their scalability with the research hypothesis and objectives around multi-scale engineering of garnet electrolytes.

Methodological foundation in Chapter 2: An integrated workflow of synthesis, characterization, and electrochemical evaluation was established to ensure reproducibility and direct correlation between processing parameters with various performances.

Synthesis Optimization and Interface Stabilization in Chapter 3: An aqueous combustion route using novel alanine fuels was optimized for maximum yield (~94%) of pristine cubic LLZO with engineered neck-fused grains at low temperature (900ºC). Introduced solvated ionic liquid (SIL) infusion in a LLZO matrix as a "liquid therapy" with enhanced interfacial stability and excellent full cell performance in various cathode chemistries (LMO, LFP, and NMC811).

Dual Interfacial Modification in Chapter 4: Surface fluorination generated a LiF-rich passivation layer in the LLZO matrix, whereas the SIL infusion enhanced wettability and Li-ion transport across the various interfaces. Post-electrochemical XPS results confirmed the suppression of TFSI decomposition, and DRT revealed stabilized interfacial processes over long cycling. This dual strategy delivered the best performance matrix in terms of low interfacial resistance (41.17Ω), high critical current density(1.45mA.cm^{-2}), and extended symmetric and full-cell stability, which suggests the effectiveness of the dual strategy in metal batteries.

Microstructural Engineering in Chapter 5: Engineering at the microstructural level attempts to use water hyacinth as a bio template for producing plate-like Ga doped LLZO, while cellulose exo-templating produced highly interconnected frameworks with a significant reduction in grain boundary resistance. With SIL infusion in cellulose-derived LLZO matrix delivered high ionic conductivity at RT (0.215 mS cm^{-1}), long-term plating/stripping behaviour (>1350h) with superior full cell performance.

Dual Therapy in Chapter 6: A dual-therapy approach was developed, which combined the solid therapy of Ga doped LLZO via NiO sintering aid and liquid therapy using a solvated ionic liquid (SIL). NiO addition in the LLZO matrix improved densification (90%) and introduced a conductive K_2NiF_4-type phase ($Li_{0.5}La_2Al_{0.5}O_4$), which reduced the grain boundary resistance by ~7×. With SIL infusion in solid therapy, the hybrid electrolyte further delivers higher ionic conductivity, lower interfacial resistance, and excellent long-term stability.

Composite Membranes in Chapter 7: Ga doped LLZO fillers were incorporated into three distinct systems, paper, polymer, and paper-polymer composite matrices, to enhance the ionic conductivity, interfacial stability, and flexibility. Paper-based separators improved the Li-ion cell performance, dual-polymer composites deliver ~10^{-4} S·cm^{-1} conductivity at RT with good Li metal compatibility. Whereas the paper-polymer membranes show reinforced, flexible electrolytes to offer a scalable pathway toward next-generation flexible lithium batteries.

Exploratory Extensions in Chapter 8: The liquid-therapy concept was further extended beyond Li metal batteries. In NASICON-type $Na_3Zr_2Si_2PO_{12}$ (NZSP), an ether-based liquid electrolyte infusion reduced the interfacial resistance and improved Na plating/stripping. This demonstrates the broad applicability of liquid-assisted stabilization in metal batteries. An unconventional modification strategy in the LLZO matrix is tried via Al-S modification. The preliminary results suggested the conductivity improvement compared to Al-only systems, which highlights both the challenges and the potential of anion doping in garnets. Together, these explorations further broaden the scope of the thesis in other metal batteries and by an unconventional approach.

Conclusion and future perspective in Chapter 9: Summarized the various materials and design engineering in garnet electrolytes and derivatives. It also highlighted the future directions in doping, cross-chemistry strategies, and scalable processing for solid-state batteries.

Together, this thesis develops a comprehensive roadmap for garnet electrolytes. It addresses the synthesis, interfacial, microstructural, and composite challenges with extending concepts to new materials systems.

Graphical Overview

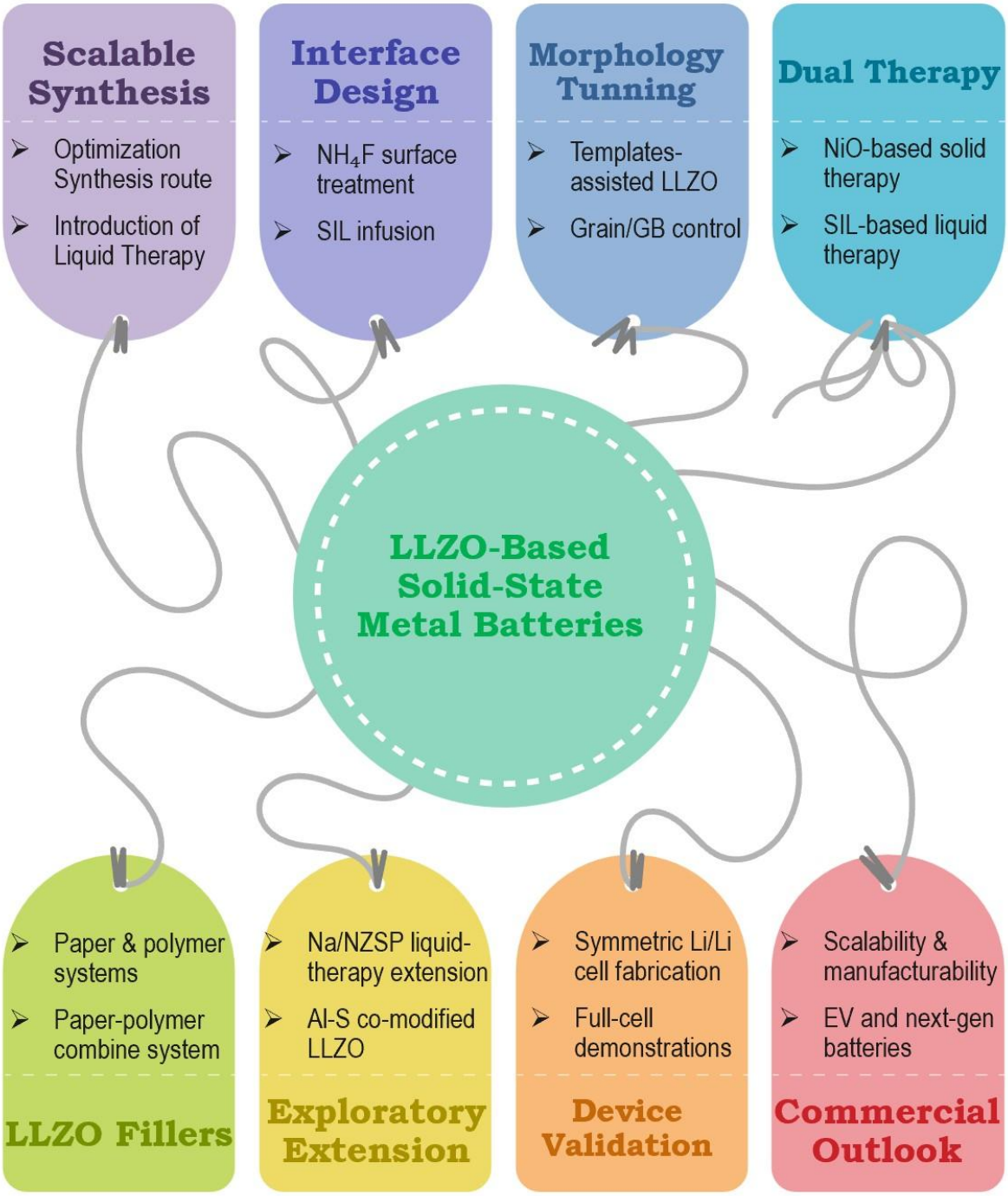

CHAPTER 1

Introduction, Motivation & Research Objective

1.1 Motivation

The steady rise in greenhouse gas (GHG) emissions is one of the defining challenges of the twenty-first century. The over-dependency on fossil fuels for electricity, heat, industrial work, and transportation has drastically altered the natural atmospheric composition of Mother Earth. The Intergovernmental Panel on Climate Change (IPCC) has already reported in its Sixth Assessment Report (AR6, 2021) that the concentration of atmospheric carbon dioxide (CO_2) has already reached higher than the pre-industrial levels of ~280 ppm[1]. Along with the CO_2, other pollutants such as Methane (CH_4) and nitrous oxide (N_2O) have also risen rapidly. The International Energy Agency (IEA) also calculated the global CO_2 emissions. It was found that the energy sector alone reached a record high of 36.8 gigatonnes in 2022, with a rough contribution of about 34% of the total emissions[2]. Whereas, the transportation contributed about 15-17%[3]. As, global warming heavily depends on the total amount of CO_2 released over time, or cumulative CO_2. Thus, CO_2 emissions must fall rapidly to keep the warming threshold as prescribed in the Paris Agreement (COP21, 2015) of staying below 1.5 °C[1]. This requires immediate action across the border to reach net zero within a few decades.

India also faces a dual challenge of sustaining rapid economic growth while keeping an eye on a sustainable low-carbon footprint. At COP26 in Glasgow, India announced its landmark commitment to achieve net-zero emissions by 2070[4]. This target is supported by the detailed plans from NITI Aayog and the Ministry of Environment, Forest and Climate Change (MoEFCC)[5]. In the near-term commitments, India pledged to reduce the carbon intensity of GDP by 45% relative to 2005 levels by 2030. Where the carbon internsity of GDP defined as the ratio of the quantity of CO_2 (or CO_2-equivalent) emitted divided by the size of the economy (GDP). India has also projected to lower down the cumulative carbon emissions by one billion tonnes by 2030 and ensure that half of the country's installed power capacity comes from non-fossil energy sources. The transport sector has been identified as a critical pillar of

decarbonization parallel to the power sector. A national policy vision has already proposed that at least 30% of all new vehicle sales should be electric by 2030 (MoEFCC, 2022; NITI Aayog, 2021)[6]. Between 2030 and 2047 in the medium term, India aims to accelerate this shift by expanded the renewable energy via a mass adoption. The success of this transformation will heavily depends on several key factors such as nationwide EV charging infrastructure, breakthroughs in battery technologies, and the integration of hydrogen based solutions for heavy-duty transport. In the long-term trajectory from 2047 to 2070, this transformation is expected to reach a mature stage with nearly complete electrification. Thus, these measures are expected to align India's development pathway with its 2070 net-zero milestone.

Thus, the electrification in the transport sector emerging as a key driver of decarbonization. In India, the transport sector contributes nearly 12% of energy-related CO_2 emissions as its heavy reliance on petroleum fuels. Thus, with a change from internal combustion engine vehicles with electric vehicles (EVs) can significantly reduce the lifecycle emissions. Beyond the climate benefits, EVs also enhanced the national energy security by reducing the dependence on imported crude oil and further promote the initiatives such as *Make in India* and *Atmanirbhar Bharat* which encourage the domestic manufacturing and innovation[5,6]. In addition, EVs provide a technological platform to integrate with other renewable energy sources through flexible charging.

These commitments towards net zero carbon footprint and EVs adaptation are also closely aligned with the United Nations (UN) Sustainable Development Goals (SDGs)[7]. The transition toward clean mobility directly contributes to SDG 7 (Affordable and Clean Energy) which further expand to sustainable energy systems. The reduction of greenhouse gas emission due to EVs adaption is also correlated with SDG 13 (Climate Action. The domestic EV manufacturing also supports SDG 9 (Industry, Innovation and Infrastructure) by developing domestic infrastructure and sustainable industrialization. Therefore, the mass adoption of EVs is not just an option anymore but an urgency for India's sustainable mobility transition and its long-term climate goals.

1.2 The Rise of Electric Mobility

The rise of electric mobility depends on energy storage systems (ESS) which balance between the energy and power densities. In general, fuel cells deliver high energy density but limited power density. Whereas the capacitors exhibit high power but lack storage capacity. But, Lithium-ion batteries provide a balance between energy and power densities. That is why LIBs

shows dominance in compared other EES for EVs. However, safety concerns, limited energy density, and reliance on liquid electrolytes remain critical constraint for EV application. This thesis is therefore motivated by the need to advance solid-state lithium batteries to deliver safer, higher-performance, and scalable solutions for future electric mobility.

1.2.1 Global Trends

Over the last decade the electric mobility has evolved from a niche technological advancement into one of key strategy for decarbonisation of any major economies across the globe. Global EV stock and annual sales have grown exponentially over last few years[8]. Countries like Norway, China, Germany, and the USA are adopted EVs aggressively through policy reforms, government subsidies, and improving support for charging infrastructure. However, China currently leading with more than 60% of the global Lithium-ion battery production[9]. Europe has also committed to get rid from internal combustion engine (ICE) vehicles by 2035. The European Union also allocates billions of funds in green transition. USA has implemented several tax benefits and boosting domestic EV manufacturing and critical mineral sourcing. The global EV sale also surpassed 26 million units in 2022, almost a ten-fold increase from 2017[8]. Global EV R&D efforts have also put significant effort to address the key technological bottlenecks of this transformation. In the United States, Battery500 Consortium initiative focusses on lithium-metal and solid-state batteries to achieve higher energy densities and longer lifetimes for EVs[10]. In Europe, programmes like Battery 2030+ and the European Battery Alliance promote breakthroughs in sustainable materials, digital design tools, and recycling pathways[11]. China has invested heavily in manufacturing, next-generation chemistries including lithium iron phosphate (LFP), high-nickel NMC, sodium-ion, and early solid-state prototypes. Japan and South Korea continue to push innovations in solid-state, lithium-sulfur, and high-safety electrolytes through their leading automotive and electronics industries (Toyota, Panasonic, Samsung SDI, LG Energy Solution). Collectively, these R&D efforts are strategically linked to industrial policies that recognise batteries as a core technology for competitiveness, energy security, and climate mitigation.

1.2.2 Indian Landscape

India's electric mobility ecosystem has grown very rapidly in recent years. It has driven by the governmental incentives, industrial policy, and a steadily growing research base across the country. The most prominent national initiative is the Faster Adoption and Manufacturing of Hybrid and Electric Vehicles (FAME) programme to catalysed the EV adoption[12]. As reported

in 2023, more than 1.17 million EVs had been supported through purchase incentives under the scheme[13]. This including nearly one million electric two-wheelers, while over 2,800 charging stations were sanctioned across 68 cities. Also, for industries the Production-Linked Incentive (PLI) schemes are very beneficial[14]. The PLI for the automotive sector, with a budget of ₹25,900 crore, was designed to stimulate domestic manufacturing of EVs and components. Whereas PLI for Advanced Chemistry Cells (ACC), with ₹18,100 crore, planning to established various manufacturing unit for 50 GWh of battery production capacity within India[15]. Additional support measures, such as the reduction of GST on EVs from 12% to 5% and on chargers from 18% to 5%, together with road tax waivers and green license plates, further promotes the EV adoption[16]. As a result of these combined efforts, EV penetration reached nearly 5% of all vehicle sales in 2022-23[13]. It was projected to increasing a upto 40% by 2030. Importantly, the early growth of India's EV market has been concentrated in two- and three-wheelers, as well as compact cars.

India has also developed a robust research and development ecosystem that support the EV adoption. Among the various Indian Institutes of Technology (IITs), IIT Delhi, IIT Roorkee, and IIT Jammu have contributed to electrode and cathode materials research. Whereas, IIT Gandhinagar focused on various solid-state chemistry. IIT Bombay has advanced in diagnostics, modelling, and prototyping. IIT Indore and IIT Hyderabad have pursued dual-ion and lithium-sulfur systems, along with hybrid battery-supercapacitor developments. IIT Madras has work on solid electrolytes and nanostructured electrodes. IIT Kharagpur and IIT BHU have work on prototyping and solid-state battery development.

Among the various Council of Scientific and Industrial Research (CSIR) lab, CSIR-CECRI in Karaikudi has led R&D on lithium-ion electrochemistry, cell fabrication, and recycling. CSIR-CGCRI in Kolkata has specialised in glass- and ceramic-based solid electrolytes for solid state battery development and paper based sustainable separator for Lithium-ion cell. Whereas, CSIR-NCL in Pune has contributed significantly to electrode materials and polymer electrolytes. CSIR-IMMT in Bhubaneswar has already established in battery recycling and mineral recovery technologies. Beyond IITs and CSIR labs, other premier institutions strengthen the ecosystem further, such as IISc Bangalore, JNCASR, and CPRI have emphasised oxide and polyanion cathodes and prototyping. And, IISERs in Pune, Kolkata, and Thiruvananthapuram have pursued solid electrolytes and advanced materials. ARCI in Chennai and C-MET centres have worked extensively on materials scale-up and industrial prototyping. ISRO's VSSC has developed high-reliability batteries for aerospace applications which

provides key insights into safety and performance under extreme operating conditions. IACS, TCG-CREST in Kolkata continues to contribute to advanced solid-state materials research. Also establishment of Battery Research Society (BRS) has emerged as a professional platform linking academia, industry, and policymakers to accelerate the translation of laboratory research into commercially viable technologies.

In summary, India's EV policy framework, emerging market adoption, distributed R&D capabilities, and professional networks reflect a deliberate strategy to build Make in India product for the entire value chain. This approach is essential for the challenges of affordability, tropical climate durability, and infrastructure readiness, sustainable electric mobility.

1.2.3 Role of Batteries in EVs

Battery is like the heart of any electric vehicle system. It directly controls in the performance, cost, and sustainability of EVs. In simple terms, the energy density of a battery tells us how far a vehicle can travel on a single charge. Whereas, the power density controls the dynamic performance, such as acceleration and fast charging[17]. Lifecycle, stability and safety of a battery cell further correlate with the economic viability of EVs, especially under India's hot and humid climatic conditions.

Currently, lithium-ion batteries (LIBs) dominate the EV market because they offer a favourable balance between energy density and power density compared to other energy storage devices alternatives such as fuel cells or supercapacitors. However, LIBs still face critical challenges due to the flammable organic electrolyte. Thermal runaway risks due to the presence of polypropylene based polymer separator and limited driving range due to utilizing graphite anode instead of Li metal restrict it successful large-scale adoption[17]. Moreover, battery cost is directly controlling the affordability of EVs.

These challenges highlight the need for next-generation better batteries for affordable EVs. Solid-state lithium metal batteries (SSLMBs) are widely considered as a promising alternative because they replace flammable liquid electrolytes with solid electrolytes. It also offers higher energy density due to the use of Li metal which have the highest theoretical capacity ($3860 mah.g^{-1}$), improved safety, and longer cycling stability. However, large interfacial resistance at the metal/electrolyte interface, uncontrolled dendrite penetration, and scalable processing remain bottlenecks for successful commercialization. Thus, the role of batteries in EVs is therefore not only in technological aspect but also strategic as always. Improvements in

battery chemistry, design, and manufacturing can directly accelerate the EV adoption, enhance the national energy security by reducing the oil imports, and can enable integration of renewable energy into the grid through flexible charging and vehicle-to-grid (V2G) applications. For India, indigenising battery innovation and manufacturing is essential to achieving long-term goals such as Atmanirbhar Bharat and Make in India. Thus the primary of this thesis is to address the limitations of current LIB technology and advancing the solid-state solutions, particularly through interface engineering and microstructural optimisation of solid-state electrolytes, to deliver safer, high-performance, and scalable batteries for future electric mobility.

1.3 Li-ion Batteries and Beyond

Since the commercialization of Li-ion batteries (LIBs) by Sony in 1991, it revolutionized the portable electronics market and have become a strong candidate for electric vehicles[18,19]. Here, we will discuss about the basic principle of Li-ion batteries, their limitation and about next-generation energy storage devices.

1.3.1 Basic Principle of Li-ion batteries

Lithium-ion batteries (LIBs) are generally a primary rechargeable electrochemical device. It converts chemical energy into electrical energy and also it can store energy. A typical LIB consists of three key components, a positive electrode (cathode), a negative electrode (anode), and an ionically conducting and electronically insulator, electrolyte separated by a porous polymeric membrane, as shown in ***Figure 1.1***. The electrodes are generally electronically connected through an external circuit. It allows the flow of electrons in the external circuit, while the electrolyte selectively transports lithium ions (Li^+) between two electrodes during charge and discharge[18].

The cathode is usually a lithium transition metal oxide with a layered or olivine structure. Such as lithium cobalt oxide ($LiCoO_2$), lithium manganese oxide ($LiMn_2O_4$), or nickel-manganese-cobalt oxides (NMC). Whereas, the anode most commonly consists of graphite, which can host the lithium ions into its layered structure via intercalation. The electrolyte typically contains a lithium salt such as $LiPF_6$ dissolved in organic carbonate solvents (ethylene carbonate, diethyl carbonate, etc.). To prevent short-circuiting, a microporous polypropylene (PP) or polyethylene (PE) based separator soaked with the liquid electrolyte is used to physically isolate the electrodes but conduct ion through its pore[19].

The basic operation of a LIB depends on the principle of reduction and oxidation (redox) reactions at the electrode/electrolyte interfacial boundary. During charging, Li^+ ions are deintercalated from the cathode host lattice and migrate through the electrolyte via porous separator, and intercalate into the anode. Similarly, electrons also travel through the external circuit from cathode to anode. During discharge, the reverse process, i.e. Li^+ ions leave the anode and return to the cathode via intercalation with electrons flow through the external load. In this way we are powering our devices.

Positive electrode

$$LiMO_2 \leftrightarrow LiMO_{1-x} + Li_x + xe^-$$

Negative electrode

$$C + xLi^+ + xe^- \leftrightarrow Li_xC$$

Overall reaction

$$LiMO_2 + C \leftrightarrow Li_xC + LiMO_{1-x}$$

[M = transition metal]

Thus, the main driving force for the overall process is the difference in chemical potential between the cathode and anode materials and which further translates into the cell voltage. So, the operation of LIBs can be understood as a reversible "shuttling" of lithium ions between the two host structures and electrons complete the race in externally[18,19].

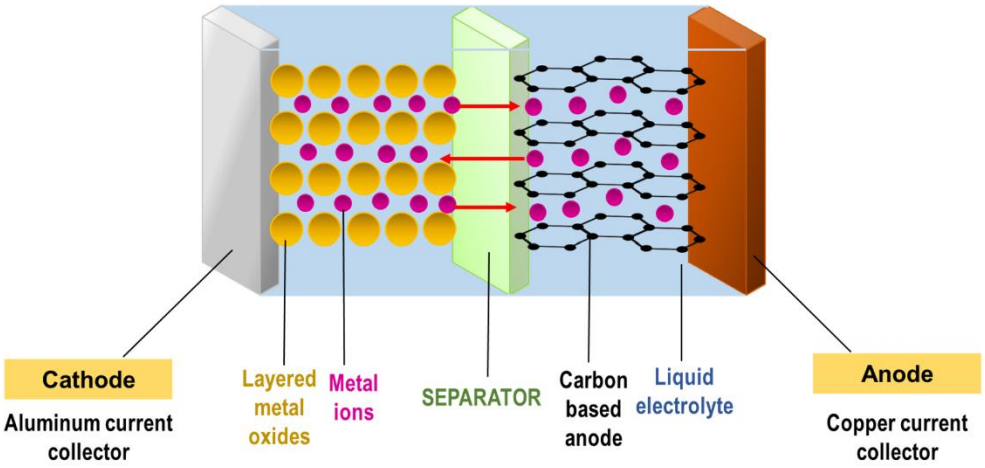

Figure 1.1 *Schematic representation of a typical Lithium-ion battery*

In the present scenario, the LIB deployment has started from consumer devices to grid-scale storage and electric mobility, their inherent limitations have become increasingly evident. Various Challenges related to safety, restricted energy density, life cycle degradation, and

material sustainability restrict their successful commercialization for large-scale electrification. Thus, a critical assessment of these limitations is required to identify the parameters at which the improvement is necessary for current the successful commercialization of current LIBs or next-generation systems such as solid-state batteries.

1.3.2 Limitation in Safety, Energy Density and Lifecycle

LIBs system revolutionizes the electric vehicle electrification with their balance energy density, power capability, and manufacturing maturity. However, their intrinsic limitations present a formidable barrier in terms of long-term scalability. The foremost concern is safety. LIBs contain flammable organic carbonate electrolytes and polymer separators. In any abusive condition (overcharge, mechanical abuse, thermal shock, or internal short-circuits), the cell can go to thermal runaway. This initiation resulting in accumulation of local heating and exothermic electrolyte decomposition with release of oxygen from cathode and that easily goes to an uncontrollable fire accident. The risk of accident heavily depends on tropical region, where the high ambient temperature and poor thermal management system can make two or three wheelers very vulnerable[20–22].

Another bottleneck is the energy density. Conventional LIBs use the graphite anodes (372 mAh g^{-1}), which has very low capacity as compared to lithium metal (3860 mAh g^{-1}). So, even with high-nickel layered oxide cathodes (NMC, NCA), the system should carry sufficient amount of graphite and thus the energy density significantly reduced. The current densities are also remained insufficient for long-range EVs without increasing battery mass and cost. Efforts have been made to use silicon or high voltage cathode but it often creates instability, mechanical degradation and ultimately reduced safety in Li-ion cell[18,23,24].

Another Equally critical parameter is cycle life and performance degradation over time. LIBs generally deteriorate its performance due to multiple coupled processes. Such as the growth of the solid electrolyte interphase (SEI), cathode structural degradation, pollutant the electrolyte, and lithium plating during fast charging[23–25]. These processes fading capacity over time and as a result of that the cell resistance increases during long cycling. In India's hot and humid climate, the side reaction also accelerates which further reduced the calendaring and cycle life. It also directly negatively impacts on the reliability and affordability of EVs adoption. Thus, we need more advanced battery system that can provide safer operation, higher energy density, and longer durability.

1.3.3 Solid-State Batteries as Next-Generation Technology

Solid-state batteries (SSBs) have gained significant attention due to its theoretical advantages against the intrinsic weaknesses of LIBs[26,27]. The main building block of the solid-state battery is the solid electrolyte. It replaces flammable liquid electrolytes that we use in Li-ion cell. There are two types of the solid electrolyte, inorganic solid electrolyte and organic solid electrolyte. We will discuss about them in the later section. In general, solid electrolytes improve safety by eliminating leakage and suppressing thermal runaway mainly observed in Li-ion cells. Also, solid electrolytes offer wider electrochemical stability windows, and can operate at higher operating temperatures[26,27]. It making them attractive for a region like India where climatic resilience is critical. A second advantage lies in the energy density enhancement by using lithium metal as anodes which has highest theoretical capacity of 3860 mAh g^{-1}. Thus, it is quite expected that the SSBs can easily surpass the energy-density achieved in the graphite cell. Thus, it has the potential to deliver longer driving ranges and reduced pack sizes by using Li metal for EVs. This is a crucial step toward the successfully commercialization of EVs. Also, their inherently low self-discharge rate and resistance to dendrite growth hold a key promise for longer service lifetimes[27,28]. However, it seems to be a perfect solution for existing hurdles in liquid battery but the promise of SSBs comes with some serious challenges that will discuss in the later section.

1.4 Solid Electrolytes: Classification and Ion Transport Mechanism

Solid state battery promises to address the primary challenges in conventional LIBs by replacing volatile organic solvents with the ion-conducting solids which also acted as physical separators. Thus, a solid electrolyte is expected to facilitate the lithium-ion transport across electrodes and prevent the electronic short-circuiting just like the liquid electrolyte in lithium-ion cell. It will also offer the additional advantages in safety, thermal stability, and energy density. Thus, the ideal solid electrolyte therefore should satisfy a combination of electrochemical, mechanical, and practical requirements for solid state battery development. An ideal electrolyte should satisfy following requirement[26,27].

- The lithium-ion conductivity at room temperature comparable to or exceeding 10^{-3} S cm^{-1}, similar to that of the liquid carbonate electrolytes.
- A wide electrochemical stability window compatible with high-voltage cathodes and lithium-metal as anodes.

- Purely ionic conduction with negligible electronic conductivity to avoid internal short-circuiting.
- Excellent chemical and mechanical stability with the electrodes.
- The ability to form stable, low-resistance interfaces with the both anode and cathode materials.
- Higher critical current density for fast charging.
- Low cost and easy scalability for large-format cell manufacturing.

In practical scenario, no single class or materials meets the most of the criteria of an ideal electrolyte for successful commercialization. Therefore, it becomes essential to systematically classify the solid electrolytes and critically analyse their unique advantages and limitations with their ion transport mechanism. This perspective not only highlights the progress made so far but also points toward rational design of composite and hybrid systems that may meet the requirement of an "ideal" solid electrolyte.

1.4.1 Inorganic Electrolytes and Their Ion Transport

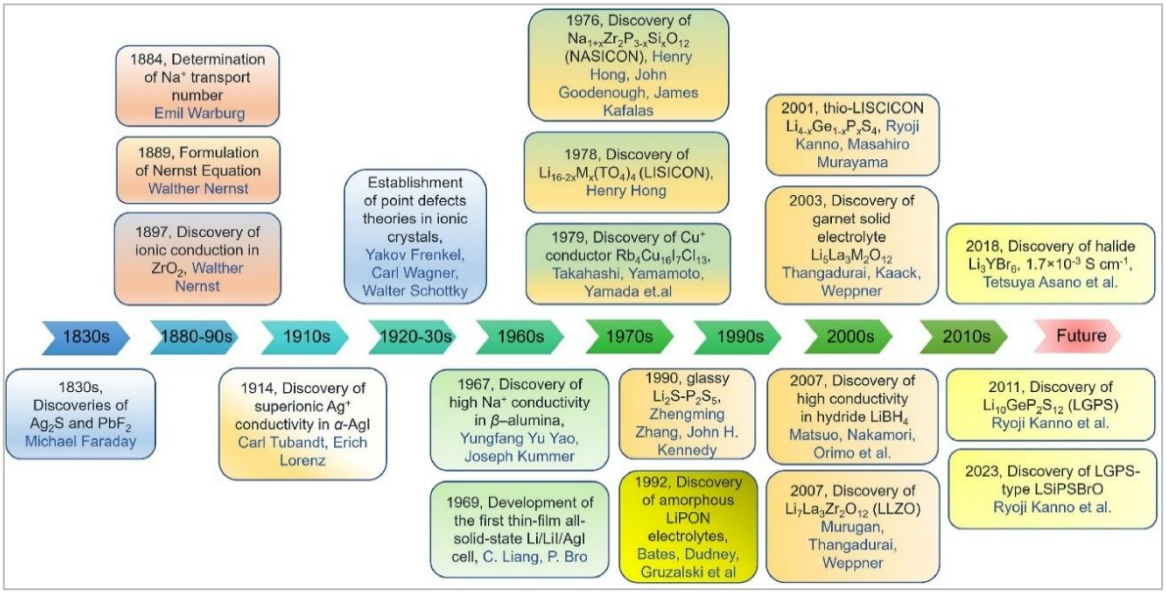

Figure 1.2 *Historical evolution of development of inorganic solid electrolytes. Reproduced from [29]*

The fascinating fields solid-state ionics began with Faraday's discovery of ionic conduction in 1830. After that, significant evolution happened through α-AgI, β-alumina, NASICON/LISICON, LiPON and Garnet systems[29]. The evolution of various inorganic solid electrolytes was presented in ***Figure 1.2***. Among the various types of solid electrolytes,

inorganic solid electrolytes (ISEs) have the most research due to their properties being very close to an ideal electrolyte. It consists of various types of electrolytes and is mainly divided into amorphous glasses, glass-ceramics or partially crystalline, and crystalline. Inorganic solid electrolytes generally deliver the highest ionic conductivity at room temperature among the various types of solid electrolytes, thanks to their crystalline nature. Also, it has a wide potential window, excellent thermal stability and excellent Li-ion efficacy with lower activation energy. The ion transport mechanism of inorganic solid electrolytes is completely different from that of their liquid counterparts. In conventional liquid electrolytes, as we know that the both the ion are behave like a mobile charge carriers. The overall conductivity also depends on the intrinsic properties of the solvent. According to the Stokes-Einstein relation, higher ionic conductivity in liquids can be achieved by increasing ion dissociation in solvents with large dielectric constants. Also, by lowering the viscosity to enhance the mobility of solvated ions[30,31].

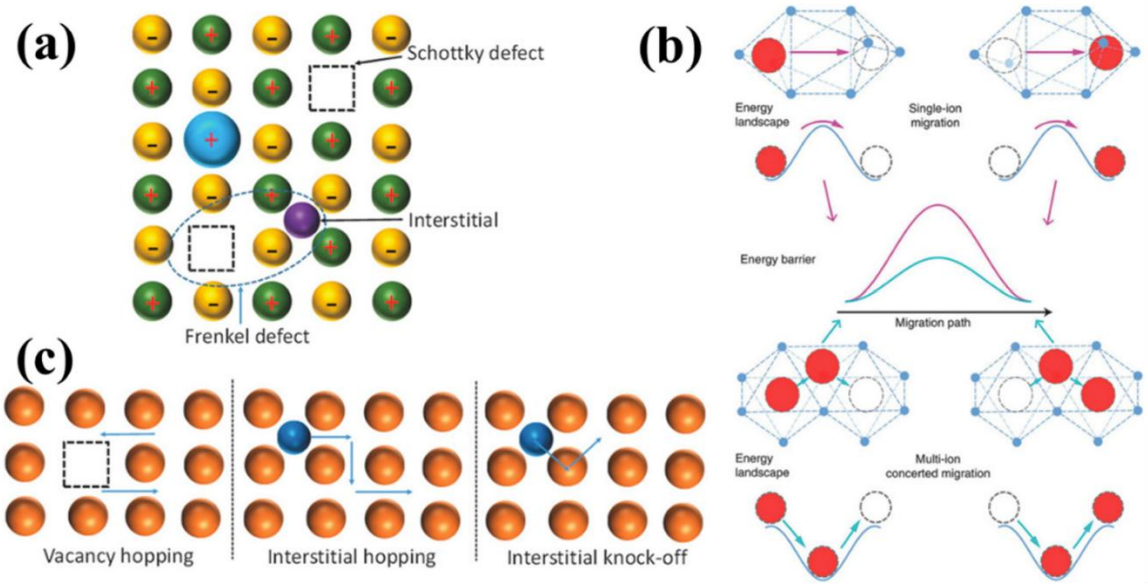

Figure 1.3 *Mechanism of ion transfer process in inorganic solid electrolyte via (a) defect, (b) migration pathway,[32] (c) migration mechanism[33]. Reproduced with permission from [34].*

However, in inorganic solid-state electrolytes, only lithium ions act as mobile carriers. Here, ionic conduction is mainly depended on the crystal structure, availability of vacant sites, and the interaction between lithium ions and the structural skeleton. Ion transport occurs predominantly via three mechanisms: (i) the vacancy mechanism, where Schottky-type defects provide unoccupied sites for lithium hopping; (ii) the interstitial mechanism, where lithium migrates through Frenkel defects created by displaced ions; and (iii) the interstitial-

substitutional exchange mechanism, where diffusion proceeds through coordinated ion exchange across adjacent lattice sites as shown in ***Figure 1.3***. In some systems such as garnet-type oxides, a combination of these pathways enables relatively high conductivities[34,35].

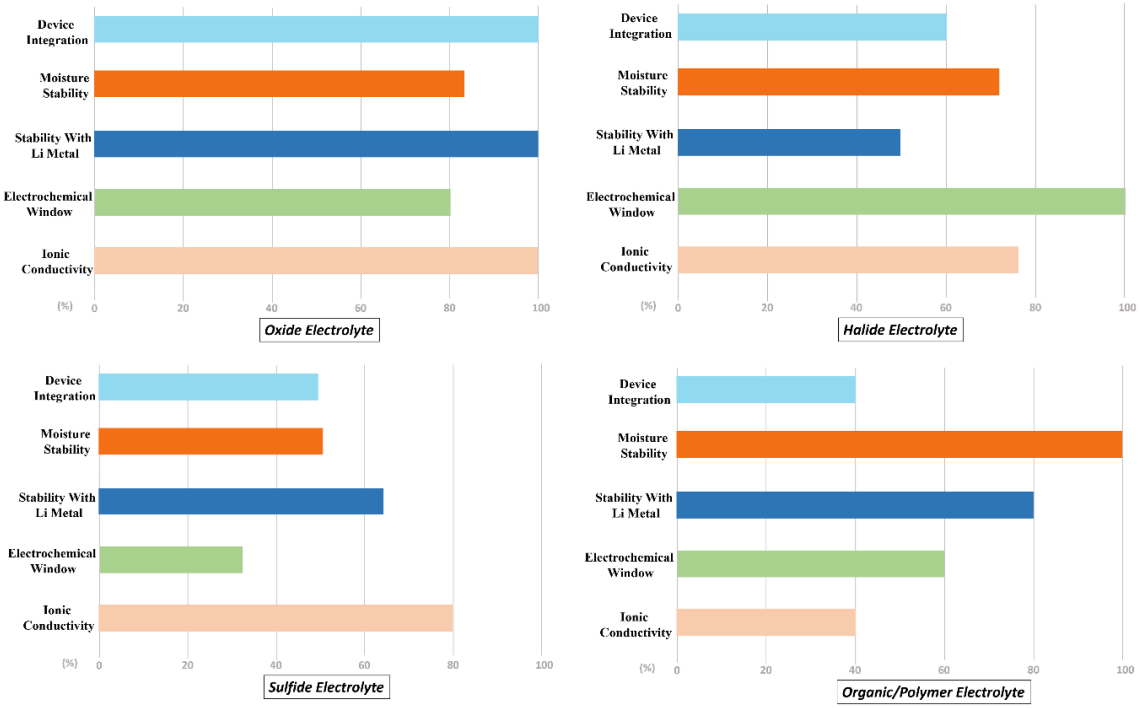

Figure 1.4 *Comparative chart of the various advantages and disadvantages of four major solid electrolytes: oxide, sulfide, halide, and polymer. Idea taken from [29]*

On the other hand, glassy and amorphous electrolytes which lacks any long-range crystalline order but retain short- and medium-range ordered structure that can still facilitate lithium-ion conduction. In these systems, lithium transport is generally described as localised hopping between energetically similar sites. It is followed by the collective diffusion at the macroscopic scale. The mobility of lithium ions is strongly influenced by the density of defects and the nature of their interaction with the disordered glassy framework. Thus, designing high-performance inorganic conductors therefore requires three essential conditions, (i) the presence of wide conduction channels or disordered sublattices large enough for Li^+ ions to move through, (ii) a continuous network of interconnected vacancies or interstitial sites with low migration barriers, and (iii) a stable framework with weak ion-lattice interactions to minimise trapping[36–39].

1.4.1.1 Solid Oxide Electrolytes

Oxide-based solid electrolytes are among the most extensively studied classes of inorganic solid-state electrolytes because of their high thermal stability, wide electrochemical windows, and good compatibility with high-voltage cathodes as shown in ***Figure 1.4***. They include NASICON-type, garnet-type, LISICON-type, perovskites, anti-perovskites, and LiPON group electrolytes[40–47]. Despite their several advantages, these materials often face challenges such as high processing temperatures, surface impurities, rigid structures, and interfacial resistance against lithium metal.

1.4.1.1.1 NASICON-type Electrolytes

The sodium superionic conductor (NASICON) structure was first introduced by Goodenough et al. in 1976[48]. It consists of a 3D framework of corner-sharing MO_6 octahedra and PO_4 tetrahedra, where Na^+ (or Li^+ in the Li-substituted analogues) ions migrate through interconnected channels[49]. When Na is replaced by Li, compositions of the general form $LiM_2(PO_4)_3$ (M = Ge, Ti, Zr) can be obtained[38,49]. Ionic conductivity in NASICONs can be improved via substitution at the at the M sites. For example, Al doping in $LiTi_2(PO_4)_3$ and $LiGe_2(PO_4)_3$ forms $Li_{1+x}Al_xTi_{2-x}(PO_4)_3$ (LATP) and $Li_{1+x}Al_xGe_{2-x}(PO_4)_3$ (LAGP), respectively, which show the room-temperature ionic conductivities close to 10^{-3} S.cm^{-1}[50–54]. Conductivity in NASICON structure (***Figure 1.5***) is generally governed by the bottleneck size and site percolation, with larger bottleneck dimensions lowering activation energy[50,55].

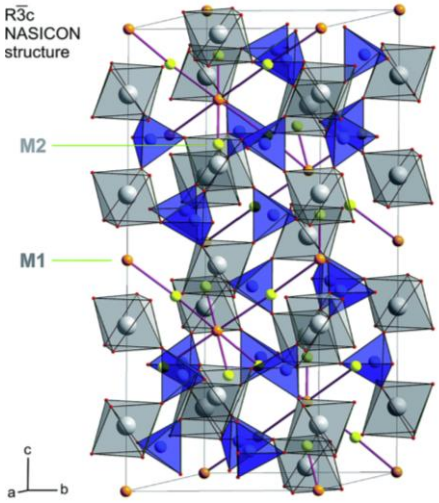

Figure 1.5 *NASICON-type LATP Structure. Reproduced from [51].*

1.4.1.1.2 Garnet-type Electrolytes.

Garnet-type solid electrolytes $Li_7La_3Zr_2O_{12}$ (LLZO) are the most researched and considered one of the promising candidates for the commercialization. It shows good conductivity (10^{-4}–10^{-3} S cm^{-1}) at room temperature, wide potential window (up to 6 V vs. Li^+/Li) and excellent stability against Li metal[26,28,56–59]. It belongs to the garnet-type family ($Li_7A_3B_2O_{12}$). In general, the La occupies

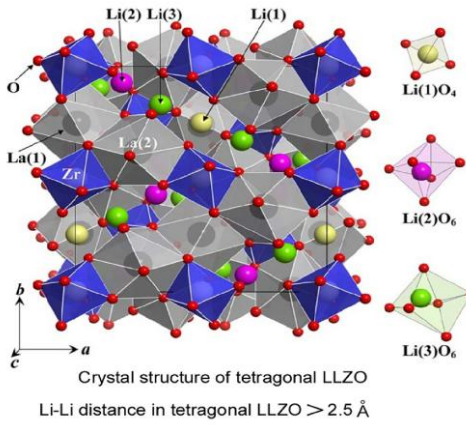

Figure 1.6 *Garnet-type tetragonal LLZO Reproduced from [29].*

dodecahedral eight-coordinated sites and Zr resides in octahedral six-coordinated sites. The crystal lattice are existed in two polymorphs, tetragonal phase with a space group $I4_1/acd$ and cubic phase with a space group $Ia3d$[60]. In the tetragonal structure as shown in ***Figure 1.6*** and ***Figure 1.8(b)***, Li ions fully occupy tetrahedral 8a sites and octahedral 16f and 32g sites. It resulted in a highly ordered distribution but poor ionic mobility ~10^{-6} S cm^{-1} at room temperature. However, in the cubic structure as show in ***Figure 1.7*** and ***Figure 1.8(a)***, Li partially occupies in filled 24d tetrahedral and 96h octahedral sites. It provides 64 vacant sites that enable fast Li-ion migration via a 3D hopping pathway with a higher conductivity ~ 10^{-3}-10^{-4} S cm^{-1} at room temperature). Doping with Al, Ga, Ta, Nb, W, or Te is a common strategy to stabilize the cubic polymorph and reduce sintering temperatures[29].

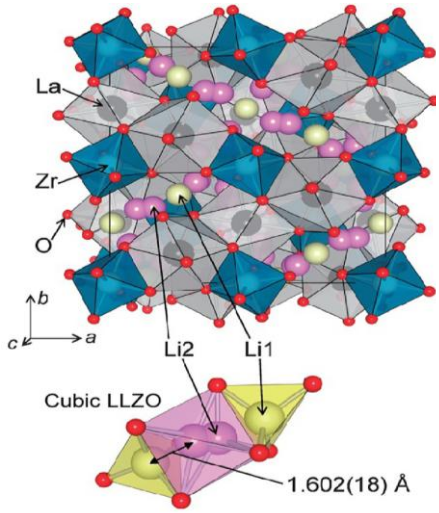

Figure 1.7 *Garnet-type cubic LLZO. Reproduced from [29].*

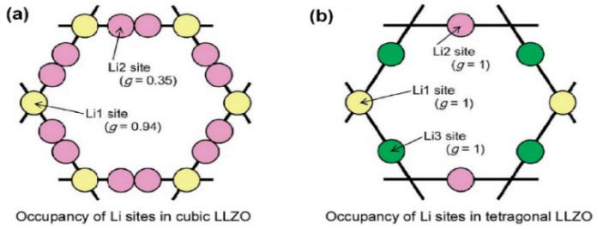

Figure 1.8 Crystal Structure of Li sites and occupancy in (a) Cubic and (b) tetragonal LLZO. *Reproduced from [29].*

Despite these important advantages, garnets electrolytes often face challenges including high-temperature processing, grain-boundary impedance, and surface degradation in contact with atmospheric CO_2/H_2O leading to Li_2CO_3 formation[29,61,62].

1.4.1.1.3 LISICON-type Electrolytes

Structural features of Lithium superionic conductors (LISICONs) very similar to γ-Li_3PO_4. Substitution at the P sites (e.g., P^{5+} to Si^{4+}) can modify and expand the lattice and as a result, improves conductivity[63,64]. However, oxide LISICONs typically delivered low

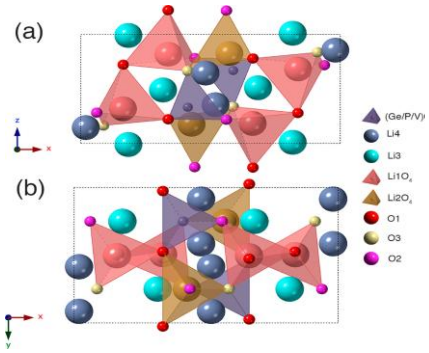

Figure 1.9 *LISICON type Structure along two directions. Reproduced with permission from [68].*

conductivities ~10^{-7} S cm^{-1} at room temperature. If oxygen replace sulfur can generates thio-LISICONs with excellent ionic conductivity. Notably, $Li_{10}GeP_2S_{12}$ (LGPS) shows room-temperature conductivity of ~10^{-3} S.cm^{-1}. Mainly due to enlarged ion channels and weaker Li-framework interactions. Alternative compositions such as Li_4GeS_4, Li_3PS_4, and doped analogues have also been explored[63–67]. Different views of the crystal structure of $Li_{3.53}(Ge_{0.75}P_{0.25})_{0.7}$ $V_{0.3}O_4$ from Rietveld refinement of neutron diffraction data are shown in ***Figure 1.9 (a)***View along the y-axis and ***(b)*** view along the z-axis show a close-packed arrangement of oxide atoms[68].

1.4.1.1.4 Perovskite-type Electrolytes.

Perovskite oxides or ABO_3 type structure such as $Li_{3x}La_{2/3-x}TiO_3$ (LLTO) have gain much attention due to the bulk conductivities reach to 10^{-3} S cm^{-1}[69,70]. However, the conduction mechanism is highly sensitive to Li content, vacancy concentration, and lattice bottleneck size. For example, $Li_{0.34}La_{0.56}TiO_3$ shows the highest reported conductivity among various perovskite-type SSEs. However, LLTO suffers from high grain boundary resistance and poor compatibility with Li metal due to the Ti^{4+} reduction to Ti^{3+}. It leads to electronic conduction and poor cycling[69–75].

1.4.1.1.5 Anti-Perovskites and LiPON.

Anti-perovskites material i.e. Li_3OCl first reported in 2012[76]. These 3D-structured electrolytes mainly combine with the reasonable amount of conductivity with the stability against lithium metal. However, their strong sensitivity to moisture and synthesis difficulties under ambient conditions limit large-scale use[76–80]. Lithium phosphorus oxynitride (LiPON), with general formula LixPOyNz, has lower conductivity (~10^{-5} S cm^{-1})[77]. But the stability with the Li metal is exceptional nature (up to 5.5 V). It can be fabricated as thin film via sputtering[81]. As a result, LiPON is widely used as a protective interfacial layer in real solid-state cells with other electrolyte[82]. In ***Figure 1.10***, typical crystal structure of perovskite and anti-perovskite solid electrolyte are shown.

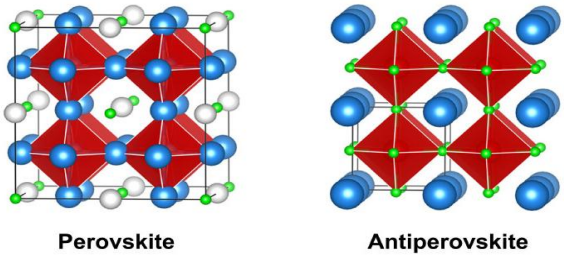

Figure 1.10 *Typical Perovskite and Anti-perovskite structure (with Li atom in green sphere. Reproduced with permission from [180].*

In summary, among the various type of oxide solid electrolytes, NASICONs and garnets showing higher conductivities of ~10^{-3} -10^{-4} S cm^{-1} and wide electrochemical windows. However, limitations such as interfacial instability at metal/electrolyte interface, moisture

sensitivity, high grain boundary resistance and high temperature processing requirements are quite challenging. The hybrid and composite approaches are increasingly explored to compensate such challenges. We will discuss about their advantages in the later section.

1.4.1.2 Sulfide Electrolytes

Recently, Sulfide-based solid electrolytes have attracted much attention due to their excellent ionic conductivity with relatively low temperature processing. This processing often facilitates the densification and intimate particle contact. A key route involves the preparation of the glass ceramic electrolytes is typically obtained by the low-temperature heat treatment of amorphous precursors after mechanical milling. In sulfide group composition generally strongly influence the overall ion transport behaviour. One of the most researched compounds $Li_7P_3S_{11}$ was derived from the Li_2S-P_2S_5 system and can deliver room-temperature ion conductivities on the order of 4.2×10^{-3} S.cm^{-1}. It combines a three-dimensional framework with one-dimensional diffusion channels along the their c-axis, which mainly promotes its transport characteristics[83–85].Crystal structure of Li6PS5I with I^- in an fcc lattice, PS_4 in octahedral voids, and S^{2-} on 4d sites; Li^+ occupies 24g and 48h positions. (b) Li^+ transport is governed by the intercage 48h–48h jump through windows formed by 4a iodine and PS_4 sulfur atoms.

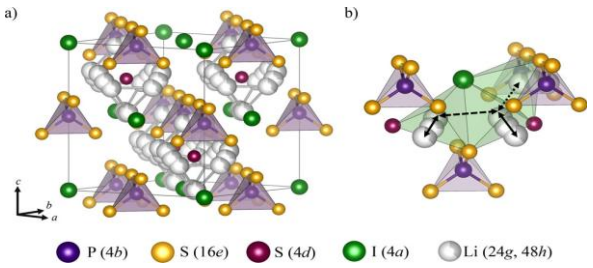

Figure 1.11 *Li_6PS_5I crystal structure with Li transportation sites. Reproduced with permission from [83].*

In comparison, the crystalline sulfides such as $Li_{10}GeP_2S_{12}$ (LGPS) also deliver very high conductivity. Using ab initio simulations, Ceder and co-workers showed that the Li transport in LGPS is strongly anisotropic and occurs preferentially along the one-dimensional c-axis channels. They also further clarified the mechanism, showing that conduction is not limited to isolated ion hopping, but involves concerted multi-ion migration with low activation barriers, enabling superionic behavior[86]. Complementary solid-state NMR studies by Feng et al. revealed distinct activation energies for transport: ~0.16 eV along the 1D channels and ~0.26 eV for in-plane two-dimensional pathways, together forming a highly efficient diffusion network[87].

Earlier generations of glassy sulfides such as $Li_2S.P_2S_5$, $Li_2S.SiS_2.Li_xMO_\gamma$, $Li_2S.GeS_2$, and $Li_2S.SiS_2$.LiI had already demonstrated room-temperature conductivities in the 10^{-4}-10^{-3} S cm^{-1}

range. These sulfides showed high ionic conductivity and softer than oxides, as a result they improves the electrode-electrolyte contact and reduces interfacial resistance in all-solid-state lithium batteries (ASSLBs)[88–92].

From a device perspective, sulfide SSEs have shown promising performance in real cell application. Several group integrated 80Li2S.20P2S5 glass-ceramic with various commercial cathodes to construct ASSLBs that achieved stable long-term cycling[93–95]. More recently, Kanno's group fabricated LGPS-based cells that delivered discharge capacities exceeding 120 mAh g^{-1} with high Coulombic efficiency[96].

However, despite so much potential, sulfide electrolytes face significant challenges too. Their chemical instability in air remains a major barrier. It react with moisture and leads to decomposition and the release of toxic H_2S gas which is very poisonous for safety and processing challenges. In addition, their limited electrochemical stability at high voltages and compatibility issues with oxide cathodes complicate practical integration.Overall, sulfides stand out as the most conductive family of solid electrolytes, surpassing oxides in ionic transport by orders of magnitude. However, their environmental sensitivity and chemical reactivity demand careful encapsulation strategies, protective coatings, or engineered hybrid systems before they can be considered viable for scalable commercial solid-state batteries.

1.4.1.3 Halide Solid Electrolytes

Halide solid electrolytes have recently emerged as promising candidates for solid-state batteries due to their unique combination of high ionic conductivity, electrochemical stability against high-voltage cathodes, and mechanical deformability. Their general chemical formula can be expressed as Li_a-M-X (X = Cl, Br, F; M = metal cation), which is conceptually derived from the introduction of high-valence transition metal cations into lithium halides (LiX). Among the halide family, chloride-based electrolytes have gained the most attention because they offer better deformability, excellent room-temperature ionic conductivity, and stability over wide voltage ranges compared to bromides, while fluorides generally exhibit poor conductivities[97–101]. Typical crystal structure of Li_3ScCl_6 is shown in ***Figure 1.12***.

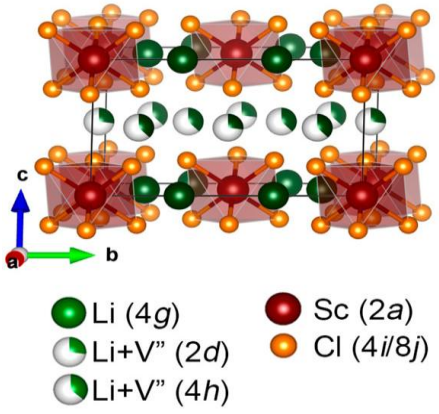

Figure 1.12 *Typical crystal structure of Li_3ScCl_6. Reproduced with permission from [101]*

The favorable transport behavior of halides mainly originates from their relatively large ionic radii. These radii which are comparable to sulfide anions and substantially larger than oxides. This weaker Coulombic interaction within halide frameworks enables lithium ions to remain in a highly mobile state within many crystal structures, supporting fast-ion conduction. However, their tendency to undergoes into phase transitions at different temperatures can influence the ionic conductivity. In addition, the halides are highly sensitive to moisture and easily hydrolyze to form corrosive by-products, which complicates handling and increases synthesis costs[102–104].

Overall, halide electrolytes combine the high ionic transport of sulfides with improved electrochemical stability against high-voltage cathodes, making them strong candidates for all-solid-state battery cathode interfaces. However, their air/moisture sensitivity and possible reactivity with lithium metal anodes remain substantial obstacles. Progress in dopant engineering, synthesis optimization, and encapsulation strategies will therefore be central to their practical deployment[102–105].

1.4.2 Organic/Polymer Electrolytes and Their Ion Transport

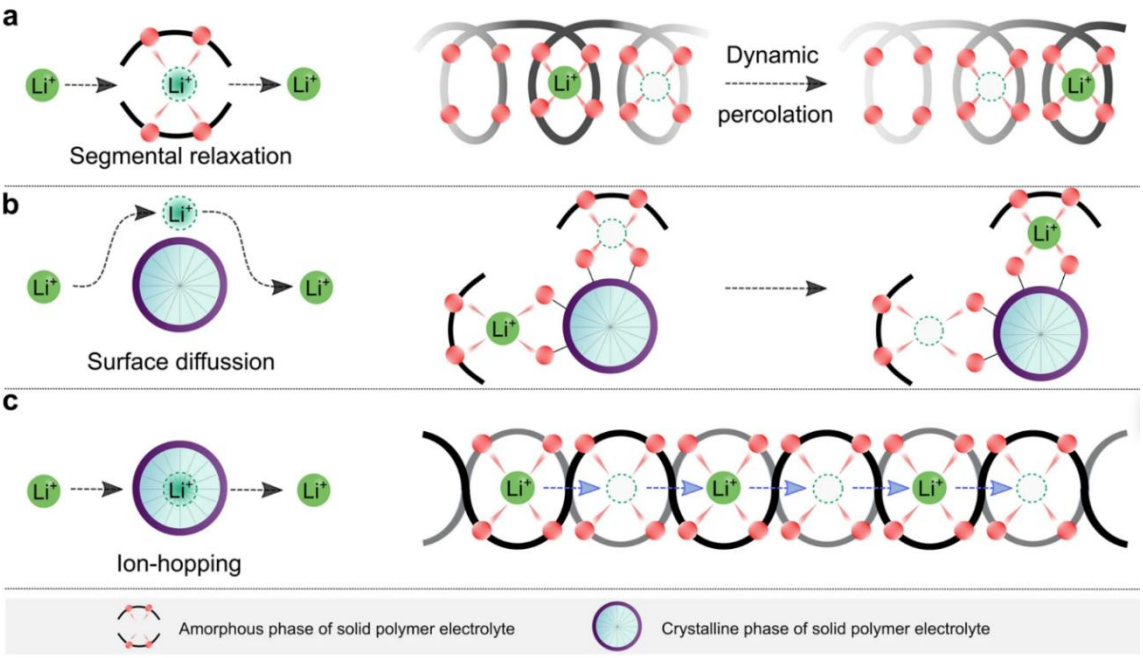

Figure 1.13 *Schematic illustration of lithium-ion transport mechanisms in solid polymer electrolytes: (a) Segmental relaxation- Li^+ moves with the motion of polymer chains, creating dynamic percolation pathways. (b) Surface diffusion -Li^+ migrates along the surface of crystalline domains aided by local polymer interactions. (c) Ion hopping - Li^+ jumps between*

coordination sites through the amorphous polymer matrix, forming continuous conduction pathways. Reproduced from [106]

Solid polymer electrolytes (SPEs) have considered attractive candidates for solid-state batteries from a long time due to their combining electrochemical functionality with mechanical flexibility. The concept was first introduced when Wright demonstrated ion conduction in poly(ethylene oxide) (PEO) alkali complexes in 1973[107]. After that, Armand subsequently highlighted their application in lithium batteries later[108]. After that, extensive research has been conducted on both the fundamentals of ion transport in polymers and the engineering of practical polymer-based solid electrolytes.

The transport mechanism of lithium ions in SPEs fundamentally differs from that in conventional liquid electrolytes as shown in ***Figure 1.13***. In liquids, the ion conduction is dominated by solvated species moving within the solvent medium. In contrast, in polymers the migration of Li^+ ions is strongly coupled with the local motion of polymer chain segments. Functional groups such as ether (-O-), nitrile (-CN), or amide (-NH-) groups act as coordination sites for Li^+. Thus, this way the ion transport occurs via successive coordination/decoordination events as the polymer segments undergo conformational rearrangements[106,108–110].

SPEs are usually classified into three main categories based on their composition and conduction mechanism. I. *Salt-in-polymer electrolytes*: It contain a polymer host (e.g., PEO, PAN, PMMA, PVDF) with a relatively small fraction of lithium salt (typically < 50 wt.%). Although they were mechanically robust and shows low room-temperature ionic conductivity (10^{-6}-10^{-7} S cm^{-1}) due to crystallinity and limited segmental mobility. II. *Polymer-in-salt electrolytes*: They generally embedding a polymer binder within a lithium salt-rich matrix (> 50 wt.%). This composition increases the population of charge carriers and often enhances ionic conductivity, though at the expense of mechanical flexibility. III. *Single-ion conducting polymers*: They immobilize the anion on the polymer backbone, leaving Li^+ as the sole mobile species. This approach increases the lithium-ion transference number (t_{Li^+}~1), thereby suppressing concentration polarization and improving interfacial stability. Ion transport in SPEs is also strongly dependent on the degree of crystallinity in the polymer matrix. Lithium conduction predominantly occurs in the amorphous domains, where chain-segment mobility above the glass-transition temperature (Tg) facilitates local site-to-site hopping. By contrast, crystalline domains restrict ion motion, though some studies suggest limited Li^+ migration can occur through interstitial channels. Most reports agree that reducing crystallinity and lowering

Tg are essential strategies for enhancing ionic conductivity[107–114].From a practical overview, SPEs provide several advantages over liquid electrolytes. In general, they are lightweight, nonflammable, mechanically flexible, and capable of ensuring uniform lithium deposition during cycling. However, their key limitation remains low ionic conductivity at ambient temperature. Typically, room-temperature conductivities remain two to three orders of magnitude below the benchmark of ~10^{-3} S cm^{-1} required for solid-state battery commercialization. To address this bottleneck, a variety of material-engineering strategies have been done, such as Polymer blending and copolymerization, Crosslinking and grafting, use of plasticizers and ionic liquids and Hybridization with inorganic fillers or ceramic particles[115–119].

In summary, polymer electrolytes offer intrinsic advantages of flexibility, processability, and stable electrode contact, which are particularly relevant for mitigating interfacial issues in solid-state batteries. however, their low ionic conductivity at room temperature remains the major roadblock.

1.4.3 Composite/ Hybrid Electrolytes

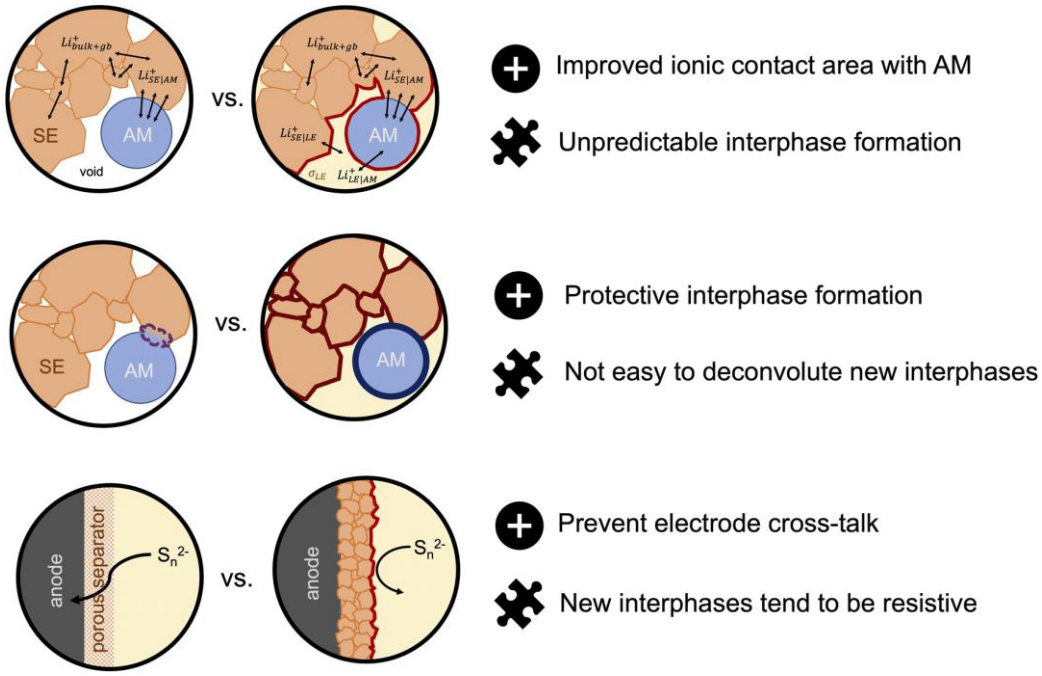

Figure 1.14 *Advantages and disadvantages of a Hybrid electrolyte in metal batteries. Reproduced from [120].*

The concept of hybrid electrolytes has recently emerged as a promising pathway to tackle the intrinsic limitations of both inorganic solid electrolytes and polymer/liquid counterparts in

solid-state lithium batteries. It generally combines the advantages of both these electrolytes. Rigid oxide ceramics such as garnet-type $Li_7La_3Zr_2O_{12}$ (LLZO) offer high Li^+ conductivity and chemical stability but suffer from poor interfacial contact with electrodes and susceptibility to Li dendrite penetration at high current densities. On the other hand, polymer electrolytes and liquid phases exhibit superior electrode wettability and flexibility, but their relatively low mechanical strength and reduced transference numbers limit their application in long-life, high-voltage cells. Hybrid electrolyte systems comprising solid/solid, solid/polymer, or solid/liquid combinations are therefore being developed to combine the favourable advantages of each class while mitigating their shortcomings[121–123].

A common strategy is the integration of fast-ion conducting ceramics into polymer matrices to form composite hybrid electrolytes. This approach combines the advantages of the high room-temperature conductivity of garnet ceramics while enhancing the interfacial compliance through polymer incorporation. For example, Al, Ta, and Nb-doped LLZO ceramics combined with polyethene oxide (PEO) or PVDF-HFP matrices display conductivities in the range of 10^{-4}-10^{-3} S cm^{-1} at ambient conditions. These ceramic-polymer hybrids simultaneously provide mechanical rigidity for dendrite suppression and sufficient flexibility to maintain intimate electrode-electrolyte interfaces, demonstrating long-term cycling stability in Li-metal cells[121,122,124].Beyond polymers, ionic liquids (ILs) have also been incorporated into garnet scaffolds to create inorganic-organic hybrid electrolytes. These systems utilise the dual function of ILs, which is acting as plasticisers to reduce interfacial resistance while also providing additional ion transport pathways. However, challenges remain regarding IL volatility under extended cycling and the potential formation of resistive interphases at LLZO/IL interfaces[120]. ***Figure 1.14*** describes the advantages and disadvantages of a hybrid electrolyte. A more direct hybridisation is achieved by the infiltration of liquid electrolytes into ceramic frameworks, resulting in quasi-solid systems, which will be discussed in a later section. Such solid-liquid hybrid electrolytes bridge the gap between conventional liquid electrolytes and rigid solid-state platforms. Recent reports suggest that the liquid infiltration enhances the ionic connectivity and electrode wetting. It also introduces a new interphase known as the solid-liquid electrolyte interphase (SLEI), which can become resistive and detrimental to long-term stability. In LLZO/$LiPF_6$-based hybrids, decomposition reactions lead to Li_2CO_3, LiF, and La/Zr-fluorides within the SLEI, which further contributed to interfacial impedance growt[125,126]h. Interestingly, the choice of lithium salt and solvent strongly dictates interphase chemistry. Thus, it is very important to balance and choose the solid electrolyte and liquid

electrolyte system very carefully. For example, LiBOB-based systems promote significant Li depletion and high resistances, LiTFSI-based hybrids form comparatively stable SLEIs with minimal compositional change to LLZO. Moreover, solvent coordination strength plays a decisive role. Such as glyme-based solvents that generally fully coordinate with Li^+ can prevent the nucleophilic attack on thiophosphate or garnet structures. As a result, the stability increases. These insights highlight that hybrid solid-liquid electrolytes need very careful selection of each component[127–131].

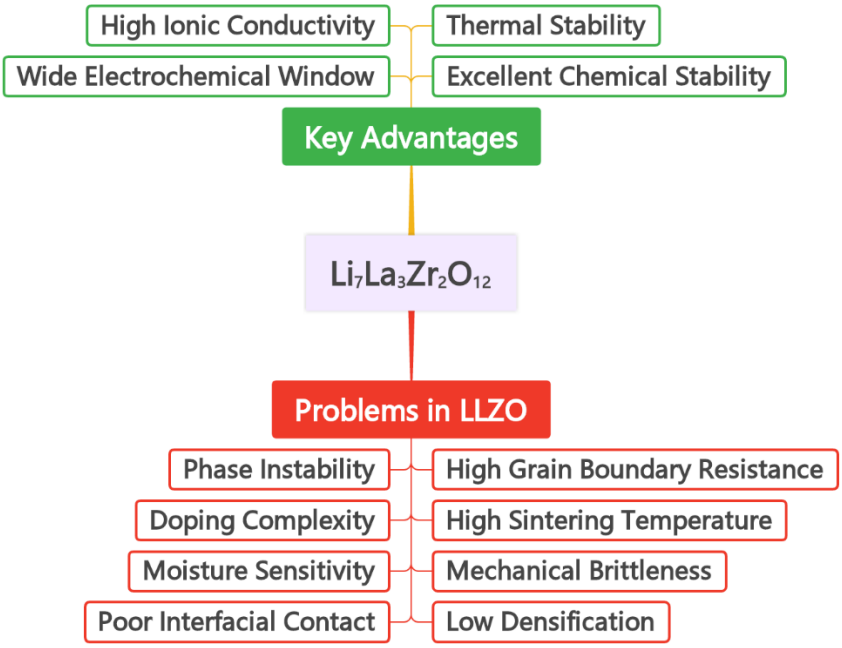

Figure 1.15 *Advantage and Disadvanges of Garnet based electrolyte.*

Hybrid electrolytes thus represent a versatile design platform which can combine the advantages of ceramic stability, polymer/IL flexibility, and liquid-phase connectivity. However, the success of such systems is hindered by the controlling interfacial reaction, dopant chemistry, or passivation layers. Thus, systematic studies with electrochemical evaluation in symmetric and full cells will be essential to unravel the interphase formation mechanisms. Hybrid and quasi-solid system thus opens a new design to combine the stability of ceramic scaffolds with the flexibility and ionic connectivity of polymeric, liquid, or ionic-liquid phases. However, their ultimate effectiveness still depends on how well they address the intrinsic bottlenecks of garnet electrolytes themselves. This thesis therefore explores targeted approaches such as solvated ionic liquid infusion, surface fluorination, and microstructural and sintering engineering to mitigate the interfacial resistance, dendrite penetration, and phase instability. With this context, the next section we will discusses the opportunities and challenges

in garnet solid electrolytes highlights both the unique advantages and the critical hurdles that shape their practical application in solid-state lithium batteries.

1.5 Opportunity and Challenges in Garnet Electrolytes

Garnet-type $Li_7La_3Zr_2O_{12}$ (LLZO) and its doped derivatives present several attractive features for solid-state lithium batteries as discussed in the earlier section and shown in the ***Figure 1.15***. In summary, their high room-temperature Li^+ conductivity (10^{-4}-10^{-3} $S.cm^{-1}$), wide electrochemical stability window, and chemical robustness against lithium metal make them one of the most promising inorganic solid electrolytes[56,57,59,121,132–135]. The ceramic's mechanical rigidity also provides a physical barrier against lithium dendrite growth which offered an inherent safety advantage over polymer- and liquid-based systems.

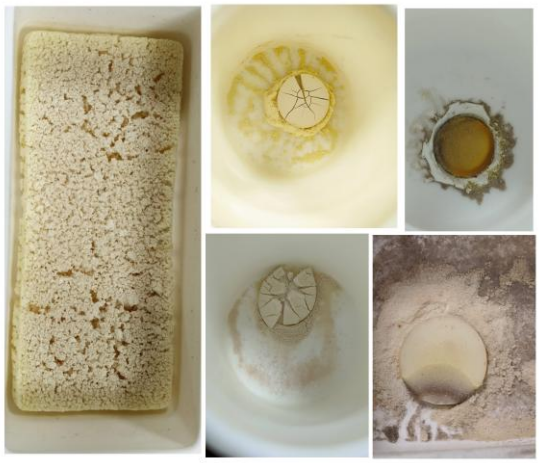

Figure 1.16 *Representative images of unsuccessful garnet calcination/sintering attempts.*

However, in this section we will explore the critical gap and challenges that hindered the successful application towards commercialization. In practice, however, garnet electrolytes possess various challenges as described in ***Figure 1.15***. These problems include phase and surface instability, large grain-boundary resistance, poor metal/electrolyte contact and complex cathode/electrolyte chemistry. ***Figure 1.16*** present such images of unsuccessful garnet calcination and sintering attempts which highlight the challenges. These problems strongly enhanced the impedance and reduced overall conductivity. The following subsections discuss these failure modes critically, and summarise the principal strategies and remaining gaps reported in recent literature.

1.5.1 Phase Instability

Garnet oxides show two phases as shown in ***Figure 1.17***, a high-symmetry cubic phase with high Li^+ mobility and a lower-conductivity tetragonal phase[56]. Thus, although doping and process optimisation have produced compositions with the desirable cubic phase as shown in ***Figure 1.18***, stability remains conditional, and reproducibility is challenging; thus, more in-depth studies are required for large-scale production.

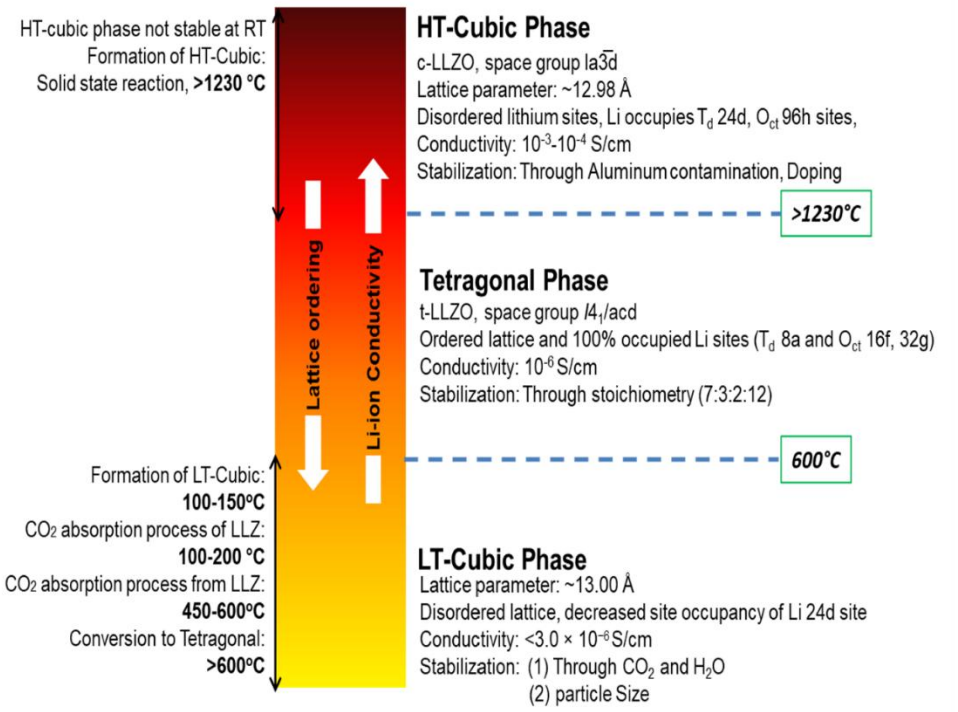

Figure 1.17 *Schematic representation of the phase evolution of garnet-type $Li_7La_3Zr_2O_{12}$ (LLZO) as a function of temperature, showing the transition between low-temperature cubic, tetragonal, and high-temperature cubic phases with corresponding lithium-ion conductivity.*

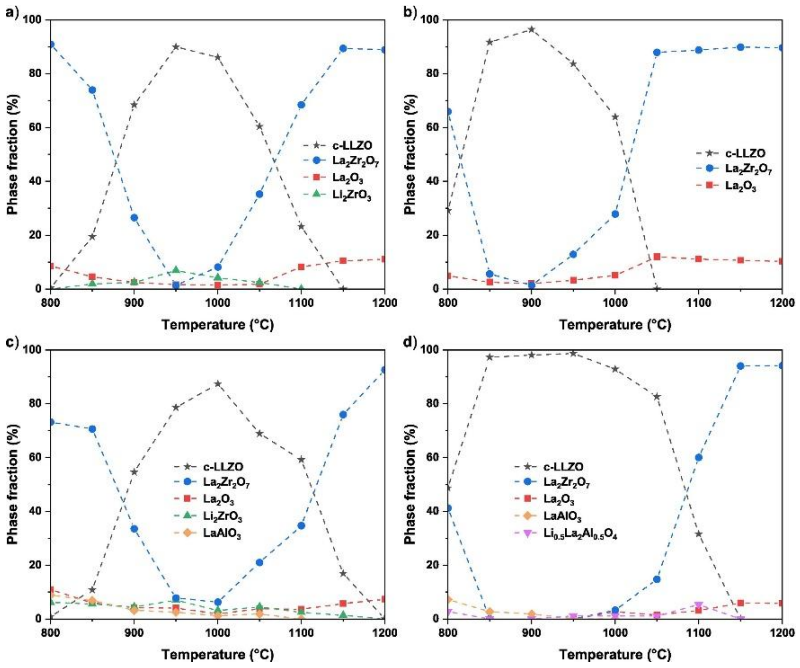

Figure 1.18 *Phase evolutions of LLZO pristine material using (a) solid state synthesis and (b) sol-gel synthesis, Al-doped LLZO using (c) solid state and (d) sol-gel synthesis methods with sintering temperature. Reproduced from [136]*

1.5.2 Large Grain-Boundary Resistance

In any polycrystalline solid electrolyte material, the total ionic resistance is majorly dominated by grain boundaries (GBs). Various resistance originating by using solid inorganic electrolyte are shown in ***Figure 1.19***. Quantitatively, GB resistance has been reported to contribute on the order of 40–50% of the total impedance in typical polycrystalline LLZO pellets[56,121]. Achieving high relative density and low-resistance GBs is therefore essential to realise the bulk conductivity in practical samples. The microstructural origins of GB resistance are can be originated from various reason such as, incomplete densification leaving pores, secondary phases at grain boundaries, and segregation of dopants or carbonate/hydroxide impurities to GB regions. These raises local activation barriers for Li^+ hopping.

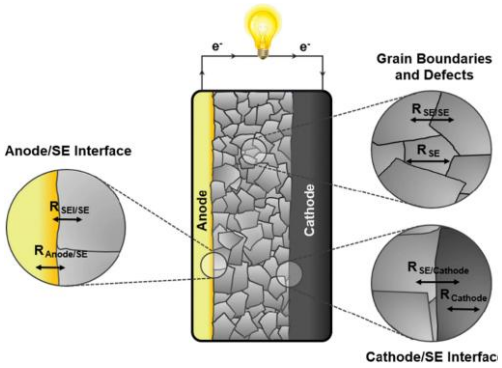

Figure 1.19 *Various interfaces present in a solid-state battery. Reproduced from [181].*

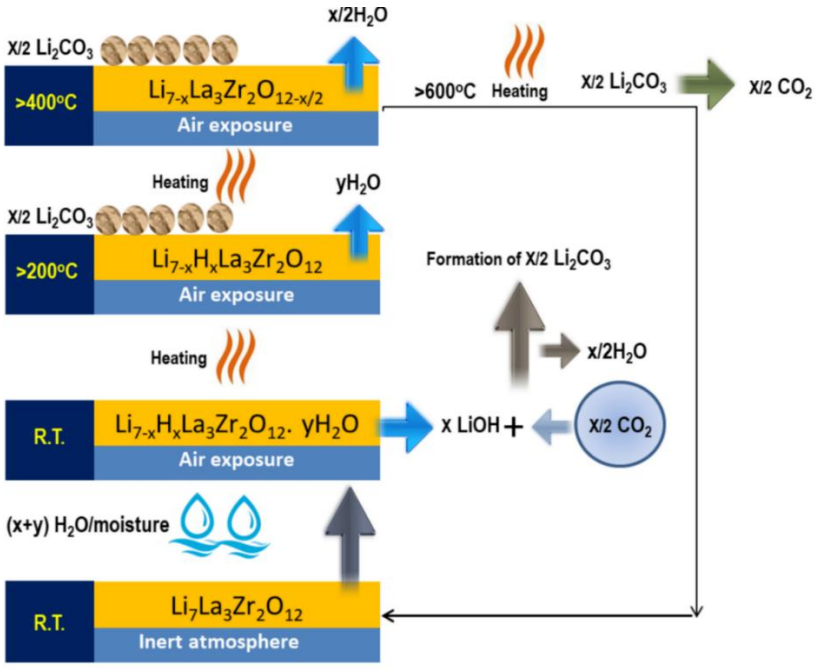

Figure 1.20 *Schematic illustration of LLZO surface degradation upon air/moisture exposure.*

Different strategies can be implemented to reduced the GB resistance, such as via advanced sintering process i.e. hot-pressing, field-assisted or spark plasma sintering, or by using sintering aids and controlled co-doping strategies. As these methods can produce very low GB

resistances in some times, but they generally comes with some challenges such as they promote undesirable phase formation at the grain boundaries or interdiffusion within the cathode during co-sintering[137–140]. Thus, the grain-boundary engineering is both necessary and technically demanding for any route that aims to convert garnet powders into practical membranes.

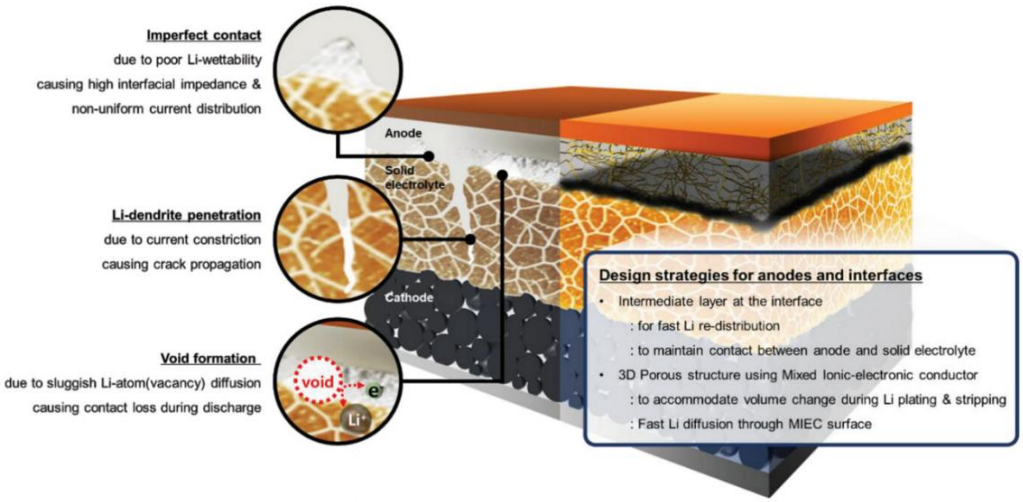

Figure 1.21 *Issues and strategies related to the anodes and Li metal–solid electrolyte interfaces. Reproduced from [141]*

1.5.3 Electrolyte / Metal Interface Instability

The interface between metallic lithium and garnet electrolytes controls the practical cell impedance and the system's ability to plate/strip Li uniformly. Surface contamination acquired during air exposure (notably LiOH and Li_2CO_3) severely degrades wettability, contact angles with molten Li[142–145]. This surface reaction is uncontrollable as shown in ***Figure 1.20*** and sevely damage the true cell performance. The impact of these surface impurities is described in ***Figure 1.21***. First-principles and experimental studies also indicate that certain surface impurities and dopant chemistries are more prone to reduction or Li insertion, which can generate mixed-conducting interphases and propagate reduced zones into the bulk. Several Mitigation strategies are already applied at the metal/electrolyte interface that include (i) surface cleaning and controlled thermal treatments to remove carbonates and hydroxides, (ii) thin artificial interlayers or lithiophilic coatings (LiF, Li_3PO_4, $LiNbO_3$, or polymeric lithiophiles) to improve wetting and block deleterious reactions, (iii) applying moderate stack pressure to maintain contact and suppress voids, and (iv) designing mixed ionic-electronic interlayers that homogenise current[56,146,147]. Each approach reduces particular failure modes in

laboratory cells, but scalability is a major issue. Thus, further effort should be made to reduced the interfacial resistance at the metal/electrolyte boundaries.

1.5.4 Cathode / Electrolyte Interface

Making a cell with LLZO and oxide cathodes presents a separate set of chemical-mechanical challenges. Practical cathodes are composite in type whose fabrication frequently requires elevated temperatures or sintering to ensure electronic percolation and intimate contact with the electrolyte. High-temperature processing generally trigger the elemental interdiffusion and the formation of various secondary phases (e.g., $La_2Zr_2O_7$, $LaCoO_3$ or nickel- and cobalt-containing reaction products) at LLZO-cathode interfaces. Such reaction layers increase the charge-transfer resistance, and may also alter local lithium chemical potential and trigger deleterious space-charge layers[56,148].

Practical solution include low-temperature composite fabrication (introducing limited amounts of ionic liquids or room-temperature wetting agents), protective cathode coatings (Li_3PO_4, $LiNbO_3$, tailored halide coatings), and engineered cathode-electrolyte composites that avoid vigorous co-sintering. While these measures can reduce immediate chemical reactivity and impedance but they often lack long-term mechanical and electrochemical stability under repeated cycle[149–152]. Thus, for successful long-term operation we have engineered the cathode/electrolyte interface and enhanced the stability.

In summary, garnet electrolytes bring an attractive combination of ionic conductivity, mechanical stiffness and excellent electrochemical window. But their successful deployment depends on solving designing the material and processing very carefully. Stabilising the desired cubic phase with reproducibility and minimising the grain-boundary resistance with engineered microstructures, and forming chemically inert and lithiophilic Li interfaces can be challenging but fruitful effort for the successful development of garnet electrolyte in practical metal batteries. The literature reports numerous promising laboratory-scale remedies, co-doping, rapid densification, surface chemistry control, interlayers and composite cathode design. Yet, most of the times the path from small-area demonstrations to robust, low-cost manufacturing remains incomplete. Thus, the current effort should be made to correlate in phase stability, interfacial surface chemistry, densification and processing with real cell application.

1.6 Cell Architectures in Solid-State Batteries

The translation of solid-state electrolyte research into functional devices requires very careful consideration of the overall cell architecture. In this direction, the materials development and configuration or architecture is critical. It generally dictate the overall the electrochemical performance and practical scalability of solid-state batteries (SSBs). The design such robust configuration is equally important with making ideal solid electrolyte. In broader aspect, three major architectural strategies have emerged, all-solid-state batteries, which rely exclusively on the solid electrolytes, quasi- or semi-solid-state batteries, where a small liquid or gel fraction is used to stabilize the interfacial or mechanical issues, and anode-free or beyond-lithium systems, which represent the frontier of electrochemical storage by pushing energy density and sustainability boundaries[141,153–155].

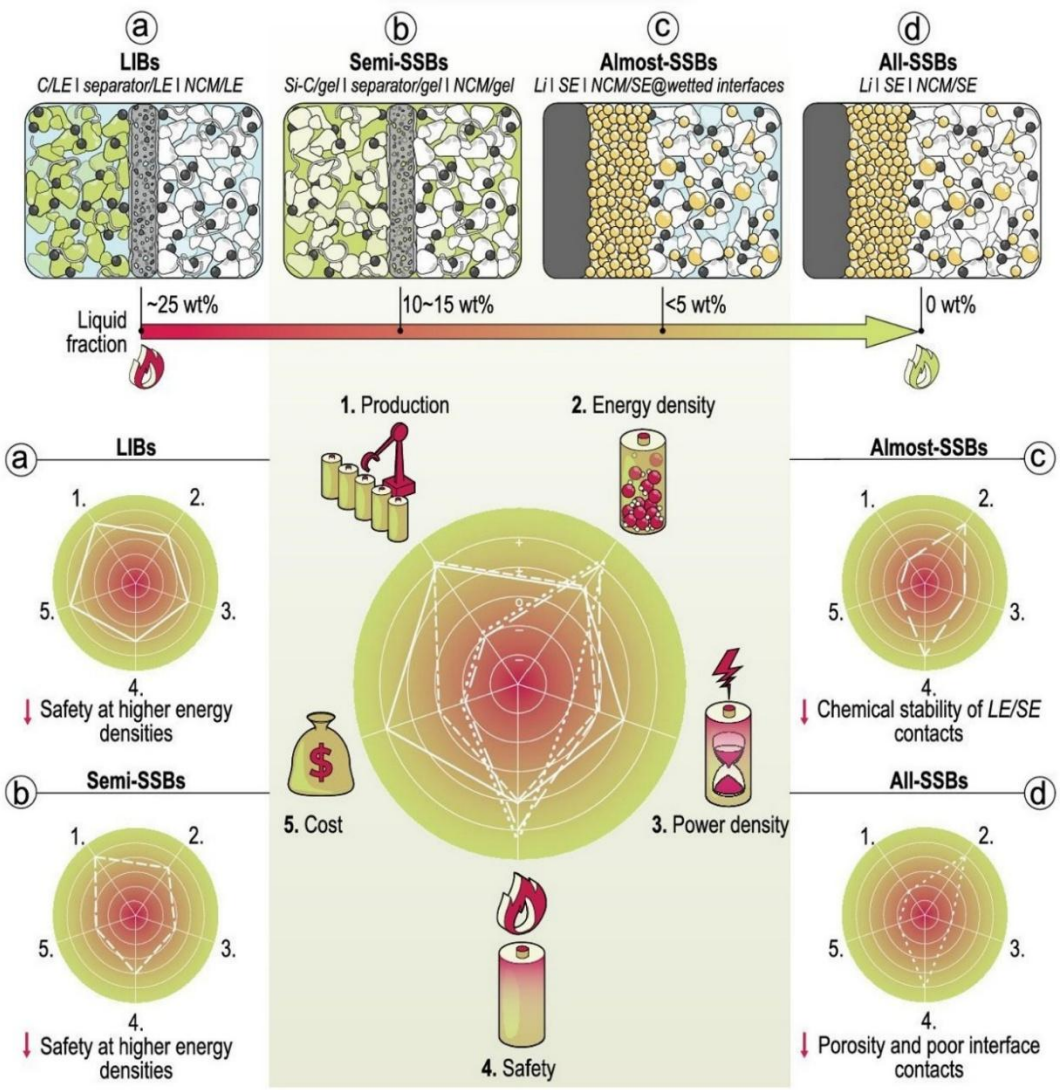

Figure 1.22 *Schematic comparison of LIBs, semi-SSBs, almost-SSBs, and all-SSBs showing liquid fraction, configuration, and key performance. Reproduced from [153]*

1.6.1 All-Solid-State Batteries (Polymer-based, Inorganic-based)

All-solid-state batteries (ASSBs) represent the "idealized" architecture where both electrodes are mostly considered with a purely solid electrolyte, without the use of any flammable liquid phase. Depending on the electrolyte, these systems can be polymer-based or inorganic-based. Polymer-based SSBs mostly used polyethylene oxide (PEO) or related polymers which enable intimate electrode-electrolyte contact and mechanical flexibility as we discussed earlier but their room-temperature ionic conductivity remains insufficient, restricting operation to elevated temperatures. In contrast, inorganic electrolytes particularly sulfides, oxides, and halides offer conductivities approaching or exceeding those of liquid electrolytes (10^{-3}-10^{-2} S cm^{-1})[156–159]. However, their rigidity complicates processing, and poor physical contact with electrodes often results in large interfacial resistance.

To address these challenges, interlayers have emerged as a critical architectural element in ASSBs. Functional interlayers, such as Li-philic metals (e.g., Ag, Au), lithiated alloys (Li–Al, Li–Mg), or chemically stable thin films ($LiNbO_3$, Li_3PO_4, LiF) are introduced at the electrolyte/electrode interfaces to homogenize current distribution, suppress dendrite initiation, and reduce interfacial impedance[146,147,160–162]. Thus, the interlayers are no longer optioal but are becoming the central to the practical design of ASSBs, bridging the gap between high-performance materials and manufacturable architectures.

1.6.2 Quasi-/Semi-Solid-State Batteries

Despite significant progress in ASSBs, purely solid-solid interfaces remain difficult to stabilize at scale. Quasi- or semi-solid-state batteries (QSSBs/SSSBs) have therefore emerged as potential alternatives, incorporating a small fraction of liquid or gel electrolyte to combine the advantages of solid-state safety with improved interfacial wetting and lower impedance. These systems are highly diverse. Polymer-inorganic composite systems, where ceramic fillers are dispersed in a polymer host, strike a balance between mechanical robustness and ion transport, creating continuous percolation pathways for Li^+ conduction. Another important category is quasi-solid-state hybrids, where a solid electrolyte scaffold (e.g., garnet or sulfide) is infiltrated with small quantities of ionic liquid that ensure the intimate contact without sacrificing too much thermal stability[126,163,164].

The performance of QSSBs is strongly dependent on the liquid fraction. Too little liquid fails to resolve interfacial voids and too much compromises safety and stability. Recent advances in in-situ polymerization techniques, where liquid monomers are polymerized inside the electrode

pores, have further improved the interfacial contact and mechanical adhesion. Critically, quasi-solid-state batteries can mitigate some of the bottlenecks in ASSBs, such as dendritic penetration and brittle fracture, by introducing compliant liquid-like domains. For this reason, QSSBs are often viewed as an intermediate as shown in ***Figure 1.22***, but commercially attractive step toward fully solid-state cells, and they are particularly relevant to near-term large-format EV applications in regions with high ambient temperatures, such as India. Thus, a systematic effort should be necessary to establish the correlation an understanding the benefits and limitation of liquid used with the solid counterpart.

1.6.3 Anode-Free and Beyond-Lithium Chemistries

A particularly promising but challenging direction is the anode-free SSB architecture where the cell is assembled without a pre-deposited lithium metal. Instead, lithium is reversibly plated onto a current collector (commonly Cu or stainless steel) during the initial charging process. This design offers a significant increase in energy density by eliminating excess lithium and reducing cell weight, while also simplifying manufacturing. However, it promotes the interfacial instability. As the repeated nucleation and dissolution of lithium can lead to void formation, uneven plating, and eventual short-circuiting. The Solid electrolytes with high critical current densities and carefully engineered nucleation interlayers are essential to enable stable cycling in such systems[165–167].

Beyond lithium, the same architectural principles are being extended to sodium, potassium, magnesium, and calcium solid-state batteries. Sodium and potassium offer the advantage of the elemental abundance and lower cost. Whereas, Mg^{2+} and Ca^{2+} chemistries promise higher volumetric capacity and reduced dendrite tendencies due to multivalent ion transport[168–170]. However, the sluggish ion diffusion and limited compatible electrolytes remain critical barriers for multivalent systems. Anode-free sodium and potassium SSBs are currently under intensive investigation[168]. Thus, while these chemistries remain at an earlier stage compared to lithium, they broaden the technological horizon and align with global electrification for resource diversification and sustainable scaling of electrochemical storage.

1.6.4 Critical Challenges

In summary, cell architectures represent the translational dimension of solid-state battery research, transforming materials into practical systems. All-solid-state batteries promise the highest safety and energy density but require carefully engineered interlayers to manage interfacial instabilities. **Figure 1.22**, represent a comparison of liquid, semi-solid, almost solid,

and all-solid-state batteries in terms of liquid fraction, cell configuration, and performance. Quasi- and semi-solid-state designs provide a transitional pathway, with small liquid fractions to overcome processing and contact challenges. These making them attractive for near-term commercialization. Anode-free and beyond-lithium architectures push the limits of energy density and sustainability but face great challenges in interfacial stability and multivalent ion transport. Together, these diverse architectures needs materials innovation and innovative engineering design. As illustrated in ***Figure 1.23***, liquid electrolytes allow facile ion transport but suffer from dendrite growth and continuous SEI formation, whereas solid-state electrolytes face interfacial instability, void formation, and sluggish ion transport due to grain boundary resistance. Thus, the successful transition will be critical in terms of material engineering and in developing robust electrode-electrolyte interfaces that ensure both high ionic conductivity and long-term electrochemical stability.

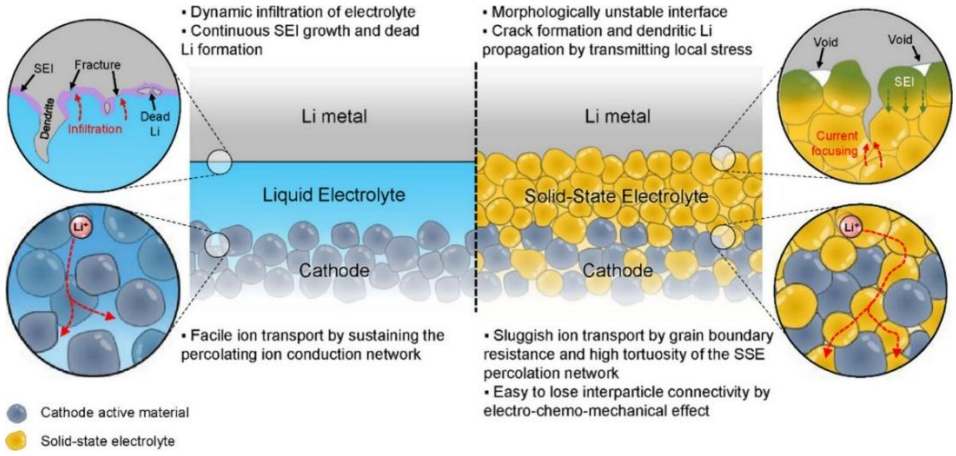

Figure 1.23 *Schematic comparison of liquid and solid-state electrolytes highlighting interfacial instability, dendrite formation, and ion transport limitations. Reproduced from [148]*

1.7 Synthesis Process of Garnet Solid Electrolytes

The stability of cubic LLZO is typically achieved at elevated temperatures (450-1000 K) but the sintering temperature can be reduced with less surface reaction at room temperature through aliovalent doping (Al^{3+}, Ta^{5+}, Ga^{3+}, Nb^{5+}) that creates Li vacancies, broadens bottleneck sizes, and enhances conductivity. Computational studies further confirm that octahedral 96h sites show higher Li occupancy than tetrahedral 24d sites, with the partial disorder at Li sites being critical for high ionic conductivity. Despite its advantages, cubic LLZO is sensitive to air/moisture, where surface reactions with H_2O/CO_2 form Li_2CO_3 and degrade performance.

There are several synthesis processes to prepared cubic LLZO. Few of them are discussed briefly.

1.7.1 Solid-State Reaction

The conventional solid-state route remains the most widely used method due to its simplicity, low cost, and scalability. It involves mixing stoichiometric precursors such as Li_2CO_3, La_2O_3/$La(OH)_3$, and ZrO_2 with dopant oxides (e.g., Al_2O_3, Ta_2O_5), followed by calcination (900-1000°C) and high-temperature sintering (1100-1250°C) . Murugan et al.[57] (2007) first reported cubic LLZO via this route, achieving conductivities on the order of 10^{-4} S cm^{-1}. However, there are several disadvantages such as Li loss at high temperature, impurity formation from crucibles (e.g., Al contamination from Al_2O_3), and the need for long processing timesLLgarnet[56,57,171].

1.7.2 Combustion & Wet-Chemistry Routes

To mitigate high-temperature issues, wet-chemical methods such as sol-gel, Pechini, and combustion synthesis have been developed. These approaches ensure better mixing at the molecular level, leading to uniform particle size and reduced calcination temperature. For instance, sol-gel-derived LLZO can crystallize at ~60 °C, and produced nano-sized powders with high reactivity. Combustion methods (glycine nitrate, citric acid assisted) produce highly porous powders with shorter synthesis times and facilitate subsequent densification. However, these methods may suffer from carbon contamination, difficulty in controlling stoichiometry and uncontrolled surface reaction[172–177].

1.7.3 Template-Assisted Methods

Template-assisted routes, including electrospinning and porous-template impregnation have been explored to design the LLZO with tailored morphologies. Electrospinning combined with calcination can produce LLZO nanowires (~100-200 nm diameter) that crystallize at relatively low temperatures (~700 °C) with reducing Li volatilization. Such 1D architectures improve sintering behavior and Li-ion transport but often require careful optimization of precursor viscosity, calcination conditions, and phase purity[178].

1.7.4 Green/Alternative Routes

Recently, environmentally sustainable and scalable synthesis strategies have gained attention. Solvent-free mechanochemical milling, nebulized spray pyrolysis, and aqueous wet-chemistry

enable LLZO synthesis with lower environmental impact. For example, aqueous precipitation followed by annealing has produced cubic LLZO with conductivities of ~10^{-4} S cm^{-1}. Similarly, co-doping strategies combined with lower-temperature synthesis (e.g., Ta, Ce dual-doping) have resulted in cubic LLZO showing $\sigma \sim 1 \times 10^{-3}$ S cm^{-1} and stable cycling against Li metal. Despite progress, scalability and moisture sensitivity remain major barriers[179].

In summary, LLZO can be synthesized by various synthesis methods. However, pristine LLZO without dopants still shows poor conductivity, and the role of various impurities on the electrical and electrochemical performances remains unresolved. Thus, optimization of synthesis and microstructure engineering are essential to realize the intrinsic potential of garnet electrolytes for solid-state batteries.

1.8 Research Hypothesis

This present research work hypothesized that that the electrochemical bottlenecks of garnet solid electrolytes are not inherent to their bulk composition alone. But are strongly governed by microstructural design, interfacial chemistry, and processing pathways. By systematically tailoring these aspects through coupled “solid” and “liquid” interventions, it should be possible to mitigate interfacial degradation, reduce grain boundary resistance, and enhance lithium-ion transport and thereby unlocking the true potential of garnet electrolytes for SSLMB applications.

Specifically, it is hypothesized that:

1. Phase stabilization of the cubic LLZO can be achieved through doping and synthesis optimization (e.g., Ta/Ga/Al substitution, controlled sintering), which can suppress tetragonal transformation and stabilize high-conductivity frameworks.
2. Microstructural engineering, particularly through template-assisted synthesis and incorporation of controlled porosity, can tune grain boundary connectivity and minimize interfacial resistance without sacrificing mechanical integrity.
3. Interface modification at the Li/LLZO boundary using fluorination, interlayers, or solvated ionic liquids (SILs) can improve wettability, suppress uncontrolled SEI growth, and homogenize lithium deposition, thereby mitigating dendrite penetration.

4. Composite integration of LLZO with polymeric or hybrid matrices can provide mechanical flexibility, accommodate volume changes, and reduce processing cost, thereby improving both performance and manufacturability.
5. Liquid therapy concepts, when combined with solid engineering, can synergistically bridge the gap between classical all-solid-state systems and quasi-solid-state approaches and enables more reliable cycling performance under practical conditions.

In this direction, this works generally diverse into multi-scale design strategy from atomic-level doping to mesoscale grain boundary engineering and macroscopic composite formation, which can collectively overcome the intrinsic challenges of garnet electrolytes. Such a strategy not only enhances the immediate performance of LLZO-based systems but also establishes design principles extendable to other solid electrolyte chemistries, such as NASICON, sulfides, and halides.

1.9 Objectives and Scope

The objective of this thesis is to establish a coherent roadmap for advancing garnet-based solid electrolytes from laboratory-scale synthesis to scalable, application-ready designs for solid-state lithium metal batteries. The scope of work is structured into the following research aims:

1. Scalable Synthesis: Develop cost-effective, reproducible synthesis strategies (aqueous combustion, bio-templating) to obtain phase-pure cubic LLZO with controlled microstructures.
2. Interface Engineering: Employ chemical (e.g., surface fluorination) and liquid-phase (solvated ionic liquid infusion) modifications to stabilize the Li/LLZO interface and suppress dendrite growth.
3. Microstructure Tuning: Engineer mesoscale architectures using bio-templates (water hyacinth, cellulose) to reduce grain boundary resistance and enhance ionic pathways.
4. Grain Boundary Engineering: Utilize sintering aids (NiO) and dopants to promote densification and introduce beneficial secondary phases.
5. Composite Integration: Incorporate LLZO fillers into polymeric, paper, and hybrid membranes to improve flexibility, mechanical strength, and manufacturability.
6. Exploratory Extensions: Extend the “liquid therapy” concept to NASICON-type electrolytes and probe unconventional lattice modifications (Al-S co-doping).

Collectively, these objectives aim to bridge the gap between fundamental material challenges and practical solid-state battery applications.

1.10 Reader's Guide to the Thesis

This thesis is structured to provide a progressive narrative, moving from fundamental motivation to experimental realization and future outlook:

- **Chapter 1** introduces the motivation, reviews Li-ion battery limitations, and presents the promise of solid-state electrolytes, with a focus on garnet LLZO.
- **Chapter 2** describes the methodological framework for synthesis, characterization, and electrochemical testing.
- **Chapters 3-4** address synthesis optimization and interfacial engineering, highlighting aqueous combustion routes, surface fluorination, and liquid infusion strategies.
- **Chapter 5** focuses on microstructural engineering via bio-templating and its effect on ionic transport.
- **Chapter 6** presents a dual-therapy approach combining solid and liquid interventions to enhance performance.
- **Chapter 7** expands toward composite electrolytes, demonstrating polymer, paper, and hybrid membranes as scalable solutions.
- **Chapter 8** explores unconventional and cross-chemistry extensions, broadening the applicability of the developed strategies.
- **Chapter 9** summarizes the findings, identifies limitations, and outlines future perspectives and commercial outlook.

This structured roadmap ensures the reader can follow the trajectory from hypothesis to demonstration, while critically evaluating the strategies proposed for overcoming the intrinsic challenges of garnet electrolytes in solid-state batteries.

1.11 References

1 Intergovernmental Panel on Climate Change (IPCC), *Climate Change 2021: The Physical Science Basis. Contribution of Working Group I to the Sixth Assessment Report (AR6)*, 2021.

2 International Energy Agency (IEA), *Global Energy-Related CO_2 Emissions Rose to 36.8 Gt in 2022*, 2023.

3 *OECD*, preprint, DOI: 10.1787/co2-data-en.

4 United Nations Framework Convention on Climate Change (UNFCCC) & UK Government (hosted in partnership with Italy), *26th UN Climate Change Conference of the Parties (COP26)*, Glasgow, United Kingdom, 2021.

5 F. and C. C. (MoEFCC), G. of I. Ministry of Environment, *India's Long-Term Low Emission Development Strategy (LT-LEDS)*, 2022.

6 NITI Aayog & Rocky Mountain Institute (RMI), *India's Electric Mobility Vision 2030*, 2021.

7 United Nations (UN), *Transforming Our World: The 2030 Agenda for Sustainable Development*, 2015.

8 International Energy Agency (IEA), *Global EV Outlook 2023*, .

9 J. Yuan, Z. Liu, T. Zhou, X. Tang, J. Yuan and W. Yuan, *Sustainability*, 2023, **15**, 7962.

10 US Department of Energy (DOE), *Battery500 Consortium Updates (2022–2023)*, .

11 Fraunhofer Institute (Germany), *Fraunhofer Solid-State Battery Roadmap 2035+*, .

12 Ministry of Heavy Industries (Government of India), *FAME-II Dashboard Report 2023*, .

13 NITI Aayog & Rocky Mountain Institute (RMI), *India EV Report 2023*, .

14 Ministry of Heavy Industries (Government of India), *PLI Scheme for Automobile and Auto Components 2021*, .

15 NITI Aayog & Ministry of Heavy Industries, *PLI Scheme for Advanced Chemistry Cell (ACC) Battery Storage 2021*, .

16 Government of India / Ministry of Finance, *Union Budget Announcements & GST Council Updates (2019–2022)*, .

17 J.-M. Tarascon and M. Armand, *Nature*, 2001, **414**, 359–367.

18 A. K. Koech, G. Mwandila, F. Mulolani and P. Mwaanga, *S Afr J Chem Eng*, 2024, **50**, 321–339.

19 Y. Nishi, in *Lithium-Ion Batteries*, Elsevier, 2014, pp. 21–39.

20 X. Zeng, M. Li, D. Abd El-Hady, W. Alshitari, A. S. Al-Bogami, J. Lu and K. Amine, *Adv Energy Mater*, DOI:10.1002/AENM.201900161.

21 L. Lu, X. Han, J. Li, J. Hua and M. Ouyang, *J Power Sources*, 2013, **226**, 272–288.

22 S. Bourlot, P. Blanchard and S. Robert, *J Power Sources*, 2011, **196**, 6841–6846.

23 S. Aphale, A. Kelani, V. Nandurdikar, S. Lulla and S. Mutha, in *2020 IEEE International Conference on Power and Energy (PECon)*, IEEE, 2020, pp. 288–292.

24 M. Şen, M. Özcan and Y. R. Eker, *Next Sustainability*, 2024, **3**, 100036.

25 U. S. Meda, L. Lal, S. M and P. Garg, *J Energy Storage*, 2022, **47**, 103564.

26 Z. Wang, J. Liu, M. Wang, X. Shen, T. Qian and C. Yan, *Nanoscale Adv*, 2020, **2**, 1828–1836.

27 S. Antony Jose, A. Gallant, P. L. Gomez, Z. Jaggers, E. Johansson, Z. LaPierre and P. L. Menezes, *Batteries*, 2025, **11**, 90.

28 Y. Luo, Z. Rao, X. Yang, C. Wang, X. Sun and X. Li, *Energy Environ Sci*, 2024, **17**, 7543–7565.

29 E. J. Cheng, H. Duan, M. J. Wang, E. Kazyak, H. Munakata, R. Garcia-Mendez, B. Gao, H. Huo, T. Zhang, F. Chen, R. Inada, K. Miyazaki, S. Ohno, H. Kato, S. Orimo, V. Thangadurai, T. Abe and K. Kanamura, *Energy Storage Mater*, 2025, **75**, 103970.

30 K. Xu, *Chem Rev*, 2004, **104**, 4303–4418.

31 K. Xu, *Chem Rev*, 2014, **114**, 11503–11618.

32 B. Zhang, R. Tan, L. Yang, J. Zheng, K. Zhang, S. Mo, Z. Lin and F. Pan, *Energy Storage Mater*, 2018, **10**, 139–159.

33 X. He, Y. Zhu and Y. Mo, *Nat Commun*, 2017, **8**, 15893.

34 Z. Gao, H. Sun, L. Fu, F. Ye, Y. Zhang, W. Luo and Y. Huang, *Advanced Materials*, DOI:10.1002/adma.201705702.

35 Z. Deng, Y. Mo and S. P. Ong, *NPG Asia Mater*, 2016, **8**, e254–e254.

36 P. P. Kumar and S. Yashonath, *Journal of Chemical Sciences*, 2006, **118**, 135–154.

37 R. Kanno and M. Murayama, *J Electrochem Soc*, 2001, **148**, A742.

38 V. Thangadurai and W. Weppner, *Ionics (Kiel)*, 2006, **12**, 81–92.

39 W. VAN GOOL, in *Solid Electrolytes*, Elsevier, 1978, pp. 1–5.

40 W. Xia, Y. Zhao, F. Zhao, K. Adair, R. Zhao, S. Li, R. Zou, Y. Zhao and X. Sun, *Chem Rev*, 2022, **122**, 3763–3819.

41 S. Sicolo and K. Albe, *J Power Sources*, 2016, **331**, 382–390.

42 K. Khan, H. Xin, B. Fu, M. Bilal Hanif, P. Li, B. Admasu Beshiwork, Z. Fang, M. Motola, Z. Xu and M. Wu, *J Colloid Interface Sci*, 2023, **642**, 246–254.

43 D. Zuo, L. Yang, Z. Zou, S. Li, Y. Feng, S. J. Harris, S. Shi and J. Wan, *Adv Energy Mater*, DOI:10.1002/aenm.202301540.

44 A. Manthiram, X. Yu and S. Wang, *Nat Rev Mater*, 2017, **2**, 16103.

45 M. Inoue, H. Iwane, H. Kikuyama, Y. Tasaki, Y. Honda and T. Abe, *J Alloys Compd*, 2022, **923**, 166350.

46 H. AONO, *Solid State Ion*, 1990, **40–41**, 38–42.

47 Y. Inaguma, C. Liquan, M. Itoh, T. Nakamura, T. Uchida, H. Ikuta and M. Wakihara, *Solid State Commun*, 1993, **86**, 689–693.

48 J. B. Goodenough, H. Y.-P. Hong and J. A. Kafalas, *Mater Res Bull*, 1976, **11**, 203–220.

49 C. R. Mariappan, C. Yada, F. Rosciano and B. Roling, *J Power Sources*, 2011, **196**, 6456–6464.

50 P. Wu, W. Zhou, X. Su, J. Li, M. Su, X. Zhou, B. W. Sheldon and W. Lu, *Adv Energy Mater*, DOI:10.1002/aenm.202203440.

51 S. Breuer, D. Prutsch, Q. Ma, V. Epp, F. Preishuber-Pflügl, F. Tietz and M. Wilkening, *J Mater Chem A Mater*, 2015, **3**, 21343–21350.

52 A. M. Cruz, E. B. Ferreira and A. C. M. Rodrigues, *J Non Cryst Solids*, 2009, **355**, 2295–2301.

53 A. MEI, X. WANG, Y. FENG, S. ZHAO, G. LI, H. GENG, Y. LIN and C. NAN, *Solid State Ion*, 2008, **179**, 2255–2259.

54 H. Morimoto, H. Awano, J. Terashima, Y. Shindo, S. Nakanishi, N. Ito, K. Ishikawa and S. Tobishima, *J Power Sources*, 2013, **240**, 636–643.

55 B. E. Francisco, C. R. Stoldt and J.-C. M'Peko, *Chemistry of Materials*, 2014, **26**, 4741–4749.

56 P. Kodgire, B. Tripathi and P. Chandra, *J Electron Mater*, 2024, **53**, 2203–2228.

57 R. Murugan, V. Thangadurai and W. Weppner, *Angewandte Chemie International Edition*, 2007, **46**, 7778–7781.

58 E. Rangasamy, J. Wolfenstine, J. Allen and J. Sakamoto, *J Power Sources*, 2013, **230**, 261–266.

59 R. Murugan, V. Thangadurai and W. Weppner, *Angewandte Chemie - International Edition*, 2007, **46**, 7778–7781.

60 M. M. Raju, F. Altayran, M. Johnson, D. Wang and Q. Zhang, *Electrochem*, 2021, **2**, 390–414.

61 A. J. Samson, K. Hofstetter, S. Bag and V. Thangadurai, *Energy Environ Sci*, 2019, **12**, 2957–2975.

62 H. El Shinawi and J. Janek, *J Power Sources*, 2013, **225**, 13–19.

63 H. Kim, Y. Ding and P. A. Kohl, *J Power Sources*, 2012, **198**, 281–286.

64 H. Y.-P. Hong, *Mater Res Bull*, 1978, **13**, 117–124.

65 R. D. Shannon, B. E. Taylor, A. D. English and T. Berzins, *Electrochim Acta*, 1977, **22**, 783–796.

66 N. Kamaya, K. Homma, Y. Yamakawa, M. Hirayama, R. Kanno, M. Yonemura, T. Kamiyama, Y. Kato, S. Hama, K. Kawamoto and A. Mitsui, *Nat Mater*, 2011, **10**, 682–686.

67 G. Zhao, K. Suzuki, T. Seki, X. Sun, M. Hirayama and R. Kanno, *J Solid State Chem*, 2020, **292**, 121651.

68 G. Zhao, K. Suzuki, M. Yonemura, M. Hirayama and R. Kanno, *ACS Appl Energy Mater*, 2019, **2**, 6608–6615.

69 S. Stramare, V. Thangadurai and W. Weppner, *Chemistry of Materials*, 2003, **15**, 3974–3990.

70 T. Takahashi and H. Iwahara, *Energy Conversion*, 1971, **11**, 105–111.

71 O. BOHNKE, *Solid State Ion*, 2008, **179**, 9–15.

72 Y. Harada, *Solid State Ion*, 1998, **108**, 407–413.

73 Y. INAGUMA, L. CHEN, M. ITOH and T. NAKAMURA, *Solid State Ion*, 1994, **70–71**, 196–202.

74 J. B. Goodenough, *Annu Rev Mater Res*, 2003, **33**, 91–128.

75 O. Bohnke, *Solid State Ion*, 1996, **91**, 21–31.

76 Y. Zhao and L. L. Daemen, *J Am Chem Soc*, 2012, **134**, 15042–15047.

77 X. Lü, G. Wu, J. W. Howard, A. Chen, Y. Zhao, L. L. Daemen and Q. Jia, *Chem. Commun.*, 2014, **50**, 11520–11522.

78 J. Zhu, S. Li, Y. Zhang, J. W. Howard, X. Lü, Y. Li, Y. Wang, R. S. Kumar, L. Wang and Y. Zhao, *Appl Phys Lett*, DOI:10.1063/1.4962437.

79 Z. Lu, C. Chen, Z. M. Baiyee, X. Chen, C. Niu and F. Ciucci, *Physical Chemistry Chemical Physics*, 2015, **17**, 32547–32555.

80 Z. Deng, B. Radhakrishnan and S. P. Ong, *Chemistry of Materials*, 2015, **27**, 3749–3755.

81 N. Gavrilov, A. Kamenetskikh, P. Tretnikov, A. Nikonov, L. Sinelnikov, D. Butakov, V. Nikolkin and A. Chukin, *Membranes (Basel)*, 2021, **12**, 40.

82 J. LaCoste, Z. Li, Y. Xu, Z. He, D. Matherne, A. Zakutayev and L. Fei, *ACS Appl Mater Interfaces*, 2020, **12**, 40749–40758.

83 M. A. Kraft, S. Ohno, T. Zinkevich, R. Koerver, S. P. Culver, T. Fuchs, A. Senyshyn, S. Indris, B. J. Morgan and W. G. Zeier, *J Am Chem Soc*, 2018, **140**, 16330–16339.

84 A. Hayashi, K. Minami, S. Ujiie and M. Tatsumisago, *J Non Cryst Solids*, 2010, **356**, 2670–2673.

85 J. Zhou, P. Chen, W. Wang and X. Zhang, *Chemical Engineering Journal*, 2022, **446**, 137041.

86 Y. Mo, S. P. Ong and G. Ceder, *Chemistry of Materials*, 2012, **24**, 15–17.

87 X. Liang, Y. Jiang, W. Cai, S. Wu, L. Wang, Z. Lei, J. Chen, Y. Lei, L. Yang and J. Feng, *ACS Appl Mater Interfaces*, 2020, **12**, 27029–27036.

88 F. Mizuno, A. Hayashi, K. Tadanaga and M. Tatsumisago, *Solid State Ion*, 2006, **177**, 2721–2725.

89 T. Baba and Y. Kawamura, *Front Energy Res*, DOI:10.3389/fenrg.2016.00022.

90 S. Kondo, K. Takada and Y. Yamamura, *Solid State Ion*, 1992, **53–56**, 1183–1186.

91 Y. Kim, J. Saienga and S. W. Martin, *J Phys Chem B*, 2006, **110**, 16318–16325.

92 J. Saienga and S. W. Martin, *J Non Cryst Solids*, 2008, **354**, 1475–1486.

93 M. Tatsumisago, *Solid State Ion*, 2004, **175**, 13–18.

94 A. Ahniyaz, I. de Meatza, A. Kvasha, O. Garcia-Calvo, I. Ahmed, M. F. Sgroi, M. Giuliano, M. Dotoli, M.-A. Dumitrescu, M. Jahn and N. Zhang, *Advances in Applied Energy*, 2021, **4**, 100070.

95 M. Tatsumisago, *Solid State Ion*, 2004, **175**, 13–18.

96 A.-K. Hatz, R. Calaminus, J. Feijoo, F. Treber, J. Blahusch, T. Lenz, M. Reichel, K. Karaghiosoff, N. M. Vargas-Barbosa and B. V. Lotsch, *ACS Appl Energy Mater*, 2021, **4**, 9932–9943.

97 K. Kim, D. Park, H.-G. Jung, K. Y. Chung, J. H. Shim, B. C. Wood and S. Yu, *Chemistry of Materials*, 2021, **33**, 3669–3677.

98 I. Kochetkov, T.-T. Zuo, R. Ruess, B. Singh, L. Zhou, K. Kaup, J. Janek and L. Nazar, *Energy Environ Sci*, 2022, **15**, 3933–3944.

99 L. Huang, L. Zhang, J. Bi, T. Liu, Y. Zhang, C. Liu, J. Cui, Y. Su, B. Wu and F. Wu, *Energy Material Advances*, DOI:10.34133/energymatadv.0092.

100 S. Yang, S. Y. Kim and G. Chen, *ACS Energy Lett*, 2024, **9**, 2212–2221.

101 J. Liang, X. Li, S. Wang, K. R. Adair, W. Li, Y. Zhao, C. Wang, Y. Hu, L. Zhang, S. Zhao, S. Lu, H. Huang, R. Li, Y. Mo and X. Sun, *J Am Chem Soc*, 2020, **142**, 7012–7022.

102 C. Wang, J. Liang, J. T. Kim and X. Sun, *Sci Adv*, DOI:10.1126/sciadv.adc9516.

103 X. Nie, J. Hu and C. Li, *Interdisciplinary Materials*, 2023, **2**, 365–389.

104 B. Tao, D. Zhong, H. Li, G. Wang and H. Chang, *Chem Sci*, 2023, **14**, 8693–8722.

105 B. Tao, D. Zhong, H. Li, G. Wang and H. Chang, *Chem Sci*, 2023, **14**, 8693–8722.

106 Z. Song, F. Chen, M. Martinez-Ibañez, W. Feng, M. Forsyth, Z. Zhou, M. Armand and H. Zhang, *Nat Commun*, 2023, **14**, 4884.

107 P. V. Wright, *British Polymer Journal*, 1975, **7**, 319–327.

108 M. Armand, *Solid State Ion*, 1983, **9–10**, 745–754.

109 D. Bresser, S. Lyonnard, C. Iojoiu, L. Picard and S. Passerini, *Mol Syst Des Eng*, 2019, **4**, 779–792.

110 Z. Li, J. Fu, X. Zhou, S. Gui, L. Wei, H. Yang, H. Li and X. Guo, *Advanced Science*, DOI:10.1002/advs.202201718.

111 K. S. Ngai, S. Ramesh, K. Ramesh and J. C. Juan, *Ionics (Kiel)*, 2016, **22**, 1259–1279.

112 V. Di Noto, S. Lavina, G. A. Giffin, E. Negro and B. Scrosati, *Electrochim Acta*, 2011, **57**, 4–13.

113 R. P. S., V. Prasannavenkadesan, V. Katiyar and A. S. Achalkumar, *RSC Applied Polymers*, 2025, **3**, 499–531.

114 P. G. Bruce and C. A. Vincent, *Journal of the Chemical Society, Faraday Transactions*, 1993, **89**, 3187.

115 G. Yang, Y. Song, Q. Wang, L. Zhang and L. Deng, *Mater Des*, 2020, **190**, 108563.

116 Y. Liu, Q. Zeng, Z. Li, A. Chen, J. Guan, H. Wang, S. Wang and L. Zhang, *Advanced Science*, DOI:10.1002/advs.202206978.

117 N. G. Ningappa, A. K. Madikere Raghunatha Reddy and K. Zaghib, *Batteries*, 2024, **10**, 454.

118 K. Karuppasamy, J. Theerthagiri, D. Vikraman, C.-J. Yim, S. Hussain, R. Sharma, T. Maiyalagan, J. Qin and H.-S. Kim, *Polymers (Basel)*, 2020, **12**, 918.

119 N. G. Ningappa, A. K. Madikere Raghunatha Reddy and K. Zaghib, *Batteries*, 2024, **10**, 454.

120 H. M. Woolley and N. M. Vargas-Barbosa, *J Mater Chem A Mater*, 2023, **11**, 1083–1097.

121 Y. Mao, J. Liu, W. Chen, W. Zhang and C. Sun, *Mater Horiz*, 2025, **12**, 6082–6123.

122 H. Im, D. U. Park, Y. J. Lee, J. Moon, S. Lee, T.-M. Choi, T. Lee, G. Lee, J.-M. Oh, W. H. Shin, S. G. Pyo, A. Seubsai and H. Sohn, *Materials*, 2025, **18**, 1536.

123 S.-Y. Du, G.-X. Ren, N. Zhang and X.-S. Liu, *ACS Omega*, 2022, **7**, 19631–19639.

124 L. Han, M. L. Lehmann, J. Zhu, T. Liu, Z. Zhou, X. Tang, C.-T. Heish, A. P. Sokolov, P. Cao, X. C. Chen and T. Saito, *Front Energy Res*, DOI:10.3389/fenrg.2020.00202.

125 D. Yu, Z. Ma, Z. Liu, X. Jiang, H. A. Younus, X. Wang and S. Zhang, *Chemical Engineering Journal*, 2023, **457**, 141043.

126 J. Li, F. Li, L. Zhang, H. Zhang, U. Lassi and X. Ji, *Green Chemical Engineering*, 2021, **2**, 253–265.

127 M. R. Busche, T. Drossel, T. Leichtweiss, D. A. Weber, M. Falk, M. Schneider, M. L. Reich, H. Sommer, P. Adelhelm and J. Janek, *Nat Chem*, 2016, **8**, 426–434.

128 M. Keller, A. Varzi and S. Passerini, *J Power Sources*, 2018, **392**, 206–225.

129 A. Tsurumaki, R. Rettaroli, L. Mazzapioda and M. A. Navarra, *Applied Sciences (Switzerland)*, DOI:10.3390/APP12147318.

130 B. Xu, H. Duan, H. Liu, C. A. Wang and S. Zhong, *ACS Appl Mater Interfaces*, 2017, **9**, 21077–21082.

131 A. Tsurumaki, R. Rettaroli, L. Mazzapioda and M. A. Navarra, *Applied Sciences (Switzerland)*, DOI:10.3390/APP12147318.

132 I. Kokal, M. Somer, P. H. L. Notten and H. T. Hintzen, *Solid State Ion*, 2011, **185**, 42–46.

133 I. Kokal, M. Somer, P. H. L. Notten and H. T. Hintzen, *Solid State Ion*, 2011, **185**, 42–46.

134 E. Rangasamy, J. Wolfenstine, J. Allen and J. Sakamoto, *J Power Sources*, 2013, **230**, 261–266.

135 D. Wang, K. Peng, Y. Fu, C. Zhu and Y. Yang, *J Power Sources*, 2021, **487**, 229421.

136 J. Košir, S. Mousavihashemi, B. P. Wilson, E.-L. Rautama and T. Kallio, *Solid State Ion*, 2022, **380**, 115943.

137 B. Gao, R. Jalem, H. Tian and Y. Tateyama, *Adv Energy Mater*, DOI:10.1002/aenm.202102151.

138 S. Yu and D. J. Siegel, *Chemistry of Materials*, 2017, **29**, 9639–9647.

139 L. Cheng, C. H. Wu, A. Jarry, W. Chen, Y. Ye, J. Zhu, R. Kostecki, K. Persson, J. Guo, M. Salmeron, G. Chen and M. Doeff, *ACS Appl Mater Interfaces*, 2015, **7**, 17649–17655.

140 W. S. Scheld, K. Kim, C. Schwab, A. C. Moy, S. K. Jiang, M. Mann, C. Dellen, Y. J. Sohn, S. Lobe, M. Ihrig, M. G. Danner, C. Y. Chang, S. Uhlenbruck, E. D. Wachsman, B. J. Hwang, J. Sakamoto, L. F. Wan, B. C. Wood, M. Finsterbusch and D. Fattakhova-Rohlfing, *Adv Funct Mater*, DOI:10.1002/adfm.202302939.

141 G. Yoon, S. Kim and J. Kim, *Advanced Science*, DOI:10.1002/advs.202302263.

142 A. Sharafi, S. Yu, M. Naguib, M. Lee, C. Ma, H. M. Meyer, J. Nanda, M. Chi, D. J. Siegel and J. Sakamoto, *J Mater Chem A Mater*, 2017, **5**, 13475–13487.

143 Y. Jin and P. J. McGinn, *J Power Sources*, 2013, **239**, 326–331.

144 W. Xia, B. Xu, H. Duan, Y. Guo, H. Kang, H. Li and H. Liu, *ACS Appl Mater Interfaces*, 2016, **8**, 5335–5342.

145 L. Cheng, C. H. Wu, A. Jarry, W. Chen, Y. Ye, J. Zhu, R. Kostecki, K. Persson, J. Guo, M. Salmeron, G. Chen and M. Doeff, *ACS Appl Mater Interfaces*, 2015, **7**, 17649–17655.

146 A. Baniya, A. Gurung, J. Pokharel, K. Chen, R. Pathak, B. S. Lamsal, N. Ghimire, R. S. Bobba, S. I. Rahman, S. Mabrouk, A. L. Smirnova, K. Xu and Q. Qiao, *ACS Appl Energy Mater*, 2022, **5**, 648–657.

147 J. Fu, P. Yu, N. Zhang, G. Ren, S. Zheng, W. Huang, X. Long, H. Li and X. Liu, *Energy Environ Sci*, 2019, **12**, 1404–1412.

148 E. P. Alsaç, D. L. Nelson, S. G. Yoon, K. A. Cavallaro, C. Wang, S. E. Sandoval, U. D. Eze, W. J. Jeong and M. T. McDowell, *Chem Rev*, 2025, **125**, 2009–2119.

149 J. Ma, R. He, Y. Jiang, L. Zhang, H. Xu, H. Zeng, C. Wang, X. Xu, Y. Deng, J. Wang and S. Chi, *Battery Energy*, DOI:10.1002/bte2.70009.

150 Y. Xiao, L. J. Miara, Y. Wang and G. Ceder, *Joule*, 2019, **3**, 1252–1275.

151 E. J. Cheng, M. Shoji, T. Abe and K. Kanamura, *iScience*, 2022, **25**, 103896.

152 D. Yu, Z. Ma, Z. Liu, X. Jiang, H. A. Younus, X. Wang and S. Zhang, *Chemical Engineering Journal*, 2023, **457**, 141043.

153 H. Huo and J. Janek, *Natl Sci Rev*, DOI:10.1093/nsr/nwad098.

154 X. B. Cheng, R. Zhang, C. Z. Zhao and Q. Zhang, *Chem Rev*, 2017, **117**, 10403–10473.

155 X. B. Cheng, R. Zhang, C. Z. Zhao, F. Wei, J. G. Zhang and Q. Zhang, *Advanced Science*, DOI:10.1002/ADVS.201500213.

156 F. Han, J. Yue, C. Chen, N. Zhao, X. Fan, Z. Ma, T. Gao, F. Wang, X. Guo and C. Wang, *Joule*, 2018, **2**, 497–508.

157 S. Randau, D. A. Weber, O. Kötz, R. Koerver, P. Braun, A. Weber, E. Ivers-Tiffée, T. Adermann, J. Kulisch, W. G. Zeier, F. H. Richter and J. Janek, *Nat Energy*, 2020, **5**, 259–270.

158 Y. Kato, S. Hori, T. Saito, K. Suzuki, M. Hirayama, A. Mitsui, M. Yonemura, H. Iba and R. Kanno, *Nat Energy*, DOI:10.1038/NENERGY.2016.30.

159 F. Zheng, M. Kotobuki, S. Song, M. O. Lai and L. Lu, *J Power Sources*, 2018, **389**, 198–213.

160 S. A. Pervez, G. Kim, B. P. Vinayan, M. A. Cambaz, M. Kuenzel, M. Hekmatfar, M. Fichtner and S. Passerini, *Small*, DOI:10.1002/SMLL.202000279.

161 L. Wang, Z. Li, J. Luo, H. Fan and R. Zhao, *Chemical Communications*, 2022, **58**, 6962–6965.

162 J. Lou, G. Wang, Y. Xia, C. Liang, H. Huang, Y. Gan, X. Tao, J. Zhang and W. Zhang, *J Power Sources*, DOI:10.1016/J.JPOWSOUR.2019.227440.

163 S. Afyon, F. Krumeich and J. L. M. Rupp, *J Mater Chem A Mater*, 2015, **3**, 18636–18648.

164 J. Li, F. Li, L. Zhang, H. Zhang, U. Lassi and X. Ji, *Green Chemical Engineering*, 2021, **2**, 253–265.

165 D. Cao, T. Ji, Z. Wei, W. Liang, R. Bai, K. S. Burch, M. Geiwitz and H. Zhu, *Nano Lett*, 2023, **23**, 9392–9398.

166 K. Cai, M. Zhang, G. Zhong, G. Kang, J. Biao, C. Li, Y. Liu, G. Zhou, F. Kang and Y. Cao, *J Mater Chem A Mater*, 2024, **12**, 11719–11729.

167 M. J. Counihan, T. Kim, R. Pathak, T. Zagorac, Y. Yang, M. E. Burns, J. Cabana, R. F. Klie, L. Hanley, J. G. Connell, A. U. Mane, J. W. Elam and S. Tepavcevic, *Frontiers in Batteries and Electrochemistry*, DOI:10.3389/fbael.2023.1292622.

168 G. Deysher, J. A. S. Oh, Y.-T. Chen, B. Sayahpour, S.-Y. Ham, D. Cheng, P. Ridley, A. Cronk, S. W.-H. Lin, K. Qian, L. H. B. Nguyen, J. Jang and Y. S. Meng, *Nat Energy*, DOI:10.1038/s41560-024-01569-9.

169 M. Tang, S. Dong, J. Wang, L. Cheng, Q. Zhu, Y. Li, X. Yang, L. Guo and H. Wang, *Nat Commun*, 2023, **14**, 6006.

170 J. Wang, Y. Zhou, Y. Zhuo, K. Fang, S. Wang, B. Zhao, J. Zhou and H. Wang, *Chem Sci*, 2025, **16**, 552–574.

171 X. Huang, T. Xiu, M. E. Badding and Z. Wen, *Ceram Int*, DOI:10.1016/j.ceramint.2017.12.217.

172 C. Deviannapoorani, L. Dhivya, S. Ramakumar and R. Murugan, *J Power Sources*, 2013, **240**, 18–25.

173 C. Deviannapoorani, L. Dhivya, S. Ramakumar and R. Murugan, *J Power Sources*, 2013, **240**, 18–25.

174 N. Janani, C. Deviannapoorani, L. Dhivya and R. Murugan, *RSC Adv*, 2014, **4**, 51228–51238.

175 C. Deviannapoorani, L. Dhivya, S. Ramakumar and R. Murugan, *J Power Sources*, 2013, **240**, 18–25.

176 H. Xie, Y. Li and J. B. Goodenough, *Mater Res Bull*, 2012, **47**, 1229–1232.

177 I. Quinzeni, D. Capsoni, V. Berbenni, P. Mustarelli, M. Sturini and M. Bini, *Mater Chem Phys*, 2017, **185**, 55–64.

178 T. Yang, Z. D. Gordon, Y. Li and C. K. Chan, *The Journal of Physical Chemistry C*, 2015, **119**, 14947–14953.

179 M. M. Raju, F. Altayran, M. Johnson, D. Wang and Q. Zhang, *Electrochem*, 2021, **2**, 390–414.

180 W. Xia, Y. Zhao, F. Zhao, K. Adair, R. Zhao, S. Li, R. Zou, Y. Zhao and X. Sun, *Chem Rev*, 2022, **122**, 3763–3819.

181 Z. D. Hood and M. Chi, *J Mater Sci*, 2019, **54**, 10571–10594.

CHAPTER 2

Experimental Methodology and Characterization Techniques

Summary & Flow of Work

This chapter presents the experimental methodology used to design, fabricate, and evaluate advanced solid electrolytes for next-generation solid-state metal batteries. The synthesis strategies include various wet-chemical and solid-state synthesis processes that are scalable in nature. The synthesis processes are optimized to achieve controlled phase formation, microstructure tailoring, and improved interfacial properties. Efforts are made to reproduce the synthesis process for similar electrical and electrochemical performances throughout the thesis work. All the cells are tested in a 2032-coin cell with a commercial cathode and Li metal with various types of electrolytes developed under this work. A comprehensive set of various characterization techniques was used to establish the correlations between processing conditions, material properties, and electrochemical behavior. Thus, this chapter provides a robust framework for the evaluation of solid electrolyte systems and guides their optimization for next-generation metal batteries.

Objectives

1. Synthesize and modify LLZO-based solid and hybrid electrolytes.

2. Correlate structure, properties, and performance in solid-state cells.

Strategy

Adopt systematic synthesis, modification, and multi-technique characterization.

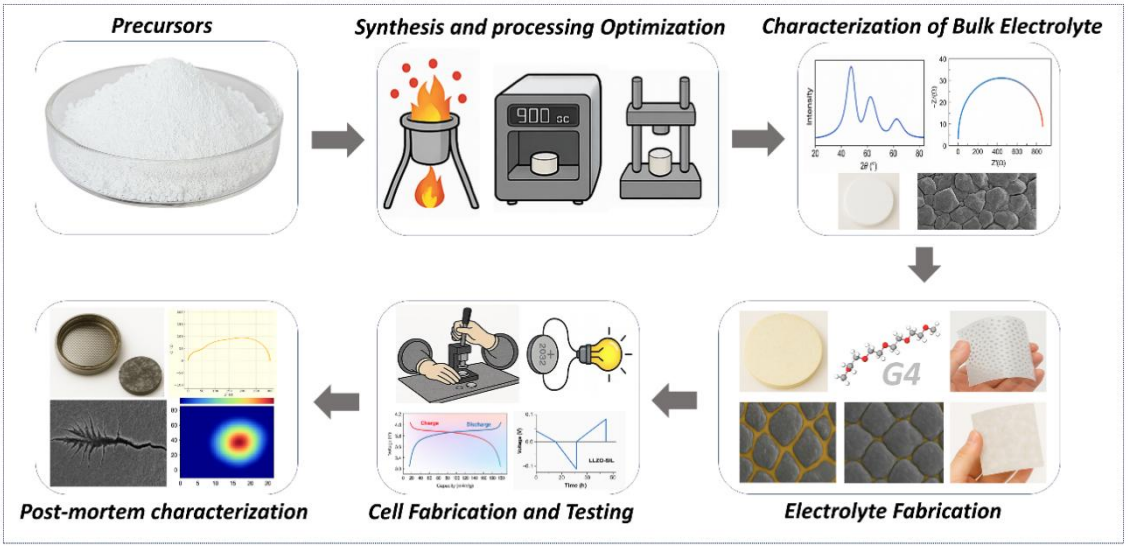

Figure 2.1 *Schematic of the flow of experimental work followed in this thesis work.*

2.1 Overview

The study of solid electrolytes for solid-state metal batteries generally involves both material synthesis and in-depth evaluation of their properties. This journey starts with the synthesis of solid electrolytes and their composite configurations from various approaches, such as combustion, template-assisted synthesis, or the solid-state synthesis method. Each synthesis process has some advantages and limitations in terms of phase purity, particle size, morphology, and scalability, which directly impact the cell performance during real-world applications. Thus, optimization and reproducibility are important factors in the synthesis process.

Beyond the synthesis process, an equally important aspect of electrolyte research lies in their characterization methods. In general, thermal studies always provide insight into the stability and phase evolution process. While, the structural and microstructural analyses confirm crystallinity, grain connectivity of the solid electrolyte, and interfacial features at various boundaries. In electrical and electrochemical techniques, we studied the impedance spectroscopy, plating/stripping behaviors, critical current density measurement, and long-term cycling, which are essential to probe ionic transport and interfacial resistance at the cell chemistry. Post-electrochemical and surface studies are also very crucial to correlate with degradation products, interphase formation, mechanisms of failure, and a correlation with the previous characterization. Thus, this way we can optimize and design the material's properties and use it in various functional applications.

In this chapter, we mainly focus on the methodologies that are generally used for the synthesis, fabrication, evaluation of solid electrolytes and their composite membranes in the present study. The techniques and protocols presented in this chapter establish a correlation between the fundamental concepts that were introduced in Chapter 1 and the detailed experimental studies discussed in the subsequent chapters.

2.2 Materials and Chemicals

The present thesis work focuses on the development of advanced solid electrolytes for metal batteries. A set of various types of chemicals was used to carry out this research work. ***Table 2.1*** represents a dedicated list of the chemicals and reagents used in this thesis. All the chemicals are used without any further purification. Highly moisture-sensitive materials were always handled inside an argon-filled glove box (H_2O and $O_2 < 0.1$ ppm) to avoid any exposure, degradation, or parasitic side reactions during synthesis, storage, and cell fabrication.

Table 2.1 List of chemicals and materials used in the current research work

S. No.	Material	Source	Purity
1	Lithium nitrate ($LiNO_3$)	SRL	≥99.5%
2	Lanthanum nitrate hexahydrate ($La(NO_3)_3 \cdot 6H_2O$)	SRL	99.9%
3	Zirconyl nitrate hydrate ($ZrO(NO_3)_2 \cdot xH_2O$)	Sigma-Aldrich	≥99%
4	Alanine ($C_3H_7NO_2$)	Merck	≥99%
5	Nickel oxide (NiO)	Alfa Aesar	99.9%
6	Ammonium fluoride (NH_4F)	Merck	98%
7	Li_2S	Merck	≥99.5%
8	Alumina crucibles (Al_2O_3)	MTI Corp.	99.8%
9	Zirconia crucibles (ZrO_2)	MTI Corp.	99.9%
10	LiTFSI	Sigma-Aldrich	99.95%
11	Tetraglyme (G4)	Sigma-Aldrich	≥99% anhydrous
12	1M $LiPF_6$ in EC/DMC	Sigma-Aldrich	99.9%
13	Polypropylene (PP) separator	Celgard Inc.	~20±2 µm
14	Lithium metal foil	MTI Corp.	99.9%
15	Stainless steel (SS) electrodes	MTI	316L grade
16	$LiMn_2O_4$ (LMO) powder	MTI Corp.	≥99%
17	$LiFePO_4$ (LFP) powder	MTI Corp.	≥99%
18	$Li(Ni_{1/3}Mn_{1/3}Co_{1/3})O_2$ (NMC111)	MTI Corp.	≥99%
19	Polyvinylidene fluoride (PVDF)	MTI Corp.	≥99%
20	Polyvinylidene fluoride-hexafluoropropylene (PVDF-HFP)	Sigma-Aldrich	≥99%
21	Polyethene oxide (PEO)	Sigma-Aldrich	≥99%
22	Active carbon (Super P)	Alfa Aesar	≥99%
23	N-Methyl-2-pyrrolidone (NMP)	Sigma-Aldrich	≥99.5%
24	Dimethylformamide (DMF)	Merck	≥99.5%
25	Deionized (DI) water	In-house Milli-Q	18.2 MΩ·cm
26	Deuterium oxide (D_2O)	Sigma-Aldrich	99.9 atom% % D
27	Sodium carbonate (Na_2CO_3)	Merck	≥99.5%
28	Zirconia (ZrO_2) powder	Sigma-Aldrich	99.9%
29	Silicon dioxide (SiO_2, amorphous/fumed/quartz) source	Sigma-Aldrich	≥99.5%
30	Ammonium dihydrogen phosphate ($NH_4H_2PO_4$)	Sigma-Aldrich	≥99%
31	NaPF6	Sigma-Aldrich	≥99%

2.3 Synthesis and Processing of Solid Electrolytes

As discussed earlier in Chapter 1, the development of solid-state batteries depends heavily on the main building block, i.e, solid electrolytes. High ionic conductivity, phase stability, and scalable synthesis routes are essential for an ideal solid-state battery. Garnet-type oxides, particularly $Li_7La_3Zr_2O_{12}$ (LLZO) and its doped version, have recently received much attention across the globe due to their wide electrochemical stability window, chemical compatibility with high-voltage cathodes, and potential dendrite resistance when interfaced with lithium metal. However, their practical handling is often restricted by issues such as Li loss during high-temperature sintering, large grain boundary resistance, and sensitivity to moisture and CO2. Hence, careful design of the synthesis route is very important to stabilize the cubic phase of LLZO and maintain reproducibility.

In this work, LLZO was synthesized in pristine, doped, engineered, and surface-modified forms using various approaches. The details about these approaches will be discussed in this section. These modifications are beneficial to achieve better grain connectivity, reduced interfacial resistance, and improved compatibility with polymer and hybrid electrolyte systems. While the primary focus of this thesis remains on LLZO, a brief exploratory study using NASICON-type NZSP($Na_3Zr_2Si_2PO_{12}$) and modified LLZO compositions has also been carried out, which is discussed in Chapter 8.

2.3.1 Synthesis of Pristine LLZO

Pristine LLZO solid electrolytes were synthesized via a wet-chemical assisted auto-combustion method, selected for its energy efficiency, compositional homogeneity, and scalability compared to traditional solid-state synthesis. The combustion synthesis process of LLZO has been schematically presented in ***Figure 2.2***. The process was carried out by mixing a stoichiometric amount of $LiNO_3$, $La(NO_3)_3$, $ZrO(NO_3)_2$ in deionized water (*referred to as Solution A*). A saturated solution of alanine was then prepared separately in aqueous medium (*referred to as Solution B*) with optimized stoichiometric ratios to that of nitrate. Both solutions A and B were then mixed together in a beaker and kept on a hot plate with constant magnetic stirring inside the fume hood. The input temperature of the hot plate was fixed to 150-250°C. The stirring was continued till the solution turned into a viscous gel. A small portion of gel was collected for thermal analysis, and the rest was allowed to further heat. Thereafter, small volcanic openings were found at places on the top surface of the gel, and subsequently, auto-ignition was triggered. After some time, the gel was burnt momentarily with the evolution of a

large amount of gaseous species, resulting in a flappy white mass carrying ultrafine particles (called as-synthesized powder or ash). It is mandatory that, as the combustion process involves uncontrolled heat surge and evolution of a large amount of noxious gases, for personal and lab safety, the whole synthesis process was carried out inside a fume hood to avoid any unwanted happenings. The as-synthesized powder after combustion synthesis was then calcined at 900°C for 10 hours in air to obtain cubic LLZO. To measure various physio-chemical parameter, the 900°C calcined powder was pelletized under a pressure of 3-5 tonns for 3-5 minutes using a uniaxial hydraulic press and sintered at 1000°C for 10 hours in air.

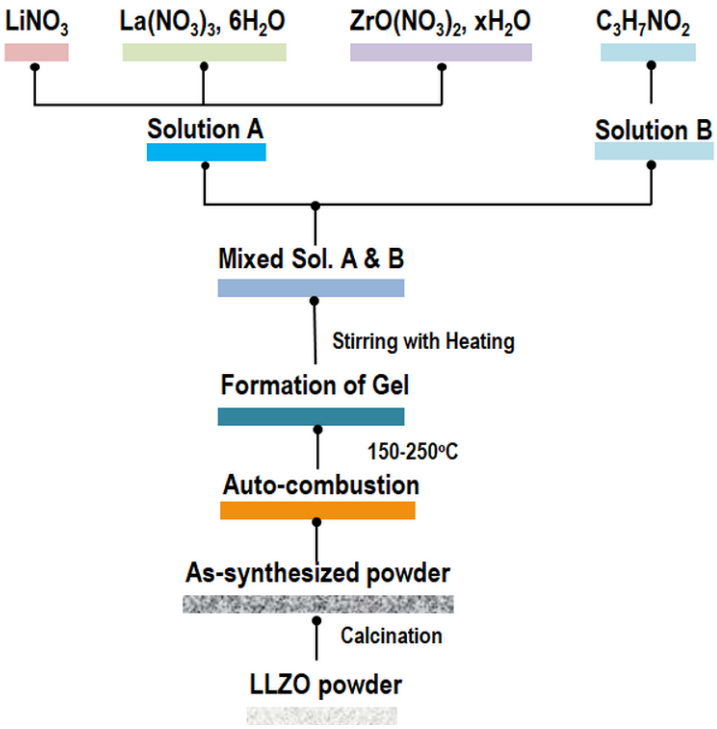

Figure 2.2 *Schematic representation of the alanine-assisted combustion process for making LLZO powder.*

2.3.2 Synthesis of Ga doped LLZO

To further stabilize the cubic phase and reduce grain boundary resistance, Ga-doped LLZO ($Li_{6.25}Ga_{0.25}La_3Zr_2O_{12}$ with 10% excess Li) was synthesized using the same alanine-assisted auto-combustion process described in ***Section 2.3.1***. The introduction of Ga^{3+} at the Li sites has been widely reported. Mainly, the ionic mobility with additional vacancies increases with the introduction of dopant material in the LLZO matrix by suppressing unwanted tetragonal distortions, as already discussed in the earlier chapter.

In a typical combustion process, different constituent salts such as $LiNO_3$, $La(NO_3)_3$, $ZrO(NO_3)_2$, and $Ga(NO_3)_3$ were dissolved in deionized water under constant stirring, a

chelating agent named alanine was dissolved separately in deionized water (with optimized fuel to nitrate ratio) and was mixed slowly with the metal nitrate solution. With constant heating (150°C) and stirring, the solution was finally converted to a viscous gel, allowing further heating (200°C). After some time, the gel was burnt momentarily with the evolution of large amounts of gaseous species, and a fluffy white powder (named Ash) was produced. The ash powder was further calcined at 900°C for 10 hours with a ramp rate of 120°C/h in a Carbolite Gero furnace to get the cubic phase of LLZO.

The calcined powders were then finely ground, pelletized using a uniaxial hydraulic press (10-19 mm diameter, 3-5tonnes, 3-5 min), and sintered at 1000°C for 10 h in covered alumina crucibles with sacrificial powder beds to minimize lithium volatilization. The final pellets exhibited dense microstructures with phase-pure cubic garnet characteristics. All powders and pellets were transferred and stored in an argon-filled glove box (H_2O and O_2 < 0.1 ppm) immediately after calcination/sintering to prevent surface degradation by CO_2 and moisture.

2.3.3 Synthesis of Engineered LLZO

LLZO-based materials were further prepared using various methods to engineer the grain boundary, particle morphology, and surface modification. These engineering at the bulk level are crucial to reduce the intergranular resistance, suppress uncontrollable lithium dendrite growth, and improve interface compatibility with electrodes.

2.3.3.1 Neck-fused LLZO

Neck-fused pristine LLZO particles were synthesized by carefully optimizing the fuel-to-nitrate (F/N: 0.10, 0.15, 0.20, and 0.30) ratio during the alanine-assisted combustion process. A higher fuel concentration (F/N~0.2) controls the exothermicity of the reaction. This raises the localized combustion temperature and promotes partial grain coalescence and inter-particle fusion during the rapid combustion stage. As a result, formation of neck-fused LLZO grains in the as-combusted powder is observed. Further enhancement in the F/N ratio might produce hard agglomeration due to high exothermicity.

The precursor mixture was prepared as described in Section 2.3.1, but the F/N ratio was systematically adjusted in the range of 0.10-0.30. After auto-combustion, the fluffy ash-like product was collected and calcined at 900 °C for 10 h in air to remove residual carbon and organics. The resulting powders exhibited partially sintered and fused morphologies, even

before final pellet sintering. Subsequent pelletization under 1000°C further enhanced the neck-fusion of grains.

2.3.3.2 Plate-like LLZO

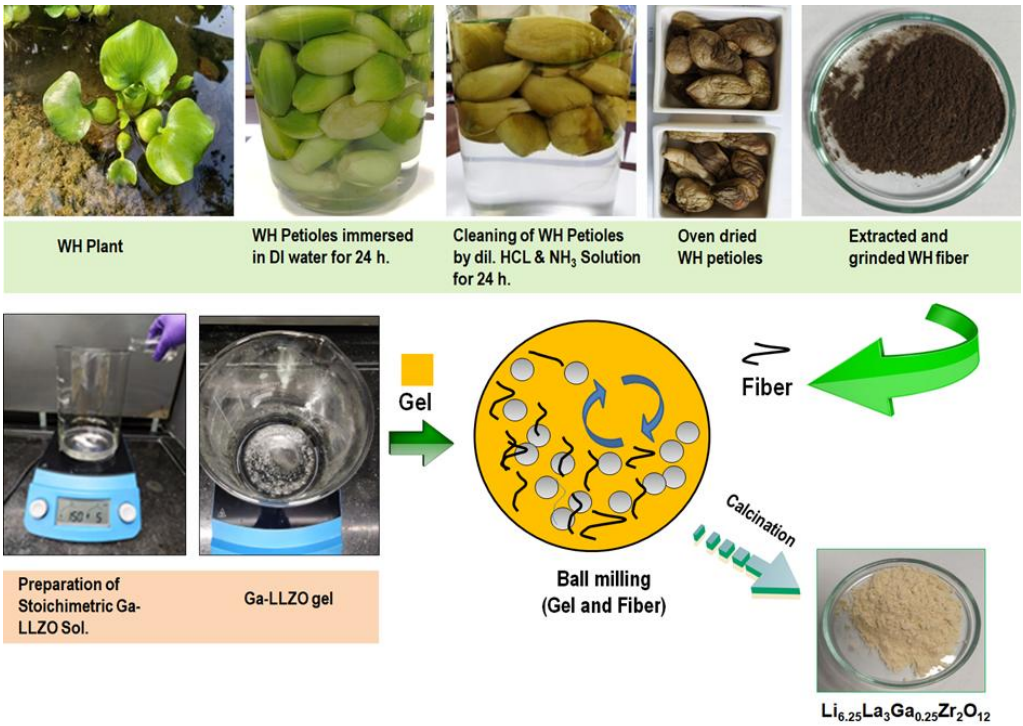

Figure 2.3 *The different steps involved in the synthesis process of plate-like Ga-doped LLZO powder (LLZOWH).*

In the present thesis, a unique "plate-like" microstructure was developed by mimicking the intercellular structure of Water hyacinth (*Eichhornia crassipes*). Here, we particularly emphasize a facile synthesis process of preparing Gallium-doped $Li_7L_3Z_2O_{12}$ ($Li_{6.25}La_3Ga_{0.25}Zr_2O_{12}$, henceforth referred to as LLZOWH) based garnet solid-state electrolyte for its application in Solid State Lithium Batteries (SSLBs) using Water Hyacinth (*Eichhornia Crassipes*) as sacrificial bio-template.

Water hyacinth plants were collected from a local water body, and the green petioles were cut into pieces. The petioles were first cleaned thoroughly with deionized water, followed by dilute acid and alkali solution to remove impurities. The cleaned petioles were then oven-dried at 250°C for about 3-4 hours and ground into powder. The WH powder was kept in a desiccator to avoid moisture contamination.

A stoichiometric amount of $LiNO_3$, $La(NO_3)_3$, $ZrO(NO_3)_2$, $Ga(NO_3)_3$ was taken considering a nominal composition of $Li_{6.25}La_3Ga_{0.25}Zr_2O_{12}$ (with 10% excess Li) along with alanine as complexing agent in aqueous medium. The mixture was heated with constant stirring on a hot

plate at 150-250 ˚C to obtain a clear viscous gel (Ga-LLZO-Gel). The Ga-LLZO-Gel was then mixed with WH Fiber in 10:1 v/w ratio and ball milled for 12-24 hours. The milled slurry was pre-calcined at 500˚C and finally at 900˚C for 5 hours in air to obtain cubic LLZOWH powder. The different steps involved in the synthesis process are schematically presented in ***Figure 2.3***.

2.3.3.3 Interconnected LLZO

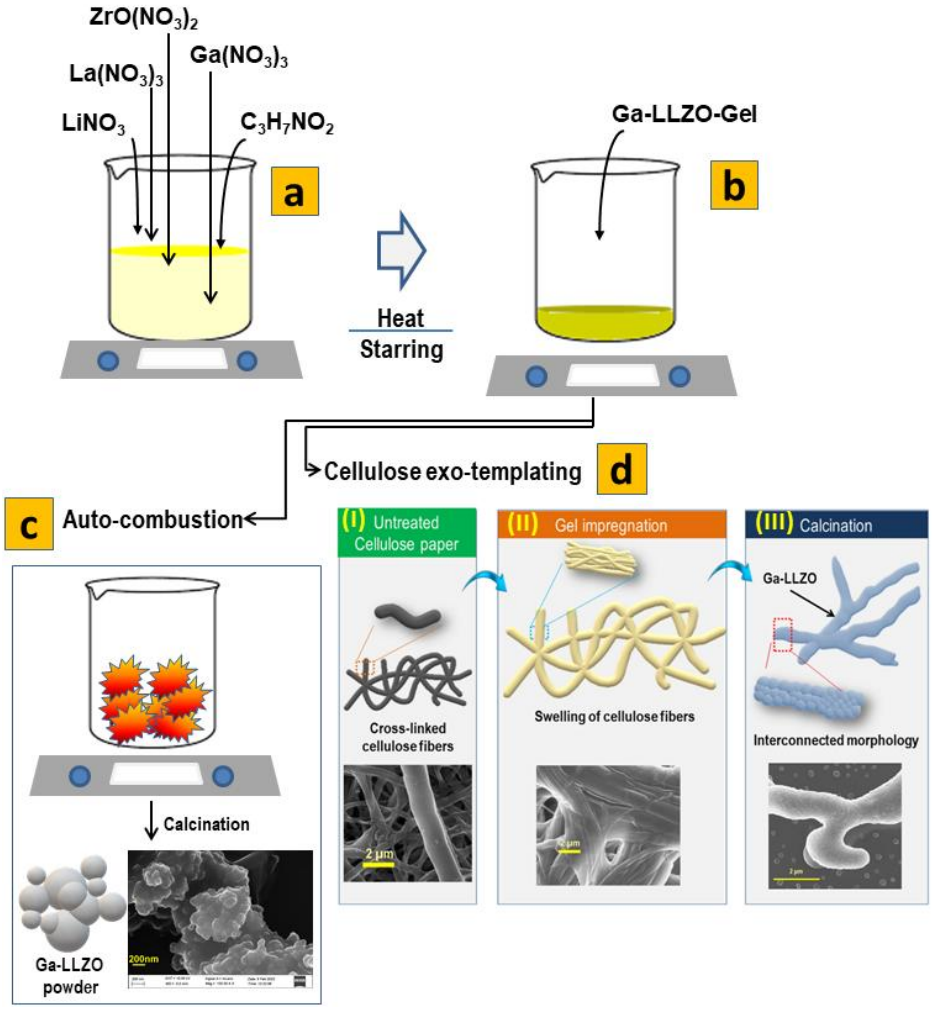

Figure 2.4 *Schematic representation of synthesis of Ga doped LLZO powder using (a-b-c) conventional gel-combustion (GC) process and (a-b-d) cellulose exo-templating (CET) process. The morphologies of Ga doped LLZO powders are also given in the inset for comparison.*

The template method is a simple and effective approach to control nucleation and growth during synthesis, which enables the formation of unique particle morphologies. Commercial cellulose paper was used as a soft template and sacrificial in nature, which at the end of the synthesis process produced interconnected/networked Ga-doped LLZO garnet by controlled nucleation across the entangled cellulosic fibers of paper.

Preparation of Gel

To synthesize Ga-LLZO, a solution was first prepared by dissolving constituent metal salts- $LiNO_3$, $La(NO)_3$, $ZrO(NO_3)_2$, $Ga(NO_3)_3$, and a chelating agent, alanine ($C_3H_7NO_2$) in deionized water. With constant stirring and heating(~150°C), the solution finally turned into a viscous gel.

The obtained gel was divided into two portions:

(i) One portion of the gel was allowed to further heat for gel combustion. (***Figure 2.4*(a-b-c))**

(ii) The residual portion was used to conduct the cellulose exo-templating process by impregnating the gel in commercial pure cellulosic paper. (**Figure 2.4(a-b-d)**).

Cellulose exo-templating (CET) process

Commercially available cellulosic paper was first demystified under a vacuum oven for 6 hours. The dry paper was then carefully soaked with the gel. The quantity of gel impregnated in the paper substrate could be estimated as 2:3 w/v % with respect to dry paper and precursor gel. The swelling of the cellulosic fiber could be visible under a microscope even after gel impregnation. The impregnation of gel into the fiber bundles is mainly controlled through capillary action. The gel-soaked paper was then placed in a muffle furnace, and controlled calcination was carried out by heat treating the sample to 900 °C in air for 10 hours to get cubic interconnected Ga-LLZO as shown in ***Figure 2.4d(III)***. Thus, two different Ga-doped LLZO powders were obtained: LLZOGC via the direct gel combustion route, and LLZOCET via the cellulose exo-templating method. A schematic representation of the synthesis processes and the resulting morphologies is presented in **Figure 2.4**.

2.3.3.4 Grain Boundary Engineered LLZO

Ga-doped LLZO ($Li_{6.25}Ga_{0.25}La_3Zr_2O_{12}$ with 10% excess Li) was first prepared using the fuel-assisted auto-combustion method as described in ***Section 2.3.2***. To engineer the grain boundaries, different percentages of NiO (0wt%, 0.25wt%, 0.50wt%,0.75wt%, and 1.00wt%) were mixed with the Ga doped LLZO calcined powder (900°C at 10h) and ball-milled overnight in a PE container with a proportionate amount of zirconia balls and isopropyl alcohol. The ball-milled powder was then dried in a vacuum oven and stored inside the glove box for further experiments. The different solid electrolyte powders were pelletized in a uniaxial hydraulic pellet maker with an optimized pressure and then sintered at 1000°C for 10 hours.

Figure 2.5 represents the synthesis and sintering process schematic of solid therapy in Ga doped LLZO solid electrolyte material.

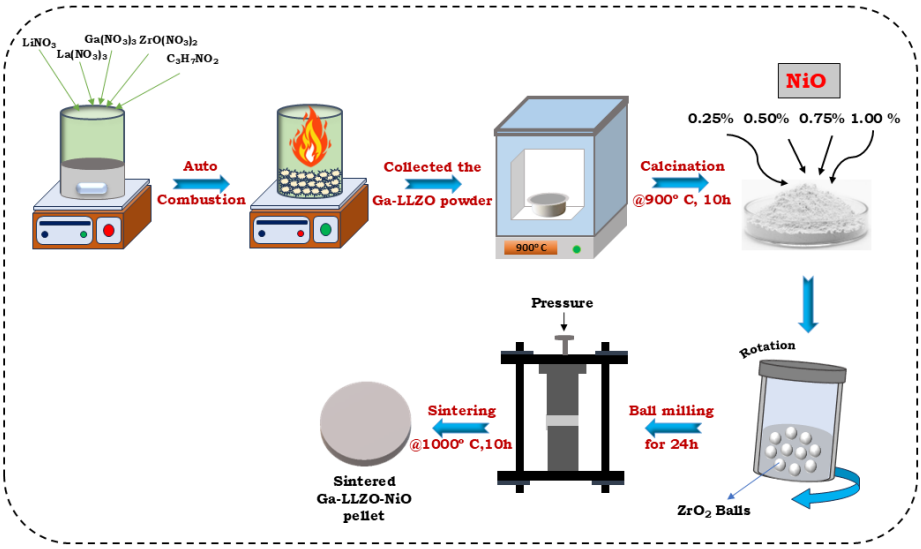

Figure 2.5 *Schematic representation of the synthesis and sintering process of solid therapy in Ga doped LLZO solid electrolyte material.*

2.3.4 Synthesis of Surface-modified LLZO

Figure 2.6 *Schematic representation of surface-modified LLZO material using the low-temperature wet chemical method*

Pristine LLZO ($Li_7La_3Zr_2O_{12}$ with 10% excess Li) was first prepared using the alanine-assisted auto-combustion method as described in detail in ***Section 2.3.2***. The goal of this modification was to mitigate the instability of LLZO against ambient moisture/CO_2 and to form a stable passivation layer that improves interfacial compatibility with lithium metal. For surface modification of the LLZO pellet sintered at 1000°C, a low-temperature wet chemical process was used. In this process, NH_4F solution was prepared using 25 mg of NH_4F in 10ml of dimethyl sulfoxide (DMSO). Then, the solution was vigorously stirred at 40°C for 48h to obtain

a homogeneous solution. A small amount (~50 µL) of the NH_4F solution was further drop-cast onto the polished surface of LLZTO pellets, as shown in ***Figure 2.6***. Then, it was dried at about 200 °C inside a glove box for 20 minutes. As a result, the DMSO is evaporated rapidly, and NH_4F reacts with surface contaminants (Li_2CO_3 and LiOH). This mostly converted the surface impurities into a LiF-rich passivation layer. This process was repeated 20 times to ensure uniform surface distribution of LiF.

2.3.5 Synthesis of NZSP Solid Electrolyte

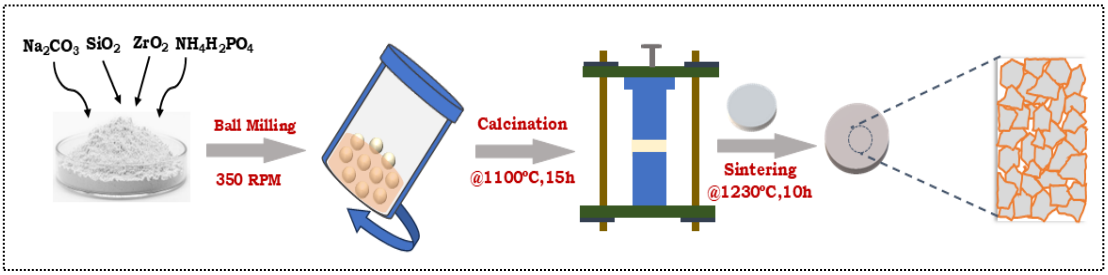

Figure 2.7 *Schematic representation of the synthesis process of NZSP solid electrolyte preparation via the conventional solid-state method.*

Sodium superionic conductor or $Na_3Zr_2Si_2PO_{12}$ (NZSP) was first synthesized using a conventional solid-state route, as shown in ***Figure 2.7***. The stoichiometric ratio of the precursor powders, i.e., Na_2CO_3, SiO_2, ZrO_2, and $NH_4H_2PO_4$, was first weighed according to the nominal composition of NZSP (10% Excess Na_2CO_3 taken due to Na volatility at high temperature). These precursors were mixed via high-energy ball milling at 350 rpm for overnight using zirconia balls and isopropanol as the solvent. The slurry was collected and dried in a vacuum oven. It was then ground to obtain fine precursor powder.

The dried powders were calcined at 1100 °C for 15 h in air to promote the formation of the NASICON phase. The calcined powders were then pelletized under a uniaxial pressing machine. The green pellets were finally sintered at 1230 °C for 10 h in air for a high-density NZSP solid electrolyte.

This solid-state synthesis approach is simple and scalable. However, it often requires careful optimization of sintering parameters to minimize the formation of secondary phases and to achieve high ionic conductivity. The as-prepared NZSP pellets were stored in an argon-filled glove box prior to further characterizations and electrochemical studies.

2.3.6 Synthesis of Al and S-modified LLZO

Al-doped LLZO with a nominal composition of $Li_{6.25}La_3Al_{0.25}Zr_2O_{12}$ was first synthesized using the alanine-assisted auto-combustion method as described in ***Section 2.3.1***. $Al(NO_3)_3$ was introduced as a dopant precursor. The as-synthesized powder was further calcined and sintered to measure the various electrical and electrochemical process properties.

Based on this Al-stabilized cubic LLZO matrix, sulfur substitution was further attempted at the oxygen sites, yielding $Li_{6.25}La_3Al_{0.25}Zr_2O_{12-x}S_x$ with x = 0.01 to 0.1. The same combustion synthesis process was used to synthesize the Al and S-modified LLZO. Li_2S was introduced as the source material of S in the combustion synthesis process. A series of compositions was synthesized, and optimization was found in the intermediate range of 0.02-0.07. Although direct sulfur incorporation could not be confirmed by elemental analysis, changes in XRD patterns, surface morphology, zeta potential, and ionic conductivity indicated a strong influence of S addition on phase purity and surface chemistry. In particular, the impurity profile was markedly altered compared to Al-only LLZO, suggesting a role of sulfur in modifying grain boundary or surface reactions during synthesis

2.4 Development of Solid Hybrid Electrolytes via Liquid Therapy

One of the major challenges in solid-state battery development for the oxide-based solid electrolytes (LLZO and its derived) is their inherently high grain boundary resistance and poor interfacial wettability with lithium metal. These lead to inhomogeneous and non-uniform current distribution across the interface, unstable solid electrolyte interphase (SEI) layer, and, as a result, lithium dendrite penetration was observed. To tackle such issues in metal batteries, a solid hybrid electrolyte (SHE) approach was introduced. SHE was fabricated by infusing a viscous gel termed as solvated ionic liquid (SIL) into the solid LLZO matrix. This strategy helps to retain the robust structural framework of LLZO and maintain good interfacial stability as offered by SIL. Thus, a quasi-solid-state system was formed, which provides much improved electrochemical performance.

2.4.1 Preparation of Solvated Ionic Liquid (SIL)

The SIL was prepared inside an argon-filled glove box by dissolving lithium bis(trifluoromethanesulfonyl)imide (LiTFSI) in tetraglyme (G4) in a 1:1(w/v%) molar ratio under continuous stirring until a homogeneous viscous gel was obtained. This solvated ionic liquid behaves like a room-temperature ionic liquid, where Li^+ ions are strongly coordinated by the ether oxygens of tetraglyme, forming a $[Li(G4)]^+$ solvation complex. The remaining

$TFSI^-$ anions remain either loosely associated or dissociated. The presence of such mobile species provides fast Li-ion pathways and improves wettability at the electrolyte/electrode interface.

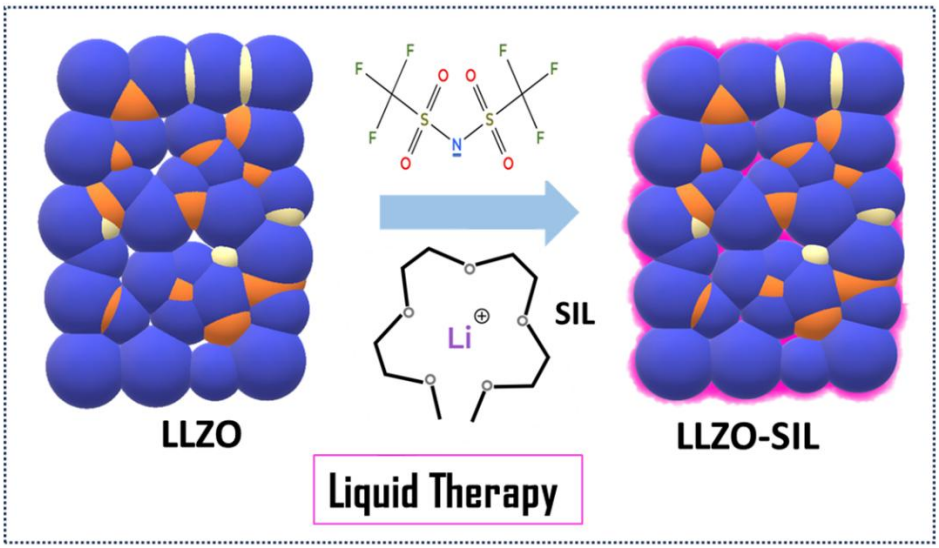

Figure 2.8 Liquid Therapy via solvated ionic liquid in LLZO-based material for metal batteries.

2.4.2 Liquid Therapy in LLZO Matrices

All synthesized LLZO variants, including pristine LLZO, Ga-doped LLZO, neck-fused LLZO, plate-like LLZO, interconnected LLZO, grain boundary engineered LLZO, and surface-modified LLZO (NH_4F treated), were infused with SIL (***Figure 2.7***). In a typical process, the sintered and polished pellets were immersed in the viscous SIL gel for approximately 2 h. The uptake of SIL into the pellet was measured gravimetrically and was found to be ~5-18 wt% across all variants. This indicates uniform infiltration through grain boundaries and open porosity of the garnet framework.

This SIL infusion into the LLZO matrix results in the formation of solid hybrid electrolytes (SHEs) that provide dual characteristics.

- Mechanical strength and thermal stability due to the solid LLZO backbone.
- Interfacial wettability with ion-conduction channels from the SIL phase throughout the bulk LLZO.

Thus, this dual introduction is further termed as “Liquid Therapy” in metal batteries.

The systematic use of SIL across pristine, engineered, and surface-modified LLZO matrices enables a direct performance comparison. This also highlights the influence of microstructure, grain boundary chemistry, and surface treatments on Li-ion transport and electrochemical stability. Thus, the SIL-LLZO hybrid approach addresses interfacial limitations, which is the key issue in solid-state metal batteries. Thus, it serves as a versatile platform to evaluate the effectiveness of different LLZO engineering strategies under practical battery-relevant conditions.

2.4.3 Extension to NZSP Solid Electrolyte

The SIL strategy was also broadened to other metal batteries in the present thesis work. In this direction, an exploratory study was also conducted on NASICON-type $Na_3Zr_2Si_2PO_{12}$ (NZSP). For this, a 1M $NaPF_6$ solution in tetraglyme was used as the wetting medium. Unlike LLZO, NZSP shows very low uptake (<2 wt%) due to its high relative density (>95%). The modified NZSP still showed superior Na-metal interfacial stabilization compared to untreated pellets. This study uncovers the potential of liquid-assisted stabilization or liquid therapy in other solid electrolyte systems.

2.5 Composite Membrane

Solid electrolytes or SIL-modified solid hybrid electrolytes deliver high bulk lithium ionic conductivity and excellent interfacial stability with Li metal. However, their inherent brittleness and poor processability always restrict their application in device integration. On the other hand, solid polymer electrolytes (SPEs) are ideal candidates for metal batteries, which offer flexibility, stability, high ionic conductivity, and compatibility with lithium metal. The fabrication process is also industry-friendly and has great potential for scaling up. However, poor ionic conductivity at room temperature and limited electrochemical stability against Li metal in long cycling hinder their successful application. To bridge these gaps, a scalable and versatile pathway towards flexible metal batteries is introduced by developing a composite membrane.

Three major classes of composite membranes were explored in this thesis work. Firstly, a paper-based composite membrane for high-performance metal ion batteries was studied preliminarily. Secondly, the dual-polymer-based composite membrane for metal batteries, and thirdly, the paper-polymer-based electrolyte for flexible batteries. In all three systems, Ga doped LLZO particles were incorporated to find the role of solid electrolyte material in these

composite structures. The main advantages of this system are mostly underlying two factors: the garnet filler, which contributes fast Li^+ transport pathways and thermal robustness, and the polymer or paper substrate provides structural flexibility, processability, and improved interfacial adhesion. The distribution and interaction of LLZO particles within these matrices are also expected to disrupt polymer crystallinity, which enhances the segmental motion and Li^+ mobility of the polymer matrix.

2.5.1 LLZO incorporated paper-based composite membrane

By impregnation of LLGZO, the present study aims to transform the paper substrate from a passive separator into a high-performance separator. This approach improves ionic conductivity, Li-ion transference, and reinforces the mechanical framework of the paper fibers. This interaction provides better electrolyte affinity and more stable electrochemical performance compared to base paper and inert Al_2O_3-loaded membranes.

Figure 2.9 *Digital image of the in-house designed semi-automated separator fabrication machine. (A) Loading section for cellulose-based commercial paper rolls, (B) coating unit, (C) upper infrared drying chamber, (D) lower infrared drying chamber, and (E) final separator output in roll format.*

The Ga doped LLZO (LLGZO) is prepared using an alanine-assisted auto combustion synthesis process as described in ***Section 2.3.2*** in this chapter. The ash synthesized powder was calcined at 900°C for 10h and used without any modification. The calcined LLGZO powder incorporated paper separator was fabricated in continuous "roll-to-roll" form using an industry-compatible dip-coating technique with an in-house developed double-decker coating machine (as presented in ***Figure 2.9***). Commercial cellulose paper of 20 µm thickness and ~65% porosity was used as the base substrate. Prior to coating, the paper roll (62 mm wide, 100 m length) was dried overnight at 80 °C in a vacuum oven to eliminate residual moisture.

For the coating suspension, a solution of 5.0 wt% PVDF was prepared in N-methyl-2-pyrrolidone (NMP) at 70 °C with continuous stirring (400 rpm) for 6 h. To this solution, 30 wt% of finely milled Ga-doped LLZO powder (relative to polymer weight) was gradually introduced, followed by ultrasonication for 30 min and repeated stirring to ensure homogeneity. The resulting polymer–ceramic slurry was uniformly deposited on both sides of the dehydrated cellulose paper using the dip-coating machine, with simultaneous in-line infrared drying to remove solvent. The coated paper was subsequently compacted and collected as continuous rolls. It is worth mentioning here that the optimization process of Ga doped LLZO incorporated paper separator was already explored in our publication with the pristine LLZO, where the 30wt% concentration was found to be optimum.

The final LLGZO-incorporated paper separator, designated as G03, exhibited a uniform thickness of 20 ± 2 μm. For comparison, a control separator containing 30 wt% Al_2O_3 (A03) and an uncoated base paper were also prepared by the same procedure.

2.5.2 Dual Polymer-LLZO-based composite membrane

Cellulose has some intrinsic limitations, such as fiber inhomogeneity, mechanical anisotropy, and poor compatibility with lithium metal anodes, which restrict its application in next-generation metal batteries. Composite solid polymer electrolytes (CSPEs), which integrate polymer matrices with active garnet-type fillers, provide a versatile platform to address these challenges. In this context, dual-polymer-based CSPEs incorporating Ga-doped LLZO were developed to synergistically combine the mechanical stability of PVDF-HFP, the ionic transport of PEO, and the active role of LLZO fillers. The following section presents their structural, electrical, and electrochemical characteristics in detail.

A simple solution casting method was utilized to develop PVDF-HFP/PEO/LLGZO-based CSPE. To optimize the concentration of LLGZO (calcined at 900°C), in the duo polymer matrix, a series of CSPEs is prepared using 0.9g of PVDF-HFP, 0.1g of PEO, and 0.5g of LiTFSI, with various concentrations of LLGZO (0, 5, 10, 15 wt%). These components are mixed and uniformly dispersed subsequently under stirring at a 45-55°C temperature. The dispersed solution was cast onto the miller paper in an automated casting machine. The CSPE was then carefully peeled off after being kept in a vacuum oven overnight.

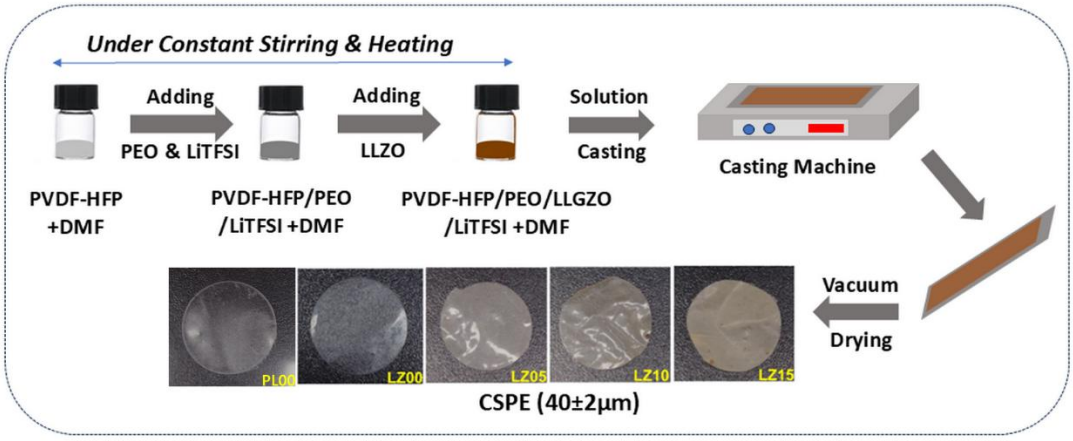

Figure 2.10 *Schematic representation of the fabrication process for dual-polymer-based electrolyte CSPEs via the solution-casting method, with digital images of various CSPEs*

The concentration of LLGZO was set at 0 (LZ00), 5 (LZ05), 10 (LZ10), and 15 (LZ15) wt% of the total weight of polymers. To check the effect of the duo-polymer matrix, a CSPE (PL00) is also developed using 1 g of PVDF-HFP and 0.5g of LITFSI. It is worth mentioning here that the PVDF-HFP: PEO ratio is set in this study at 9:1 to balance between ionic conductivity and mechanical strength. The thickness of all the CSPEs was found to be 40±2 µm. The CSPE films were prepared and cast several times, keeping the preparation conditions the same, to check their reproducibility, and all the physico-chemical and electrochemical parameters were fully reproducible for the CSPEs prepared at different times. The preparation step and digital image of all the CSPEs were represented in ***Figure 2.10***.

2.5.3 Paper-Polymer-LLZO Composites Membrane

Cellulosic paper substrate has excellent porosity, electrolyte affinity, and mechanical reinforcement. But it suffers from fiber inhomogeneity, anisotropic strength, and limited compatibility with lithium metal. Similarly, composite polymer solid electrolytes (CSPEs) deliver excellent flexibility and interfacial adhesion. However, the mechanical strength, processability, and dendrite suppression were limited for the CSPE system. To maximize the benefits of both systems, a paper-polymer composite was introduced. It combined the CSPEs slurry incorporated into a sustainable paper matrix for a single, mechanically robust, multifunctional electrolyte.

This strategy converts the passive paper substrate into a Li-ion active paper-polymer electrolyte membrane. The Ga-doped LLZO (LLGZO) fillers were used as fast Li^+ conduction pathways and stabilize the interfacial incompatibility. The dual-polymer matrix reduces crystallinity, enhances flexibility, and promotes homogeneous dispersion of active particles.

For fabrication, Ga-doped LLZO was synthesized using the alanine-assisted auto-combustion route as discussed in ***Section 2.3.2***, calcined at 900 °C for 10 h, and directly used as filler. The dual-polymer-LLZO solution was prepared as discussed in the earlier ***section 2.5.2***. An optimized 10wt% LLGZO particle was used as filler in the dual polymer matrix. After ultrasonication and prolonged stirring, the slurry was uniformly coated onto both sides of a pre-dried cellulose paper substrate (20 μm thick, ~65% porosity) using an in-house designed semi-automated "double-decker" casting machine (***Figure 2.9***). After initial drying by the infrared drying chambers, the paper-polymer-LLZO composite membrane was transferred to a vacuum oven. The coated paper was subsequently compacted and collected in a continuous roll with a uniform thickness of ~60 ± 2 μm. This multifunctional configuration provides a promising platform for next-generation solid-state and flexible lithium batteries.

2.6 Cell Fabrication

2.6.1 Symmetric Cells

To investigate the interfacial stability and long-term Li plating/stripping behavior, symmetric cells (Li/Electrolyte/Li) were fabricated. LLZO-based solid hybrid electrolytes (SIL-infused pristine, doped, engineered, and surface-modified as described in ***Sections 2.3*** and ***2.4***) were used as electrolytes (diameter~17-18mm, thickness 0.8-1.0mm). For a paper-based membrane (thickness~20±2μm), a commercial 1M $LiPF_6$ in ethylene carbonate (EC) and dimethyl carbonate (DMC) (1:2) soaked paper separator was used. A dual polymer composite membrane (40±5μm) or hybrid paper polymer membrane (60±5μm) was directly used as an electrolyte in the fabrication process without further modification. All cell assembly was performed inside an Ar-filled glovebox (O_2 and H_2O < 0.1 ppm) to prevent reaction of Li/solvents with ambient air or moisture. Commercial Li foils (100 μm thickness) were cut into discs (15mm diameter) and carefully stacked on both sides of the electrolyte pellet/membrane. The stack was crimped into CR2032-type coin cells with stainless steel spacers and spring components to maintain intimate contact. A moderate pressure of ~800-1200psi was applied during assembly to minimize interfacial voids, ensuring reproducible electrochemical performance. These symmetric cells were used for impedance spectroscopy, DC polarization, critical current density (CCD) determination, and long-term cycling stability tests. Other than this, cells with Li-ion blocking electrodes, such as SS, were fabricated for the measurement of ionic and electronic conductivity for solid hybrid electrolyte and composite electrolyte. For bulk solid electrolyte pellets (diameter 10-12mm, thickness 0.9-1.2mm), both sides of the pellet are

coated with Au via a gold sputtering machine. Then the pellets were dried in a vacuum at 90°C and further used for EIS measurement. For NZSP solid electrolyte (diameter 18mm, thickness 0.6mm), Na metal was attached with the same procedure, and a 1M $NaPF_6$ solution in tetraglyme was used as the wetting medium for long cycling stability and impedance study.

2.6.2 Full Cells

To evaluate the practical application of developed electrolytes, full cells (Li/Electrolyte/Cathode) were fabricated. Lithium metal was used as an anode, and commercial LiFePO4 (LFP), LiMn2O4 (LMO), and LiNi1/3Mn1/3Co1/3O2 (NMC111) were used as cathodes in different studies. Homogeneous cathode slurries were prepared by mixing the active material (80 wt%), Super P carbon (10 wt%), and PVDF binder (10 wt%) in NMP. Then, the slurry was cast onto the aluminum foil using a doctor blade and dried at 100 °C overnight under vacuum. The active mass of various cathodes was discussed in the specific chapter. The dried cathode sheets were roll-pressed, punched into discs, and transferred into the glovebox. Coin-cell (CR2032) were assembled, depending on the testing requirements. A drop of liquid electrolyte (<20µl) is added at the cathode side during cell fabrication with a solid hybrid electrolyte (diameter 17-19mm, thickness 0.8-1.0mm). For the paper separator membrane, commercial liquid electrolyte ($LiPF_6$) is used. No liquid electrolyte is used in a dual polymer-based solid composite membrane. For NZSP, commercial NVP as a cathode and Na metal as an anode are used. The NVP cathode was cast in the same ratio (80:10:10), and 1M $NaPF_6$ solution in tetraglyme was used as the wetting medium.

2.7 Characterization Techniques

A comprehensive set of structural, physico-chemical, electrical, and electrochemical techniques was used to investigate the functional properties of the developed electrolyte in metal batteries. An effort was made to correlate the synthesis route and processing strategies with microstructure, ion-transport, interfacial stability, and post-electrochemical studies. In this way, an end-to-end correlation was established, starting from material design to real cell application and diagnostics.

2.7.1 Structural, Morphological, and Surface characterization techniques

2.7.1.1 X-ray Diffraction

X-ray diffraction (XRD) is a non-destructive fundamental tool in material science and studies the crystal structure of any material. It basically works on the principle of constructive interference of X-rays scattered by the periodic atomic planes. The resultant diffraction pattern provides information about crystallinity and phase formation of the material based on Bragg's law. In this study, the XRD was used to evaluate the phase stabilization of the cubic polymorph, along with the identification of various impurity phases that originate during synthesis, the calcination process, or after electrochemical studies.

In the present study, XRD was carried out using an X′pert Pro MPD XRD system (PANalytical, Netherlands) with nickel-filtered Cu Kα (λ = 1.5406 Å) radiation and irradiated at 40 kV and 40 mA with a step size of 0.02°/Sec. The phase quantification was further analyzed using Rietveld refinement with PANalytical HighScore Plus with the PDF-4+/PDF-5+ database for referencing. Crystallinity Index (CI) of the CSPE film was calculated from the XRD pattern using the Gaussian peak fitting method by using the following equation [1,2]:

$$Crystallinity\ Index\ (CI) = \frac{A_c}{A_c + A_a} \times 100\% \quad (2.1)$$

Where A_c, A_a, and (A_c+A_a) are the area of the crystalline peaks, amorphous peaks, and the total sum of all the crystalline and amorphous peaks combined.

So, in general, the CI can be calculated from the XRD pattern by using the following equation:

$$Crytallinity\ Index = \frac{Area\ of\ a\ the\ targeted\ peak}{Area\ of\ all\ the\ crytalline\ and\ amorphous\ peaks} \quad (2.2)$$

2.7.1.2 SEM, FESEM, and TEM

Scanning Electron Microscopy (SEM), Field Emission Scanning Electron Microscopy (FESEM), and Transmission Electron Microscopy (TEM) were used to study the morphology and microstructural features of the synthesized electrolyte materials. SEM basically works by scanning a focused electron beam over the sample surface. It produces microscopic images from the secondary and backscattered electrons to reveal the grain size distribution, surface porosity, and overall morphology. FESEM is the advanced version of SEM, which used a field emission source. It provides a finer beam with much higher resolution and depth of field. This current study provides detailed observations about neck-fusion, plate-like structures, or other engineered morphology and filler distribution in composite membranes. Energy-dispersive X-ray spectroscopy (EDX) coupled with FESEM was also used for elemental mapping or line scanning, extremely beneficial for the visualization of any impurity distribution at the grain

boundaries. TEM, on the other hand, transmits a high-energy electron beam through an ultrathin specimen, giving direct information on crystallinity, lattice fringes, and local structural defects at the nanoscale. Together, these microscopic techniques provides critical insights into grain connectivity, interfacial features, and particle distribution, which were directly correlated with the electrochemical performance of LLZO-based electrolytes and their composites before and after electrochemical studies.

In the present study, SEM was performed using Phenom TM, Model Pro-X, USA. Whereas, FESSEM and TEM were performed using a Supra VP35 Carl Zeiss model from Germany and a Tecnai G2 30ST (FEI) microscope operated at an accelerating voltage of 300 kV.

2.7.1.3 Fourier Transform Infrared Spectroscopy

Fourier Transform Infrared Spectroscopy (FTIR) is a spectroscopy technique used to find the bond vibration between various functional groups. It was based on the absorption of infrared light by molecular vibrations, which correspond to specific chemical bonds. Each functional group shows characteristic peaks, allowing identification of bonding environments. In this work, FTIR was used to study the various metal-oxygen vibrations. The presence of different surface impurities can be detected by studying the FTIR spectra. It also helps to understand polymer–filler interactions in composite membranes. In the thesis work, FTIR was performed using a JASCO FTIR-6300 spectrometer.

2.7.1.4 Raman Spectroscopy

Raman spectroscopy relies on inelastic scattering of monochromatic light (Raman effect) where part of the light shifts in frequency depending on the vibrational modes of the material. This technique provides structural and bonding information as similar to FTIR. In this thesis, Raman spectroscopy was used to probe the garnet stabilization and detection of any secondary impurity phases. It was performed using using a Horiba LaBRam HR Evolution Raman spectrometer under a 488 nm Ar ion laser of 20 mW power.

2.7.1.5 X-ray Photoelectron Spectroscopy

X-ray Photoelectron Spectroscopy (XPS) is generally a surface-sensitive technique. It is based on the photoelectric effect. An incident X-rays eject core electrons from atoms and the measured binding energies. This reveals the chemical composition and oxidation states within the top few nanometers of the surface. In this work, XPS was used to check the decomposition product after cycling at the electrode/electrolyte interface. The surface impurities are also

examined by this method. In this work, X-ray Photoelectron Spectroscopy (XPS) measurements were performed by using a monochromatic Aluminum K_alpha focused X-ray (1486.6 eV) beam and a multi-channeltron hemispherical electron energy analyzer (PHI 5000 VERSAPROBE II, Physical Electronics). One set of data was acquired, and the next set of data was taken after 10-15 minutes of sputtering with Ar ion at 1 keV.

2.7.1.6 Particle size and Zeta Potential

Dynamic light scattering (DLS) was used to determine the agglomerated size distribution of the synthesized LLZO powders in suspension. The technique is based on the scattering of incident laser light by particles undergoing Brownian motion. The time-dependent fluctuations in scattered intensity are analyzed to calculate the hydrodynamic diameter of agglomerates. This measurement provided insights into the degree of agglomeration present in the powders after synthesis and grinding, which is critical for understanding their sintering and densification behavior.

In parallel, zeta potential measurements were performed to evaluate the surface charge of LLZO particles dispersed in ethanol. Zeta potential is an indicator of suspension stability, with higher absolute values corresponding to better electrostatic stabilization and a lower tendency for agglomeration. The combined DLS and zeta potential data were thus used to assess the agglomerated size distribution and dispersion stability of LLZO powders, which influence subsequent processing and microstructural evolution. All measurements were carried out using a Malvern Zetasizer Nano series instrument after ultrasonication-assisted dispersion of the powders in ethanol or DMF solvent.

2.7.2 Physico-Chemical

2.7.2.1 Proton Nuclear Magnetic Resonance

Proton nuclear magnetic resonance (^{1}H NMR) spectroscopy was used to investigate the coordination environment of alanine complexes with lithium, lanthanum, and zirconium precursors. The technique is based on the interaction of nuclear spins with an applied magnetic field and radiofrequency pulses, which provides information about the chemical environment of hydrogen atoms. In this work, the nature of the complexes formed between alanine and different metal ions (La and Zr) was studied using ^{1}H NMR spectroscopy (Bruker-FT300 MHz spectrometer) by dissolving alanine and different metal nitrates in a D_2O solvent. These results

were used to gain insights into the precursor chemistry and the role of alanine in controlling phase evolution and dopant incorporation in LLZO.

2.7.2.2 Thermogravimetric and Differential Thermal Analysis

Thermogravimetric analysis (TGA) is a powerful thermal technique that actually measures the weight loss of a sample as a function of temperature or time under a controlled atmosphere. It provides important information on dehydration, evaporation, decomposition, and phase transitions of a material. On the other hand, Differential thermal analysis (DTA) is recorded simultaneously to identify endothermic and exothermic events corresponding to chemical or structural transformations.

In this work, TGA/DTA was used extensively to study the thermal behaviour of alanine-nitrate gel, exo-template, and LLZO ash powder. The thermal stability of polymer electrolytes, composite solid polymer electrolytes (CSPEs), and solvated ionic liquid-infused systems was also explored. TGA/DTA was performed using a NETZSCH thermal analyzer (Germany).

2.7.2.3 Density

The density of sintered pellets was evaluated using both geometrical calculations and Archimedes' principle. In the geometrical method, the mass (m) of the dried pellet was measured using a high-precision balance. Then the volume(V) was calculated from its dimensions. The geometrical density (ρ_{geo}) was then calculated using the relation,

$$\rho_{geo} = \frac{m}{V} = \frac{m}{\pi r^2 h} \tag{2.3}$$

Where r and h are the radius and thickness of the cylindrical pellet.

The density of sintered LLZO pellets was also measured using the Archimedes' principle with toluene as the immersion medium. Initially, the dried mass of the pellet (m_{dry}) was recorded after keeping the pellet at about 150ºC. The pellets were then soaked in toluene for 24 h to fill the available pores. The soaked mass in air (m_{soaked}) was measured and recorded. Finally, the apparent mass of the soaked pellet when suspended in toluene ($m_{immersed}$) was recorded. The bulk density was then calculated according to the relation:

$$\rho_{arc} = \frac{m_{dry}}{m_{soaked} - m_{immersed}} \rho_{toluene} \tag{2.4}$$

Where $\rho_{toluene}$ is the known density of toluene and depends on the temperature.

The relative density was measured by dividing the theoretical density of the solid electrolyte material. The calculated relative density was used to correlate the sintering behaviour with electrical and electrochemical performance.

2.7.2.4 Dilatometry

Dilatometry was generally used to study the dimensional changes of LLZO pellets during heating. It gives important information about the sintering behavior and densification kinetics of the solid electrolyte material. In this technique, the change in specimen length was continuously monitored as a function of temperature (T). The relative shrinkage is calculated from the initial length of the pellets. The shrinkage curves provide information about the onset temperature of densification, grain growth, and the maximum shrinkage rate. In the present work, dilatometry was used to optimize the calcination and sintering conditions of LLZO pellets by identifying the temperature window for effective densification while minimizing lithium volatilization. The results were further correlated with the relative density and microstructural features to establish a relationship between sintering kinetics, pellet densification, and ionic transport properties. Dilatometry was performed in Netzsch STA 409C (Simultaneous Thermal Analyzer).

2.7.2.5 Tensile Tests

The tensile properties of various composite membranes were investigated to evaluate their mechanical robustness and flexibility, and their ability to resist deformation under applied stress. Rectangular strips of membranes were cut to uniform dimensions and tested to obtain stress-strain behavior, from which tensile strength was calculated. An average of five specimens taken from different positions of each membrane was analyzed to minimize sample-to-sample variation. The mean curve with standard deviation was presented to ensure clarity and reproducibility. The tensile measurements were carried out using a Universal Testing Machine (Model 5500R, INSTRON, UK) equipped with a 1 kN load cell and operated at a crosshead speed of 10 $mm \cdot min^{-1}$.

2.7.2.6 Gurley Value

The Gurley test was employed to evaluate the air permeability and porosity of the fabricated paper-based separators. This method measures the time required for a fixed volume of air (typically 100 mL) to pass through a given area of the membrane under standardized pressure. A higher Gurley number corresponds to lower porosity and reduced gas permeability, whereas

a lower value indicates higher porosity and easier air flow through the separator. In this work, the Gurley values were used to estimate pore size distribution and connectivity, which were further correlated with electrolyte uptake and ionic conductivity. The measurements were performed using a Gurley precision instrument (Model 4110N).

2.7.2.7 Liquid Uptake

Electrolyte uptake is an important parameter that reflects the ability of membranes to absorb and retain liquid electrolyte, which in turn governs ionic conductivity and interfacial wettability. For polymer-based separators, 19 mm diameter circular disks of each sample were cut and soaked in a standard liquid electrolyte (1M $LiPF_6$ in Ethylene carbonate (EC): Dimethyl carbonate (DMC) (1:2)) for 2 hours inside a glove box. The electrolyte uptake was calculated using the following equation:

$$Electrolyte\ Uptake = \frac{W_{wet} - W_{dry}}{W_{dry}} \times 100\% \quad (2.5)$$

where Wdry and Wwet are the respective separator weights before and after the absorption of liquid electrolyte.

A similar protocol was followed for quantifying solvated ionic liquid (SIL) uptake in hybrid LLZO electrolytes. Polished LLZO pellets were immersed in the SIL for 2 h inside the glove box. Then the uptake was calculated gravimetrically. The uptake values were expressed in weight percentage relative to the dry pellet mass and were typically ~5-18 wt% depending on the modification made on the LLZO electrolyte. This measurement was essential to evaluate the role of SIL infusion in improving interfacial contact and establishing continuous Li^+ conduction pathways within the hybrid electrolyte. All weighing was performed using a high-precision analytical microbalance (Model AUW220D, Shimadzu, Japan).

2.7.3 Electrical and Electrochemical Techniques

2.7.3.1 Electrochemical impedance spectroscopy

Electrochemical impedance spectroscopy (EIS) was generally used to evaluate the ionic transport behavior of the developed electrolytes. The technique involves by applying a small alternating current (AC) perturbation over a wide frequency range and recording the corresponding voltage response. This provides information about bulk resistance, grain boundary contribution, and interfacial polarization. The data are typically represented as Nyquist plots (Z′ VS -Z″), where the high-frequency intercept corresponds to bulk electrolyte

resistance, semicircular arcs reflect grain boundary and charge-transfer contributions, and the low-frequency tail is associated with electrode polarization or diffusion kinetics. In this work, symmetric cells with Li-ion conductive (Li) or blocking (SS, Au, Ag) electrodes were fabricated depending on the measurement requirement. EIS was used to calculate the total ionic conductivity as well as the interfacial resistance. The bulk resistance was approximated from the intercept on the real Z′ axis at high frequencies, and Li^+ ion conductivity was calculated using the relevant equation.

$$\sigma = \frac{1}{R_b} \times \frac{l}{a} \quad (2.6)$$

The ionic conductivity (σ) was assessed using the bulk resistance (R_b) of the cell, along with the thickness of the composite membrane (l) and the area of the working electrode (a).

The equivalent circuit fitting was performed using ZView software to separate contributions from bulk, grain boundary, and electrode processes. Electrochemical impedance spectroscopy (EIS) was carried out in a ZIVE SP1 or Autolab across a frequency range of 1 mHz to 1 MHz at room temperature. EIS was recorded in each fabricated cell after kept it few hours for stabilization.

2.7.3.2 Distribution of Relaxation Times

Electrochemical impedance spectroscopy (EIS) helps analyze the different electrochemical processes during electrochemical cycling. However, resolving electrochemical processes from EIS spectra using conventional equivalent circuit models (ECMs) is challenging due to overlapping time constants, which can lead to misinterpretations[3–6]. In contrast, the distribution of relaxation times (DRT) method simplifies EIS analysis by distinguishing individual electrochemical processes through unique time constants.

The impedance response $Z(\omega)$ of an electrochemical system can be expressed as an integral of relaxation processes over a continuous distribution of characteristic times τ,

$$Z(\omega) = R_\infty + \int_0^\infty \frac{\gamma(\tau)}{1+j\omega\tau} d ln\tau \quad (2.7)$$

Where, R_∞ is the ohmic resistance (high-frequency intercept), $\gamma(\tau)$ is the distribution function of relaxation times, τ is the relaxation time and ω is the angular frequency is described as,

$$\omega = 2\pi f \quad (2.8)$$

The function $\gamma(\tau)$ reveals the intensity of individual relaxation processes. The sharper peaks correspond to distinct resistive or capacitive processes, while broader peaks indicate overlapping processes. In general, the high-frequency peak corresponds to bulk ionic transport in the electrolyte, and the mid-frequency peak corresponds to grain boundary or interphase contribution. The Low-frequency peak corresponds to the electrode-electrolyte interface polarization and charge transfer.

To decouple the electrochemical process, EIS was also taken at different SOC and DOD levels using ZIVE SP1 over a frequency range of 0.01 Hz–1 MHz by applying 50 mV AC amplitude. The distribution of relaxation time (DRT) was used to decouple the interfacial kinetics [7]. The open-source MATLAB-based software and the DRTtools algorithm were used to derive the DRT from impedance data [8]. Gaussian method with a second-order Tikhonov regularization was applied, and the regularization parameter was set at 0.0001. Real and imaginary components of the EIS data were duly fitted, and the inductive part was ignored. The resulting intensity distributions are further compiled into a two-dimensional map in MATLAB software, where the x-axis represents relaxation time (τ), the y-axis denotes cycling time (h), and the color scale corresponds to normalized DRT intensity. Fitting of DRT is further analyzed in a custom script in MATLAB software. The evolution of resistance was also shown in 2d contour map.

2.7.3.3 DC Polarization

DC polarization experiments were performed to separately evaluate the ionic transference number and the electronic conductivity of the developed electrolytes. For ionic transference number measurements, symmetric Li/electrolyte/Li cells were fabricated to allow reversible Li^+ exchange. When a small DC potential (ΔV) is applied, the current response initially contains contributions from both ionic and electronic charge carriers. With time, polarization of Li^+ at the electrode-electrolyte interfaces leads to a decay in current until a steady state is reached. The ionic transference number was calculated using the Bruce-Vincent-Evans (BVE) equation[9], as follows,

$$t_{Li^+} = \frac{I_{SS}(\Delta V - I_0 R_0)}{I_0(\Delta V - I_0 R_0)} \quad (2.9)$$

Where, I_0 and I_{SS} are the initial and steady state current before and after polarization, respectively, and R_0 and R_{SS} are the electrolyte/electrode interfacial resistance before and after polarization, respectively, with an applied DC polarization voltage ΔV of 10 mV.

To further investigate the electronic conductivity of the hybrid electrolyte, a higher DC potential (0.5 V) was applied in SS/SS symmetric cells. In this configuration, the SS electrodes act as ion-blocking contacts, and hence the steady-state current originates primarily from electronic leakage. The electronic conductivity was calculated using the relation,

$$\sigma_e = \frac{I_{SS} \times L}{A \times V} \tag{2.10}$$

where Iss is the steady-state current, L is the electrolyte thickness, A is the electrode-electrolyte contact area, and V is the applied DC potential. This analysis enabled quantification of electronic leakage pathways and correlation of various modifications in the LLZO matrix with suppression of dendrite growth or critical current density. All DC polarization experiments were carried out using a ZIVE SP1 workstation.

2.7.3.4 Linear sweep voltammetry

Linear sweep voltammetry (LSV) was generally used to evaluate the electrochemical stability window of the developed electrolytes for successful application against high voltage cathode material. In this technique, the potential of the working electrode is swept linearly with time relative to the counter/reference electrode while recording the current response. The potential at which a sharp rise in current is observed corresponds to the onset of electrolyte decomposition. thereby defining the oxidative stability limit.

In this study, LSV measurements were carried out using asymmetric Li/electrolyte/stainless steel (Li/SS) cells, where lithium metal served as both the counter and reference electrode and stainless steel acted as the working electrode. The applied potential was swept from the open-circuit voltage to 7 V vs. Li/Li^+ at a scan rate of 10 $mV \cdot s^{-1}$. The resulting current-voltage response was analyzed to determine the electrochemical window of the solid hybrid electrolytes. All LSV experiments were performed using a ZIVE SP1 electrochemical workstation.

2.7.3.5 Critical Current Density

Critical current density (CCD), or maximum endurable current density of battery cycling without cell failure, is a crucial parameter for evaluating the efficacy of the solid electrolytes

(SEs) and determining the Li kinetics rate at the Li-solid state electrolyte (SSE) interface. Several parameters can influence a solid electrolyte's critical current density (CCD) [10]. Key internal factors influencing CCD include ionic conductivity, electronic conductivity, and density of the solid electrolyte. External factors such as stack pressure, sintering temperature, and measurement temperature significantly determine CCD and overall battery efficiency. In our study, all external factors were kept constant during the measurement of the CCD for different solid hybrid electrolytes, allowing the electrical properties of the solid electrolytes to influence the CCD values primarily. Here, with the increment of current density, the voltage due to polarization drop increases, and suddenly, after a few plating/stripping cycles, a spike is observed. This spike rapidly grows, resulting in a distortion in the voltage profile. The current density up to which such distortion does not appear can be termed the critical current density due to the soft short circuit. In our present study and our previous study, no hard short circuit is observed, which might be due to the presence of SIL at the Li metal/electrolyte interface.

To determine the CCD, symmetric cells with various hybrid electrolytes are fabricated and subjected to galvanostatic charge-discharge cycles at various current densities increased stepwise (typically in increments of 0.05-0.1 $mA \cdot cm^{-2}$), with each step maintained for 30 minutes charge and 30 minutes discharge. The CCD values obtained provided a direct measure of interfacial stability and the ability of the electrolytes to suppress lithium dendrite growth under practical operating conditions. The CCD was also measured in ZIVE SP1.

2.7.3.6 Symmetric Li/Li Cycling

Symmetric Li/electrolyte/Li cells were cycled galvanostatically to evaluate the long-term electrochemical stability and interfacial compatibility of the electrolytes with lithium metal. In this technique, equal and opposite currents are alternately applied to both the lithium electrodes, leading to repeated lithium plating and stripping across the electrolyte. The evolution of overpotential with cycling time provides direct information on the stability of the electrode-electrolyte interface, the resistance to dendrite formation, and the overall durability of the system.

In this study, symmetric cells were subjected to continuous plating/stripping cycles at fixed current densities for extended periods ranging from several hundred to over a thousand hours. The voltage response was recorded as a function of cycling time, and the absence of sudden short-circuiting or sharp voltage drops was taken as evidence of stable lithium deposition and dendrite suppression. The measurements were carried out using an Arbin automated battery

tester (Arbin Instruments, USA), and the data were further correlated with CCD values and post-mortem analysis to assess the reliability of the developed electrolytes under long-term operation. EIS was measured at ZIVE SP1 before and after the cycling test to decouple various electrochemical processes and to understand the impact of lithium dendrite penetration.

2.7.3.7 Galvanostatic Cycling of Full Cells

Galvanostatic charge-discharge cycling of full cells was performed to evaluate the practical electrochemical performance of the developed electrolytes under operating battery conditions. In this method, a constant current is applied during charge and discharge processes within a defined voltage window, and the cell voltage response is recorded as a function of capacity and cycle number. The cycling behavior provides key parameters such as specific capacity, coulombic efficiency, capacity retention, and interfacial stability, thereby serving as a direct assessment of the electrolyte's suitability in full-cell configurations.

The fabrication of a full cell using various types of electrolytes is already discussed in *Section 2.6.2*. The cells were stabilized, and EIS was taken after some time at ZIVE SP1. Then all the cells were cycled at various current densities within a potential range that depends on the cathode chemistry. For instance, for the Li/LMO cell, the voltage range is 3.0-4.5 V. The long-term cycling stability and capacity retention were analyzed to understand the impact of interfacial modifications. All galvanostatic cycling experiments were carried out using an Arbin automated battery testing system (Arbin Instruments, USA). An isothermal vacuum oven was used to maintain a temperature of 27ºC throughout battery cycling for a full cell with hybrid electrolyte (LLZO-SIL).

2.8 Data Analysis and Reliability

All electrochemical data were analyzed with the help of Microsoft Excel and Origin Software. The EIS data were fitted with Zview software using equivalent circuit modelling. To ensure reproducibility, each sample preparation and cell assembly was repeated at least three times for a specific developed electrolyte under identical conditions. Standard deviations and error bars were mostly reported wherever applicable. These measures ensure statistical reliability and minimize errors arising from batch-to-batch variations in synthesis and cell fabrication.

2.9 Flow of Work

The overall experimental flow in this thesis is presented schematically in ***Figure 2.10***. Starting from raw precursors, solid electrolyte powders were synthesized via auto-combustion, exo-

templating, or solid-state synthesis methods. These powders were calcined to get the desired phase and then processed into pellets or composite membranes. The fabricated electrolytes were subjected to a combination of structural, morphological, physico-chemical, and various electrical characterizations, followed by cell fabrication and testing in symmetric and full-cell configurations for practical applicability. Finally, advanced analysis tools such as DRT and post-mortem microstructural imaging, XPS analysis were used to correlate among various parameter.

2.10 References

1 E. Tarani, I. Arvanitidis, D. Christofilos, D. N. Bikiaris, K. Chrissafis and G. Vourlias, *J Mater Sci*, DOI:10.1007/s10853-022-08125-4.

2 M. Doumeng, L. Makhlouf, F. Berthet, O. Marsan, K. Delbé, J. Denape and F. Chabert, *Polym Test*, DOI:10.1016/j.polymertesting.2020.106878.

3 C. Plank, T. Rüther, L. Jahn, M. Schamel, J. P. Schmidt, F. Ciucci and M. A. Danzer, *J Power Sources*, DOI:10.1016/j.jpowsour.2023.233845.

4 R. Soni, J. B. Robinson, P. R. Shearing, D. J. L. Brett, A. J. E. Rettie and T. S. Miller, *Energy Storage Mater*, DOI:10.1016/j.ensm.2022.06.016.

5 A. Subhakumari, T. Thomas and N. P. B. Aetukuri, *ACS Energy Lett*, 2024, 9, 6109–6116.

6 Y. Lu, C. Z. Zhao, J. Q. Huang and Q. Zhang, 2022, preprint, DOI: 10.1016/j.joule.2022.05.005.

7 F. Ciucci and C. Chen, *Electrochim Acta*, DOI:10.1016/j.electacta.2015.03.123.

8 T. H. Wan, M. Saccoccio, C. Chen and F. Ciucci, *Electrochim Acta*, DOI:10.1016/j.electacta.2015.09.097.

9 J. Evans, C. A. Vincent and P. G. Bruce, *Polymer (Guildf)*, 1987, 28, 2324–2328.

10 S. Sarkar and V. Thangadurai, 2022, preprint, DOI: 10.1021/acsenergylett.2c00003.

CHAPTER 3

Pristine $Li_7La_3Zr_2O_{12}$: Exploring Aqueous-based Synthesis Route and Interfacial Engineering using Solvated Ionic Liquid

Summary & Graphical Abstract

Achieving the cubic phase of pristine LLZO via the solid-state route remains challenging due to Li volatility, secondary phase formation, and high sintering requirements. It often leads to poor ionic conductivity and unstable interfaces against the Li metal anode. In this chapter, an aqueous-based synthesis process was optimised using alanine as fuel to obtain cubic, microstructurally altered cubic LLZO. The role of surface impurities in electrical and electrochemical performances is explored in detail. Interfacial liquid therapy was introduced using a solvated ionic liquid (SIL) for improved Li wettability, reduced interfacial resistance, and enhanced ionic conduction across grain boundaries. Together, this synergistic approach demonstrated improved stability in symmetric cells, high coulombic efficiency, and improved tolerance against dendritic penetration. Thus, this chapter establishes the synergistic role of aqueous synthesis and interfacial liquid therapy to enhance faster Li-ion conduction as well as resistance to Li dendritic growth, providing a path for developing high-performance SSLMBs.

Objectives

1. Stabilize the cubic phase of pristine LLZO.
2. Origin and role of surface Impurities in the electrochemical process.

Strategy

Optimization of aqueous synthesis process with interfacial liquid therapy.

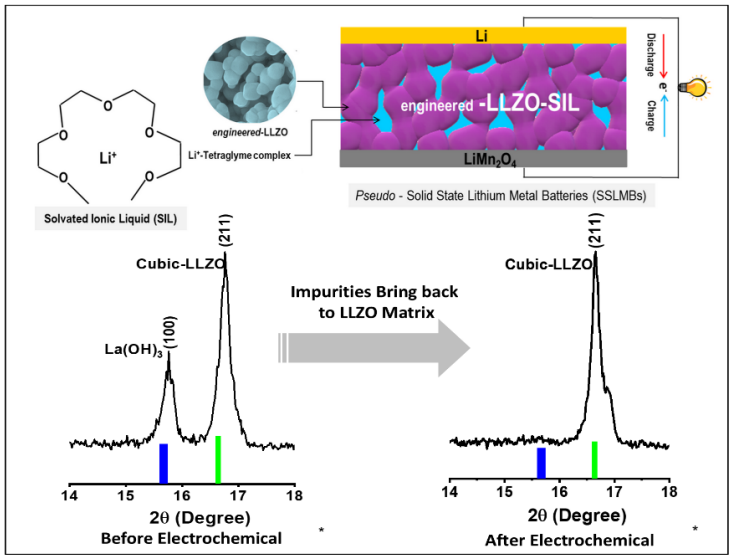

Figure 3.1 *Graphical abstract summarizing the effects of aqueous synthesis and interfacial liquid therapy on pristine LLZO-based solid electrolytes.*

3.1 Introduction

In the post-"Rocking-Chair" era of Lithium-ion battery technology, a new configuration of Solid State Lithium Metal Batteries (SSLMBs) now emerges with promise to deliver high energy and high power density batteries. Such a configuration relies on the use of Li-metal anode (3860 mAh g^{-1}) instead of conventional low capacity graphite (372 mAh g^{-1}) and a fast Li-ion conducting ceramic electrolyte instead of organic liquid electrolyte[1,2]. It is envisaged that the solid electrolyte can (i) eliminate safety issues which are major concerns of flammable liquid electrolytes, (ii) impede lithium dendritic growth, creating an opportunity to use a lithium metal anode, and (iii) control parasitic side reactions resulting in longer cycle life of the batteries[2,3]. Despite several advantages, making of All Solid-State Lithium Batteries (ASSLBs) using ceramic electrolytes still possesses serious scientific and engineering challenges related to establishing stable solid electrolyte-electrode interfaces.

One of the possible solutions is to build an electrolyte that can satisfy the benefits of both solid-state and liquid electrolytes[4]. Here, the concept of "hybrid electrolyte" comes into the picture. Therefore, by definition, the "Solid State" configuration could be renamed as pseudo-SSLMBs. While developing hybrid electrolytes, most commonly used solid electrolyte matrix is $Li_7La_3Zr_2O_{12}$ (LLZO). However, successful fabrication of hybrid electrolyte heavily depends on the nature of the solid electrolyte used in terms of their particle size, microstructure, sinterability, mechanical strength etc. While optimizing all those parameters, it was well noted that the engineered microstructure of the solid-state electrolyte can significantly influence the ion transport properties. While developing engineered LLZO, optimization of synthesis conditions and parameters were found crucial. Thus, an in-depth probing was necessary to regulate the microstructure in final LLZO powder.

Cubic LLZO, first proposed by Murugan et al.[5] in 2007, is conventionally synthesized following high temperature (1100-1200°C) solid state processing technique, but with a substantial risk of phase transformation from cubic $Li_7La_3Zr_2O_{12}$ to more thermodynamically stable $La_2Zr_2O_7$ pyrocholore structure[6,7]. In such high temperatures, lithium loss also becomes unavoidable, resulting in compositional inhomogeneity. Even in post synthesis condition, the exposure of single-phase cubic LLZO in ambient atmosphere reportedly triggers severe surface reaction involving Li^+/H^+ exchange and subsequent formation of Li_2CO_3 by the reaction with atmospheric CO_2[8]. The appearance of impurities such as La_2O_3, $LiAlO_2$, low conducting tetragonal-LLZO, pyrochlore type $La_2Zr_2O_7$ etc. were also common while synthesizing LLZO

material[6]. To tackle these problems, low-temperature synthesis processes were adopted to achieve cubic LLZO with sufficient ionic conductivity below 1000°C. Among various other wet chemical methods such as sol-gel[9], pechini[10], co-precipitation[11] etc, combustion synthesis of producing multi-component oxides are now considered as one of the low cost, less time consuming, single-step synthesis process which can results in desired powder properties ranging from nano to micro domain.

In this chapter, we first developed a first-of-its-kind hybrid electrolyte comprising morphologically engineered LLZO impregnated with SIL and extensively analyzed its electrochemical performance in pseudo-SSLM configuration against Li-metal anode and commercial $LiMn_2O_4$ cathode. The reason for using SIL in making a hybrid electrolyte is of great interest now for battery researchers. Equimolar mixtures of Li-salt (e.g., LiTFSI) and glymes (tri or tetraglyme) are most commonly used solvated ILs wherein a large complex cation $[Li(glyme)]^+$ is produced and functions as a weakly coordinating ion[12]. The use of SILs is reportedly more advantageous compared to conventional ILs; as Li-ions are already present in the ILs, clustering of anions around the Li+ can thus be avoided during electrochemical cycling. Thus, an attempt has been made here to impregnate SIL with in solid engineered-LLZO matrix for studying their synergetic effect in pseudo SSLMBs.

3.2 Experimental

3.2.1 Material Synthesis and Characterization

Pristine LLZO material is synthesized by the alanine-assisted auto combustion method. The detailed steps and optimization process were already discussed in ***Chapter 2***, ***Section 2.3.1*** and ***Section 2.3.3.1***. In short, aqueous nitrate precursors (Li, La, Zr) were mixed with alanine fuel and heated until auto-ignition produced a fluffy ash-like powder. The as-synthesized powder was calcined at 900 °C (10 h) and then pelletized and sintered at 1000 °C (10 h) to obtain cubic LLZO. Fuel-to-nitrate ratios were varied (F/N: 0.10, 0.15, 0.20, and 0.30) and optimized to tune the microstructure of pristine LLZO material. To record the temperature profile of the gel at various stages of the combustion process and also to measure the temperature surge during auto-ignition, an optical pyrometer (AMPROBE IR 720 IR thermometer) was used to collect the temperature readings, and with this, a time-dependent temperature profile was plotted. The nature of combustion at different fuel/nitrate ratios was photographed and presented. The detailed characterization techniques are already discussed in ***Section 2.7***. The calcined

powders thus obtained using different fuel-to-nitrate ratios (F/N) will be henceforth referred to in the text by the given codes, as described in ***Table 3.1***.

Table 3.1 *(F/N) ratio and corresponding sample codes of LLZO solid electrolyte Material.*

Fuel/Nitrate Ratio	Termed as
0.10	Ala010
0.15	Ala015
0.20	Ala020
0.30	Ala030

3.2.2 Cell Fabrication and Testing

The detailed cell fabrication and testing techniques are already discussed in ***Chapter 2***, ***Section 2.6*** and ***Section 2.7***, respectively. In Short, all the sintered pellets were infused with a solvated ionic liquid (LiTFSI/tetraglyme, 1:1 mol ratio). Symmetric (Li/Li, SS/SS), asymmetric (Li/SS), and full (Li/LMO, Li/LFP, and Li/NMC111) coin cells were then fabricated using the procedures described in ***Chapter 2, Section 2.6***.

3.3 Results & Discussion

3.3.1 Thermal Studies

The nature of combustion during synthesis is directly related to the product yield and the quality of the as-synthesized powder. In a perfect gel-combustion, where all the constituents (metal-fuel complexes) are completely decomposed under controlled exothermicity, a desired quality powder with maximum yield is typically produced. Here, the product throughput efficiency or combustion yield (%) we defined as the relative amount of as-synthesized powder obtained after combustion synthesis with respect to their estimated theoretical batch size. In ***Figure 3.2(a)***, the real-time images were shown, which were taken during the auto-combustion process with different fuel-to-nitrate ratios (F/N). As shown in the images, it is clear that as the fuel-to-nitrate ratio increases, the nature of combustion gradually changes from a sluggish to vigorous type of combustion (called volume combustion). At a smaller F/N ratio of 0.10, the combustion is much more delayed and incomplete in nature, with the evolution of a very small amount of gaseous species. The propagation of the reaction front at a lower F/N ratio was found to be limited, and the overall combustion process resulted in a sticky mass along with a small amount of ash powder, with a combustion yield estimated to be 38%.

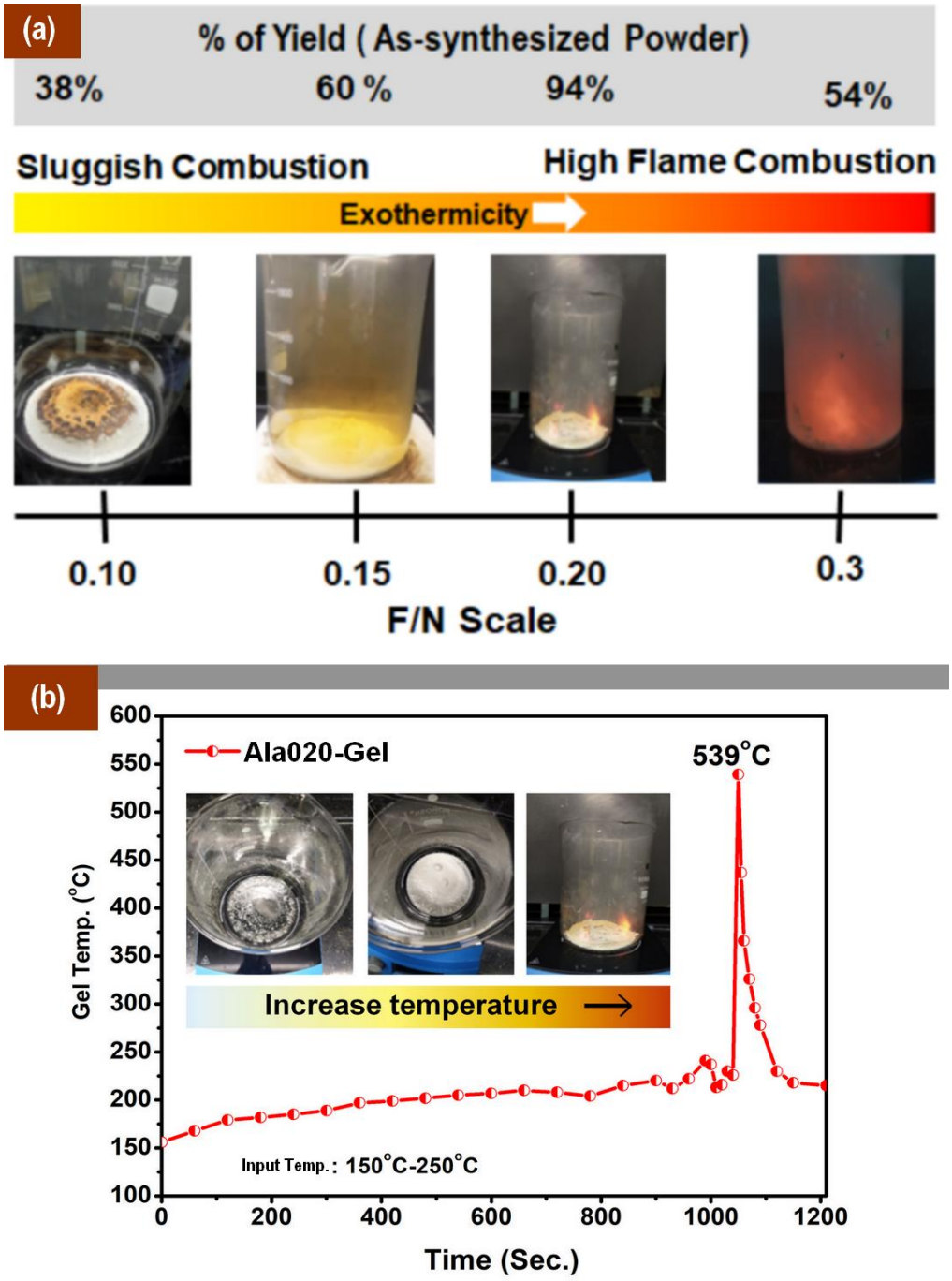

Figure 3.2 *(a) The effect of fuel-to-nitrate ratio (F/N) on product powder yield (%) and (b) time-dependent thermal profile of Ala020-Gel measured using optical pyrometer; inset shows the nature of combustion with constant heating.*

With further increase in F/N ratio to 0.15, the combustion still appeared to be sluggish in nature with evolution of small amount of yellowish nitrogenous (NO_x) fumes originated from decomposition nitrate precursors. The powder yield was found to be increased to a value of 60% at F/N=0.15 compared to the previous one.

Table 3.2 *Summary of nature of combustion, powder properties and moisture sensitivities of as-synthesized powder derived using different F/N ratio.*

Code	Nature of Combustion	Flame Temp. (°C)	Yield	Morphology	Mass loss due to moisture (%) measured from TGA/DTA
Ala010	Sluggish, no flame, sticky mass	-	38%	Agglomerated	29.68
Ala015	Sluggish, gaseous emission, no flame, coarse powder	-	60%	Agglomerated	18.36
Ala020	Controlled, significant gaseous emission, fine powder	539°C	94%	Soft Agglomeration	20.26
Ala030	Violent, uncontrolled combustion	>670°C	54%	Hard Agglomeration	0.183

Ash: as-synthesized powder; Cal. Calcined powder at 900°C; Yield: Efficiency of combustion process to produce as-synthesized powder; Code: sample nomenclatures, Mass loss due to moisture (%) as referred to ***Figure 3.5(a)*** in supporting information.

At F/N=0.20, the flame appeared first time during combustion resulting in white flappy mass and maximum powder yield of 94%. At F/N=0.20, during pre-combustion stage, a volcanic mouth was formed on the gel surface which gradually turned into a reaction center creating a self-propagating reaction front which moved in all directions and momentarily converted the whole gel into ultrafine white LLZO as-synthesized powder. On further increase in F/N ratio to 0.30, the combustion reaction was found to be very fast, uncontrolled and vigorous with long flame height. In this case, large volume of gaseous species evolved forcing the resulting powder to be spilled over from the reaction pot. The combustion yield was estimated to be 54% by considering the powder left over inside the reaction pot. The overall nature of combustion and estimated yield obtained by varying fuel to nitrate ratios thus suggested that at F/N=0.20 the product throughput efficiency was found maximum (94%) with controlled exothermicity, as summarized in ***Table 3.2***. Thus, this ratio may be considered as optimum F/N ratio, where a control combustion reaction might be carried out with high product output.To understand the temperature profile during the synthesis of LLZO, starting from gel formation to auto ignition, an optical pyrometer was used with utmost caution to measure the surface temperature of the

gel and flame temperatures. A time-dependent temperature profile of gel to auto-ignition is thus plotted in **Figure 3.2(b)**, which shows that gel temperature remained almost constant (~200°C) over time, and suddenly it increased to a value of 539°C during the peak of combustion, as shown in the inset of ***Figure 3.2(b)***. This abrupt increase in temperature during auto-combustion might originate from the decomposition of metal-fuel complexes, resulting in the formation of corresponding metal oxides and other desired phases in the as-synthesized product powder. To study the combustion behaviour of LLZO gel which comprises of complexes formed by multiple metal ions (Li, La, Zr) and reducing fuel alanine in aqueous medium, individual metal-alanine complexes were prepared and named as Li-alanine (Li-Ala), La-alanine (La-Ala) and Zr-Alanine (Zr-Ala) complexes. To obtain those gels, saturated solution of alanine was prepared and mixed with metal nitrate solutions in stoichiometric proportions with constant heating and stirring. During heating, the evaporation of water resulted in a clear viscous gel of corresponding metal-alanine complexes. It is reported elsewhere that a univalent metal ion (M^{+}) can bind with one molecule of alanine (M^{+}-Ala), whereas the bivalent metal ions (M^{2+}) generally bind two molecules of alanine to form simpler complexes[13]. The charge on the metal ion is typically satisfied by the bidentate ligand alanine forming a stable chelate like compounds. However, for tri- and tetra-valent ions like La^{3+} and Zr^{4+} respectively, the mechanism of formation of M^{3+}-Ala and M^{4+}-Ala complexes (M=La, Zr) may differ. The complexation reaction reportedly proceeds through formation of several transient intermediates. Alanine here might be coordinated with trivalent cation like La^{3+} only through

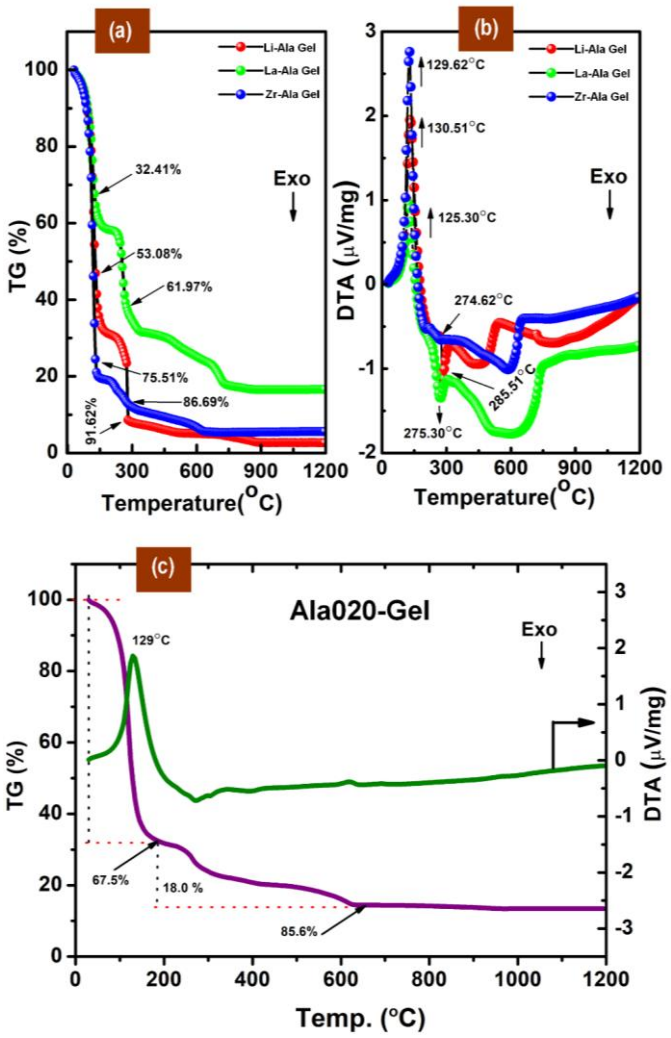

Figure 3.3 *(a)-(b) TGA and its corresponding DTA plot of Li-alanine, La-alanine and Zr-alanine gel; (c) TGA/DTA profile of Ala020-Gel from RT to 1200 ℃.*

carboxyl oxygen atom, while its nitrogen lone pair remains intact without coordination. The ^{1}H NMR spectra of mixture of Alanine and La^{3+}/Zr^{4+} in D_2O as shown in ***Figure 3.4*** also exhibited significant downfield shifting of -CH_3 doublet (1.39 ppm (J = 8.0 Hz) for alanine, 1.42 ppm (J = 8.0 Hz) for La^{3+}-alanine complex and 1.47 ppm (J = 8.0 Hz) for Zr^{4+}-alanine complex) and -CH quartet (3.70 ppm (J = 12.0 Hz) for alanine, 3.77 ppm (J = 12.0 Hz) for La^{3+}-Alanine complex and 3.98 ppm (J = 12.0 Hz) for Zr^{4+}-alanine complex) supporting the covalent interaction between alanine and metal ions. Alanine-NH_2 may not be available in NMR spectra due to rapid proton exchange with D_2O in the NMR time scale.

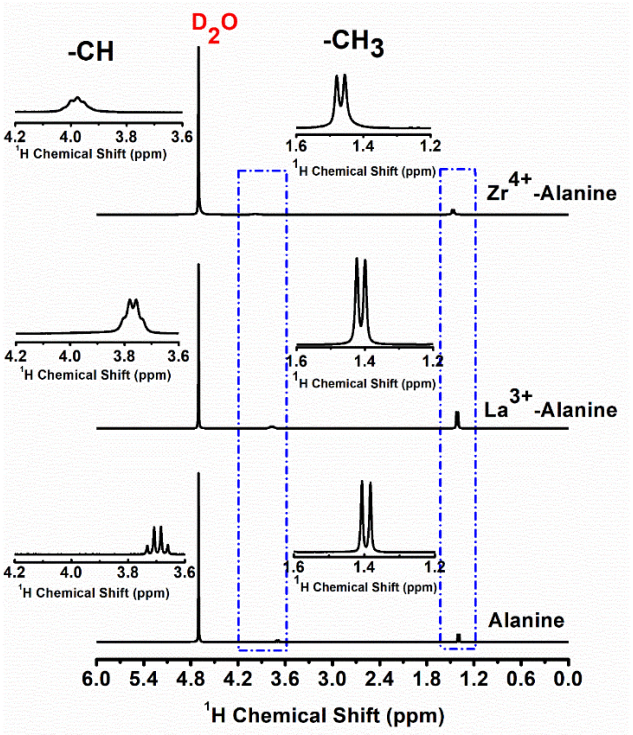

Figure 3.4 *^{1} H NMR spectra of (a) Alanine, (b) La^{3+}-Alanine complex, (c) Zr^{4+}-Alanine complex on D_2O solvent*

A similar trend was also found in the formation of [Fe^{3+}-Ala] type complexes as reported by Djurdjević et al.[14] who proposed that the formation of say M^{3+}-alanine complex may follow the reaction path as stated below:

$$M^{3+} \rightarrow [MOH] \rightarrow [M(OH)HAla]^{\text{Metastable phases}} \rightarrow [M^{3+}\text{-Ala}]^{\text{Metal-alanine complex}}$$

The above reaction path indicates that the [M-Ala] complex (where OS of M $>2^{+}$) is formed possibly in two ways; (a) either alanine zwitter ion may attach with the hydrolytic product of tri/tetra valent metal ions resulting in metastable phases or (b) by hydroxide ions (OH^{-}) and hydronium ions (H_3O^{+}) formed via protolysis of water, which further can coordinate to M (=M^{3+}/M^{4+}) in [MHAla] metastable complexes. This metastable phase may exist in solution over prolonged period forming an equilibrium between [M(OH)HAla] and [M-Ala][14,15].

The thermal profiles of individual metal-alanine gels (Li-Ala, La-Ala and Zr-Ala) were further studied by TGA/DTA which provided important information about the decomposition behaviour of complexes during combustion. ***Figure 3.3(a)-(b)*** showed the TGA and corresponding DTA plots of Li-Ala, La-Ala and Zr-Ala gels in the temperature range of RT-1200°C. All three gel samples initially showed sharp weight losses up to 150ºC due to dehydration and removal of trapped water from the gels, as shown in ***Figure 3.3(a)***. At around 275°C, Li-Ala gel showed the highest weight loss of 91.62% compared to La-Ala (61.97%) and Zr-Ala (86.69%). As understood from these mass loss values, the removal of water from the viscous gel becomes more difficult once the valence state of the corresponding metal ion increases. The multi-valent metal ions generally form several intermediates (as discussed in the earlier section) through the protolysis of water molecules, which makes it difficult to be dehydrated. From 300-900°C, all the three gel samples showed multi-step sluggish mass loss and beyond 900°C, no further weight loss could be seen. The dehydration process of gel was reflected in their corresponding DTA plot, as shown in ***Figure 3.3(b)***, from endothermic peaks at 130.5°C (Li-Ala), 125.3°C (La-Ala), and 129.6°C (Zr-Ala), respectively. The decomposition of nitrates (metal) that took place at around 275-285°C for all the gel samples were reflected in the DTA plot through exothermic peaks. ***Figure 3.3(c)*** shows the thermal decomposition profile of LLZO gel (with F/N=0.2) along with its corresponding DTA plot along the Y-axis. A sharp weight loss of 67.5 % could be measured up to 200°C, which is assigned to the loss of water molecules from the gel. The decomposition of all metal-alanine complexes took place between 200°C-630°C, which was also reflected in a broad exothermic peak in the DTA curve. No further weight loss could be detected in LLZO gel beyond 630°C, suggesting formation of corresponding metal oxides (as-synthesized product powder).

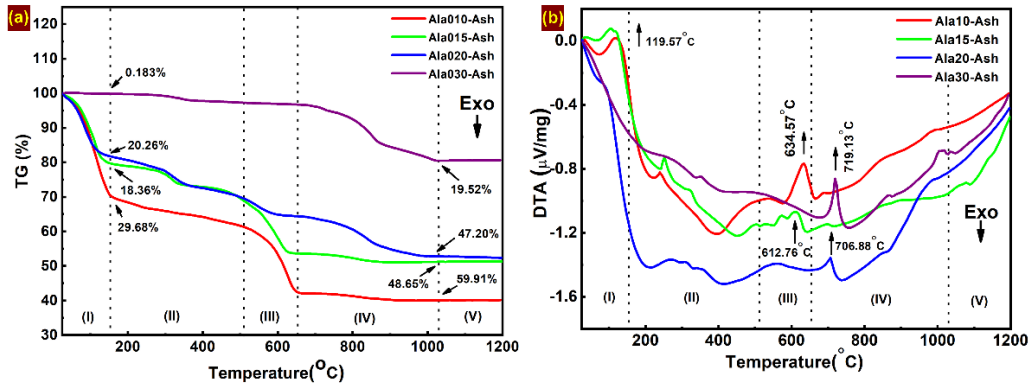

Figure 3.5 *(a) TGA and (b)DTA profile of LLZO as-synthesized powders with different fuel to nitrate ratios (F/N= 0.10,0.15,0.20, and 0.30) describe the thermal behaviour of ash-synthesized powder.*

The thermal study of individual metal-alanine and LLZO precursor gels thus suggested that the combustion reaction was actually triggered by the decomposition reaction of metal-alanine complexes, which produced enough exothermicity to further propagate the reaction, resulting in ultrafine product powder of corresponding metal oxides and desired phases. The thermal behavior of pristine LLZO ash powders with varying fuel-to-nitrate ratios in ***Figure 3.5(a)-(b)*** revealed multi-step weight losses and corresponding endo/exothermic events. The optimum F/N = 0.20 (Ala020) shows controlled decomposition (~20% mass loss) with distinct exothermic peaks between 600–720 °C, suggesting efficient combustion and formation of crystalline LLZO precursor phases, whereas lower ratios showed incomplete combustion (Ala01 and Ala015) and higher ratios loss carbonaceous residues at the time of synthesis process due to vigorous flame. The mass loss due to moisture is attached in ***Table 3.2***. Thus, it is interesting to study the phase present in ash-synthesized powder as well as calcined powder, which were discussed in the later section.

3.3.2 Structural Studies

X-ray diffractograms of as-synthesized powders with different fuel to nitrate ratios were plotted in ***Figure 3.6(a)*** along with standard JCPDS patterns of tetragonal-LLZO (PDF 00-064-0140), cubic-LLZO (PDF 00-064-0141) and pyrocholre-$La_2Zr_2O_7$ (PDF 01-080-3408). It is clearly visible from the diffractograms $La_2Zr_2O_7$ phase predominantly formed in as-synthesized product powder along with other metal oxides. For lower F/N ratio, the amorphous content is much higher than that of ash powder with higher F/N ratio suggesting the presence of unburned carbonaceous materials and small amount of metal oxides (La_2O_3) with lower crystallinity, however, with increase in fuel content, the $La_2Zr_2O_7$ phase appeared as major dominant phase which certain degree of crystallinity. As the fuel content increases, the more exothermic heat produced helping in crystalline growth of $La_2Zr_2O_7$ as observed for F/N-0.20 and F/N-0.30 respectively. Pyrochlore-$La_2Zr_2O_7$ is described as LZO, a framework which reorients to produce either tetragonal-LLZO (t-LLZO) or cubic-LLZO (c-LLZO) by atomic rearrangement depending on the synthesis conditions and sintering schedules. In previous literature, similar types of formation of pyrochlore structure were also reported for LLZO synthesized via sol-gel methods which upon heating converted into garnet LLZO[9,16,17]. The XRD profiles of as-synthesized powders obtained by varying fuel to nitrate ratio thus revealed that at lower F/N, the desired crystalline phase could not be obtained rather it produced un-burnt non-detectable amorphous phases. In summary, both in terms of product yield and desirable phase content in

as-synthesized powder, F/N=0.20 might be an optimum choice of fuel to metal ratio for further progress in obtaining LLZO product powder through calcination.

In the FTIR spectra, a sharp characteristic peak of -OH vibrations at 3450 cm^{-1} could be detected originating from absorbed moisture as shown in the enlarged view of spectra in ***Figure 3.6(b)***. It was seen from the spectra that the intensity of the peak reduced once the F/N ratio increased. Similar results could also be found in the case of $-CO_3$ vibration originating from Li_2CO_3 surface impurities, as shown in the enlarged view of spectra in ***Figure 3.6(c)***. The intensity of the $-CO_3$ vibrational peaks was found to be drastically reduced when the F/N ratio increased.

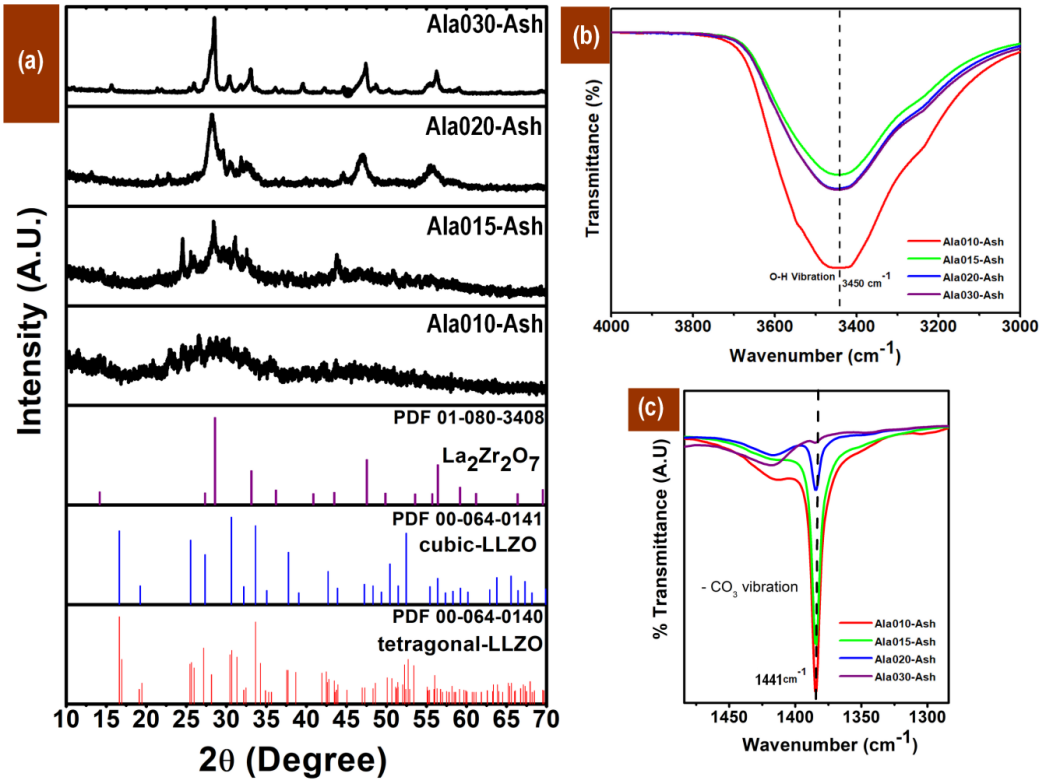

Figure 3.6 *(a) X-Ray diffractogram and FTIR spectra of (b) -OH vibrations originated from absorbed moisture and (c) $-CO_3$ vibrations originated from Li_2CO_3 impurities of as-synthesized powder (ash) of LLZO with varying fuel to nitrate ratio.*

Figure 3.7(a) showed the XRD diffractograms of LLZO (Ala020) as-synthesized powder and powders calcined at 700°C, 900°C and 1000°C. At a lower calcination temperature of 700°C, it was clearly visible that only the pyrochlore structure was formed along with some impurities of metal oxides. However, in both the diffractograms of 900°C and 1000°C, all the intense peaks could be indexed as c-LLZO along with detectable impurities of $La(OH)_3$ and Li_2CO_3. Quantitative phase analysis revealed that at 700°C, Li_2CO_3 appeared as major phase (52.9%)

along with Pyrochlore $La_2Zr_2O_7$ (22.6%) and $La(OH)_3$ (21.9%). Only a trace amount of c-LLZO could be detected. With increase in calcination temperature at 900°C, c-LLZO appeared as major phase (73.7%),

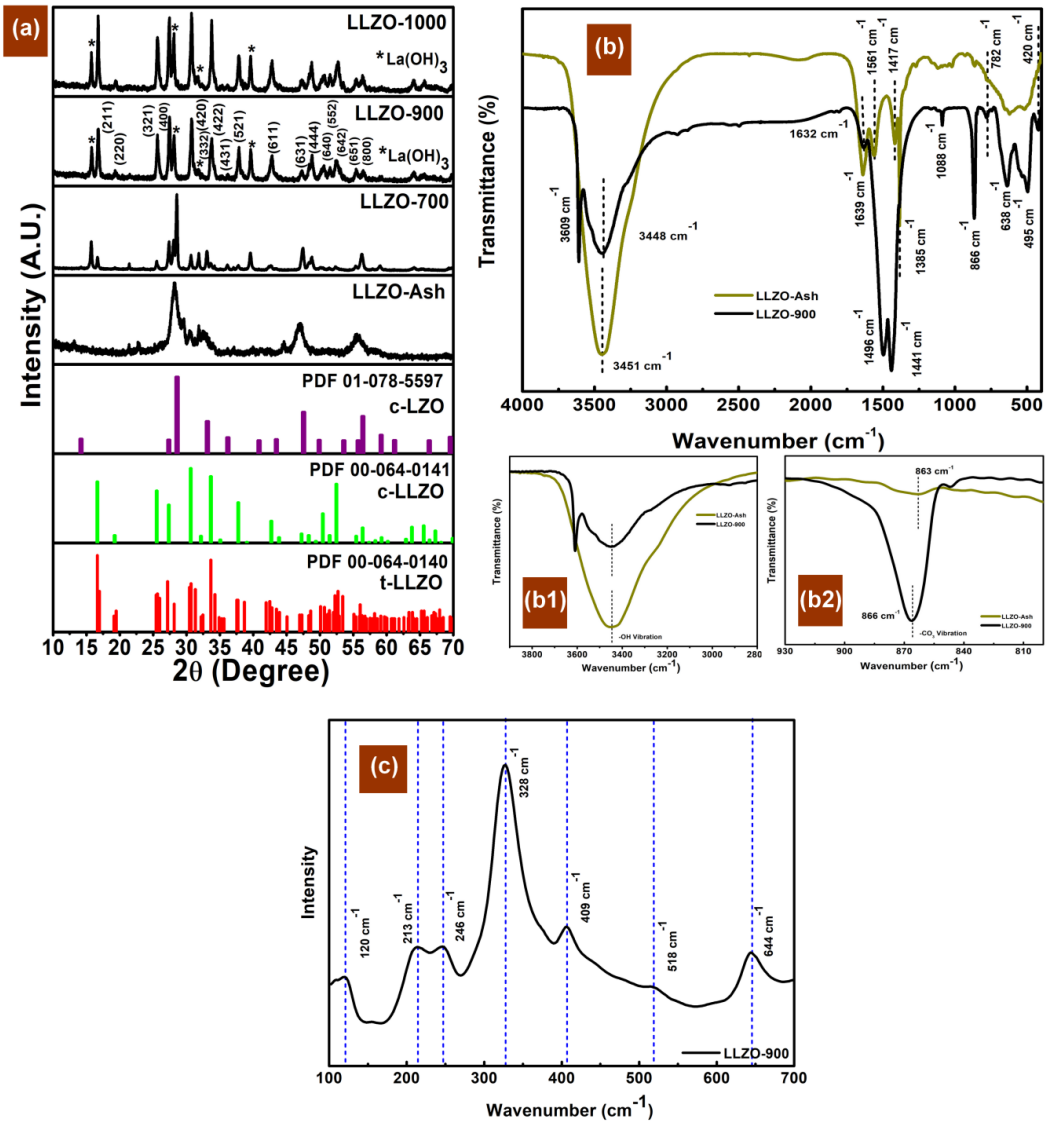

Figure 3.7 *(a) X-ray diffractogram of LLZO (Ala020) as-synthesized (ash) and powders calcined at 700, 900, and 1000℃; (b) FTIR spectra of LLZO (Ala020) as-synthesized and calcined powder at 900°C; (b1) and (b2) are enlarged versions of showing characteristic peaks responsible for -CO_3 and -OH vibrations both in as-synthesized and calcined Ala020 powders; (c) RAMAN spectra of LLZO (Ala020) powder calcined at 900℃.*

however, the amount of $La(OH)_3$ still remained similar in percentage (26.3%). The presence Li_2CO_3 could not be detected at 900°C. At 1000°C, Amount of c-LLZO increased to a value of 75.7% along with 24.3% of $La(OH)_3$.Therefore, it is cleared that $La(OH)_3$ appeared to be one

of the secondary phases in all calcined samples. It was reported that in lanthana (La containing) materials the $La(OH)_3$ phase as surface impurity might be generated when the materials were synthesized, calcined and exposed in an open atmosphere which initially triggered through formation of LaO(OH) and $La_2O_2CO_3$ intermediates and finally converts into $La(OH)_3$ when calcinations temperature increased beyond 700°C[18]. This rate of formation of $La(OH)_3$ is highly dependent on surface area and morphology of the powder as examined by Fleming et al.[18]. On the other hand, the presence of Li_2CO_3 as surface impurity in LLZO powder is now well established which is due to the Li^+/H^+ exchange between garnet and moisture forming a Li^+ insulating Li_2CO_3 surface layer[8,19,20]. Sometimes such impurities are responsible for lowering the Li-ion conductivity and impede densification process of LLZO pellets. Professor Goodenough thus recently raised serious concern relating to the practical and economical storage of this garnet material due its unstoppable surface activities[21]. In our case, the impurity profiling of LLZO was further examined using FTIR spectroscopy and Raman spectroscopy. The FTIR spectra of as-synthesized and calcined powders were compared and shown in ***Figure 3.7(b)***. The existence of $La(OH)_3$ in as-synthesized could not be detected, however it was reflected in calcined powder by a strong peak at 3609 cm^{-1}. Strong -OH vibration peaks at 3451 and 3448 cm^{-1} as obtained in ash and calcined powders respectively, were attributed to the absorbed moisture[22]. The intensity of -OH peak was found to be less for the calcined powder as shown in the enlarged view of spectra in ***Figure 3.7(b1)***. The characteristic peak of Li_2CO_3 attributed to C-O stretching was also detected at peak positions 1441 and 866 cm^{-1} in as-synthesized powder as well as calcined powder[23]. However, the intensity of such peak (863 cm^{-1}) in as-synthesized powder were found less as shown in the enlarged view in ***Figure 3.7(b2)*** revealing that high temperature calcinations enhanced the surface activity of LLZO powder due to the Li^+/H^+ ion exchange process and resulting the formation of Li_2CO_3 impurities. In as-synthesized powder several other strong peaks were detected at 1632 cm^{-1}, 1639 cm^{-1},1496 cm^{-1}, 1441 cm^{-1} and 1088 cm^{-1}, which were attributed to the different stretching and bending vibrations of residual hydrocarbons and organic moieties present in as-synthesized powder. Few low intense peaks as reflected below 800 cm^{-1} could be assigned to the characteristics Zr-O and La-O vibrations as present both in ash and calcined powders[24]. The structural profile of LLZO calcined powder was further confirmed by Raman spectroscopy as shown in ***Figure 3.7(c)***. The Raman spectra could be typically categorized in three regions - (I) below 300 cm^{-1}, attributed to the translational modes of mobile cations in LLZO, (II) 300-550 cm^{-1} , where cubic phase exhibits broad and partly overlapping band and tetragonal phase shows higher

number of peaks, (III) frequency range above 550 cm^{-1}, assigned to the vibrational stretching of ZrO_6 octahedra[8]. The Raman spectra thus further confirmed the presence of cubic phase LLZO in calcined powder.

3.3.3 Microstructural and Dilatometry Studies

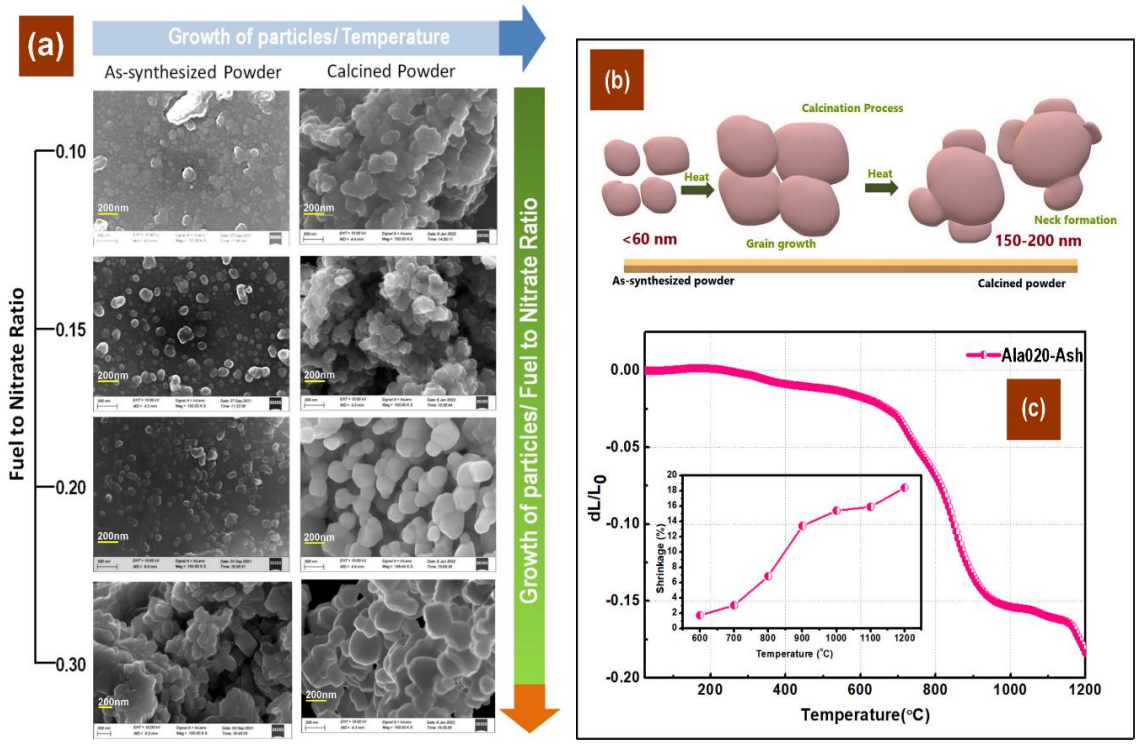

Figure 3.8 *(a) FESEM images of as-synthesized and calcined powders (900 °C) of pristine LLZO synthesized using different F/N ratios, (b) Schematic demonstration of grain growth with respect to calcination temperatures, and (c) Shrinkage profile of LLZO green compact with respect to sintering temperature under Dilatometric study.*

Fuel in combustion synthesis plays an important role in defining the nature and quality of the product powder. While urea, citric acid, and glycine are the most common and popular fuels to produce nanocrystalline powders with uniform particle size, alanine has also been used for certain advantages as a chelating fuel during combustion. The zwitterionic character of alanine facilitates the complexation process with most of the metal ions in aqueous solution. Alanine has extra branched methyl group which liberates more gaseous species during combustion making ultrafine product powder. More carbon in the side-chain in alanine helps to increase the reaction temperature momentarily up to 800°C and subsequently, such exothermicity facilitates corresponding phase formation[25,26]. It was observed in our earlier studies that most of the alanine metal complexes decompose at a lower temperature, reducing

the chances of formation of hard agglomerates and the substantial risk of partial sintering of primary particles during combustion[26]. In the present study, various alanine-nitrate ratios (F/N; 0.10-0.30) were used to execute the combustion process, and the effect of this process on morphological and microstructural changes in LLZO as-synthesized and calcined powders was examined. In ***Figure 3.8(a)***, the FESEM image of as-synthesized powders with different F/N ratios was displayed. It was found that, in all cases, soft agglomerated particles were formed. The average primary particle size of LLZO as-synthesized powders, as estimated from the micrographs, was already mentioned in ***Table 3.3***.

Table 3.3 *Average agglomeration size (PSD) and particle size distribution (FESEM) of LLZO ash and calcined powders at different F/N ratios.*

Code	Average Agglomeration Size by PSD (nm)		Particle Size Distribution by FESEM (nm)	
	Ash	Cal.	Ash	Cal.
Ala010	615.1	987.6	10-52	32-80
Ala015	458.7	814.3	15-85	30-120
Ala020	531.2	745.5	17-72	50-310
Ala030	255.0	593.8	50-230	75-375

The nanoparticles as obtained in the post-combustion stage having high surface energy resulted in soft agglomerates for all F/N ratios without partial sintering between primary particles, rather all the particles were appeared to be loosely bound to each other. However, the microstructure of powders (with different F/N ratio) calcined at 900°C, a significant change in morphology could be observed. At lower F/N ratio (0.10 and 0.15), the particles were found highly agglomerated in nature with limited grain growth. With further increase in F/N ratio, i.e., at 0.20, a unique multifaceted morphological feature was visualized. It was seen, the neck formation occurred between grains and the particles were found coalesced together resulting in a significant change in microstructure compared to lower fuel to nitrate ratio powder samples. A schematic representation of grain growth and subsequent neck formation has been presented in ***Figure 3.8(b)***. On further increase in F/N ratio (0.30), it was observed that hard agglomerates were formed with coarse particles and irregular grain growth. Therefore, it can be suggested that the microstructural evolution in calcined powder was found to be highly dependent on the fuel to nitrate ratios which may also affect the sintering behaviour and densification process during palletisation of LLZO powder sample at high temperature. To

measure the sinterability, LLZO with an F/N ratio of 0.20, the dilatometric measurement was carried out using a green compact made with Ala020 as-synthesized powder and presented in ***Figure 3.8(c)***. From the graph, it was observed that the densification process started around 300°C, which further continued up to 1000 °C. The amount of densification in terms of shrinkage was estimated to be ~15.0 % at 1000 °C. It is assumed that apart from the removal of unburnt carbonaceous species, the transformation of $La_2Zr_2O_7$ pyrochlore to the cubic LLZO phase could also occur during this high-temperature measurement process. The shrinkage as estimated was mainly due to the fusion of grains and formation of multifaceted morphology, which might have increased the packing density of particles during thermal treatment.

3.3.4 Electrical Studies

3.3.4.1 Solid Electrolyte

The ionic conductivity of the LLZO material is strongly influenced by the crucible material used during the sintering study. As shown in ***Figure 3.9***, samples sintered in Zr-based crucibles show lower conductivities in the range of 10^{-7} S/cm, whereas those delivered higher conductivity up to ~10^{-6} in Al-based crucibles. This difference can be attributed to cationic exchange and impurity incorporation from the crucible walls during high-temperature treatment, and is well established in the literature[27–31]. Al crucibles can promote partial Al-doping, which stabilizes the cubic phase of LLZO material and enhances Li-ion transport across the grain boundaries. In contrast, Zr crucibles tend to suppress such incorporation, often leading to less conductive phases or higher grain boundary resistance.

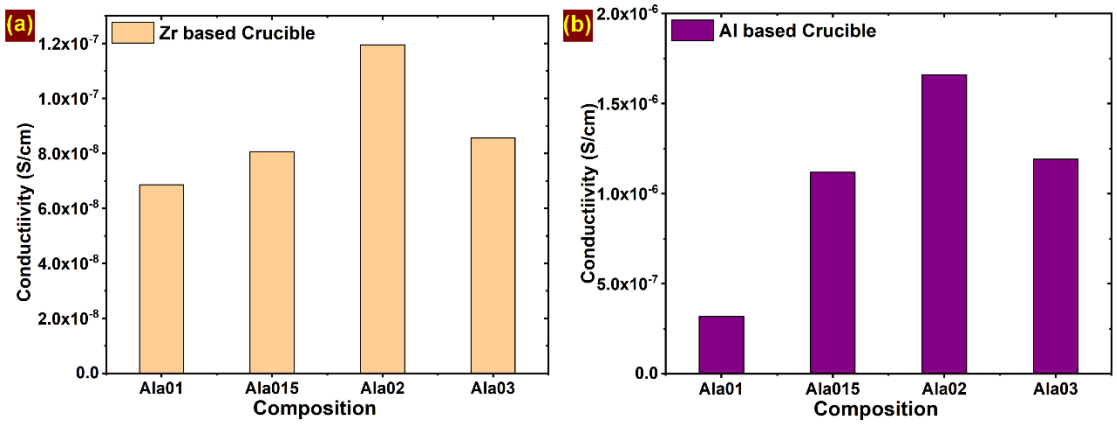

Figure 3.9 *Ionic conductivity of LLZO pellets with different fuel-to-nitrate (F/N) ratios (Ala01-Ala03) measured after sintering in (a) Zr-based crucibles and (b) Al-based crucibles.*

The temperature-dependent EIS spectral analysis was carried out for pristine LLZO pellets (Ala02) sintered at 1000 °C for 10 hours in air in a Zr-based crucible (after calcination in an Al-based crucible). The measurement was conducted from room temperature to 150°C at

intervals. The Nyquist plots of EIS spectra of the LLZO pellet coated on both sides using an Au electrode at different temperatures are presented in ***Figure 3.10(a)***. All the spectra showed typical depressed semicircular characteristics of Li-blocking symmetrical cells comprising grain and grain boundary contributions from LLZO solid electrolyte.

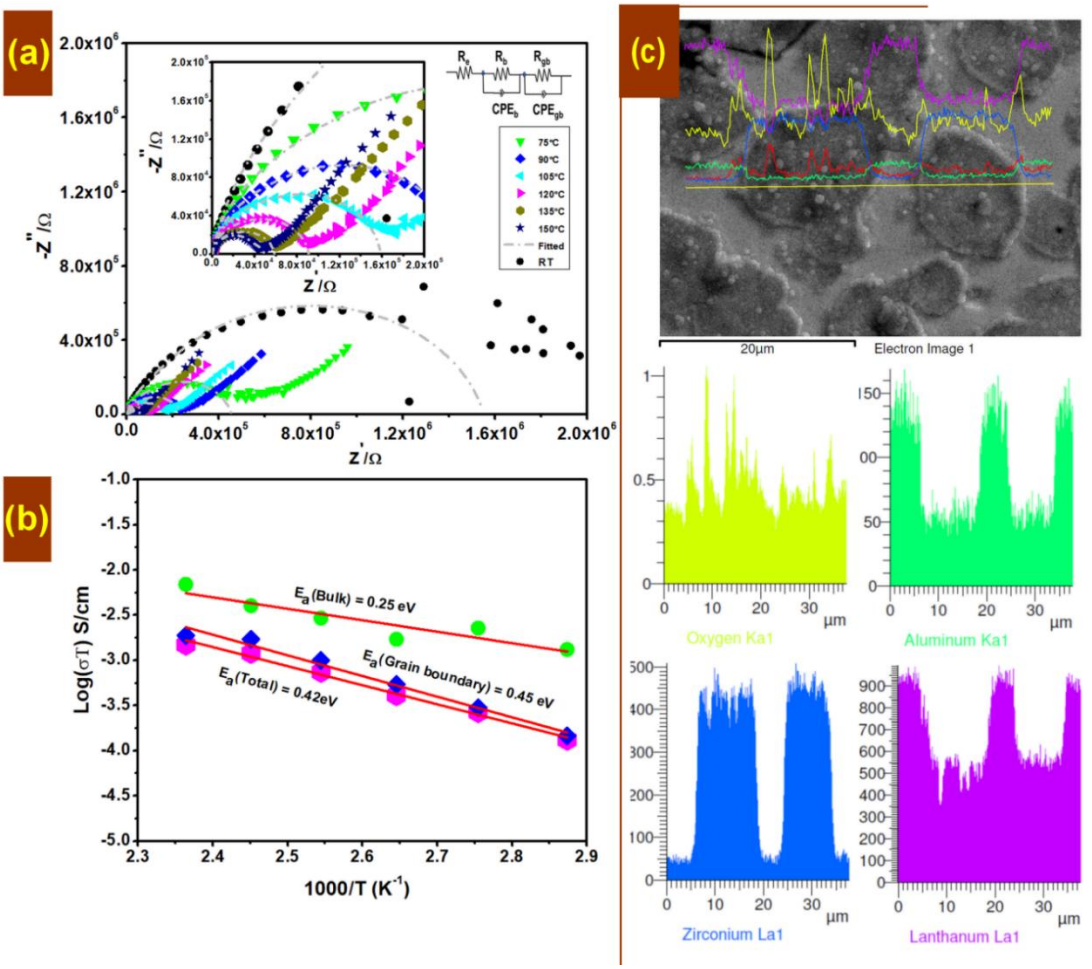

Figure 3.10 *(a) Nyquist plot of LLZO pellet sintered at 1000 ℃ for 10 hours in air taken in the temperature range between RT to 150°C, and corresponding (b) Arrhenius plot showing variation of conductivities of LLZO pellet with respect to temperature and calculated activation energies, (c) FESEM micrograph of fractured surface of LLZO sintered pellet and their corresponding elemental line spectrum carried out by EDX.*

Although, the semicircles responsible for grain and grain boundary contributions could not be visible in the spectrum separately, however, the data could be resolved by fitting the curve with an equivalent circuit model comprising all the circuit elements; $R_e(R_bCPE_b)(R_{gb}CPE_{gb})$, where R_b, R_{gb}, and R_e are the resistances attributed to bulk, grain boundaries and Au electrodes; CPE_b and CPE_{gb} represents the constant phase elements (CPE) originated from grain and grain boundaries. The equivalent circuit was given at the inset of ***Figure 3.10(a)***. Apart from the semicircles, the appearance of a straight line in the lower

frequency region, as observed in the spectrum, clearly suggested the intrinsic Li-ion conduction property of LLZO garnet. The room temperature EIS conductivity as measured showed somewhat noisy profiles at lower frequency region. However, with the increase in temperature, the EIS plots reflected the typical profiles of Li-ion blocking symmetrical electrodes. To measure the conductivity at different temperatures including grain and grain boundary contributions equation, σ=1/R.L/A was used; where, R; Resistance, L; thickness, A; area of the pellet. It is clearly visible from the plot that the total conductivity of LLZO garnet increased by an order of magnitude with an increase in temperature. The impedance imparted by the grain and grain boundaries was also found to be reduced at higher temperatures. The results obtained after fitting the plots with Z-view software were summarized in ***Table 3.4***.

Table 3.4 *Variation in electrical properties at different temperatures (RT – 423K) of LLZO pellets sintered at 1000℃ for 10 hours in air.*

Temp. (K)	L (cm)	A (cm^2)	R_b (Ω)	R_{gb} (Ω)	σ_b ($S.cm^{-1}$)	σ_{gb} ($S.cm^{-1}$)	σ_{total} ($S.cm^{-1}$)
RT	0.132	0.7698	68261	1.48E+06	2.51213E-06	1.16E-07	1.10E-07
348			45359	4.09E+05	3.78051E-06	4.20E-07	3.78E-07
363			27422	2.07E+05	6.25338E-06	8.28E-07	7.31E-07
378			38005	1.20E+05	4.51204E-06	1.42E-06	1.08E-06
393			23033	6.78E+04	7.44498E-06	2.53E-06	1.89E-06
408			17470	4.09E+04	9.8157E-06	4.19E-06	2.94E-06
423			10486	3.84E+04	1.63533E-05	4.46E-06	3.51E-06

It is worthy to mention here that although the total conductivity at room temperature (1.10×10^{-7} $S.cm^{-1}$) as obtained for developed LLZO garnet was found to be somewhat lower than the pristine LLZO materials synthesized by other reported high temperature solid state routes and/or wet chemical methods. The total activation energy [$\sigma T = Ae^{-Ea/TK_B}$, where, A is the pre-exponential factor, E_a is the activation energy for ionic conduction, and K_B is the Boltzmann constant] as calculated from the slope of the log(σT) versus 1000/T plot [as shown in ***Figure 3.10(b)***] was estimated to be 0.42 eV, well matched to the other literature reports[28,31]. A comparison chart of pristine LLZO synthesized by different methodologies and their corresponding properties are dully summarized in **Table 3.5**. To further probe the reduction of conductivity at RT in developed LLZO, sintered pellets were polished and studied under FESEM microscope, and elemental mapping was carried out using EDX. It is believed that the presence of Li_2CO_3 surface impurities as formed due to the exposure of sample in ambient

atmosphere can diminish the ionic conductivity of LLZO to some orders[19,20]. However, no literature was found describing the role of La(OH)3 impurities produced in situ during the synthesis of LLZO garnet. As analysed by XRD (refer to ***Figure 3.7(a)***), we initially found $La(OH)_3$ was typically formed as bulk impurities and during sintering, its crystallinity gradually increased, and we expected that $La(OH)_3$ would probably remain at the grain boundaries. This definite loss of lanthanum from the LLZO matrix by making lanthanum-deficient garnet LLZO during the synthesis process might be one of the reasons in our case for obtaining lowered conductivity. The FESEM micrograph and its corresponding line spectrum for elemental mapping, as shown in ***Figure 3.10(c)***, revealed that La was present both in grains and at the grain boundaries of LLZO. The line profiles of O, Al (originated from the crucible during calcination), La, and Zr, as shown in ***Figure 3.10(c)***, further demonstrated that lanthanum is predominantly found at the grain boundary, where the presence of Zr was very low or negligible. Although the conductivity is somewhat compromised, such a distribution of La at grain boundaries could possibly be beneficial to impede dendritic growth and could act as a sintering aid, improving the compact density of LLZO particles in pellets. Similar kinds of sintering aids were also used by several researchers to contain transgranular lithium migration[32].

The overall EIS studies thus demonstrated that Li-ion conductivity in engineered LLZO was found ($1.1x10^{-7}$ $S.cm^{-1}$) lowered due to presence of impurities such as Li_2CO_3 and $La(OH)_3$, still activation energy as calculated was comparable to LLZO produced by different synthesis methodologies[29,31]. The presence of $La(OH)_3$ as traced at the grain boundaries might be helpful in impeding Li dendritic migration. As reported in earlier literature, the interfacial modification to resist dendritic penetration was generally carried out by addition of sintering aids in LLZO matrix such as Li_3PO_4, Li_3BO_3, CuO, SiO_2 etc[31–34].The presence of such lithiated or non-lithiated compounds helped in compaction of grains, suppression of additional phase formation, and also reduced grain boundary resistance. Therefore, it is expected that in-situ formed $La(OH)_3$ at grain boundaries might be playing a similar kind of role in the present case also. It has been discussed in detail in the later sections by analysing electrochemical results and post-electrochemical findings.

3.3.4.2 Solid Hybrid Electrolyte

A solid hybrid electrolyte was prepared by impregnating the solvated ionic liquid into engineered LLZO pellets. The preparation and details steps were already discussed in ***Chapter 2***, ***Section 2.4***. The detailed electrical measurement of the hybrid electrolyte was presented in

Figure 3.11. The SIL preferentially wets grain boundaries and surface pores. As a result, it creates a thin and ionically conductive interfacial layer where pre-solvated Li^+ ($[Li(G4)]^+$) can desolvate in a controlled way and feed into the 3-D Li^+ pathways of LLZO. The hybrid electrolyte, therefore, aims to keep the mechanical and safety advantages of a ceramic with an improvement in wetting and interfacial kinetics.

The ionic conductivity of solvated ionic liquid electrolyte was measured by fabricating an SS/SS cell with SIL soaked commercial PP separator. ***Figure 3.11(a)*** represents the Nyquist plot of PP-SIL and LLZO-SIL material. The ionic conductivity of LLZO-SIL and PP-SIL was found to be 8.20×10^{-5} S.cm^{-1} and 1.13×10^{-4} S.cm^{-1}, respectively. Thus, the ionic conductivity of the LLZO-SIL hybrid is slightly lower than that of the liquid-dominated PP–SIL system. This is quite common, as the ionic transport in the hybrid must also traverse the ceramic matrix. However, the overall ionic conductivity of the LLZO pellet was enhanced to a significant extent after making a hybrid electrolyte. To measure the transference of LLZO-SIL hybrid electrolyte,

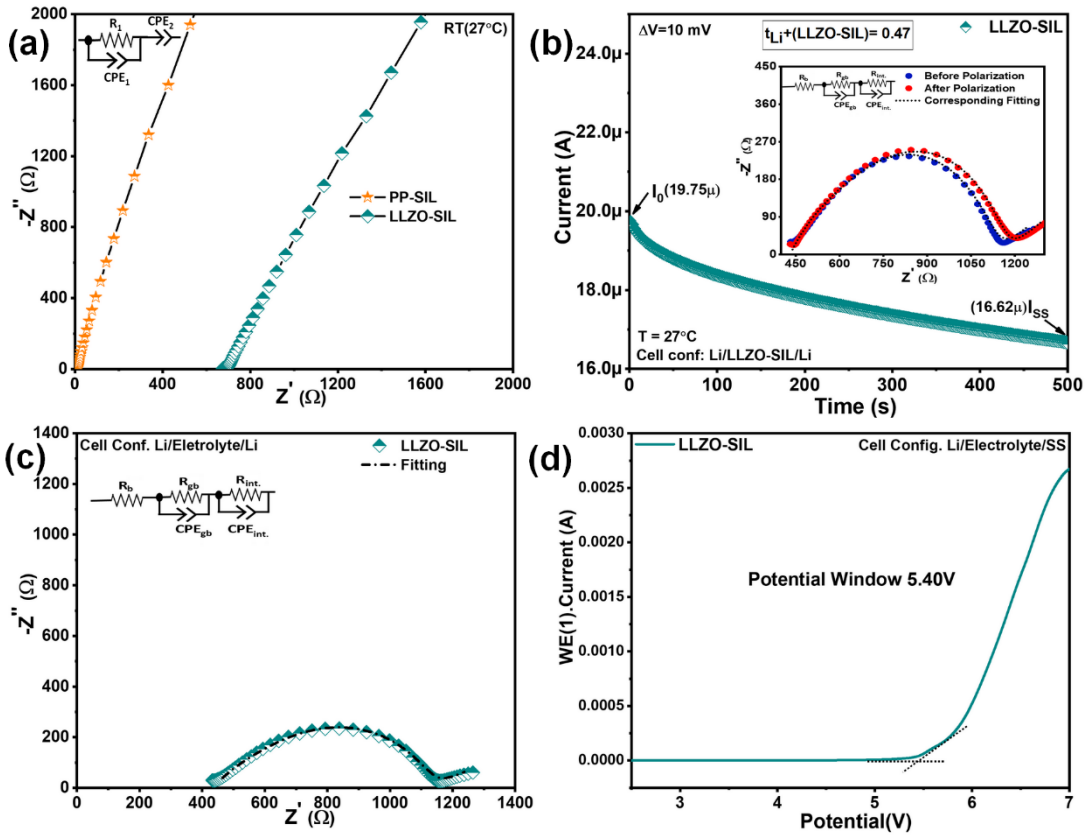

Figure 3.11 *(a) EIS spectra of PP-SIL, LLZO-SIL for conductivity measurements. (b) DC polarization curve of LLZO-SIL, along with the EIS spectra before and after polarization, (c) Nyquist plot of LLZO-SIL solid hybrid electrolytes in Li/Li symmetric cell, (d) Current vs. potential linear sweep voltammetric (LSV) plot at a scan rate of 2.0 mV s^{-1} of LLZO-SIL.*

DC polarization was measured in a Li/Li symmetric cell at ΔV = 10 mV as shown in ***Figure 3.11(b)***. The EIS was measured before and after polarization. The transference number as calculated using the Bruce-Vincent-Evans equation[35] (***Equation 2.9*** in ***Chapter 2***), was found to be 0.47. This value is significantly higher than the ionic or liquid electrolyte system. These results suggest that the hybrid electrolyte can support efficient Li^+ transport with minimal polarization losses.

To measure the interfacial resistance between the metal and solid hybrid electrolyte, EIS was taken in a Li/Li cell and presented in ***Figure 3.11(c)*** along with the equivalent circuit.

Table 3.5 *A comparison chart of pristine LLZO synthesized by different methodologies and their corresponding properties.*

Electrolyte composition	Synthesis Method	Processing steps /Morphology	Cond. (S.cm^{-1})/ Activation energy (eV)	Properties	Ref.
Cubic-$Li_7La_3Zr_2O_{12}$	Solid-State	Multistep, 1200°C, 36h /-	3 ×10^{-4}/ 0.30	High Conductivity, Low activation energy	5
	Solution method	One step, Calcination temp.750ºC, 4h/ Agglomerated	2.85 × 10^{-6} /0.36	Cubic LLZO at low temperature	36
	Solid-State	Multistep, High Sintering Temperature/ Grain sized:10-30 µm	2.1 × 10^{-4} /0.34	High Conductivity, low Activation Energy	37
	Sol-gel	Multi-step, 1200°C, 6h / Agglomerated	5.1 × 10^{-6} /0.57	High temperature sintering, c-LLZO	38
	Molten Salt Synthesis	Single step/ Calcination Temp. 900°C, 6h, Sintering Temp. 1100°C, 6-18h/ 0.5- 2 µm sized facted structure	-	c-LLZO can be produced in a large volume	39
	Alanine Assisted Combustion	Single step, one pot synthesis, Calcination Temp. 900°C, 10h, Sintering temp. 1000°C, 10h/ engineered nanocrystalline Neck-fused morphology	1.10 × 10^{-7}/ Hybrid mode: 3.3 × 10^{-4}/0.42	Single step, one pot low temperature synthesis, morphologically Engineered c-LLZO with excellent electrochemical properties	This Work

The full cell electrochemical data of the developed pristine LLZO electrolyte in the cited references were not published yet.

After analyzing in the ZView software, the interfacial resistance is found to be 452.60Ω, suggesting good compatibility between the electrolyte and Li metal. The electrochemical stability window of the hybrid system was evaluated by linear sweep voltammetry (LSV) at ascan rate of 2.0 mV s^{-1} as presented in ***Figure 3.11(d)***. A high potential window of 5.44V was observed for LLZO-SIL, which suggest that this hybrid electrolyte was suitable for any existing high-voltage cathode material lithium batteries. In summary, the hybrid electrolyte shows reduced grain boundary resistance, moderate lithium transference number, low interfacial resistance and a wide potential window. Thus, it will be interesting to measure the symmetric cell stability and full cell performance in the later section.

3.3.5 Electrochemical Studies

3.3.5.1 Long cycling performance

Li-symmetric cells provide a platform to describe the behaviour of Li metal anodes, since all electrochemical half-reactions occur on a Li surface[40]. Therefore, examination of Li metal plating/stripping processes in symmetric cell configuration helps in probing metal-ceramic interfacial activities and subsequent formation of Li dendrites. Here, Li-symmetrical cells were fabricated using optimized LLZO pellets soaked in SIL and cycled under incremental current densities ranging from 0.05 mA.cm^{-2} to 1.0 mA.cm^{-2} at RT. The DC cycling profiles of the fabricated symmetric cell was presented in ***Figure 3.12(a)***. With lower current densities smooth cycling profiles are obtained, however, after reaching to a critical current density of 0.45 mAcm^{-2}, the profile showed typical pattern of soft short circuit. The CCD thus obtained here found comparably higher than the previously reported CCD values of pristine LLZO electrolytes[41].

The time dependent voltage profile of symmetric cell was given in ***Figure 3.12(b)***; the four dotted regions marked as I-IV are further displayed in their enlarged versions. The average polarization value of symmetric cells under cycling at a current density of 0.05 mA.cm^{-2} was estimated to be ~ 0.12V, which reflected the lower energy barrier for both plating and stripping processes. It is mainly due to the fact that the engineered LLZO-SIL electrolyte matrix might have lowered the energy barrier required for the Li plating/stripping process, and reduced overall polarization of the cell. To further probe the efficiency of the LLZO electrolyte in symmetric configuration, the Li/LLZO-SIL/Li cell was galvanostatically charge-discharged at different temperatures of 30°C, 40°C, 50°C and 60°C respectively and their corresponding potential vs. time profiles during cycling were shown in ***Figure 3.12(d)***. It was observed from

the plots that with increase in temperature, the energy barrier of Li plating/stripping process at metal-ceramic interfaces gradually decreased resulting in lowering of over potential. The initial polarization value at 30°C was found to ~ 0.15V, which at 60°C decreased to a value of ~ 0.05V.

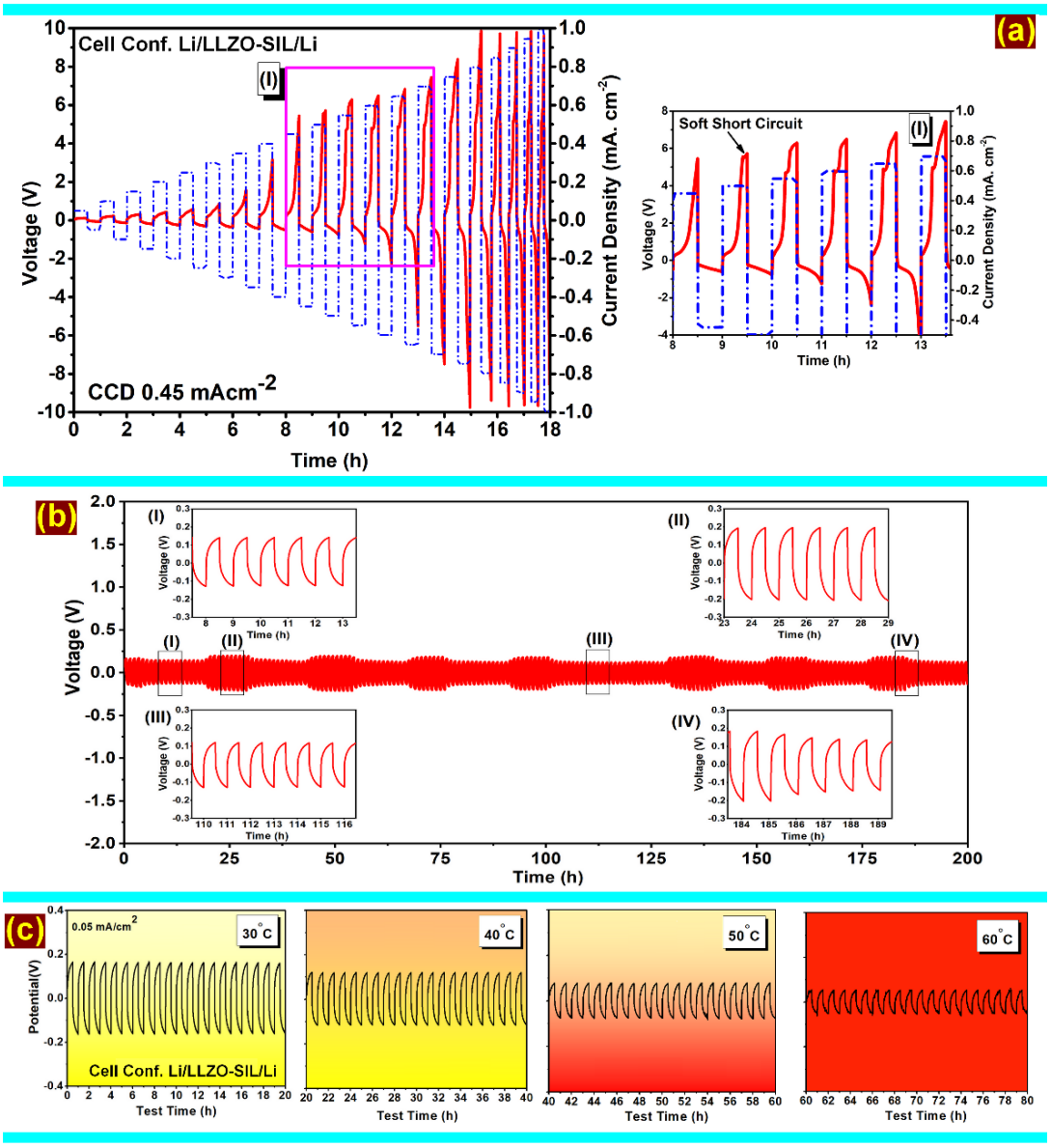

Figure 3.12 *(a) DC cycling profile of Li/Li cells at room temperature with step current density of 0.05 to 1 mA cm^{-2} (b) Galvanostatic cycling profile of Li/LLZO-SIL/Li symmetric cell at 0.05 mA.cm^{-2} for 200 hrs. (enlarged cycling profiles marked as (I–IV)). (d) Galvanostatic cycling profile of Li/LLZO-SIL/Li symmetric cell at temperature range of 30-60 ℃, current density of 0.05 mA.cm^{-2}.*

Apart from that, the smooth cycling profiles as shown in ***Figure 3.12(c)*** also suggested that Li-ion transport phenomena became more facile through the LLZO-SIL hybrid structure at elevated temperatures. Thus, the above results revealed that the combined effect of

engineered LLZO and impregnated SIL has a distinct influence in minimizing overpotential by lowering the energy barrier for Li plating/stripping at the metal-ceramic electrolyte interfaces, improving unimpeded Li-ion transport through grains due to its lower grain boundary areas.

3.3.5.2 Full Cell Performance

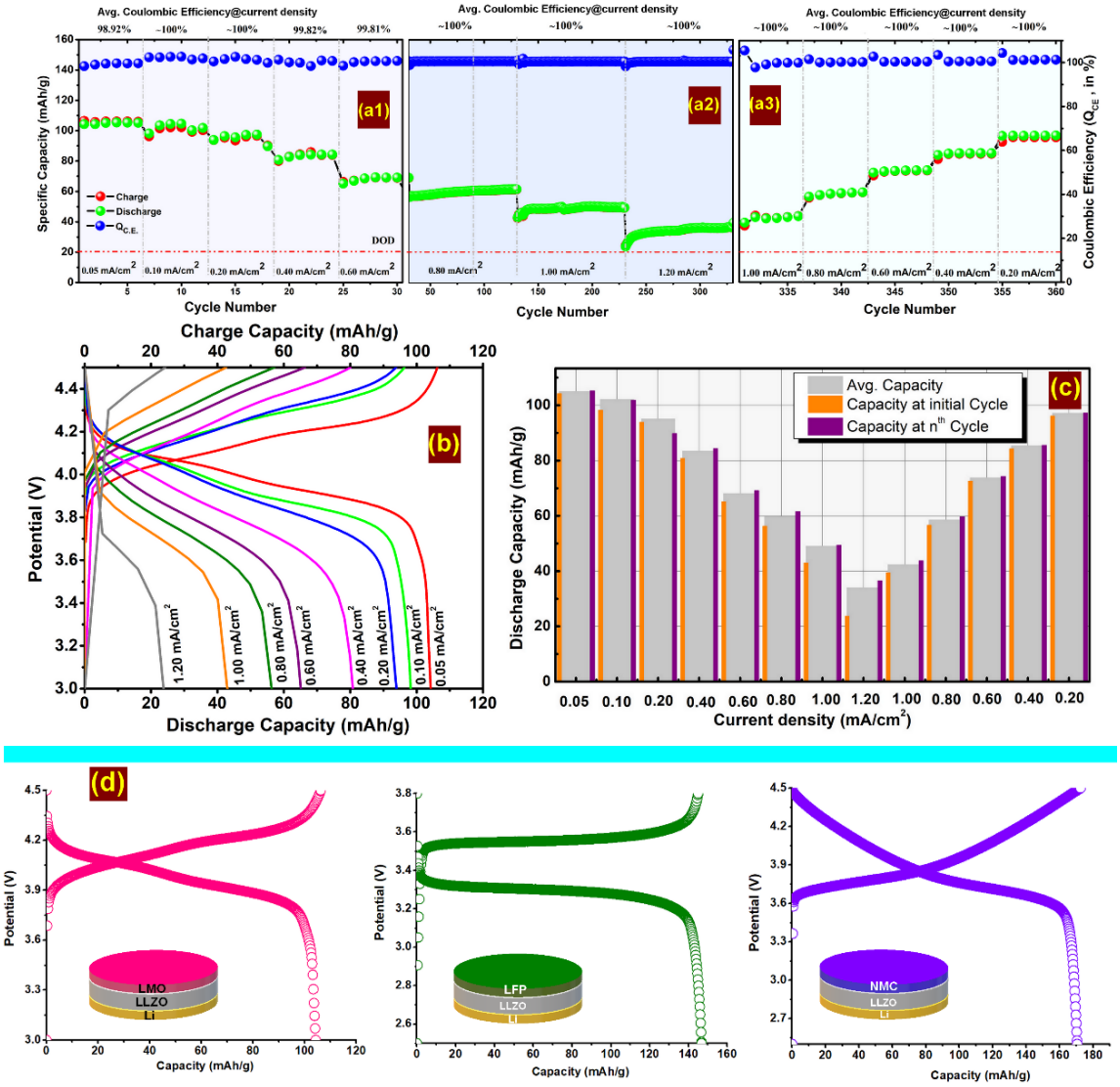

Figure 3.13 *(a) Specific capacity vs cycle number plot of Li/LLZO-SIL/LMO full cell at different current densities; a1(step up;0.05-0.60 mA.cm^{-2}), a2(step up ; 0.80-1.20 mA.cm^{-2}) and a3(step down; 1.00-0.20 mA.cm^{-2}), (b) typical charge discharge profiles of Li/LLZO-SIL/LMO full cell at different current densities (0.05-1.20 mA.cm^{-2}), (c) their corresponding discharge capacity vs current density plots, (d) electrochemical impedance spectra for as-fabricated cell and the cell taken after cycling at various current densities and their corresponding equivalent circuit in the inset., (e) multi-cathode compatibility showing typical charge-discharge profiles of Li/LLZO-SIL/LMO, Li/LLZO-SIL/LFP and Li/LLZO-SIL/NMC111 full cell.*

The electrochemical performance of solid-state lithium cell has been demonstrated in ***Figure 3.13***. The cycle number vs capacity plot with step-up current densities ranging from 0.05-1.2 mA.cm^{-2} is shown in ***Figure 3.13(a)***. The respective coulombic efficiencies were also plotted along with their cycling profiles. The cycling profiles as shown in ***Figure 3.13(a)*** of solid-state lithium cell were divided into three parts with respect to the current densities applied during testing; (a1) cycling profile (6 cycles each) at lower current densities ranging from 0.05-0.60 mA.cm^{-2}, (a2) high current densities comprising 100 cycles each and (a3) reverse current densities of 1.00-0.20 mA.cm^{-2}.In ***Figure 3.13(a1)***, at a lower current density of 0.05 mA.cm^{-2}, the cell delivered an average discharge capacity of 104.91 mAh.g^{-1} with >98 % coulombic efficiency. With further increase in current density to 0.10 mA.cm^{-2}, a marginal decrease in average discharge capacity could be observed delivering average discharge capacity of 102.15 mAh.g^{-1}. The current densities then continuously increased to values of 0.20, 0.40 and 0.60 mA.cm^{-2} and after 30 cycles, the average discharge capacity value of 68.04 mAh.g^{-1} was obtained at current density of 0.60 mA.cm^{-2}. The average discharge capacities as obtained in each of the said current densities (0.80, 1.00 and 1.20 mA.cm^{-2}) were found to be 59.71 mAh.g^{-1}, 48.95 mAh.g^{-1} and 33.98 mAh.g^{-1} with ~100% coulombic efficiency respectively. After running 330 cycles in incremental current densities, the cell was subjected to reversing back by decreasing the current densities and their profiles are represented in ***Figure 3.13(a3)***. No significant changes in average discharge capacities could be observed while reversing the current densities. It clearly suggested that the cell delivered excellent rate capability in almost all current densities as given both in forward and backward steps maintaining their overall coulombic efficiency >98%. ***Figure 3.13(b)*** demonstrates typical charge discharge profiles at constant current (CC) mode between 3.0V-4.5 V at all current densities (0.05 -1.20 mA.cm^{-2}) using engineered LLZO hybrid electrolyte against Li metal and LMO cathode delivering excellent coulombic efficiencies and charge-discharge characteristics of Li-LMO cell. To probe the cycling performance in terms of capacity fading at different current densities of Li/LLZO-SIL/LMO was further represented in ***Figure 3.13(c)***. The plot describes the initial capacity, average capacity and capacity delivered at nth cycle at a particular current density. The results revealed that almost no capacity fading could be observed. This further corroborates that the ionic transport of Li across the hybrid electrolyte comprising engineered LLZO and SIL remained unimpeded thought out the tested current densities. On the other way, it also reflected the enhanced interfacial stability and well wettability of Li metal on LLZO-SIL hybrid electrolyte surface. The excellent rate performance at 0.80 mA.cm^{-2} (2C), 1.00 mA.cm^{-2} (4C), and 1.20 mA.cm^{-2} (6C), thus obtained in LLZO solid electrolyte, might be due to the

contributions from both engineered LLZO and SIL filler, which probably minimized the grain boundary resistance, enhancing fast lithium ion migration through the solid matrix. The details of electrochemical findings at different current densities were summarized and presented in ***Table 3.6***.

Table 3.6 *Summary of electrochemical performance at different current densities of LLZO-SIL hybrid electrolyte in full cell configuration (Li/LLZO-SIL/LMO).*

Current density ($mA.cm^{-2}$)	Avg. C-rate	Avg. Charge Capacity ($mAh.g^{-1}$)	Avg. discharge capacity ($mAh.g^{-1}$)	Coulombic Efficiency (%)	Initial discharge capacity ($mAh.g^{-1}$)	Discharge capacity at n^{th} cycle ($mAh.g^{-1}$)
0.05	0.085C	106.06	104.91	98.92	104.26	105.15
0.10	0.17C	100.33	102.15	101.81	98.20	101.80
0.20	0.37C	94.28	95.04	100.83	93.89	89.70
0.40	0.85C	83.53	83.37	99.82	80.77	84.30
0.60	1.57C	68.16	68.04	99.81	65.12	69.12
0.80	2.39C	59.57	59.71	100.24	56.32	61.51
1.00	3.64C	48.87	48.95	100.17	42.96	49.35
1.20	6.34C	33.94	33.984	100.17	23.77	36.46
1.00	4.22C	42.21	42.31	100.34	39.44	43.71
0.80	2.44C	58.28	58.50	100.37	56.68	59.63
0.60	1.45C	73.12	73.66	100.75	72.55	74.19
0.40	0.84C	84.40	85.26	101.02	84.29	85.49
0.20	0.37C	95.44	97.07	101.72	96.14	97.15

The electrochemical performance of engineered LLZO was further extended to evaluate its multi-cathode compatibility against commercial $LiFePO_4$ (LFP) and NMC-111 cathodes. The typical charge discharge profiles were presented in the ***Figure 3.13(d)*** along with LMO. The discharge capacities as obtained were calculated to be 104.26 $mAh.g^{-1}$ (LMO), 146.77 $mAh.g^{-1}$ (LFP) and 170.54 $mAh.g^{-1}$ (NMC111) respectively. The charge-discharge profiles using Li metal and engineered LLZO hybrid electrolyte against the commercial cathodes revealed excellent capacity retention both in charge and discharge modes.

The electrochemical performances as obtained from the pseudo solid state cell against Li metal using engineered LLZO garnet in hybrid mode demonstrated excellent high rate capability

(0.05-1.20 mA.cm^{-2}, equivalent to C/12-6C rate), coulombic efficacy (>98%) and long-term cycling performance (tested up to 360 cycles). This may be due to the fact that multifaceted microstructure in engineered LLZO with reduced grain boundary area (neck-formed) facilitated intergranular Li-ion transport, whereas transgranular dendritic growth might have retarded due to the presence of impurities at grain boundaries. The LLZO voids filled with SILs in hybrid electrolyte might have contributed fast ionic transport at high current density. To probe these phenomena, the cycled cells were further dismantled and the exhausted LLZO electrolyte was analyzed by XRD and FESEM.

3.3.6 Post Electrochemical Studies

Lihtium dendritic growth in metal batteries is inevitable due to the point contacts at the metal-electrolyte interface[42]. Therefore, to observe the Lithium dendrite phenomena, Li/LLZO-SIL/LI symmetric cells were cycled in step current densities ranging from 0.05-6.40 mA.cm^{-2} at regular intervals of ~50 cycles, and impedance spectra were recorded both before cycling and after cycling. The EIS profiles along with its corresponding equivalent circuit in the in-set as shown in ***Figure 3.14****(c)* of freshly prepared and cycled cells also revealed a dramatic change in charge transfer resistance, R_{ct} considered as cumulative impedance (R_1 and R_2) of both electrolyte and interfacial resistances, suggesting the metallic penetration of Lithium[43].

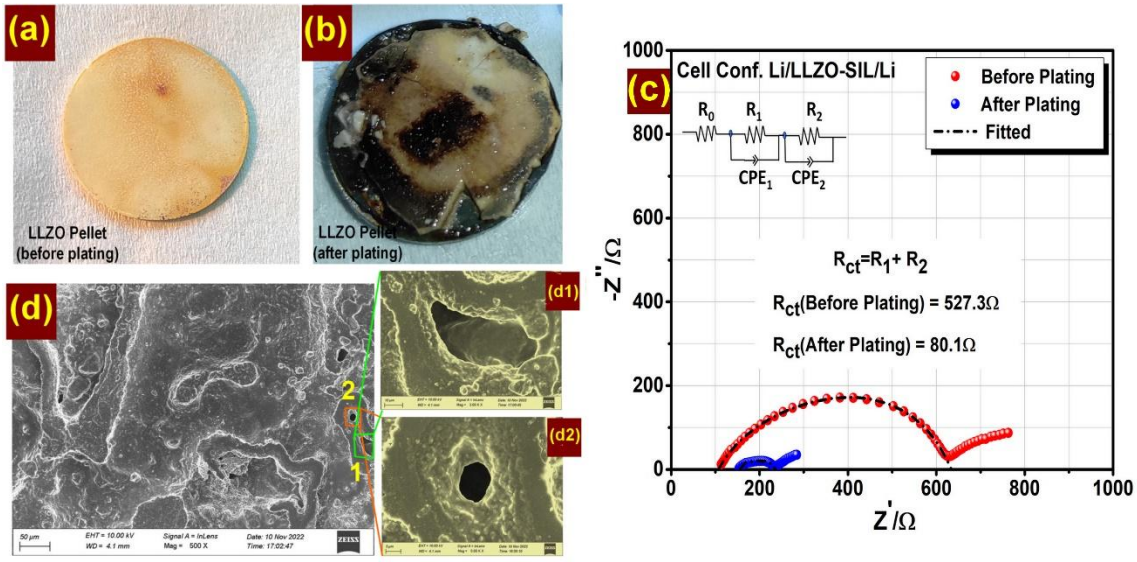

Figure 3.14 *The digital images* ***(a)*** *taken for LLZO pellet before and* ***(b)*** *after plating of Li-symmetric cell,* ***(c)*** *Impedance spectra Li-symmetric cell cycled cell before and after cycling at high current density of 6.4 mA.cm^{-2} for testing short-circuit,* ***(d)*** *FESEM micrographs of top surface of LLZO-SIL hybrid electrolyte showing "glacier flow" pattern (d1) and deep penetrating holes at places (d2).*

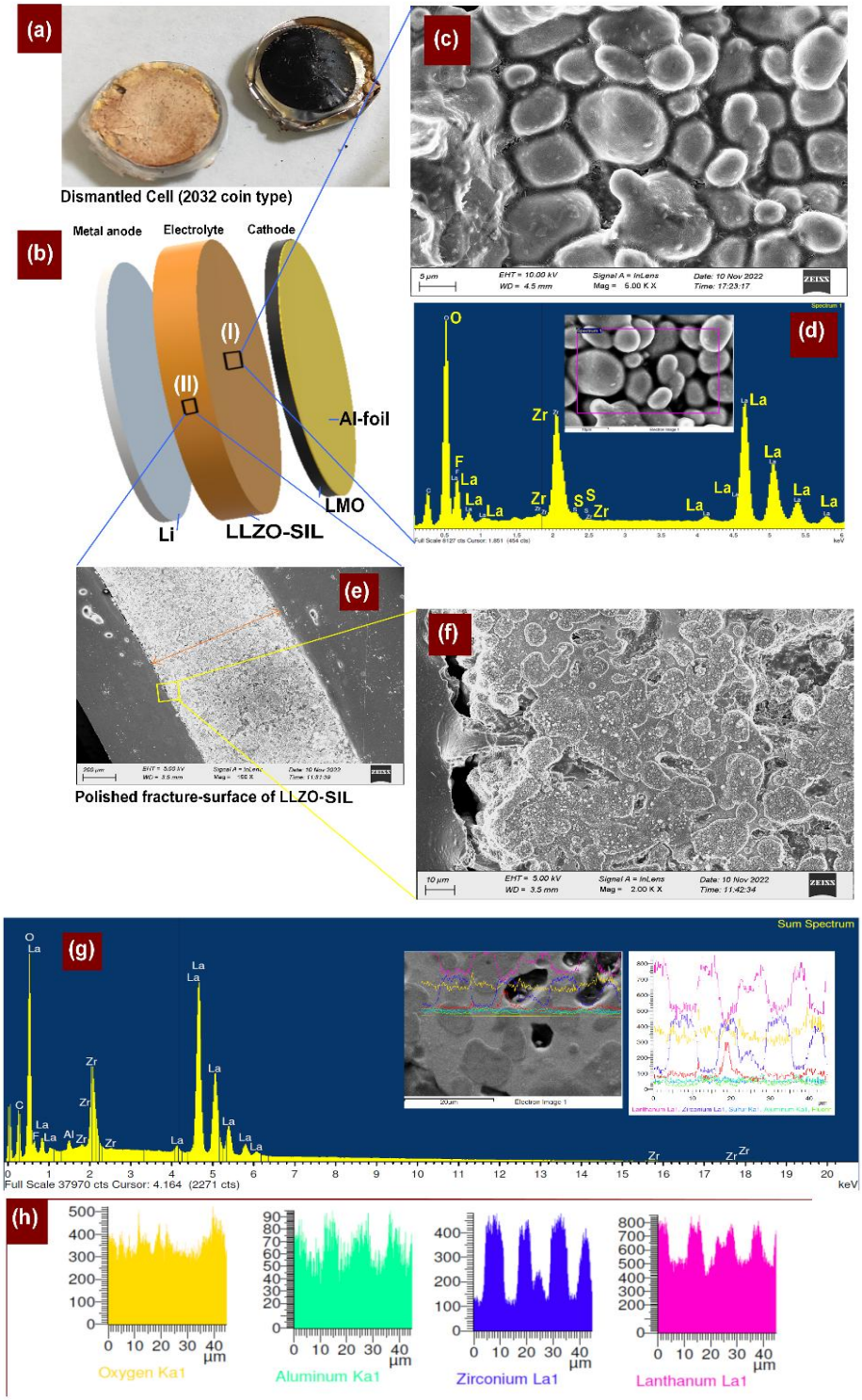

Figure 3.15 *(a) digital images taken at the interior of 2032 coin cell showing circular cathode films and LLZO electrolyte soaked in SIL, (b) Schematic representation of lithium solid state cell and the places where FESEM imaging done, (c)-(d) FESEM micrographs and corresponding elemental mapping of LLZO-SIL electrolyte, (e) FESEM micrographs of fractured surface and its enlarged version show in (f), Corresponding elemental mapping and line spectrum as presented in (g) & (h).*

The symmetric cell was then dismantled, and the surface morphology was examined under FESEM as shown in ***Figure 3.14 (a),(b),*** and ***(d)***. It was observed that the colour of the freshly prepared LLZO pellet was completely changed and turned blackish [***Figure 3.14(a)*** *and* ***Figure 3.14(b)***]. It was reported elsewhere that the black spots on the short-circuited LLZO surface was probably due to lithium, growing through the grain boundaries or voids in LLZO[44]. Utilizing backscattered electron SEM and EDS, Ren et al.[45] proposed that Li might grew through grain boundaries and interconnected pores in short-circuited LLZO. In this study, the surface morphology of cycled LLZO-SIL pellet as shown in ***Figure 3.14(d)*** showed large number of cavities at places. On further magnification, the cavities (as shown in ***Figure 3.14(d1)*** and ***(d2)***) were found to be deep and hollow in nature with interesting non-geometrical openings suggesting forceful penetration of unknown moiety, most probably lithium dendrites needle. This may be the first indirect observation as per our knowledge of lithium penetration through LLZO hybrid electrolytes. The post-electrochemical study (full cell) was also carried out by dismantling the 2032 coin cells, as shown in ***Figure 3.15(a)***. The colour of cycled electrolyte pellets was found to remain the same as the as-fabricated one. The FESEM analysis was performed at the surface facing towards the cathode and at the cross-section of the cycled pellet, schematically presented and marked in ***Figure 3.15(b)***.

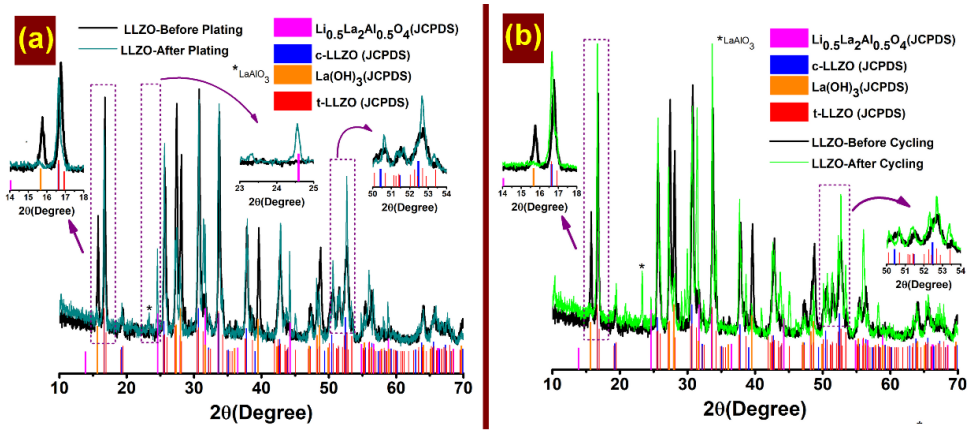

Figure 3.16 *(a) X-ray diffractograms of LLZO pellet before and after plating (b) The comparison of X-ray diffractograms of the LLZO pellet before and after cycling (Cell Configuration Li/LLZO-SIL/LMO).*

The microstructure and morphology of the particles found at the cathode facing surface of LLZO was similar to that of calcined LLZO powder (refer to ***Figure 3.8(a)***). The neck-formed grains with faceted microstructure could also be observed here. The selected area EDX profile, as shown in ***Figure 3.15(d)***, and the quantitative elemental mapping on the cathode-facing surface of LLZO revealed that the molar ratio (in atomic wt.%) of Zr and La was nearly 2:3, the typical stoichiometric proportion exists in LLZO garnet. The presence of aluminum

was also detected, which might have originated from the alumina crucible used for powder processing and sintering. At the fractured surface, the microstructure as shown in ***Figure 3.15(e)*** and its magnified version in ***Figure 3.15(f)***, was found to be somewhat changed due to the surface contamination of LLZO cycled pellet as the specimen had to exposed during polishing and sample preparation in ambient atmosphere. To understand the compositional features of the grain and grain boundaries at the cross-section of the LLZO pellet, qualitative line mapping was carried out using EDX, and the presence of elements both at grain and grain boundaries across the line is examined and shown in ***Figure 3.15(g)-(h)***. It was interesting to note that the presence of lanthanum at the grain boundary was found to be higher than that of grains, whereas Zr was detected inside the grains only. The results also corroborated the finding observed in LLZO sintered pellets as earlier.

To further confirm the phases present in cycle LLZO, XRD was carried out, and the diffractograms are presented in ***Figure 3.16***. A comparison of XRD profiles of cycled-LLZO powder along with sintered LLZO powder revealed trace amount of $La(OH)_3$, whereas an appearance of a new phase, $Li_{0.5}Al_{0.5}La_2O_4$ in cycled LLZO powder. This particular phase $Li_{0.5}Al_{0.5}La_2O_4$ probably originated during electrochemical cycling of LLZO electrolyte. The accumulation of lithium to form that particular phase might occur either by diffusing from the LLZO grains or from the SIL used for hybridization of the LLZO solid electrolyte. Such in-situ formation of Li containing stable phase in the LLZO solid electrolyte matrix might be one of the reasons for the high-rate capability and long cycling performance without short-circuit. Similar observation could also be detected for Li-symmetric cell operation of 200 hours configured with LLZO-SIL hybrid electrolyte as shown in the XRD patterns in ***Figure 3.16(a)***.

3.4 Conclusion

In this chapter, a one-step alanine-assisted combustion process was optimized to synthesize engineered LLZO with neck-fused microstructures. Pristine LLZO showed reduced conductivity due to residual impurities. But when hybridized with solvated ionic liquid (SIL), the engineered LLZO delivers excellent electrochemical performance. Li/LLZO-SIL/LMO full cells delivered long-term cycling stability (>360 cycles), high coulombic efficiency (>99%), and superior rate capability, while symmetric cells demonstrated stable operation for over 200 hours. A first-of-its-kind visualization of dendritic penetration by lithium inside the LLZO-SIL hybrid electrolyte matrix was demonstrated in a symmetric cell at a high current density of 6.4 $mA.cm^{-2}$. Post-cycling studies revealed that dendrite growth was mitigated by the engineered microstructure and the in situ formation of $Li_{0.5}Al_{0.5}La_2O_4$ at the grain boundaries. Furthermore, multi-cathode tests (LMO, LFP, NMC111) confirmed the versatility of the hybrid electrolyte.

Overall, this work establishes that engineered LLZO-SIL hybrid electrolytes offer a scalable and effective route for developing high-performance pseudo-solid-state lithium metal batteries.

3.5 References

1 F. Zheng, M. Kotobuki, S. Song, M. O. Lai and L. Lu, *J Power Sources*, 2018, **389**, 198–213.

2 Q. Zhao, S. Stalin, C.-Z. Zhao and L. A. Archer, *Nat Rev Mater*, 2020, **5**, 229–252.

3 J. Wang, G. Huang and X. Zhang, *Batter Supercaps*, 2020, **3**, 1006–1015.

4 M. Keller, A. Varzi and S. Passerini, *J Power Sources*, 2018, **392**, 206–225.

5 R. Murugan, V. Thangadurai and W. Weppner, *Angewandte Chemie International Edition*, 2007, **46**, 7778–7781.

6 M. M. Raju, F. Altayran, M. Johnson, D. Wang and Q. Zhang, *Electrochem*, 2021, **2**, 390–414.

7 A. Paolella, W. Zhu, G. Bertoni, S. Savoie, Z. Feng, H. Demers, V. Gariepy, G. Girard, E. Rivard, N. Delaporte, A. Guerfi, H. Lorrmann, C. George and K. Zaghib, *ACS Appl Energy Mater*, 2020, **3**, 3415–3424.

8 G. Larraz, A. Orera and M. L. Sanjuán, *J Mater Chem A Mater*, 2013, **1**, 11419.

9 I. Kokal, M. Somer, P. H. L. Notten and H. T. Hintzen, *Solid State Ion*, 2011, **185**, 42–46.

10 Y. Jin and P. J. McGinn, *J Power Sources*, 2013, **239**, 326–331.

11 K. Kim, S.-H. Yang, M. Y. Kim, M. S. Lee, J. Lim, D. R. Chang and H.-S. Kim, *Journal of Industrial and Engineering Chemistry*, 2016, **36**, 279–283.

12 K. Ueno, K. Yoshida, M. Tsuchiya, N. Tachikawa, K. Dokko and M. Watanabe, *J Phys Chem B*, 2012, **116**, 11323–11331.

13 Q. A. ISLAM, M. W. RAJA, C. SATRA and R. N. BASU, *Bulletin of Materials Science*, 2015, **38**, 1473–1478.

14 P. Djurdjević and R. Jelić, *Transition Metal Chemistry*, 1993, **18**, 457–461.

15 D. D. Perrin, *Journal of the Chemical Society (Resumed)*, 1958, 3125.

16 P. Badami, S. Smetaczek, A. Limbeck, D. Rettenwander, C. K. Chan and A. N. M. Kannan, *Mater Adv*, 2021, **2**, 5181–5188.

17 N. Janani, S. Ramakumar, L. Dhivya, C. Deviannapoorani, K. Saranya and R. Murugan, *Ionics (Kiel)*, 2011, **17**, 575–580.

18 P. Fleming, R. A. Farrell, J. D. Holmes and M. A. Morris, *Journal of the American Ceramic Society*, 2010, **93**, 1187–1194.

19 L. Cheng, J. S. Park, H. Hou, V. Zorba, G. Chen, T. Richardson, J. Cabana, R. Russo and M. Doeff, *J. Mater. Chem. A*, 2014, **2**, 172–181.

20 M. Rosen, R. Ye, M. Mann, S. Lobe, M. Finsterbusch, O. Guillon and D. Fattakhova-Rohlfing, *J Mater Chem A Mater*, 2021, **9**, 4831–4840.

21 Y. Li, X. Chen, A. Dolocan, Z. Cui, S. Xin, L. Xue, H. Xu, K. Park and J. B. Goodenough, *J Am Chem Soc*, 2018, **140**, 6448–6455.

22 A. Ansari, A. Ali, M. Asif and S. Shamsuzzaman, *New Journal of Chemistry*, 2018, **42**, 184–197.

23 S. Pratibha, N. Dhananjaya, A. Pasha and S. Khasim, *Appl Nanosci*, 2020, **10**, 1927–1939.

24 K. Ghosh and M. Wasim Raja, *ACS Omega*, 2022, **7**, 33385–33396.

25 I. M. Weiss, C. Muth, R. Drumm and H. O. K. Kirchner, *BMC Biophys*, 2018, **11**, 2.

26 M. W. Raja, S. Mahanty, P. Ghosh, R. N. Basu and H. S. Maiti, *Mater Res Bull*, 2007, **42**, 1499–1506.

27 J. Sakamoto, E. Rangasamy, H. Kim, Y. Kim and J. Wolfenstine, *Nanotechnology*, 2013, **24**, 424005.

28 J. Tan and A. Tiwari, *ECS Solid State Letters*, 2012, **1**, Q57–Q60.

29 H. Buschmann, J. Dölle, S. Berendts, A. Kuhn, P. Bottke, M. Wilkening, P. Heitjans, A. Senyshyn, H. Ehrenberg, A. Lotnyk, V. Duppel, L. Kienle and J. Janek, *Physical Chemistry Chemical Physics*, 2011, **13**, 19378.

30 E. A. Il'ina, O. L. Andreev, B. D. Antonov and N. N. Batalov, *J Power Sources*, 2012, **201**, 169–173.

31 E. Rangasamy, J. Wolfenstine, J. Allen and J. Sakamoto, *J Power Sources*, 2013, **230**, 261–266.

32 N. Janani, C. Deviannapoorani, L. Dhivya and R. Murugan, *RSC Adv.*, 2014, **4**, 51228–51238.

33 N. C. Rosero-Navarro, T. Yamashita, A. Miura, M. Higuchi and K. Tadanaga, *Journal of the American Ceramic Society*, 2017, **100**, 276–285.

34 Y. Luo, X. Li, H. Chen and L. Guo, *Journal of Materials Science: Materials in Electronics*, 2019, **30**, 17195–17201.

35 J. Evans, C. A. Vincent and P. G. Bruce, *Polymer (Guildf)*, 1987, **28**, 2324–2328.

36 H. Xie, Y. Li and J. B. Goodenough, *Mater Res Bull*, 2012, **47**, 1229–1232.

37 A. Dumon, M. Huang, Y. Shen and C.-W. Nan, *Solid State Ion*, 2013, **243**, 36–41.

38 L. Dhivya, K. Karthik, S. Ramakumar and R. Murugan, *RSC Adv*, 2015, **5**, 96042–96051.

39 J. M. Weller, J. A. Whetten and C. K. Chan, *ACS Appl Energy Mater*, 2018, **1**, 552–560.

40 Q. Wang, C. Yang, Y. Zhang, J. Yang, K. Wu, C. Hu, J. Lu, W. Liu and H. Zhou, *ACS Appl Energy Mater*, 2019, **2**, 4602–4608.

41 L. Porz, T. Swamy, B. W. Sheldon, D. Rettenwander, T. Frömling, H. L. Thaman, S. Berendts, R. Uecker, W. C. Carter and Y. Chiang, *Adv Energy Mater*, DOI:10.1002/aenm.201701003.

42 T.-Q. Yang, C. Wang, W.-K. Zhang, Y. Xia, Y.-P. Gan, H. Huang, X.-P. He and J. Zhang, *Rare Metals*, 2022, **41**, 1870–1879.

43 D. Wang, K. Peng, Y. Fu, C. Zhu and Y. Yang, *J Power Sources*, 2021, **487**, 229421.

44 R. Sudo, Y. Nakata, K. Ishiguro, M. Matsui, A. Hirano, Y. Takeda, O. Yamamoto and N. Imanishi, *Solid State Ion*, 2014, **262**, 151–154.

45 Y. Ren, Y. Shen, Y. Lin and C.-W. Nan, *Electrochem commun*, 2015, **57**, 27–30.

CHAPTER 4

Stabilization of Metal-Solid Electrolyte Interface via Functional Layer (NH_4F) and Solvated Ionic Liquid

Summary & Graphical Abstract

Stabilizing interfaces in solid-state lithium metal batteries remains challenging due to incompatibility, parasitic reactions, and uneven Li deposition at the metal/electrolyte boundaries. Here, we present a novel dual-interfacial engineering strategy combining rapid NH_4F surface treatment and solvated ionic liquid (SIL) infusion in garnet-type pristine LLZO electrolytes to construct robust LiF-rich solid hybrid electrolytes (SHEs). This synergistic modification suppresses parasitic reactions, reduces interfacial degradation, and stabilizes lithium plating/stripping over extended cycling. Post-cycling analysis confirms the presence of chemically stable interfaces and interphases. In full-cell configurations, the dual-modified LLZO hybrid electrolyte demonstrates superior compatibility and excellent electrochemical performance at a higher current density. Thus, this chapter establishes that NH_4F-SIL-assisted dual interfacial engineering is an effective and scalable approach to overcome interfacial limitations of garnet electrolytes for next-generation solid-state lithium metal batteries.

Objectives

1. Improve interfacial wettability and Li^+ transport.
2. Suppress parasitic reactions and dendrite growth.

Strategy

Dual strategy via NH_4F surface treatment and SIL

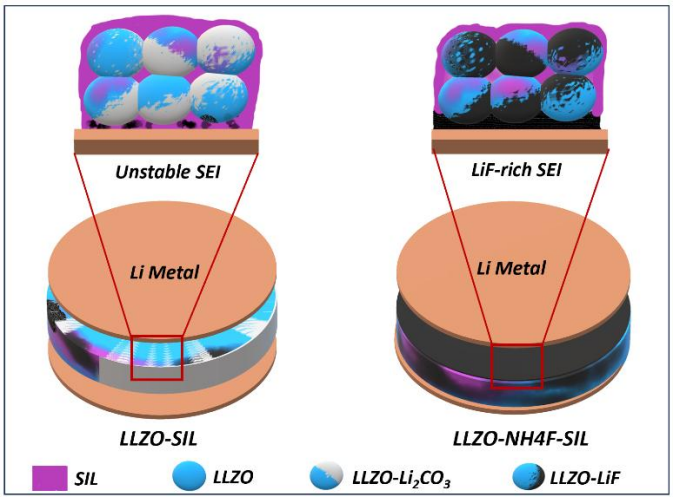

Figure 4.1 *Graphical abstract summarising the effects of dual interfacial strategy in pristine LLZO-based solid electrolytes for metal batteries.*

4.1 Introduction

Solid-state lithium metal batteries (SSLMBs) have recently gathered significant attention as one of the promising candidates among the various next-generation energy storage devices for high energy density and intrinsic safety towards electrification[1,2]. Conventional liquid electrolyte system fails miserably due to their limited energy density and safety issues with flammable electrolytes. The successful commercialisation of SSLMBs thus critically depends on the development of a robust solid electrolytes that can ensure both high ionic conductivity and interfacial stability against lithium metal[1–4]. Among the various groups of inorganic solid electrolytes, garnet-type $Li_7La_3Zr_2O_{12}$ (LLZO) satisfies most of the requirements for an ideal solid electrolyte due to its wide electrochemical stability window, high thermal stability, and reasonable bulk ionic conductivity. However, the practical deployment of LLZO in SSLMBs is hindered by two main interfacial challenges: (i) poor wettability and chemical instability at the metal/electrolyte interface, and (ii) surface contamination from atmospheric exposure, which results in rapid resistive layer formation (such as Li_2CO_3 and LiOH) during exposure to the air atmosphere. These challenges further lead to higher interfacial resistance and non-uniform and uneven Li plating/stripping, resulting in premature death of the cell due to uncontrolled dendrite penetration[1–4].

To stabilise the metal/electrolyte interface, various strategies are explored. Mainly, two distinct approaches were chosen by the researchers worldwide: (1) either by doing engineering at the metal anode-electrolyte interface using functional interlayers (nanosized fumed silica[5], Si_3N_4[6], MoS_2[7], Indium Tin Oxide layer[8] and an Ag nanoparticle[9]) or (2) by changing the cell configurations e.g., by designing a monolithic cell[10], application of molten Lithium as a metal anode[11,12] or by making composites[13–16] /hybrid[15,17,18] Solid-state electrolytes using Ionic liquids. Room temperature SILs are of particular interest owing to their thermal stability, low flammability, and wide potential window[19].

In this chapter, we introduce a dual interfacial engineering approach that combines (i) a rapid, low-temperature NH_4F surface via wet chemical treatment and (ii) the solvated ionic liquid (SIL) infusion in a porous LLZO matrix. The NH_4F treatment on the top of the bulk surface of LLZO material reacts with surface impurities, such as Li_2CO_3/LiOH species, to form a stable LiF-rich passivation layer[20,21]. As a result, the interfacial stability between Li metal and LLZO electrolyte was improved by reducing the parasitic reaction. However, the large grain boundary resistance with pores and voids of pristine LLZO restricted its performance in all solid-state

cell configurations[1,2]. Thus, a solid hybrid electrolyte is designed to improve the Li/LLZO interface further. Thus, infusion with the SIL ($[Li(G4)]^+TFSI^-$ complex) enhances the ionic conductivity and interfacial wettability[22,23]. It also reduces the electronic leakage pathways, one of the major issues in cell failure[19,24]. Together, these modifications demonstrate the creation of a hybrid organic–inorganic interface that simultaneously improves the chemical stability, suppresses dendrite growth, and facilitates homogeneous Li^+ flux during cycling. By systematically investigating the structural, microstructural, electrochemical, and post-mortem characteristics of solid hybrid electrolyte, this chapter establishes the efficacy of synergistic interfacial modification in enabling high-rate, dendrite-free, and long-life SSLMBs.

4.2 Experimental

4.2.1 Material Synthesis and Characterization

The preparation of solid hybrid electrolytes involves three major steps. The first one was the preparation of cubic LLZO by alanine-assisted auto-combustion methods. Followed by wet chemical treatment via NH_4F, and finally, the infusion of solvated ionic liquid into the pristine LLZO scaffold. The detailed steps of the synthesis process are already discussed in ***Chapter 2***, ***Section 2.3.1***. The wet chemical treatment on the top of the LLZO pellets was discussed in ***Section 2.3.4***. Whereas the preparation of a solid hybrid electrolyte is discussed in ***Section 2.4***. It is worth mentioning here that the solid hybrid electrolyte, after surface modification and SIL treatment, was directly compared with the surface-unmodified system to better assess the impact of surface modification on overall performance. However, the SIL uptake for both cases was almost equal, 15±2wt%. Thus, it will be very interesting to measure various electrical and electrochemical performances in these systems. ***Table 4.1*** describes the nomenclature of various electrolytes developed in this study. The details of characterization techniques are already discussed in ***Section 2.7***.

Table 4.1 *Various modifications and corresponding nomenclature of NH4F and SIL modified solid or solid hybrid electrolyte.*

Modification	Termed as
Pristine LLZO	LLZO
Pristine LLZO with NH_4F	LLZO-NH4F
Pristine LLZO with SIL	LLZO-SIL
Pristine LLZO with NH_4F and SIL	LLZO-NH4F-SIL

4.2.2 Cell Fabrication and Testing

The details of the cell fabrication and testing techniques are already discussed in ***Chapter 2***, ***Section 2.6*** and ***Section 2.7,*** respectively. In Short, after preparing the solid hybrid electrolyte (LLZO-SIL and LLZO-NH4F-SIL), various cells, symmetric (Li/Li, SS/SS) and full (Li/LMO) or asymmetric (Li/SS) coin cells were assembled as discussed in ***Chapter 2***.

4.3 Results and Discussion

4.3.1 Microstructural Study

The surface morphology of the pristine LLZO material before and after NH_4F treatment is examined via FESEM, as illustrated in ***Figures 4.2 (a)-(i)***. In ***Figures 4.2(a)***, pristine LLZO powder calcined at 900°C shows a highly porous and interconnected network of agglomerated particles. It is worth mentioning here that a prominent lamellar-type structure of Li2CO3 is formed at the surface of the LLZO particle due to uncontrollable reactions between LLZO and atmospheric moisture, leading to Li^+/H^+ exchange reaction and carbonate deposition as discussed earlier. The presence of such insulating by-products is widely reported in LLZO systems and poses a significant barrier to Li^+ transport at the electrolyte-electrode interface, contributing to increased interfacial resistance and dendrite formation[20,21]. Thus, removal of such phase is beneficial in terms of reducing interfacial resistance and retarded the penetration. ***Figures 4.2(b)*** and ***4.2(c)*** show the top view of cross-sectional FESEM images of the sintered LLZO pellet at two different magnifications. At a magnified version, it is clearly seen that the surface of LLZO is greatly impacted due to the formation of Li_2CO_3 across the surface. After the surface treatment with NH_4F, significant changes in the surface morphology of the LLZO top surface are observed. The surface in ***Figures 4.2(d)*** and ***4.2(e)*** appears to be smooth and more uniformly covered with fine particles or a film-like structure, which might be due to the formation of a LiF-rich layer at the top surface of the pellet. Thus, a more homogeneous reaction of NH_4F with surface impurities such as Li_2CO_3 and LiOH in the LLZO is expected. To further confirm the chemical transformation induced by NH_4F treatment, elemental mapping is performed. The elemental distributions of oxygen, lanthanum, zirconium, and fluorine are shown in ***Figures 4.2(f)-(i)***, respectively. A uniform distribution of Oxygen (***Figures 4.2f***), Lanthanum (***Figures 4.2g***), and zirconium (***Figures 4.2h***) is observed across the surface, suggesting the formation of LLZO material. Most notably, ***Figures 4.2(i)*** clearly confirms the homogeneous incorporation of fluorine across the surface, validating the possible successful formation of a LiF-rich passivation layer following NH_4F treatment. This LiF-rich interfacial

layer might play a critical role in enhancing interfacial stability by suppressing parasitic reactions, minimizing interfacial voids, and facilitating uniform Li-ion flux during cycling. Thus, it is interesting to see the structural, electrical, and electrochemical properties after NH_4F surface treatment of pristine LLZO electrolyte.

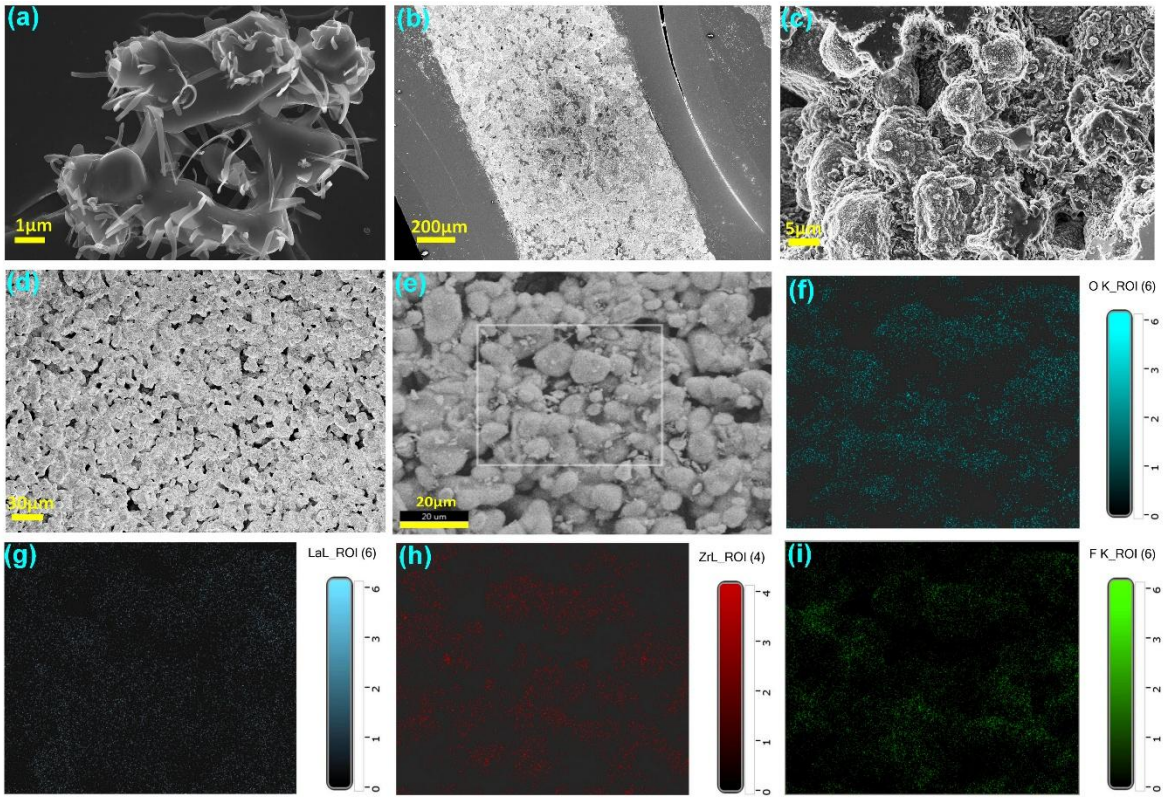

Figures 4.2 *(a) FESEM micrographs of LLZO powder, (b) and (c) FESEM micrographs of the polished surface of LLZO sintered pellets at two different scales, (d) & (e) NH4F modified top surface of LLZO pellets at different scales. (f)-(i) Elemental mapping of NH4F modified LLZO pellet for O, La, Zr, and F, respectively.*

4.3.2 Structural Studies

Figure 4.3(a) represents the X-ray diffraction patterns of pristine and NH_4F-treated LLZO pellets sintered at 1000 °C along with the JCPDS data of cubic (c-LLZO, PDF 00-064-0141). The major peak of both samples is consistent with the cubic garnet structure, along with impurities such as $La(OH)_3$. The formation of such impurities and their effect on electrical and electrochemical properties are discussed in our previous work. In short, this phase, $La(OH)_3$, can be treated as a surface impurity in La-containing materials, particularly under atmospheric exposure during synthesis and calcination. Importantly, the comparison between pristine and NH_4F-treated LLZO reveals that the surface fluorination process does not cause any distortion

or secondary phase formation within the bulk crystal lattice. The absence of peak shifts or additional reflections in the treated sample confirms that NH_4F selectively modifies the surface chemistry without compromising the structural integrity of the cubic garnet framework. Complementary evidence is provided by the Fourier transform infrared (FTIR) spectra shown in ***Figure 4.3(b)***. The pristine LLZO sample displays a distinct vibrational band at ~860–880 cm^{-1}, which corresponds to carbonate ($-CO_3^{2-}$) stretching modes, indicative of Li_2CO_3 formation due to Li^+/H^+ exchange and subsequent reaction with atmospheric CO_2. After NH_4F treatment, this carbonate band is markedly suppressed, demonstrating the effective removal of Li_2CO_3 from the surface. Such a surface modification is particularly important because carbonate and hydroxide impurities are known to hinder interfacial wetting with lithium metal and increase charge-transfer resistance. Therefore, selective fluorination emerges as a viable strategy to tailor the surface chemistry of LLZO without compromising its intrinsic structural or electrochemical stability.

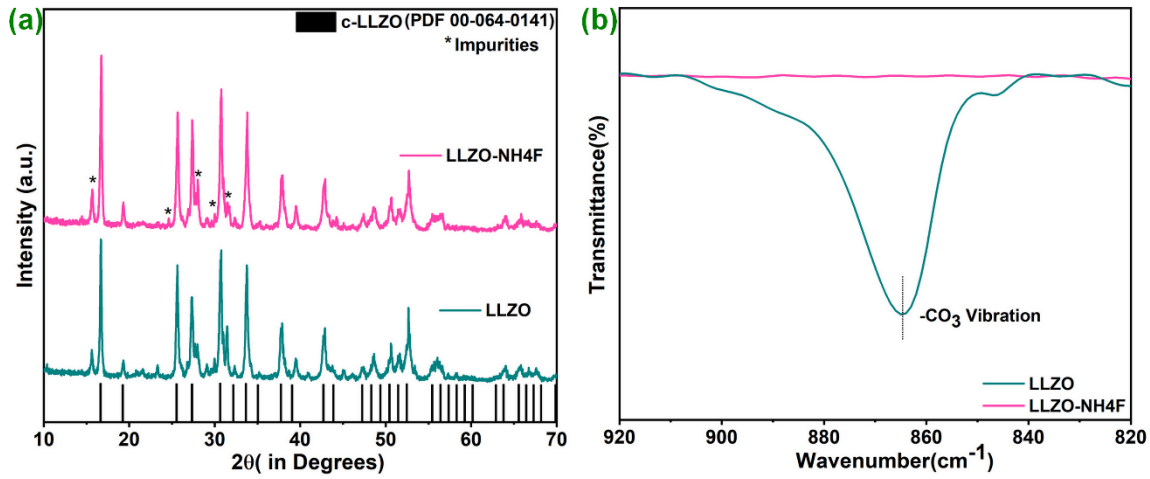

Figure 4.3 *(a) X-ray diffraction pattern of LLZO and LLZO-NH4F pellets sintered at 1000°C along with the JCPDS file of cubic LLZO (c-LLZO). (b) FTIR spectra of -CO_3 vibration for LLZO and LLZO-NH4F pellets.*

4.3.3 Electrical Studies

In ***Figure 4.4(a)***, the Nyquist plot of the LLZO and LLZO-NH4F pellet is presented along with the equivalent circuit. The total conductivity is found to be 1.10×10^{-4} mS/cm for LLZO and 2.43×10^{-3} mS/cm for NH4F-treated LLZO. Thus, the overall conductivity increases by a significant margin after the surface treatment. But, the overall conductivity of pristine c-LLZO is somewhat lower than the reported one (~10^{-5} S/cm), which might be due to the formation of $La(OH)_3$ impurities, which are deposited at the grain boundaries as discussed in our previous

work. The Arrhenius plot as presented in ***Figure 4.4(b)*** reveals a notable reduction in activation energy from 0.42 eV (LLZO) to 0.39 eV (LLZO-NH_4F). Thus, the electrical measurement clearly established that the surface treatment improved the overall Li^+ transport kinetics by reducing interfacial impedance due to the elimination of the insulating Li_2CO_3/LiOH layer. It is worth discussing here that the chemically treated LLZO showed a significant increment in overall conductivity, but the sintered pellet still delivered lower conductivity. To compensate for such a reduction, solvated ionic liquid is infused into the matrix of LLZO and LLZO-NH4F to enhance the Li metal anode/electrolyte interface stability and facilitate the lithium-ion movement across the thick electrolyte. Thus, it is interesting to investigate the combined effect of NH_4F treatment and SIL infusion on the ionic conductivity and electrochemical behaviour of the hybrid electrolyte.

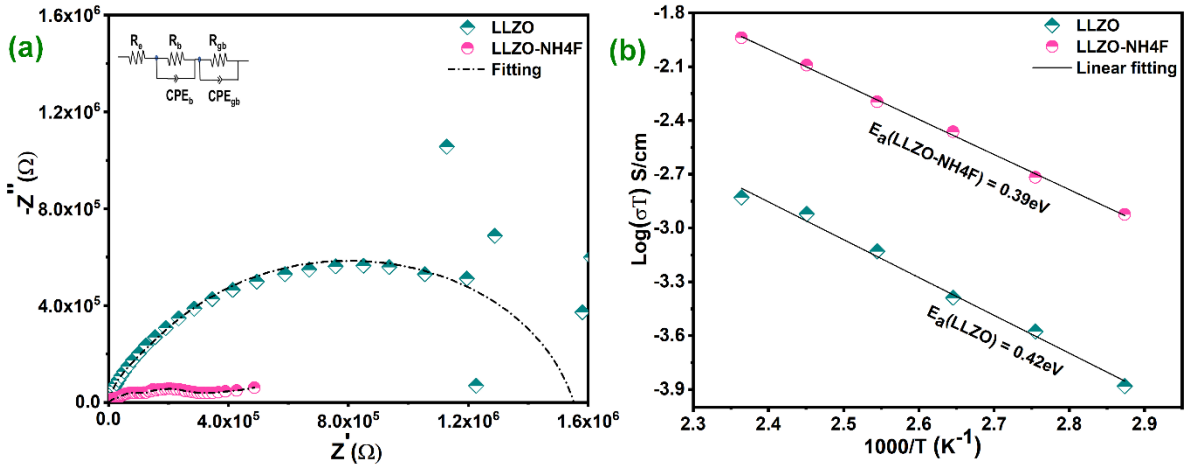

Figure 4.4 *(a) Nyquist plot of LLZO and LLZO-NH4F pellets at RT, (b) Arrhenius plot showing variation of conductivities with respect to temperature to calculate the activation energies for both the developed electrolytes.*

The pristine LLZO solid electrolyte suffers from low ionic conductivity and poor interfacial compatibility with lithium metal due to Li_2CO_3 surface contaminants and limited Li^+ mobility across grain boundaries, as discussed in the previous chapter (***Chapter 3, Sec. 3.3.3***). To tackle both issues, solvated ionic liquid and NH_4F are used to modify the LLZO matrix. As earlier, we observed that the LLZO matrix provides better ionic transport with lower activation energy after modification with NH_4F chemical treatment. To evaluate the combined impact of SIL and NH_4F in the LLZO matrix, a series of electrochemical analyses is carried out and presented in ***Figure 4.5***. To understand the role of solvated ionic liquid (SIL) in enhancing the ionic conductivity of LLZO-based hybrid electrolytes, the ionic contribution of SIL was separately estimated using a polypropylene (PP) separator soaked with SIL placed between two blocking

stainless-steel electrodes. The corresponding Nyquist plots of PP-SIL, LLZO-SIL, and LLZO-NH4F-SIL are presented in ***Figure 4.5(a)***. Although SIL appears to enhance the conductivity of the LLZO matrix to a certain extent. However, LLZO-NH4F-SIL shows a conductivity of 7.43×10^{-4} S·cm^{-1}, which is significantly higher than that of LLZO-SIL (8.20×10^{-5} S·cm^{-1}) and PP-SIL (1.13×10^{-4} S·cm^{-1}). This enhancement may be due to both the improved interfacial wetting and percolative conduction pathways facilitated by the LiF-rich NH_4F-treated surface.

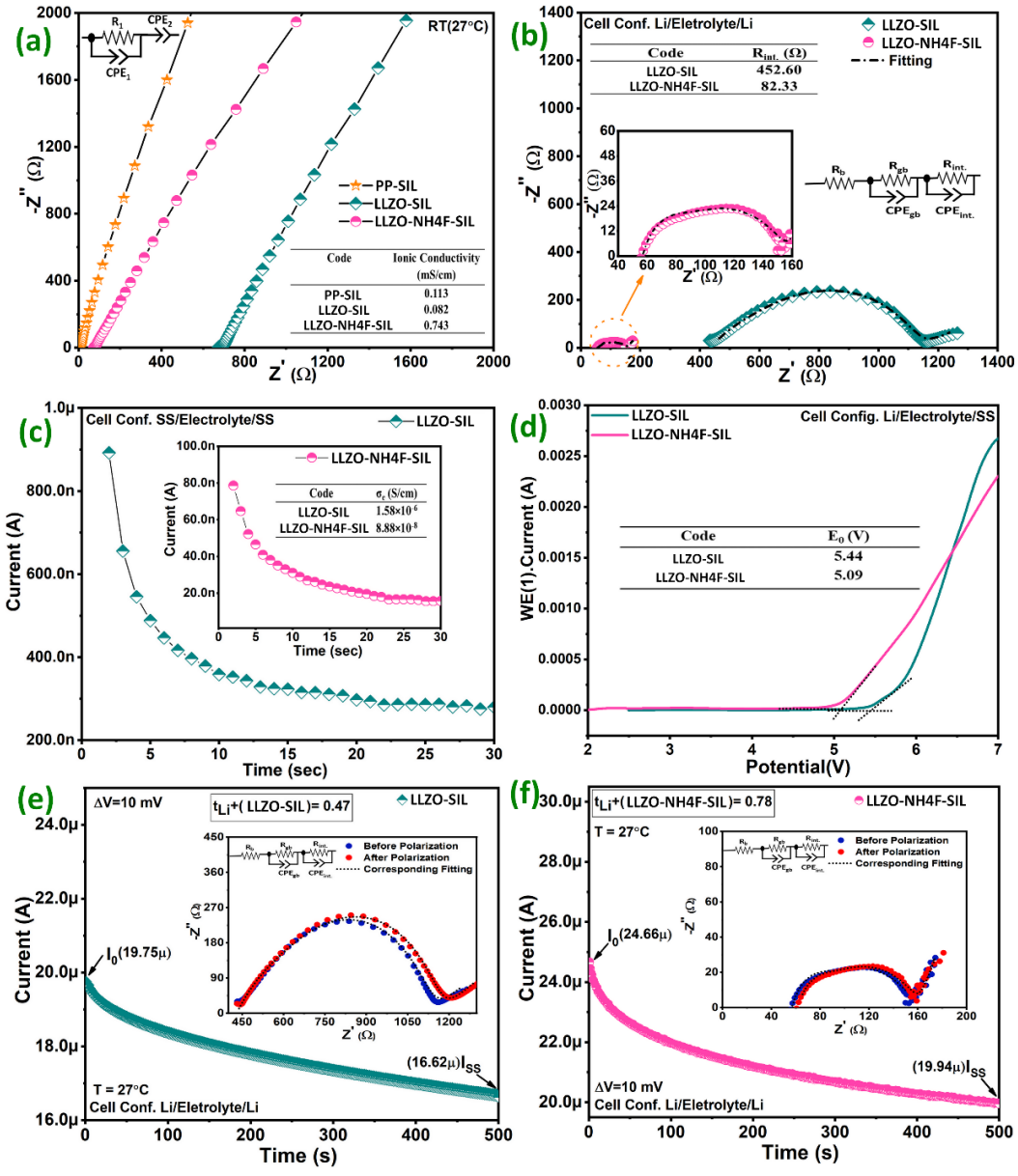

Figure 4.5(a) *EIS spectra of PP-SIL, LLZO-SIL, and LLZO-NH4F-SIL for conductivity measurements. (b) Nyquist plot of LLZO-SIL and LLZO-NH4F-SIL solid hybrid electrolytes in Li/Li symmetric cell, with an inset showing the enlarged version of the plot. (c) DC polarization of LLZO-SIL and LLZO-NH4F-SIL using an ion-blocking SS electrode. (d) Current vs.*

potential linear sweep voltammetric (LSV) plot at a scan rate of 2.0 mV s^{-1} of LLZO-SIL and LLZO-NH4F-SIL. (e) and (f) DC polarization curve of LLZO-SIL and LLZO-NH4F-SIL, respectively, along with the EIS spectra before and after polarization.

It is worth mentioning here that although the ionic conductivity of both matrices is significantly altered, the SIL uptake for pristine and NH_4F-treated LLZO is almost the same (~15±2 wt%). To understand the interface compatibility between Li metal and LLZO solid electrolyte, the interfacial resistance is estimated from the EIS spectra taken after fabricating a Li/Li symmetric cell with both the electrolyte and is presented in ***Figure 4.5(b)***, along with the corresponding equivalent circuit. It is found that the Li/LLZO interfacial resistance is reduced from 226.30 Ω (LLZO-SIL) to 41.17 Ω (LLZO-NH4F-SIL), demonstrating the superior compatibility of the treated electrolyte with Li metal. Thus, the EIS result suggests an improved Li^+ flux at the electrode-electrolyte interface due to the LiF stabilizing interphases. Apart from the ionic conductivity and electrode-electrolyte interfacial resistance, the electronic conductivity of the hybrid electrolyte is a key parameter to assess the dendrite penetration in the metal batteries. Typically, in the steady state condition in an ion-blocking electrode system, the steady state current can be due to electronic conduction of the electrolyte. To measure the steady state current, a DC polarization of 0.5V is applied to both electrolytes in an ion-blocking symmetric cell. The electronic conductivity from ***Figure 4.5(c)*** is found to be 1.58×10^{-6} S/cm for LLZO-SIL and 8.88×10^{-8} S/cm for LLZO-NH4F-SIL. Thus, NH_4F treatment likely forms a stable LiF-rich passivation layer across the LLZO top surface, which can effectively block parasite reaction and reduce the risk of dendrite propagation. It will be interesting to evaluate critical current density and long-term plating/stripping behaviour with both electrolytes. The electrochemical stability window of both systems was evaluated by linear sweep voltammetry (LSV) at a scan rate of 2.0 mV s^{-1} as presented in ***Figure 4.5(d)***, revealing that both electrolyte has a wide potential window>5V, suitable for high-voltage lithium batteries. The lithium transference number is also estimated using the Bruce-Vincent-Evans equation and presented in ***Figures 4.5(e)*** and ***4.5(f)*** for LLZO-SIL and LLZO-NH4F-SIL, respectively. The inset shows the EIS spectra before and after polarization, along with the equivalent circuit. The transference number is found to be 0.47 for LLZO-SIL and 0.78 for LLZO-NH4F-SIL, suggesting that the insulating LiF layer suppresses the electron-likage pathways and improves percolation of Li^+ carriers. In summary, the combination of NH_4F surface treatment and solvated ionic liquid infusion significantly enhances the ionic conductivity, interfacial compatibility, and electrochemical stability of LLZO-based solid electrolytes. The NH_4F-

derived LiF-rich interphase reduces interfacial resistance and electronic conductivity while improving Li^+ transport efficacy. These results demonstrate the effectiveness of dual interfacial engineering in overcoming critical limitations of garnet-type electrolytes and provide a strong foundation for further evaluation of lithium metal stability and high-rate cycling, as explored in the following sections.

4.3.4 Electrochemical Studies

4.3.4.1 Critical Current Density Measurement

Critical current density (CCD) is the maximum endurable current density for a solid electrolyte before a short circuit or cell failure. It is an important parameter that directly reflects the rate of kinetics at the Li/solid electrolyte interface. CCD is directly influenced by both intrinsic factors, such as ionic/electronic conductivity of the electrolyte and surface chemistry, and extrinsic conditions like stack pressure, cell temperature, and pellet thickness, etc. Thus, in this study, all the external variables are held constant, allowing for a fair comparison between the intrinsic properties of LLZO-SIL and LLZO-NH_4F-SIL hybrid systems. To determine CCD, Li/Li symmetric cells were cycled using a stepwise current density protocol (ΔI = 0.05 $mA \cdot cm^{-2}$) starting from 0.05 $mA \cdot cm^{-2}$, as shown in ***Figures 4.6(a)*** for LLZO-SIL and ***Figure 4.6(b)*** for LLZO-NH4F-SIL. Initially, a stable polarization for both the cells, followed by a sudden voltage drop, which indicates a soft short circuit in the system. It is interesting to observe that the presence of SIL reduced the risk of hard short circuit of the cell. The current density, just before the soft short circuit, is defined as the CCD. Thus, the CCD is found to be 0.45 mA. cm^{-2} for LLZO-SIL and 1.45 mA. cm^{-2} for LLZO-NH4F-SIL, highlighting the superior interfacial stability and high-rate capability of the NH_4F-treated system. To understand the voltage changes in correspondence with plating/stripping behaviour, the voltage profile in the critical current density test can be divided into three distinct segments. Firstly, the pre-spike region, where a stable plating/stripping with uniform distribution of Li^+ flux is expected with low polarization voltage. Secondly, post-spike to pre-distortion region, where the metal filament started to grow rapidly, as a result of which an increasing trend in polarization voltage is observed. Lastly, the post-distortion region, where uncontrolled growth of metal filaments is expected to propagate and cause an internal short circuit. The prolonged stability of LLZO-NH4F-SIL containing cells in the pre-spike region indicates effective mitigation of dendrite initiation and propagation. This is largely due to the LiF-rich interfacial layer formation during NH_4F surface treatment. Also, the presence of SIL further assists in Li^+ wetting and homogenization at the metal/electrolyte interface.

4.3.4.2 Long Cycling Performance

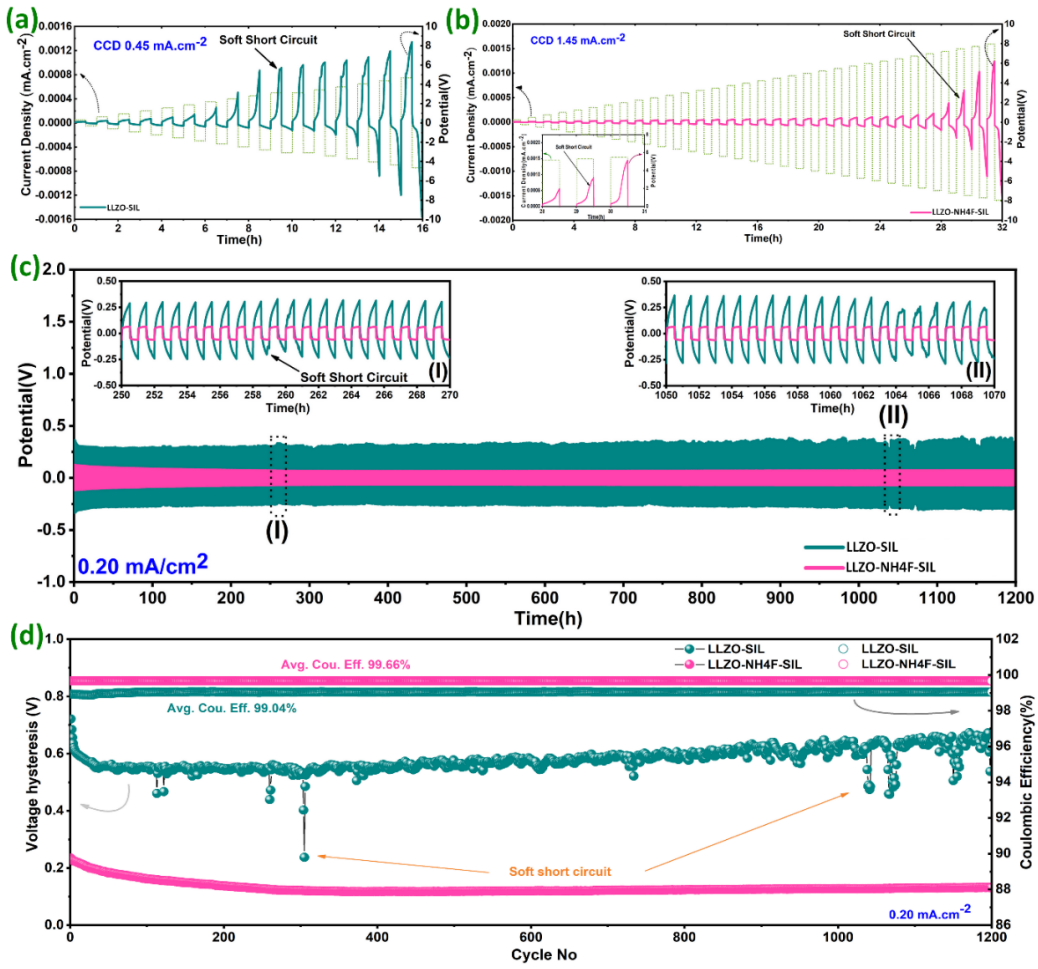

Figure 4.6 *(a) & (b) DC cycling profile of LLZO-SIL and LLZO-NH4F-SIL hybrid electrolyte at RT with step current density of 0.05mA.cm^{-2} for the measurement of critical current density (CCD) respectively, (c) Voltage profile and (d) Voltage hysteresis of Li/Li Symmetric cells at RT over 1200 cycles at a current of 0.20 mA.cm^{-2} for LLZO-SIL & LLZO-NH4F-SIL.*

To evaluate the long-term cycling behaviour and interfacial stability of the developed hybrid electrolytes, a symmetric cell in Li/electrolyte/Li is fabricated. The galvanostatic plating/stripping behaviour was measured at 0.20 mA.cm^{-2} at room temperature for over 1200h for both cells and presented in ***Figures 4.6(c)***. In the voltage profile, both cells displayed a stable cycling behaviour to a certain extent. However, after a few initial cycles, a sudden voltage drop is observed for LLZO-SIL electrolytes, which indicates a soft short circuit. This is likely caused by the unstable interfacial Li deposition and uncontrolled filament growth due to point contact. In comparison, the LLZO-NH4F-SIL cell delivers excellent long-term stability with low polarization voltage over 1200 hours. No sign of soft circuit is also observed throughout the test. The observed voltage hysteresis, as shown in ***Figure 4.6(d)***, remained low,

which confirms the formation of a chemically and mechanically stable interface that can sustain prolonged lithium plating/stripping without any degradation. This enhanced performance might be due to the LiF-rich interphase formation by the NH_4F treatment, which not only improves wetting and interfacial contact with lithium metal but also acts as an electronically insulating, ionically conductive barrier that suppresses dendritic growth and parasitic reactions. The evolution of voltage hysteresis and coulombic efficiency (CE) during the entire cycling period is presented in ***Figure 4.6(d)***. The LLZO-NH4F-SIL system maintained an average hysteresis of approximately 0.22 V with an average coulombic efficiency of ~99.66%. This is due to efficient charge transport and minimal accumulation of interfacial resistance, and the highly reversible nature of Li plating/stripping and minimal formation of inactive "dead Li." In contrast, the LLZO-SIL cell shows an increase in voltage hysteresis with cycling with repetitive short circuit, and an average CE of ~99.04% is observed. This behavior suggests an interfacial degradation, which is due to unstable Li nucleation and non-uniform current distribution. Thus, these results clearly demonstrate that the dual interfacial strategy combining NH_4F surface modification with SIL infusion significantly enhances interfacial robustness and electrochemical reversibility.

To investigate the interfacial behavior under various current densities, both the symmetric cells are subjected to stepwise cycling from 0.05 $mA \cdot cm^{-2}$ to 0.40 $mA \cdot cm^{-2}$, followed by a step down to 0.05 $mA \cdot cm^{-2}$, as shown in ***Figure 4.7(a)***. Cells with LLZO-SIL hybrid electrolyte deliver stable behavior at 0.05 and 0.10 $mA \cdot cm^{-2}$ but show rapid voltage polarization and instability beyond 0.20 $mA \cdot cm^{-2}$. At 0.40 $mA \cdot cm^{-2}$, the voltage reached the voltage cutoff limit (±1 V), which indicates the large polarization due to instability at Li/LLZO. However, the presence of SIL successfully recovers the cell when cycled again at 0.05 $mA \cdot cm^{-2}$. This suggests that the SIL can mitigate the interfacial instability to some extent at a lower current density. However, a stable interface is necessary for long-term suppression of dendrite propagation at higher current densities. In comparison, the LLZO-NH4F-SIL cell demonstrated stable and symmetric voltage profiles across all current densities. Even after the current density was returned to 0.05 $mA \cdot cm^{-2}$, the cell retained its original behavior, which reflects the high interfacial stability at the metal/electrolyte interface. ***Figure 4.7(b)*** presents the corresponding voltage hysteresis and coulombic efficiency. For LLZO-SIL, the hysteresis increased significantly at 0.40 $mA \cdot cm^{-2}$. A sign of soft circuit is also visible at 0.20 $mA.cm^{-2}$ with an increase in coulombic efficiency (>101%). Interestingly, LLZO-NH4F-SIL maintained consistently low hysteresis and a high coulombic efficiency above 99.8% throughout the test.

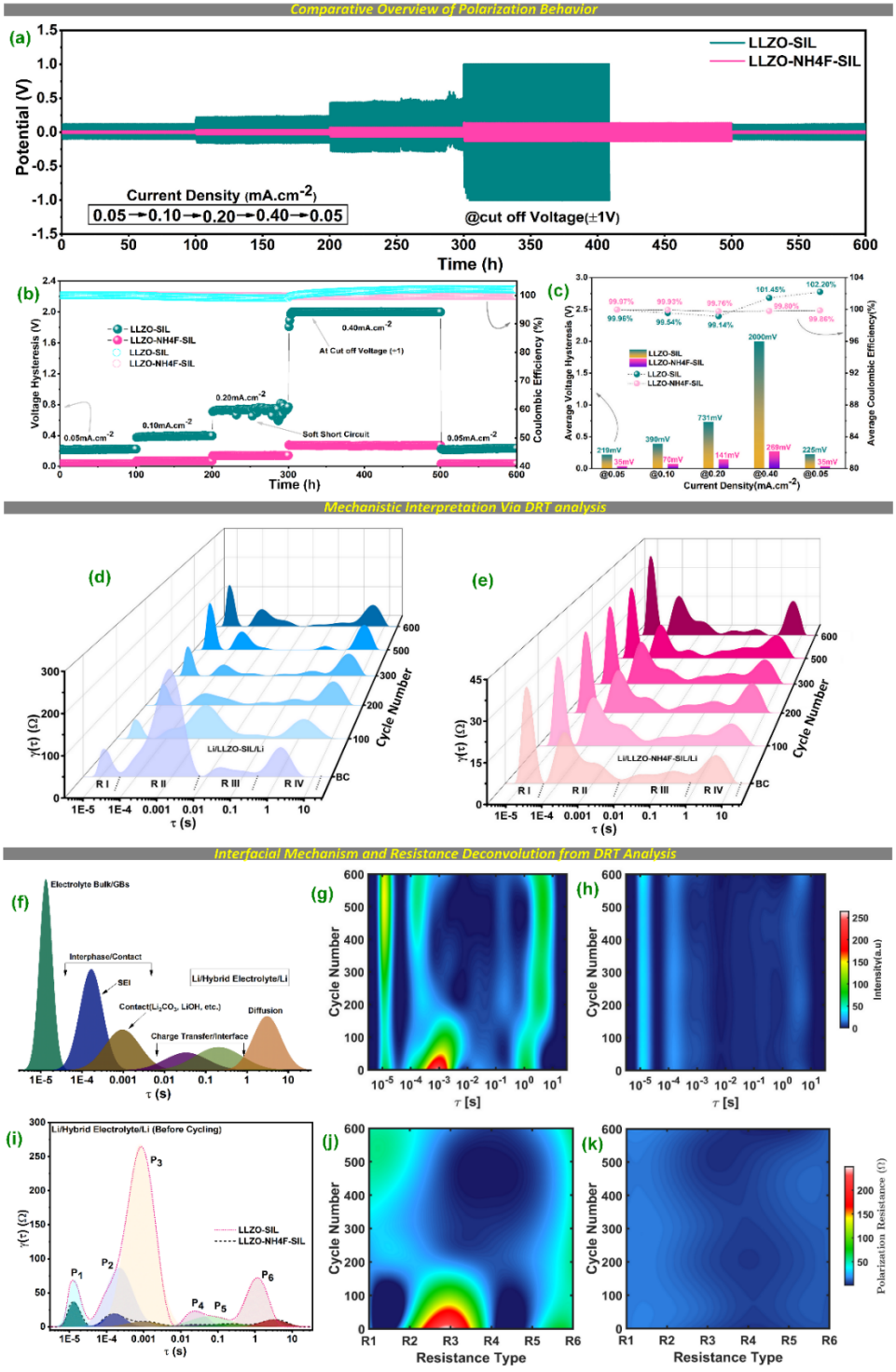

Figure 4.7 *(a) Voltage profile and (b) Voltage hysteresis of Li/Li Symmetric cells at RT over 600 cycles at different current densities (0.05-0.40 mA. cm^{-2}) for LLZO-SIL & LLZO-NH4F-SIL. (c) A summary plot denoting average voltage hysteresis and average coulombic efficiency at various current densities for both cells. 3D DRT pattern taken at before cycling (BC), after 100, 200, 300, 500, and 600 cycles for Li/Li cells containing (d) LLZO-SIL, (e) LLZO-NH4F-SIL electrolytes. (f) Typical Fitted deconvoluted DRT pattern corresponding to various*

electrochemical process in the relaxation time scale for hybrid electrolyte (LLZO-NH4F-SIL) (Before Cycling). 2D contour plots of DRT intensities vs. cycling time for (g) LLZO-SIL and (h) LLZO-NH4F-SIL. (i) Fitted deconvoluted DRT pattern for both the hybrid electrolyte taken at before cycling. 2D contour plot showing the Variation of resistances during cycling associated with different polarization peaks for (j) LLZO-SIL and (k) LLZO-NH4F-SIL electrolyte.

Figure 4.7(c) presents a summary of the corresponding average voltage hysteresis and coulombic efficiency with respect to current densities. This clearly highlights the superior interfacial reversibility, mechanical integrity, and current-handling capability of LLZO-NH4F-SIL-based electrolyte. In summary, it is clearly evident that the synergistic effect of SIL with NH_4F treatment in the LLZO matrix likely enhances the surface lithophilicity, stabilizes the interphase, and suppresses dendritic growth.

4.3.4.3 Post-mortem Studies after Long Cycling Performance

4.3.4.3.1 Dynamic Interfacial Evolution via DRT

To maintain long-term cycling stability, it is very important to understand the interfacial evolution under dynamic Li plating/stripping conditions. Post-cycling EIS followed by Distribution of Relaxation Times (DRT) analysis is carried out on Li/LLZO-SIL/Li and Li/LLZO-NH4F-SIL/Li cells after each current density of operation, as presented in ***Figure 4.7***. The 3D DRT plots as presented in ***Figures 4.7(d)*** for LLZO-SIL and ***Figure 4.7(e)*** for LLZO-NH4F-SIL, provide a temporal fingerprint of resistance contributions at different relaxation times. Both the DRT patterns can be categorized into four different regions according to their relaxation time. The region *R I* is situated at the high frequency region or with have lowest relaxation time ($\tau \sim 6\times10^{-6}$ to 4×10^{-5} s) corresponding to peak P_1. Mainly, the contribution of grain boundary (GB) resistance and contact resistance is observed in the regions. It is worth noting that the bulk resistance of the hybrid electrolyte is beyond the measurable resolution due to the negligible contribution to the total resistance. In our scenario, the contribution of contact resistance can be ignored due to the presence of SIL throughout the interfaces. The resistance R_1 corresponds to peak P_1, almost stable for LLZO-NH4F-SIL, but it keeps increasing for LLZO-SIL, which suggests that the NH_4F surface modification effectively suppresses the grain boundary degradation of LLZO material. Similarly, in region R II ($\tau \sim 4\times10^{-5}$ to 6×10^{-3} s), the observed peaks reflect the interphase-related kinetics, such as SEI formation and evolution (P_2), along with possible contributions from electrochemically active

or resistive secondary phases (P_3)[25]. It is clearly seen that the intensity of both the peaks (P_2 and P_3) for the LLZO-NH4F-SIL cell does not change significantly, which suggests the formation of a stable and robust interfacial layer. This suggest that the interfacial layer effectively maintains ion transport and suppresses further degradation. For the LLZO-SIL cell, the high intensity P_3 peak before cycling suggests the formation of a resistive interfacial layer due to the presence of surface impurities, and consequently, poor wettability is expected. However, the subsequent decrease in P_3 intensity upon cycling suggests that the infused solvated ionic liquid (SIL) improves the interface compatibility. It is possibly by redistributing the surface species and forming a more uniform and ionically conductive interphase. The intensity corresponding to peak P_2, which denotes the SEI resistance, for the LLZO-SIL cell initially decreases during low current density operation, indicating the formation of a stable solid electrolyte interphase initially. However, a significant increase in P_2 after the soft short-circuit, suggests that interfacial instability or SEI breakdown due to uncontrolled Li dendrite penetration Peak P_4 and P_5 at the region R III correspond to interfacial resistance (due to physical contact) and charge transfer resistance at the metal/electrolyte interface[25–29]. Interestingly, the intensities of peak P_4 vanish completely after the voltage reaches the cutoff limit (at 0.40 mA. cm^{-2}) for LLZO-IL, suggesting a collapse or transformation of the interfacial zone. This is possibly due to localized short-circuiting, mechanical breakdown of the interphase, or dendrite-induced disruption of the charge transfer pathway. Although the intensities of both peaks remain stable for the LLZO-NH4F-SIL electrolyte. At the lower frequency region, the kinetics due to diffusion or mass transfer are generally observed. The peak intensities for both electrolytes are changed to a certain extent. However, a significant peak shift is observed for the LLZO-SIL cell at high current density operation. This may be due to sluggish diffusion kinetics, likely arising from interfacial degradation or increased tortuosity in Li^+ transport pathways after the formation of dead Li.

A typical fitted deconvoluted DRT pattern of LLZO-NH4F-SIL is presented in ***Figure 4.7(f)*** to understand the series of electrochemical processes with respect to the relaxation time scale. Typically, six relaxation peaks (P_1-P_6) can be resolved as discussed earlier. At high frequencies, P_1 corresponds to grain boundary resistance. The intermediate frequency region shows P_2 and P_3. They are associated with interphase kinetics such as SEI formation (P_2) and contributions from resistive surface impurities or secondary phases(P_3). In the mid-frequency regime, P_4 and P_5 may be due to charge-transfer resistance at the Li/electrolyte interface. At the low-frequency region, peak P_6 mostly represents the diffusion-related kinetics[26,27]. The comparative spectra

before cycling, as presented in ***Figure 4.7(i)***, describe the distinct interfacial characteristics of the two hybrid electrolytes. LLZO-SIL shows relatively stronger intensities for P_2 and P_3, suggesting the presence of unstable SEI components and poorer interfacial wettability. Also, the broader P_4 and P_6 peaks indicate higher charge-transfer kinetics and sluggish Li^+ transfer pathways. In comparison, LLZO-NH4F-SIL shows very low polarization contributions across all regions, suggesting that the surface fluorination effectively stabilizes various interphases and interfaces, resulting in improved Li^+ transfer kinetics and homogeneous transport across the modified interface.

The two-dimensional contour plots provide deeper insight into the temporal evolution of resistance contributions during Li plating/stripping more clearly. For LLZO-SIL (***Figure 4.7(g)***), the contour intensity gradually increases with cycling, especially relaxation time associated with P_1, P_2, P_5, and P_6. As discussed earlier, SIL successfully solves the wettability issues with cycling, which is clearly seen(P_3). The growth of P_1 and P_2 signifies the continuous SEI breakdown, accumulation of resistive phases, and non-uniform interphase evolution. In the later cycle, the contours broaden and the intensity increases, which indicates the accelerated interfacial instability and uncontrolled dendritic activity at higher current densities. As a result, we observe a soft short circuit and an abrupt increase in coulombic efficiency in later cycles. Thus, the unstable contour pattern reflects the failure of the SIL-only hybrid system at higher current densities to maintain a robust and stable interface. In comparison, LLZO-NH4F-SIL (***Figure 4.7(h))*** shows a remarkably stable contour profile throughout prolonged cycling. The intensities corresponding to P_2 and P_3 remain nearly unchanged, and no new resistive features emerge. This stability confirms that dual strategies suppress resistive interphase growth and sustain homogeneous Li^+ transport across the electrolyte interface. There is no contour broadening over 600 h, which clearly establishes the robustness of the modified hybrid electrolyte in resisting dendrite-related interfacial disruption.

The 2D contour plots of polarization resistances provide the complementary evidence of these contrasting behaviors as observed earlier. In LLZO-SIL (***Figure 4.7(j)***), the resistances associated with grain boundaries (R_1), interfacial (R_2), and diffusion (R_6) kinetics increase steadily with cycling, reflecting progressive interfacial degradation. The polarization map becomes more intense and uneven at the higher current densities. This may be due to localized resistance build-up and non-uniform Li deposition. Conversely, LLZO-NH4F-SIL (***Figure 4.7(k)***) demonstrates almost constant polarization resistances throughout extended cycling.

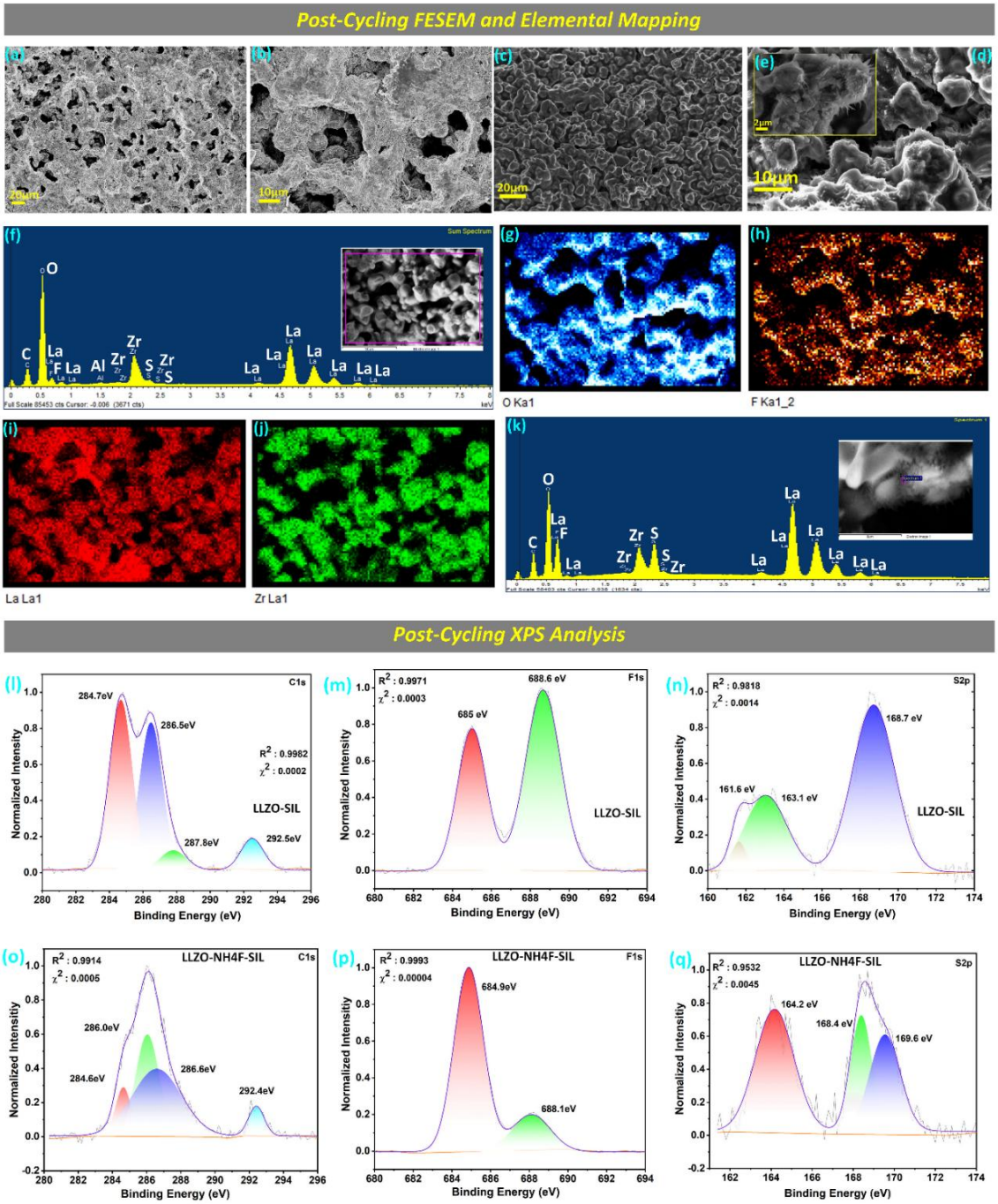

Figure 4.8 *FESEM micrographs and corresponding EDX and elemental mapping after long cycling (1200h). (a) & (b) FESEM micrograph of LLZO-SIL electrolyte at two different scales, (c), (d), (e) FESEM micrograph of LLZO-NH4F-SIL electrolyte at three different scales. (f)-(j) corresponding to EdX and elemental mapping of LLZO-NH4F-SIL electrolytes. (k) Corresponding EdX at the localized crystalline area. High-resolution XPS spectra of post-cycled symmetric Li/LLZO-SIL/Li and Li/LLZO-NH$_4$F-SIL/Li cells after long-term cycling (1200h). (l) & (o) C 1s spectra, (m) & (p) F 1s spectra. (n) & (q) S 2p spectra.*

The resistance contributions remain stable and uniform, indicating that the fluorinated hybrid electrolyte sustains a mechanically and electrochemically stable interface. Thus, the comparative DRT analysis highlights the critical importance of surface engineering with liquid therapy for stabilizing various interfaces and interphases during long-term cycling. It will be interesting to relate this signature to microstructures and structural evidence in the later section.

4.3.4.3.2 Microstructural and Structural Studies

To further validate the interfacial stabilization of the dual strategy, post-mortem structural and surface analyses were carried out on both the symmetric cells after long-term cycling and are presented in ***Figure 4.8***. The FESEM micrographs of LLZO-SIL, as shown in ***Figures 4.8(a)*** and ***(b)***, reveal surface degradation, with porous and fragmented features due to severe dendrite penetration and unstable SEI growth during long cycling. This is expected from our earlier observation in DRT studies. Although the LLZO-NH4F-SIL hybrid electrolyte (***Figures 4.8(c)-(e))*** shows a dense and uniform surface morphology without evidence of any dendritic growth. At higher magnification, as shown in ***Figure 4.8(e)***, a crystalline microdomain is visible, which was further probed by localized EDX analysis (***Figure 4.8(k)).*** Interestingly, this region not only shows La, Zr, O, and F elements but also a noticeably stronger sulfur signal compared to the surrounding region. This suggests that decomposition products from the TFSI anion in the solvated ionic liquid may preferentially accumulate in certain crystalline sites of the modified interphase. The presence of sulfur at this localized crystalline region could indicate partial trapping of anion-derived fragments within the stabilized fluorinated matrix. This can immobilize and prevent further propagation of parasitic decomposition across the interface. EdX and Elemental mapping of the NH_4F-treated electrolyte is further studied and presented in ***Figures 4.8(f)-(j)***. The elemental mapping and EdX also showed homogeneous distributions of La, Zr, O, and F, with localized sulfur enrichment. But no severe phase segregation is observed. The strong and uniform F distribution suggests the formation of a LiF-rich interphase that ensures uniform and homogeneous ion movement with a stable SEI. High-resolution XPS spectra were recorded for both cycled symmetric cells to probe the surface chemistry after long-term operation (1200 h). For the LLZO-SIL hybrid electrolyte as presented ***Figures 4.8(l)-(n)***, the C 1s spectrum shows strong peaks ~284.6 eV (C–C/C–H) and ~286.5 eV (C–O/C-O-C for G4), 287.8 eV (O-C-O, C=O) and 292.5 eV (-CF3). These findings indicate that during extended cycling, parasitic reactions between Li metal and residual carbonate impurities with solvent-derived decomposition may generate an insulating layer at the interface. The F 1s spectrum shows a weak 685 eV (LiF) and a strong peak near 688.6 eV (-CF3), which suggests

that LiF formation is uneven and discontinuous across the interface. The S 2p region shows multiple peaks at ~161.5 eV and ~163.1 eV, which generally correspond to reduced S species or degraded $TFSI^-$. These contributions suggest a continuous decomposition of the TFSI anion in the SIL, which destabilizes the interface and correlates with the rising polarization resistances as seen earlier. In comparison, the LLZO-NH4F-SIL hybrid electrolyte shows markedly different spectral features as presented in ***Figures 4.8(o)-(q)***. The C 1s spectrum in ***Figure 4.8(o)*****,** multiple peaks are observed at ~284.6 eV (C–C/C–H) and ~286.0 eV (C–O/C-O-C for G4), 286.6 eV (O-C=O), and 292.4 eV (-CF3). Thus, suppression of carbonate species via NH4F treatment suggests that it may mitigate the parasitic reactions at the interface. The F 1s spectrum is dominated by a sharp and intense peak at ~684.9 eV, which is characteristic of LiF. A minor peak at 688.1 eV corresponds to residual fluorinated organic fragments. This suggests that the surface treatment by NH_4F further promotes a stable LiF-rich interphase formation. The S 2p spectra show weaker features overall. Mainly, the peaks shifted toward higher binding energies (~164-169 eV), which are typically associated with oxidized sulfonyl species ($-SO_2^-$, $-SO_3^-$). The reduced intensity and upward binding energy shift suggest that instead of widespread TFSI decomposition as seen in LLZO–SIL, sulfur species are stabilized in localized domains (consistent with the sulfur enrichment observed in the crystalline region), where they are immobilized and less electrochemically active. Thus, the comparative XPS analysis clearly demonstrates that while LLZO-SIL undergoes extensive carbonate and sulfonyl decomposition with poor LiF formation, LLZO-NH4F-SIL develops a robust LiF-enriched interphase with suppressed carbonate formation and stabilized sulfur species. These chemical features directly correlate with the stabilization of various interfaces and interphases via a dual strategy. Thus, it will be interesting to measure the full cell application using this hybrid system.

4.3.4.4 Full Cell Performance

Figure 4.9 (a) describes the effect of the dual interfacial strategy in metal batteries. The electrochemical performance of full cells containing LLZO-SIL and LLZO-NH4F-SIL hybrid electrolytes with a $LiMn_2O_4$ (LMO) cathode and lithium metal anode in a quasi-solid-state configuration is presented in ***Figure 4.9 (b)-(e)***. ***Figure 4.9(b)*** presents the rate perforamnce at various current densities from 0.05 to 1.20 $mA \cdot cm^{-2}$ and then returns to 0.05 $mA \cdot cm^{-2}$ to check the reversibility. Both cells show stable cycling with high coulombic efficiencies (>98%) across all current steps, which validates the quasi-solid nature of the hybrid electrolytes.

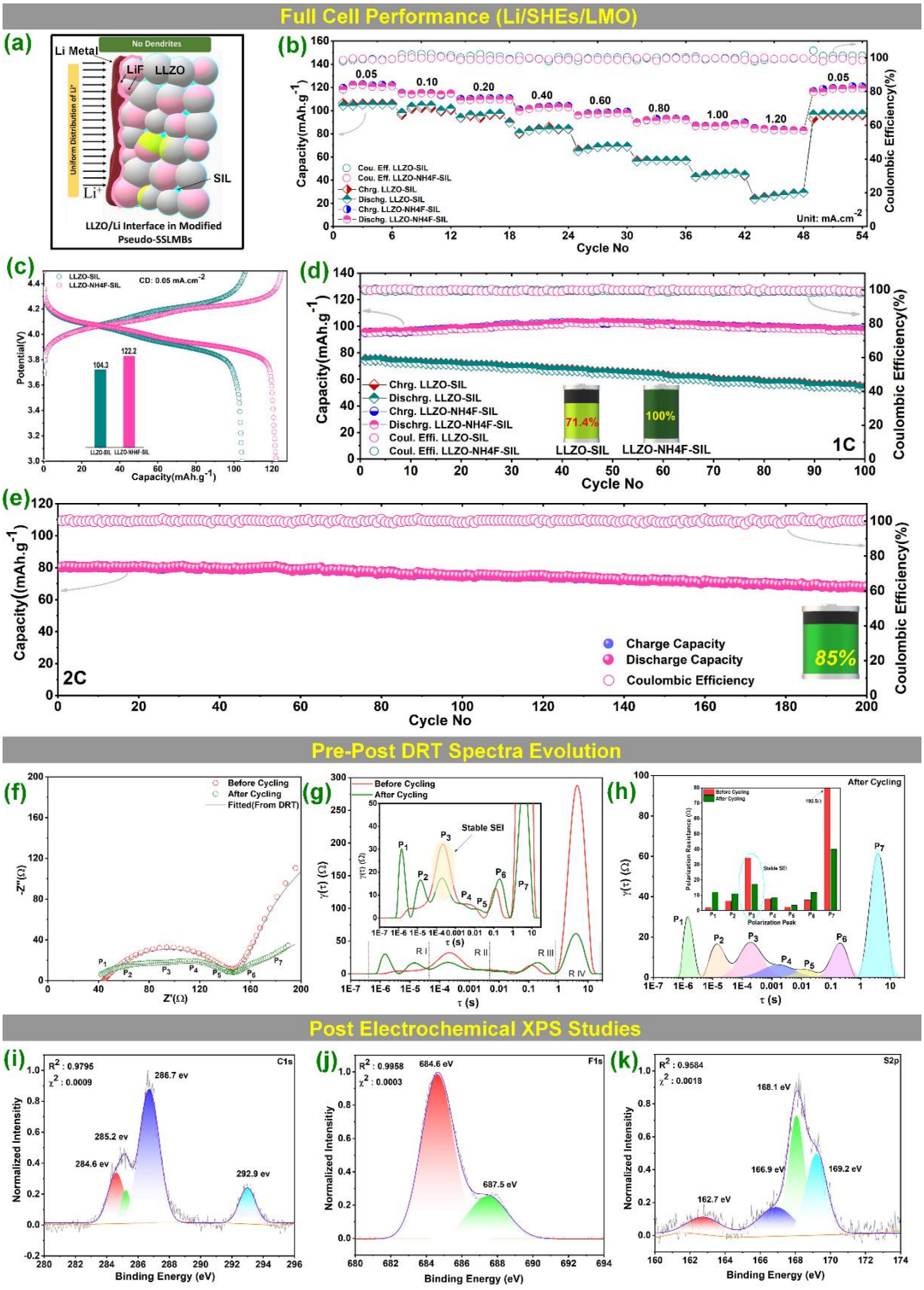

Figure 4.9 *(a) Schematic representing stabilization of interfaces via dual strategies. Electrochemical full cell performance of LLZO-SIL and LLZO-NH4F-SIL using $LiMn_2O_4$ cathode and Li anode, (b) Rate performance study at different current densities ranging from 0.05-1.20 $mA.cm^{-2}$, (c) Typical charge-discharge profile at a current density of 0.05$mA.cm^{-2}$, (d) High-rate capability at 1C, (e) High-rate capability of LLZO-NH4F-SIL hybrid electrolyte at 2C. (f) Nyquist plot of LLZO-NH4F-SIL before and after cycling, along with fitted data*

derived from DRT, (g) Corresponding DRT Plot, (h) Fitted DRT data with distinct peaks after cycling, with an inset showing the variation in polarization resistances corresponding to different peaks before and after cycling. XPS analysis after post cycling of LLZO-NH4F-SIL cell showing (i) C 1s, (j) F1s, and (k) S2p spectra.

However, the LLZO-SIL cell shows noticeable capacity degradation beyond 0.6 $mA \cdot cm^{-2}$, whereas the LLZO-NH4F-SIL cell maintains higher capacities at all the current densities. At 0.05 $mA.cm^{-2}$, LLZO-SIL delivers an average discharge capacity of 104.91 $mAh.g^{-1}$, whereas, LLZO-NH4F-SIL delivers a capacity of 120.64 $mAh.g^{-1}$. Similarly, at 0.60 and 1.20 $mA.cm^{-2}$, LLZO-NH4F-SIL deliver an impressive discharge capacity of 97.14 and 83.44 $mAh.g^{-1}$, respectively. Whereas, the LLZO-SIL cell shows very poor discharge capacity of 68.04 and 26.78 $mAh.g^{-1}$, respectively, at that current density. When the current density is reduced to the initial value, LLZO-SIL and LLZO-NH4F-SIL deliver an average discharge capacity of 97.07 and 117.9 $mAh.g^{-1}$, which suggests that both the electrolytes maintain reversibility even after high current density of operation. The galvanostatic charge-discharge (GCD) profiles at 0.05 $mA \cdot cm^{-2}$ are shown in ***Figure 4.9(c)***. The cell with LLZO-NH4F-SIL electrolyte delivers a higher initial discharge capacity of 122.24 $mAh \cdot g^{-1}$. Whereas, LLZO-SIL delivers an initial discharge capacity of 106.25 $mAh \cdot g^{-1}$. This might be due to the formation of a stable interfacial layer and low overpotential as estimated earlier. The high-rate cycling behavior at 1C is shown in ***Figure 4.9(d)***, where the LLZO-NH4F-SIL hybrid electrolyte outperforms the LLZO-SIL cell after 100 cycles. The cell with LLZO-SIL electrolyte retains about 71% of its capacity after 100 cycles. Whereas, no capacity loss is observed for the LLZO-NH4F-SIL cell. It is worth mentioning here that the increase in capacity around the 40th cycle for LLZO-NH4F-SIL might be due to electrolyte redistribution, SIL wetting, and activation of interfacial pathways. It is a common phenomenon in quasi-solid-state systems during initial stabilization cycles. The LLZO-SIL cell suffers from gradual capacity fading, likely due to interphase instability and Li depletion at the interface, which aligns well with the symmetric cell performance as discussed earlier section. The high-rate capability at 2C is tested using the LLZO-NH4F-SIL hybrid electrolyte to validate the mechanical and electrochemical robustness of this dual interfacial strategy as presented in ***Figure 4.9(e)***. The cell retains about 85% of its initial discharge capacity even after 200 cycles with an excellent average coulombic efficiency of >98%. This performance thus correlates with the stable plating/stripping behaviour and minimal resistance fluctuation during stability performance in the earlier section. In summary, the LLZO-NH4F-SIL system demonstrates superior interfacial compatibility, high-rate capability, and long-term

cycling stability. To understand the interfacial behaviour, DRT and XPS measurements are discussed in the later section.

4.3.4.5 Post-mortem Studies after Full Cell Performance

To further probe the interfacial stability of LLZO-NH4F-SIL hybrid electrolyte after electrochemical full cell performance, post-cycling EIS and DRT analyses were conducted, followed by surface chemical characterization via XPS, and presented in ***Figure 4.9(f)-(k)***. The Nyquist plots before and after cycling (***Figure 4.9(f)***) clearly show that the impedance profile of the cell remains unchanged due to improved interfacial stabilization. In the corresponding DRT plot as presented in ***Figure 4.9(g)***, the deconvoluted relaxation peaks corresponding to grain boundaries, interphase kinetics, contact or interfacial kinetics, charge-transfer resistance, and diffusion contribution, no significant change was observed according to their position. Although a significant reduction was observed in intensities corresponding to peaks P_3 and P_7, this further strongly suggests the formation of a stable SEI layer and faster diffusion kinetics even after repeated charge-discharge operation. Importantly, a new ultrafast relaxation mode (P_1, $\tau \sim 10^{-6}$s) appears after cycling, which is absent or merged with the grain boundary distribution before cycling. This might be due to the redistribution of the solvated ionic liquid (SIL) within the LLZO matrix during electrochemical cycling. The corresponding polarization resistance distribution in the inset in **Figure 4.9(h)**, along with the fitted DRT peaks, suggests the formation of a stable SEI. The increment in P_1 and P_2 might be due to the decomposition of SIL during cycling. Thus, the dual interfacial modification in the LLZO system successfully stabilizes the various interfaces and interphases. Post-mortem XPS spectra as presented in ***Figure 4.9(i)-(k)*** provide a key chemical pattern further supporting this electrochemical stability. The C 1s spectrum in ***Figure 4.9(i)*** shows hydrocarbon (284.6eV) and ether/carbonyl peaks (286-287 eV) with no carbonate contamination. On the other hand, the F 1s spectrum (***Figure 4.9(j)***) is dominated by a sharp LiF peak (684.6 eV) and a small contribution from organic -CF_x fragments at ~687.5 eV. This correlates with our earlier observation, suggesting a LiF-rich layer in stabilizing the interface. The S 2p region at ***Figure 4.9(k)*** shows peaks between 166-169 eV corresponding to oxidized sulfonyl species, but with reduced intensity and absence of low-binding-energy reduced sulfur species. This suggests that the decomposition of the TFSI anion is minimized. These results are in strong agreement with the earlier observation in symmetric cell performance, where uniform F distribution and localized sulfur trapping in crystalline interfacial regions were observed in the FESEM spectra. Overall, the combined EIS, DRT, and XPS results validate that the dual modification strategy produces

a chemically robust, LiF-rich interphase that sustains stable electrochemical kinetics during full-cell cycling. This explains the excellent long-term cycling performance and high Coulombic efficiency observed in ***Figure 4.9(b)-(e)***, and further reinforces the conclusion that NH_4F and SIL dual interfacial engineering provides a scalable route to overcoming interfacial instability in garnet-type solid electrolytes. The interfacial stabilization is further probed in detail during the 1^{st} and 10^{th} charge and discharge cycles by measuring EIS at various SOC and DOD, which were presented in ***Figure 4.10***. The upper two rows (a–f) present the fitted DRT spectra for the first charge (a) and first discharge (d) together with their corresponding 2-D intensity contours (b, e) and normalized resistance maps (c, f), while the lower two rows (g–l) show the same sequence after ten cycles (10th charge g, 10th discharge j with contours h, k and resistance maps i, l). In the fitted spectra (a, d, g, j) the same set of principal relaxation features (P_2–P_7) is observed throughout, occupying consistent relaxation-time windows that can be associated with bulk conduction, interphase kinetics, charge-transfer processes and diffusion-controlled behaviour; however, the character of these peaks evolves substantially between the 1st and 10th cycles. During the 1st cycle the spectra are broader, especially in the high-frequency/short-τ region, and the high-frequency response appears as a smeared shoulder rather than a discrete feature, indicating an immature, heterogeneous interfacial state where very fast processes are masked by overlapping polarizations. The 2-D DRT intensity contours (b, e) make this clear: intensity during the first cycle is concentrated in the intermediate τ bands with SOC/DOD-dependent growth and a diffuse high-frequency background, signifying active formation and modulation of interfacial layers under polarization. By the 10th cycle the fitted spectra sharpen markedly and a distinct ultrafast component at the shortest relaxation times becomes resolvable, while P_2–P_7 retain their nominal positions but with reduced broadening and less SOC/DOD drift, consistent with interphase maturation and homogenization of ion-transport pathways. The corresponding 2-D intensity maps (h, k) therefore show well-confined, narrow bands for each relaxation mode and a clear separation of the ultrafast band from the mid-frequency interphase features, reflecting stabilized kinetics across charge and discharge. The resistance contribution maps (c, f, i, l) further corroborate this temporal evolution: in the first cycle the bulk of the transient resistance changes are borne by the mid-frequency channels (R_2–R_4), which track interphase formation and charge-transfer modulation, whereas by cycle 10 the resistance landscape has re-partitioned so that a small but distinct short-τ resistance (R_1) is measurable and the mid-frequency resistances settle to nearly constant values. Together, these observations indicate that the cell transitions from a formation regime—dominated by

evolving interfacial chemistry and heterogeneous contact—to a steady state in which interfacial contacts and transport pathways are consolidated.

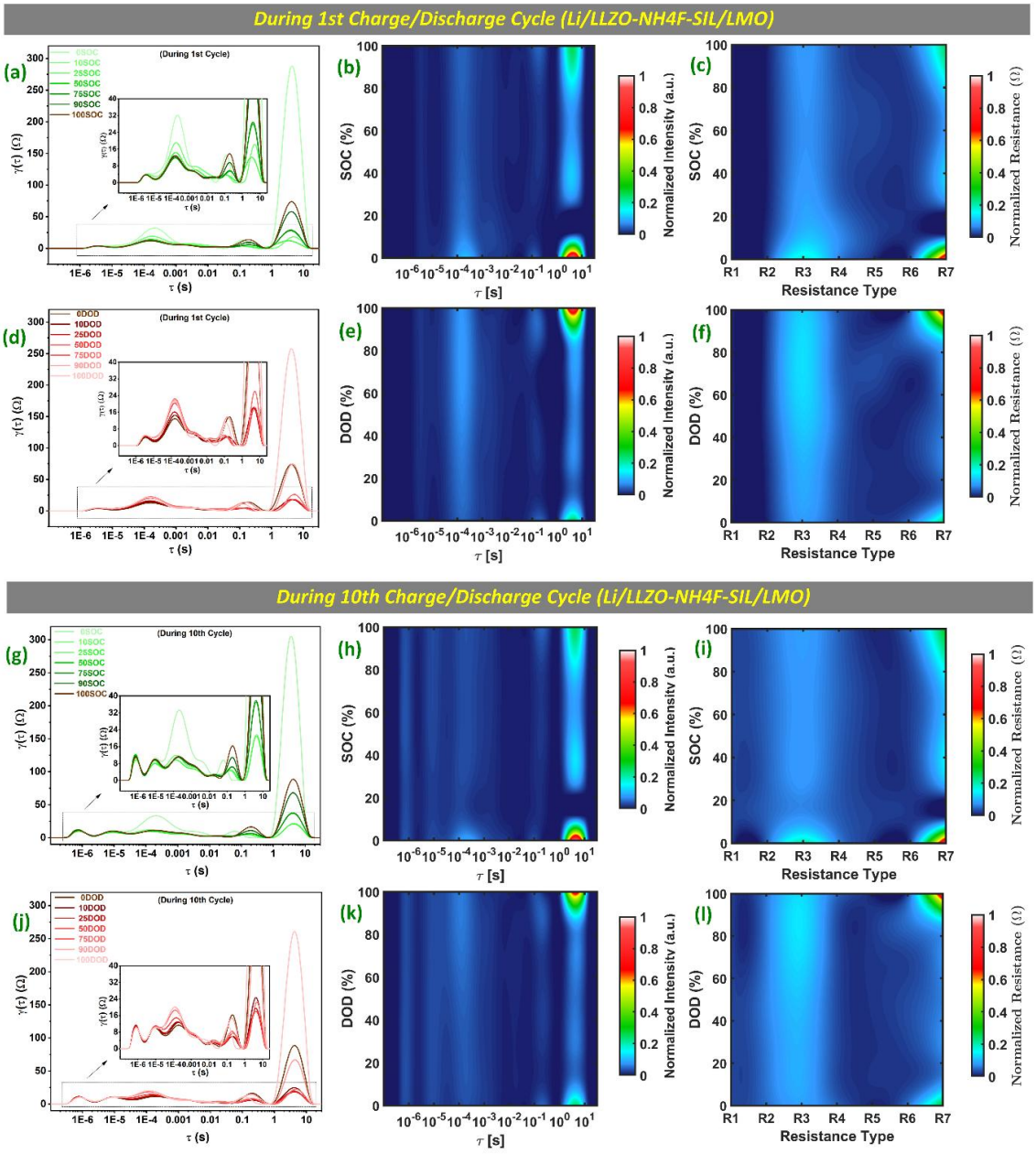

Figure 4.10 *Deconvolution of electrochemical process via DRT analysis. DRT spectra at various (a) SOC and (d) DOD during 1St cycle. Corresponding 2d intensity contour during (b) charge and (e) discharge, and their normalized resistance contour in (c), (f), respectively. Similarly, DRT spectra at the 10th cycle during (g) charge and (j) discharge. Their corresponding intensity contour at (h) and (k) during charge and discharge, respectively. The 2d contour of normalized resistance during (i) charge and (l) discharge process.*

Also, the ultrafast contact/GB dynamics are separated out, and the overall polarization is reduced and more uniform across SOC/DOD, explaining the improved electrochemical stability recorded elsewhere in this work. ***Figure 4.10*** presents the evolution of interfacial processes via DRT in the Li/LLZO-NH4F-SIL/LMO full cell during the 1st and 10th charge/discharge cycles. The DRT spectra at the 1st charge (***Figure 4.10(a)***) and discharge (***Figure 4.10(d)***) show broad and overlapping relaxation features that can be denoted as peaks P_2-P_7, consistent with multiple simultaneous processes including grain boundary contribution, interphase kinetics, charge-transfer reactions, and diffusion contributions in the earlier studies. However, in the very high-frequency region (τ ~10^{-6}-10^{-5} s), no discrete ultrafast peak is observed during the 1st cycle. This might be due to the fact that the initial interface is immature, dominated by the dynamic formation of SEI-like layers and unstable contact resistances. The corresponding 2D intensity contours presented in ***Figures 4.10(b)*** and ***4.10(e)*** further support this interpretation. The normalized resistance maps shown in ***Figures 4.10(c)*** and ***4.10(f)*** reveal that most of the resistance contributions during the first cycle arise from R_2-R_4 and R_6 (interphase and charge-transfer and diffusion regimes), indicating that the interface is still undergoing active reorganization. In comparison, after 10 cycles in ***Figures 4.10(g)*** and ***4.10(j)***, the spectra sharpen significantly, and a rise of a distinct ultrafast relaxation mode (P_1 at τ ~10^{-6} s) is visible. This feature might be due to the redistribution of the solvated ionic liquid (SIL) within the LLZO matrix and the interaction at the cathode interface (due to liquid electrolyte), which creates a new rapid Li^+ transport pathway. Importantly, the positions of P_2-P_7 remain consistent with the 1st cycle, but their intensities become narrower and more stable. The 2D contour maps of normalized intensity as presented in ***Figures 4.10(h)*** and ***4.10(k)*** display well-confined, sharp relaxation bands with minimal SOC/DOD drift. This suggests that the ion-transport pathways have homogenized. In nature. Correspondingly, the resistance contour plots in ***Figures 4.10(i)*** and ***4.10(l)*** show that by the 10th cycle, the mid-frequency resistances stabilize, while a small but discrete contribution from R_1 appears, consistent with ultrafast interfacial kinetics separated from the slower interphase dynamics. Overall, the comparison between the 1st and 10th cycles clearly demonstrates the transition from a "formation regime" to a "steady state regime". Thus, this dual interfacial engineering (NH_4F+SIL) establishes a robust LiF-rich and organic-inorganic hybrid interphase. These results strongly correlate with the low hysteresis, stable coulombic efficiency, and robust morphology evidenced in the earlier section. Thus, the dual-modification approach is a powerful interfacial engineering strategy in metal batteries.

4.4 Conclusion

In this chapter, a dual interfacial engineering (via NH_4F chemical treatment and SIL infusion) strategy was systematically investigated to overcome the intrinsic interfacial limitations of garnet-type pristine LLZO solid electrolytes in lithium metal batteries. Structural and microstructural studies suggest that the surface treatment via NH_4F removed surface impurities and produced a LiF-rich passivation layer without a change in the cubic garnet framework. Complementary SIL infusion in the LLZO matrix, enhancement in Li^+ transportation by improving interfacial wettability was observed. Extensive electrical, electrochemical, and post-electrochemical studies demonstrate that dual interfacial engineering via NH_4F treatment and SIL infusion synergistically enables both chemical stabilization and kinetic enhancement at the Li/LLZO interface. The combined strategy establishes a scalable route toward high-performance, dendrite-free, and long-life solid-state lithium metal batteries, providing critical insights into the role of hybrid organic-inorganic interphases in garnet electrolytes.

4.5 References

1 M. Pasta, D. Armstrong, Z. L. Brown, J. Bu, M. R. Castell, P. Chen, A. Cocks, S. A. Corr, E. J. Cussen, E. Darnbrough, V. Deshpande, C. Doerrer, M. S. Dyer, H. El-Shinawi, N. Fleck, P. Grant, G. L. Gregory, C. Grovenor, L. J. Hardwick, J. T. S. Irvine, H. J. Lee, G. Li, E. Liberti, I. McClelland, C. Monroe, P. D. Nellist, P. R. Shearing, E. Shoko, W. Song, D. S. Jolly, C. I. Thomas, S. J. Turrell, M. Vestli, C. K. Williams, Y. Zhou and P. G. Bruce, *J. Phys. Energy*, 2020, **2**, 32008.

2 J. Janek and W. G. Zeier, *Nature Energy 2023 8:3*, 2023, **8**, 230–240.

3 W. D. Richards, L. J. Miara, Y. Wang, J. C. Kim and G. Ceder, *Chemistry of Materials*, 2016, **28**, 266–273.

4 Y. Xiao, Y. Wang, S. H. Bo, J. C. Kim, L. J. Miara and G. Ceder, *Nat Rev Mater*, 2020, **5**, 105–126.

5 L. Wang, Z. Li, J. Luo, H. Fan and R. Zhao, *Chemical Communications*, 2022, **58**, 6962–6965.

6 A. Baniya, A. Gurung, J. Pokharel, K. Chen, R. Pathak, B. S. Lamsal, N. Ghimire, R. S. Bobba, S. I. Rahman, S. Mabrouk, A. L. Smirnova, K. Xu and Q. Qiao, *ACS Appl Energy Mater*, 2022, **5**, 648–657.

7 J. Fu, P. Yu, N. Zhang, G. Ren, S. Zheng, W. Huang, X. Long, H. Li and X. Liu, *Energy Environ Sci*, 2019, **12**, 1404–1412.

8 J. Lou, G. Wang, Y. Xia, C. Liang, H. Huang, Y. Gan, X. Tao, J. Zhang and W. Zhang, *J Power Sources*, 2020, **448**, 227440.

9 B. Pang, Z. Wu, W. Zhang, H. Huang, Y. Gan, Y. Xia, X. He, X. Xia and J. Zhang, *J Power Sources*, 2023, **563**, 232836.

10 I. Madinabeitia, J. Rikarte, A. Etxebarria, G. Baraldi, F. J. Fernández-Carretero, I. Garbayo, R. Cid, A. García-Luis and M. Á. Muñoz-Márquez, *ACS Appl Energy Mater*, 2022, **5**, 12120–12131.

11 B. Kinzer, A. L. Davis, T. Krauskopf, H. Hartmann, W. S. LePage, E. Kazyak, J. Janek, N. P. Dasgupta and J. Sakamoto, *Matter*, 2021, **4**, 1947–1961.

12 S. Kim, J.-S. Kim, L. Miara, Y. Wang, S.-K. Jung, S. Y. Park, Z. Song, H. Kim, M. Badding, J. Chang, V. Roev, G. Yoon, R. Kim, J.-H. Kim, K. Yoon, D. Im and K. Kang, *Nat Commun*, 2022, **13**, 1883.

13 T.-Q. Yang, C. Wang, W.-K. Zhang, Y. Xia, Y.-P. Gan, H. Huang, X.-P. He and J. Zhang, *Rare Metals*, 2022, **41**, 1870–1879.

14 W. Lu, M. Xue and C. Zhang, *Energy Storage Mater*, 2021, **39**, 108–129.

15 H. W. Kim, P. Manikandan, Y. J. Lim, J. H. Kim, S. Nam and Y. Kim, *J Mater Chem A Mater*, 2016, **4**, 17025–17032.

16 M. Wu, D. Liu, D. Qu, Z. Xie, J. Li, J. Lei and H. Tang, *ACS Appl Mater Interfaces*, 2020, **12**, 52652–52659.

17 M. Keller, A. Varzi and S. Passerini, *J Power Sources*, 2018, **392**, 206–225.

18 D. Zhou, M. Zhang, F. Sun, T. Arlt, J. E. Frerichs, K. Dong, J. Wang, A. Hilger, F. Wilde, M. Kolek, M. R. Hansen, P. Bieker, I. Manke, M. C. Stan and M. Winter, *Nano Energy*, 2020, **77**, 105196.

19 M. C. Buzzeo, R. G. Evans and R. G. Compton, *ChemPhysChem*, 2004, **5**, 1106–1120.

20 A. Sharafi, S. Yu, M. Naguib, M. Lee, C. Ma, H. M. Meyer, J. Nanda, M. Chi, D. J. Siegel and J. Sakamoto, *J Mater Chem A Mater*, 2017, **5**, 13475–13487.

21 G. Larraz, A. Orera and M. L. Sanjuán, *J Mater Chem A Mater*, 2013, **1**, 11419.

22 K. Ghosh and M. Wasim Raja, *ACS Appl Energy Mater*, 2023, **6**, 4035–4052.

23 K. Ghosh and M. Wasim Raja, *Chemical Engineering Journal*, DOI:10.1016/J.CEJ.2023.148200.

24 K. Ueno, K. Yoshida, M. Tsuchiya, N. Tachikawa, K. Dokko and M. Watanabe, *J Phys Chem B*, 2012, **116**, 11323–11331.

25 R. Soni, J. B. Robinson, P. R. Shearing, D. J. L. Brett, A. J. E. Rettie and T. S. Miller, *Energy Storage Mater*, 2022, **51**, 97–107.

26 C. Plank, T. Rüther, L. Jahn, M. Schamel, J. P. Schmidt, F. Ciucci and M. A. Danzer, *J Power Sources*, 2024, **594**, 233845.

27 C.-Y. Yu, J. Choi, J. Dunham, R. Ghahremani, K. Liu, P. Lindemann, Z. Garver, D. Barchiesi, R. Farahati and J.-H. Kim, *J Power Sources*, 2024, **597**, 234116.

28 Y. Lu, C.-Z. Zhao, J.-Q. Huang and Q. Zhang, *Joule*, 2022, **6**, 1172–1198.

29 A. Subhakumari, T. Thomas and N. P. B. Aetukuri, *ACS Energy Lett*, 2024, **9**, 6109–6116.

CHAPTER 5

Probing the Microstructural Effect of Solid Electrolytes on the Performance of Solid-State Lithium Metal Batteries

Summary & Graphical Abstract

Garnet-type solid electrolytes often show large voids and irregular grain structures, resulting in high grain boundary resistance and uncontrolled lithium dendrite growth in metal batteries. In this chapter, a bio-inspired exo-templating approach was introduced to address these challenges. An attempt for the first time using water hyacinth demonstrated the feasibility of transferring plant-derived microstructures into Ga-doped LLZO, yielding plate-like morphologies with moderate ionic conductivity and stable cycling at the symmetric cell level. In this direction, a cellulose exo-templating strategy was developed to produce a highly interconnected structure, which significantly reduced grain boundary resistance and enhanced lithium-ion transport. Further infusion of solvated ionic liquid (SIL) into the engineered LLZO matrix improved wettability at the Li/electrolyte interface, suppressed dendrite penetration, and enabled stable cycling for extended durations with high critical current density. Thus, this chapter systematically compares engineered LLZO with conventionally prepared garnets and highlights the benefits of hybrid solid electrolytes for high-performance lithium metal batteries.

Objectives

1. To facilitate the ionic movement across grains and grain boundaries.

2. Impeded the Li dendritic growth in metal batteries.

Strategy

Microstructural engineering with Liquid therapy.

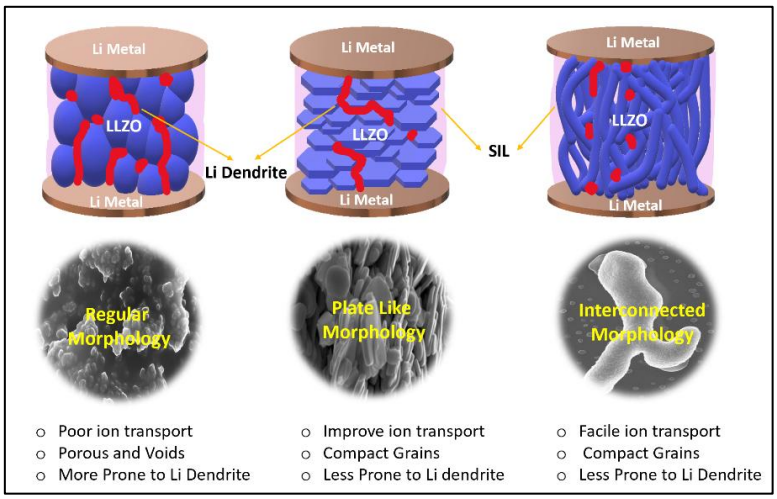

Figure 5.1 *Graphical abstract illustrating the effects of microstructure engineering of solid electrolyte in metal batteries.*

5.1 Introduction

Garnet-type LLZO, despite its high ionic conductivity and chemical stability, often suffers from high grain boundary resistance, interfacial instability with Li metal, and uncontrolled dendrite growth. These issues are closely linked to the presence of voids, irregular grain structures, and poor interfacial contact[1]. Microstructural engineering of solid electrolytes is one of the most promising ways to restrict these problems[2,3]. Recently, Heo et al. explored a mesoscopic computational method capable of establishing the significance of microstructure for ion conduction in garnet-type cubic phase LLZO material, and also correlated the synthesis conditions of garnet to its performance[4]. Horii et al. developed a 1-D continuum model and predicted that grain size, grain boundary thickness, and void fraction have a profound effect on overall battery performance at high-rate conditions[5].

The templates or bio-scaffolds offer plenty of room to engineer the material structures, similar to the template's morphology. In the last two decades, varieties of bio templates such as bacteria,[6,7] egg shell membrane,[8] paper,[9] fruits,[10] etc have been used to synthesize metals, alloys, metal oxides, semiconductors, ceramics, and composite materials. Depending on the nature of their synthesis, Ozin et al.[11] proposed that Bio-templating methods may be classified in three broad categories, i.e., Negative Template method, Positive Template method, and Surface Step Edge Template method. Among them, Exo-templating offers an easy synthesis option where a bio-scaffold is used as a sacrificial template and removed at the end of the synthesis process, resulting in an exo-pattern of the template used. Recently, Raja et al. successfully synthesized $BaBi_{0.2}Co_{0.35}Fe_{0.45}O_{3-\delta}$ (BBCF) perovskite-type oxygen separation membrane with "Nano-rod" microstructure using Water Hyacinth (*Eichhornia crassipes*) as exo-template and obtained a two-fold increase in electronic conductivity compared to the conventionally prepared BBCF materials.[12] However, the impact of the engineered microstructure of the solid electrolyte on electrical and electrochemical performances remains limited in the literature. One of the probable reasons is due to the complexity and bottleneck in making all-solid-state lithium metal batteries (ASSLMBs). There are major bottlenecks reported in ASSLMBs: (i) instability of the interface between SSEs and the electrode, causing unwanted chemical reactions with the generation of large interfacial impedance, and finally loss of anodic contact, and (ii) transgranular lithium dendritic migration across the grain boundaries of the solid electrolyte, posing a threat to short circuit[13,14]. Thus, careful engineering of microstructure and configuration is needed to address high-performance metal batteries.

In the present chapter, we aimed to develop an engineered Ga doped LLZO ($Li_{6.25}La_3Ga_{0.25}Zr_2O_{12}$) solid inorganic electrolyte scaffold infused with solvated ionic liquid (SIL) as a hybrid solid electrolyte (HSE). The garnet electrolyte was microstructurally engineered to develop (1) a unique "plate-like" LLZO (LLZOWH) by mimicking the intercellular structure of WH fibers, (2) interconnected LLZO (LLZOCET) via a cellulose exo-templating process to achieve high Li-ion mobility across the grains. The pore filled with solvated ionic liquid (SIL) was introduced to enhance the wettability between LLZO and Li metal- a process may be termed as "liquid therapy," which is very effective, as we observed in ***Chapter 3.*** This dual modification is designed to reduce the interfacial resistance, suppress dendritic penetration, and improve electrochemical performance. Thus, this chapter systematically compares engineered LLZO with conventionally prepared garnets via gel combustion process (LLZOGC) and highlights the benefits of bio-templating and SIL infusion for high-rate, long-life lithium metal batteries.

5.2 Engineered Plate-like LLZO

5.2.1 Experimental

5.2.1.1 Material Synthesis and Characterization

Gallium-doped $Li_7L_3Z_2O_{12}$ ($Li_{6.25}La_3Ga_{0.25}Zr_2O_{12}$, LLZOWH) was synthesized using a water hyacinth (*Eichhornia crassipes*) bio-template to obtain a plate-like microstructure. A sol-gel precursor with 10% excess Li was mixed with WH powder (10:1 v/w), followed by calcination at 500 °C and 900 °C to get cubic LLZOWH powder. Detailed synthesis steps are described in ***Chapter 2***, ***Section 2.3.3.2***. The detailed characterization techniques are already discussed in ***Section 2.7***. Various synthesis processes and corresponding sample codes of Ga doped LLZO solid electrolyte Material were presented in ***Table 5.1***.

Table 5.1 *Synthesis process and corresponding sample codes of Ga doped LLZO solid electrolyte Material.*

Synthesis Process	Termed as
Gel Combustion	LLZOGC
Exo-templating using WH	LLZOWH
Exo-templating using Cellulose	LLZOCET

5.2.1.2 Cell Fabrication and Testing

The detailed cell fabrication and testing techniques are already discussed in ***Chapter 2***, ***Section 2.6*** and ***Section 2.7***, respectively. In Short, all the sintered pellets were infused with a solvated ionic liquid (LiTFSI/tetraglyme, 1:1 mol ratio). Symmetric (Li/Li, SS/SS), asymmetric (Li/SS), and full (Li/LMO) coin cells were then fabricated using the procedures described in ***Chapter 2, Section 2.6***.

5.2.2 Results and Discussion

5.2.2.1 Thermal Studies

The major component in raw water hyacinth (WH) biomass is 20% cellulose, 33% hemicellulose, and 10% lignin as estimated by Bolenz et al.[15], and Gressel et al.[16]. Therefore, the study of the thermal behaviour of raw WH fiber is necessary before conducting the exo-templating process. It is also required to estimate the ash content in WH fiber after thermal treatment. The thermal analysis is carried out using TGA-DTA for raw WH fibers (oven dried at 250°C for 4 h) from RT to 1200 °C at a heating rate of 10 °C /min in air and presented in ***Figure 5.2(a)***. The profile revealed three distinct weight losses of 10%, 85% and 91% at temperatures around 250°C, 535 °C, and 900 ºC, respectively. From RT to 250°C, the initial weight loss of 10% corresponds to the removal of water from WH fibers. Thereafter, the decomposition of cellulose, hemicellulose, and lignin in WH fibers takes place, which is reflected by two exothermic peaks at 334°C and 535°C in the DTA curve. The weight loss continued up to 900°C resulting in total weight loss of 91%. No significant weight loss could be observed up to 1200°C. From the above thermogram, the ash content in raw WH fiber as estimated to be around 9% up to 900°C. It also suggested that the alkali and acid pre-treatment might be able

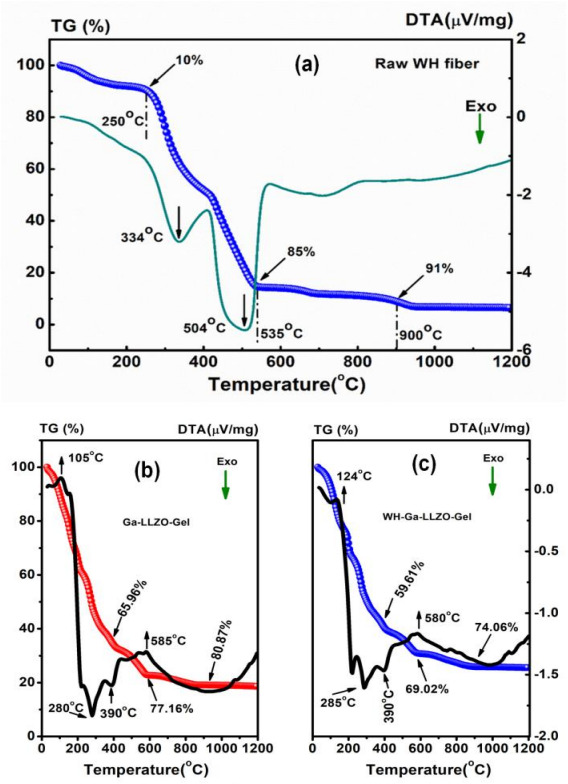

Figure 5.2 *TGA and its corresponding DTA plots of (a) raw WH fiber, (b) Ga-LLZO-Gel, and (c) WH-Ga-LLZO-Gel from RT to 1200°C.*

to remove some impurities[17–19]. However, the intrinsic metallic elements present in the WH fiber, which were converted into metal oxide during thermal treatment, remained as residual ash. The elemental composition of the ash is presented in ***Figure 5.3***. ***Figure 5.2(b)*** and ***Figure 5.2(c)*** describe the thermal behaviour of Ga-LLZO-Gel produced by dehydrating a stoichiometric mixture of nitrate salts of Li, La, Zr, and Ga in aqueous medium using alanine as a chelating agent and WH fiber mixed Ga-LLZO-Gel (10:1 v/w %), termed as WH-Ga-LLZO-Gel, respectively.

The thermal decomposition profile of Ga-LLZO-Gel showed multi-step weight losses up to 900°C. An initial sharp weight loss measuring ~66% up to 400°C is attributed to the exothermic decomposition of nitrates and metal-alanine complexes, followed by another weight loss of 11% up to 585ºC, which is due to the formation of the tetragonal phase of Ga-doped LLZO, accompanied by the release of absorbed CO2 and atomic rearrangement of the pyrochlore $La_2Zr_2O_7$ phase[20]. A weight loss estimated to be ~ 4% in the temperature range of 585°C-900°C is assigned to phase transition from Tetragonal to Cubic phase in Ga doped LLZO, which is also reflected by the corresponding endothermic peak at ~585°C in the DTA curve. No significant weight loss could be detected after 900°C for Ga-LLZO-Gel, as shown in ***Figure 5.2(b)***. The thermal profile of WH fiber mixed with Ga-LLZO-Gel also followed a similar trend to that of Ga-LLZO-Gel, as shown in ***Figure 5.2(c)***. No significant change in the nature of the thermal profile could be observed apart from a slight difference in total weight loss of ~6% compared to Ga-LLZO-Gel, which might be arising due to the presence of impurities in raw WH fiber (ash content).

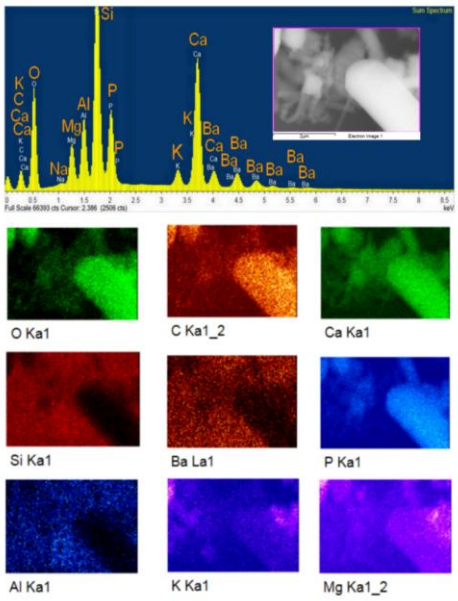

Figure 5.3 *Typical EDX spectrum and its corresponding elemental map of raw WH fiber, calcined at 900ºC.*

5.2.2.2 Structural Studies

X-ray diffractograms of WH fiber and LLZOWH, both calcined at 900ºC for 5 h in air, are presented in ***Figure 5.4(a)*** along with standard JCPDS files of cubic-LLZO (PDF 00-064-0141) and tetragonal-LLZO (PDF 00-064-0140). The WH fibers showed two small peaks at 2θ =17.9°and 21.7°, which correspond to the 101 and 002 planes of crystalline cellulosic phases.[36]

Several other peaks were found in the calcined powder of WH fibers might have originated due to inherent metal oxide impurities such as PbO_2, MgO, CdO, Fe_3O_4, Mn_3O_4, Cr_2O_3, etc[12]. The quantitative phase analysis of the powder XRD pattern of LLZOWH powder calcined at 900°C revealed the presence of both cubic (42.5%) and tetragonal (56.9%) LLZO phases along with a trace amount of non-detectable impurities.

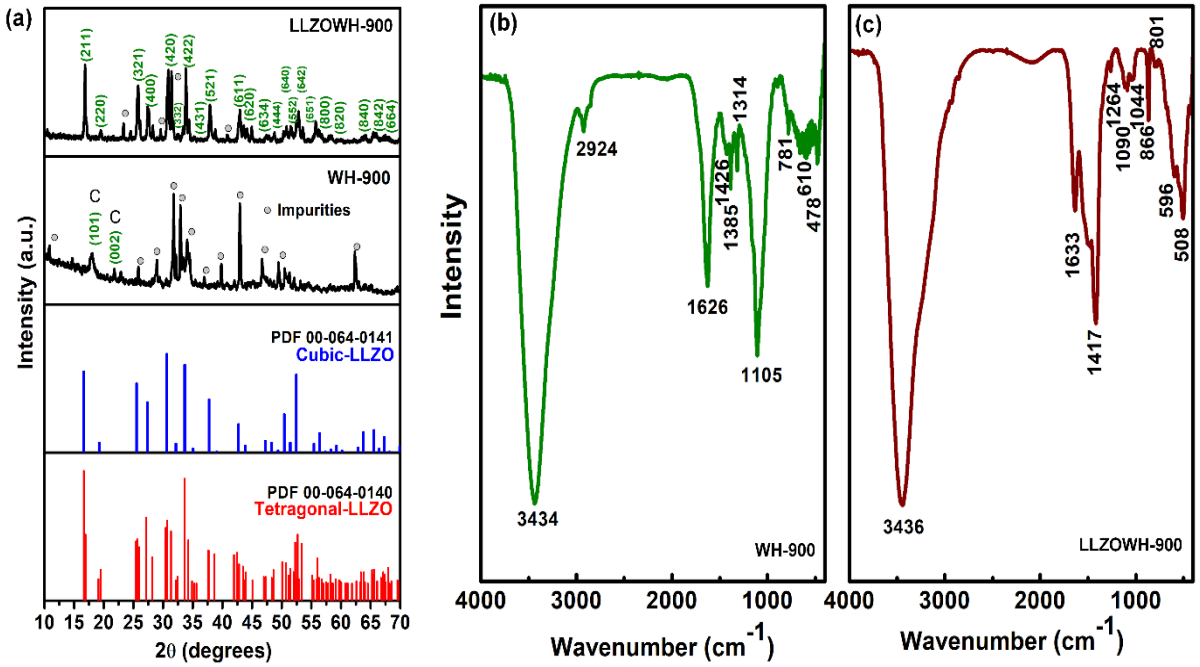

Figure 5.4 *(a) X-ray Diffractograms of raw WH fiber and LLZOWH powders calcined at 900°C for 5 h in air. (b) FTIR spectra of raw WH fiber and (c) FTIR spectra of LLZOWH powder calcined at 900°C.*

FTIR spectroscopy is carried out to identify the changes in (a) raw WH fiber dried at 250°C and (b) LLZOWH powder after being calcined at 900°C. WH fiber consists of three main functional groups, namely cellulose, hemicelluloses, and lignin, along with metal salt impurities. The characteristic peaks of cellulose, lignin, and hemicelluloses for WH-fiber are thus reflected in the spectra as shown in ***Figure 5.4(b)*** at peak positions 1626, 1426, 1314, 1105 cm^{-1} [21,22]. A broad peak appeared at 3434 cm^{-1} is assigned to the O-H vibration of absorbed water by the fiber[21,23,24]. Several minor peaks are also recorded at 781, 610, 478 cm^{-1}, which might be originated from the metal oxide impurities in the fiber. The FTIR spectra of exo-templated LLZOWH powder calcined at 900°C is shown in ***Figure 5.4(c)***. Similar to that of WH fiber, distinct peaks of O-H vibration are also observed at 3436 and 1633 cm^{-1} due to absorbed moisture by LLZOWH calcined powder. The LLZO powder readily reacts with moisture and spontaneously takes part in Li^+/H^+ ion exchange to form surface active Li_2CO_3 layer[25].In ***Figure 5.4(c)***, two distinct characteristics peaks of Li_2CO_3 are also detected at peak

positions 1417 and 866 cm^{-1} suggesting the formation of surface active Li_2CO_3 phase in LLZOWH[25]. Such surface contamination is unavoidable and is responsible for lowering ionic conductivity in the garnet. The spectra also reflected two minor peaks appeared at the lower wavenumber region of 596 and 508 cm^{-1} and assigned to M-O vibrations of Zr-O and La-O respectively[25,26].

Table 5.2 *The peak positions and its corresponding assignment for raw WH fiber and LLZOWH powder calcined at 900 °C.*

Raw WH fiber		**LLZOWH Powder**	
Peak Position (cm^{-1})	Peak assignment	Peak Position (cm^{-1})	Peak assignment
3434 (Broad, sharp)	O–H stretching, Moisture	3436 (Broad, sharp)	O–H stretching, Moisture
2924 (Narrow, sharp)	C–H stretching,Cellulose	1633 (Sharp)	δ(H_2O) Absorbed Moisture
1626 (Sharp)	C=O vibration, characteristic group of lignin and Hemicellulose	1417 (Sharp)	C-O stretching, characteristic peak of Li_2CO_3
1426 (minor)	C-H bending, the presence of lignin contents in the fiber. Or C-O cellulose	1264 (minor)	unknown
1385 (minor)	O-H organic/Phenolic type	1090 (minor)	unknown
1314 (minor)	characteristic group of lignin and hemicellulose, C-H	1044 (minor)	unknown
1105 (Sharp)	- C–O–C vibration in cellulose and hemicelluloses	866 (Sharp)	C-O stretching, characteristic peak of Li_2CO_3
781 (minor)	Unknown	801 (minor)	unknown
610 (minor)	Unknown	596 (minor)	Zr-O Characteristic band
478 (minor)	Unknown	508 (minor)	La–O vibration

The FTIR findings obtained in the present study are summarized in ***Table 5.2,*** describing peak positions and their corresponding peak assignment. To further confirm the phases, Raman spectra were recorded for LLZOWH-900 calcined powder. It is reported that the LLZO tetragonal phase shows a higher number of spectral features compared to its cubic polymorph due to its distorted Li^+ ion arrangement and/or lower symmetry[27]. The Raman spectra as observed in ***Figure 5.5*** could be typically categorized in three regions - (I) a low frequency region below 300 cm^{-1} responsible for translational modes of mobile cations, (II) an intermediate frequency range between 300-550 cm^{-1} where cubic phase exhibits broad and partly overlapping band and tetragonal phase shows higher number of peaks, (III) the high frequency range above 550 cm^{-1} could be assigned to the vibrational stretching of ZrO_6 octahedra. In ***Figure 5.5***, at low frequency region number of peaks are found at 96 cm^{-1}, 159 cm^{-1}, 178 cm^{-1}, 191 cm^{-1}, 258 cm^{-1} representing the existence of tetragonal phase along with cubic phase, which showed broad and overlapping peaks characteristics of cubic phase LLZO in the intermediate region. Apart from these two phases, possible appearance of impurity phases particularly Li_2CO_3 during calcination process of LLZO garnet material is unavoidable and it is treated as surface contaminant for LLZO[25,27].

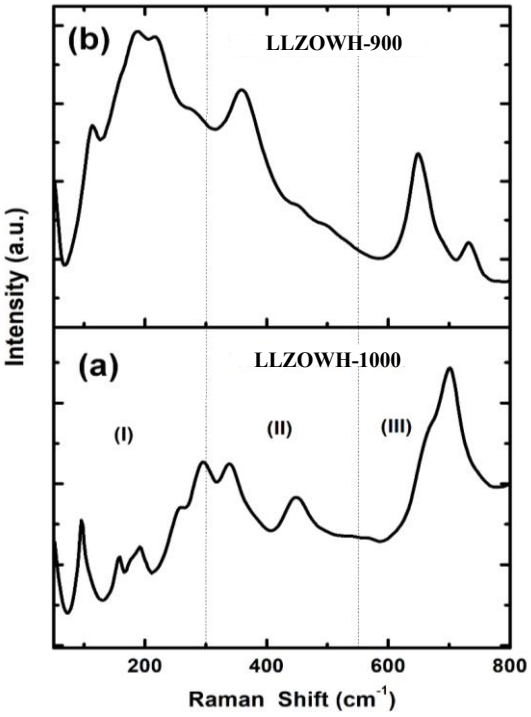

Figure 5.5 *Raman Spectra for LLZOWH powders calcined at (a) 900°C and (b) 1000°C in air.*

It is also believed that Li_2CO_3 formation occurred between interaction of H_2O and LLZO through Li^+/H^+ exchange when exposed to ambient atmosphere[26,28,29]. Although trace surface contamination of Li_2CO_3 could not be verified by XRD, but detected during FTIR analysis as presented in the next sub-section. A very minute quantity of constituent oxide such as La_2O_3 could also be present in the calcined powder which formed due to loss of lithium at high temperature. It is previously observed in TGA analysis that WH fiber produces an ash amounting to ~ 9 wt % in the final product powder when calcined at 900°C (as observed in

Figure 5.2(a)). Thus, the appearance of few unknown metal oxides peaks in the diffractogram of LLZOWH-900 possibly be originated from the ash of WH fiber.

5.2.2.3 Microstructural Studies

In exo-templating synthesis methodology the process and place (i.e., confined space) of impregnation of precursor gel inside targeted template play an important role for defining particle's morphology. Inside WH petiole fibrous unit, two confined spaces are available for gel impregnation namely vascular *tissue* xylem and aerenchyma cells. Raja et al. reported on BBCF-based MIEC membrane; we carefully impregnated BBCF precursor gel into the empty tubular spaces confined by the cell walls of WH-fiber[12].

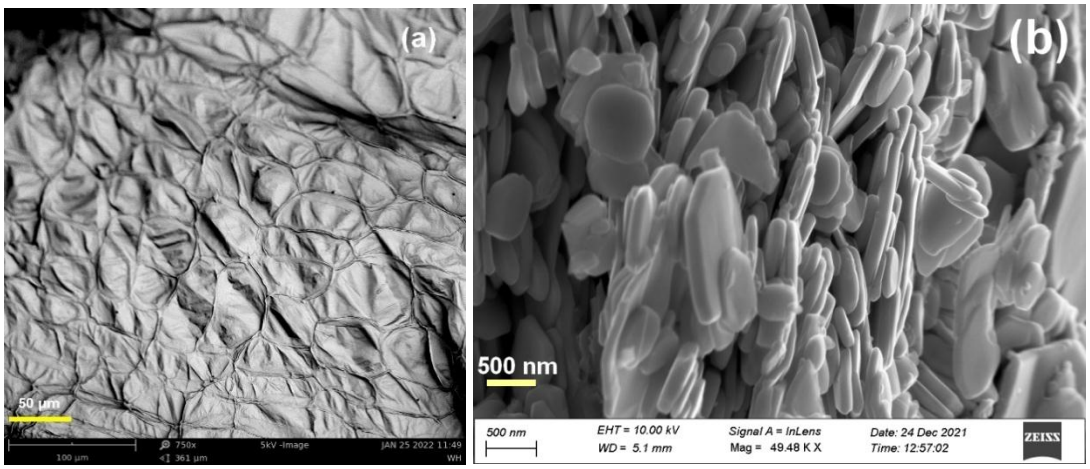

Figure 5.6 *(a) SEM micrograph of WH dried petioles and (b) FESEM image of LLZOWH powder calcined at 900°C*

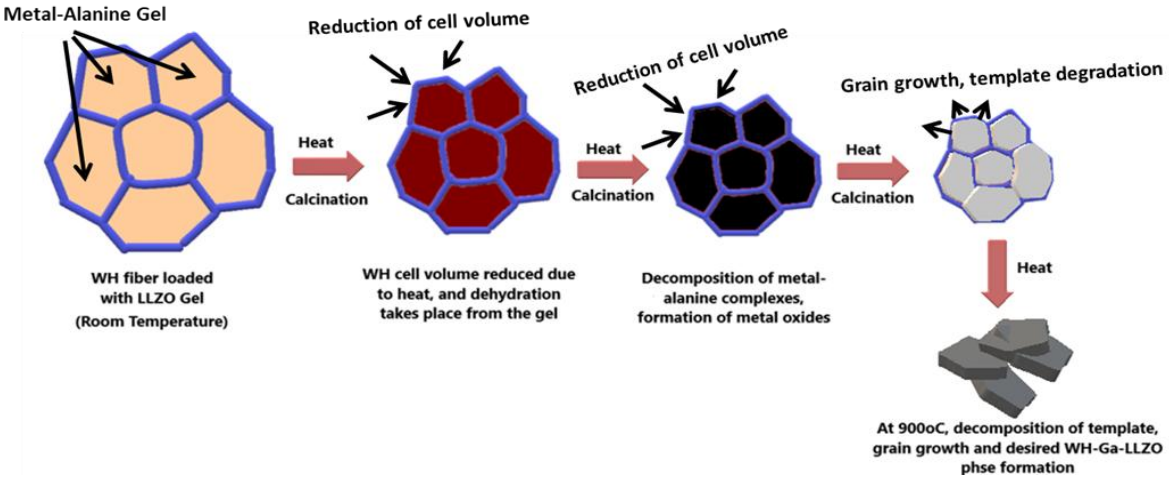

Figure 5.7 *Schematic illustration of origin of plate like morphology of LLZOWH(WH-Ga-LLZO) powder calcined at 900°C(The colour of the impregnated gel gradually changes to darker shade as the temperature increases prior to decomposition and nucleation)*

Controlled heat treatment for the removal of the template resulted in a nanorod-like BBCF morphology. In the present study we attempted to load the gel in aerenchyma cells (a tissue with large, empty, and polygonal cell structure) to mimic its polygonal pattern. Polygonal-shaped aerenchyma cells with discrete cell boundaries are observed in the SEM image as given in ***Figure 5.6(a)***, which resulted in multifaceted "plate-like" morphology after exo-templating. ***Figure 5.6(b)*** shows the FESEM micrograph of LLZOWH calcined powder showing plate-like particles with an average thickness of 100-120 nm.

Such unique morphology in LLZOWH powder might originate from mimicking the polygonal-shaped aranchyma cells present in the WH fiber, which provided a scaffold for the synthesis of Ga-LLZO.The formation mechanism of plate-like morphology has been illustrated schematically in ***Figure 5.7***. During the gel loading process, the cellular confined space of the WH fiber becomes filled with the constituent gel of LLZO. On heat treatment, two processes simultaneously occur: (1) thermal shrinkage of the WH template and (2) dehydration of the aqueous LLZO-Gel in the confined space. Therefore, a reduction in WH template dimension (volume) is expected whereas the volume of gel is also reduced due to the removal of water from its matrix. On further heating, the gel decomposition starts, resulting in nucleation and grain growth of the desired phase inside the thermally squeezed template. On further increase calcination temperature, the WH scaffold or template is finally removed producing plate like exo-templated microstructure of LLZO garnet. As shown in SEM micrograph of ***Figure 5.6(a)***, the raw WH fiber showed an average length of the template around 50-100 µm, however the 900ºC calcined LLZO powder revealed a plate like morphology with average length scale of 0.5-1.0 µm (***Figure 5.6(b)***).

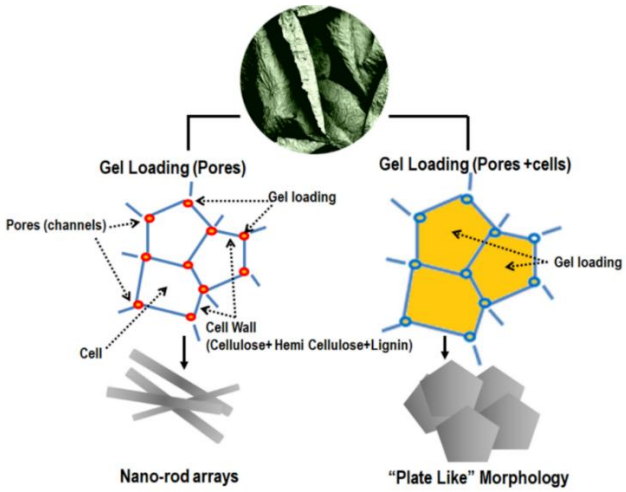

Figure 5.8 *The schematic representation showing proposed path to obtain (Left) Nano-rod arrays[12] and (Right) 'Plate like" morphology via exo-templating method mimicking inter-*

cellular structures (pore channels for nanorod arrays and aerenchyma cells for plate like morphology) of WH fiber

The reason behind of such reduction of length scale from raw fiber to calcined powder is due to the dimensional shrinkage of template at high temperature as explained above. It is worthy to mention here that the use WH fiber as an exo-template can offer typically two types of morphologies; (a) when the gel impregnation occurs in the tubular xylem of WH fiber, it produces nanorods,[14] and (b) when gel loading is done inside aerenchyma cells, it develops "Plate like" morphology as observed in LLZOWH calcined powder. This formation process of nanorods and plate-like morphology is illustrated schematically in ***Figure 5.8*** for understanding the above phenomena happening during the gel loading process.

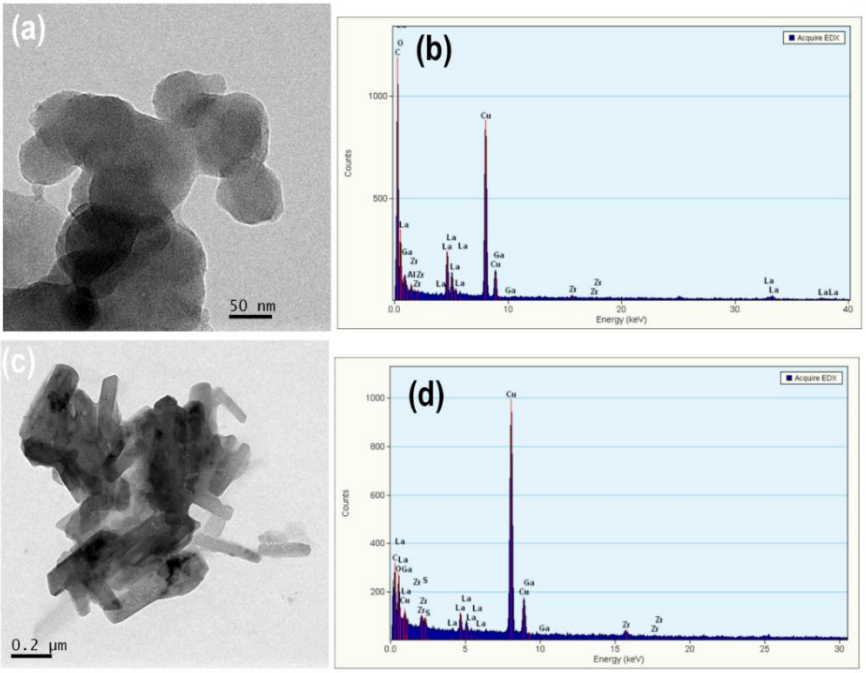

Figure 5.9 *(a)-(b) TEM images and corresponding elemental compositions of LLZOWH at 900°C and (c)-(d) for 1000°C calcined powders.*

To further analysis of microstructure and morphology, TEM images are taken for LLZOWH powders calcined at 900°C and 1000°C along with their elemental composition using EDX and the micrographs are presented ***Figure 5.9(a)-(d)***. The average particle size as measured for 900°C calcined powder is found to be less than 100 nm. The presence of agglomerated morphology could also be visible in ***Figure 5.9(a)***. The elemental composition as shown in ***Figure 5.9(b)*** revealed the presence of La, Zr, Ga along with trace amount of Al, likely originated from the Al-crucible during calcination. In ***Figure 5.9(c)***, a discrete plate-like morphology of LLZOWH powder calcined at 1000 °C could be identified. The thickness of oriented plates is measured in the range of 40-120 nm. The EDX profile as shown in ***Figure***

5.9(d) is found to be similar in nature to that of LLZOWH powder calcined at 900ºC. The cryptographic information by analyzing HRTEM could not be realized this time due to electron beam-irradiation damage to the samples. It needs further refinement in imaging parameters and specimen preparation procedures.

5.2.2.4 Electrical Studies

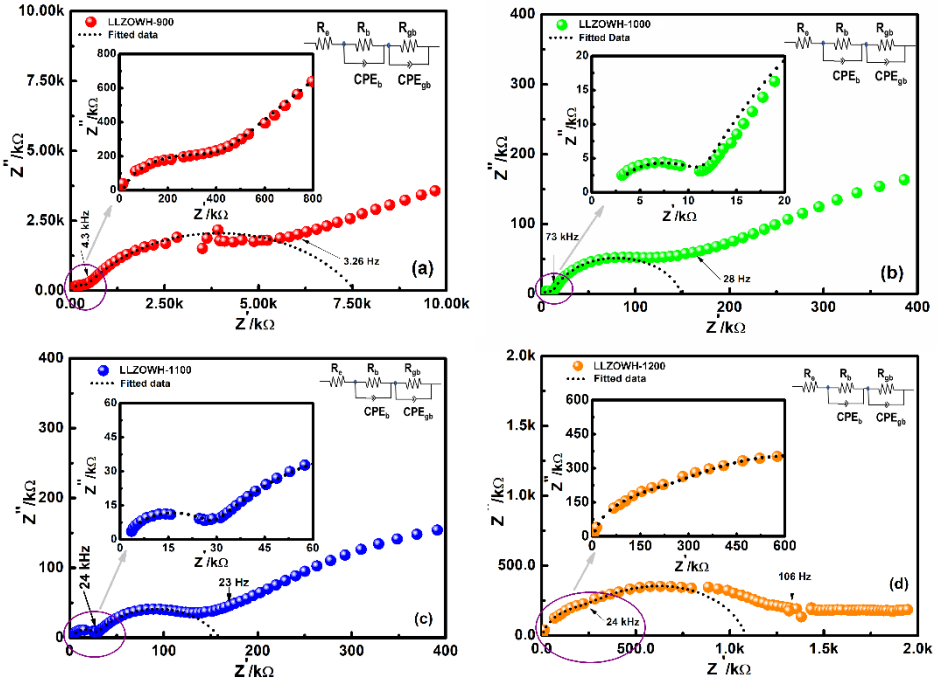

Figure 5.10 *Room temperature AC impedance plots of LLZOWH pellets sintered at (a) 900 °C, (b) 1000 °C, (c) 1100 °C, and (d) 1200 °C. The inset shows the corresponding equivalent circuit.*

Figure 5.10 shows the room temperature AC impedance plots of LLZOWH pellets sintered at (a) 900°C, (b) 1000°C, (c) 1100°C and (d) 1200°C in air. All the profiles comprise of two depressed semicircles along with diffusion tail; the first semicircle appeared at low frequency region is due to the contribution of the grain boundary and second at high frequency is attributed to the grain or bulk properties of LLZOWH pellets. The appearance of a straight-line tail at a lower frequency using Li-ion blocking Ag electrodes suggests that the synthesized LLZOWH garnet is intrinsically Li-ion conductive in nature[30]. An equivalent circuit model comprising circuit elements $R_e(R_bCPE_b)(R_{gb}CPE_{gb})$ has been used here to fit the curves as shown in the inset of ***Figure 5.10(a)-(d)*** , where R_b, R_{gb}, and R_e are the resistances representing bulk, grain boundaries and Ag electrodes; CPE_b and CPE_{gb} represents constant phase elements originated from grain and grain boundaries. The total conductivity is determined by adding R_b and R_{gb}. The contribution of grain and grain boundaries in total conductivity of LLZOWH

pellets sintered at different temperatures is summarized in ***Table 5.3***. The conductivity values (S/cm) are calculated using the equation, $\sigma=\frac{1}{R}.\frac{l}{A}$; where, R=Resistance, l= thickness, A=area of the pellets.

The sintering temperature vs conductivity values which include σ_b, σ_{gb} and σ_{total} are plotted in ***Figure 5.11***. The plot showed that a highest bulk conductivity (σ_b) value of $3.94x10^{-5}$ S/cm could be obtained for LLZOWH sample sintered at 1000°C. It also observed that the bulk conductivity (σ_b) gradually reduces as the sintering temperature increases. On the other hand, with the increase in sintering temperature from 900°C to 1000°C, the grain boundary resistance initially decreased, however no further significant reduction in impedance could be observed on elevated sintering temperature. This may due to the fact that with increase in sintering temperature, a slight stoichiometric loss of lithium may result in appearance of secondary phases which may accumulate at the grain boundary blocking Lithium-ion migration. To identify the phases, present in the pallets sintered at 1000°C, 1100°C and 1200°C, XRD is performed and the corresponding X-diffractograms are shown in the ***Figure 5.12(a)***. The XRD profile of the pellet sintered at 1000°C showed all the major peaks assigned for cubic garnet, however, with increase in sintering temperature, pyrochlore type $La_2Zr_2O_7$ phases started appearing as visible in the inset of ***Figure 5.12(a)***. It is observed that the magnitude of splitting of peaks (640, 552, 642 peaks) in cubic phase of LLZO gradually increases with the increase in sintering temperature. A phase transformation from cubic to pyrochlore type structure could be observed for the pellet sintered at 1200°C. To further confirm the phases formed at different

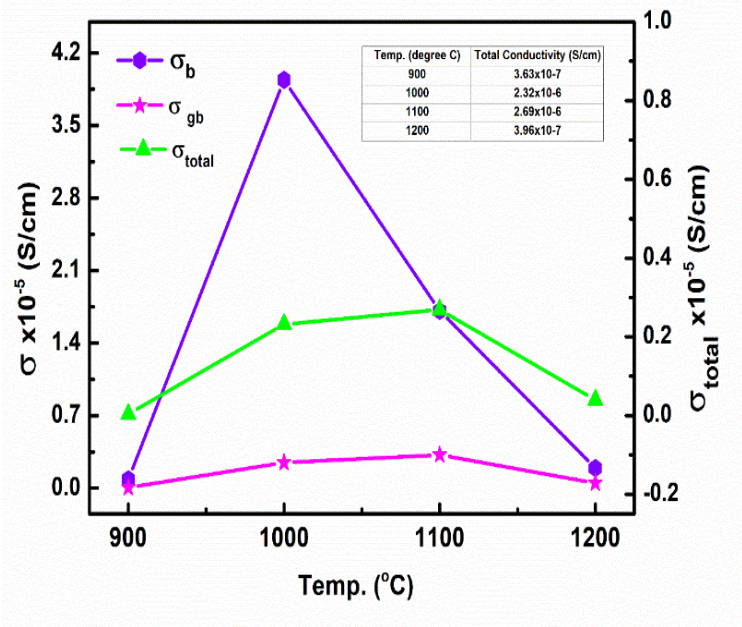

Figure 5.11 *Plot showing variation of Grain, grain boundary and total conductivities of the pellets w.r.t to sintering temperatures (900°C, 100°C, 1100°C and 1200°C).*

sintering temperatures of 1000°C, 1100°C and 1200°C, quantitative phase analysis is carried out.

Table 5.3 *Variation of conductivity of LLZOWH pellets sintered at different temperatures.*

Temp./ °C, 10 hours	Thickness (cm)	Area (cm^2)	R_b (Ω)	σ_b (S/cm)	R_{gb} (Ω)	σ_{gb} (S/cm)	$R_{Total} = R_b + R_{gb}$ (Ω)	σ_{Total} (S/cm)
900	0.22	0.8075	330000	8.33×10^{-7}	7.23×10^{6}	3.8×10^{-8}	7.56×10^{6}	3.63×10^{-7}
1000	0.145	0.42545	8658	3.94×10^{-5}	1.38×10^{5}	2.46×10^{-6}	1.38×10^{5}	2.32×10^{-6}
1100	0.180	0.42545	24737	1.71×10^{-5}	1.32×10^{5}	3.2×10^{-6}	1.56×10^{5}	2.69×10^{-6}
1200	0.172	0.4026	220000	1.94×10^{-6}	8.61×10^{5}	4.96×10^{-7}	1.08×10^{6}	3.96×10^{-7}

The results revealed that at 1000°C, the major phase is cubic amounting to 71.6%, with 25.8% Li_2CO_3 surface impurity phase which appeared during post-sintering stage due to unavoidable surface reaction[25,29]. The cubic phase of sintered at 1000°C is further confirmed by Raman spectroscopy as shown in ***Figure 5.5***, which indicated less number of peaks characteristic to the cubic LLZO type phase

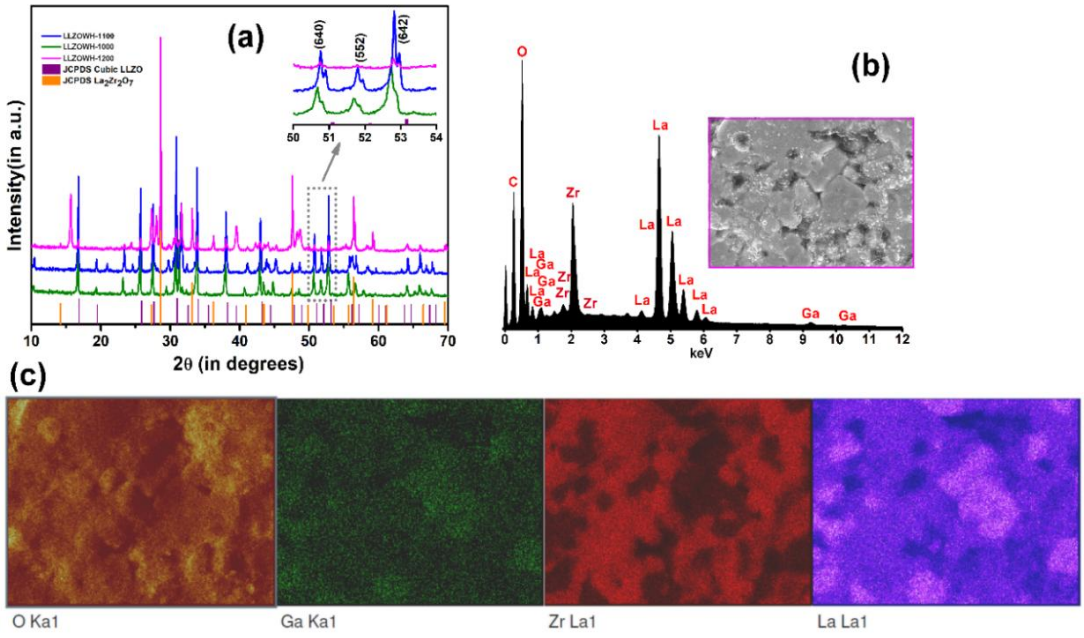

Figure 5.12 *(a) XRD diffractograms of LLZOWH pellets sintered at 1000ºC,1100ºC and 1200ºC in air, (b)-(c) EDX profile and elemental map of the LLZOWH pellet sintered at 1000ºC in air.*

With increase in sintering temperature at 1100ºC, the amount of cubic phase reduced to 63.3% along with Li_2CO_3 (32.3%) and trace amount of other oxide impurities. At 1200ºC, the cubic phase found transformed into pyrochlore type $La_2Zr_2O_7$ phases (24.2%), $La(OH)_3$ (34.5%) and Li_2CO_3 (31.8%) phases.

In summary, EIS results revealed that the maximum exhibited total Li-ion conductivity (bulk + grain boundary) is found to be $2.69x10^{-6}$ S/cm for Ga-LLZO pellet sintered at 1100°C, whereas the highest bulk conductivity of $3.94x10^{-5}$ S/cm could be measured in the pellet sintered at 1000°C. Similar kind of trend in bulk conductivities are also observed by Afyon et al. due to slight reduction of density from 76% at 950°C to 69% at 1100°C for Ga doped LLZO sample synthesized by modified Sol-gel method[31]. The total conductivity value is appeared to be somewhat lower than the previously reported literature values for Ga-doped LLZO with similar compositions which might be due to the poor densification of the LLZOWH pellets[32–34]. The presence of large number of voids is confirmed by FESEM micrographs on fractured surface of the pellet sintered at 1000°C and shown in ***Figure 5.12(b)*** with corresponding EDX profile. Elemental mapping carried out on the fractured surface of the pellet is also given ***Figure 5.12(c)*** describing the presence of constituent elements both at grain and grain boundaries in fractured surface apart from void areas.

5.2.2.5 Electrochemical Studies

To evaluate galvanostatic cycling performance with configuration of Li/LLZOWH/Li, lithium symmetric cell is fabricated and tested by step ascending current densities at room temperature. For that purpose, in the present study we have introduced solvated ionic liquid (SIL) to effectively reduce the interfacial resistance and enhance the interfacial stability of metallic Li at both surfaces of LLZOWH pellet. Ionic liquids (ILs) offer intrinsic ionic conductivity and its use considered as one of the best well-known procedures where one can achieve good interfacial wettability of lithium metal anode with LLZO SSE garnet[35–37]. The galvanostatic cycling performance of lithium symmetric cells tested at different current densities are presented in ***Figure 5.13(a)***. The initial current density is fixed to 28 $\mu A/cm^2$ and gradually increased every after completion of 50 cycles. The cycles are performed with an initial set program of [Charging @+28 $\mu A/cm^2$, 30 min] - Rest (10 min)- [discharging@ -28$\mu A/cm^2$, 30 min] -Rest (10 min), Voltage range ± 1.0V. The positive and negative potentials

in the curve signify the corresponding Li stripping and plating processes. It is observed that at lower current density of 28 μA/cm^2, the cell performed lithium stripping/plating process continuously up to 50 cycles with stable polarization. With further increase in the current

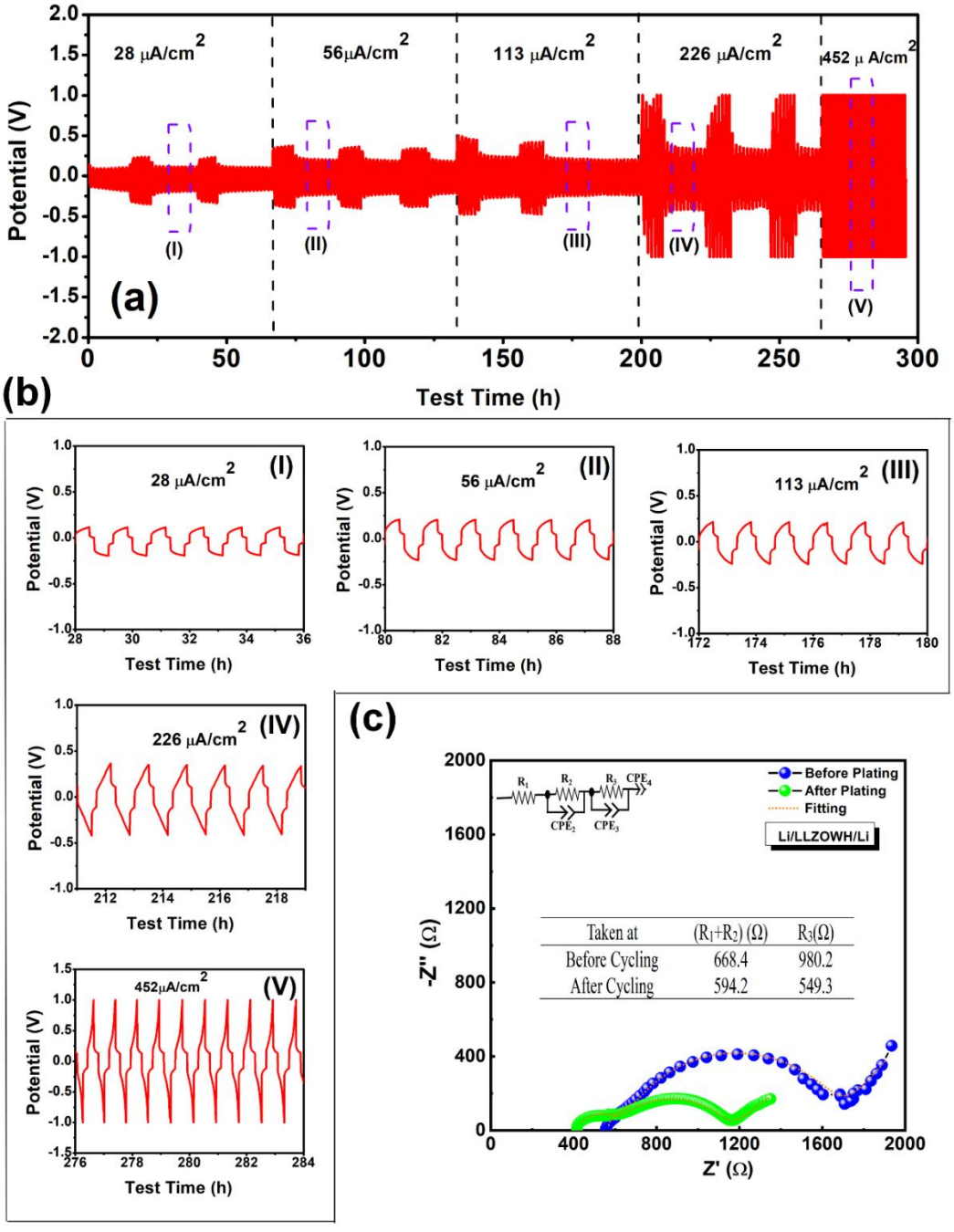

Figure 5.13 *Electrochemical galvanostatic profile of Li/LLZOWH/Li symmetric cell (a) at various current densities from 28-452 μA.cm^{-2} (b) enlarged cycling profiles as marked (I)-(V) in (a), (c) Electrochemical impedance plot of symmetric cell before and after plating.*

density step wise, smooth cycling profiles are recorded. The enlarged view of cycling profiles at ascending current densities as marked I to V in the ***Figure 5.13(a)*** by dotted lines are

presented in ***Figure 5.13(b)*** describing the symmetrical polarization during lithium stripping/plating process. At high current density of 452 μA/cm^2, a large polarization could be detected which might be originated from the loss of contact of Li electrode to the solid electrolyte surface, which increased the Lithium/electrolyte interfacial resistance. This is very common issue faced during cycling of garnet electrolytes because of the poor contact wettability and lack of interphase between Li metal and electrolyte[35,37]. A drastic increase in polarization, instead of a short circuit, forced the cell to be disconnected after completion of 295 hours of lithium stripping/plating process. To measure the effect of dendritic penetration of metallic lithium anode in to the LLZOWH solid state electrolyte, impedance spectroscopy is taken for the symmetric cell before and after lithium plating and the spectra is given in ***Figure 5.13(c)***. It described that the electrolyte and interfacial resistance of LLZOWH-SIL electrolyte slightly decreases after 295 h of operation. This may be due to the fact that the penetration of lithium metal through grain boundary of LLZOWH electrolyte might be sluggish in nature. It is also proposed that the unique plate like grain might be responsible to increase the lithium dendritic diffusion path length through grain boundaries.

5.2.2.6 Post-Electrochemical Studies

To understand the lithium deposition through grain boundaries in LLZOWH, the cycled cell is dismantled and the pellets are examined under FESEM as shown ***Figure 5.15(a)-(d)***. A significant change in colour of both the surfaces of the cycled pellet is observed. The black spots are found at places on the surfaces suggesting the point of metallic contacts or growth. The FESEM micrographs of top and fracture surfaces as shown in ***Figure 5.15(c)*** and ***Figure 5.15(d)***, revealed that the primary grain structure as seen before plating is found to be somewhat distorted from its original structure (as shown in ***Figure 5.12(b)***). This may be due to the penetration of metallic anode through grain boundaries or voids during cycling. A very few numbers of micro-cracks were found in the grain boundary region of cycled pellet as seen in the FESEM micrographs of fracture surface of the cycled pellet, which might be due to the dendritic penetration of metallic lithium across the grain boundary. EDX spectrum taken at the fractured surface of

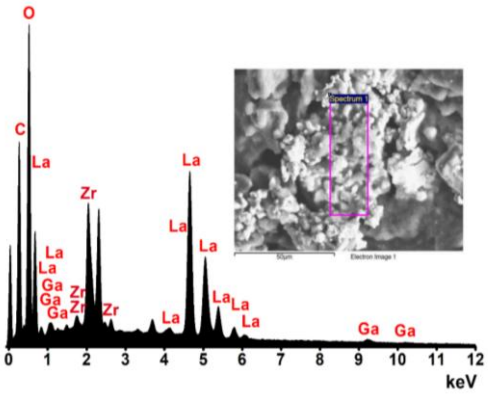

Figure 5.14 *EDX spectrum of the fracture surface of LLZOWH after galvanostatic cycling.*

cycled LLZOWH pellet also presented ***Figure 5.14*** to better understand the topographic change in grains and grain boundaries. It showed that no significant changes either in the grain structure or elemental homogeneity of LLZOWH electrolyte could be found. The unique microstructure as obtained through exo-templating process possibly hindered the dendritic migration of metallic anode in LLZOWH electrolyte by increasing the diffusion path length across the grain boundaries. The increased polarization with incremental current densities without short-circuits in the fabricated lithium symmetric solid-state cell comprising LLZOWH electrolyte might be due to the effect of unique microstructure obtained by exo-templating process, as presented illustrated schematically in ***Figure 5.15(e)***.

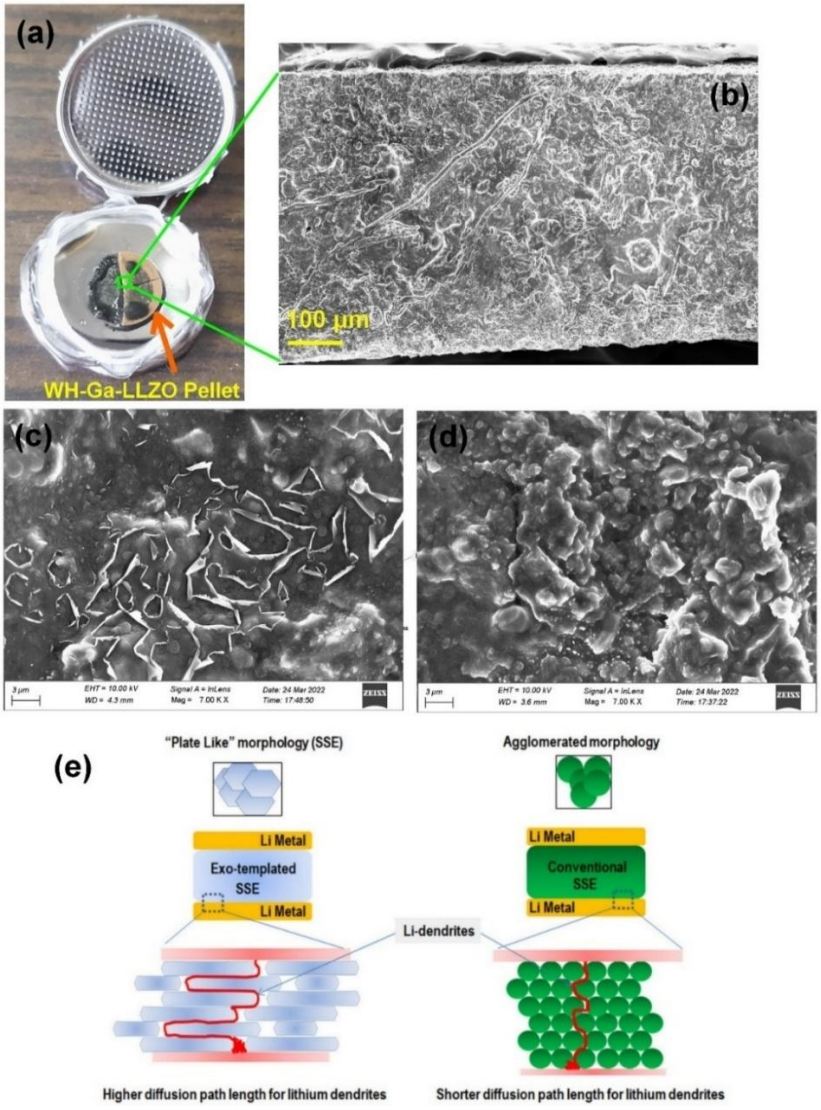

Figure 5.15 *(a) Dismantling of 2032 Coin cell after galvanostatic cycling, (b) FESEM micrograph of cycled LLZOWH pellet, (c) & (d) FESEM micrographs of top and fracture surfaces of cycled LLZOWH pellet and (e) Schematic illustration of metallic anodic deposition through exo-templated and conventionally prepared solid-state electrolyte*

5.3 Engineered Interconnected LLZO

5.3.1 Experimental

5.3.1.2 Material Synthesis and Characterization

Gallium-doped $Li_7L_3Z_2O_{12}$ ($Li_{6.25}La_3Ga_{0.25}Zr_2O_{12}$, LLZOWH) was synthesized using a cellulose paper to obtain an engineered interconnected morphology. The detailed synthesis process is described in ***Chapter 2***, ***Section 2.3.3.3***. In short, a sol-gel precursor (constituent nitrates with a stoichiometric ratio along with fuels in DI water) was prepared. The gel was dropped carefully on the commercial cellulose paper for soaking via capillary action. After the process, the soaked paper was transferred to the furnace for calcination. Similarly, the remaining gel was allowed to further heat for gel combustion. Various synthesis processes and corresponding sample codes of Ga doped LLZO solid electrolyte Material were presented in ***Table 5.1***. The detailed characterization techniques are already discussed in ***Section 2.7***.

5.3.1.2 Cell fabrication and testing

The detailed cell fabrication and testing protocols are already discussed in ***Chapter 2***, ***Section 2.6*** and ***Section 2.7***, respectively. In Short, all the developed solid electrolyte pellets were infused with a solvated ionic liquid (LiTFSI/tetraglyme, 1:1 mol ratio). Various coin cells were then fabricated using the procedures described in ***Chapter 2, Section 2.6***.

5.3.2 Results and Discussion

5.3.2.1 Thermal Studies

The calcination temperature for the exo-templating process was selected by performing the TGA/DTA analysis of pure cellulosic paper and the gel-impregnated paper up to 1200 °C in air. Their thermal profiles were given in ***Figure 5.16***, which described that after 900 °C, no weight loss could be detected in gel-soaked paper. On the other hand, the TGA plot of pure cellulosic paper also suggested that around 3 wt.% of residual ash could be found after thermal

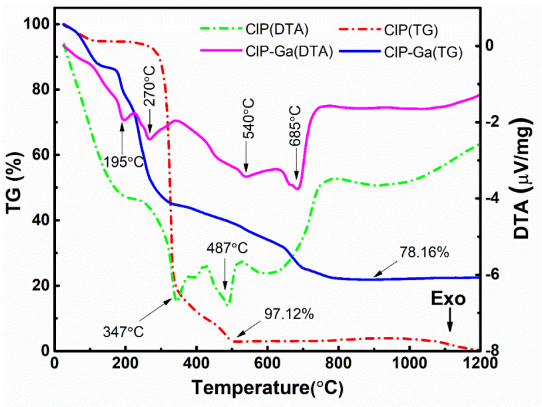

Figure 5.16 TGA and its corresponding DTA plot of bare Cellulose paper (ClP) and Ga doped LLZO gel-soaked Cellulose paper (ClP-Ga) from RT to 1200°C.

degradation of pure cellulosic paper. Therefore, it is expected that such residual mass could also be present in the Ga doped LLZO powder when calcined in air at 900 °C for 10 hours.

5.3.2.2 Structural Studies

X-ray diffractogram of LLZOCET and LLZOGC powders calcined at 900°C and 1000°C along with standard JCPDS patterns of tetragonal-LLZO (PDF 00-064-0140) and cubic-LLZO (PDF 00-064-0141) are presented in ***Figure 5.17(a)***. At 900°C, all the major peaks in the diffractograms could be indexed as cubic LLZO (c-LLZO) for LLZOCET and LLZOGC powders along with impurities of $La(OH)_3$ and Li_2CO_3. However, these impurities were found to be disappeared when calcination temperature was elevated to 1000°C. At this temperature, a new secondary phase La_2O_3 appeared along with cubic LLZO. In our previous experience, we found that $La(OH)_3$ and La_2O_3 usually present as secondary phase along with cubic polymorph of LLZO. The origin of such impurities was well described in our previous reports.[38] Typically lanthanum based impurities such as $La(OH)_3$ or La_2O_3 in any lanthana material appeared as surface impurities during high temperature calcination and exposure of bulk powder in open atmosphere.[38,39] Recently, Fleming et al. established a correlation between the rate of formation of surface impurities such as $La(OH)_3$ or La_2O_3in lanthana materials with respect to surface area and morphological features of the materials.[39]On the other hand, the origin of formation of Li_2CO_3 phase particularly during synthesis LLZO garnetis mainly due to the Li^+/H^+ exchange process between the garnet and atmospheric moisture.[40–42]The presence of such Li_2CO_3non-conducting surface layer on LLZO garnet sometimes may cause lowering the Li-ion conductivity and can impede the densification process of LLZO during sintering.

To further confirm the presence of desired cubic LLZO phases, Raman Spectroscopy and FTIR spectroscopy were carried out for LLZOCET calcined powder. ***Figure 5.17(b)*** shows the Raman spectra of LLZOCET samples calcined at 900°C and 1000°C. Earlier Raman studies on LLZO and related lithiated materials demonstrated that vibration of heavy La cation observed at 100 cm^{-1} and 150 cm^{-1} and the Zr-O bond stretching observed around 640 cm^{-1} and the internal mode of LiO_6 and LiO_4 appeared in the range of 200-300 cm^{-1} and 350-500 cm^{-1} range respectively.[43,44] It is reported that the LLZO tetragonal phase exhibit a greater number of spectral features when compared to its cubic polymorph.[43–45] This distinction arises primarily due to the distorted arrangement of Li^+ ions and the lower symmetry present in the tetragonal structure. Thus, Raman spectra of LLZOCET can be categorized into three distinct regions. Firstly, a low-frequency region below 300 cm^{-1}, which corresponds to the translational

modes of mobile cations. Secondly, in the mid-frequency range between 300 and 550 cm^{-1}, where the cubic phase exhibits a broad and partially overlapping band, while the tetragonal phase shows a higher number of distinct peaks. Lastly, in the high-frequency range above 550 cm^{-1}, where the peaks can be assigned to the vibrational stretching of ZrO_6 octahedra.[43–45]

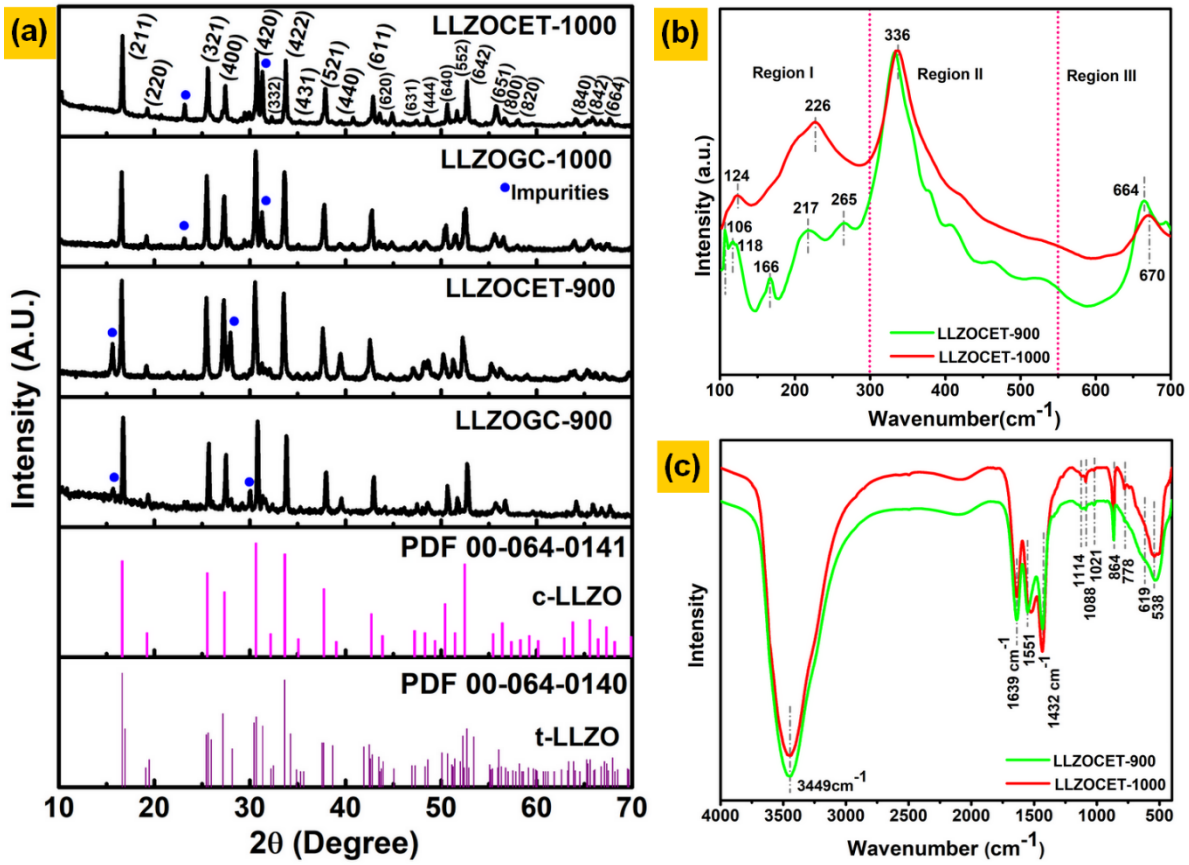

Figure 5.17 *(a) X-ray diffractogram of LLZOGC and LLZOCET calcined at 900°C and 1000 °C in air; (b) & (c) Raman and FTIR spectra of LLZOCET powders calcined at 900 °C and 1000°C respectively.*

Figure 5.17(c) describes the FTIR spectra of LLZOCET powders calcined at 900°C and 1000°C. In the FTIR spectra, no evidence of $La(OH)_3$ was detected in the LLZOCET sample calcined at 900°C. However, prominent -OH vibration peaks at 3449 $cm^{-1}$was observed in both the samples, which were attributed to absorbed moisture. Additionally, characteristic peaks corresponding to Li_2CO_3 were identified, showing C-O stretching at peak positions of 1432 and 866 cm^{-1} in both the calcined powders. Moreover, various strong peaks were also observed at 1639, 1551, 1114, 1088, and 1021 cm^{-1} in both the calcined powders which were associated with different stretching and bending vibrations of residual hydrocarbons and organic moieties. Furthermore, several low-intensity peaks below 800 cm^{-1} were observed, indicating the

presence of characteristic Zr-O and La-O vibrations in both the calcined powders.[38,46]So, FTIR and Raman Spectroscopy results as obtained validated the existence of cubic phase of LLZO in all the calcined powders.

5.3.2.3 Microstructural Studies

Typically, within polycrystalline materials, the diversity in microstructure arises from a range of factors, including grain size, grain shape, the favoured alignment of distinct grains, the coexistence of different phases, and the spatial arrangement of these phases.[47] In our scenario, although the presence of different impurity phases is same in both the powders (LLZOGC and LLZOCET) but the grains and grain boundaries and their orientation are significantly influenced the overall performance of solid electrolyte as they play a crucial role to provide accessible conduction pathways for lithium ion across the solid state electrolyte. Recent computational studies employing phase-field grain growth model as reported by Heo et al. described that in LLZO the microstructural features at both the atomistic and mesoscopic scales can make a significant impact in ionic conductivity.[4] Here, we tried to focus on the effect of microstructure and interconnectedness among the particles in LLZO obtained via cellulose exo-templating process directly on the electrochemical performance in pseudo-solid state lithium metal cell. And for comparison, LLZO powder has also been synthesized by conventional gel combustion process. ***Figure 5.18(a)*** and ***Figure 5.18(b)*** showed the FESEM images of LLZO calcined powders synthesized via GC and CET methods respectively. LLZOGC revealed an agglomerated morphology with wide distribution in their primary particle size ranging from 40-100 nm. The local sintering effect was also seen as large numbers of neck-fused particles are observed; which further formed hard agglomerates to reduce their high surface energy. On the contrary, LLZO synthesized by CET method showed distinct interconnected morphology with fused-grain structure. The growth of the particles as seen in ***Figure 5.18(b)*** seemed to be followed along the direction of crosslinked cellulosic fibrous during high temperature calcination, which on removal of cellulosic template resulted in networked type interconnected morphology. Therefore, FESEM studies clearly revealed two distinct microstructures of LLZO synthesized by two different methods. The further confirm the grain growth in LLZOCET along entangled fibers of cellulosic template, TEM images were taken and presented in ***Figure 5.18(c)***. A spectacular networked morphology was observed with interconnected sub-micron sized grains in LLZOCET. To further understand the microstructural features of LLZO after sintering at 1000°C for 10 hours, the FESEM images were taken on the LLZO pellets both on the top surfaces and fractured surfaces.

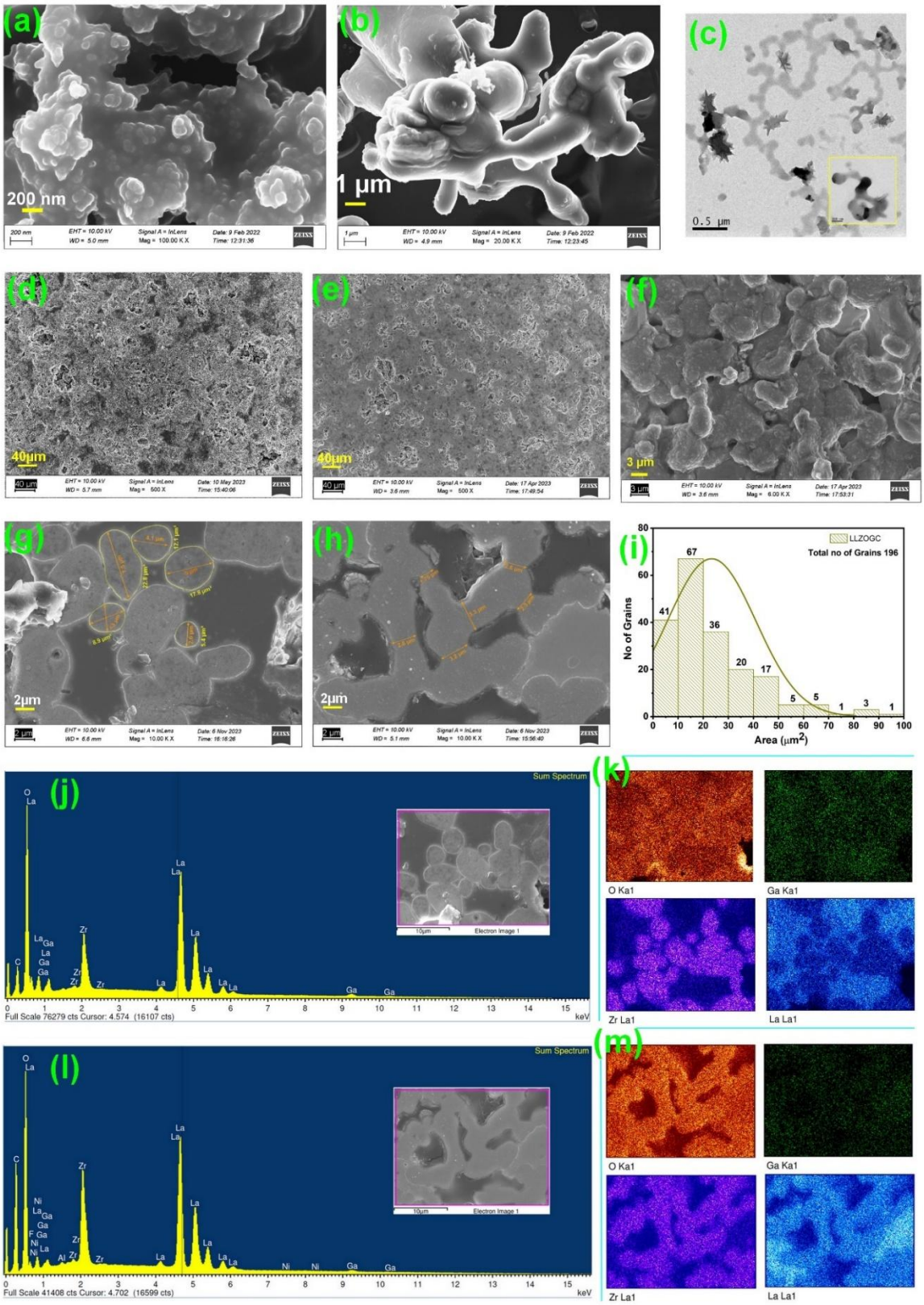

Figure 5.18 *(a) & (b)FESEM micrographs of LLZOGC and LLZOCET, respectively, (c) TEM micrographs of LLZOCET along with its enlarged view in the in-set;(d) & (e) FESEM micrographs of top surfaces of LLZOGC, LLZOCET pellets respectively along with enlarge*

version (f), FESEM micrographs of polished and fractured surface of (g) LLZOGC and (h) LLZOCET pellets; (i) Grain size distribution of LLZOGC, (j) &(k) are EDX profiles and elemental map of LLZOGC pellet; (l) & (m) EDX profile and elemental map of LLZOCET pellet.

Figure 5.18(d) and ***Figure 5.18(e)*** represent the FESEM images of the top surface of LLZOGC and LLZOCET pellets, respectively. It is suggested that LLZO synthesized by gel combustion is likely to be more porous with a large number of cavities/voids on the top surface than that of LLZOCET. The surface topology of sintered LLZOCET pellets, as shown in ***Figure 5.18(f)*** at high magnification, corroborated the nature of the interconnectedness of the grains even after high-temperature sintering at 1000 °C. To explore more microstructural characteristics and probe close to the grains and grain boundaries in LLZOGC and LLZOCET, their sintered pellets were fractured and polished properly. In ***Figure 5.18(g),*** the micrograph of the fractured surface of LLZOGC revealed agglomerated particles, whereas in ***Figure 5.18(h)***, the networked type morphology of LLZOCET grains was clearly visible. Few irregular shaped grains in LLZOGC were marked in ***Figure 5.18(g)*** and their corresponding distribution was calculated using ImageJ software resulting a wide distribution in their corresponding grain sizes, as shown in ***Figure 5.18(i)***. EDX and elemental mapping was also carried out at the fracture polished surfaces of both the pellets- LLZOGC and LLZOCET. ***Figure 5.18(j)*** and ***Figure 5.18(k)*** represented the EDX and elemental mapping of the LLZOGC pellet, respectively, demonstrating the presence of the constituent elements both at the grains and grain boundaries. In case of LLZOCET, the EDX and elemental mapping of LLZOCET were also carried out to confirm the presence of constituent elements at the interconnected grains was and the results were shown in ***Figure 5.18(l)*** and ***Figure 5.18(m)***. It will be thus of interesting to correlate such unique microstructural features obtained via CET method with other interfacial phenomena, its electrical and electrochemical properties.

5.3.2.4 Electrical Studies

Microstructure plays a crucial role in ion transport phenomena for polycrystalline materials. In such ion transport process grain boundary between the crystals in a polycrystalline body behaved differently from its bulk counterparts and their presence markedly affects the properties of the material. The diffusion or ionic transport is usually faster at grain boundaries compared to the grains. In the present scenario, the network interconnected morphology of Ga-LLZO was obtained by high temperature sintering process. The X-ray diffraction analysis also

suggested the presence of secondary phases as La_2O_3, Li_2CO_3 etc. (***Figure 5.17(a)***). Therefore, the possibility of coherent boundaries between the grains may arise along the unlike phases. To study the effect of grain boundaries on the lithium ionic transport properties of synthesized cellulose templating materials, thus electrochemical impedance spectroscopy was carried out of sintered LLZO pellet with Au blocking electrode. The EIS spectra of both LLZOGC and LLZOCET sintered pellets are presented in ***Figure 5.19(a)*** along with their equivalent circuits. Here, equivalent circuit consists of two major resistive parts originated from grain (R_b) and grain boundary (R_{gb}).

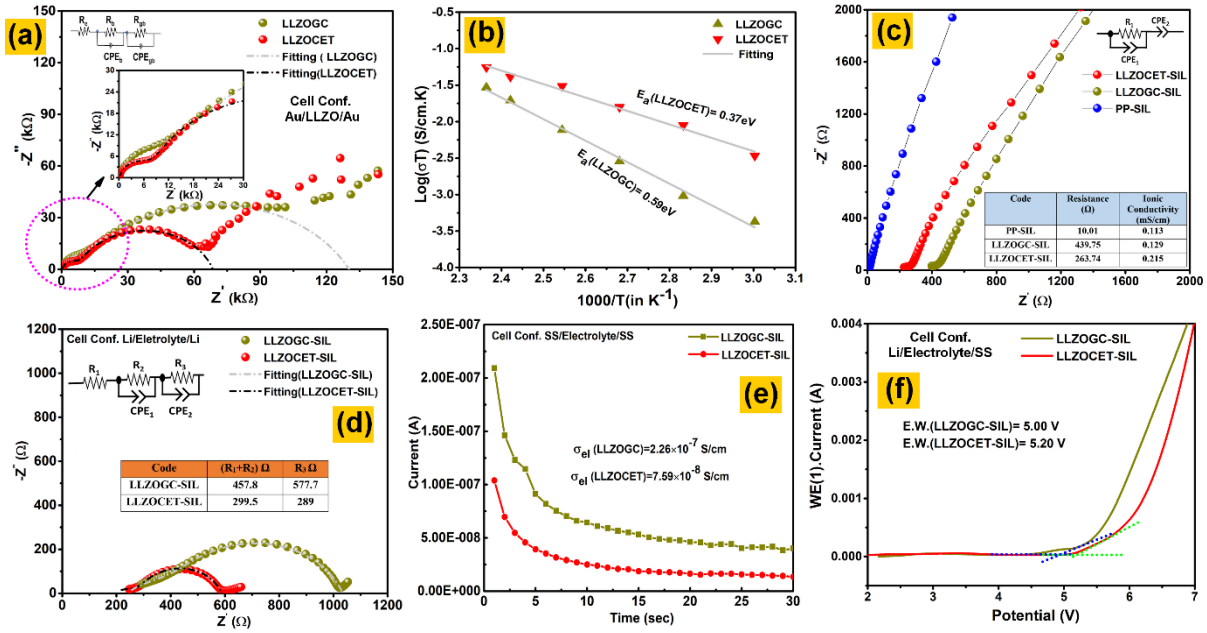

Figure 5.19 (a) Nyquist plot of LLZOGC and LLZOCET pellets sintered at 1000°C at RT. (b) Arrhenius plot of LLZOGC and LLZOCET and calculated activation energies from slopes. (c) EIS spectra of PP-SIL, LLZOGC-SIL and LLZOCET-SIL using SS blocking electrode. (d) Nyquist plot of LLZOGC-SIL and LLZOCET-SIL in Li/Li symmetric cell (e) DC polarization of LLZOGC-SIL and LLZOCET-SIL using ion blocking stainless steel electrode (f) Current vs potential linear sweep voltammetric (LSV) plot at a scan rate of 2.0 mV s^{-1} of LLZOGC-SIL and LLZOCET-SIL.

The Z' vs-Z'' plot as obtained further analysed with Z-view software which suggested the grain resistance of 8.6kΩ and 6.7kΩ and grain boundary resistance of 121.4kΩ and 61.5kΩ for LLZOGC and LLZOCET respectively. The values revealed two times decrease in grain boundary resistance obtained for LLZO material synthesized by templating method compared to LLZOGC. The total conductivity as calculated from the EIS spectrum for LLZOGC and LLZOCET were found to be 1.28×10^{-3}mS/cm and 2.52×10^{-3}mS/cm respectively. The overall

ionic conductivity of LLZO garnet as measured was found to be somewhat lower than by other reported LLZOs synthesized by high-temperature solid-state routes and/or other wet chemical methods.[23,34,36,37,39] The obvious reasons might be due to the formation different secondary phases during synthesis.[38,41,44,46]The activation energies for lithium-ion conduction process for both LLZOGC and LLZOCET were calculated based on Arrhenius equation [$\sigma T = Ae^{-E_a/TK_B}$, where A is the pre-exponential factor, E_a is the activation energy for ionic conduction, and K_B is the Boltzmann constant] from 333-423K. ***Figure 5.19(b)*** represents log(σT) vs 1000/T plot of LLZOGC and LLZOCET with resultant activation energies of 0.59eV and 0.37eV respectively. As the lithium transport phenomena in solid electrolyte predominately follow the grain boundary path, therefore it is expected that having lowered activation energies of the lithium-ion mobility through LLZOCET might be much faster than LLZOGC.

It is worthy to mention here although the microstructurally altered (LLZOCET) electrolyte showed reduces grain boundary resistance compared to LLZOGC with regular morphology, the sintered pellet still delivered lower conductivity due to the presence of secondary phases (La_2O_3, Li_2CO_3 etc.). To compensate such reduction in conductivity, solvated ionic liquid (SIL) was infused in Ga-LLZO. The presence of SIL assisted in two ways; *1)* enhance Li metal anode and hybrid electrolyte compatibility and *2)* facilitated lithium movement across thick sintered electrolyte (thickness ~0.8-0.9mm). The use of SIL thus has been termed here as "liquid therapy" to acquire the required conductivity for solid state metal battery operation. Here, the contribution in conductivity offered by the SIL in LLZO sintered pellets was separately estimated using a polypropylene (PP) separator soaked with SIL sandwiched between two blocking electrodes.

The soaking ability of PP was estimated to be 952 % with respect to its dry weight. The EIS spectrum of PP-SIL is presented in ***Figure 5.19(c)*** along with SIL impregnated LLZOGC and LLZOCET pellets. The nature of the spectrum and corresponding equivalent circuit showed quasi-capacitance type straight line behaviour which on analysis revealed the ionic conductivity value of 0.113 mS/cm for PP-SIL, 0.129 mS/cm for LLZOGC and 0.215 mS/cm for LLZOCET-SIL. Thus, the ionic conductivity offered by SIL definitely aided to enhance the ionic conductivity at least two order of magnitudes than that of LLZO pellet. To further refinement of resistive contributions in solid electrolytes during electrochemical cycling against lithium, EIS were further carried out for LLZGC-SIL and LLZOCET-SIL sandwiched between Li metal anode (symmetric cell). EIS spectrum along with equivalent circuit was

demonstrated in ***Figure 5.19(d)*** which indicated that the charge transfer resistance was found to be around two times less in case of LLZOCET-SIL cell compared to LLZOGC-SIL cell, although the amount of impregnation of SIL in both the cells was found to be same (~ 18% w/w ratio).

Furthermore, the Li metal wettability with the developed ceramic electrolytes also significantly differs between LLZOGC and LLZOCET. The 3D interconnected network morphology of LLZOCET electrolyte offered better wettability with Li metal interface which reflected by the reduction of charge transfer resistance. The entangled LLZOCET grains (***Figure 5.18(f)***) have better access to SIL than the agglomerated LLZOGC electrolyte. Hence, it is expected that the interfacial compatibility of networked LLZO definitely be beneficial in solid state full cell and also Li metal symmetric cell performance. Apart from ionic conductivity, the electronic conductivity of developed hybrid electrolytes is also measured by applying DC polarization at 0.5V in anion blocking symmetric cell as shown in ***Figure 5.19(e)***. Typically, in a steady state condition, the steady state current can be attributed to electronic conduction as the electrodes are acting as ion blocking.[48]Thus, the electronic conductivity as calculated from the DC polarization curve was found to be 2.26×10^{-7} S/cm for LLZOGC-SIL cell and 7.59×10^{-8} S/cm for LLZOCET-SIL cell. These values of electronic conductivity are well matched with the previous literatures.[48,49]In general, solid electrolyte with low electronic conductivity is expected to be less affected by lithium dendritic formation and help in increase in critical current densities (CCD) of the solid electrolytes.[49] It will be thus interesting to calculate the CCD in symmetric cell for both the electrolytes. In later section, it has been discussed in details.

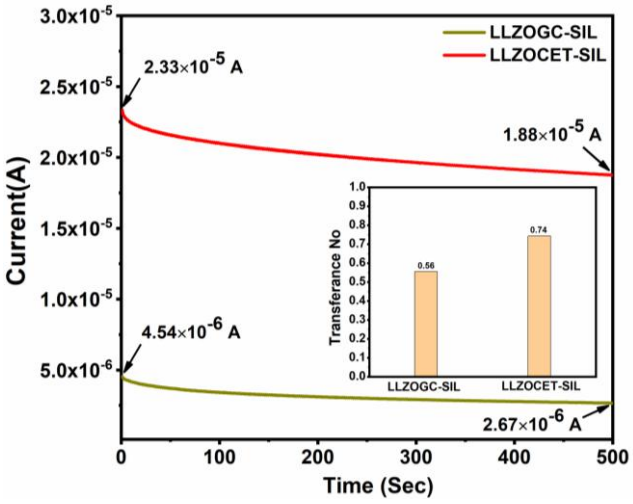

Figure 5.20 *DC polarization curve of LLZOGC-SIL and LLZOCET-SIL with an inset plot showing no transference variation.*

The working electrochemical potential window is one of the important factors to check the durability of lithium batteries as well as the suitability of electrolyte materials against commercial cathode materials. As shown in ***Figure 5.19(f)*** the curve displayed the profiles of the developed electrolytes using linear sweep voltammetry (LSV) ranging from 0 to 7V at room

temperature. The electrochemical potential window thus obtained were found to be 5.0V for LLZOGC-SIL and 5.2V for LLZOCET-SIL which suggested that the both the hybrid electrolytes seemed to be suitable for high voltage lithium batteries. DC polarization curve of LLZOGC-SIL and LLZOCET-SIL with initial and steady state current before and after polarization was presented in ***Figure 5.20***. The t_{Li^+} was calculated using Bruce-Vincent-Evans equation (Equation 1) and the it was found to be 0.56 for LLZOGC-SIL and 0.74 for LLZOCET-SIL respectively. In summary, the measured electrical properties of developed electrolytes inferred that template assisted synthesis as produced engineered morphology delivered significant reduction in grain boundary resistance, enhancement in lithium-ion transport efficacy at room temperature and lowered activation energy than the conventionally prepared LLZO. The potential window as measured was also found to be compatible with most of the existing commercial cathodes.

5.3.2.5 Electrochemical Studies

5.3.2.5.1 Critical Current Density Measurement

To calculate the critical current density (CCD) of the electrolytes (LLZOGC and LLZOCET), the symmetric cells were galvanostatically charge discharge at a current density of 0.05 to 1.0 mA/cm^2 with a step current density of 0.05 mA/cm^2. The potential vs time plot for both the electrolytes was presented together in ***Figure 5.21(e)***. The regions (Region I and Region II) were identified in the profile where soft short circuit could be detected for both the electrolytes. The CCD for LLZOGC-SIL was estimated to be 0.40 mA/cm^2 and 0.70 mA/cm^2 for LLZOCET-SIL symmetric cell describing two times increase in current density for engineered LLZO electrolyte. Hence, the aforementioned findings illustrates that the combined influence of the engineered LLZO and incorporated SIL exerts unique effect in diminishing overpotential. Therefore, the results obtained from EIS and CCD studies provides additional support for the significant role played by the engineered microstructure. It helps in inhibiting the growth of lithium dendrites and reducing the charge transfer resistance at the solid metal interface.

5.3.2.5.2 Long cycling performance

Solid state lithium metal batteries (SSLMBs) suffer from failure related to Li dendritic induced short circuit and contact loss at metal anode-ceramic electrolyte interface. [1,4,5,7-10] The kinetic involved in such failures are related to the platting and stripping of Li at the interface.

Such failure may also be facilitated in reduction of critical current density (CCD), the rate determining state of lithium kinetics in solid state battery. At solid electrolyte interface, several phenomena such as ion diffusion, lithium metal nucleation growth, formation of voids and parasite reactions are found to be detrimental for successful operation of SSLMBs.[50–54]

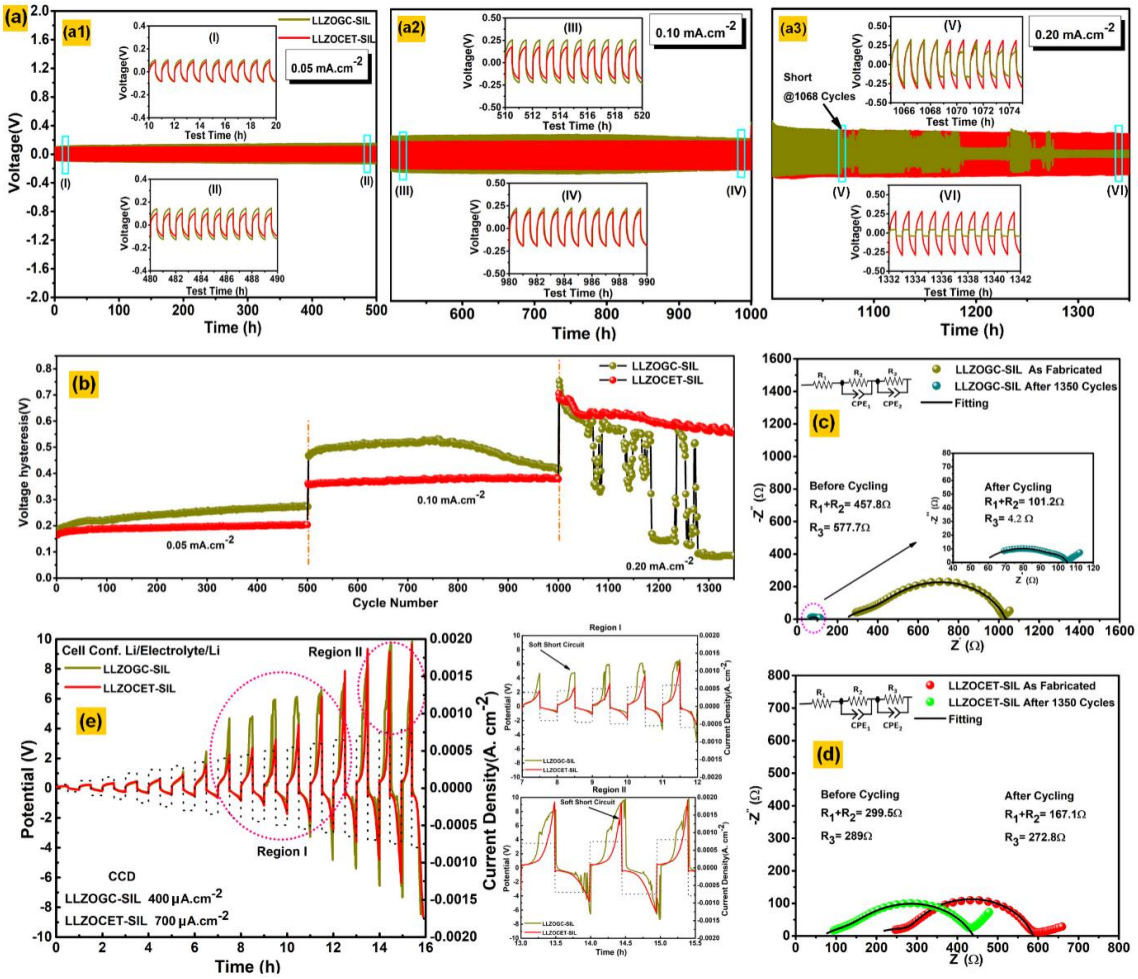

Figure 5.21 *(a) Voltage profile and (b) voltage hysteresis of Li/Li Symmetric cells at RT over 1350 cycles at different current density (1-500 at 0.05* mA.cm^{-2}*, 501-1000 at 0.10* mA.cm^{-2} *and 1001-1350 at 0.20* mA.cm^{-2}*)with two distinct hybrid electrolytes(LLZOGC-SIL & LLZOCET-SIL), (c) and (d) EIS spectra before and after electrochemical cycling of LLZOGC-SIL and LLZOCET-SIL cell, (e) DC cycling profile of Li/Li symmetric cell of both the electrolyte at RT with step current density of 0.05* mA.cm^{-2} *in the range of 0.05 to 1.00* mA.cm^{-2}.

The study of electrochemical behaviour of LLZO sandwiched between two lithium metal foil is thus a useful technique to understand the solid electrolyte compatibility with Li metal in SSLMBs. Here, lithium symmetric cells were fabricated using LLZOGC-SIL and LLZOCET-SIL electrolytes and undergone lithium platting/stripping process for more than 1350 hours at room temperature (27°C). The platting/stripping profiles at different current

densities such as 1 to 500 hours at 0.05 mA/cm^2, 501-1000 hours at 0.10 mA/cm^2 and 1001-1350 hours at 0.20 mA/cm^{2}weredemonstrated in ***Figure 5.21(a)(a1-a3)*** respectively. For current density 0.05 mA/cm^2, LLZOCET-SIL cell showed an average polarization of 0.082V at 1st cycle and 0.102V at 500th cycle, whereas LLZOGC-SIL cell showed 0.087V and 0.136V; which suggests that the Li platting/Stripping process was more stable in LLZOCET-SIL cell compared to LLZOGC-SIL cell. The insets in ***Figure 5.21(a)(a1)***, (as marked I and II) shows the symmetrical lithium platting stripping profiles of two electrolytes. From 501-1000 hours of operation, the current density increases to a 0.10 mA/cm^2 as shown in ***Figure 5.21(a)(a2)***. Such two-fold increase in current densities resulted a slight increase in average polarization of 0.246V and 0.187V for LLZOGC-SIL and LLZOCET-SIL electrolyte respectively. In the inset the symmetric charge discharge profile as presented were taken from the portion as marked III and IV from the profile. On further increasing of current density to0.20 mA/cm^2, the LLZOGC-SIL cell was showed asymmetrical platting stripping profile as shown in ***Figure 5.21(a)(a3)***. After 1068 cycles (hours) LLZOGC-SIL cell was found to be short circuited as presented (as marked V and VI in the inset). On the other hand, engineered LLZOCET-SIL cell performed exceptionally, where cycling stability with negligible voltage fluctuations and no sign of short circuit was observed till 1350 cycles which corroborated the Li dendritic growth might be significantly retarded in LLZOCET. The cycling stability and short circuit phenomena could also be observed in voltage hysteresis curve as shown in ***Figure 5.21(b)***. In general, the voltage hysteresis is the difference between the voltages of Li stripping and platting. This voltage hysteresis mainly originated due to the interfacial instability and can be determined by the current density, different interfacial properties and overall charge transfer resistance of the cell. At a current density of 0.05 mA/cm^2 and 0.10 mA/cm^2, the voltage hysteresis remained almost constant for LLZOCET-SIL cell than that of LLZOGC-SIL cell. At current density of 0.20 mA/cm^2, the Li platting/stripping of LLZOGC-SIL cell showed an irregular fluctuating voltage profile due to the unstable interfacial stability between Li metal and ceramic electrolyte. A certain drop in hysteresis voltage was observed for LLZOGC-SIL cell after 1068 cycles because of the dendrite induced soft short-circuit. The voltage hysteresis of Li plating/stripping of LLZOCET-SIL cell was found to be stable without any irregularities. The result thus obtained from stripping/platting behaviour suggested that interconnected engineered morphology facilitated the lithium platting and stripping kinetics and also abled to impede short circuit. To look into the fate of charge transfer process, electrochemical impedance spectroscopy was also carried out for both the symmetric cells before and after cycling. The Nyquist plots of LLZOGC-SIL and LLZOCET-SIL cells before and after electrochemical

cycling were presented in ***Figure 5.21(c)*** and ***Figure 5.21(d)*** along with their equivalent circuit. It is worth to mentioned here that we have denoted R_1 and R_2 as a bulk and grain boundary resistances of hybrid electrolyte and R_3 as an interfacial resistance between Li metal and electrolyte which further termed as charge transfer resistance or $R_{ct.}$ The charge transfer resistance of LLZOGC-SIL cell was found drastically reduced to 577.7Ω to 4.2 Ω revealing short circuit phenomena inside the cell after prolonged operation of 1350 cycles, whereas engineered LLZOCET-SIL cell showed no such significant change in charge transfer resistance. The R_{ct} values remained 289.0 Ω to 272.8 Ωbefore and after cycles.

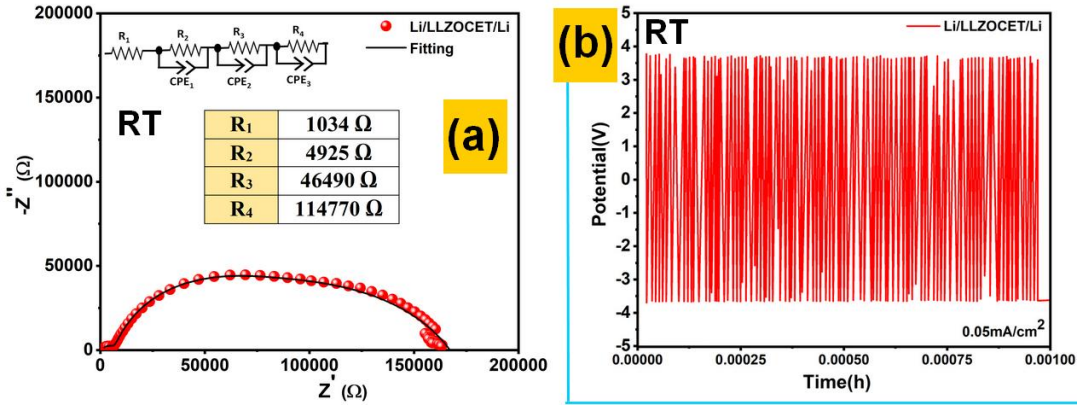

Figure 5.22 *(a) EIS spectra of a lithium symmetric cell of LLZOCET electrolyte pellet without using SIL, (b) Symmetric cell performance of LLZOCET electrolyte without SIL showing very high polarization voltage at a current density of 0.05* mA.cm^{-2}.

It is worthy to mention here that the solid-state cells with LLZOCET electrolyte (without impregnating SIL) could not be found operational due the high interfacial resistance and large polarization voltage at room temperature offered by metal-ceramic electrode electrolyte interface. The results were demonstrated in EIS plot in ***Figure 5.22(a)*** and symmetrical cell performance in ***Figure 5.22(b)***. The charge transfer resistance of LLZOCET without SIL was found to be 114.7kΩ, a significantly higher value which can retard facile Li transport at the metal-electrolyte interface. The symmetric cell performance as measured in Li/LLZOCET (without SIL)/Li also suggested a large polarization voltage around 4V even at a lower current density of 0.05 mA/cm^2 during room temperature operation. Therefore, such observation typically compelled us to use SIL into LLZOCET matrix.

5.3.2.5.3 Electrochemical Cell Performance

In ***Figure 5.23(a)***, we envisaged the lithium transport mechanism across the developed electrolytes. The Li-ion movement through conventionally prepared LLZOGC possibly

hindered due to large grain boundary resistances offered by the irregular microstructure, whereas, Li-flux across the networked LLZOCET structure proved to be higher. To support this hypothesis, SSLMBs were fabricated with both the electrolytes using $LiMn_2O_4$ cathode and Li anode. ***Figure 5.23(b)*** and ***Figure 5.23(c)***, displayed the typical charge discharge profiles at current densities 0.1-3.0 mA/cm^2 of LLZO electrolyte derived from two synthesis methods. The severe loss in discharge capacity at high current density could be found for LLZOGC-SIL cell compared to LLZOCET-SIL. ***Figure 5.23(d)(d1-d3)*** demonstrate the cycling profile of LLZOGC-SIL (Li/LLZOGC-SIL/LMO) and LLZOCET-SIL (Li/LLZOCET-SIL/LMO) at current densities ranging from 0.10 to 3.0 mA/cm^2.

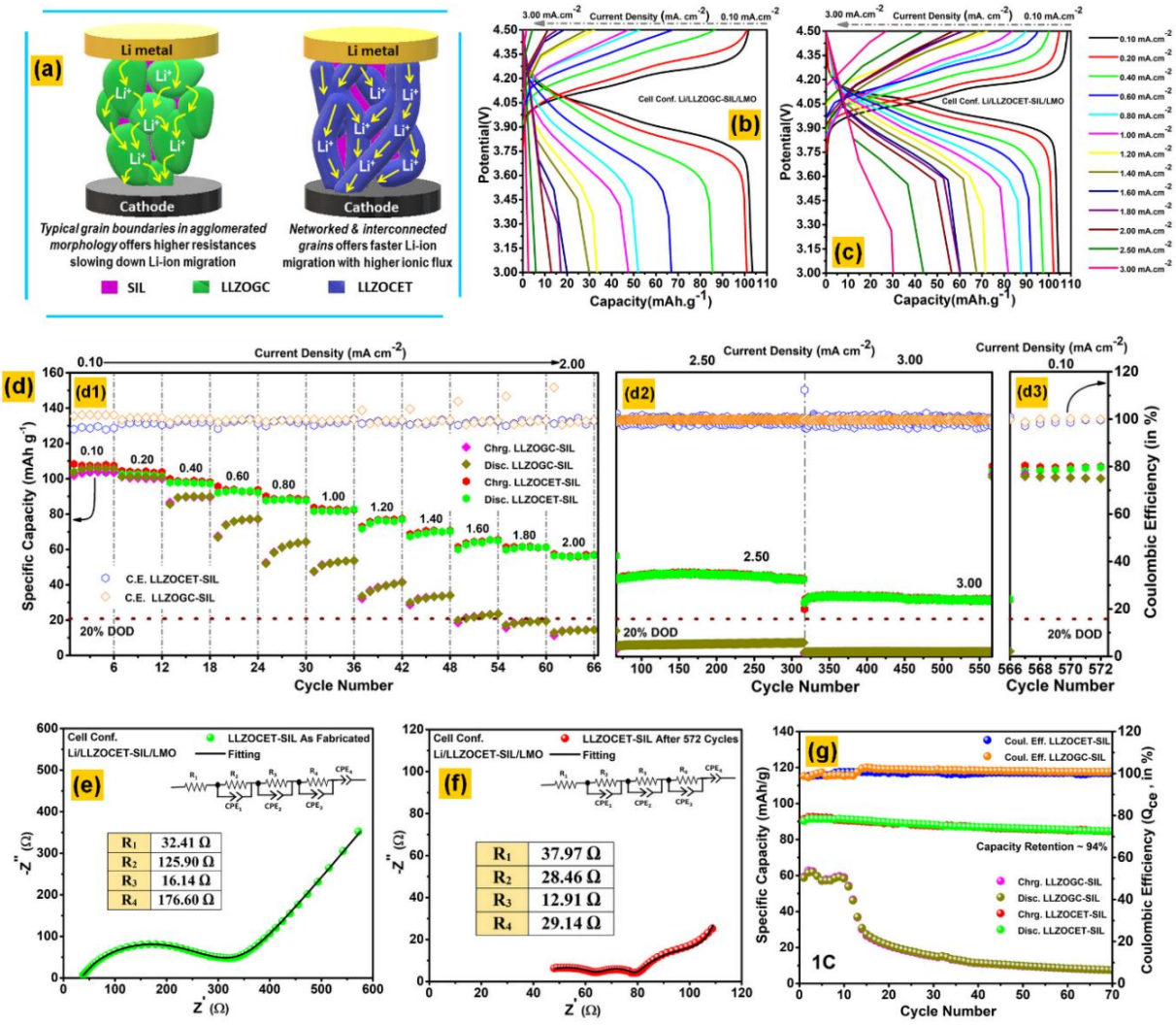

Figure 5.23 *(a) Schematic representation of Li-ion transport across LLZO prepared by two different methodologies (GC and CET processes); (b-c) Typical charge-discharge profiles of LLZOGC and LLZOCET electrolytes (cell configuration Li/LLZO-SIL/LMO) at different current densities; (c) Typical charge-discharge profiles of LLZOGC cell at different current*

densities.; (d) Rate performance study of LLZOGC and LLZOCET electrolytes up to 572 cycles comprising different current densities- (d1) 1-66 cycles @ 0.1-2.0 mAcm^{-2}, (d2) 67-566 cycles @ 2.5-3.0 mAcm^{-2} and (d3) 567-572 cycles @ 0.1 mA.cm^{-2}.; (e-f) showing the EIS spectra of LLZOCET cells before and after cycling along with their equivalent circuit in the in-set.; (g) High rate capability study at 1C rate for both LLZOGC and LLZOCET electrolytes along with their coulombic efficiencies.

A comparison of specific capacities and coulombic efficiencies were also been reflected in the plot at various current densities. It is worthy to mention here that an initial decrease in capacities could be observed for both the cells, which might be due the sudden change in the step current densities, however both the cells recovered their capacities in later cycles. At a lower current density of 0.1 to 0.2 mA/cm^2 both the cells showed average discharge capacity of ~105-101 mAh/g and ~104-102 mAh/g respectively. The average coulombic efficiency at those current densities is also found more than 98%. With further increasing current densities, from 0.4 to 3.0 mA/cm^2, a significant decrease in specific capacity could be observed at LLZOGC-SIL cell compared to LLZOCET-SIL cell. However, coulombic efficiency offered by both the cell was found similar. The average discharge capacity along with their average coulombic efficiency, corresponding C-rate and capacity retention with respect to initial capacities were summarised in ***Table 5.4***. At current density of 1.6 mA/cm^2, LLZOGC-SIL cell was found to suffer ~80% fading of its initial capacity whereas engineered LLZOCET-SIL still delivered 61.1% of its initial capacity. The cells were cycled at high current density of 2.5 and 3.0 mA/cm^{2}for more than 250 cycles each. It was found that the specific discharge capacity of LLZOGC-SIL cell was measured to be 7.16 and 2.79 mAh/g equivalent to 6.79% and 2.64% retention of its initial capacity. Interestingly, at those same current densities, engineered LLZO cell still delivered 45.46 and 32.87 mAh/g discharge capacities which were equivalent to the 43.77% and 31.65% retention of capacity. After performing 566 cycles, the current density was reduced to its initial current density of 0.10 mA/cm^2 and both the cell was found to delivered more than ~95% of their initial specific capacities. The cycling profile carried out for more than 570 cycle using both LLZOGC-SIL and LLZOCET-SIL Electrolyte suggested that the Li mobility across the solid electrolyte is highly dependent on its microstructure. The network LLZO possible facilitated lithium-ion conduction at higher current densities than that of conventionally prepared solid electrolyte (Gel combustion method).

Table 5.4 *Summary of electrochemical performance at different current densities of developed hybrid electrolytes in full cell configuration (Li/LLZO-SIL/LMO) (showing excellent rate capability and coulombic efficiency).*

Current Density (mA cm^{-2})	Corres. Avg. C-rate (Up to 20% DOD)		Avg. Coulombic Efficiency (in %)		Avg. Discharge Capacity (mAh g^{-1})		Cap. Reten. W. r. t. initial/ Reversible Capacity loss (in %)	
	LLZO GC	LLZO CET	LLZO GC	LLZO CET	LLZO GC	LLZO CET	LLZO GC	LLZO CET
0.10	0.2C	0.2C	101.99	96.51	105.39	103.86	-	-
0.20	0.4C	0.4C	100.72	98.41	101.03	102.29	95.86	98.49
0.40	0.8C	0.8C	100.02	98.93	89.12	97.68	84.56	94.05
0.60	1.4C	1.3C	99.88	98.88	74.61	92.71	70.79	89.26
0.80	2.3C	1.8C	99.74	98.99	60.35	87.93	57.26	84.66
1.00	3.4C	2.4C	99.90	98.94	51.78	81.87	49.13	78.82
1.20	5.5C	3.1C	100.12	98.97	38.19	75.30	36.24	72.50
1.40	7.6C	4.0C	100.29	98.90	32.46	69.21	30.80	66.64
1.60	-	4.9C	100.49	98.99	21.95	63.47	20.82	61.11
1.80	-	5.8C	100.92	99.14	18.55	60.84	17.60	58.57
2.00	-	7.0C	101.47	99.31	13.93	56.21	13.22	54.12
2.50	-	10.8C	100.15	99.47	7.16	45.46	6.79	43.77
3.00	-	18.0C	100.12	99.41	2.79	32.87	2.64	31.65
0.10	0.2C	0.2C	99.84	98.67	100.58	105.18	-4.56	0

In both cell the contribution of solvated ionic liquids (SIL) in lithium-ion movement across the electrolyte is similar thus, the poor performance of LLZOGC-SIL might be due its polycrystalline grain and corresponding grain boundary resistance which retarded fast ionic mobility at high current densities. To understand the intrinsic charge transfer mechanism at electrode-electrolyte interface EIS techniques was carried out before and after electrochemical cycling of LLZOCET-SIL cell as shown in ***Figure 5.23(e)*** and ***Figure 5.23(f)*** respectively. Post electrochemical impedance study further revealed that the charge transfer resistance significantly decreases even after performing 572 cycles. This finding corroborated the facile ionic mobility across network LLZOCET electrolyte.

Table 5.5 A comparison chart of different electrochemical performances of engineered LLZO.

Electrolyte	σ at RT (S/cm)	t (μm)	E_0 (V)	t_{Li}^+ at RT	Stability (h)	Initial Capacity ($mAh.g^{-1}$) /Cathode	Capacity retention properties	Ref.
3D coral like LLZO/PVDF – LiClO4/CPE	1.51×10^{-4}	100	4.7	0.47	Stable over 200 cycles	168.3 @0.1C /$LiFePO_4$	95.2% over 200 Cycles at 1C	[55]
3D LLZAO/PEO-LiTFSI/CPE	2.51×10^{-4}	240	5.58	0.53	stable over 400 cycles	167.2 @0.1C /$LiFePO_4$	80 % after 100 cycles at 0.2C	[56]
LLZO Templated by Bacterial Cellulose /PEO-LiTFSI/CPE	1.12×10^{-4}	70-100	6.0	-	-	-	-	[57]
LLZO Templated by Silk Template/ PEO-LiTFSI/CPE	8.89×10^{-5} (30°C)	-	5.1	0.49 (50° C)	stable over 700 cycles	149.3 @0.2C (50°C) /$LiFePO_4$	107.2 mAh g^{-1} after 500 cycles at 1 C (50°C)	[58]
LLZO fibers using bio-mass template Kapok	1.13×10^{-4}	-	-	-	-	-	-	[59]
LLZO derived from lignosulfonate/ cellulose nanofiber (LS-CNF) / PEO-LiTFSI/CPE	1.37×10^{-4}	-	5.4	0.59	stable over 400h	146 @0.1C /$LiFePO_4$	100% after 100 cycles at0.5C	[60]
Hydrogel-derived LLTO framework/ PEO/CPE	8.8×10^{-5}	-	-	-	-	-	-	[61]

3D garnet framework using the polyurethane foam as template/ PEO-LiTFSI/CPE	1.2×10^{-4}	260	5.6	0.33	stable over 360 cycles	138 @0.5C /$LiFePO_4$	92.1% after 50 cycles at 0.5C	[62]
Neck-fused Engineered LLZO/ Solvated Ionic liquid/SHE	3.3×10^{-4}	~800 - 1000	5.44	-	stable over 200h	104.91 @0.05 mA/cm^2 /$LiMn_2O_4$	-	[38]
Interconnected LLZO/Solvated Ionic liquid/SHE	2.15×10^{-4}	~800 -900 (Bulk)	5.2	0.74	Stable over 1350h	103.8 @0.1 mA/cm^2 /$LiMn_2O_4$	94% after 70 cycles at 1C	This Work

CPE, SHE, and CD stand for composite polymer electrolyte, solid hybrid electrolyte, and current density, respectively.

The interconnectedness in particle morphology thus found responsible for faster ionic mobility as well as small grain boundary resistance.

A summary of the electrochemical performances of engineered solid electrolyte materials was presented in ***Table 5.5*** comparing with LLZOs synthesized by different methodologies. While doing literature survey, a limited number of articles were found which used engineered LLZO as solid matrix to make SHE, rather composite type electrolytes were available which are made of engineered solid electrolyte incorporated or embedded within the matrix of polymer and lithium ion conducting salts. It is worthy to mention here that the degradation of capacity at high-rate condition is directly related to the interrupted Li-ion movement both across the electrolyte and electrodes (anode and cathode) used. Here, LLZOCET thus needs to be further probed to explore the structural integrity (cubic polymorph) after cycling. In this context, the cycled cells were dismantled and their structural and microstructural features were examined under FESEM, XRD, FTIR. The details of the study will be discussed in next sub-section.

5.3.2.6 Post-electrochemical Studies

Figure 5.24 focuses major three aspects of post-mortem analysis of LLZOCET cycled cells; *(1)* (a) & (b) morphological features of lithium facing surfaces of LLZOCET electrolyte in symmetric cell configuration (Li/LLZOCET-SIL/Li), *(2)* (c)-(e) deterioration of Li-LLZO interface due to dendritic growth in full cell configuration (Li/LLZOCET-SIL/$LiMn_2O_4$) and

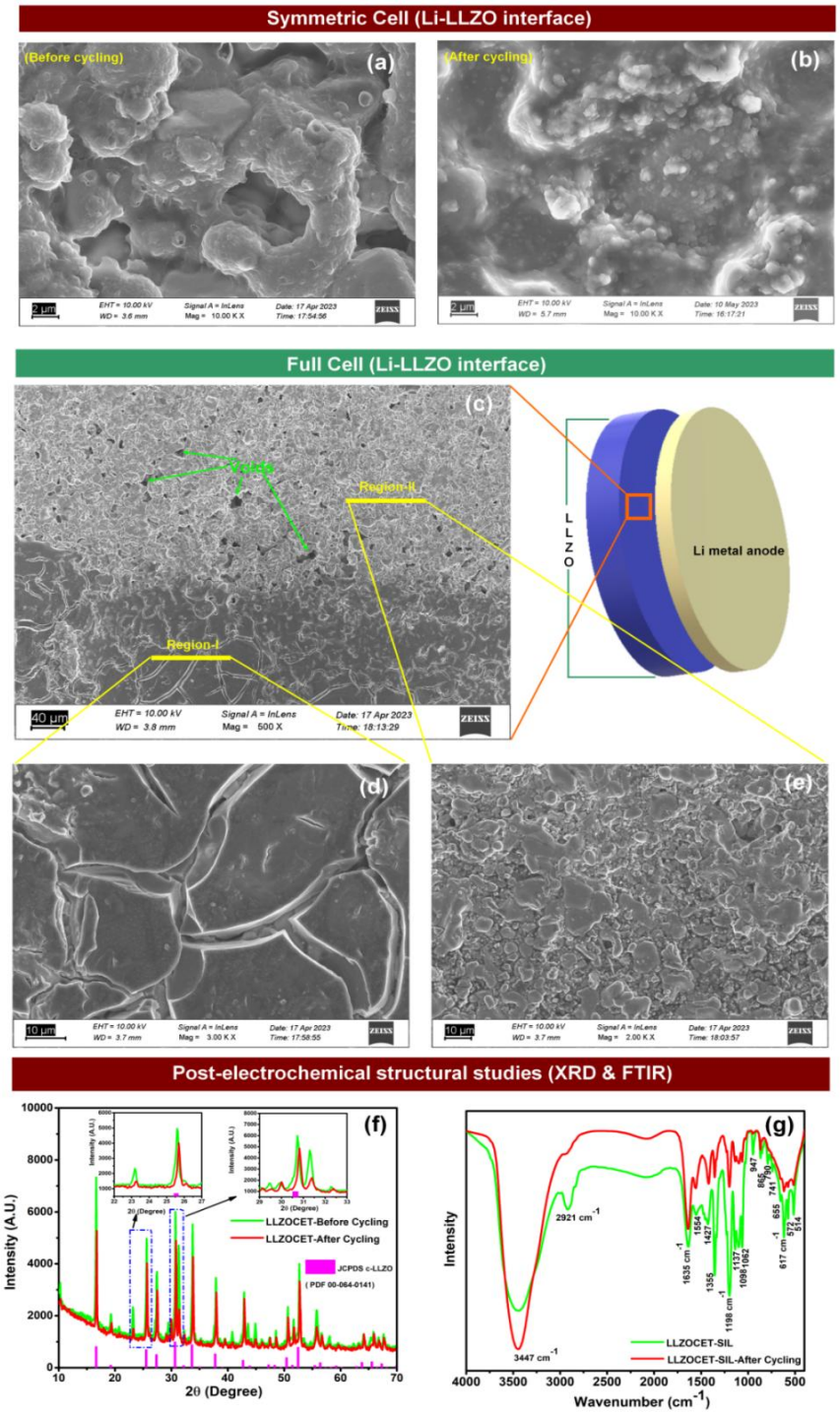

Figure 5.24 *Microstructures of anode facing surfaces of LLZOCET electrolyte in symmetric cell configuration (Li/LLZOCET-SIL/Li) (a) before cycling and (b) after cycling; In full cell configuration (Li/LLZOCET-SIL/$LiMn_2O_4$) (c) showing the microstructure of anode facing surface of LLZO electrolyte comprising microcracks (region-I) and voids (region-II); The magnified view of microstructures of (d) region-I and (e) region-II; (f) X-ray diffraction patterns of LLZOCET electrolyte before and after cycling along with enlarged view of significant peaks; (g) FTIR spectra of LLZOCET-SIL electrolyte before and after cycling.*

(3) structural changes in compositional level in LLZOCET electrolyte due to long term cycling**.** In a symmetric cell configuration, the FESEM images of the top surfaces of the LLZOCET electrolyte both before and after cycling revealed that the networked microstructure almost remained the same even after prolonged charge-discharge cycles, as shown in ***Figures 5.24(a)*** and ***(b)***. However, in full configuration, the results seemed to be different. The top surface of the LLZOCET cycled electrolyte facing the lithium anode side showed a few black spots (Region-I) and voids, which were found to be different compared to the overall surface (Region-II) of the electrolyte, as demonstrated in ***Figure 5.24(c)***. The dark spots (region-II) were further magnified to look into the details. Several interlinked cracks were found, which might be due to the penetration of dendrites originating from point contacts between the Lithium metal anode and the ceramic LLZOCET electrolyte, as shown in ***Figure 5.24(d)***. On the contrary, in region II, the major fraction of the electrolyte surface showed unchanged interconnected morphology as it was before cycling, as shown in ***Figure 5.24(e)***.

The selected area EDX profile of anode facing LLZOCET-SIL pellet after full cell performance (572 Cycles) was also presented in ***Figure 5.25***, suggesting the presence of all the constituent metal ions (La, Zr, and Ga) along with F and S from SIL. The cycled electrolyte was further probed to understand the compositional changes or phase changes after cycling of the LLZOCET electrolyte. ***Figure 5.24(f)*** describes the X-ray diffractograms of the LLZOCET electrolyte both before and after cycling. The diffraction patterns clearly indicate that the desired cubic phase remained intact even after long cycling. Moreover, the major impurities, such as La_2O_3, which were present initially in the electrolyte powder, were found to be reduced. The quantitative phase analysis of cycled LLZOCET electrolyterevealed93.5% cubic LLZO phase along with 0.3% La_2O_3 and $La_2Zr_2O_7$ pyrochlore phase, amounting to 6.2% (initially, before electrochemical, the phase of c-LLZO was found to be 87.4%, La_2O_3 was found to be 11.5%, and $LaAlO_3$ was 1.2% in calcined powder). The XRD analysis thus suggested lanthanum deficiency as present in the LLZOCET electrolyte before cycling electrochemically, fulfilled by the formation of a more cubic phase and lanthanum diffused to the garnet electrochemically. Such phenomena were also detected in our

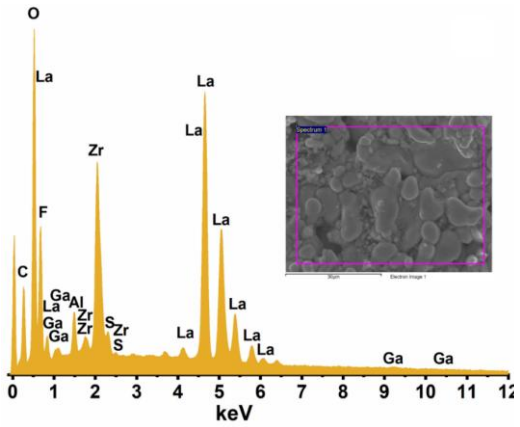

Figure 5.25 *EDX profile of LLZOCET-SIL pellet after full cell performance (572 Cycles).*

previous report, where lanthanum was present as $La(OH)_3$ impurity in pristine LLZO powder, diffused back to the LLZO matrix during cycling. [38] The structural effect was further investigated and compared using FTIR spectra of LLZOCET electrolyte before and after cycling, as described in ***Figure 5.24(g)***. All the characteristic peaks of LLZO, as appeared in the spectra, remained the same even after cycling. Several other residual peaks were visible, which correspond to the solvated ionic liquids used in the LLZOCET electrolyte. The overall post-mortem analysis revealed no change in interconnected engineered morphology in LLZOCET, which might be responsible for long cycle life and high C-rates. Lithium dendritic penetration in terms of cracks and voids could be visible on the anode-facing surface due to point contacts of electrolyte with the metallic anode surface.

Table 5.6 *Pictorial representation of various properties/parameters of Ga doped LLZO material synthesized by three different synthesis processes*. *(SHE: Solid Hybrid Electrolyte)*

Properties/ Parameter	**Gel Combustion**	**WH Exo-Templating**	**Cellulose Exo-Templating**
Phase	c-LLZO+Impurities	c-LLZO+Impurities	c-LLZO+Impurities
Powder Morphology	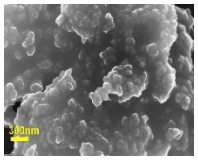	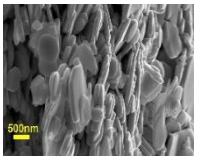	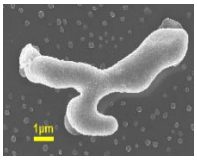
TEM Morphology	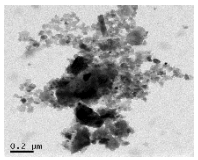	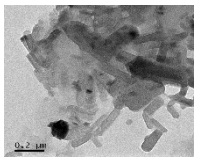	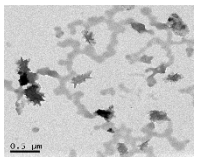
Pellet Morphology	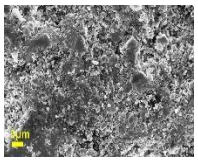	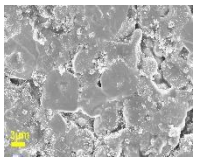	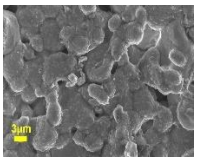
σ_b (mS/cm)	0.019	0.039	0.026
σ_{SHE}(mS/cm)	0.129	0.179	0.215
$R_{int.}$ ($\Omega.cm^{-2}$)	655.70	245.05	328.47
Cycling Stability	Short at 1068h	295h without short	1350h without short

5.4 Conclusion

This chapter demonstrated the successful application of bio-inspired exo-templating routes to engineer the microstructure of Ga-doped LLZO garnet electrolytes for SSLMBs. In the first case, a biowaste material is used for deriving a unique 'plate-like' microstructure of a cubic Ga-doped LLZO ($Li_{6.25}La_3Ga_{0.25}Zr_2O_{12}$) solid-state electrolyte by mimicking the intercellular polygonal structure of WH fibrous tissues. The developed exo-templating method resulted in cubic phase LLZO at a lower temperature of 1000 °C. The synthesized Ga-doped LLZO solid electrolyte showed a bulk Li-ion conductivity in the order of 10^{-5} S/cm. The results obtained by three different synthesis processes, resulting in three distinct morphologies, are summarized in ***Table 5.6***. Where shaded regions describe the SIL incorporation in the LLZO matrix.

In a similar direction, commercial cellulose paper was used as a sacrificial template to obtain an interconnected LLZO microstructure through an exo-templating process. Compared to conventionally prepared LLZO by gel-combustion process, the developed engineered electrolyte showed a twofold reduction in grain boundary resistance with lower activation energy. Further infusion with solvated ionic liquid (SIL) resulted in improved wettability, suppressed dendritic penetration, and delivered stable Li plating/stripping for over 1300 h with a critical current density of 700 μA cm^{-2}. Full-cell studies with $LiMn_2O_4$ cathodes and Li anode delivered superior rate performance and cycling stability. Overall, this chapter establishes that microstructural engineering plays a critical role in delivering the high performance of garnet-based solid-state electrolytes for lithium metal batteries.

5.5 References

1 P. Kodgire, B. Tripathi and P. Chandra, *J Electron Mater*, 2024, **53**, 2203–2228.

2 M. Wu, D. Liu, D. Qu, Z. Xie, J. Li, J. Lei and H. Tang, *ACS Appl Mater Interfaces*, 2020, **12**, 52652–52659.

3 F. Okur, H. Zhang, D. T. Karabay, K. Muench, A. Parrilli, A. Neels, W. Dachraoui, M. D. Rossell, C. Cancellieri, L. P. H. Jeurgens, K. V. Kravchyk and M. V. Kovalenko, *Adv Energy Mater*, 2023, **13**, 2203509.

4 T. W. Heo, A. Grieder, B. Wang, M. Wood, T. Hsu, S. A. Akhade, L. F. Wan, L. Q. Chen, N. Adelstein and B. C. Wood, *NPJ Comput Mater*, DOI:10.1038/S41524-021-00681-8.

5 M. Horii, R. J. Christianson, H. Mutha and J. C. Bachman, *J Power Sources*, DOI:10.1016/J.JPOWSOUR.2022.231177.

6 S. Shivaji, S. Madhu and S. Singh, *Process Biochemistry*, 2011, **46**, 1800–1807.

7 J. R. Stephen and S. J. Macnaughton, *Curr Opin Biotechnol*, 1999, **10**, 230–233.

8 R. Camaratta, A. N. Correia Lima, M. D. Reyes, M. A. Hernández-Fenollosa, J. Orozco Messana and C. P. Bergmann, *Mater Res Bull*, 2013, **48**, 1569–1574.

9 G. Kale, S. Arbuj, U. Kawade, S. Kadam, L. Nikam and B. Kale, *Journal of Materials Science: Materials in Electronics*, 2019, **30**, 7031–7042.

10 C. Zhang, J. Wang, R. Hu, Q. Qiao and X. Li, *Sens Actuators B Chem*, 2016, **222**, 1134–1143.

11 G. A. Ozin, *Advanced Materials*, 1992, **4**, 612–649.

12 M. W. Raja, Q. A. Islam and R. N. Basu, *J Memb Sci*, 2017, **522**, 168–174.

13 J. Janek and W. G. Zeier, *Nature Energy 2023 8:3*, 2023, **8**, 230–240.

14 M. Pasta, D. Armstrong, Z. L. Brown, J. Bu, M. R. Castell, P. Chen, A. Cocks, S. A. Corr, E. J. Cussen, E. Darnbrough, V. Deshpande, C. Doerrer, M. S. Dyer, H. El-Shinawi, N. Fleck, P. Grant, G. L. Gregory, C. Grovenor, L. J. Hardwick, J. T. S. Irvine, H. J. Lee, G. Li, E. Liberti, I. McClelland, C. Monroe, P. D. Nellist, P. R. Shearing, E. Shoko, W. Song, D. S. Jolly, C. I. Thomas, S. J. Turrell, M. Vestli, C. K. Williams, Y. Zhou and P. G. Bruce, *J. Phys. Energy*, 2020, **2**, 32008.

15 S. Bolenz, H. Omran and K. Gierschner, *Biological Wastes*, 1990, **33**, 263–274.

16 J. Gressel, *Plant Science*, 2008, **174**, 246–263.

17 M. N. Eshtiaghi, *Afr J Biotechnol*, DOI:10.5897/AJB11.4045.

18 A. Kumar, G. L. Devnani and D. B. Pal, *Biomass Convers Biorefin*, DOI:10.1007/S13399-025-06765-5.

19 P. E. Ndimele, C. A. Kumolu-Joh and M. A. Anetekhai, *Res J Environ Sci*, 2011, **5**, 509–520.

20 I. Quinzeni, D. Capsoni, V. Berbenni, P. Mustarelli, M. Sturini and M. Bini, *Mater Chem Phys*, 2017, **185**, 55–64.

21 E. Abraham, B. Deepa, L. A. Pothen, J. Cintil, S. Thomas, M. J. John, R. Anandjiwala and S. S. Narine, *Carbohydr Polym*, 2013, **92**, 1477–1483.

22 M. Asrofi, H. Abral, A. Kasim and A. Pratoto, *Journal of Metastable and Nanocrystalline Materials*, 2017, **29**, 9–16.

23 C. S. Julie Chandra, N. George and S. K. Narayanankutty, *Carbohydr Polym*, 2016, **142**, 158–166.

24 M. K. Nacos, P. Katapodis, C. Pappas, D. Daferera, P. A. Tarantilis, P. Christakopoulos and M. Polissiou, *Carbohydr Polym*, 2006, **66**, 126–134.

25 K. Ghosh and M. Wasim Raja, *ACS Appl Energy Mater*, 2023, **6**, 4035–4052.

26 M. Rosen, R. Ye, M. Mann, S. Lobe, M. Finsterbusch, O. Guillon and D. Fattakhova-Rohlfing, *J Mater Chem A Mater*, 2021, **9**, 4831–4840.

27 F. Tietz, T. Wegener, M. T. Gerhards, M. Giarola and G. Mariotto, *Solid State Ion*, 2013, **230**, 77–82.

28 C. Galven, J. L. Fourquet, M. P. Crosnier-Lopez and F. Le Berre, *Chemistry of Materials*, 2011, **23**, 1892–1900.

29 G. Larraz, A. Orera and M. L. Sanjuán, *J Mater Chem A Mater*, 2013, **1**, 11419–11428.

30 V. Thangadurai, R. A. Huggins and W. Weppner, *J Power Sources*, 2002, **108**, 64–69.

31 S. Afyon, F. Krumeich and J. L. M. Rupp, *J Mater Chem A Mater*, 2015, **3**, 18636–18648.

32 M. A. Howard, O. Clemens, E. Kendrick, K. S. Knight, D. C. Apperley, P. A. Anderson and P. R. Slater, *Dalton Transactions*, 2012, **41**, 12048–12053.

33 J. F. Wu, E. Y. Chen, Y. Yu, L. Liu, Y. Wu, W. K. Pang, V. K. Peterson and X. Guo, *ACS Appl Mater Interfaces*, 2017, **9**, 1542–1552.

34 J. Wolfenstine, J. Ratchford, E. Rangasamy, J. Sakamoto and J. L. Allen, *Mater Chem Phys*, 2012, **134**, 571–575.

35 J. Li, F. Li, L. Zhang, H. Zhang, U. Lassi and X. Ji, *Green Chemical Engineering*, 2021, **2**, 253–265.

36 H. Zhao, X. Zhang, N. Wang, Y. Xiao, S. Liang, W. Zhuang, J. Yang and X. Huang, *J Alloys Compd*, DOI:10.1016/J.JALLCOM.2024.174460.

37 S. A. Pervez, G. Kim, B. P. Vinayan, M. A. Cambaz, M. Kuenzel, M. Hekmatfar, M. Fichtner and S. Passerini, *Small*, DOI:10.1002/SMLL.202000279.

38 K. Ghosh and M. Wasim Raja, *ACS Appl Energy Mater*, 2023, **6**, 4035–4052.

39 P. Fleming, R. A. Farrell, J. D. Holmes and M. A. Morris, *Journal of the American Ceramic Society*, 2010, **93**, 1187–1194.

40 L. Cheng, J. S. Park, H. Hou, V. Zorba, G. Chen, T. Richardson, J. Cabana, R. Russo and M. Doeff, *J Mater Chem A Mater*, 2014, **2**, 172–181.

41 G. Larraz, A. Orera and M. L. Sanjuán, *J Mater Chem A Mater*, 2013, **1**, 11419–11428.

42 M. Rosen, R. Ye, M. Mann, S. Lobe, M. Finsterbusch, O. Guillon and D. Fattakhova-Rohlfing, *J Mater Chem A Mater*, 2021, **9**, 4831–4840.

43 F. Tietz, T. Wegener, M. T. Gerhards, M. Giarola and G. Mariotto, *Solid State Ion*, 2013, **230**, 77–82.

44 A. Sharafi, S. Yu, M. Naguib, M. Lee, C. Ma, H. M. Meyer, J. Nanda, M. Chi, D. J. Siegel and J. Sakamoto, *J Mater Chem A Mater*, 2017, **5**, 13475–13487.

45 L. Dhivya, K. Karthik, S. Ramakumar and R. Murugan, *RSC Adv*, 2015, **5**, 96042–96051.

46 K. Ghosh and M. Wasim Raja, *ACS Omega*, 2022, **7**, 33385–33396.

47 S. Patnaik, M. Jokar, W. Ding and F. Semperlotti, *npj Computational Materials 2022 8:1*, 2022, **8**, 1–7.

48 Y. T. Chen, A. Jena, W. K. Pang, V. K. Peterson, H. S. Sheu, H. Chang and R. S. Liu, *Journal of Physical Chemistry C*, 2017, **121**, 15565–15573.

49 F. Han, A. S. Westover, J. Yue, X. Fan, F. Wang, M. Chi, D. N. Leonard, N. J. Dudney, H. Wang and C. Wang, *Nature Energy 2019 4:3*, 2019, **4**, 187–196.

50 J. Wang, B. Ge, H. Li, M. Yang, J. Wang, D. Liu, C. Fernandez, X. Chen and Q. Peng, *Chemical Engineering Journal*, 2021, **420**, 129739.

51 L. M. Riegger, R. Schlem, J. Sann, W. G. Zeier and J. Janek, *Angew. Chem. Int. Ed.*, 2021, **60**, 6718–6723.

52 X. Zhao, C. Wang, H. Liu, Y. Liang and L. Z. Fan, *Batter Supercaps*, 2023, **6**, e202200502.

53 M. Keller, A. Varzi and S. Passerini, *J Power Sources*, 2018, **392**, 206–225.

54 X. B. Cheng, R. Zhang, C. Z. Zhao and Q. Zhang, *Chem Rev*, 2017, **117**, 10403–10473.

55 M. Wu, D. Liu, D. Qu, Z. Xie, J. Li, J. Lei and H. Tang, *ACS Appl Mater Interfaces*, 2020, **12**, 52652–52659.

56 D. Cai, D. Wang, Y. Chen, S. Zhang, X. Wang, X. Xia and J. Tu, *Chemical Engineering Journal*, 2020, **394**, 124993.

57 H. Xie, C. Yang, K. (Kelvin) Fu, Y. Yao, F. Jiang, E. Hitz, B. Liu, S. Wang and L. Hu, *Adv Energy Mater*, DOI:10.1002/aenm.201703474.

58 P. Pan, M. Zhang, Z. Cheng, L. Jiang, J. Mao, C. Ni, Q. Chen, Y. Zeng, Y. Hu and K. (Kelvin) Fu, *Energy Storage Mater*, 2022, **47**, 279–287.

59 X. Yang, X. Han, Z. Chen, L. Zhou, B. Zhao, H. Su and W. Jiao, *Mater Lett*, 2018, **217**, 271–275.

60 H. Zhang, X. An, Z. Lu, L. Liu, H. Cao, Q. Xu, H. Liu and Y. Ni, *J Power Sources*, 2020, **477**, 228752.

61 J. Bae, Y. Li, J. Zhang, X. Zhou, F. Zhao, Y. Shi, J. B. Goodenough and G. Yu, *Angewandte Chemie International Edition*, 2018, **57**, 2096–2100.

62 Z. Li, W.-X. Sha and X. Guo, *ACS Appl Mater Interfaces*, 2019, **11**, 26920–26927.

CHAPTER 6

Introduction of Dual Therapy in Solid-State Lithium Metal Batteries

Summary & Graphical Abstract

Large grain boundary resistance, uneven pores, and uncontrolled dendrite growth in solid electrolytes hinder their practical use in solid-state lithium metal batteries. These issues lead to poor ionic transport, uneven lithium deposition, and premature failure. In this direction, this chapter explores a dual approach combining solid therapy (via NiO sintering aid) and liquid therapy (using a solvated ionic liquid, SIL) in the Ga-doped $Li_7La_3Zr_2O_{12}$ (Ga-LLZO) matrix. Solid therapy is effective in reducing the grain boundary resistance and enhancing the densification of the LLZO matrix. Whereas liquid therapy helps in facile ion transportation across the metal/electrolyte interface. This synergistic dual strategy successfully minimizes the SIL uptake, reduces interfacial impedance, and suppresses dendrite growth in workable solid-state lithium metal batteries.

Objectives

1. Enhanced stability at the metal/electrolyte interface.

2. Retarded Transgranular Li dendritic migration across the grain and grain boundaries.

Strategy

Solid (Via NiO sintering aid) and Liquid Dual Therapy (Via Solvated Ionic Liquid).

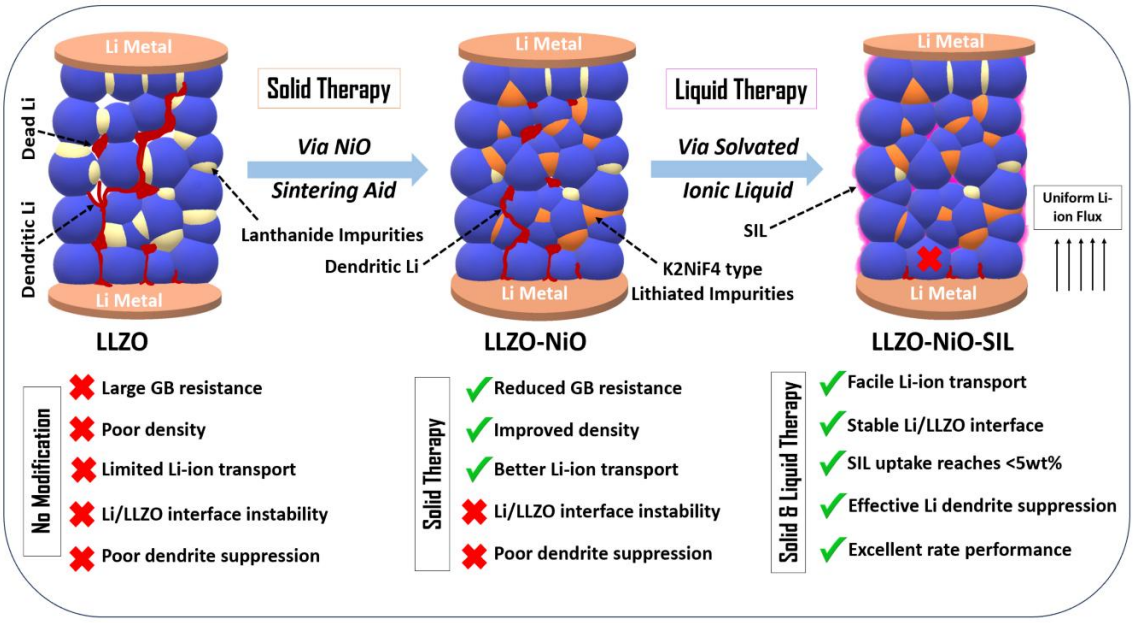

Figure 6.1 *Graphical abstract illustrating the effects of dual therapy in metal batteries.*

6.1 Introduction

All-solid-state lithium batteries (ASSLBs) emerged as an alternative battery configuration comprising solid electrolytes, which have the potential to offer higher energy/power density, temperature stability, and safety for the successful deployment in EVs. It can also unlock the possibility of using Lithium metal anode (specific capacity 3860 $mAhg^{-1}$) and high voltage cathode (~5V) [1,2]. Among the various type of solid electrolyte, garnet $Li_7La_3Zr_2O_{12}$ (LLZO) is one of the most researched solid electrolytes due to its excellent chemical stability, high ionic conductivity (~1 mS cm^{-1}), wide potential window of 0-6 V vs. Li^+/Li and low electronic conductivity of ~10^{-8} S cm^{-1} (RT) [3,4]. Owing to these several advantages of LLZO, this solid electrolyte still needs to be further refined prior to use in ASSLBs [5,6]. The lowering of interfacial resistance at the anodic interface (Li side), fast Li-ion transportation across the thick solid LLZO during cycling, and prevention of dendrite growth through grain boundary still pose challenges to its successful application in ASSLBs [7].

Recently, researchers tried to increase the density in the LLZO matrix to improve the overall ionic conductivity, lowering the thickness of the electrolyte and suppressing the dendrite growth [8–12]. One of the strategies to achieve higher densification in LLZO solid electrolytes is to use additives with LLZO powder. Qin et al. reported that 5wt% excess of La_2O_3 additive can enhance the ionic conductivity, critical current density (CCD), and overall electrochemical performance of Ta-doped LLZO (LLZTO)[12]. The addition of sintering aids, such as Li_3PO_4, CuO, Li_4SiO_4, etc, is also found to be effective in increasing densification through the formation of new intermediate phases at grain boundaries[8–14]. While most of these previous studies were found to be focused on improving the ionic conductivities of the LLZO compositions, it is now essential to probe the overall battery performance, which establishes a correlation between the densification of LLZO with interface-related kinetics, cycling behavior, dendrite formation, etc.

In ***Chapter 5***, we demonstrated that the engineering of the microstructure in LLZO is effective for faster ionic mobility and stable cycling performance. However, this engineered LLZO was found to be inadequate in lowering interfacial resistance to a greater extent. We also explored a strategy to use SIL both at the anode-electrolyte interface & in the bulk of the LLZO ceramic. The results obtained from the studies clearly demonstrated that faster Li-mobility could be achieved using SIL, a strategy we named “liquid therapy” for obtaining excellent cyclability and high coulombic efficiency (up to 6C) (***Chapter 3***). While using SIL-based liquid therapy in SSEs, it is worth mentioning here that SIL does not provide enough support during prolonged

operation at high currents. The post-mortem analysis of the cycled cells revealed an interesting phenomenon: the surface of the solid electrolyte was attacked by Li-dendrite penetration discretely at places. This is probably due to the SIL failure at that region, which triggers the contact of Li metal with the electrolyte surface, resulting in dendritic growth (***Chapter 5***).

In this chapter, a first-of-its-kind approach is introduced where both "liquid therapy" (via solvated ionic liquid) and "solid therapy" (using NiO sintering aid) have been used in LLZO SEs. The choice of NiO as a sintering aid in the LLZO system is based on a rational design strategy targeting solid-phase sintering behavior. On further modification, solvated ionic liquid (SIL) was also infused in LLZO to increase Li ion mobility, which we called liquid therapy. NiO addition improves densification and reduces the grain boundary resistance by forming lithiated K_2NiF_4-type phase at the grain boundary. Thus, the SIL concentration reduces. This synergistic approach is expected to minimize interfacial resistance, suppress dendrite formation, and enhance long-term cycling stability. This chapter thus explored a new dimension of using solid and liquid therapy in LLZO-based SEs for application in SSLMBs by systematically analyzing electrochemical responses and cell performance.

6.2 Experimental

6.2.1 Material synthesis and characterization

The detailed material synthesis and characterization techniques are already discussed in ***Chapter 2***, ***Section 2.3.3.4*** and ***Section 2.7,*** respectively. In Brief, Ga-doped LLZO was synthesized by the alanine-assisted auto-combustion method, followed by the incorporation of NiO in varying amounts (0-1 wt%) before sintering at 1000°C for 10h. Composition and corresponding sample codes of NiO-incorporated solid electrolyte were presented in ***Table 6.1***.

Table 6.1 *Composition and corresponding sample codes of NiO-incorporated solid electrolyte composites.*

Composition	Termed as
0wt% NiO	GN000
0.25wt% NiO	GN025
0.50wt% NiO	GN050
0.75wt% NiO	GN075
1 wt% NiO	GN100

6.2.2 Cell fabrication and testing

The detailed cell fabrication and testing techniques are already discussed in ***Chapter 2***, ***Section 2.6*** and ***Section 2.7,*** respectively. In Short, after densification with various concentrations of NiO, the pellets were infused with a solvated ionic liquid (LiTFSI/tetraglyme, 1:1 mol ratio), which was termed as liquid therapy. For various electrochemical testing, symmetric (Li/Li, SS/SS) and full (Li/LMO) or asymmetric (Li/SS) coin cells were assembled as discussed in ***Chapter 2***.

6.3 Results and Discussion

6.3.1 Structural and Dilatometry study

X-ray diffractogram of all developed electrolytes sintered at 1000°C and commercial NiO powder, along with the JCPDS file of c-LLZO, is presented in ***Figure 6.2(a)***. In all the developed electrolytes, the significant peaks could be indexed as cubic LLZO powder along with the impurities such as $La(OH)_3$, La_2O_3, $LaAlO_3$, $La_2Zr_2O_7$, $Li_{0.5}La_2Al_{0.5}O_4$ and $Li_{0.5}La_2Ni_{0.5}O_4$ [15]. Interestingly, despite NiO's addition, no characteristic NiO peak is detected in the X-ray diffraction (XRD) patterns of the NiO-added Ga-doped LLZO samples. It is worth mentioning here that the disappearance of NiO peaks in the XRD patterns of the NiO-added Ga-doped LLZO samples suggests that NiO either fully reacts with the LLZO matrix during high-temperature sintering, becomes highly dispersed or amorphous, falling below the XRD detection limit. However, a notable trend is observed in the presence of different impurity phases and their relative intensities. Here, we have divided the impurities into two distinct categories: lithiated impurities (such as $Li_{0.5}La_2Al_{0.5}O_4$ and $Li_{0.5}La_2Ni_{0.5}O_4$) and non-lithiated lanthanide-based impurities (such as $La(OH)_3$, La_2O_3, $LaAlO_3$, $La_2Zr_2O_7$). The calculation of lithiated and non-lithiated impurity phases was performed using Rietveld refinement of XRD patterns with PANalytical HighScore Plus with the PDF-4+ database for referencing. All GN samples (GN000 to GN100) were refined using the same procedure and refinement model to ensure consistency across the series. The software internally calculates phase fractions based on refined scale factors and crystallographic constants. Lithiated impurities included $Li_{0.5}La_2Ni_{0.5}O_4$ and $Li_{0.5}La_2Al_{0.5}O_4$, while non-lithiated phases included La_2O_3, $La_2Zr_2O_7$, $LaAlO_3$, and $La(OH)_3$.

In any lantana material, lanthanide impurities such as $La(OH)_3$ and La_2O_3 appear as surface impurities formed during high-temperature calcination or exposure to an air atmosphere[16–18]. In our previous chapter (***Chapters 3*** and ***5***), the origin of such impurities and

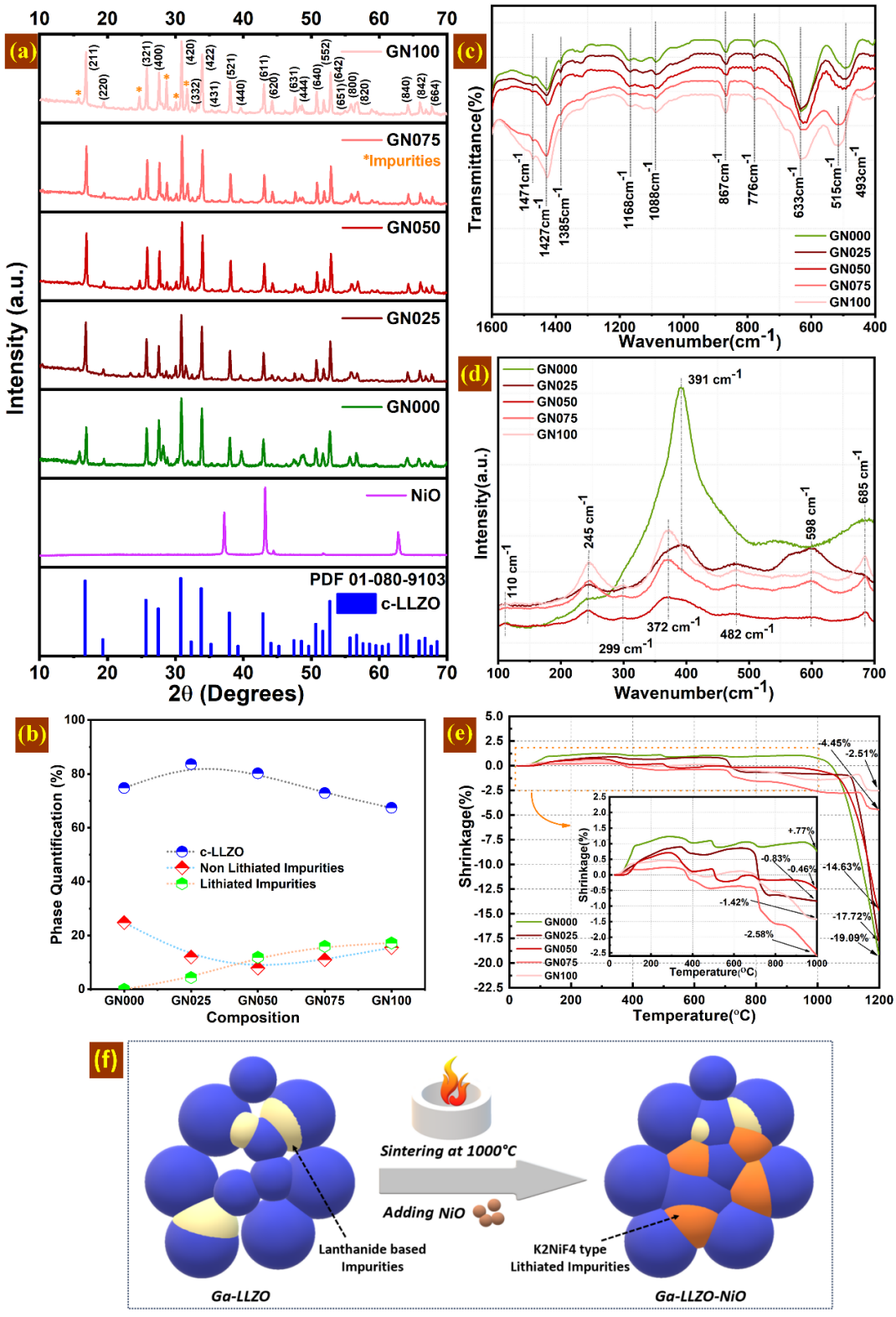

Figure 6.2 *(a) X-ray diffractograms of developed electrolytes along with commercial NiO powder, (b) Variation of quantification of phases concerning the different solid electrolytes composition, (c) & (d) FTIR and RAMAN spectra of all developed solid electrolytes respectively, (e) Dilatometry study to measure the linear shrinkage of all developed sintered*

pellets as a function of temperature from RT-1200°C. (f) Schematic representation illustrating the effect of NiO as a sintering aid in the Ga-doped LLZO matrix.

their effect on electrical and electrochemical performances are discussed in detail [17,19]. In short, these surface impurities are generally deposited at the grain boundaries and increase the overall grain boundary resistance of the solid electrolyte [20]. The formation of $La_2Zr_2O_7$ in cubic LLZO is now well understood and is attributed to lithium loss during high-temperature sintering [21]. This secondary phase can coexist with the c-LLZO matrix. On the other hand, contamination of aluminium (Al) from the alumina crucible during the sintering process is another significant factor impacting the LLZO matrix [22]. The uncontrolled incorporation of Al leads to other secondary phases, such as $LaAlO_3$ and $Li_{0.5}La_2Al_{0.5}O_4$ [4,17]. Specifically, the presence of non-lithiated lanthanide-based impurities such as $La(OH)_3$, La_2O_3, $La_2Zr_2O_7$, and $LaAlO_3$ varies with the concentration of NiO. For the GN000 sample, non-lithiated lanthanide impurities constitute 24.8% of the total phase, with $La(OH)_3$ alone accounting for 21.5%, while the remaining 74.8% consists of cubic-phase LLZO (c-LLZO). As the NiO content increases in the Ga-doped LLZO matrix, the non-lithiated lanthanide impurities initially decrease but then increase with the further addition of NiO. Specifically, these impurities are 12% in GN025, 7.9% in GN050, 11% in GN075, and 15.5% in GN100. These non-lithiated lanthanide phases tend to accumulate in the grain boundaries, reducing the overall grain boundary conductivity of the LLZO materials. In addition to non-lithiated lanthanide impurities, new K_2NiF_4-type lithiated impurities, specifically $Li_{0.5}La_2Al_{0.5}O_4$ and $Li_{0.5}La_2Ni_{0.5}O_4$, are observed in the NiO-added samples. The formation of the K_2NiF_4-type layered oxide phase, specifically $Li_{0.5}La_2Ni_{0.5}O_4$, in the GN system is attributed to the solid-state reaction between NiO and the La-rich LLZO matrix during high-temperature sintering (1000 °C). Mechanistically, Ni^{2+} from NiO can react with excess La_2O_3 in the local environment to form a Ruddlesden–Popper (K_2NiF_4-type) structure, which is known to accommodate layered perovskite-type stacking $(AO)(ABO_3)_n$, particularly in La-Ni-O systems. The formation is promoted in the presence of Li^+, La^{3+}, and Ni^{2+}, especially under slightly reducing or Li-rich conditions at high temperature. This transformation is consistent with literature reporting the in situ formation of $Li_{0.5}La_2Cu_{0.5}O_4$ and related phases during sintering of CuO with garnet-type LLZO. In this study, the presence of the K_2NiF_4 phase $Li_{0.5}La_2Cu_{0.5}O_4$ was found at 700°C when 1 wt% of CuO was added as a sintering aid in Ta-doped LLZO material[10]. In the present study, as the NiO content increases in the Ga-doped LLZO matrix, the presence of these K_2NiF_4-type lithiated impurities also rises from 4.4% in GN025 to 17.2% in GN100. Consequently, the

amount of $Li_{0.5}La_2Ni_{0.5}O_4$ is expected to increase, as the amount of Al in Ga-doped LLZO depends on its reaction with the alumina crucible and the specific experimental conditions. This phase may then accumulate at the grain boundaries in the Ga-doped LLZO matrix. It is worth mentioning here that we also detected the presence of $Li_{0.5}La_2Al_{0.5}O_4$ in the same samples, despite Al already being present in the LLZO matrix (Source: Al crucible). This Al-based phase was not observed in Ni-free samples, suggesting that the presence of NiO promotes the segregation or crystallization of both Al- and Ni-containing K_2NiF_4-type phases. The Rietveld refinement showed good agreement with the measured data as discussed earlier, but inclusion of both $Li_{0.5}La_2Al_{0.5}O_4$ and $Li_{0.5}La_2Ni_{0.5}O_4$ phases resulted in only a marginal change over models with a single K_2NiF_4-type phase. Also, the increasing trend in K_2NiF_4-type phase with an increase in NiO concentration suggests the possible solid solution behavior or overlapping features.

Table 6.2 *The quantification of various phases present in all the developed electrolytes*

Compound	**Quantification (%)**				
	GN000	GN025	GN050	GN075	GN100
cubic-LLZO	74.8	84.3	80.2	72.9	67.4
La_2O_3	1.5	6.1	3.0	2.4	2.7
$La(OH)_3$	21.5	2.8	1.7	1.8	3.0
$La_2Zr_2O_7$	2.2	2.5	2.6	6.6	9.5
Lithiated K_2NiF_4-type compounds	0	3.1	11.9	16	17.2
LaAlO3	0	1.2	0.6	0.2	0.3

However, the contribution of such a phase could not be resolved as both belong to the K_2NiF_4-type phase with space group I4/mmm. The site occupancy refinement may resolve this, but it could not be performed due to limitations of the existing software version. Given the complexity in precisely identifying the variation of these K_2NiF_4 phases with increasing NiO content in c-LLZO, complementary techniques such as neutron diffraction or X-ray absorption spectroscopy may be necessary for accurate differentiation between $Li_{0.5}La_2Al_{0.5}O_4$ and $Li_{0.5}La_2Ni_{0.5}O_4$ phases. ***Figure 6.2 (b)*** illustrates the variation of phase quantification concerning the different compositions of solid electrolytes. The variation of different phases in all the developed electrolytes is further summarized in ***Table 6.2***. The c-LLZO phase is 83.6% in GN025, 80.2% in GN050, 72.9% in GN075, and 67.4% in GN100 solid electrolytes. The

quantitative refinement parameters of all the samples, including profile residual (R_p), weighted profile residual (R_{wp}), expected R-factor (R_{exp}), and goodness-of-fit (χ^2), are summarized in ***Table 6.3***. All samples have χ^2 values between 1.61 and 2.06 and good Rp, Rwp values, indicating excellent fitting quality and reliable structural modeling. These results confirm the preservation of the cubic LLZO phase across all samples and support the presence of Ni-induced K_2NiF_4-type phases, consistent with phase evolution trends discussed. In summary, as the NiO content increases in the Ga-doped LLZO matrix, the amount of cubic LLZO decreases. Concurrently, the amount of non-lithiated lanthanide impurities initially decreases and then increases. Additionally, the amount of K_2NiF_4-type lithiated impurities, such as $Li_{0.5}La_2Ni_{0.5}O_4$, steadily increases.

Table 6.3 *Rietveld refinement parameters for all the developed electrolytes.*

Sample	R_p (%)	R_{wp} (%)	R_{exp} (%)	χ^2
GN000	9.66	13.93	8.64	1.61
GN025	3.72	5.04	2.99	1.68
GN050	4.16	5.88	2.98	1.97
GN075	4.19	5.80	2.90	1.99
GN100	4.20	5.95	2.88	2.06

To further confirm the presence of the c-LLZO phase in all the sintered pellets, FTIR and RAMAN spectroscopy are carried out. In ***Figure 6.2(c)***, FTIR spectra of GN000, GN025, GN050, GN075 and GN100 materials are presented. Characteristic peaks of C-O stretching at 1427 and 867 cm^{-1} are present for all the sintered pellets due to the formation of Li_2CO_3 [23]. The origin of the Li_2CO_3 phase in the LLZO matrix is now well established, which formed due to the Li^+/H^+ exchange process during air exposure. Other characteristic peaks such as 1471, 1385, 1188, and 1081 cm^{-1} are observed, attributed to the different stretching and bending vibrations of residual hydrocarbons and organic moieties. Additionally, several low-intensity peaks below 800cm^{-1} are detected, suggesting the presence of La-O and Zr-O vibration in the FTIR spectra of all the sintered pellets. The RAMAN spectra of GN000, GN025, GN050, GN075, and GN100 materials are illustrated in ***Figure 6.2(d)***. Heavy La cation vibration is observed at 100cm^{-1} and 150$cm^{-1,}$ and Zr-O bond vibration is observed above 550 cm^{-1} [17,] The LiO_6 and LiO_4 vibrations become evident in the 200-300 cm^{-1} and 350-600 cm^{-1} range, respectively, as earlier studies on LLZO and related lithium-containing material suggested.

Additionally, the tetragonal polymorph of LLZO exhibits more spectral features than its cubic form. In the low-frequency range below 300 cm^{-1}, the vibrations are attributed to the translational modes of the mobile cations. The cubic phase shows few broad and partially overlapping peaks in the mid-frequency range (300-550 cm^{-1}). Peaks above 550 cm^{-1} are likely due to the vibrational stretching of ZrO_6 octahedra. Thus, the FTIR and Raman spectroscopy results confirm and further support the presence of the cubic phase of LLZO in all the developed electrolyte materials. It is worth mentioning here that the Li-O vibrational modes associated with the lithiated K_2NiF_4 type phases were observed at 602 cm^{-1} and 560 cm^{-1}, which indicates the partial contributions from Li-containing layered structures such as $Li_{0.5}La_2Ni_{0.5}O_4$. However, the La-O and Ni-O vibrational modes, indicative to K_2NiF_4-type phase are likely due to spectral overlap with the dominant cubic LLZO modes and the relatively low intensity of signals[10].

The dilatometry study on the sintered pellets aims to evaluate thermal expansion properties and any volume changes associated with NiO addition. ***Figure 6.2(e)*** presents the shrinkage variation over time for all the sintered pellets. Due to the difference between the actual sintering condition (1000°C for 10 hours with a rate of 2°/min) and the conditions during the dilatometry measurement (RT-1200°C with a rate of 10°/min, holding 30mins), these results offer a general indication of shrinkage behavior with temperature rather than an exact quantification. ***Figure 6.2(e)*** shows a dramatic difference in the shrinkage behaviors between Ga-doped LLZO material and NiO-added LLZO materials. For all the solid electrolyte samples, the initial grain growth can be attributed to the coarsening of particles and the formation of grain boundaries [24]. Among the different solid electrolytes, a high initial grain growth of 1.23% was observed at 300°C for the GN000 solid electrolyte, whereas the least grain growth of 0.24% was observed for GN075 at 284°C. Maximum initial growths of 0.90% around 340°C, 0.71% around 294°C, and 0.46% around 264°C are observed for GN025, GN050, and GN100, respectively. Similarly, GN000 shows a grain growth of 0.77% at 1000°C, whereas GN075 shows a maximum linear shrinkage of 2.58% at that temperature. After 1200°C, GN000 shows a maximum linear shrinkage of 19.09%, and GN100 shows a minimum shrinkage of 2.51%. This sudden shrinkage may be attributed to converting the c-LLZO phase to the pyrochlore $La_2Zr_2O_7$ structure due to severe lithium loss at high temperatures. A systematic change in initial grain growth and linear shrinkage at higher temperatures was observed after NiO was added to the Ga-doped LLZO matrix. A schematic was presented in ***Figure 6.2(f)*** illustrating the possible role of NiO as a sintering aid in the Ga-doped LLZO matrix. The formation of a

K_2NiF_4-type lithiated phase might be deposited at the grain boundaries of LLZO. Thus, NiO can be used to tailor the microstructural stability of the solid electrolyte, and it will be interesting to correlate the structural and microstructural features in the next section.

6.3.2 Microstructural Study

In polyphase materials, microstructural diversity is influenced by geometrical factors and the mutual distribution of multiple impurity phases[25]. In this scenario, the presence of different impurity phases and their distribution are altered after NiO is added to the Ga-doped LLZO matrix, as suggested by the X-ray diffraction pattern. This alteration in impurity phase distribution could significantly affect the material's overall performance, particularly in ionic conductivity and density. Also, the X-ray diffraction data suggests that NiO interacts with the Ga-doped LLZO matrix, potentially diffusing into grain boundaries, leading to changes in phase composition and microstructural evolution. Recent computational studies using a phase-field grain growth model, as reported by Heo et al., demonstrate that in LLZO, microstructural characteristics at both the atomic and mesoscopic scales can significantly influence ionic conductivity[26]. ***Figures 6.3 (a)-(c)*** represent the FESEM micrographs of polished and fractured sintered pellets (sintered at 1000°C for 10 hours) of GN000, GN050, and GN100, respectively. For GN000, a less compact structure with large pores and cavities is observed. In contrast, GN050 displays a more compact structure with fewer and smaller pores and cavities, although more NiO-containing phases at the surface are observed for GN100. Such porosity and phase distribution variations could influence the overall electrical and electrochemical properties. For instance, a dense structure with fewer pores, as seen for GN050, might offer reduced ionic resistance compared to a more porous structure like GN000. Conversely, the increased presence of NiO in GN100 may enhance specific surface reactions but can also lead to potential issues such as increased grain boundary resistance. The FESEM micrograph and line spectra of GN100, as shown in ***Figure 6.3(d)***, reveal the presence of La at both grain and grain boundaries and the presence of Zr maximum at the grain and minimum at the grain boundaries. Conversely, the presence of Ni is prominent at maximum at the grain boundaries and minimum at the grain, as shown in ***Figure 6.3(d1-d4)***. Point EdX is taken to investigate the elements present at the grain and grain boundaries, as shown in ***Figures 6.3(e) and (f)***. At the grain, La, Al (originating from the crucible during the calcination process), Zr, Ga, and O suggest the presence of c-LLZO material in GN100. The absence of Ni in the grain thus further corroborates that Nickel's role is more related to microstructural modifications than bulk doping. On the contrary, at the outside of the grain, the presence of La, Ni, Al, and O indicates the formation of new K_2NiF_4-

type lithiated impurities at the grain boundary. It is worth mentioning here that from the quantitative elemental mapping at the grain of GN000 and GN100, the molar ratio (in atomic wt.%) of (La/Zr) is found to be 1.57 and 1.48 (the typical stoichiometric ratio is 1.5), respectively, ensuring the formation of c-LLZO material. Similarly, at the outside of the grain, the molar ratio (in atomic wt. %) of La/(Ni+Al) is found to be 3.8 whereas, in the K_2NiF_4-type lithiated impurities (**$Li_{0.5}La_2Al_{0.5}O_4$** and $Li_{0.5}La_2Ni_{0.5}O_4$), the ratio is 4. Thus, Ni is expected to diffuse at the grain boundaries along with Al, and a new K_2NiF_4-type lithiated impurity originated. Therefore, it will be exciting to measure the effect of such impurities on electrical and electrochemical performances.

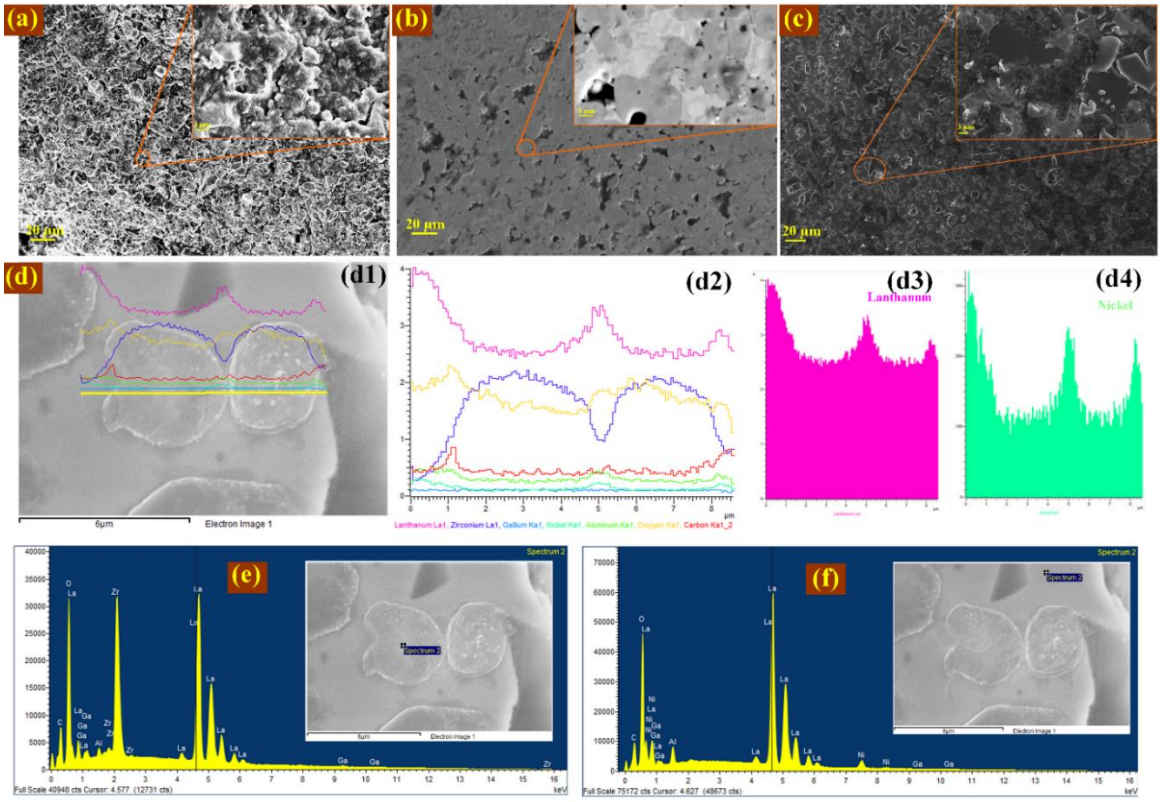

Figure 6.3 *FESEM micrographs of a polished and fractured surface of (a) GN000, (b) GN050, and (c) GN100, respectively. (d) FESEM micrograph (d1) and corresponding elemental line spectrum (d2-d4) of GN100. (e) EdX profile at the grain of GN100. (f) EdX profile at the grain boundaries of GN100.*

6.3.3 Electrical Studies

The ion transport properties of polyphase or porous materials depend highly on their microstructural features. However, the microstructure of a polyphase material involves not only its geometrical factors, such as grain size, grain shape, or grain boundary orientation but also

the mutual distribution of other phases. As the relative distribution of lithiated and non-lithiated phases varies with the increment of NiO percentage in the LLZO matrix, as suggested by the XRD and FESEM studies, thus it is expected that the ionic transport or diffusion at the grain and grain boundaries will vary with or without the addition of NiO in the Ga-doped LLZO material. Thus, the electrochemical impedance spectroscopy is carried out for different compositions of sintered pellets with Au-blocking electrodes using ZIVE SP1 over a frequency range of 0.1 Hz–1 MHz by applying 300 mV AC amplitude. The EIS spectra of Ga-doped LLZO pellets and different percentages of NiO-added Ga-doped LLZO pellets are presented in ***Figure 6.4(a)*** along with their equivalent circuit, which consists of grain resistance (R_b) and grain boundary resistance (R_{gb}) along with constant phase elements (CPE_{gb} & CPE_w). Nyquist plots of all samples are further analyzed in ZView software, and it is found that the grain or bulk resistance is 5.5kΩ, 6.5kΩ, 6.2kΩ, 7.0kΩ and 6.8kΩ and grain boundary resistance is 106.7kΩ, 20.3kΩ, 15.4kΩ, 31.6kΩ and 45.5kΩ for GN000, GN025, GN050, GN075, and GN100 materials respectively as shown in ***Figure 6.4(b)***. The values reveal a significant change in grain boundary resistance due to the addition of NiO sintering aid. Among the different NiO-modified materials, GN050 offered the lowest R_{gb}, almost seven times decrease compared to GN000. The total conductivities, as calculated from the EIS spectrum, are 1.25×10^{-3} mS/cm, 5.70×10^{-3} mS/cm, 7.06×10^{-3} mS/cm, 3.96×10^{-3} mS/cm, and 2.92×10^{-3} mS/cm for GN000, GN025, GN050, GN075, and GN100 materials respectively. However, the total conductivity of all the samples is somewhat lower than that of the other reported LLZO materials synthesized by the solid-state method or other wet chemical processes[13,18,27]. This might be due to the formation of different secondary phases originating during the calcination or sintering process.[17,19] The activation energy, i.e., the energy required for lithium-ion transportation from one site to another within a crystal lattice, can be calculated from the Arrhenius equation [$\sigma T = Ae^{-E_a/TK_B}$, where A is the pre-exponential factor, E_a is the activation energy for ionic conduction, and K_B is the Boltzmann constant]. ***Figure 6.4(c)*** represents the log(σT) vs. 1000/T plot of GN000, GN025, GN050, GN075, and GN100 materials with resultant activation energies found to be 0.59eV, 0.34eV, 0.32eV, 0.40eV, and 0.42eV respectively. GN050 offers the lowest activation energy (0.32eV), indicating smooth lithium-ion transportation across grain boundaries. So, NiO addition in the Ga-doped LLZO matrix significantly affects lithium-ion transportation by decreasing the grain boundary resistance to a certain extent. The density, as calculated from the Archimedes principle, is found to be 3.73 g/cc, 4.28g/cc, 4.44g/cc, 4.69g/cc, and 4.61g/cc, and geometrical density is found to be

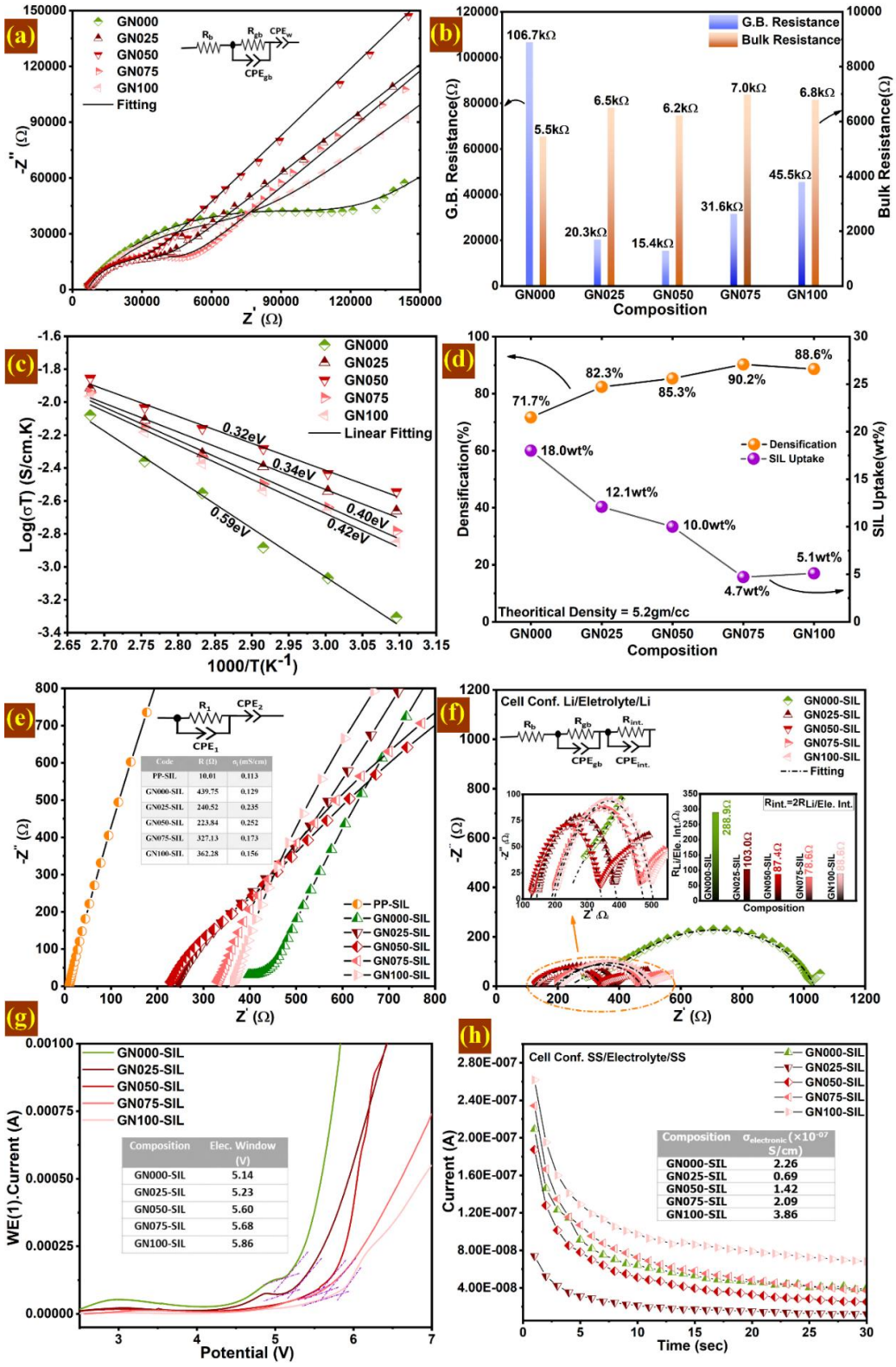

Figure 6.4 *(a) Nyquist plot of GN000, GN025, GN050, GN075 and GN100 pellets sintered at 1000°Cat RT. (b) Variation of bulk and grain boundary resistances with different compositions of solid electrolytes. (c) Arrhenius plot of all sintered pellets and activation energies are calculated from the slopes. (d) Densification vs. different compositions of solid electrolytes and*

variation of SIL uptake concerning the composition. (e) EIS spectra of PP-SIL, GN000-SIL, GN025-SIL, GN050-SIL, GN075-SIL and GN100-SIL for conductivity measurements. (f) Nyquist plot of all SIL-soaked solid electrolytes in Li/Li symmetric cell with inset shows the enlarged version of the plot and variation of electrolyte-metal interface resistance concerning the composition. (g) Current vs. potential linear sweep voltammetric (LSV) plot at a scan rate of 2.0 mV s^{-1} of different SIL-soaked solid electrolytes composition. (h) DC polarization of GN000-SIL, GN025-SIL, GN050-SIL, GN075-SIL, and GN100-SIL using ion-blocking SS electrode.

3.66g/cc, 4.24g/cc, 4.36g/cc, 4.64g/cc and 4.58g/cc for GN000, GN025, GN050, GN075, and GN100 sintered pellets respectively. The densification vs. composition plot for the solid electrolytes is presented in ***Figure 6.4 (d)***, where the densification is calculated by the relative change of density calculated from Archimedes principle to that of the theoretical density (5.20g/cc) of Ga doped LLZO material. So, NiO addition in Ga-doped LLZO matrix not only facilitates lithium-ion transport by decreasing the grain boundary resistance but also contributes to improved densification, which is crucial for the performance of solid electrolytes in actual electrochemical cell performance. It is important to discuss here that adding NiO in Ga-doped LLZO material successfully decreased the grain boundary resistance and increased the overall density. However, the sintered pellet delivers lower conductivity for successful cell operation at room temperature due to the presence of secondary impurity phases (La_2O_3, $La_2Zr_2O_7$, $La_2Li_{0.5}Al_{0.5}O_4$, and Li_2CO_3, etc.) in the Ga doped LLZO matrix. Thus, solvated ionic liquid (SIL) was prepared and infused with all the sintered pellets to compensate for the reduced conductivity and better compatibility between Li metal and the electrolyte material. Although LLZO contains lithium ions, the addition of LiTFSI salt in tetraglyme (G4) solvent was essential to form a viscous gel termed as solvated ionic liquid (SIL). This viscous gel is then infused into the LLZO matrix to conduct Li^+ more efficiently at the bulk as well as at the electrode-electrolyte interfaces. Thus, it is used in enhancing the bulk conductivity of the hybrid electrolyte also improves wettability between Li metal and LLZO. Without LiTFSI, G4 can functions only as a neutral coordinating solvent with negligible ionic conductivity, due to its natural tendency to form chelate like compounds with Lithium may interrupt the facile transfer of lithium ions across the interface. Whereas, the LiTFSI-G4 complex forms a solvated structure, typically composed of $Li(G4)^+$ cations and free or partially coordinated $TFSI^-$ anions. In comparison, G4 alone (without LiTFSI) would lack mobile lithium carriers, which resulted in poor ionic conductivity and ineffective charge transfer at the LLZO interface[17,19,28,29]. As the

densities of different solid electrolyte compositions are different, the soaking ability of SIL in these materials is expected to be varied. The soaking abilities of GN000, GN025, GN050, GN075, and GN100were estimated to be 18.0wt%, 12.1wt%, 10.0wt%, 4.7wt%, and 5.1wt% to their dry weight, respectively as shown in ***Figure 6.4(d)***. So, with the increasing densities of solid electrolytes, the SIL uptake was lowered to a minimum value of 4.7wt% for GN075 with a maximum relative density of 90.2%. Thus, measuring the electrical and interfacial properties of developed hybrid electrolytes will be interesting. Here, the conductivity of SIL was measured separately by a Polypropylene (PP) separator soaked with SIL sandwiched between two SS electrodes. The EIS spectra of PP-SIL, GN000-SIL, GN025-SIL, GN050-SIL, GN075-SIL, and GN100-SIL were presented in ***Figure 6.4(e)***, along with their equivalent circuit. The ionic conductivity was estimated to be 0.113mS/cm, 0.129mS/cm, 0.235mS/cm, 0.252mS/cm, 0.173mS/cm and 0.156mS/cm for PP-SIL, GN000-SIL, GN025-SIL, GN050-SIL, GN075-SIL and GN100-SIL respectively. NiO addition in the Ga-doped LLZO matrix, even after liquid therapy via solvated ionic liquid, also enhances ionic conductivity. It is worth discussing here that in ***Figure 6.4(a)***, the NiO added Ga doped LLZO samples (GN) were measured as sintered pellets in a blocking electrode configuration (Au|GN|Au). The total ionic conductivity in this case is governed purely by the LLZO ceramic matrix and includes the contribution from both bulk and grain boundary resistance, which are known to be relatively high in garnet systems. In comparison, the GN-SIL samples in ***Figure 6.4(e)*** represent a hybrid electrolyte system, where SIL (LiTFSI-G4) is infused into the pores of the LLZO matrix. In this hybrid configuration, the measured conductivity reflects the combined effect of LLZO and SIL. The SIL effectively enhanced the Li^+ percolation pathways via $Li(G4)^+$ complexes and reduced interfacial resistance, resulting in improved interface wettability. Therefore, while the LLZO phase remains constant, the presence of SIL fundamentally alters the ionic transport mechanism, from being limited by ceramic grain boundaries to being supported by a percolated Li^+-rich network. This accounts for the observed two-order-of-magnitude increase in effective ionic conductivity. All the sintered pellets were soaked with SIL and sandwiched between two Li metal electrodes to measure the interfacial compatibility between solid hybrid electrolytes (SHEs) and Li metal. EIS spectra, along with their corresponding equivalent circuits, are shown in ***Figure 6.4(f)***. The electrolyte-metal interface resistance, which constitutes about half of the total interface resistance of a cell, is estimated to be 288.9Ω, 103.0Ω**,** 87.4Ω**,** 78.6Ω, and 88.6Ω for GN000-SIL, GN025-SIL, GN050-SIL, GN075-SIL, and GN100-SIL electrolytes, respectively**.** So, adding NiO as a sintering aid in the Ga-doped LLZO matrix has reduced the metal-electrolyte interface resistance by almost three to four times. Such interfacial

compatibilities between the electrolyte and Li metal are expected to benefit electrochemical cell performance, which will be discussed later.The electrochemical potential window is a critical parameter for an electrolyte since it defines the voltage range in which it remains stable and effective, impacting battery efficiency, safety, and lifespan. Generally, an electrolyte with a potential window of more than 5V is compatible with most commercial cathodes [30]. Thus, linear sweep voltammetry (LSV) is performed for all the SIL-impregnated solid electrolytes in a Li/SS asymmetric cell from OCV to 7V at room temperature, as shown in ***Figure 6.4(g)***. The electrochemical potential window is estimated to be 5.14V, 5.23V, 5.60V, 5.68V, and 5.86V for GN000-SIL, GN025-SIL, GN050-SIL, GN075-SIL, and GN100-SIL electrolytes, respectively, which suggests that all of the hybrid electrolytes are suitable for high-voltage lithium batteries. The minor rise in current near 4.8 V, particularly for the GN000-SIL and GN025-SIL samples, is not indicative of electrolyte decomposition. This increasing trend might be due to the voltage fluctuations and baseline noise, which become more visible due to normalized current scaling used for consistent comparison across samples. Notably, with an increase in NiO content in the Ga-doped LLZO matrix, the electrochemical potential window also increases, indicating that NiO may improve the electrolyte's stability and prevent decomposition at higher voltages. Although LSV is widely used to estimate the oxidative stability limit of solid electrolytes, long-term cycling validation is essential to confirm real-world applicability.

To further understand the impact of NiO addition in the Ga-doped LLZO matrix, the electronic conductivity was also measured by applying DC polarization 0.5 V in an ion-blocking symmetric cell, as shown in ***Figure 6.4(h)***. In a steady-state condition, the steady-state current observed in an electrochemical cell is primarily due to electronic conduction, as the electrodes act as barriers to ionic transport, effectively blocking the movement of ions. So, we can calculate the electronic conductivity from the steady-state current under steady-state conditions. The electronic conductivities are thus found to be 2.26×10^{-7} S/cm, 0.69×10^{-7} S/cm, 1.42×10^{-7} S/cm, 2.06×10^{-7} S/cm and 3.86×10^{-7} S/cm for GN000-SIL, GN025-SIL, GN050-SIL, GN075-SIL and GN100-SIL electrolytes respectively.

A comparative chart was also provided as ***Table 6.4***, highlighting the role of sintering aids in solid electrolyte and metal batteries. The addition of NiO to the Ga-doped LLZO matrix initially decreases electronic conductivity due to NiO's insulating nature, which disrupts the existing conductive pathways. However, as the NiO content increases, electronic conductivity may increase due to the improved microstructural interactions of the conductive network within the Ga-doped LLZO matrix.

Table 6.4 *A comparison chart of garnet-type solid electrolytes with various sintering aids reported in recent times*

SEs	Sintering Aid (SA)	Sintering profile	σ_t (mS. cm^{-1}) / E_g (eV) / Relative Density (%)		$R_{Li/Ele.}$ (Ω) / CCD (mA. cm^{-2})		Ref.
			W/o SA	With SA	W/o SA	With SA	
LLZTO	5 wt% Li_3PO_4	1140°C for 16 h	0.46 / 0.3 /-	0.14 / 0.3 / -	2080 / -	1008 / -	31
LLZTO	1 wt% CuO	1100°C for 20 h	0.028 / 0.33 / 84.2	0.106 / 0.43 / 90.4	- / -	- / -	32
LLZO	8 wt% Li_3BO_3	1100°C for 8h	0.00598 / -/ 58	0.0161/ - / 77	- / -	- / -	33
LLAZO	1 wt% Li_4SiO_4	1200°C for 12h	0.11 / 0.38 / 79	0.61 / 0.34 / 96	- / -	- / -	34
LLZNO	6.5 wt% Li_3BO_3/$LiBO_2$	900°C for 10h	0.0001 / - / 55	0.07 / 0.35 / 86	- / -	- / -	35
LLZTO	6 wt% Li_2O	1170°C for 6h	0.22 / 0.41 / 91.5	0.64 / 0.30 / 97.2	- / -	- / -	36
LLZTO	5 wt % La_2O_3	1150°C for 10h	0.65 /- /-	~1 /- / 98	- / 1.50	- / 2.12	37
LLGZO	0.50 wt% NiO	1000°C for 10h	0.0012 (0.129 With SIL) / 0.59 / 71.7	0.0071 (0.252 With SIL) / 0.32 / 85.3	289.9 / 0.40	87.4 / 0.55	This Work

Where, σ_t and E_g refers to the total ionic conductivity, activation energy of electrolyte, whereas $R_{Li/Ele.}$ and CCD refers to resistance at metal/electrolyte interface and critical current density, respectively.

Typically, a solid electrolyte with low electronic conductivity is less prone to lithium dendrite formation, which can increase the critical current density (CCD) and, consequently,

the power densities of metal batteries. Therefore, measuring the critical current density of all the electrolytes will be particularly interesting, which will be discussed in the subsequent section. Adding NiO as a sintering aid significantly reduces grain boundary resistance and activation energy, improves densification and lithium-ion transport, and decreases metal-electrolyte interface resistance, enhancing the solid electrolytes' overall performance.

6.3.4 Electrochemical Studies

6.3.4.1 CCD Measurement

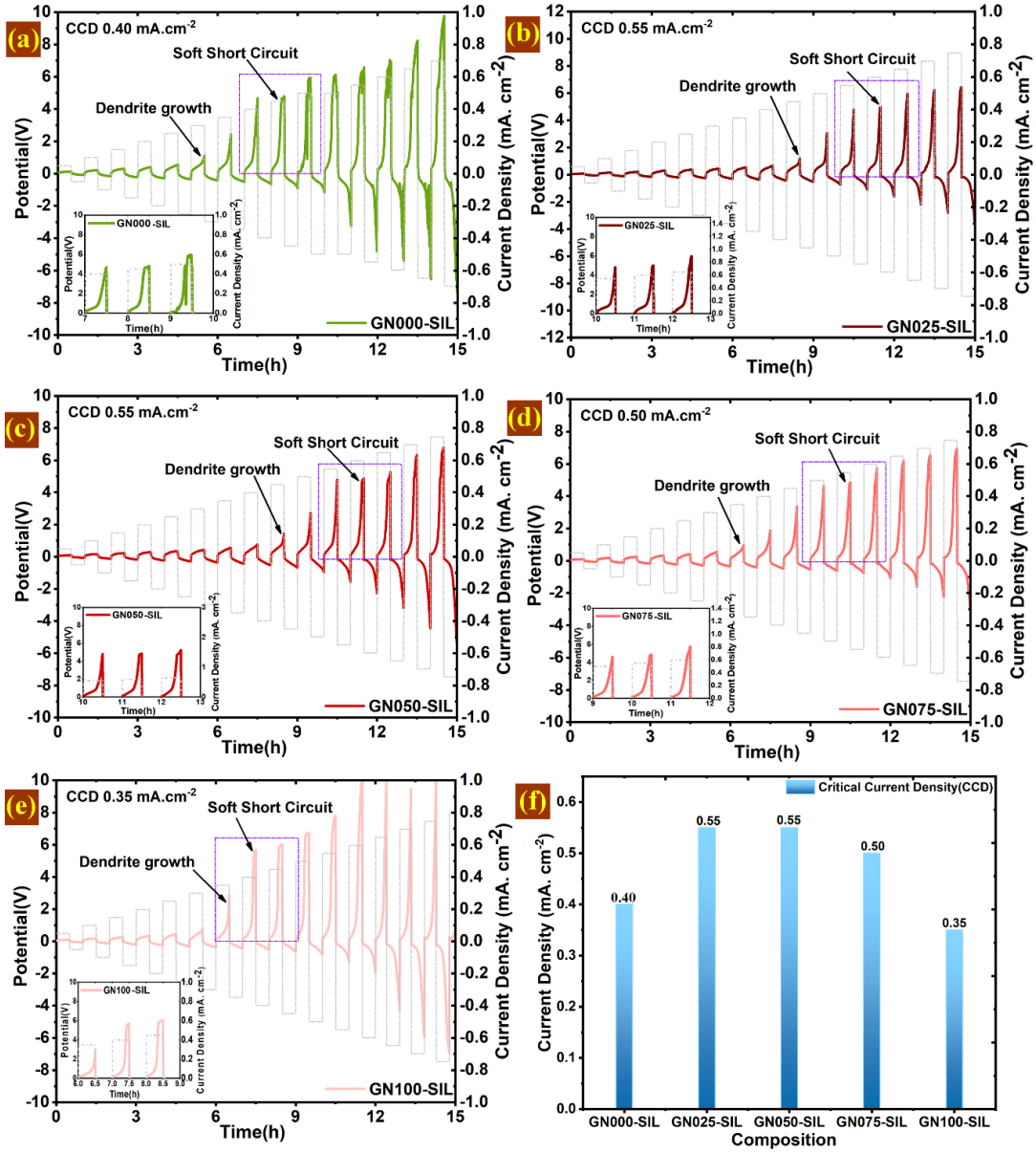

Figure 6.5 *DC cycling profile of Li/Li symmetric cell of (a) GN000-SIL, (b) GN025-SIL, (c) GN050-SIL, (d) GN075-SIL and (e) GN100-SIL hybrid electrolyte at RT with step current*

density of 0.05mA.cm^{-2} in the range of 0.05 to 0.75mA.cm^{-2}, (f) Variation of CCD values concerning different electrolyte compositions.

To determine the CCD, symmetric cells with various hybrid electrolytes are fabricated and subjected to galvanostatic charge-discharge cycles at current densities ranging from 0.05 to 0.75 mA.cm^{-2} with a step current density of 0.05 mA.cm^{-2}, as illustrated in ***Figure 6.5(a)-(e)*** with the corresponding focused version in the inset. Here, with the increment of current density, the voltage due to polarization drop increases, and suddenly, after a few plating/stripping cycles, a spike is observed. This spike rapidly grows, resulting in a distortion in the voltage profile. The current density up to which such distortion does not appear can be termed the critical current density due to the soft short circuit. In our present study and our previous study, no hard short circuit is observed, which might be due to the presence of SIL at the Li metal/electrolyte interface. In the present scenario, this spike originated around a current density of 0.30mA.cm^{-2} for GN000-SIL, 0.45mA.cm^{-2} for GN025-SIL, 0.45mA.cm^{-2} for GN050-SIL, 0.35mA.cm^{-2} for GN075-SIL and 0.35mA.cm^{-2}for GN100-SIL. So, introducing NiO as a sintering aid within the Ga-doped LLZO matrix extends the pre-spike region. This extension indicates a delay in the onset of metal filament growth, allowing a more stable voltage profile under higher current densities. The ability to extend the pre-spike region is significant, as it enhances the overall performance and durability of the electrolyte system by delaying the formation of lithium dendritic growth. ***Figure 6.5(a)*** shows that after three galvanostatic charge-discharge cycles during the post-spike to pre-distortion region, GN000-SIL reaches its critical current density limit of 0.40 mA.cm^{-2}. Whereas the critical density for GN025-SIL, GN050-SIL, GN075-SIL, and GN100-SIL has been estimated as 0.55mA.cm^{-2},0.55mA.cm^{-2}, 0.50mA.cm^{-2} and 0.35mA.cm^{-2} respectively as shown in ***Figure 6.5(b)-(e)***. A variation in CCD values for the different compositions of solid electrolytes is summarized in ***Figure 6.5(f)***. Thus, this study reveals that with the increasing addition of NiO in the Ga-doped LLZO matrix, the CCD values increase to a maximum of 0.55mA.cm^{-2} for GN025-SIL and GN050-SIL and then reach a minimum of 0.35mA.cm^{-2}for GN100-SIL.This trend suggests that NiO in the Ga-doped LLZO matrix initially enhances the CCD values by delaying dendritic growth to a certain extent; a further increase in NiO content leads to a decline in CCD values.

6.3.4.2 Long Cycling Performance

The capacity loss in solid-state lithium metal batteries can be attributed to electrochemically inactive “dead Li” formation during repeated lithium plating/stripping cycles. Accumulated

dead Li at the metal-solid electrolyte interface further increases the internal resistance of the cell, leading to significant polarization, which not only hampers the battery performance but also severely reduces its energy efficiency. Thus, examining the behavioral patterns of Li plating/stripping over an extended period of time is essential for evaluating the compatibility of solid electrolytes with lithium metal in solid-state lithium metal batteries (SSLMBs).[38] Accordingly, lithium symmetric cells are fabricated with different solid hybrid electrolytes and subjected to the Li plating/stripping process for 1000 hours at RT (27°C) at a current density of 0.1mA.cm^{-2}. The Li plating/stripping voltage profiles of different solid hybrid electrolytes are presented in ***Figure 6.6(a)***. During the first cycle of testing, the average polarization values recorded for the various samples are as follows: 0.252V for GN000-SIL, 0.205V for GN025-SIL, 0.215V for GN050-SIL, 0.209V for GN075-SIL, and 0.228V for GN100-SIL. GN000-SIL exhibits the highest polarization among these hybrid solid electrolytes, while GN025-SIL shows the lowest polarization during the initial Li plating/stripping cycle. Similarly, during the 300th plating/stripping cycle, the average polarization values observed are 0.194V for GN000-SIL, 0.157V for GN025-SIL, 0.166V for GN050-SIL, 0.164V for GN075-SIL, and 0.181V for GN100-SIL.These results suggest that all the NiO-added solid hybrid electrolytes exhibit lower polarization values initially and maintain lower polarization over multiple cycles. This indicates their superior long-term stability and performance compared to the unmodified GN000-SIL electrolyte. Among all the samples, the first soft short circuit was observed for GN075-SIL after 378 hours of operation, followed by GN100-SIL after 407 hours. GN000-SIL experienced a soft short circuit after 519 hours, and GN025-SIL showed a soft short circuit after 875 hours. In contrast, the GN050-SIL cell performed exceptionally well, exhibiting cycling stability with negligible voltage fluctuations and no signs of a soft short circuit even after 1000 hours. This performance suggests that the addition of 0.50 wt% NiO as a sintering aid in the Ga-doped LLZO matrix significantly retards lithium dendritic growth. The results from the plating/stripping behavior indicate that the optimal addition of NiO enhances lithium plating and stripping kinetics and effectively delays the onset of short circuits.

Electrochemical impedance spectroscopy (EIS) was conducted on all the symmetric cells before and after cycling to gain deeper insights into the charge transfer process. By examining the Nyquist plots and fitting the data with appropriate equivalent circuit models, we can monitor the changes in electrolyte bulk resistance and metal-electrolyte interface resistance due to prolonged cycling. Generally, a "short circuit" refers to the unintended creation of an electrical path with very low resistance, comparable to a metal wire.

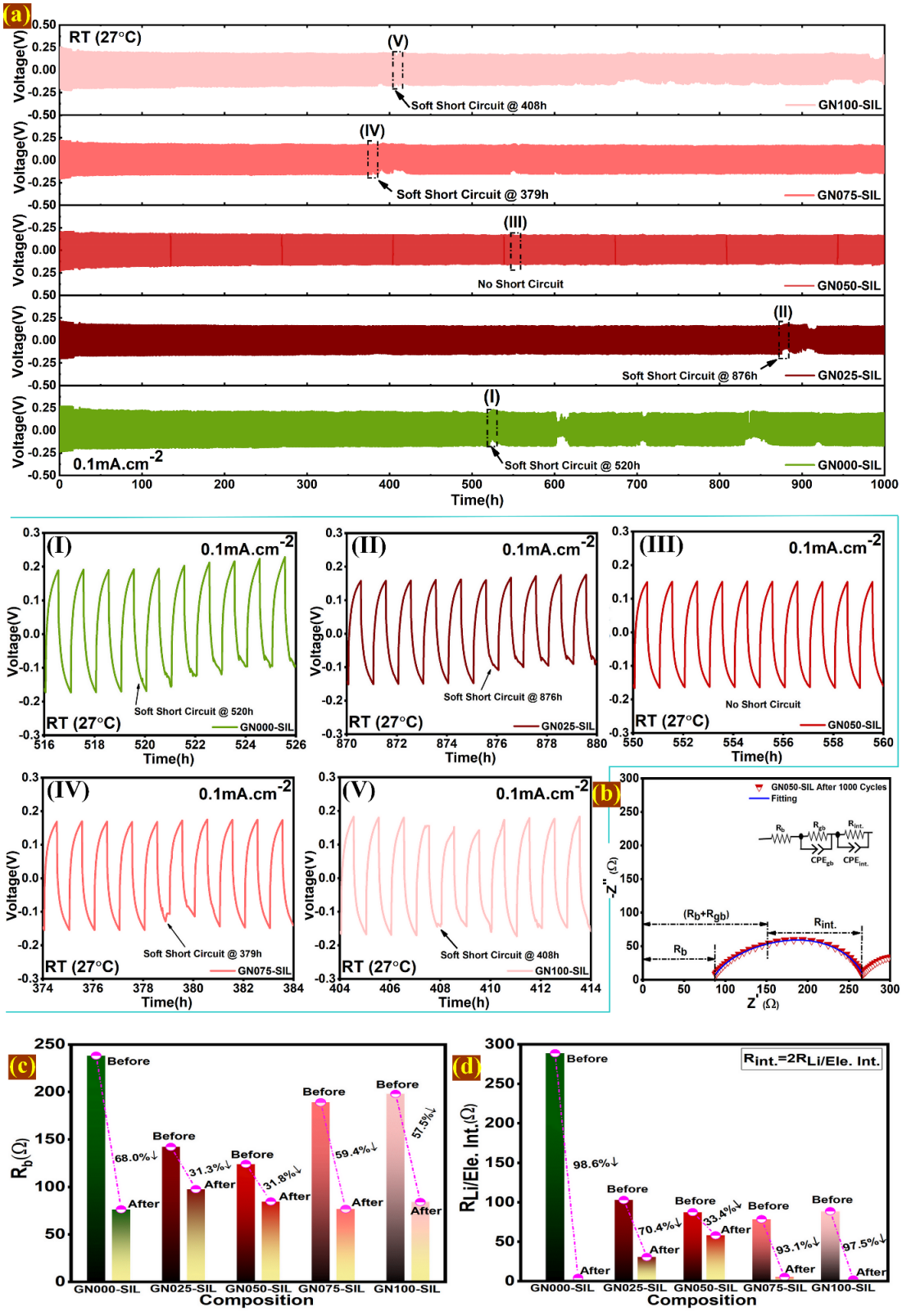

Figure 6.6 *(a) Voltage profile of Li/Li Symmetric cell at RT over 1000h at a current density of 0.1 mA.cm^{-2} with the enlarged version marked as (I)-(V) and shown separately, (b) A typical EIS spectra of GN050-SIL after symmetric cell performance along with its corresponding equivalent and different resistance components are marked, (c) Variation of electrolyte bulk*

resistance at before and after symmetric cell performance with the various composition of electrolytes, (d) Variation of metal-electrolyte interface resistance at before and symmetric cell performance with the different electrolyte composition.

Similarly, a significant reduction in bulk and metal-electrolyte interface resistance will be observed if a short circuit occurs due to lithium dendrite growth. ***Figure 6.6 (b)*** shows a typical Nyquist plot for GN050-SIL after cycling and its corresponding equivalent circuit, where various resistance components are marked. ***Figure 6.7*** displays the Nyquist plots for all the symmetric cells before and after cycling, along with their equivalent circuits. Variation of electrolyte bulk resistance before and after cycling performance for the different electrolyte compositions is illustrated in ***Figure 6.6(c)***. A significant drop of 68.0% in bulk resistance is observed for GN000-SIL, whereas GN025-SIL and GN050-SIL show reductions of only 31.3% and 31.8%, respectively. Conversely, a downfall of 59.4% and 57.5% in bulk resistance was observed for GN075-SIL and GN100-SIL. Similarly, the variation of metal-electrolyte interface resistance before and after cycling performance vs. different electrolyte compositions is presented in ***Figure 6.6 (d)***. . A dramatic reduction of over 90% in metal-electrolyte interface resistance is observed for GN000-SIL, GN075-SIL, and GN100-SIL.

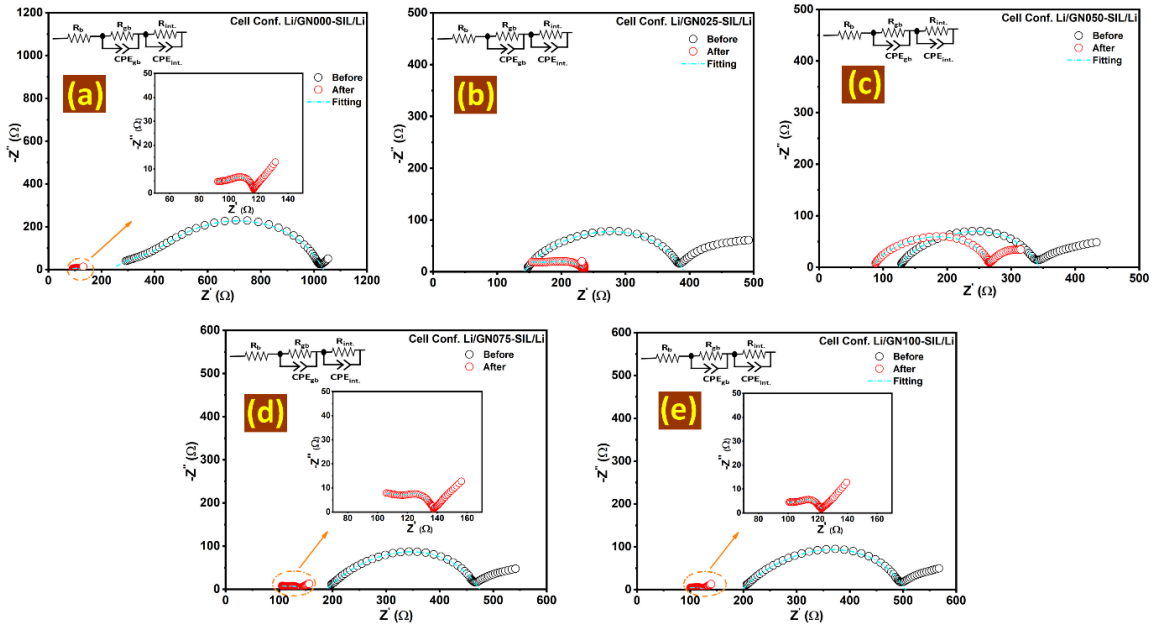

Figure 6.7 EIS spectra before and after symmetric cell performance for (a) GN000-SIL, (b) GN025-SIL, (c) GN050-SIL, (d) GN075-SIL, and (e) GN100-SIL.

In contrast, GN025-SIL shows a decrease of 70.4% in metal-electrolyte interface resistance. However, GN050-SIL only experiences a reduction of 33.4%, suggesting that adding 0.50wt%

NiO as a sintering aid in the Ga-doped LLZO matrix profoundly impedes the Li dendritic growth. Thus, it will be interesting to measure the electrochemical full-cell performance of the GN050-SIL hybrid solid electrolyte to evaluate its practical effectiveness and stability in real-world applications.

6.3.4.3 Electrochemical Cell Performance

Figure 6.8 illustrates the electrochemical full-cell performance of GN000-SIL and GN050-SIL solid hybrid electrolytes using $LiMn_2O_4$ cathode and Li metal anode in a pseudo-solid-state configuration. Typical charge-discharge profiles of GN000-SIL and GN050-SIL are displayed in ***Figures 6.8(a)*** and ***(b)*** over a current density range of 0.10 $mA.cm^{-2}$- 1.4 $mA.cm^{-2}$ revealed that the hybrid electrolyte performs excellently at a slower current density (0.05-0.40$mA.cm^{-2}$), but GN000-SIL exhibits poor performance at higher current density.

Table 6.5 *Summary of cycling results at different current densities for GN000 and GN050*

Current density ($mA.cm^{-2}$)	**GN000**			**GN050**		
	Average discharge capacity ($mAh.g^{-1}$)	Average charge capacity ($mAh.g^{-1}$)	Average coulombic efficiency (%)	Average discharge capacity ($mAh.g^{-1}$)	Average charge capacity ($mAh.g^{-1}$)	Average coulombic efficiency (%)
0.10	105.39	103.33	101.99	105.17	106.59	98.67
0.20	101.04	100.31	100.72	103.95	104.58	99.38
0.40	89.12	89.09	100.02	97.86	99.13	98.72
0.60	74.61	74.68	99.88	89.46	90.02	99.38
0.80	60.35	60.48	99.74	78.78	79.40	99.21
1.00	51.78	51.83	99.91	69.52	69.95	99.37
1.20	38.18	38.18	100.12	53.93	54.42	99.10
1.40	32.46	32.39	100.28	48.42	48.71	99.40
0.10	100.58 *[95.44% reversibility]*	100.74 *[97.49% reversibility]*	99.84 *[97.89% reversibility]*	106.19 *[100.97% reversibility]*	106.66 *[100.06% reversibility]*	99.56 *[100.90% reversibility]*

In contrast, GN050-SIL shows better performance at all current densities of operation. At 0.10 $mA.cm^{-2}$, GN000-SIL, and GN050-SIL deliver a specific discharge capacity of 103.44mAh. $g^{-1}$and 106.27 $mAh.g^{-1}$ respectively.

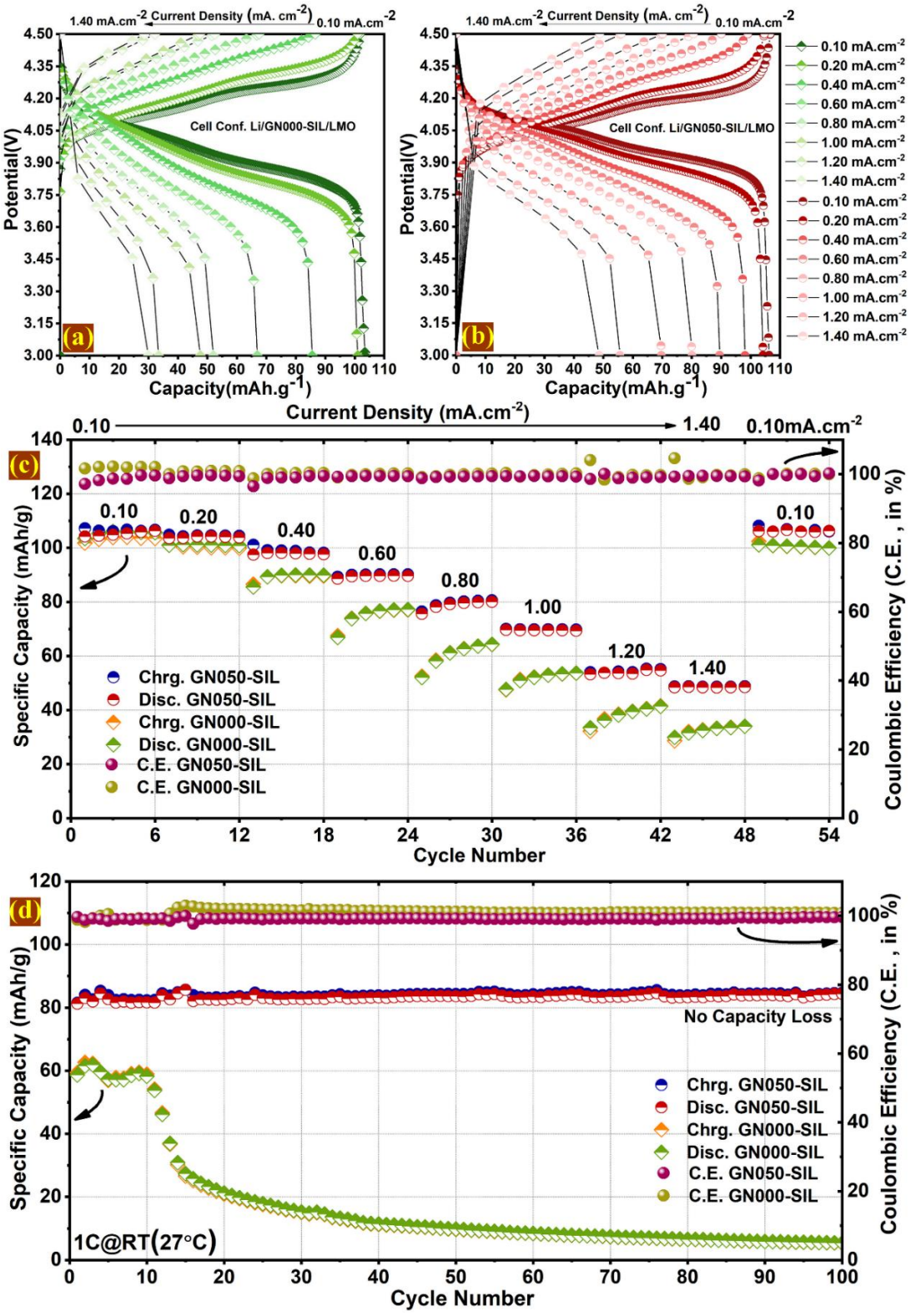

Figure 6.8 *Typical charge-discharge profile of (a) GN000-SIL and (b) GN050-SIL electrolyte at different current densities with $LiMn_2O_4$ cathode and Li metal as an anode, (c) Rate performance study of GN000-SIL and GN050-SIL hybrid electrolyte at different step current density (d) High-rate capability study at 1C using GN000-SIL and GN050-SIL electrolytes.*

At a higher current density of 1.4mA.cm^{-2}, GN000-SIL only delivers a discharge capacity of 29.95mAh. g^{-1}, whereas GN050-SIL still delivers an impressive capacity of 48.56 mAh. g^{-1}. The rate performance study of GN000-SIL and GN050-SIL was presented in ***Figure 6.8(c)***. At 0.10 and 0.2 mA.cm^{-2}, both cells show an average discharge capacity of 100-106 mAh: g-1 and excellent coulombic efficiency of more than 99%. With the further increment of current density from 0.4-1.4mA.cm^{-2}, a significant loss in discharge capacities is observed for GN000-SIL.In contrast, GN050-SIL delivers better rate performance at those current densities. Both cells maintained an impressive coulombic efficiency of more than 99% of any current density of operation. Notably, both cells exhibited an initial decrease in capacities due to the abrupt change in current densities; however, their capacities recovered in the subsequent cycles. A summary of average charge, discharge capacities, and coulombic efficiencies at each current density of operation for both cells is presented in ***Table 6.5***. After operating the cell at 1.40 mA.cm^{-2}, it is reversed back to its initial current density of 0.10mA.cm$^{-2,}$ during which GN000-SIL shows a reversibility of 95.44%in average discharge capacity, whereas GN050-SIL exhibits more than 100% reversibility. The high-rate capability tests are performed at 1C for both cells at room temperature. The previous literature cited that the typical capacity in such a configuration is around 110 mAh/g, but obtained at a lower current density[39,40]. Therefore, it is well understood that the solid and liquid therapies proved to be beneficial in fast Li-ion transactions when the current density is higher. It is worth mentioning here that the small increase in capacity around the 25th cycle for GN050-SIL is likely attributed to electrolyte redistribution, activation of interfacial pathways, or progressive wetting between the cathode and the hybrid-solid electrolyte, which is a common phenomenon in quasi-solid-state systems, particularly during early stabilization cycles[41,42].

The cell with GN000-SIL electrolyte exhibits very poor performance by losing its capacity quickly after 10 cycles at 1C, as shown in ***Figure 6.8(d)***. In contrast, no capacity loss is observed for the GN050-SIL cell even after 100 cycles. Thus, the overall electrochemical performance of GN000-SIL and GN050-SIL electrolytes suggests that adding NiO in the LLZO matrix has a notable impact at higher current density operation. As the SIL uptake in GN000-SIL is almost twice that of the GN050-SIL, their rate performances at slower current densities are expected to be more dominated by SIL rather than the solid electrolyte. At higher current densities, however, the influence of the solid electrolyte may become more pronounced as the contribution of Li-ion mobility within the LLZO matrix becomes increasingly critical. The poor performance of GN000-SIL at higher current densities, thus, might be due to its large grain

Table 6.6 *A comparison chart of garnet-type solid electrolytes with various modifications reported in recent times for hybrid or quasi-solid-state batteries.*

SEs	Modification	σ ($mS.cm^{-1}$) / $R_{int.}(\Omega)$	Li/Li Cell Stability	CCD ($mA.cm^{-2}$)	Full Cell Performance	Ref.
Al-doped LLZO	FSI IL (15 wt%) For Full Cell: FSI-LITFSI (9:1)	0.48 /-	-	-	$LiFePO_4$/HSE/Li, capacity >100 mAh g^{-1} at C/20, 89.5% retention after 10 cycles	43
Ta-doped LLZO	19 wt% $Py_{14}TFSI$, and 1 wt% LiTFSI	0.4 /-	Stable over 1000h at 0.1$mA.cm^{-2}$	-	$LiCoO_2$/HSE/Li, Capacity 140 at 0.1C, 99% retention at the 150th cycle.	44
Mg and Sr co-doped LLZO	LiN(SO2F)2 (LiFSI)/sulfolane (SL)	-	-	-	NMC622/QSE/Graphite, capacity179 $mAhg^{-1}$ at 0.2C, 89.6% retention after 100 cycles.	45
Ba and Nb co-doped LLZO	ILE (0.2 mol LiTFSI and 0.8 mol Pyr14FSI)	- / 145 $\Omega.cm^2$	stable at 0.3 mA cm^{-2}.	-	$LiFePO_4$/LLZO-ILE/Li, capacity 145 mAh g^{-1} at 20 $mA.g^{-1}$. A bipolar stacked cell (≈8V), capacity 145 mAh g^{-1}, with coulombic > 99%.	46
Ta-doped LLZO	14 wt% BMP-TFSI	0.67 /-	stable at 0.1mA cm^{-2} for more than 300 cycles without short circuit	>0.74	NMC811/HSE/Li, capacity 150 to 102 mAh g^{-1} after 200 cycles at 0.5C, LFP/HSE/Li, capacity 119 mAh g^{-1} without loss after 60 cycles at 0.2C.	47
LLZO	SIL (Equimolar mixture of LITFSI & tetraglyme)	0.33 / -	Stable over 200h at 0.05 mA cm^{-2} without short circuit	0.45	$LiMn_2O_4$/QSE/Li, capacity 104.91 $mAh{\cdot}g^{-1}$ at 0.05 $mA.cm^{-2}$ with >99%, excellent long-term cycling.	17
Ga doped LLZO	Dual Therapy (0.5wt% NiO sintering aid & SIL)	0.252 / 87.4	Stable over 1000h at 0.10 mA cm^{-2} without short circuit	0.55	$LiMn_2O_4$/QSE/Li, capacity 106.27 $mAh{\cdot}g^{-1}$ at 0.10 $mA.cm^{-2}$ with >99%, no capacity loss at 1C even after 100 cycles.	This work

Where, σ, CCD, and $R_{int.}$ refers to the total ionic conductivity, critical current density, and metal/electrolyte interface, respectively. IL: Ionic Liquid, ILE: Ionic Liquid Interlayer, SIL:Solvated Ionic Liquid, HSE: Hybrid Solid Electrolyte, QSE: Quasi-Solid Electrolyte

boundary resistance and the presence of lanthanide impurities in the grain boundaries of the LLZO matrix. GN050-SIL delivers much better rate performance, likely owing to its compact grain structure and the presence of lithiated impurities in the grain boundaries, which may facilitate improved ion transport. To understand the charge transfer mechanism at the different electrolyte-electrode interfaces of the GN050-SIL hybrid electrolyte, the pre- and post-cycling EIS studies are carried out and will be discussed in the next section. A schematic was presented in ***Figure 6.1***, highlighting the key advantages of the dual therapy strategy in metal batteries. A comparison chart of garnet-type solid electrolytes with various modifications reported in recent times for hybrid or quasi-solid-state batteries is summarized in ***Table 6.6***.

6.3.4.4 Decouple the Electrochemical Process via DRT

NiO's role in the LLZO matrix, particularly in lithium-ion transport and interfacial kinetics during and pre-post cycling, is crucial for its successful operation in commercial batteries. The distribution of relaxation times (DRT) method simplifies EIS analysis by distinguishing individual electrochemical processes through unique time constants. It is worth mentioning that the LLZO matrix contains various lithiated and non-lithiated lanthanide impurities, making it more challenging to decouple the interfacial electrochemical process, as impurities can directly or indirectly influence the overall kinetics. Thus, overlapping peaks with multiple time constants may appear in the DRT pattern. To simplify, we consider here that each major peak in the DRT pattern represents at least one time constant and avoids the presence of multiple time constants within a particular peak. Here, we focus on the position and relative intensity of the major peak rather than quantifying the polarization resistance.[48] In-depth studies will be carried out in the future to quantify the polarization resistance and to analyze the presence of multiple time constants in a broad peak, representing a series of specific electrochemical kinetics. Here, we have tried to decouple the electrochemical processes of Li/GN050-SIL/LMO cell, a first-of-its-kind study in pseudo-solid state metal batteries. ***Figure 6.9(a)*** represents the EIS spectra as fabricated and after long cycling. It is difficult to predict the number of parallel RC circuits that can be use in a ECM to resolve the EIS spectra taken in as-fabricated However, the presence of three depressed semi-circles in the EIS pattern taken after a long cycling process is clearly visible. Also, any contribution of impurities in the EIS spectra is ignored during equivalent circuit fitting. Thus, it is almost impossible to decouple the electrochemical kinetics

through equivalent circuit fitting. ***Figure 6.9(b)*** represents the corresponding DRT patterns of the GN050-SIL cell at as fabricated and after cycling conditions.

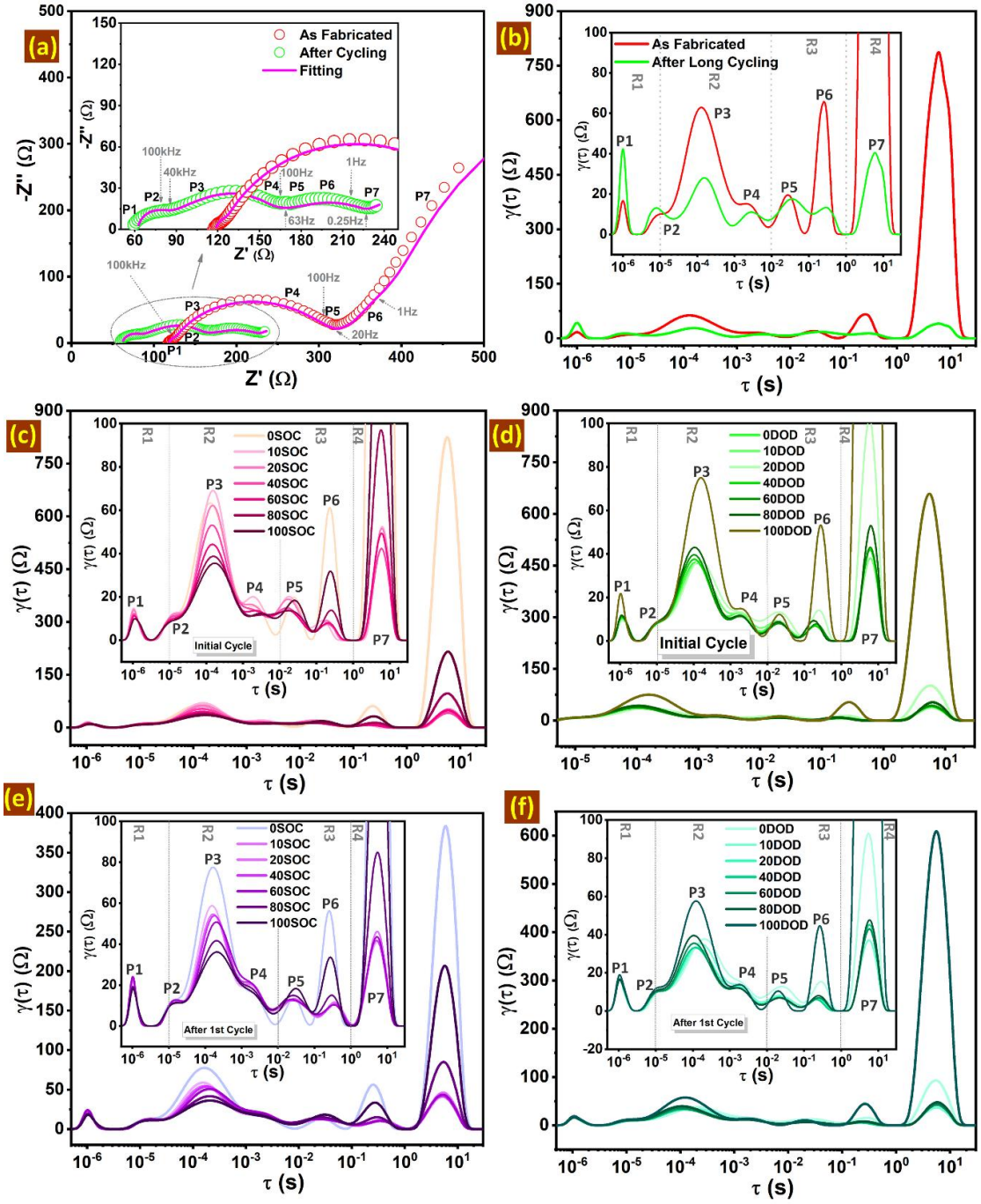

Figure 6.9 *(a) pre- and post-cycling EIS spectra of Li/LMO full cell. (b) corresponding DRT pattern. (c) & (d) DRT patterns at various states of charge (SOC) and depth of discharge (DOD) at the initial cycle, respectively. (e) & (f) DRT patterns at various SOC & DOD after the 1st cycle, respectively.*

The DRT plots show seven major peaks, each representing a resistance contribution. The overall plot can be categorized into four different regions according to their time-constant range. Regions R1 placed at ~100kHz-1MHz, i.e., at the higher frequency region. In general, the contribution of grain boundaries and contact resistance are observed. Here, peak P1 (τ~1×10^{-6} s) is referred to as the grain boundary contribution of LLZO material; interestingly, P2 is also situated at the first semicircle in EIS spectra (after cycling) with a time constant of ~8×10^{-6} s can be defined as the contribution of any lithiated impurities. As the presence of K_2NiF_4 type lithiated impurities are deposited at the GBs of LLZO matrix as confirmed by XRD, FESEM micrograph thus this peak P2 can be attributed due to the GBs resistance of K_2NiF_4 type impurities. Region R2 located at ~100kHz-100Hz, i.e., at the mid-frequency region, can be attributed to different interphase kinetics in a battery cycling, such as cathode-electrolyte interphase (CEI), anode-electrolyte interphase (commonly known as solid electrolyte interphase or SEI) kinetics. Recently, it has been observed that the SEI in metal batteries is positioned at a time constant of ~10^{-2} s, whereas for CEI, the time constant of ~10^{-3}-10^{-4} s is observed[49]. For example, the CEI of the NCM cathode is located at 3.7–6.7×10^{-3} s, whereas, for the NCA cathode, it is at 1.6×10^{-4} to 1.6×10^{-3} s. Thus, P3 peaks at ~1.3×10^{-4} s, representing the probable contribution of SEI and CEI both[49]. Intensities of peak P4 at ~2.5×10^{-3}s do not change significantly throughout the measurements. Recently, Yu. et al. discovered the mechanical contact impedance of cathode/solid electrolyte and/or electrode/current collector also contributed to the DRT pattern (peak at ~10^{-3}s) during measurement of full cell in all solid-state configurations with sulfide electrolyte[50]. In such a scenario, the presence of SIL in our hybrid system can restrict such contribution, but the formation of peak P4 is still unknown and might be due to the interaction between impurities and SEI/CEI. Peaks P5 and P6 generally attribute the contribution of anodic and cathodic charge transfer kinetics at region R3 (100Hz-1Hz), which matches well with the previous reports. P7 at the very low-frequency region (R4;<1Hz) is due to the diffusion phenomena[50,51]. These peaks are also assigned to the EIS spectra in ***Figure 6.9(a)*** according to their corresponding time constant value. Also, the bulk resistance of GN050-SIL changes from 116.7Ω to 59.5Ω, suggesting enhanced ionic transportation in the hybrid electrolyte system. In ***Figure 6.9(b)***, polarization resistance due to different interphase (SEI & CEI) (P3), cathodic charge transfer (P6), and diffusion (P7) kinetics reduced significantly after the electrochemical cycling, suggesting healthy interface stabilization in the overall ion transportation[48–52]. The resistance attributed to P5 and P4 does not significantly change upon long electrochemical cycling. However, increases in resistance corresponding to P1 and P2 can be concerning, which could arise from Li depletion, impurity

segregation, or phase instability at the grain boundaries [49]. EIS was measured at different SOC (***Figures 6.10(a)*** and ***(c)***) and DOD levels (***Figures 6.10(b)*** and ***(d)***) in as fabricated conditions and after the initial cycle to understand the changes during the electrochemical cycling as shown in ***Figure 6.10***. DRT patterns of different SOC and DOD levels are presented in ***Figure 6.9(c)*** and ***(d)*** in fabricated conditions, respectively. Similarly, ***Figures 6.9(e)*** and ***(f)*** represent the DRT patterns at different SOCs and DODs after 1st cycle.

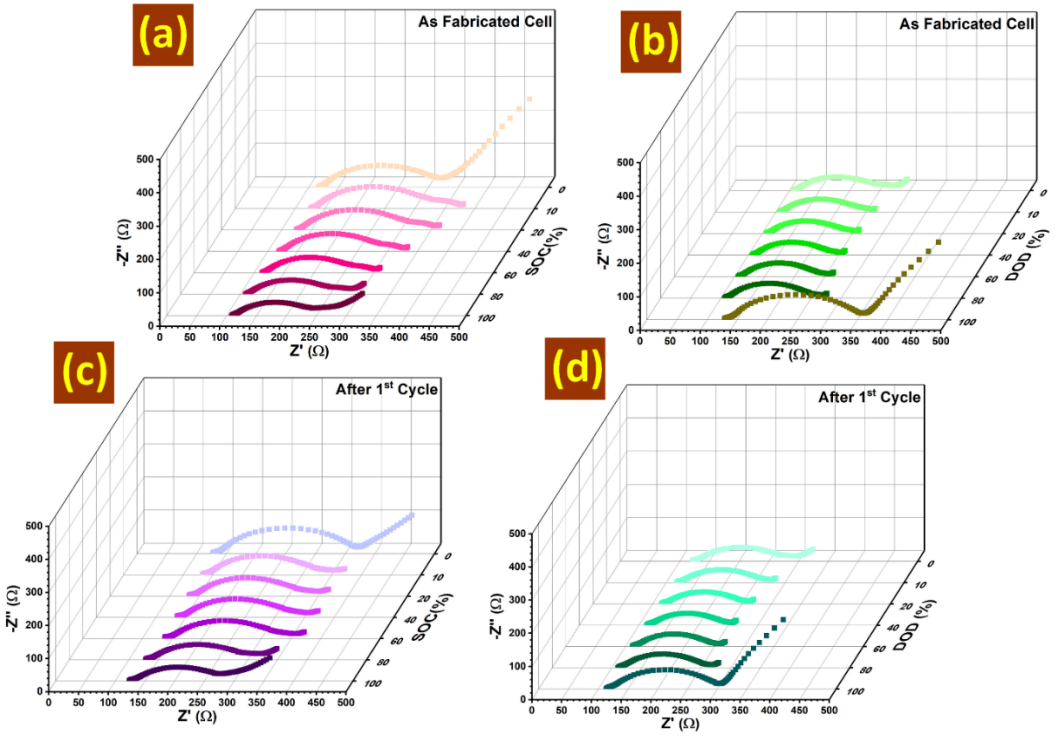

Figure 6.10 *EIS spectra during 1st cycle at various (a) SOC and (b) DOD, EIS spectra during 2nd cycle at various (a) SOC and (b) DOD.*

Higher resistance corresponding to P3, P6, and P7 at 0SOC may be due to poor interfacial contact or unstable interphase layer. A gradual decrease in resistance corresponding to P3 during different SOC levels suggests the formation of a more stable interphase layer during the charging process. Also, the intensities of peaks P5, P6, and P7 decrease abruptly along with the diffusion polarization during the charging process. However, at a higher SOC (~80-100), these resistances increase, which might be due to the sluggish Li-ion kinetics. Meanwhile, resistance corresponding to peaks P1 and P2 decreases slowly, suggesting no significant change in grain boundaries during the charging process. No significant change in peak intensities is observed in the DRT pattern during the 0-80% DOD range at the initial cycle, as shown in ***Figure 6.9(d)***, suggesting a stable charge transfer and interfacial kinetics. At a higher DOD, a sudden rise in

grain boundary (P1), different interphase (SEI & CEI) (P3), cathodic charge transfer (P6), and diffusion (P7) resistance is observed, which might be due to structural degradation and limitation in Li-ion kinetics[51,52]. Similar changes are observed when the cell undergoes different SOC and DOD levels after the initial cycle, as shown in ***Figures 6.9(e)*** and ***6.9(f)***. However, a significant drop in intensities is observed for P3, P5, and P7 after 100DOD as compared to the previous cycle, suggesting the formation of stable interphase and charge transfer kinetics could be achieved after a few cycles. In summary, DRT analysis revealed the interphase stabilization and improved charge transfer kinetics upon cycling, and the increase in grain boundary resistances of LLZO and K_2NiF_4 type impurities suggests potential degradation at long-term cycling. Thus, careful control of grain boundary chemistry and interfacial stabilization is critical for successful operation in commercial metal batteries.

Table 6.7 *Comparison of structural, interfacial, and electrochemical metrics for NiO-added Ga–LLZO pellets and with solvated ionic liquid infusion SHEs (shaded Region).*

Parameter	GN000	GN025	GN050	GN075	GN100
Phase Purity (%) c-LLZO:LI: NLI	74.8: 0:24.8	84.3: 3.1:12.6	80.2: 11.9:7.9	72.9: 16:11	67.4: 17.2:15.5
Shrinkage at 1000°C (%)	0.77	-0.83	-0.46	-2.58	-1.42
Densification (g/c.c.)	71.7	82.3	85.3	90.2	88.6
$\sigma_i \times 10^{-3}$(mS/cm)	1.25	5.70	7.06	3.96	2.92
Eg (eV)	0.59	0.34	0.32	0.40	0.42
SIL Uptake (%)	18	12.1	10	4.7	5.1
σ_i(mS/cm)	0.129	0.235	0.252	0.173	0.156
$R_{Li/Ele.}$ (Ω)	288.9	103	87.4	78.6	88.6
E_0 (V)	5.14	5.23	5.60	5.68	5.86
$\sigma_e \times 10^{-7}$(S/cm)	2.26	0.69	1.42	2.09	3.86
CCD (mA/cm^2)	0.40	0.55	0.55	0.50	0.35
Stable Li Cycling (h)	519	875	>1000	379	408
Discharge Capacity at 1.4 mA/cm^2 (mAh/g)	32.46	-	48.42	-	-
Capacity retention (%)	<20	-	~100	-	-

Here, LI: Lithiated Impurities, NLI: Non-Lithiated Impurities, σ_i: Ionic Conductivity, Eg: Activation Energy, $R_{Li/Ele.}$: Li Metal/Electrolyte Interface Resistance, E_0: Potential Window σ_e: Electronic Conductivity, CCD: Critical Current Density,

6.4 Conclusion

Introducing solid therapy via NiO as a sintering aid and liquid therapy using solvated ionic liquid (SIL) significantly contributed to the reduction of interfacial impedance and dendrite-related issues in LLZO-based solid electrolytes for its application in solid-state metal batteries (SSLMBs). While the addition of NiO (GN050; 0.5% wt.% of LLZO) promoted grain boundary transportation and improved densification through the formation of a new K_2NiF_4-type of lithiated phase, the liquid therapy using SIL (GN050-SIL) enhanced the ionic conductivity at RT (0.252 $mS.cm^{-1}$), reduced the Li/LLZO interfacial resistance (87.4 Ω), and enabled more efficient lithium-ion transportation across the metal-electrolyte interface (As summarize in ***Table 6.7***). This synergistic effect helped demonstrate a stable lithium plating/stripping behavior for LLZO-based SEs for more than 1000 hours without any short circuit and by measuring a critical current density (CCD) of 0.55 $mA \cdot cm^{-2}$. The improvised electrolyte GN050-SIL delivered improved charge/discharge cycling performance in SSLMBs (Li/SEs/$LiMn_2O_4$ configuration) at different current densities (0.1-1.4 $mA.cm^{-2}$) compared to only SIL-infused Ga doped LLZO electrolyte (GN000-SIL). The GN050-SIL electrolyte showed a high-rate capability at 1C, as tested in 100 cycles, with a coulombic efficiency of 99%. The DRT analysis clearly revealed that the dual strategy stabilized the interphases and promoted the charge transfer and diffusion process across the thick electrolyte/electrode interface. In summary, such a solid-liquid combination in LLZO proved to be a workable configuration in almost solid-state metal batteries (SSLMBs).

6.5 References

1 A. Jetybayeva, D. S. Aaron, I. Belharouak and M. M. Mench, 2023, preprint, DOI: 10.1016/j.jpowsour.2023.232914.

2 P. Albertus, V. Anandan, C. Ban, N. Balsara, I. Belharouak, J. Buettner-Garrett, Z. Chen, C. Daniel, M. Doeff, N. J. Dudney, B. Dunn, S. J. Harris, S. Herle, E. Herbert, S. Kalnaus, J. A. Libera, D. Lu, S. Martin, B. D. McCloskey, M. T. McDowell, Y. S. Meng, J. Nanda, J. Sakamoto, E. C. Self, S. Tepavcevic, E. Wachsman, C. Wang, A. S. Westover, J. Xiao and T. Yersak, *ACS Energy Lett*, DOI:10.1021/acsenergylett.1c00445.

3 X. Ma, Y. Xu, B. Zhang, X. Xue, C. Wang, S. He, J. Lin and L. Yang, *J Power Sources*, DOI:10.1016/j.jpowsour.2020.227881.

4 R. Murugan, V. Thangadurai and W. Weppner, *Angewandte Chemie - International Edition*, DOI:10.1002/anie.200701144.

5 Q. Liu, Z. Geng, C. Han, Y. Fu, S. Li, Y. bing He, F. Kang and B. Li, *J Power Sources*, DOI:10.1016/j.jpowsour.2018.04.019.

6 H. Sun, S. Kang and L. Cui, 2023, preprint, DOI: 10.1016/j.cej.2022.140375.

7 L. Chen, P. Shi, T. Gu, J. Mi, K. Yang, L. Zhao, J. Lv, M. Liu, Y.-B. He and F. Kang, *eScience*, 2024, 100277.

8 Y. Wang, P. Yan, J. Xiao, X. Lu, J. G. Zhang and V. L. Sprenkle, *Solid State Ion*, DOI:10.1016/j.ssi.2016.06.013.

9 C. Zheng, J. Su, Z. Song, T. Xiu, J. Jin, M. E. Badding and Z. Wen, *J Alloys Compd*, DOI:10.1016/j.jallcom.2022.167810.

10 C. Li, A. Ishii, L. Roy, D. Hitchcock, Y. Meng and K. Brinkman, *J Mater Sci*, DOI:10.1007/s10853-020-05221-1.

11 W. Zhang and C. Sun, *Journal of Physics and Chemistry of Solids*, DOI:10.1016/j.jpcs.2019.109080.

12 Z. Qin, Y. Xie, X. Meng, D. Qian, D. Mao, Z. Zheng, L. Wan and Y. Huang, *ACS Appl Mater Interfaces*, DOI:10.1021/acsami.2c10027.

13 N. Janani, C. Deviannapoorani, L. Dhivya and R. Murugan, *RSC Adv*, DOI:10.1039/c4ra08674k.

14 H. Zhou, Y. Zhou, X. Li, X. Huang and B. Tian, *ACS Appl Mater Interfaces*, DOI:10.1021/acsami.3c17606.

15 K. Parascos, J. L. Watts, J. A. Alarco, Y. Chen and P. C. Talbot, *RSC Adv*, DOI:10.1039/d2ra03303h.

16 S. Pratibha, N. Dhananjaya, A. Pasha and S. Khasim, *Applied Nanoscience (Switzerland)*, DOI:10.1007/s13204-020-01354-6.

17 K. Ghosh and M. Wasim Raja, *ACS Appl Energy Mater*, DOI:10.1021/acsaem.3c00291.

18 L. Dhivya, K. Karthik, S. Ramakumar and R. Murugan, *RSC Adv*, DOI:10.1039/c5ra18543b.

19 K. Ghosh and M. Wasim Raja, *Chemical Engineering Journal*, DOI:10.1016/j.cej.2023.148200.

20 W. Jeong, S. S. Park, J. Yun, H. R. Shin, J. Moon and J. W. Lee, *Energy Storage Mater*, DOI:10.1016/j.ensm.2022.10.044.

21 J. Cai, B. Polzin, L. Fan, L. Yin, Y. Liang, X. Li, Q. Liu, S. E. Trask, Y. Liu, Y. Ren, X. Meng and Z. Chen, *Mater Today Energy*, DOI:10.1016/j.mtener.2021.100669.

22 K. Liu, J.-T. Ma and C.-A. Wang, *J Power Sources*, 2014, **260**, 109–114.

23 K. Ghosh and M. Wasim Raja, *ACS Omega*, DOI:10.1021/acsomega.2c04012.

24 A. A. Hubaud, D. J. Schroeder, B. J. Ingram, J. S. Okasinski and J. T. Vaughey, *J Alloys Compd*, DOI:10.1016/j.jallcom.2015.05.067.

25 N. Lorenz, I. Gupta and T. Palberg, *Journal of Chemical Physics*, DOI:10.1063/5.0140949.

26 T. W. Heo, A. Grieder, B. Wang, M. Wood, T. Hsu, S. A. Akhade, L. F. Wan, L. Q. Chen, N. Adelstein and B. C. Wood, *NPJ Comput Mater*, DOI:10.1038/s41524-021-00681-8.

27 C. Wang, K. Fu, S. P. Kammampata, D. W. McOwen, A. J. Samson, L. Zhang, G. T. Hitz, A. M. Nolan, E. D. Wachsman, Y. Mo, V. Thangadurai and L. Hu, 2020, preprint, DOI: 10.1021/acs.chemrev.9b00427.

28 Y. Yuan, X. Peng, B. Wang, K. Xue, Z. Li, Y. Ma, B. Zheng, Y. Song and H. Lu, *J Mater Chem A Mater*, 2023, **11**, 1301–1311.

29 X. Gao, W. Yuan, Y. Yang, Y. Wu, C. Wang, X. Wu, X. Zhang, Y. Yuan, Y. Tang, Y. Chen, C. Yang and B. Zhao, *ACS Appl Mater Interfaces*, 2022, **14**, 43397–43406.

30 P. Peljo and H. H. Girault, *Energy Environ Sci*, DOI:10.1039/c8ee01286e.

31 B. Xu, W. Li, H. Duan, H. Wang, Y. Guo, H. Li and H. Liu, *J Power Sources*, 2017, **354**, 68–73.

32 C. Li, A. Ishii, L. Roy, D. Hitchcock, Y. Meng and K. Brinkman, *J Mater Sci*, 2020, **55**, 16470–16481.

33 R.-H. Shin, S.-I. Son, S.-M. Lee, Y. S. Han, Y. Do Kim and S.-S. Ryu, *Journal of the Korean Ceramic Society*, 2016, **53**, 712–718.

34 N. Janani, C. Deviannapoorani, L. Dhivya and R. Murugan, *RSC Adv.*, 2014, **4**, 51228–51238.

35 N. C. Rosero-Navarro, T. Yamashita, A. Miura, M. Higuchi and K. Tadanaga, *Solid State Ion*, 2016, **285**, 6–12.

36 X. Huang, T. Xiu, M. E. Badding and Z. Wen, *Ceram Int*, 2018, **44**, 5660–5667.

37 Z. Qin, Y. Xie, X. Meng, D. Qian, D. Mao, Z. Zheng, L. Wan and Y. Huang, *ACS Appl Mater Interfaces*, 2022, **14**, 40959–40966.

38 S. Sarkar and V. Thangadurai, 2022, preprint, DOI: 10.1021/acsenergylett.2c00003.

39 D. K. Kim, P. Muralidharan, H.-W. Lee, R. Ruffo, Y. Yang, C. K. Chan, H. Peng, R. A. Huggins and Y. Cui, *Nano Lett*, 2008, **8**, 3948–3952.

40 J. Abou-Rjeily, I. Bezza, N. A. Laziz, C. Autret-Lambert, M. T. Sougrati and F. Ghamouss, *Energy Storage Mater*, DOI:10.1016/j.ensm.2019.11.015.

41 Q. Zhao, S. Stalin, C. Z. Zhao and L. A. Archer, 2020, preprint, DOI: 10.1038/s41578-019-0165-5.

42 X. Gao, Z. Xing, M. Wang, C. Nie, Z. Shang, Z. Bai, S. X. Dou and N. Wang, 2023, preprint, DOI: 10.1016/j.ensm.2023.102821.

43 A. Tsurumaki, R. Rettaroli, L. Mazzapioda and M. A. Navarra, *Applied Sciences*, 2022, **12**, 7318.

44 H. W. Kim, P. Manikandan, Y. J. Lim, J. H. Kim, S. Nam and Y. Kim, *J Mater Chem A Mater*, 2016, **4**, 17025–17032.

45 J. Kondo, K. Otani, S. Miyamoto, H. Hikosaka, Y. Kondo, Y. Katayama and Y. Yamada, *ACS Appl Energy Mater*, 2025, **8**, 2630–2637.

46 S. A. Pervez, G. Kim, B. P. Vinayan, M. A. Cambaz, M. Kuenzel, M. Hekmatfar, M. Fichtner and S. Passerini, *Small*, DOI:10.1002/smll.202000279.

47 Z. Zhang, L. Zhang, Y. Liu, H. Wang, C. Yu, H. Zeng, L. Wang and B. Xu, *ChemSusChem*, 2018, **11**, 3774–3782.

48 A. Subhakumari, T. Thomas and N. P. B. Aetukuri, *ACS Energy Lett*, 2024, **9**, 6109–6116.

49 Y. Lu, C. Z. Zhao, J. Q. Huang and Q. Zhang, 2022, preprint, DOI: 10.1016/j.joule.2022.05.005.

50 C. Y. Yu, J. Choi, J. Dunham, R. Ghahremani, K. Liu, P. Lindemann, Z. Garver, D. Barchiesi, R. Farahati and J. H. Kim, *J Power Sources*, DOI:10.1016/j.jpowsour.2024.234116.

51 C. Plank, T. Rüther, L. Jahn, M. Schamel, J. P. Schmidt, F. Ciucci and M. A. Danzer, *J Power Sources*, DOI:10.1016/j.jpowsour.2023.233845.

52 R. Soni, J. B. Robinson, P. R. Shearing, D. J. L. Brett, A. J. E. Rettie and T. S. Miller, *Energy Storage Mater*, DOI:10.1016/j.ensm.2022.06.016.

CHAPTER 7

LLZO Fillers in Flexible Solid Electrolytes: From Paper Separators to Polymer and Paper-Polymer Systems

Summary and Graphical Abstract

Role of LLZO-based solid electrolyte as active fillers across three distinct systems studied to improve the conductivity, stability, and flexibility for next-generation lithium batteries. Firstly, Ga doped LLZO ceramic impregnated in paper-based cellulosic separator matrix using an industry-friendly dip-coating process. This composite separator membrane improves ionic conductivity and interface stability with liquid electrolyte and delivers excellent performance in a lithium-ion cell. However, the inhomogeneous fiber distribution and limited mechanical strength hindered their direct application in lithium-metal batteries. To resolve such issues, LLZO-filled dual polymer composite electrolytes are developed, which showed reduced crystallinity of polymer chain, improved Li-ion transport (~10^{-4} S/cm), and excellent electrochemical stability with Li metal batteries. Finally, a combination of paper substrated with polymer-LLZO dual matrix delivers flexible, mechanically reinforced electrolytes that synergistically combine conductivity, stability, and processability. Overall, Chapter 7 highlights that the role of LLZO fillers in paper, polymer, and paper-polymer systems provides a versatile and scalable pathway toward flexible next-generation lithium batteries.

Objectives

1. Improve the conductivity and stability of polymer electrolytes with LLZO fillers.

2. Develop a flexible, scalable composite membrane for next-generation batteries.

Strategy

LLZO fillers in paper, polymer, and paper-polymer systems.

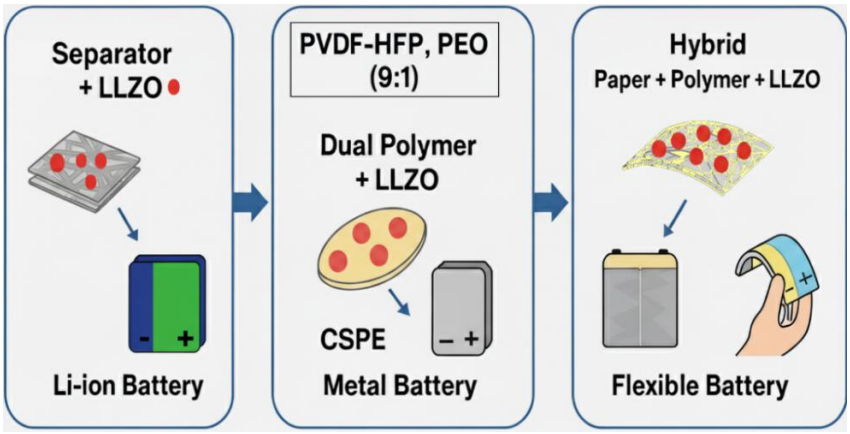

Figure 7.1 *Graphical abstract summarizing the role of solid electrolyte filler in composite membrane for next-generation batteries.*

7.1 Introduction

To mitigate environmental pollution contributed by petrol-diesel-driven transportation systems, a shift from internal combustion engines (ICE) to electric engines (EE) is imminent [1]. This typically requires powerful, long-life, and safe batteries for powering electric engines. Lithium-ion batteries (LIBs) are the first choice of energy storage systems among all other alternatives, owing to their high power and energy densities [2]. However, the major bottleneck in current LIB technology is the use of liquid electrolytes in the cell, which poses a severe threat of thermal hazard and short-circuiting, further restricting its full-scale use in electric vehicles (EVs) [3,4]. Among the other battery components, although apparently inactive, the performance and safety of LIBs heavily rely on the integrity and efficiency of the separator, an essential component that physically and electronically separates the electrodes while allowing the transport of lithium ions [5,6]. Commercially used separators, typically composed of porous polyolefins like polyethylene (PE) and polypropylene (PP), offer several advantages, such as electrochemical stability and mechanical strength. However, they exhibit shortcomings in thermal shrinkage tests, as well as display poor electrolyte wettability and high contact angle when exposed to polar organic solvents [7,8].

To address these limitations, three main strategies are explored in this chapter. Firstly, to substitute the polyolefin-based commercial separator with an eco-friendly, cost-effective, thermally stable cellulosic paper-based separator loaded with fast Li-ion conducting LLZO solid electrolyte for metal-ion batteries. The impregnation of active filler like LLZO in paper matrix using PVDF binder and DMF solvent proved superior to other inactive ceramic fillers such as Al_2O_3. Thus, this innovative approach of making paper-supported LLZO impregnated separator will pave a new pathway for the development of a sustainable, low-cost, high-performance, and safe separator for advanced LIBs.

Secondly, we developed a dual-polymer PVDF-HFP/PEO/$Li_{6.25}La_3Ga_{0.25}Zr_2O_{12}$ (LLGZO) composite solid polymer electrolyte (CSPEs) using an easily scalable solution casting method. The PVDF-HFP matrix provides mechanical robustness through its vinylidene fluoride and hexafluoropropylene units. Secondly, the PEO copolymer reduces the crystallinity of the polymer matrix, enhancing ionic conductivity. Thirdly, synthesized LLGZO acts as an active ceramic filler, aiding in the decomposition of LiTFSI and creating a fast Li^+ transport pathway. As we already know that all-solid-state lithium metal batteries (ASSLMBs) have the potential to replace the PP-based liquid system due to their enhanced safety with the use of non-flammable solid state electrolytes (SSEs) and their potential to achieve higher energy densities,

through the use of lithium metal anodes with an ultra-high theoretical specific capacity of 3860 $mAh.g^{-1}$ [9]. Among all types of solid electrolytes, CSPEs, which synergistically combine the beneficial features of both inorganic solid electrolytes and solid polymer electrolytes, are a strong candidate for the commercial viability of all-solid-state metal batteries [10].

Thirdly, developed CSPEs incorporated in paper matrix to develop paper-polymer-LLZO composites for metal batteries. LLZO-impregnated paper separators developed earlier show eco-friendliness and excellent electrochemical performance, but their intrinsic inhomogeneous fiber distribution and limited mechanical strength restrict operation in lithium-metal systems. Also, dual-polymer/LLZO composite solid electrolytes show high ionic conductivity at room temperature, but it has limited flexibility and mechanical durability. To overcome these drawbacks, a paper-polymer-LLZO composite electrolyte was developed. This reduced the structural reinforcement of cellulosic paper, the flexibility of a dual-polymer matrix, and the active ion-transport properties of LLZO fillers. The fibrous paper backbone provided a mechanically stable framework that minimized dimensional shrinkage and suppressed interfacial delamination during cycling, while its intrinsic porosity facilitated uniform infiltration of the polymer-LLZO slurry. Thus, this hybrid architecture, combined with conductivity, flexibility, and mechanical integrity, provides a versatile pathway toward practical solid-state electrolytes for advanced flexible lithium-metal batteries.

7.2 Material and electrochemical Characterization

All structural, morphological, thermal, mechanical, and electrochemical characterizations of LLGZO powders and composite membranes were performed using standard techniques (XRD, FESEM, TGA/DTA, UTM, EIS, LSV, and full-cell testing) as described in ***Chapter 2***, ***Section 2.6*** and ***Section 2.7***. Only the key results are presented here.

7.3 Paper-based composite membrane

The separator plays an important role in the electrochemical performance and safety of rechargeable batteries. Its primary role is to physically isolate the electrodes while allowing facile ionic transport and blocking electronic conduction. Conventional, widely used polyolefin separators suffer from poor wettability, limited thermal resistance, and safety concerns under high-current operation. In this context, cellulosic paper has gained attention as a low-cost, eco-friendly, and thermally stable substrate owing to its abundant porosity and excellent electrolyte uptake. However, pristine paper has limited performance at high current density and lower

mechanical strength for reliable use in advanced battery systems. To address these shortcomings, ceramic fillers have been introduced into the paper matrix, but most fillers (e.g., Al_2O_3) act only as passive stabilizers without contributing to ion transport. In comparison, Ga-doped LLZO solid electrolyte is an ion-conductive ceramic which offers fast Li-ion conduction pathways, wide electrochemical stability, and robust interfacial compatibility. By impregnation of 30wt% LLGZO in cellulose matrix, the present study aims to transform the paper substrate from a passive separator into a high-performance separator.

7.3.1 Fabrication of Paper based Composite Membrane

Ga-doped LLZO (LLGZO) was synthesized via alanine-assisted auto-combustion (details in ***Chapters 2, Section 2.3.2***), calcined at 900 °C, and incorporated into cellulose paper (20 µm, ~65% porosity) using a roll-to-roll dip-coating process (***Chapter 2, Section 2.5.1***). A slurry of 5 wt% PVDF in NMP with 30 wt% LLGZO was prepared and coated on both sides of the paper, followed by in-line drying and compaction. The final LLGZO-incorporated paper separator, designated as G03, exhibited a uniform thickness of 20 ± 2 µm. For comparison, a control separator containing 30 wt% Al_2O_3 (A03) and an uncoated base paper were also prepared by the same procedure.

7.3.2 Results and Discussion

7.3.2.1 Microstructural analysis

The microstructural characteristics of the fabricated paper separators were characterized using FESEM and EDX to understand the effect of Ga-doped LLZO impregnation in the cellulose matrix. ***Figures 7.2(a)-(d)*** present the surface morphology of cellulose paper modified with 30 wt% Ga-LLZO and Al_2O_3 material. The pristine paper shows a random network of cellulose fibers with abundant pore channels, as shown in ***Figures 7.3(a)-(b)***. After impregnation, Ga-LLZO particles are clearly observed on the fiber surfaces and at inter-fiber junctions. The particles are not uniformly distributed but appear in the form of agglomerates. This is consistent with the electrostatic repulsion between negatively charged cellulose fibers and LLZO particles. While such clustering partially blocks open pores, the ceramic domains establish ion-conducting sites that can directly contribute to Li-ion transport. Compared to Al_2O_3-filled papers, the Ga-LLZO impregnated sample displays larger clusters, reflecting the higher surface energy and stronger interaction tendency of LLZO particles.

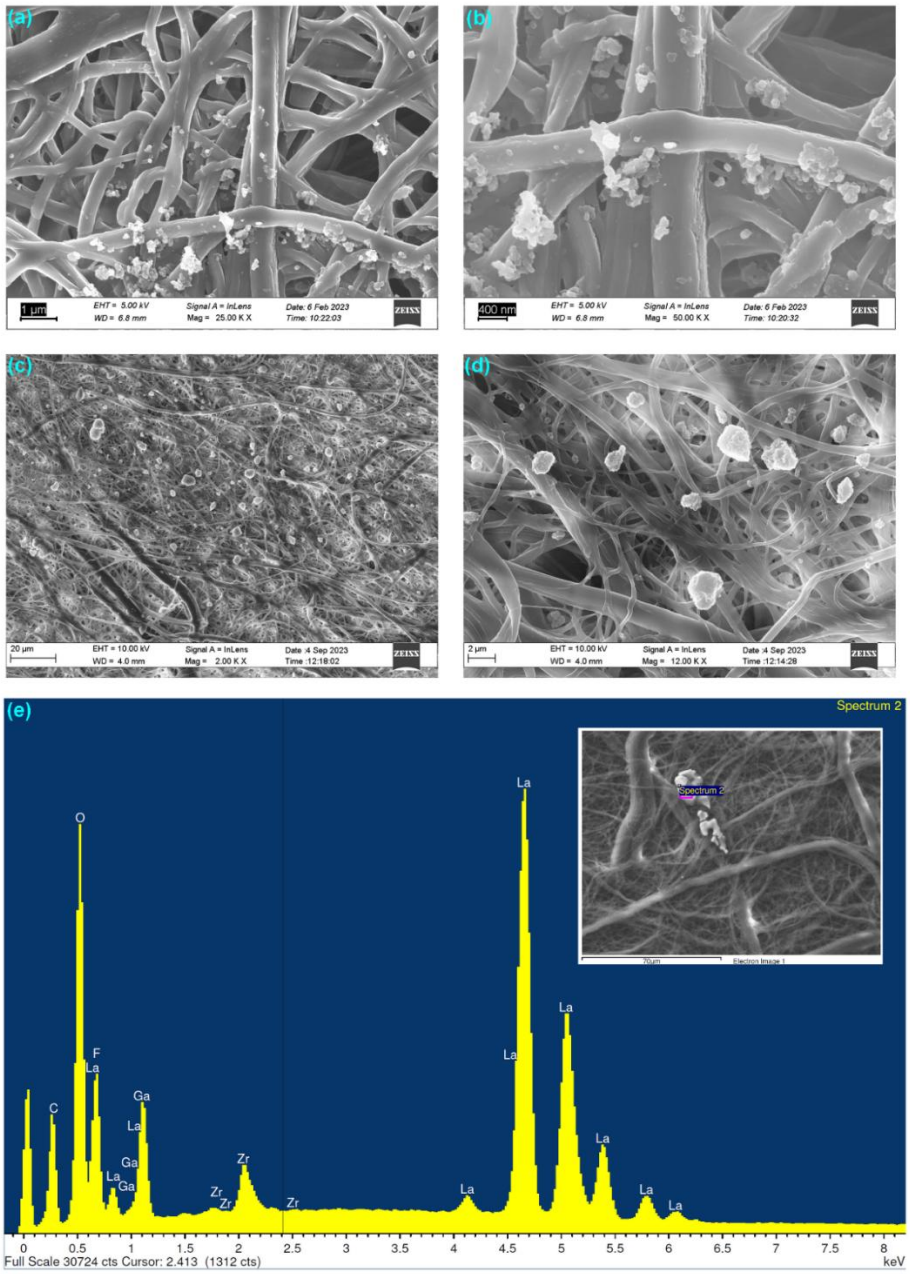

Figure 7.2 *FESEM micrograph of (a)-(b) G03 and (c)-(d) A03 at two different scales. (e) Corresponding EdX of Ga doped LLZO (G03) incorporated paper separator.*

While impregnating Al_2O_3 nanoparticles into the cellulose paper as shown in ***Figures 7.2(c)-(d)***, the overall distribution pattern was found to be similar to that of Ga-LLZO fillers. However, the size of the agglomeration was smaller. To better understand these interactions, it is essential to correlate them with the surface properties of both the filler and the paper substrate. The zeta potential can be a crucial insight into the colloidal stability of the dispersions in a matrix. The aqueous suspension of pure cellulose paper generally showed a highly negative zeta potential of -37.6 mV, which confirmed its negatively charged surface. Similarly, Ga-

LLZO powder shows a negative zeta potential of >-20 mV, which suggests its Lewis base character. Since both the cellulose fibers and LLZO particles carry negative charges, strong electrostatic repulsion occurs during slurry preparation and coating. This leads to a non-uniform diposition of agglomerates within the cellulose matrix. It is observed that the zeta potential values above 30 mV suggest stable dispersions with well-separated particles. Also, the values below 5 mV result in rapid aggregation. In the intermediate range (5-30 mV), partial agglomeration is expected. This was also consistent with the morphology observed in our FESEM analysis. In comparison, alumina nanoparticles are known to show a lower negative zeta potential. This also reduces their repulsion with cellulose fibers and favors the formation of smaller but randomly distributed agglomerates.

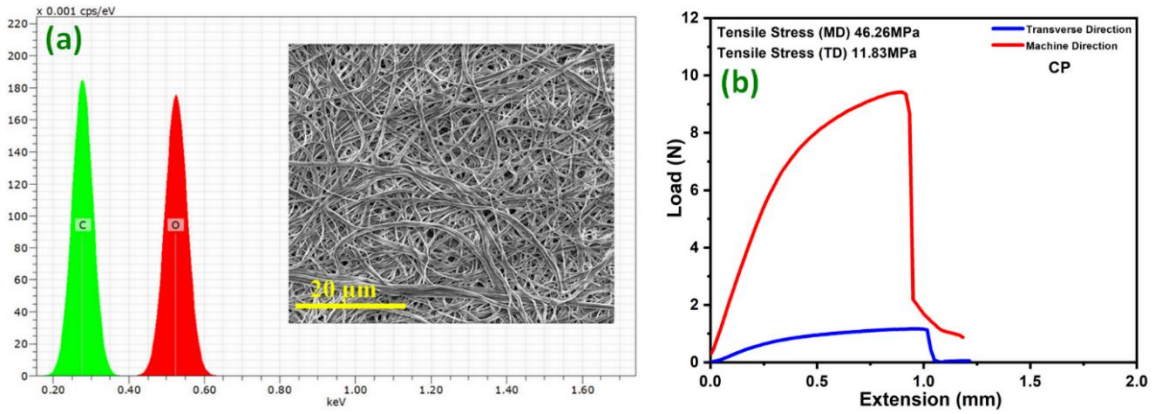

Figure 7.3 *(a) FESEM and corresponding EDX of commercial and cellulose paper and (b) Tensile strength at machine direction and transverse direction of commercial cellulose paper (CCP).*

The presence of Ga-LLZO in the paper matrix was confirmed by EDX analysis, as shown in ***Figure 7.2(e)***. Distinct peaks corresponding to La, Zr, Ga, and O show the successful incorporation of G03 in the paper matrix. Along with this, C and F signals were also shown which originate from the PVDF binder. These observations confirm that the Ga-LLZO particles are incorporated in the surface as well as the paper network, which might ensure their functional role in ionic conduction and mechanical reinforcement.

In summary, microstructural analysis confirms that Ga-LLZO particles are successfully incorporated into the cellulose paper. It forms agglomerated but well-adhered domains across the fiber network. Despite partial heterogeneity, the ceramic domains provide active ion-conducting channels, while their presence reinforces the weak fiber junctions. This might improve the electrochemical and mechanical properties compared to base paper.

7.3.2.2 Mechanical, Air permeability, Electrolyte wettability Studies

Mechanical integrity is a vital requirement for battery separators to withstand the stresses involved in electrode stacking and winding during cell fabrication. The tensile stress–strain curves of the paper separators are presented in ***Figures 7.4(a)*** and ***(b)*** for the machine direction (MD) and transverse direction (TD), respectively. As expected, the pristine cellulose paper (CCP) displayed strong anisotropy, with tensile strength values of 46.26 MPa in MD and only 11.83 MPa in TD as shown in ***Figure 7.3(b)***. The incorporation of ceramic fillers significantly improved the transverse strength, as shown in ***Figure 7.4(b)***. The Ga-LLZO (G03) and Al_2O_3 (A03) impregnated papers showed nearly a two-fold increase compared to CCP, as summarized in ***Figure 7.4(c)***. It is worthy to discuss here that the tensile stress in the MD remained almost constant in the range of 45-52 MPa as shown in ***Figure 7.4(b)*** and ***Figure 7.4(a)***. This improvement might be due to the synergistic role of the PVDF binder and ceramic particles with stronger inter-fiber adhesion and hydrogen bonding within the cellulose matrix.

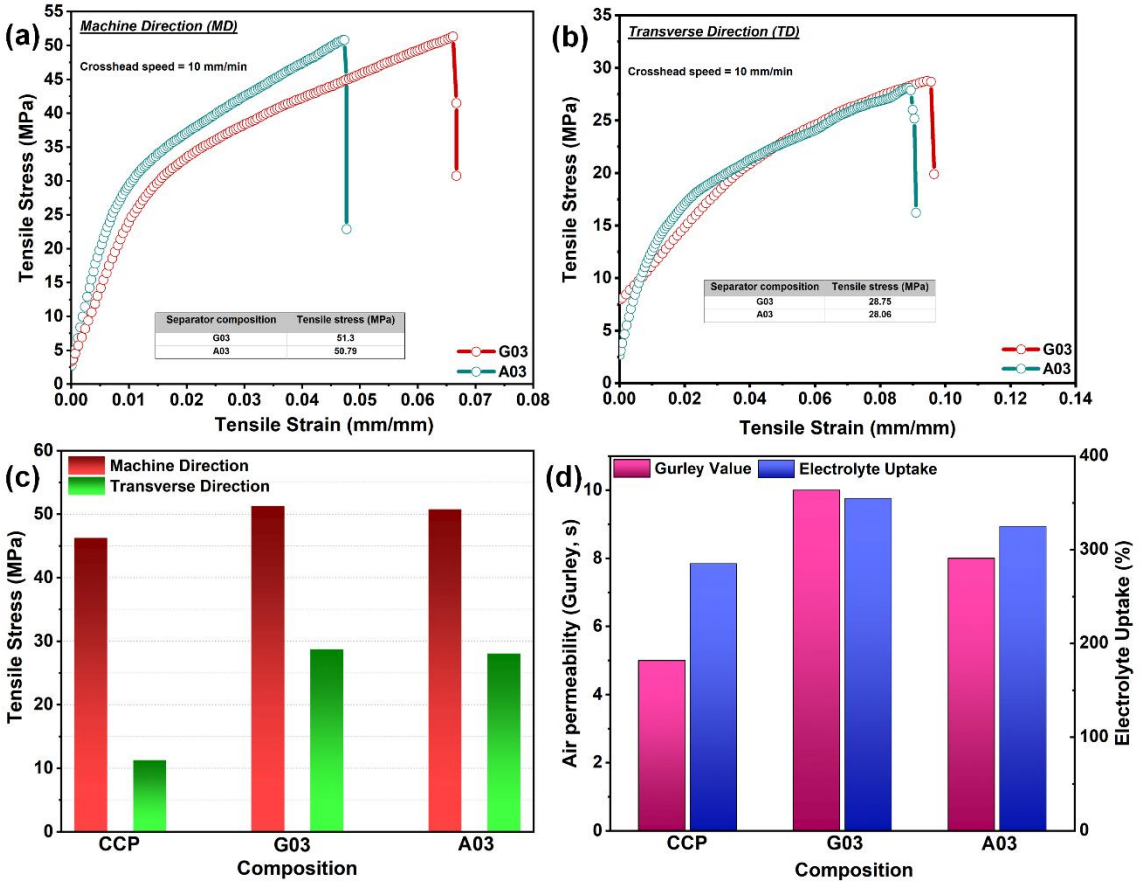

Figure 7.4 *Mechanical, air permeability, and electrolyte uptake properties of paper separators. (a) stress-strain curve in machine direction (MD) and (b) transverse direction (TD) for Ga-LLZO impregnated paper (G03) and Al_2O_3 impregnated paper (A03), (c) comparison of tensile*

strengths in MD and TD for commercial cellulose paper (CCP), G03, and A03, (d) Gurley value (air permeability) and liquid electrolyte uptake capacity of CCP, G03, and A03 separators.

Air permeability is generally assessed by the Gurley value. This provides an indication of how fast a separator can soak liquid electrolytes through the separator pores. As shown in ***Figure 7.4(d)***, the commercial cellulose paper recorded a low Gurley value of 5 s, which reflects its highly porous structure. After modification with filler particles, G03 and A03 show slightly higher values (~8-10 s), suggesting that although filler agglomerates partially occupy pore spaces. However, the overall permeability remains high for all the separators. Thus, ceramic loading does not significantly compromise the open porous architecture of the paper matrix.

Electrolyte uptake is another crucial parameter that determines separator wettability and liquid retention. Owing to the hydrophilic nature of cellulose, CCP absorbed more than ~285% electrolyte relative to its dry weight, as summarized in ***Figure 7.4(d)***. Both G03 and A03 retained high absorption capacities of ~355% and 325% respectively. The strong electrolyte affinity of the cellulose matrix, together with the active contribution of Ga-LLZO particles, ensures efficient ion conduction pathways and improved electrode–electrolyte contact during cycling.

7.3.2.3 Electrical Studies

The function of a separator is not just to prevent direct contact between anode and cathode, but rather it directly impacts the lithium-ion transport properties and consequently, the overall performance and safety of the cell. So, it's important to measure the lithium-ion transport properties of all the developed separators along with the commercial cellulose separator. ***Figure 7.5(a)*** represents the EIS spectra of electrolyte-soaked LLZO and Al_2O_3-coated paper separators along with commercial cellulose separators, measured using symmetrical blocking electrodes (SS). The corresponding equivalent circuit is also given in the inset of ***Figure 7.5(a)***. All the EIS spectra of different separators show a straight-line profile describing the characteristic behaviour of electrode-electrolyte double-layer capacitance. At the lower frequency region, the intercept on the real axis gives the bulk resistance value. The bulk resistance values extracted from the intercepts correspond to conductivities of 2.14 $mS \cdot cm^{-1}$ for CCP, 1.36 $mS \cdot cm^{-1}$ for G03, and 0.73 $mS \cdot cm^{-1}$ for A03. The relatively high conductivity of the pristine cellulose paper arises from its strong hydrophilicity and large electrolyte uptake capacity. Upon ceramic impregnation, the conductivity decreases slightly due to partial pore

blocking. However, these values suggest that the inclusion of Li-ion active LLZO in the paper matrix is showing significantly higher ionic conductivities compared to inactive Al_2O_3. The insulating nature of Al_2O_3 particles in A03 may thus contribute to offering higher resistance, which may limit its overall electrochemical effectiveness.

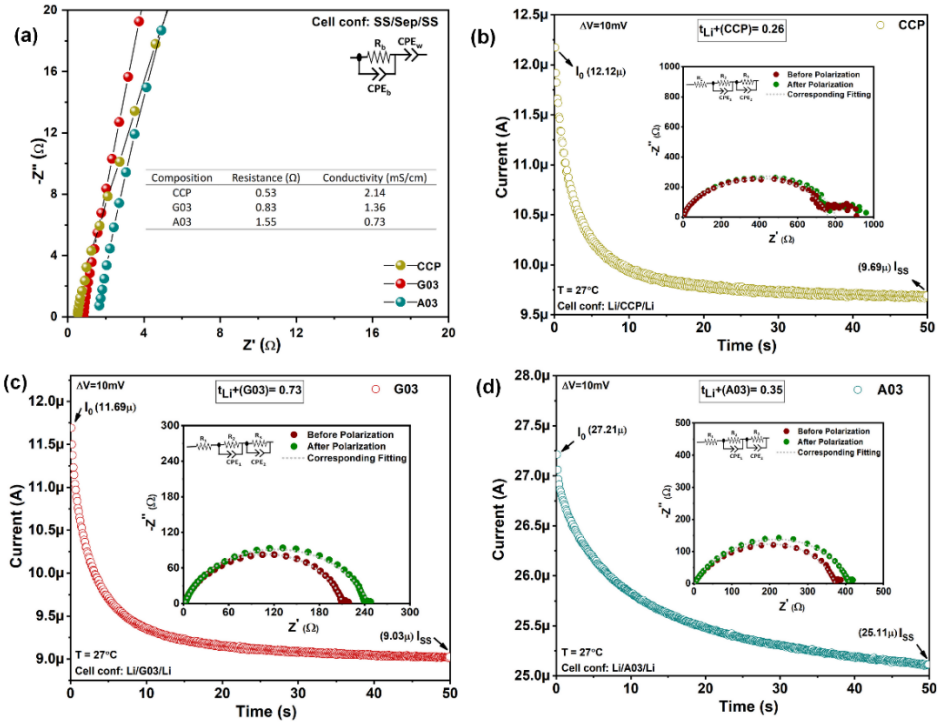

Figure 7.5 *(a) Nyquist plots of electrolyte-soaked cellulose paper (CCP), Ga-LLZO impregnated paper (G03), and Al_2O_3 impregnated paper (A03) measured with stainless steel blocking electrodes. (b-d) DC polarization profiles with corresponding impedance spectra before and after polarization for CCP, G03, and A03, respectively, used to calculate Li^+ transference numbers.*

The understanding of transport phenomena through lithium-ion transference number is essential as it describes the ion transport efficacy, reduction of concentration polarization, which in turn enhances the cycle life and power density of a battery. ***Figures 7.5(b)-(d)*** represent the DC polarization curve along with the EIS spectra before and after polarization, and their corresponding equivalent circuit is displayed in the inset for specimens CCP, G03, and A03, respectively. Lithium-ion transference number calculated using Bruce-Vincent-Evans equation as described by equation 5 and found to be 0.61 for CPP, 0.35 for A03, and 0.73 for G03 separators. This variation in transference number mainly arises due to the combined effects of the LLZO-coated separator matrix and its mutual interaction with the liquid electrolyte. The LLGZO coating on the paper separator modifies the ion transport pathways by influencing Li-

ion selectivity at the interface. A localized space-charge region at the liquid-solid interface is formed, which directly impacts the overall lithium-ion transportation. However, such benefit is absent in Al_2O_3 coated paper-based, as well as in commercial cellulose separator

Taken together, these results indicate that Ga-LLZO impregnated paper separators strike a balance between conductivity and selectivity. However, the conductivity of CCP is higher due to open pore space and high electrolyte uptake. But, low transference number may limits its practical utility. The incorporation of Ga-LLZO here not only improves structural robustness but also significantly enhances Li^+ transport efficacy. This might be a crucial factor for stable electrochemical performance in electrochemical full cells.

7.3.2.4 Electrochemical Studies

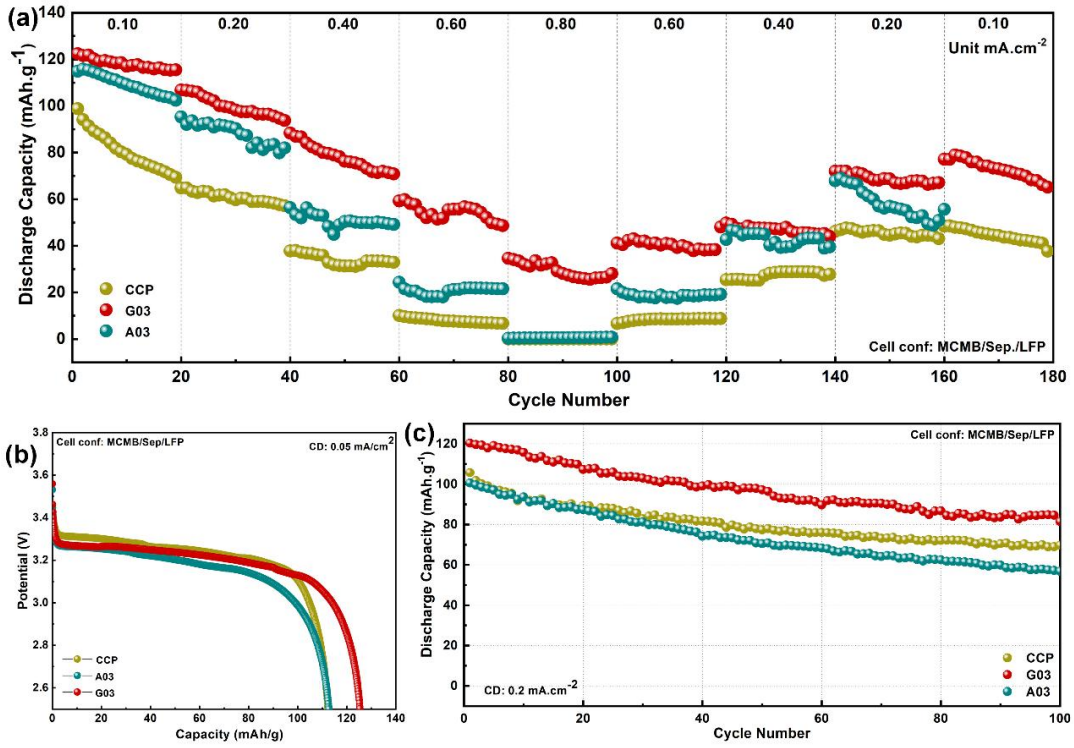

Figure 7.6 *Full-cell electrochemical performance of MCMB/LFP cells assembled with commercial cellulose paper (CCP), Ga-LLZO impregnated paper (G03), and Al_2O_3 impregnated paper (A03) separators. (a) rate performance at varying current densities (0.10–0.80 mA.cm^{-2}), (b) Typical charge-discharge voltage profiles at 0.05 mA.cm^{-2}, (c) cycling stability at 0.20 mA.cm^{-2} for 100 cycles.*

The practical applicability of ceramic impregnation in paper separators was further studied by fabricating MCMB/LFP full cells with CCP, G03, and A03 membranes. The rate performance

of these cells, tested over a wide current density range (0.10-0.80 $mA.cm^{-2}$), is shown in ***Figure 7.6(a)***. The discharge capacity decreased with increasing current densities and partially recovered when the current was stepped back down. Among all samples, the G03-based cell delivers the best capacity retention at higher current density. It maintains more than 20% of its capacity even at 0.80 $mA.cm^{-2}$. In comparison, CCP and A03 showed no retention at that current density. Thus, the superior behavior of G03 might be due to its enhanced Li^{+} transference number and stable electrode-electrolyte interface. This successfully helps to suppress the concentration polarization at higher current densities. Similarly, during step-up current densities, G03 delivers better reversibility as compared to A03 and CCP.

The typical charge-discharge voltage profiles at 0.05 $mA.cm^{-2}$ are displayed in ***Figure 7.6(b)***. All separators delivered well-defined plateaus characteristic of LFP redox chemistry. The G03 separator achieved a discharge capacity of 125.40 $mAh.g^{-1}$, which is higher than A03 (112.73 $mAh.g^{-1}$) and comparable to CCP (112.35 $mAh.g^{-1}$). This indicates that Ga-LLZO impregnation enhances ion transport thanks to the interface stabilization with the electrode.

The cycling stability of the cells at 0.20 $mA.cm^{-2}$ is presented in ***Figure 7.6(c)***. The G03-based cell delivered the most stable performance, with a capacity decay of only ~30% after 100 cycles, whereas CCP and A03 showed much larger losses of ~34% and ~44%, respectively. Importantly, the G03 separator still delivered ~84 $mAh.g^{-1}$ discharge capacity after 100^{th} cycles. In comparison, A03 and CCP deliver only ~70 and 57 $mAh.g^{-}1$ capacity. These results clearly suggest that Ga-LLZO enhances the Li-ion conduction pathways that eventually extend cycling life and high initial discharge capacity. However, the inert Al_2O_3 filler improves the mechanical robustness but lacks ionic activity, and as a result, faster capacity degradation is observed.

Overall, the full-cell studies demonstrated that the Ga doped LLZO impregnated paper separators significantly outperform commercial cellulose and Al_2O_3-loaded membranes in terms of rate capability and cycling stability. The findings highlight the importance of active ceramic fillers in enabling cellulose-based separators for high-performance lithium-ion batteries.

7.3.3 Limitation and Perspective

Although Ga-doped LLZO incorporated paper separators deliver improved electrolyte wettability, ionic conductivity, high lithium-ion transport efficacy, and better electrochemical performance compared to base paper and Al_2O_3 coated membranes, their application remains

restricted to liquid electrolyte-based lithium-ion cells. The inhomogeneous fiber distribution and limited mechanical strength of the cellulose matrix prevented their successful integration into lithium-metal systems. Because lithium dendrites easily penetrate through the modified matrix. The paper-based separators serve primarily as an eco-friendly and sustainable alternative solution in the liquid system, rather than a viable option for solid-state lithium-metal batteries. This limitation motivated the development of polymer-based and polymer-paper composite electrolytes discussed in the subsequent sections.

7.4 Composite solid polymer electrolyte (CSPE) membrane

The Ga doped LLZO impregnated paper separator delivers excellent full cell performance in lithium-ion cells. However, Cellulose suffers from inherent drawbacks, including fiber non-uniformity, anisotropic mechanical behavior, and limited interfacial compatibility with lithium metal anodes, which hinder its suitability for advanced metal battery applications. Thus, we need a more robust, flexible, and ion-conductive framework that is capable of accommodating active ceramic fillers with better stabilization with Li metal. Composite solid polymer electrolytes (CSPEs), consisting of polymer matrices reinforced with garnet-type fillers, offer a promising route to overcome the inherent limitations of conventional polymer systems. In this study, dual-polymer CSPEs incorporating Ga-doped LLZO were designed to leverage the mechanical robustness of PVDF-HFP, the ionic conductivity of PEO, and the active contribution of LLZO fillers. Their structural, electrical, and electrochemical properties are discussed in the following section.

7.4.1 Preparation of CSPE membrane

PVDF-HFP/PEO/LLGZO-based CSPEs were prepared via solution casting (PVDF-HFP:PEO = 9:1, LiTFSI as salt). LLGZO (calcined at 900 °C) was incorporated at 0, 5, 10, and 15 wt% (designated LZ00, LZ05, LZ10, LZ15). For comparison, a PVDF-HFP-only CSPE (PL00) was also fabricated. The membranes showed a uniform thickness of ~40 μm, and reproducibility was confirmed across multiple batches. The detailed preparation procedure was discussed in ***Chapter 2***, ***Section 2.5.2***.

7.4.2 Results and Discussion

7.4.2.1 Structural and Thermal Studies

Figure 7.7(a) and ***(b)*** describe the TGA and DTA profiles of PL00, LZ00, and LZ10 CSPEs in an air atmosphere from RT to 800°C. For PL00, the initial weight loss of ~5 wt% was observed from RT to 400°C. Whereas LZ00 and LZ10 showed higher weight loss ~20 wt% from RT to 320°C, which can be attributed to the decomposition of PEO and/or residual solvent trapped within the polymer matrix. A sharp decrease in weight loss is observed for all the samples, which might be due to the decomposition of the PVDF-HFP polymer matrix [21]. At the end of this decomposition process, at ~600-675°C, PL00, LZ00, and LZ10 show 98%, 93%, and 90% weight loss, respectively. In DTA profiles, the presence of an exothermic peak at 339°C for LZ00 and LZ10 CSPEs suggests the decomposition of the PEO chain in the PVDF-HFP polymer matrix. Whereas, peaks ~520-540°C represent the decomposition of the PVDF-HFP polymer chain, which appears in all the CSPEs. The peak at 679°C for LZ10 might be due to the interaction between the inorganic LLGZO particle and any organic species.

Figure 7.7(c) shows the X-ray diffraction pattern of PL00, LZ00, and LZ10 CSPEs along with the JCPDS file of cubic LLZO (PDF 00-064-0141). A broad peak centered at ~20° is visible in all the samples, which is characteristic of amorphous PVDF-HFP polymer [22,23]. Although the peak corresponding to PEO polymer in LZ00 and LZ10 (both containing 10 wt% % of PEO) is not visible clearly, or may be overlapping with the broad peak of PVDF-HFP. The major characteristics peaks of cubic LLZO are clearly seen in the LZ10 CSPEs, demonstrating the successful incorporation of crystalline LLGZO particles in the dual polymer matrix. The crystallinity index (CI) of PVDF-HFP characteristics peaks at ~20°, as calculated from *equation 1* or *equation 2*, has been found to be 37.20% for PL00, 33.65% for LZ00, and 28.54% for LZ10 (variation shown in ***Figure 7.7(f)***). So, the reduction in crystallinity in the dual polymer matrix enhances the fraction of amorphous regions in the polymer matrix. As a result, the segmental motion of polymer chains may facilitate Li^+ hopping more effectively[14,24,25]. ***Figure 7.7(d)*** presents the FTIR spectra of PL00, LZ00, and LZ10 in the wavenumber range of 1000-400 cm^{-1}. No significant change in bond vibration is observed after incorporation of PEO and LLGZO in the PVDF-HFP matrix. The transmittance peaks are identified at 949, 878, 836, 813, 791, 762, 739, 674, 616, 601, 570, 510, 481, 431, and 407 cm^{-1} mainly indicated the typical stretching and bending vibrations of -CF_2, -CH_2, and -C-O-C- groups from PVDF-HFP and PEO, along with lattice vibrations from the cubic LLGZO phase [26–29]. The absence of any additional peaks or major peak shifts suggests that their addition does not lead to any new chemical bond formation. However, the physical interaction within the polymer matrix is changed. The reduced intensity of crystalline polymer bands in the FTIR spectra further

supports enhanced polymer chain segmental motion, which may improve the electrical and electrochemical properties of CSPE.

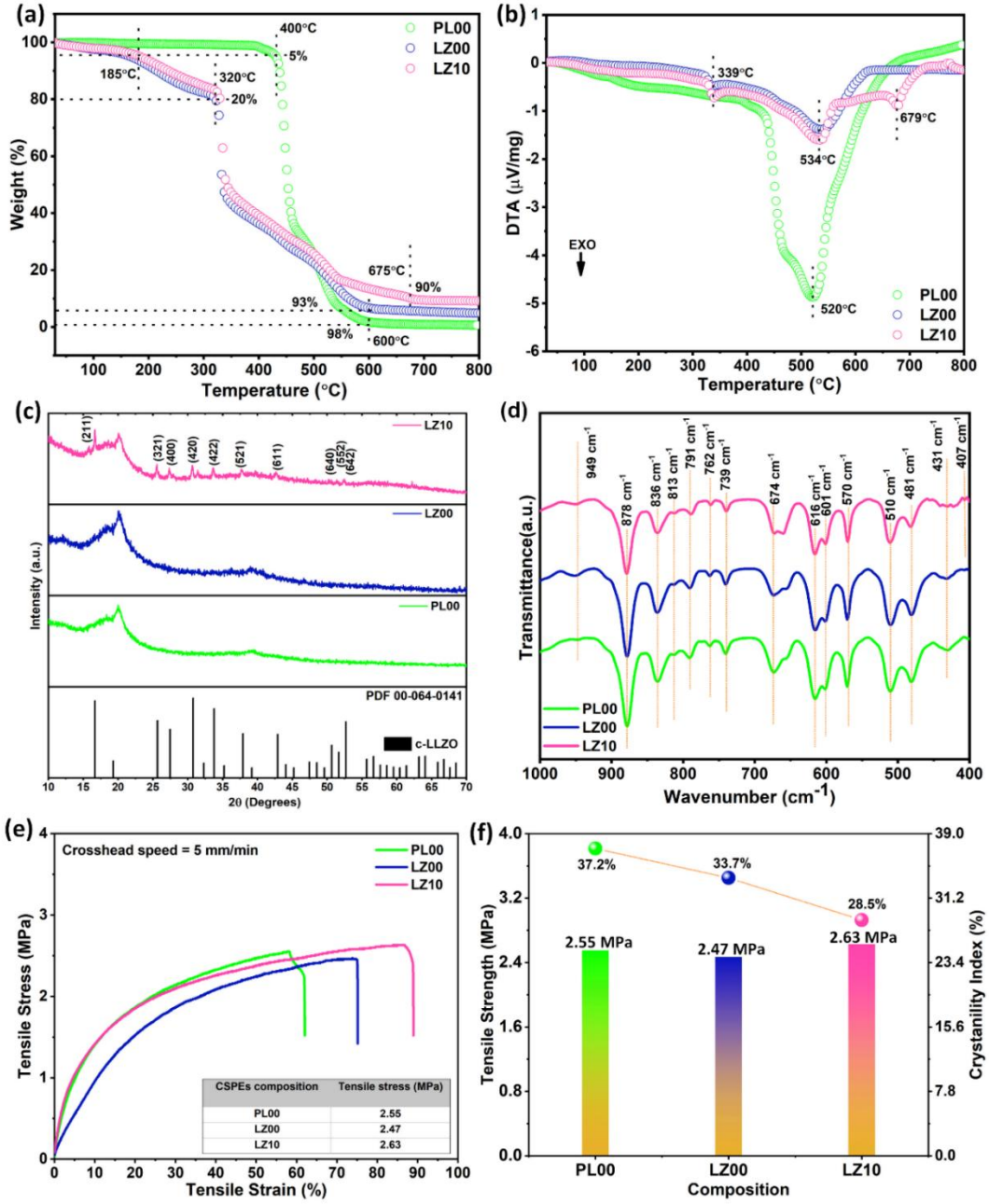

Figure 7.7 *(a) TGA and (b) DTA thermographs of PL00, LZ00, and LZ10 CSPEs from RT to 800°C. (c) X-ray diffractograms of PL00, LZ00, and LZ10 CSPEs along with the JCPDS file of cubic LLZO. (d) FTIR spectra of PL00, LZ00 and LZ10 CSPEs. (e) Tensile strength Measurement of developed CSPEs. (f) Variation of mechanical properties and crystallographic index of PL00, LZ00, and LZ10.*

7.4.2.2 Mechanical and Microstructural Studies

Figure 7.7(e) represents the tensile stress vs strain plot of PL00, LZ00, and LZ10. The samples for mechanical testing were cut from different parts of the developed CSPEs to check the homogeneity of the films as well as the reproducibility of the test results. It is observed that the incorporation of PEO in the PVDF-HFP matrix reduces the tensile strength from 2.55±0.20 MPa to 2.47±0.15 MPa. Although after adding 10 wt% of LLZO in the dual-polymer system, the tensile strength is found to be 2.63±0.20 MPa. The variation of mechanical strength and crystallinity index of PL00, LZ00, and LZ10 is shown in ***Figure 7.7(f)***. Thus, the addition of PEO and LLZO successfully increases the amorphous nature of PVDF-HFP, which might help to increase the ionic conduction through the strong electrostatic interaction of the PVDF-HFP chain. Thus, from X-ray diffraction patterns, FTIR spectra, tensile strength measurement, and thermal profile, it is clearly seen that the addition of PEO and LLGZO in PVDF-HFP matrix has a profound effect on the structural, mechanical, and thermal properties of CSPEs.

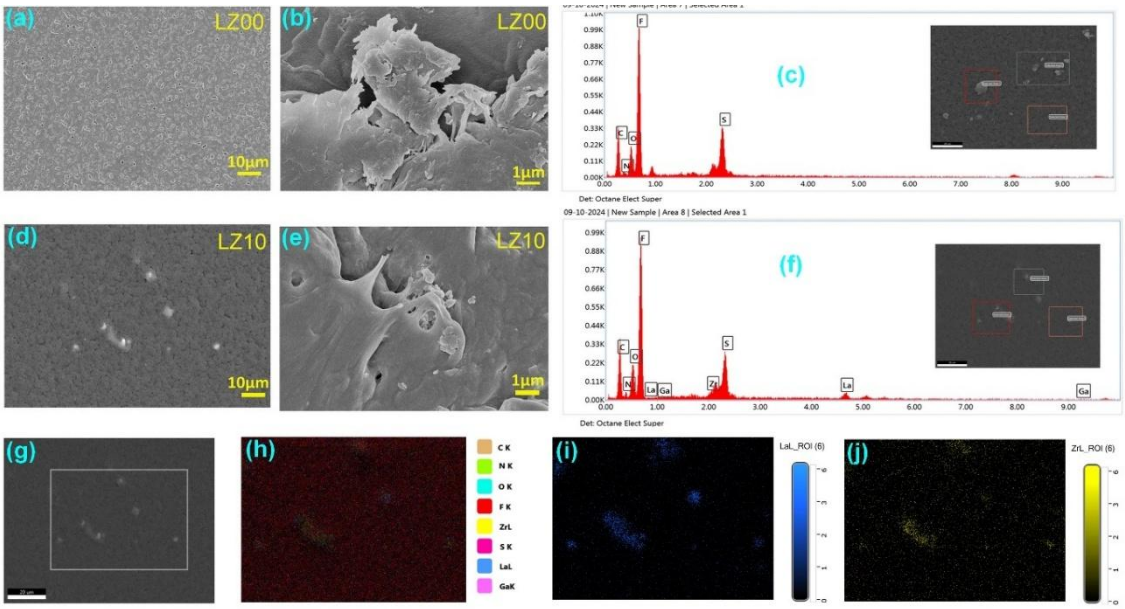

Figure 7.8 *FESEM images of LZ00 CSPEs (a) at the top surface and (b) near the edge section. (c) EdX spectrum of LZ00 CSPEs. FESEM images of LZ10 CSPEs (d) at the top surface and (e) near the edge section. (f) EdX spectrum of LZ10 CSPEs, (g) elemental mapping of the selected region in LZ10, (h) elemental mapping of all elements present in the CSPE. Distribution of (i) and (j) Zr in the developed CSPEs.*

Figures 7.8(a) and ***(b)*** show the FESEM micrographs of LZ00 CSPE at two different scales at the top surface and at the near edge section, respectively. The morphology appears more porous and less dense. The corresponding EdX spectrum is shown in ***Figure 7.8(c)***, which describes the presence of different organic species along with the N, F, and S from LITFSI.

Similarly, ***Figures 7.8(d)*** and ***(e)*** represent the FESEM of LZ10 CSPE at two different scales at the top surface and at the near edge section, respectively. The morphology here appears denser and smoother than that of LZ00. The agglomeration of the LLGZO particles is also clearly seen at the top and edge sections. The corresponding EdX spectrum of LZ10 is shown in ***Figure 7.8(f)***. The presence of La, Zr, and Ga elements in LZ10 CSPEs describes the presence of LLGZO particles. Elemental mapping analysis of LZ10 CSPEs, shown in ***Figures 7.8(g)-(j)***, provides further evidence of filler incorporation in the dual polymer matrix. The FESEM micrograph in ***Figure 7.8(g)*** highlights the analysed region. However, in the combined elemental map in ***Figure 7.8(h)*** shows the spatial distribution of C, N, O, F, S, La, Zr, and Ga across the polymer matrix. Individual La and Zr maps (***Figures 7.8(i)*** and ***(j)***) confirm the dispersion of LLGZO within the polymer host. This homogeneous distribution ensures improved polymer-ceramic contact and the formation of better Li^+ transport pathways. Thus, the structural, mechanical, thermal, and microstructural analyses demonstrate that the incorporation of PEO and LLGZO significantly influences the crystallinity, thermal stability, and microstructure of the CSPEs, which surely impact their overall electrical and electrochemical performance in lithium metal batteries.

7.4.2.3 Electrical Studies

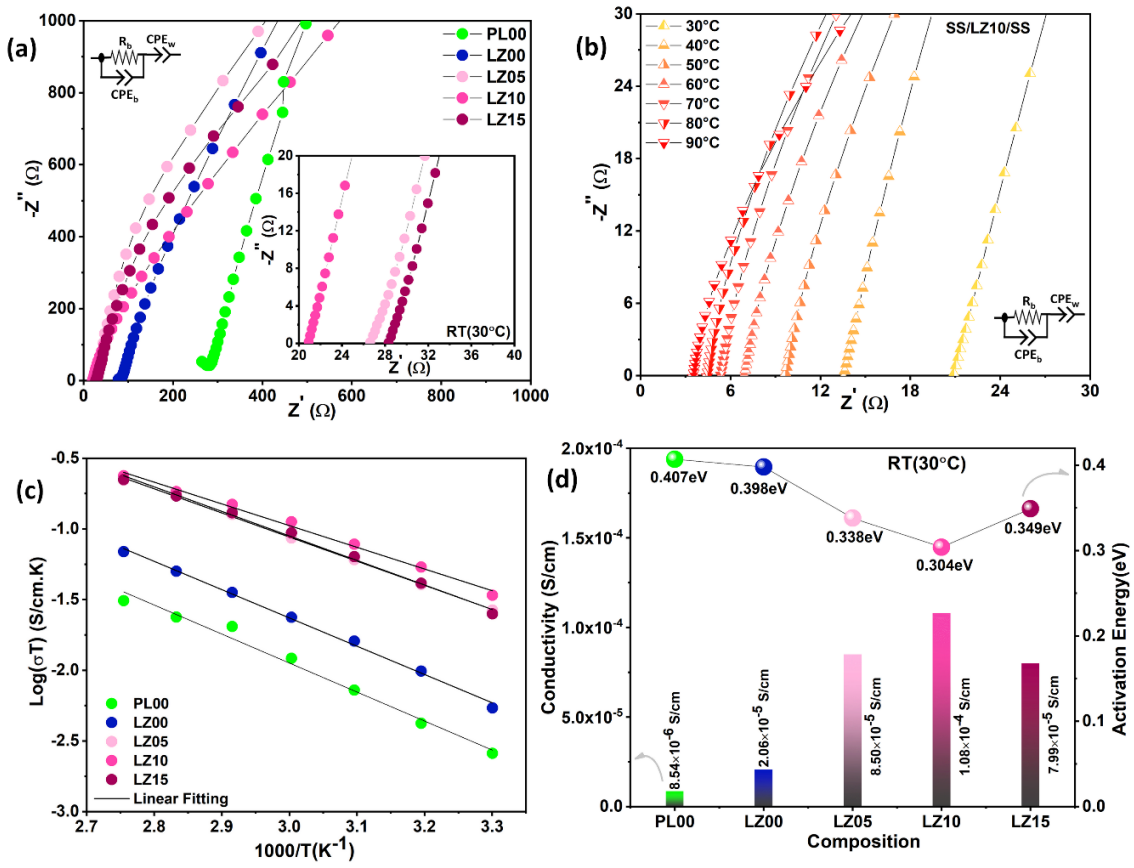

Figure 7.9 *(a) Nyquist plot of PL00, LZ00, LZ05, LZ10, and LZ15 composite solid polymer electrolytes (CSPEs) at room temperature (30 °C). (b) Electrochemical impedance spectra of LZ10 at various temperatures. (c) Arrhenius plots of PL00, LZ00, LZ05, LZ10, and LZ15 CSPEs showing temperature dependence of ionic conductivity for activation energy determination. (d) Variation of room-temperature ionic conductivity (left axis) and corresponding activation energy (right axis) for developed CSPEs.*

The ionic conductivities of PL00, LZ00, LZ05, LZ10, and LZ15 are measured using two SS ion blocking electrodes in both sides of the CSPEs that are cut from several portions of the films to confirm the homogeneity. ***Figure 7.9(a)*** represents the Nyquist plot along with the equivalent circuit, where Rb and CPE represent the bulk electrolyte resistance of CSPEs and constant phase elements, respectively. The resistance components are almost similar for all the samples for a particular composition of CSPE. The ionic conductivities as calculated from equation 3 are found to be 8.54×10^{-6}, 2.06×10^{-5}, 8.50×10^{-5}, and 1.08×10^{-4} and 7.99×10^{-5} S/cm at RT for PL00, LZ00, LZ05, LZ10, and LZ15 CSPEs respectively. Thus, 10 wt% addition of PEO in PVDF-HFP matrix (LZ00) successfully enhanced the overall ionic conductivity and reached a maximum value of 2.06×10^{-5} S/cm. It is crucial to mention here that the concentration of PEO was varied in the range of 5-20% of the total polymer and the ionic conductivity increased with the increase in the PEO content as PEO provides higher conductivity than PVDF-HFP [21,30]. However, where PVDF-HFP's crystallinity provides its high mechanical strength, the introduction of PEO disrupts the crystalline network, reducing the overall degree of crystallinity. Also, PEO acts as a plasticizer for the PVDF-HFP base matrix, that get between the polymer chains, increasing their segmental mobility and reducing the glass transition temperature [31,32]. These are the reasons that with the increase in PEO content with respect to PVDF-HFP, softer and less rigid composite polymer systems are developed. For longer cycle life and stable electrochemical operations, both high ionic conductivity and good mechanical integrity are required. Thus, from the pivotal experimental observations and the recent literature survey [33], the 9:1 ratio of PVDF-HFP and PEO has been chosen for the development of LLGZO and dual-polymer based CSPE systems. It is reported that the presence of PEO chains enhances the Li-salt dissociation and creates dynamic coordination sites, which further accelerate the Li^+ transportation in the polymer matrix[21,31]. Whereas the local ordered domain of PVDF-HFP was further disrupted by the addition of LLGZO particles due to strong Lewis acid-base interactions with the polymer chains. This also reduces the crystalline index as found earlier and creates interfacial conduction pathways more effectively. This combined effect

synergistically increases ionic conductivity for LZ10 samples. The LLGZO loading was optimized at 0, 5, 10, and 15 wt% to balance ionic conductivity, film processability, and interfacial stability. It is observed that at a higher filler content(>15wt%), LLGZO particles agglomerated and led to microstructural inhomogeneity, poor casting quality, and brittle membranes that increased interfacial polarization. On the other hand, for very low loadings (<5 wt%), the effect of LLGZO on disrupting polymer crystallinity and enhancing ionic conductivity was negligible. The intermediate range, i.e., at 5 to 15 wt%, was therefore selected to systematically evaluate the influence of filler concentration. In this study,10 wt% (LZ10) is the optimum concentration, which is consistent with the literature[30,34,35]. At this concentration, agglomeration was minimized, fillers were well dispersed within the PVDF-HFP/PEO matrix, and the composite shows the highest room-temperature conductivity, lowest activation energy, and superior Li/Li cycling stability. However, the 15 wt% composition (LZ15) showed pronounced agglomeration, increased interfacial resistance, and polarization during electrochemical performance.

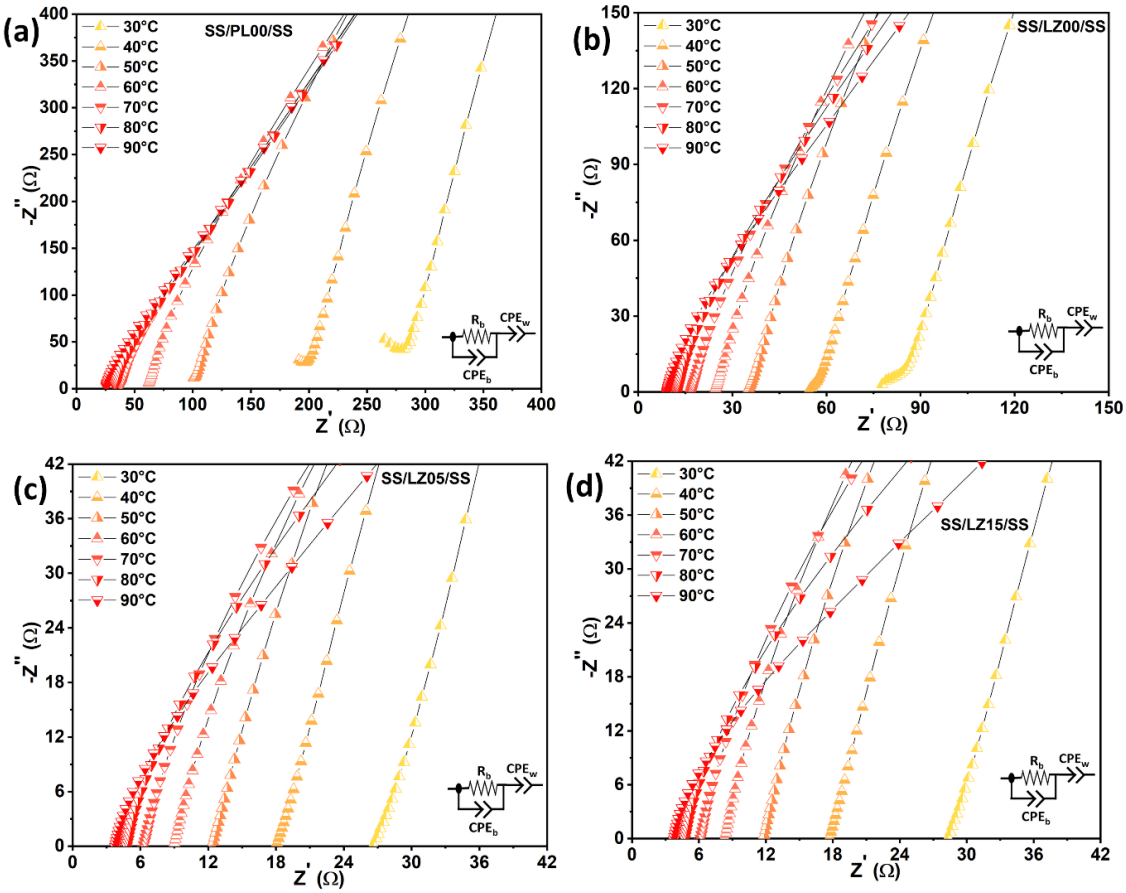

Figure 7.10 *EIS measurements at various temperatures in the SS/SS symmetric cell of (a) PL00, (b) LZ00, (c) LZ05, (d) LZ15 CSPEs.*

In comparison to the LZ00 matrix, further enhancement in ionic conductivities is observed when LLGZO particles are incorporated in the PVDF-HFP-PEO dual polymer matrix (LZ05, LZ10 and LZ15). At a concentration of 10 wt%, the ionic conductivity reaches a maximum value of 1.08×10^{-4} S/cm. To further explore the temperature dependency of ionic conductivity, the Arrhenius plots of all the developed CSPEs is also plotted in ***Figure 7.9(c)*** for a temperature range from 30°C to 90°C. The EIS spectra taken at this temperature are also presented in ***Figure 7.9(b)*** LZ10, ***Figure 7.10(a)*** PL00, ***7.10(b)*** LZ00, ***7.10(c)*** LZ05, and ***7.10(d)*** LZ15. All the developed CSPEs follow a linear Arrhenius behaviour, which indicates a thermally activated ion transport mechanism. The activation energies, as calculated from the slope (as described in *equation 4*), are shown in ***Figure 7.9(d)***. Notably, LZ10 exhibits the lowest activation energy of 0.304 eV, also providing the highest ion conductivity, which suggests facile lithium-ion conduction through a more amorphous and flexible matrix. The observed trend suggests that moderate addition of PEO and LLGZO not only enhances conductivity but also reduces energy barriers for Li^+ ion migration. However, the slight curvature observed in the Arrhenius plots at lower temperatures originates from the semi-crystalline nature of the dual-polymer matrix.[14–16,30,36] Ionic transport in such systems is coupled to polymer segmental dynamics in the amorphous domains. This becomes more active at elevated temperatures, leading to minor deviations from ideal Arrhenius behavior. No discontinuities were detected across the EIS measurement range (30–90 °C). Thus, the major phase transition was not observed, which correlates with our TGA/DTA measurement.

To investigate electrode-electrolyte interfacial properties, EIS spectra of all developed CSPE in symmetric Li/CSPE/Li cells are presented in ***Figure 7.11(a)*** along with the equivalent circuit. After analysing in ZView software, it is observed that the metal/electrolyte interfacial resistance ($R_{Li/El}$) decreased significantly with the inclusion of PEO and LLGZO. PL00 showed the highest interfacial resistance of 326.2 Ω, whereas LZ10 and LZ15 demonstrated much lower values of 105.1 Ω and 120.9 Ω, respectively. These results thus suggest that improved electrode–electrolyte contact and reduced interfacial polarization in the modified CSPEs. There are various pathways that lead to enhanced ionic conductivity and interfacial stability of the CSPEs [36,37], however, the conjugal effect of dual-polymer as well as of incorporating LLZO-based active ceramic filler is prominent in various other electrical and electrochemical phenomena that have been improved a lot. The electrochemical stability window of the CSPEs was examined using linear sweep voltammetry (LSV) in a Li/CSPE/SS configuration, as shown in ***Figure 7.11(b)***. PL00 exhibited an oxidative stability of 4.99 V, which increased with the

addition of PEO and LLGZO, reaching 5.23 V for LZ10. This enhanced electrochemical window might be due to the interaction between the polymer matrix and ceramic filler, which resulted in stabilizing the polymer backbone and delaying oxidative decomposition. So, these results demonstrated that the incorporation of PEO and LLGZO into the PVDF-HFP matrix significantly enhances the ionic conductivity, lowers activation energy, improves interfacial compatibility with lithium metal, and broadens the electrochemical stability window. It is worth discussing that the PVDF-HFP backbone in the CSPE matrix maintains structural integrity and facilitates the homogeneous dispersion of filler particles. As discussed earlier, the PEO chain further enhances Li^+ transport channels via salt dissociation[21,31,38]. Thus, even in the presence of agglomerates, the polymer matrix promotes percolative Li^+ pathways around the ceramic particles. This enhances the ionic transport in the CSPE matrix. Along with this, the interfacial Lewis acid-base interactions between LLGZO surface sites and the polymer chains are one of the reasons for reducing crystallinity and lowering the interfacial resistance. This synergistic polymer-ceramic effect likely explains why the LZ10 CSPE delivers superior performance despite some degree of particle agglomeration. However, with the increase in concentration of LLGZO particles, the agglomeration increases, and as a result, the ionic conductivity reduces.

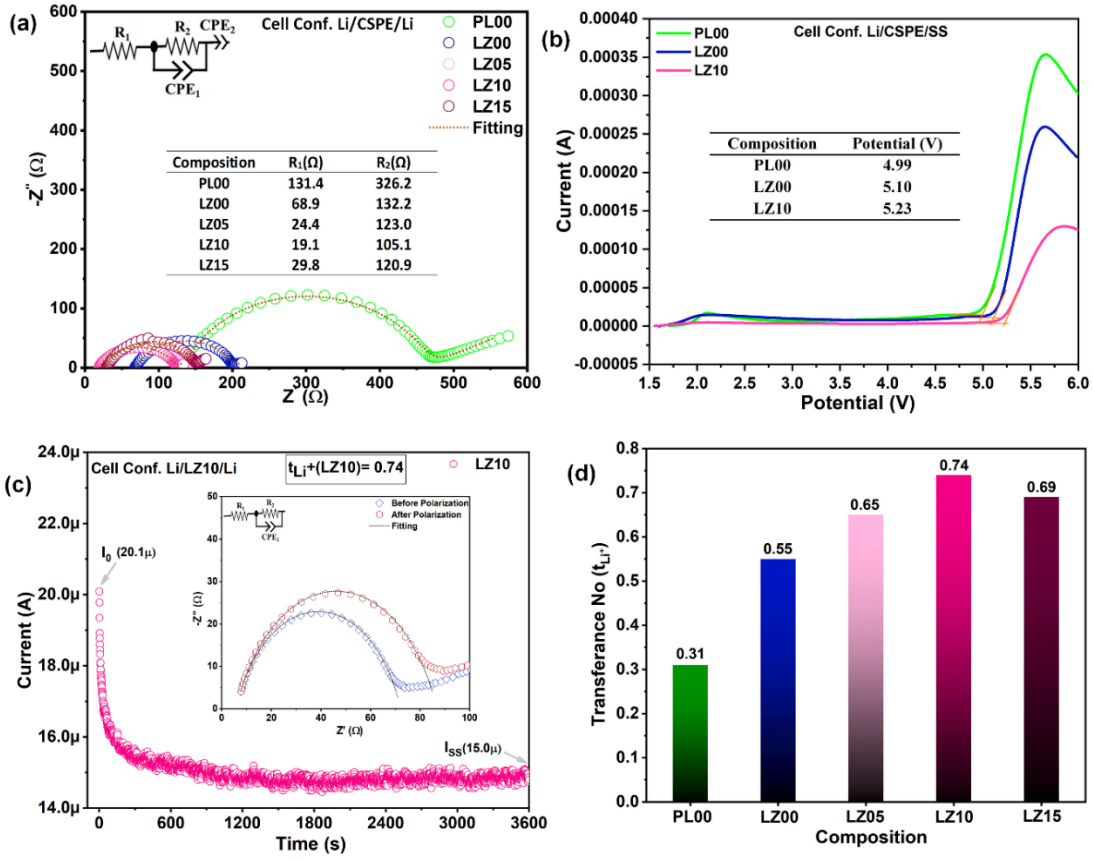

Figure 7.11 *(a) Nyquist plots of Li/CSPE/Li symmetric cells with PL00, LZ00, LZ05, LZ10, and LZ15 CSPEs at room temperature. (b) Linear sweep voltammetry (LSV) profiles of PL00, LZ00, and LZ10 in Li/CSPE/SS cells. (c) DC polarization of Li/LZ10/Li cell, (d) Summary of Li-ion transference numbers for all the developed CSPEs.*

The Li^+ transference number (tLi^+) of the developed CSPEs was evaluated at 60°C using a combination of DC polarization and EIS analysis from *equation 5* and summarized in ***Table 7.1***. DC polarization of LZ10 CSPEs, along with the EIS spectra, is presented in ***Figure 7.11(c)***. For LZ10 electrolyte, the initial and steady-state currents obtained from DC polarization deliver a t_{Li^+} of 0.74. This value is significantly higher than that of PL00 (0.31) and LZ00 (0.55). The transference number for LZ05 and LZ15 is found to be 0.65 and 0.69, respectively. A summary plot is presented in ***Figure 7.11(d)***. The enhanced t_{Li^+} of LZ10 might be due to the homogeneous dispersion of LLGZO particles within the PVDF-HFP/PEO matrix. This further promotes preferential Li^+ transport by facilitating LiTFSI dissociation and suppressing anion mobility. These results clearly demonstrate that the dual-polymer/LLGZO design provides an efficient Li^+ conduction pathway. From the results obtained so far, the importance of the development of efficient battery materials for obtaining good material characteristics as well as improved battery performance has been proven [39–41]. Now, it will be interesting to measure the long-term stability of developed CSPEs (LZ00, LZ05, LZ10, and LZ15) in the later section for the successful application in lithium metal batteries.

Table 7.1 *Lithium-ion transference no (t_{Li^+}) and corresponding resistance before and after polarization of the developed CSPEs*

CSPE	I_0 (A)	I_{ss} (A)	R_0 (Ω)	R_{ss} (Ω)	Li-ion Transference Number (t_{Li+})
PL00	2.55E-05	1.35E-05	251.2	283.0	0.31
LZ00	2.51E-05	1.50E-05	87.3	103.6	0.55
LZ05	2.43E-05	1.64E-05	72.4	89.5	0.65
LZ10	2.01E-05	1.50E-05	66.4	81.0	0.74
LZ15	2.38E-05	1.72E-05	78.2	83.7	0.69

7.4.2.4 Electrochemical Studies

7.4.2.4.1 Long cycling stability Test

Compatibility of the electrolytes with Li metal anode, as well as their mechanical integrity to inhibit Li dendritic growth, are crucial for ensuring safety and long-term stability of a battery [42–44]. To investigate the electrochemical stability and interfacial compatibility of the developed composite solid polymer electrolytes (CSPEs) against lithium metal, long-term Li/CSPE/Li symmetric cells were cycled under stepwise current densities of 0.10, 0.20, and 0.40 mA·cm^{-2}, as shown in ***Figure 7.12(a)***. At 0.10 mA. cm^{-2}, all the fabricated cells containing various CSPEs performed a stable plating/stripping behaviour over the 850 cycles (10 minutes Charge and 10 minutes discharge) except LZ015 CSPEs.

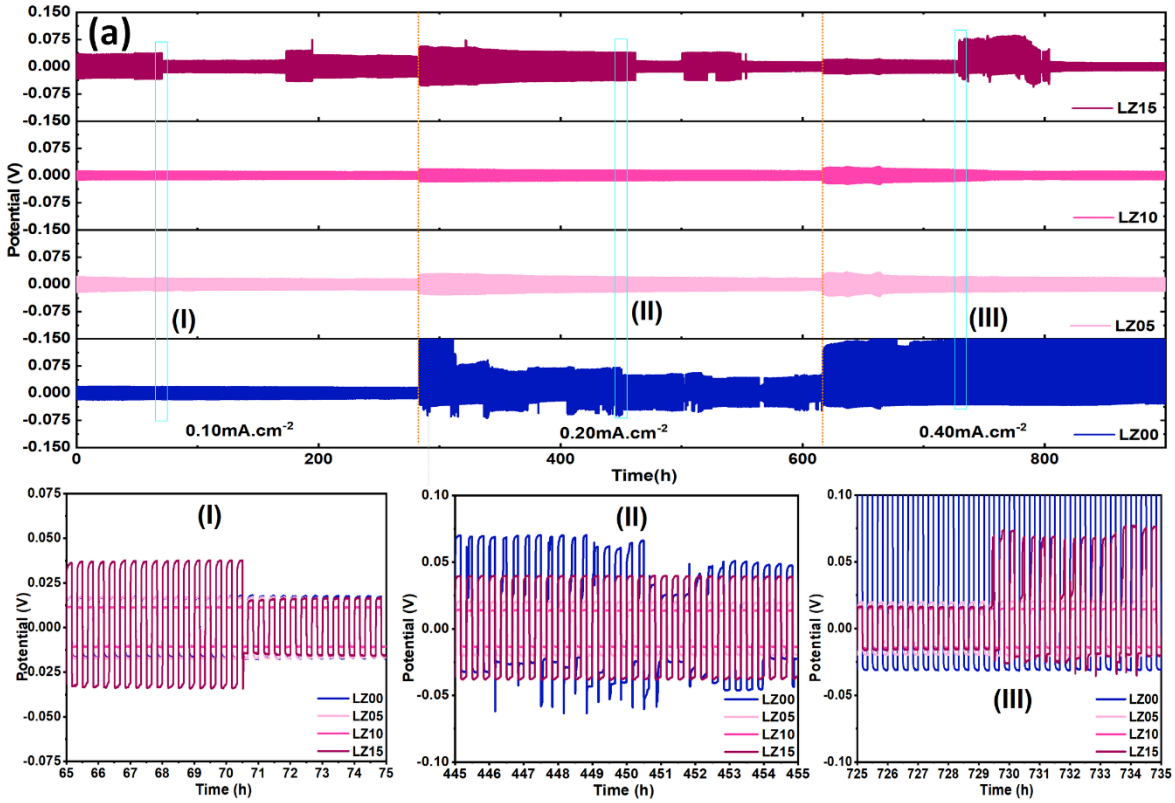

Figure 7.12 *(a) Voltage profile of Li/Li symmetric cell at 60°C at different current densities (0-850 cycles @ 0.10 mA. cm^{-2}, 851-1850 cycles @0.20 mA. cm^{-2}, and 1851-2700 cycles @0.40 mA. cm^{-2}) with three enlarged versions denoted as (I), (II), and (III).*

The cell with LZ15 electrolyte shows a large polarization and soft short circuit behaviour at around 69h. LZ00, LZ05 and LZ10 shows an average over potential ~0.17V, ~0.16 and ~0.11V respectively. Thus, in terms of lower polarization, LZ10 shows excellent stability at a lower current density of 0.10 mA. cm^{-2} as shown in inset *(I)*. At 0.2 mA.cm^{-2}, LZ00, and LZ15 suffer large fluctuations (inset (*II*)) in the plating/stripping process due to instability at the metal/electrolyte interface. Whereas, LZ05 and LZ10 show excellent stability with increasing

cycle life. After the sudden change in current density, both the cells show a larger average potential of ~0.27V for LZ05 and ~0.17V for LZ10. Whereas, around 600h, the cell undergoes more stabilization and shows an average overpotential of ~0.16V for LZ05 and ~0.12V for LZ10. At 0.4 mA.cm^{-2}, the cell with LZ00 and LZ15 undergoes abrupt fluctuation as shown in inset *(III)*. Whereas, LZ05 and LZ10 display a stable polarization. The electrochemical stability of PL00 CSPE is also measured and presented along with the LZ00 and LZ10 CSPES in Fig. S4, represent a large voltage polarization. These results highlight the critical role of active filler content (LLGZO particle) and dispersion to enhance the mechanical strength, ionic conductivity, and interfacial compatibility of CSPEs. In particular, LZ10 demonstrated the most favourable performance, which enables stable lithium plating/stripping over 900 hours across all tested current densities.

7.4.2.4.2 Full Cell Performance

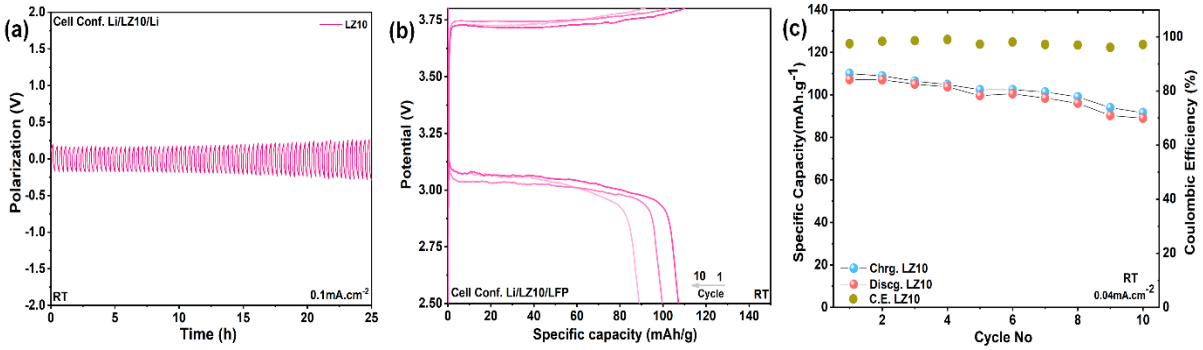

Figure 7.13 *Electrochemical performance of the optimized LZ10 CSPE at room temperature. (a) Galvanostatic Li plating/stripping profile of the Li/LZ10/Li symmetric cell at 0.1 mA·cm^{-2} over 25 h, (b) Charge-discharge voltage profiles of the Li/LZ10/LFP full cell at a current density of 0.04 mA·cm^{-2} for the 1st, 5th and 10th cycle, (c) Cycling performance of the Li/LZ10/LFP full cell at room temperature with corresponding coulombic efficiencies*

To understand the practical applicability of these CSPEs, full cells are fabricated using a Li metal anode and a commercial $LiFePO_4$ cathode. To validate the room-temperature performance of the LZ10 electrolyte, additional electrochemical measurements of the LZ10 CSPE were carried out and are presented in ***Figure 7.13***. In ***Figure 7.13(a)***, the Li/LZ10/Li symmetric cell shows plating/stripping behaviour at 0.1 mA·cm^{-2} with low polarization over 25 h. However, an increasing trend in polarization voltage is observed. In the Li/LZ10/LFP full cell in ***Figure 7.13(b)***, typical charge discharge profiles are presented at 0.04mA.cm^{-2}, and the cell delivered an initial discharge capacity of ~107 mAh·g^{-1} with an impressive coulombic

efficiency of ~97%. The rate capability plot in ***Figure 7.13(c)***, LZ10 retains ~83% capacity retention after 10 cycles at 0.04 mA·cm^{-2}. Thus, the LZ10 CSPE is capable of supporting reversible lithium storage at room temperature, although the performance is relatively limited.

EIS spectra are taken in the fabricated condition for LZ00 and LZ10 and presented in ***Figure 7.14(a)*** along with the equivalent circuit. After analysing using Zview software, it is found that boh interfacial resistance due to metal/electrolyte and cathode/electrolyte boundaries reduced significantly after the addition of 10 wt% LLGZO in the dual polymer matrix.

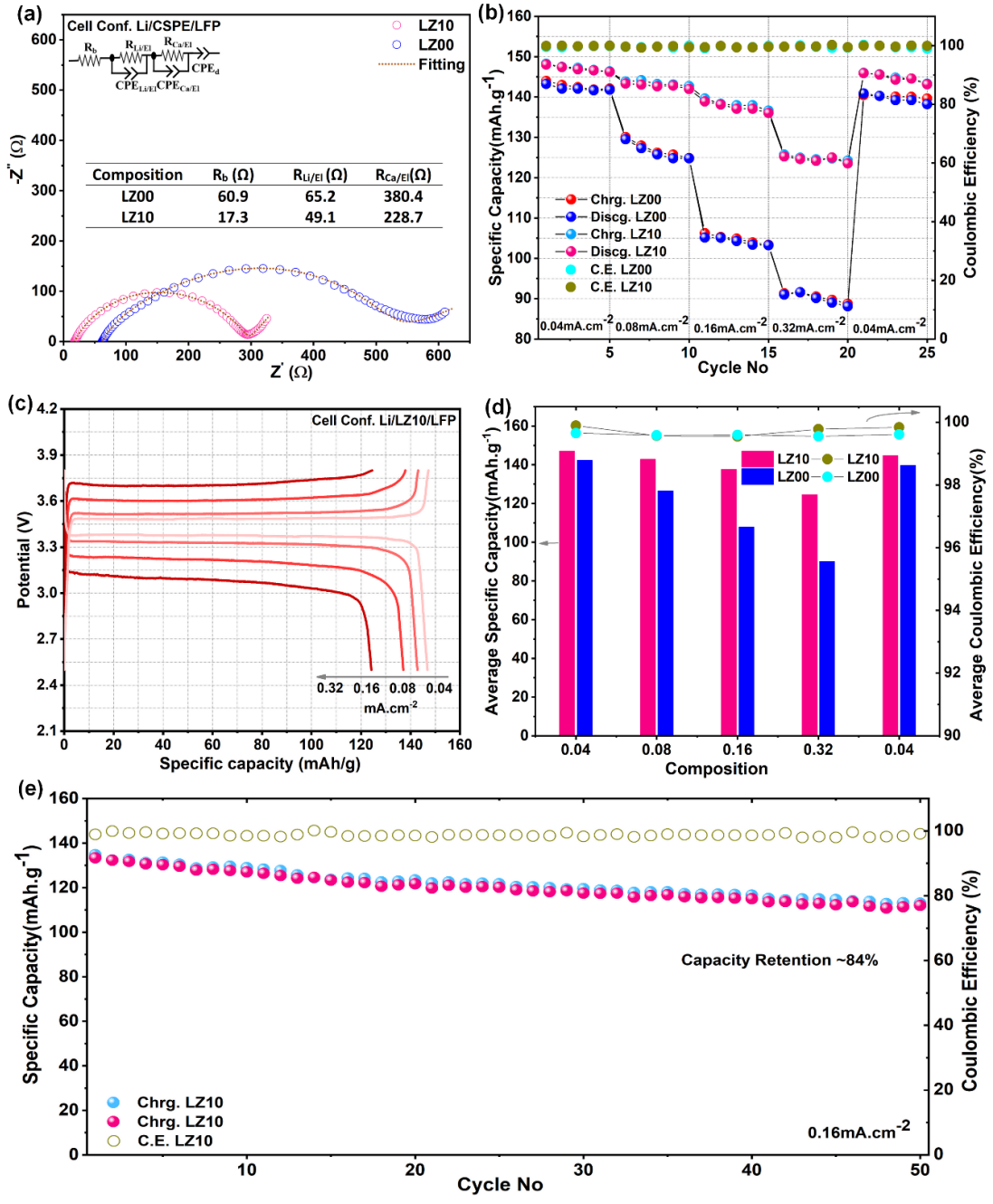

Figure 7.14 *(a) Nyquist plot of Li/LFP full cell as fabricated condition for LZ00 and LZ10. (b) Rate capability of LZ00 and LZ10 CSPEs at different current densities at 60°C. (c) Typical charge-discharge profile for LZ10 at different current densities. (d) Summary plot of the average specific capacity and average coulombic efficiency for LZ00 and LZ10 at various current densities. (e) Long cycling capacity retention test for LZ10 CSPEs.*

Table 7.2 *Comparative Performance of Composite Polymer Electrolytes with LLZO Derivatives for Solid-State Lithium Batteries.*

Composition	t (µm)	σ (S.cm^{-1})/ Eg (eV)	Electrochemical Stability	Ref
PVDF-HFP/LiTFSI/Ga-Rb-LLZO	30 ± 5	1.43×10^{-5} (30ºC)/-	Stable Li plating-stripping at 0.1 mA.cm^{-2} for >1000h; 200 cycles for Li/LFP cell with 88.29% capacity retention	45
PVDF-HFP/LiTFSI/Ga-LLZO	70	8.92×10^{-4} (RT)/-	Li/LFP cell ran in current densities from 0.1C to 2.0C and recovered well with an average coulombic efficiency of 98.7%; stable Li plating-stripping for 600h	46
PEO/LiTFSI/PVDF–HFP/LLZTO	200±100	2.65×10^{-4} (60ºC)/-	Stable Li plating-stripping for 1000h; good rate discharge stability at various current densities of 0.05, 0.10, and 0.15 mA.cm^{-2} at 60°C with >99% coulombic efficiency	21
PEO/LiTFSI/Al-LLZO	100	2.7×10^{-5} (25°C)	Stable cycling in Li-S battery at 0.75 mA.cm^{-2} and reached a high discharge capacity of 1250 mAh.g^{-1}	47
PVDF-HFP/LiTFSI/Ti@LLZTO	75	6.86×10^{-5} (30ºC)/0.24 eV	Li/Li cell cycled up to 1550h at 0.1 mA.cm^{-2} with a small polarization voltage (<40 mV); Li/LFP cycles at 0.5C for 100 times with capacity retention of 98.8% at 28ºC	48

PVDF-HFP/LiTFSI/Ga-LLZO	80	1.1×10^{-4} (RT)/-	Li/LFP cell ran for 80 cycles at 0.1C with capacity retention of 96.5% and coulombic efficiency of 98%; stable Li plating-stripping for 700h without short circuit	49
PEO/Al-doped LLZTO/LiTFSI	30	1.12×10^{-5} (25°C)/0.83 eV	Li/Li cell exhibited excellent stability with a constant polarization of 15 mV during 400h cycling at 0.10 mA.cm^{-2}; Li/LFP cell achieved a capacity of 155 mAh·g^{-1} and a Coulombic efficiency of 99% at 0.1 C at 60 °C with 87% retention after 100 cycles	50
PVDF-HFP/PEO/LiTFSI/Ga-LLZO	40±2	1.08×10^{-4} (30°C)/0.304 eV	Stable Li plating/stripping over 900h at various current densities with minimal change in electrolyte resistance, good rate capability at various current densities in Li/LFP full cell.	This Work

Metal/electrolyte resistance ($R_{Li/El}$) is reduced from 65.2Ω to 49.1Ω, whereas cathode/electrolyte resistance ($R_{Ca/El}$) is reduced from 380.4Ω to 228.7Ω. The rate capability test of LZ00 and LZ10 CSPEs is carried out at 60°C at various current densities against Li metal anode and $LiFePO_4$ (LFP) cathode and presented in ***Figure 7.14(b)***. At 0.04 mA.cm^{-2}, LZ10 and LZ00 deliver an average discharge specific capacity of 147.02 and 142.15 mAh.g^{-1}. At higher current densities, the average discharge specific capacity of LZ10 CSPEs is found to be 142.76 mAh.g^{-1}(0.08 mA. cm^{-2}), 137.45 mAh.g^{-1} (0.16 mA. cm^{-2}), and 124.51 mAh.g^{-1} (0.32 mA. cm^{-2}). Similarly, the average discharge specific capacity of LZ00 CSPEs is 126.42 mAh.g^{-1}(0.08 mA. cm^{-2}), 107.66 mAh.g^{-1} (0.16 mA. cm^{-2}), and 89.99 mAh.g^{-1} (0.32 mA. cm^{-2}). Both cells containing LZ00 and LZ10 CSPEs exhibited >99% coulombic efficiencies. When the cells are brought back to the initial current density, both cell shows good reversibility. ***Figure 7.14(c)*** represents the typical charge-discharge profile of Li/LZ10/LFP cell at various current densities at 60°C. A summary of average discharge specific capacity and average coulombic efficiencies at different current densities is also plotted and presented in ***Figure 7.14(d)***. Long Cycling performance of the Li/LZ10/LFP solid-state cell at 60°C and a current density of 0.16 mA·cm^{-2} is presented in ***Figure 7.14(e)***. The cell delivers an initial discharge capacity of ~133 mAh·g^{-}

[1] and maintains ~84% capacity retention after 50 cycles with an excellent coulombic efficiency of >98%. A Comparative Performance of Composite Polymer Electrolytes with LLZO Derivatives for Solid-State Lithium Batteries is summarized in ***Table 7.2***. Thus, these results clearly indicate that the incorporation of 10 wt% LLGZO enhances the interfacial compatibility at both the Li metal/electrolyte and cathode/electrolyte interfaces and improves the rate performance of the full cell, especially at elevated current densities. The better ionic transport and reduced interfacial resistances in the LZ10 composite electrolyte thus facilitate more stable and efficient charge/discharge processes. Thus, it can be a promising candidate for practical solid-state lithium metal batteries.

7.4.3 Critical analysis

The physico-chemical and electrochemical performance and reliability of composite solid polymer electrolytes (CSPEs) are critically governed by their crystallinity, mechanical integrity, ionic conductivity and Li-ion migration pathways. The dual-polymer/LLZO CSPEs exhibited enhanced ionic conductivity (1.08×10^{-4} S·cm^{-1}), wide electrochemical stability (5.23 V), and stable Li/Li cycling over 900 h at 60 °C. This suggests a key synergistic role of polymers and ceramic interaction. Despite these improvements, the electrolytes still have a few key limitations, Such as temperature-dependent conductivity, limited flexibility, moderate mechanical strength, and handling difficulties in free-standing form. These challenges highlight the need for more robust structural reinforcement, motivates towards the development of paper-polymer-LLZO systems.

7.5 Paper-Polymer-LLZO composite electrolytes

To address the handling difficulties and poor flexibility of standalone CSPE films, a paper-polymer-LLZO composite strategy was adopted by embedding cellulose paper within the dual-polymer/LLZO matrix. The fibrous paper scaffold provides mechanical reinforcement and flexibility, while the polymer-ceramic phase ensures ionic conductivity and interfacial stability, together forming a structurally robust and electrochemically active electrolyte membrane for the next-generation flexible battery.

7.5.1 Preparation of Paper-Polymer-LLZO Composite Membrane

Ga-doped LLZO (LLGZO) was synthesized via alanine-assisted auto-combustion, calcined at 900 °C, and used as the active filler. A dual-polymer (PVDF-HFP/PEO with LiTFSI) solution containing 10 wt% LLGZO was prepared, ultrasonicated, and stirred. The slurry was coated on

both sides of pre-dried cellulose paper (20 µm, ~65% porosity) using a semi-automated casting machine, followed by infrared drying, vacuum treatment, and compaction. The resulting paper-polymer-LLZO membrane (~60 µm) integrates the porosity and reinforcement of paper, the flexibility of polymers, and the ion transport pathways of LLGZO, forming a robust multifunctional electrolyte for next-generation flexible solid-state metal batteries. The LLGZO dual polymer-coated paper-polymer-LLZO membrane will be termed as PLZ10, and without LLGZO, PLZ00.

7.5.2 Results and Discussion

7.5.2.1 Microstructural and Mechanical Studies

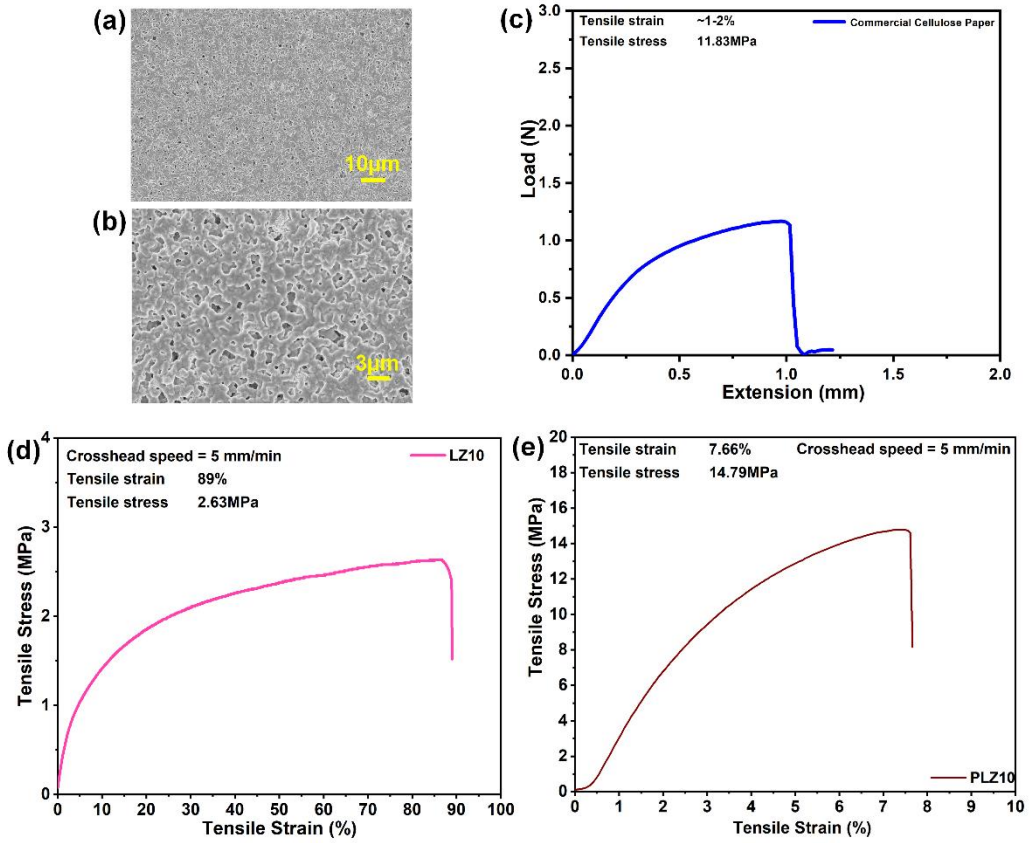

Figure 7.15*(a-b) FESEM images of PLZ10 at two different scales, Mechanical of (c) cellulose paper, (d) CSPE (LZ10), and (e) paper-polymer-LLZO membrane (PLZ10).*

The microstructural and mechanical properties of the paper-polymer LLZO (PLZ10) electrolyte demonstrated a critical insights into its robust structure compared to the commercial cellulose paper and CSPE membranes. ***Figures 7.15(a-b)*** present the FESEM images of the paper-polymer-LLZO membrane, which reveal a dense, uniform morphology with well-

dispersed filler domains. However, in the CSPE film, as we earlier discussed, a 30wt% of LLGZO ceramic impregnated paper separator shows the agglomerated LLZO particle in paper (***Section 7.3***) and for the dual polymer composite electrolyte, a relatively soft polymer-rich CSPE film was observed with agglomerated filler particle distribution. (***Section 7.4***).

The tensile profile of commercial cellulose paper (***Figure 7.15 (c)***) shows high tensile stress (11.83 MPa) but extremely low strain (~1-2%). This generally reflects the brittle structure of commercial cellulose paper with non-uniform anisotropic fibre deposition. However, the CSPE membrane, as shown in LZ10, ***Figure 7.15(d)***, demonstrates high elongation (~89% strain) but very low stress (2.63 MPa). This highlights its flexibility due to the dual polymer matrix, but poor mechanical strength to resist the dendritic growth during cycling. The PLZ10 electrolyte, as presented in ***Figure 7.15(e)***, achieves a balanced profile, i.e with tensile stress of 14.79 MPa and strain of 7.66%, it combines the strength of cellulose and improves the flexibility due to the polymer.

These results clearly establish that the paper-polymer-LLZO configuration can improve the limitations of the paper (brittleness) and CSPE (softness), by offering a mechanically robust yet flexible framework. Thus, it will be interesting to measure the electrical and electrochemical performance.

7.5.2.2 Electrical properties

The ionic transport properties and stability of the paper-polymer-LLZO electrolytes were systematically investigated and compared with those of the pristine paper-polymer (PLZ00) and the CSPE membrane. Nyquist plots of PLZ00 and PLZ10 at room temperature along with the equivalent circuit are presented in ***Figure 7.16(a)***. The PLZ10 membrane shows significantly reduced bulk resistance compared to PLZ00. This suggests the role of LLGZO fillers in facilitating the lithium ionic transportation across the paper polymer matrix. The Arrhenius plots as presented in ***Figure 7.16(b)*** further demonstrated that the PLZ10 delivers lower activation energy as compared to PLZ00, which is consistent with our earlier studies.

The temperature-dependent impedance spectra (30-80°C) of PLZ00 and PLZ10 are presented in ***Figures 7.16 (c)*** and ***(d),*** respectively. A rapid decrease in the resistance is observed with the increasing temperature, which is consistent with the enhanced segmental dynamics of the dual polymer matrix. Importantly, PLZ10 shows the lower resistance values at all the temperatures compared to PLZ00. This suggests that an improved transport pathway was formed due to the

synergistic interaction between the LLGZO filler and the polymer chains across the paper matrix. This is also consistent with our earlier observation.

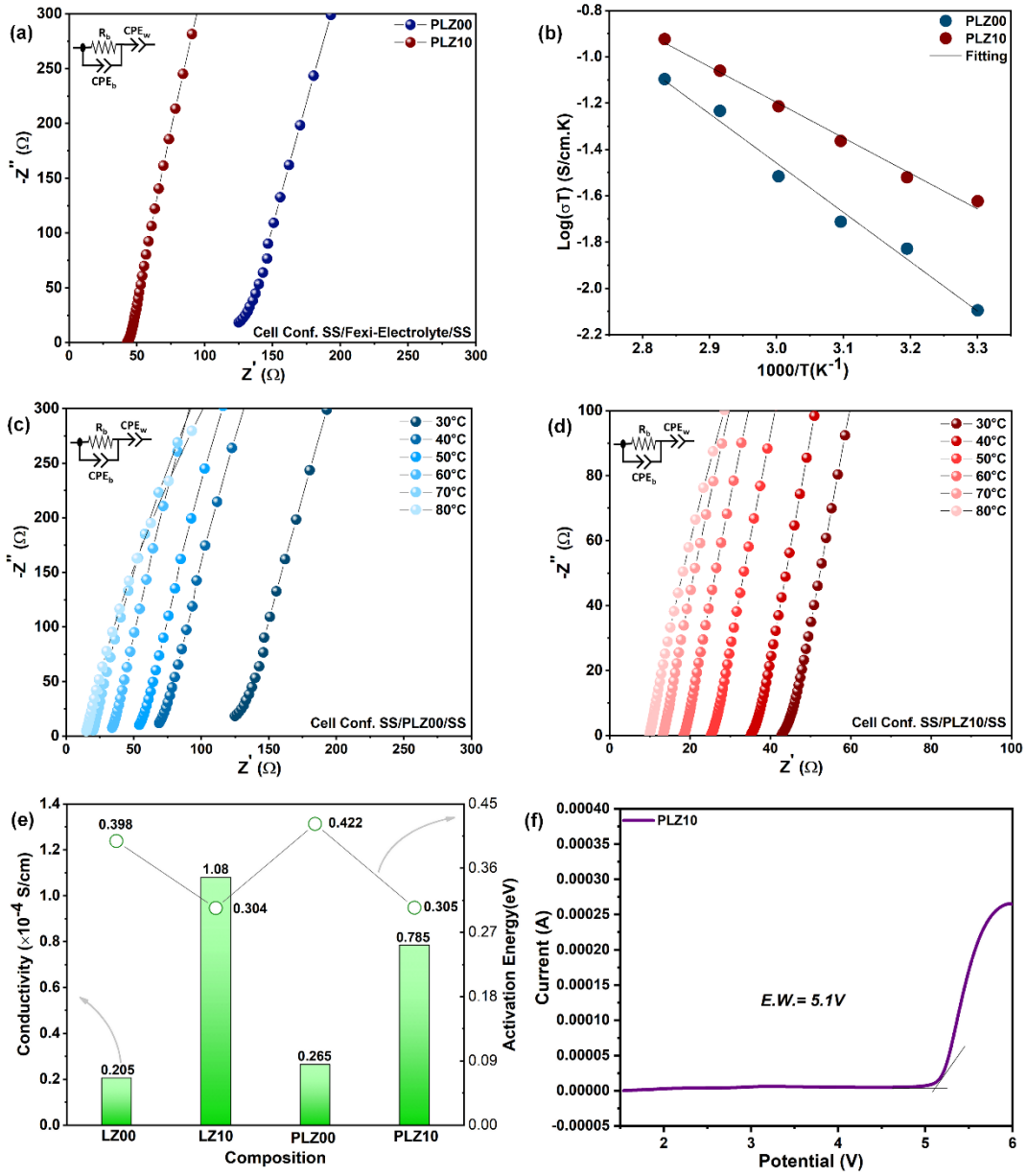

Figure 7.16 *Electrical and electrochemical properties of paper-polymer-LLZO electrolytes. (a) Nyquist plots of PLZ00 and PLZ10 at room temperature with the equivalent circuit. (b) Arrhenius plots of PLZ00 and PLZ10 for activation energy calculation. Temperature-dependent impedance spectra of (c) PLZ00 and (d) PLZ10 for a temperature range of 30-80°C. (e) Variation of room temperature ionic conductivity and activation energy with various compositions, (f) Linear sweep voltammetry of PLZ10.*

The conductivity and activation energy variation with various compositions are summarised in ***Figure 7.16(e)***. As the CSPE film (LZ10) achieved the highest conductivity (~1.08×10^{-4} S.cm^{-}

^{1} at 30°C), the PLZ10 delivered a similar conductivity of 0.785 × 10^{-4} S.cm^{-1} with a low activation energy of 0.305 eV. Whereas, the paper-based pristine polymer electrolyte shows low activation energy (0.422 eV) and similar conductivity to its CSPE's counterpart. Thus, the overall conductivity and the mechanical study suggest that the PLZ10 electrolyte successfully combines the strength of the cellulose paper and the flexibility and the ionic transport properties of the CSPEs membrane. After that, the electrochemical stability window of PLZ10, as shown in ***Figure 7.16(f)***, is way above 5V, thus any commercial high voltage cathode material can be used with this flexible paper-based electrolyte.

In summary, the PLZ10 electrolytes show an optimal balance between ionic conductivity, activation energy, electrochemical stability, and mechanical integrity. It will be very interesting to measure the Li metal computability in the later section.

7.5.2.3 Electrochemical Studies

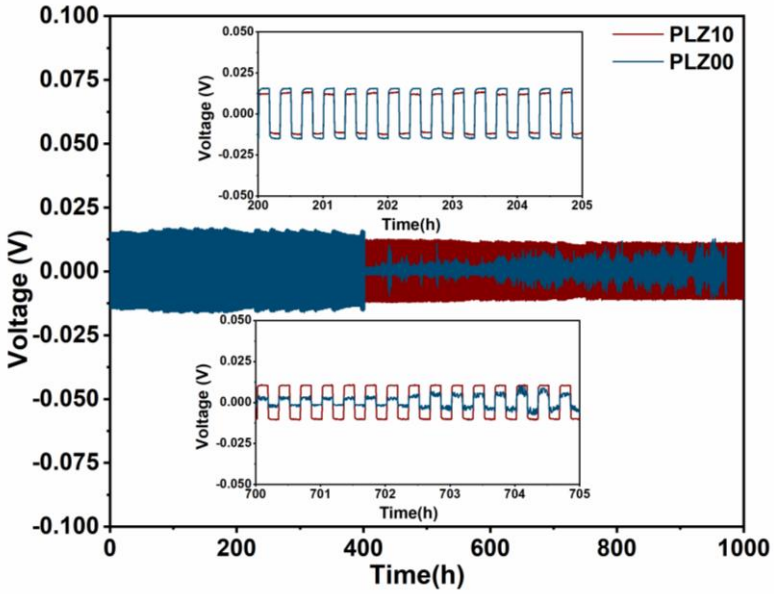

Figure 7.17 *Long-term galvanostatic cycling of Li/PLZ00/Li and Li/PLZ10/Li symmetric cells at 0.1 mA.cm^{-2}. Insets show magnified voltage profiles between 200-205 h and 700-705 h.*

The interfacial stability and dendrite suppression capability of the paper-polymer-LLZO composite membranes were evaluated using Li/electrolyte/Li symmetric cells at a current density of 0.1 mA.cm^{-2}. The long-term galvanostatic cycling profiles of PLZ00 (without LLZO) and PLZ10 (with 10 wt% LLZO) are presented in ***Figure 7.17***. Both cells showed stable lithium plating/stripping behaviour for over 900 h. However, distinct differences in polarisation trends are observed. The PLZ00 membrane shows large voltage fluctuations with increasing cycle time, which reflect the unstable voltage fluctuation and insufficient Li^{+}

transport selectivity. In comparison, PLZ10 demonstrates lower and more uniform overpotentials with smoother voltage plateaus and almost stable for longer time periods. The magnified regions at ~200-205 h and ~700-705 h clearly highlight the consistent polarization stability of PLZ10 compared to PLZ00.The improved stability of PLZ10 is due to the to the synergistic effect of the cellulose scaffold and the LLZO fillers. The paper backbone provides the structural robustness and dimensional stability. Whereas the LLGZO particles enhance the ionic conductivity and promote the homogeneous Li^+ flux. This combination effectively mitigates the localized current hotspots and delays the interfacial degradation. This way it suppresses the dendrite growth and delivered long-term stable cycling. These results clearly established that the paper-polymer composite electrolyte PLZ10 possesses superior electrochemical stability against lithium metal compared to the pristine PLZ00.

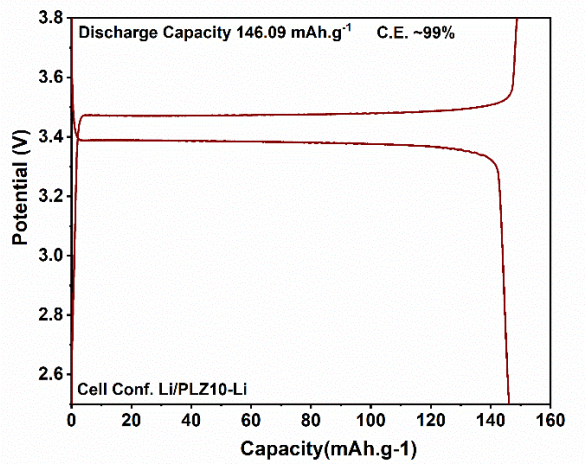

Figure 7.18 *Galvanostatic charge–discharge voltage profile of the Li/PLZ10/LFP full cell at 0.1 mA·cm⁻².*

The paper-polymer-LLZO composite electrolytes (Li/PLZ10/LFP) was further used to fabricate the full cell. ***Figure 7.18*** presents the typical charge-discharge voltage profiles of the cell at a current density of 0.1 $mA \cdot cm^{-2}$. The cell delivered an initial discharge capacity of 146.09 $mAh.g^{-1}$. This shows the efficient Li^+ transport through the PLZ10 membrane. The flat voltage plateau at ~3.4 V corresponds to the Fe^{2+}/Fe^{3+} redox couple of the LFP cathode. The coulombic efficiency (C.E.) has found to be at ~99%bwhich indicates the reversible Li plating/stripping and minimal side reactions at the electrode-electrolyte interfaces. The stable polarization during both charge and discharge further confirms the excellent interfacial compatibility of PLZ10 with both Li metal and LFP. These results validate that the incorporation of LLZO fillers and the reinforcement from the paper scaffold collectively enable a multifunctional electrolyte with strong potential for solid-state lithium metal batteries.

7.6 Conclusion

This chapter studied the role of LLZO-based fillers in three different electrolyte architectures, paper-based membranes, dual-polymer based CSPEs, and paper–polymer composite electrolytes. For paper-based membrane. It showed improved wettability and Li-ion selectivity but were brittle and unsuitable for Li metal. However, the Dual-polymer CSPEs offered high ionic conductivity (~10^{-4} S.cm^{-1}), wide electrochemical stability, and long-term symmetric cell cycling. Although, the mechanical strength was limited. Using a cellulose scaffold into the polymer-LLZO matrix produced paper-polymer-LLZO composite that balanced strength (14.8 MPa), flexibility (~7.7% strain), and conductivity (0.785 × 10^{-4} S.cm^{-1}). The paper-based electrolyte showed PLZ10 stable symmetric cycling (>900 h) and high full-cell capacity (146.09 mAh.g^{-1}, ~99% CE). Thus, paper-polymer-LLZO composite membrane represent a robust and scalable electrolyte design for next-generation flexible solid-state lithium metal batteries.

7.7 References

1 P. Albrechtowicz, *Energy Reports*, DOI:10.1016/j.egyr.2023.02.088.

2 Y. Gao, Z. Pan, J. Sun, Z. Liu and J. Wang, 2022, preprint, DOI: 10.1007/s40820-022-00844-2.

3 B. Kennedy, D. Patterson and S. Camilleri, *J Power Sources*, DOI:10.1016/S0378-7753(00)00402-X.

4 Y. Miao, P. Hynan, A. Von Jouanne and A. Yokochi, 2019, preprint, DOI: 10.3390/en12061074.

5 P. Xu, D. Zhang, Z. Shao and D. Chen, *J Appl Polym Sci*, DOI:10.1002/app.50738.

6 N. Lingappan, W. Lee, S. Passerini and M. Pecht, 2023, preprint, DOI: 10.1016/j.rser.2023.113726.

7 X. Huang, *J Power Sources*, DOI:10.1016/j.jpowsour.2014.01.080.

8 F. Liu and X. Chuan, 2021, preprint, DOI: 10.1039/d1ra02845f.

9 J. Huang, C. Li, D. Jiang, J. Gao, L. Cheng, G. Li, H. Luo, Z. Xu, D. Shin, Y. Wang, Y. Lu and Y. Kim, *Adv Funct Mater*, DOI:10.1002/adfm.202411171.

10 C. Hei Chan, H. Ho Wong, S. Liang, M. Sun, T. Wu, Q. Lu, L. Lu, B. Chen and B. Huang, *Batter Supercaps*, DOI:10.1002/batt.202400432.

11 E. Tarani, I. Arvanitidis, D. Christofilos, D. N. Bikiaris, K. Chrissafis and G. Vourlias, *J Mater Sci*, DOI:10.1007/s10853-022-08125-4.

12 M. Doumeng, L. Makhlouf, F. Berthet, O. Marsan, K. Delbé, J. Denape and F. Chabert, *Polym Test*, DOI:10.1016/j.polymertesting.2020.106878.

13 J. Evans, C. A. Vincent and P. G. Bruce, *Polymer (Guildf)*, DOI:10.1016/0032-3861(87)90394-6.

14 C. Shan, Y. Wang, M. Liang, K. Lu, C. Xiong, W. Hu and B. Liu, *Energy Storage Mater*, 2023, **63**, 102955.

15 Z. Zhang, X. Wang, X. Li, J. Zhao, G. Liu, W. Yu, X. Dong and J. Wang, *Materials Today Sustainability*, 2023, **21**, 100316.

16 S. Wang, A. La Monaca and G. P. Demopoulos, *Energy Advances*, 2025, **4**, 11–36.

17 S. Wu, C. Wang, S. Li and J. Weng, *Mater Chem Front*, 2024, **8**, 2924–2943.

18 K. Ghosh and M. Wasim Raja, *ACS Omega*, DOI:10.1021/acsomega.2c04012.

19 K. Ghosh and M. Wasim Raja, *ACS Appl Energy Mater*, DOI:10.1021/acsaem.3c00291.

20 K. Ghosh and M. Wasim Raja, *Chemical Engineering Journal*, DOI:10.1016/j.cej.2023.148200.

21 H. Gan, J. Sun, Y. Xia, P. Qiu, L. Li and W. Zhu, *Journal of Physical Chemistry C*, DOI:10.1021/acs.jpcc.3c06275.

22 J. K. Nayak, U. Shankar and K. Samal, *Chemical Engineering Journal Advances*, DOI:10.1016/j.ceja.2023.100459.

23 M. Tripathi, S. M. Bobade and A. Kumar, *Bulletin of Materials Science*, DOI:10.1007/s12034-018-1685-0.

24 K. Daems, P. Yadav, K. B. Dermenci, J. Van Mierlo and M. Berecibar, *Renewable and Sustainable Energy Reviews*, 2024, **191**, 114136.

25 H. Liang, L. Wang, A. Wang, Y. Song, Y. Wu, Y. Yang and X. He, 2023, preprint, DOI: 10.1007/s40820-022-00996-1.

26 A. Gupta, A. Jain and S. K. Tripathi, *Journal of Polymer Research*, DOI:10.1007/s10965-021-02597-9.

27 B. Jamoussi, M. N. M. Al-Sharif, L. Gzara, H. Organji, T. B. Almeelbi, R. Chakroun, B. A. Al-Mur, N. H. M. Al Makishah, M. H. F. Madkour, F. A. Aloufi and R. F. Halawani, *Polymers (Basel)*, 2024, **16**, 1738.

28 N. S. Vrandečić, M. Erceg, M. Jakić and I. Klarić, *Thermochim Acta*, DOI:10.1016/j.tca.2009.10.005.

29 M. Brogly, S. Bistac and D. Bindel, *Appl Surf Sci*, DOI:10.1016/j.apsusc.2022.154428.

30 H. Gan, H. Zhang, S. Ying, J. Dong, J. Zhang, D. Li, Q. Huang, S. Zheng, C. Hu, Q. Sun, J. Ai, J. Wang and B. Zhou, *Chemical Engineering Journal*, 2025, **522**, 167671.

31 H. B. T. Nguyen, L. Ding, B. Pohle, T. Schmeida, H. B. A. Nguyen and D. Mikhailova, *Batteries*, 2025, **11**, 45.

32 R.-A. Tong, L. Chen, B. Fan, G. Shao, R. Liu and C.-A. Wang, *ACS Appl Energy Mater*, 2021, **4**, 11802–11812.

33 W. B. Nassir, T. H. Mengesha, K. Z. Walle, Y.-S. Wu, J.-K. Chang, R. Jose and C.-C. Yang, *J Energy Storage*, 2025, **133**, 118027.

34 S. Paengson, P. Pilasuta, K. Yuzou, M. Mao, D. Mori and T. Seetawan, *J Mater Sci*, 2025, **60**, 11973–11993.

35 Y. Li, W. Zhang, Q. Dou, K. W. Wong and K. M. Ng, *J Mater Chem A Mater*, 2019, **7**, 3391–3398.

36 S. C. Sand, J. L. M. Rupp and B. Yildiz, *Chem Soc Rev*, 2025, **54**, 178–200.

37 M. Wu, D. Liu, D. Qu, Z. Xie, J. Li, J. Lei and H. Tang, *ACS Appl Mater Interfaces*, 2020, **12**, 52652–52659.

38 B. Liang, S. Tang, Q. Jiang, C. Chen, X. Chen, S. Li and X. Yan, *Electrochim Acta*, DOI:10.1016/j.electacta.2015.04.039.

39 L. Zhao, S. Bi, J. Li, Y. Wen, H. Zhang, D. Zhang, S. Lu, P. Yin, F. Shi, J. Yan, S. Pan and H. Zhang, *Energy Storage Mater*, 2025, **78**, 104256.

40 C. Chen, R. Yang, J. Zhu, W. Yao and Y. Tang, *Advanced Science*, DOI:10.1002/advs.202500756.

41 S. Yu, K. Cai, H. Zhao, T. Wang, T. Qu, L. Li, J. Li, C. Yao and X. Lang, *Appl Surf Sci*, 2025, **709**, 163863.

42 C. Wang, Y. Zhu, T. Zhang, J. Tian, F. Gao, Y. Zhao, X. Bu and T. Quan, *J Clean Prod*, 2024, **470**, 143280.

43 Z. Li, L. Gao, C. Zhang and F. Li, *J Energy Storage*, 2025, **119**, 116336.

44 J. Yu, X. Sun, X. Shen, D. Zhang, Z. Xie, N. Guo and Y. Wang, *Energy Storage Mater*, 2025, **76**, 104134.

45 H. Lee, Y.-W. Song, M.-Y. Kim, J. Lee, J. Ryu, Y. Noh, S.-J. Kim, J. Kim and J. Lim, *Solid State Ion*, 2024, **411**, 116571.

46 Y. Wang, T. Liu, C. Liu, G. Liu, J. Yu and Q. Zou, *Solid State Ion*, DOI:10.1016/j.ssi.2022.115897.

47 Y. Gong, K. Fu, S. Xu, J. Dai, T. R. Hamann, L. Zhang, G. T. Hitz, Z. Fu, Z. Ma, D. W. McOwen, X. Han, L. Hu and E. D. Wachsman, *Materials Today*, DOI:10.1016/j.mattod.2018.01.001.

48 T. Duan, H. Cheng, Q. Sun, Y. Liu, W. Nie, Y. Chu, Q. Xu and X. Lu, *J Power Sources*, DOI:10.1016/j.jpowsour.2023.233789.

49 J. Cai, T. Liu, C. Liu and G. Liu, *J Alloys Compd*, DOI:10.1016/j.jallcom.2023.171872.

50 C. Z. Zhao, X. Q. Zhang, X. B. Cheng, R. Zhang, R. Xu, P. Y. Chen, H. J. Peng, J. Q. Huang and Q. Zhang, *Proc Natl Acad Sci U S A*, DOI:10.1073/pnas.1708489114.

CHAPTER 8

Exploratory Studies: (a) Effect of Liquid Therapy in Na Metal Batteries and (b) Introduction of S in Al-doped LLZO

Summary & Graphical Abstract

This chapter presents exploratory studies designed to extend the scope of the liquid-therapy framework and to test unconventional modification strategies in solid electrolytes. In the first part, liquid therapy was applied to $Na_3Zr_2Si_2PO_{12}$ (NZSP), a NASICON-type conductor with high Na^+ conductivity but poor Na-metal interfacial stability. Even with relatively low uptake of solvated ionic liquid, the treated NZSP showed reduced interfacial resistance and improved plating/stripping response, suggesting that liquid-assisted interfacial stabilization is not limited to LLZO but can be generalized to other oxide electrolytes. In the second part, LLZO was co-modified with Al and S to explore combined cationic and anionic substitution. While sulfur incorporation could not be conclusively detected, preliminary results indicated measurable differences compared to Al-only LLZO, hinting at possible structural or conductivity modifications.

Objectives

1. To test the adaptability of liquid therapy in NZSP solid electrolytes.

2. To explore cation-anion co-modification (Al/S) in the LLZO matrix.

Strategy

Extend liquid therapy in Na metal batteries, and probe unconventional modification in garnet electrolytes.

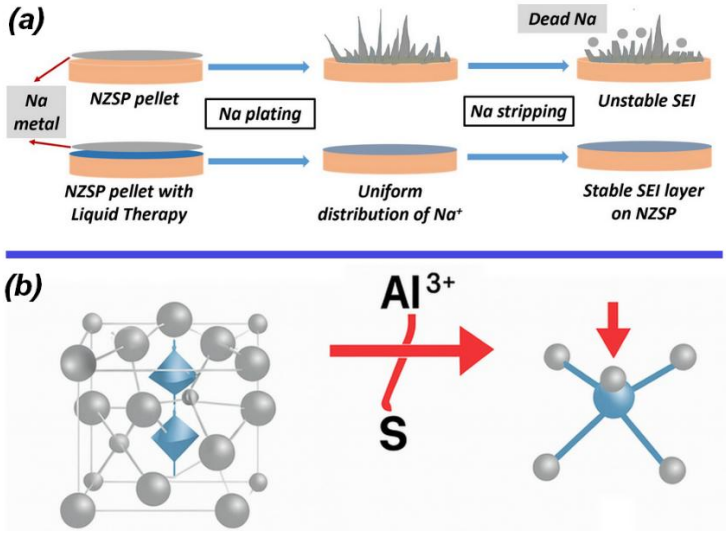

Figure 8.1 *Graphical abstract summarizing (a) the role Liquid Therapy in Na metal Batteries and (b) S incorporation in Al doped LLZO material.*

8.1 Overview

The core theme of the current thesis has been the optimization of garnet-type LLZO electrolytes and enhancement in metal/electrolyte interfacial stability via liquid therapy (***Chapter 3***), interfacial engineering (***Chapter 4***), microstructural engineering (***Chapter 5***), dual therapy (***Chapter 6***), and designing a flexible matrix (***Chapter 7***) for next-generation batteries. These studies provided key insights about the processing-structure-performance correlations in garnet-type LLZO material and its interfacial stability with Li metal. In a similar direction, it was also necessary to test whether these strategies can be extended to other solid electrolytes or metal batteries and to examine the unconventional approaches for tuning the LLZO matrix itself. The current chapter is dedicated to two crucial exploratory studies that were undertaken under the same research hypothesis: (i) liquid therapy in $Na_3Zr_2Si_2PO_{12}$ (NZSP) based Na metal batteries, and (ii) an unconventional attempt to modify the LLZO matrix via Al and S.

Among various Na superionic conductors for sodium metal batteries (SMBs), NASICON-type $Na_{1+x}Zr_2Si_xP_{3-x}O_{12}$ (NZSP, $0 \leq x \leq 3$), which was first reported by Goodenough *et al.*[1] in 1976, has gained significant attention due to high ionic conductivity (10^{-3}-10^{-2} $S \cdot cm^{-1}$) and wide electrochemical potential. Generally, NZSP has a three-dimensional framework of corner-sharing ZrO_6 octahedra and SiO_4/PO_4 tetrahedra[2]. In recent years, aliovalent doping and grain boundary engineering have been studied for improving the ionic transportation[2–5]. However, the practical use of NZSP is limited by severe instability at the Na metal interface. Several decomposition products and resistive interphases (e.g., Na_2CO_3, NaOH) were developed during preparation/cycling, and as a result, uncontrollable Na dendrite growth has been observed.[5,6] Conventional strategies to address these issues have included microstructural densification and surface modification via oxide additives such as TiO_2 or Al_2O_3, or via alloying, etc[6–9]. In this work, an alternative pathway was developed by applying the liquid therapy concept based on the previous successful application for garnet electrolyte in Li metal batteries. Although the liquid uptake was very low (<2 wt%) due to the less porous nature of NZSP compared to LLZO. The exhausted electrochemical results demonstrated that the liquid therapy successfully reduced the interfacial resistance and showed more stable Na plating/stripping at higher current density. The full cell against NVP cathodes ($Na_3V_2(PO_4)_3$) and Na anodes also delivered excellent performance throughout the measurement. Thus, these results suggest that liquid-assisted interface engineering is one of the effective strategies to enhance Na/NZSP interfacial stability. Thus, the liquid therapy, which proved to be effective in garnets, can be generalized to NASICON-type conductors as a versatile route for mitigating interfacial degradation.

The second exploratory study tried to modify the lattice structure modification in LLZO via Al and S incorporation. In the literature and in our previous study, the role of cation doping (Ga, Al, Ta, Nb) was well established in stabilizing the cubic phase, improving the conductivity by creating more Li vacancies in the matrix, and reducing the grain boundary resistance[10–12]. However, the role of anion doping in LLZO garnets remains largely unexplored. Although a few theoretical studies show the possibility of halogen-substitution on the garnets with the partial replacement of O^{2-} with F^{-} and Cl^{-}, and showed that these substitutions can reduce the tetragonal phase formation and stabilize the cubic phase[10–14]. Recently, S doping in the LATP solid state electrolyte matrix was also carried out via the sol-gel synthesis method, and the study indicated that the partial replacement of oxygen with sulfur can enhance the ionic transportation due to the lower electronegativity of the S atom as compared to oxygen[15]. Motivated by these findings, in this exploratory study, attempts have been made to incorporate sulfur. However, S modification in pristine LLZO material is challenging due to the instability of the cubic LLZO matrix. We have also tried, but no change in the crystal structure was observed. Thus, aluminium with S was tried to incorporate in the LLZO matrix during sol-gel synthesis. Sulfur generally has a larger ionic radius and lower electronegativity compared to oxygen. Thus, it has the potential to alter the local Li-O framework, which can directly influence the ionic connectivity channel. In this study, the elemental sulfur was not detected by EDX, maybe due to the volatilization during high-temperature sintering or incorporation below the detection limits. But the differences in ionic conductivities and surface features compared to Al-doped LLZO suggested that probable modification in the crystal structure[10,11]. These preliminary results highlight both the challenges and opportunities of anion co-doping. Also, the more sensitive characterization techniques (e.g., XPS, TOF-SIMS, neutron diffraction) are required to confirm the modification in the anion doping more convincing way.

Thus, these exploratory studies are very crucial to expand the scope of the thesis in two complementary directions. The NZSP investigation shows that the liquid therapy can also be useful in other chemistries to stabilize the metal/electrolyte interface. The Al/S study for the first time introduces the concept of dual cation-anion modification in garnet material. This unconventional but potentially impactful route can further fuel the study of the phase stability and Li^{+} transport in depth. Thus, these preliminary studies modify the solid electrolyte via interface and lattice engineering and have some potential to provide a new perspective for designing the next-generation solid electrolytes.

8.2 Liquid Therapy in Na metal Battery

8.2.1 Experimental

8.2.1.1 Material synthesis and characterization

The NZSP ($Na_3Zr_2Si_2PO_{12}$ with 10% excess Na) solid electrolytes were prepared following a conventional solid-state synthesis route. The detailed synthesis and processing are already discussed in ***Chapter 2***, ***Section 2.3.5***. In short, the constituent precursors are taken and ball milled overnight, followed by drying and calcination at 1100ºC for 15h. After calcination, the powders are pelletized and sintered at 1230 °C for 10 h in air. After sintering, the pellets are soaked in 1M $NaPF_6$ in tetraglyme for about 2 hours. The details preparation of making this liquid electrolyte and solid hybrid electrolyte is already discussed in ***Chapter 2***, ***Section 2.4***. It is worth discussing here that, unlike solvated ionic liquid using LiTFSI and tetraglyme as prepared and termed as solvated ionic liquid due to the formation of complex chelate structure $[Li(G4)]^+$, NaPF6 does not or partially show such complexation, thus this liquid can be termed as a liquid electrolyte rather than a solvated ionic liquid. But the whole process of hybridizing the NZSP solid electrolyte can be termed as liquid therapy. Thus, the solid hybrid electrolyte can be further referred to as NZSP-LT. The detailed characterization is already discussed in the same chapter in ***Section 2.7***.

8.2.1.2 Cell fabrication and testing

The detailed cell fabrication and testing techniques are already discussed in ***Chapter 2***, ***Section 2.6*** and ***Section 2.7,*** respectively. In Short, after preparing the solid electrolyte (NZSP), solid hybrid electrolyte (NZSP-LT), several cells (Na/Na, SS/SS, Na/NVP, etc.) are fabricated for various electrochemical testing as discussed in ***Chapter 2***.

8.2.2 Results and Discussion

8.2.2.1 Structural Studies

The structural properties of NZSP and NZSP-LT were investigated using XRD and FTIR, as presented in ***Figure 8.2***. After liquid therapy, the XRD patterns of NZSP show no shift in diffraction peak or appearance of any secondary phases, as shown in ***Figure 8.2(a)***. The X-ray pattern further analysis by Rietveld refinement confirmed that both the electrolytes, NZSP and NZSP-LT, consist of ~88% monoclinic phase, ~11% rhombohedral phase, and a minor ~1%

ZrO_2 impurity phase. This further suggests that the liquid therapy does not introduce any structural modification.

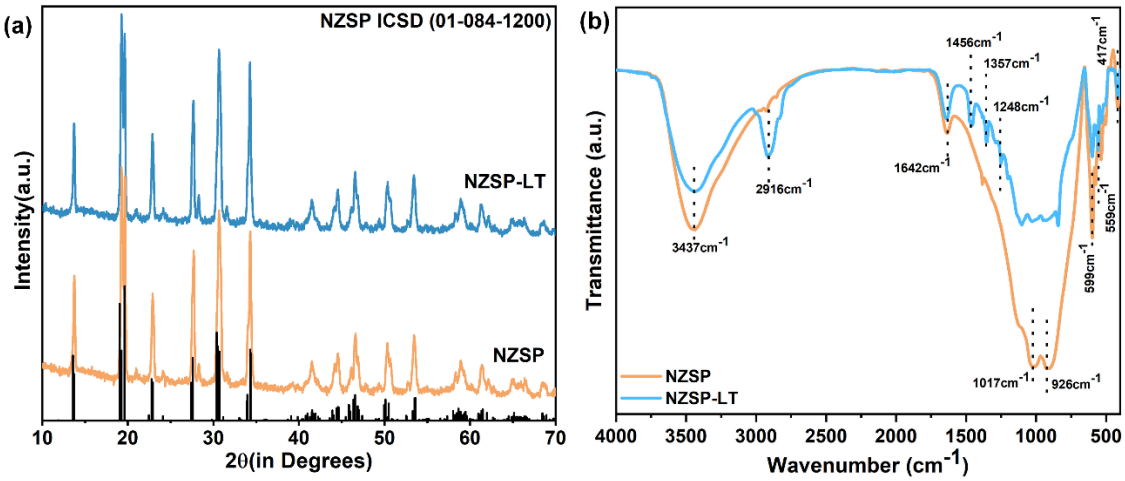

Figure 8.2 *(a) XRD patterns of pristine NZSP and liquid-treated NZSP (NZSP-LT) and (b) FTIR spectra of NZSP and NZSP-LT materials.*

FTIR spectra as presented in ***Figure 8.2(b)*** further provide key insights about the surface interaction between the liquid electrolyte and NZSP materials. In the FTIR spectra, both the materials shows the characteristic vibrational modes of phosphate stretching (P-O) around 1017 and 926 cm^{-1} and the silicate units. However, in the NZSP-LT, various new vibration modes were observed, especially at ~1456, 1337, and 1248 cm^{-1}, which may arise from the weak interactions between the $NaPF_6$-based liquid phase and the NZSP surface groups. However, no new peaks corresponding to any secondary phases of NZSP material were detected, which is consistent with earlier observations. Thus, the structural studies suggest that the liquid therapy did not alter the intrinsic NASICON structure, but the local chemical environment at the grain surface of the NZSP material was changed. This is very crucial for improving Na wetting and interfacial stability, which we discussed in the later section.

8.2.2.2 Microstructural Studies

The microstructural changes due to the liquid infusion in the NZSP matrix were further studied by FESEM (***Figure 8.3***) and corresponding EDX spectra (***Figure 8.4***). The pristine NZSP pellets as presented in ***Figure 8.3(a)-(b)*** show a highly dense structure with some intergranular pores distributed across the surface. With further magnification in ***Figure 8.3(c)***, the grains appear to have a facet-like structure with irregular edges. Some non-uniform grains and secondary particles were also visible. After the liquid therapy, the surface morphology of the NZSP solid electrolyte changed as shown in ***Figure 8.3(d)-(f)***. The liquid probably infiltrates

into the porous structure of NZSP and forms a smooth and interconnected surface texture as compared to pristine NZSP material, as shown in ***Figure 8.3(d)-(e)***. Further magnification (***Figure 8.3(f)***) suggests that the bulk microstructure of NZSP was almost unchanged. The intergranular voids appear to be filled with liquid electrolyte. This is consistent with the low uptake of liquid therapy (~2 wt%). But, due to the significant changes in surface morphology, it is expected to get some benefits during cycling with better wetting of Na metal.

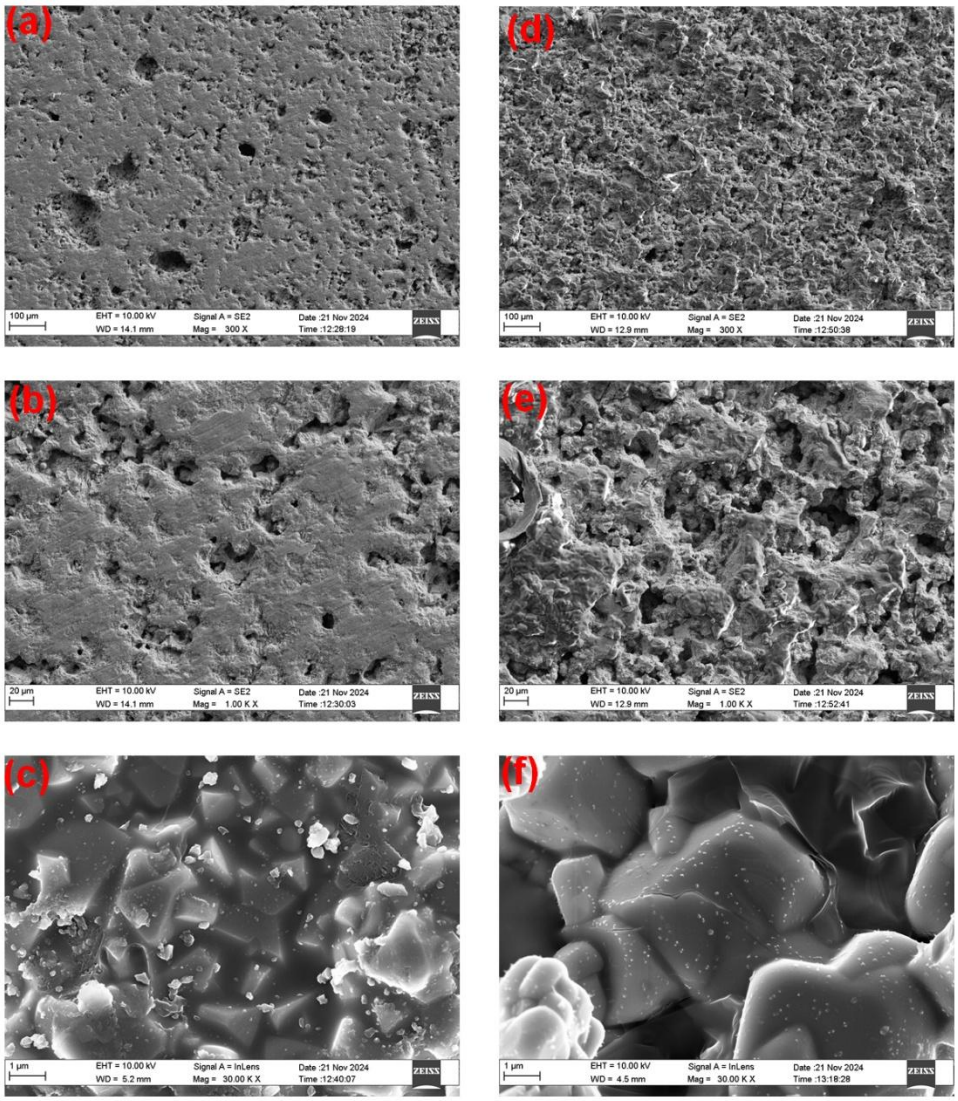

Figure 8.3 *FESEM images of (a-c) NZSP and (d-f) NZSP-LT at different magnifications.*

Elemental composition was further studied qualitatively using corresponding EDX spectra as presented in ***Figure 8.4***. The presence of Na, Zr, Si, O, and O confirms the formation of NZSP material as shown in ***Figure 8.4(a)***. Whereas, after liquid therapy, the presence of F is more prominent as shown in ***Figure 8.4(b)***, suggesting the successful incorporation of liquid electrolyte in the NZSP matrix. The presence of F mainly originated from the NaPF6-based

liquid electrolyte. Thus, FESEM and the EDX spectra further highlight that the liquid therapy does not affect the bulk crystal but modifies its surface morphology, which is crucial for Na wetting and suppressing any interface instability during electrochemical cycling.

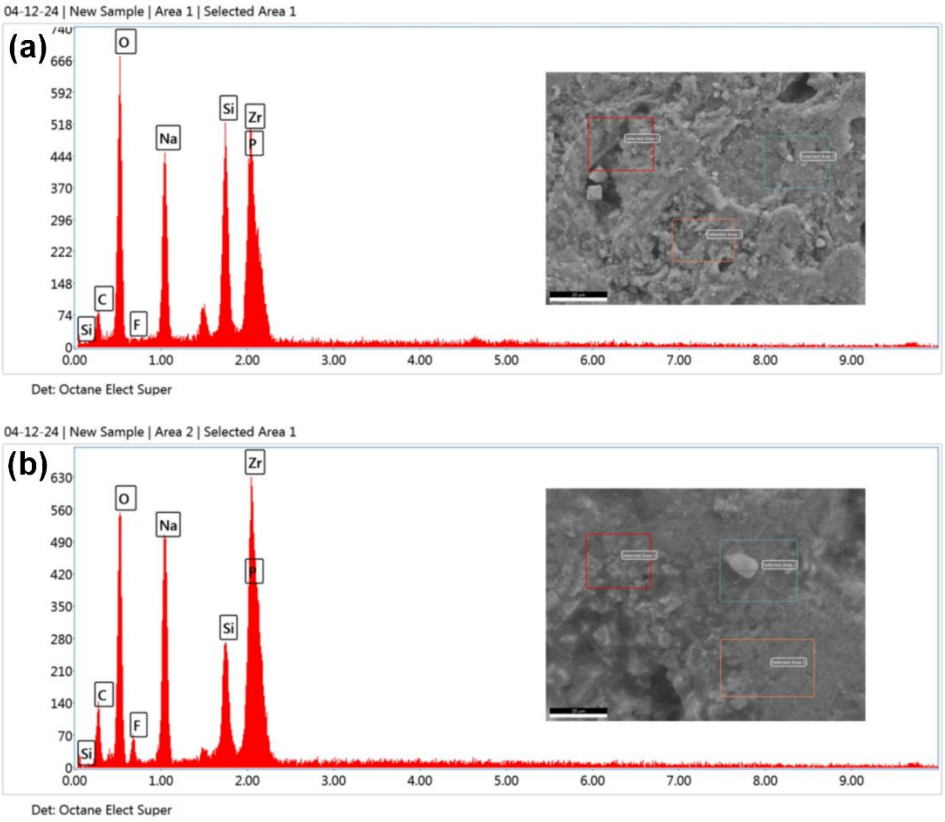

Figure 8.4 *EDX spectra of (a) NZSP and (b) NZSP-LT.*

8.2.2.3 Electrical Studies

The ionic conductivity of pristine NZSP pellets was measured using a coated Au blocking electrode at the top surface of both faces of the sintered pellets. The EIS spectrum with the corresponding equivalent circuit, as shown in Figure 8.5(a), shows a semicircle followed by a long tail. The total ionic conductivity at room temperature of pristine NZSP is found to be 2×10^{-4} S·cm^{-1}. The activation energy from the Arrhenius plot was presented in ***Figure 8.5(b)*** from the EIS measurement in a temperature range of 30ºC-120ºC. The activation energy is calculated from the slope and was found to be 0.29, well-matched with the literature. Prior to liquid therapy, it is very important to measure the ionic conductivity of the liquid electrolyte. To measure the ionic conductivity of the liquid electrolyte, a SS/SS symmetric cell was fabricated using a polypropylene-based commercial separator. The EIS spectrum presented in ***Figure 8.5(c)*** revealed that the ionic conductivity of the liquid electrolyte is found to be 1.10×10^{-4} S·cm^{-1}, which is of the same order of magnitude as pristine NZSP.

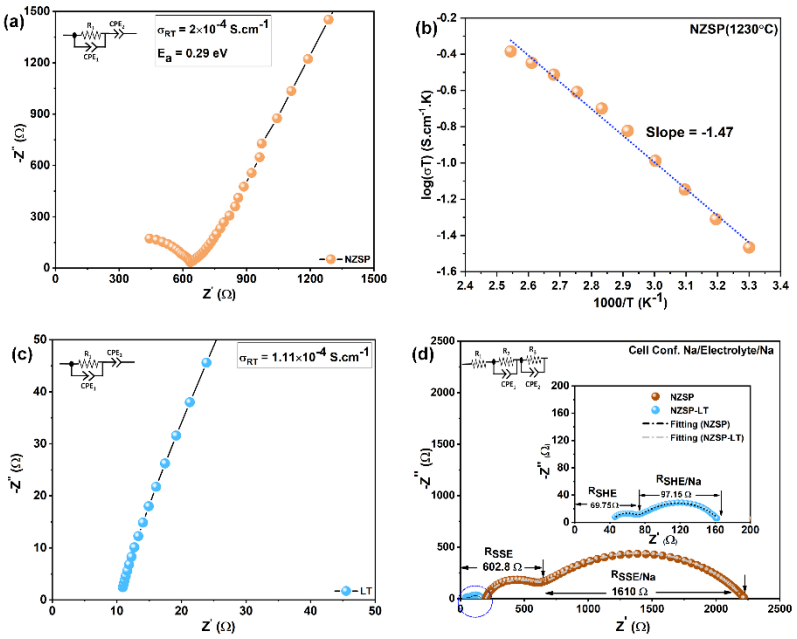

Figure 8.5. (a) Nyquist plot of NZSP solid electrolyte sintered at 1230º for 10h, (b) Arrhenius plot for calculation of activation energy from slope, (c) Nyquist plot for measurement of ionic conductivity of LT in SS/Separator/SS cell. (d) Symmetric cell impedance spectra of NZSP and NZSP-LT.

The effect of liquid therapy on interfacial resistance was further investigated in symmetric Na/NZSP/Na and Na/NZSP-LT/Na cells. The EIS spectra along with the equivalent circuit were presented in ***Figure 8.5(d)***. The EIS spectra were fitted in Zview software for measuring the interfacial resistance. For pristine NZSP, the interfacial resistance was found to be 1610 Ω with a total electrolyte resistance of 602.8 Ω, which is consistent with earlier observations. to the earlier measurement in the ion blocking electrode. It is worthy to discuss that in the earlier measurement, the contribution of bulk and grain boundary resistance was not clearly visualized. But with the Na/Na electrode, the contribution of bulk and grain boundary is easily visible and found to be 196.5 for bulk and 406.3 for grain boundary. After liquid therapy, all the resistance was found to be decreased. The interfacial resistance is found to be ~97 Ω, which is a nearly 16-fold reduction in interfacial resistance. Thus, these results suggest that the liquid therapy can enhance the stabilization at the metal/electrolyte interface in metal batteries. The electrolyte resistance can also be calculated and found to be 69.75Ω. The corresponding total ionic conductivity was 1.82×10^{-3} S·cm^{-1}. These results confirm that liquid therapy, even at a very low uptake (~2 wt%), can reduce the interfacial impedance and enhance the ion transport across the NZSP matrix. Thus, it will be interesting to measure the long-term stability and electrochemical cell performance in the latter section.

8.2.2.4 Electrochemical Studies

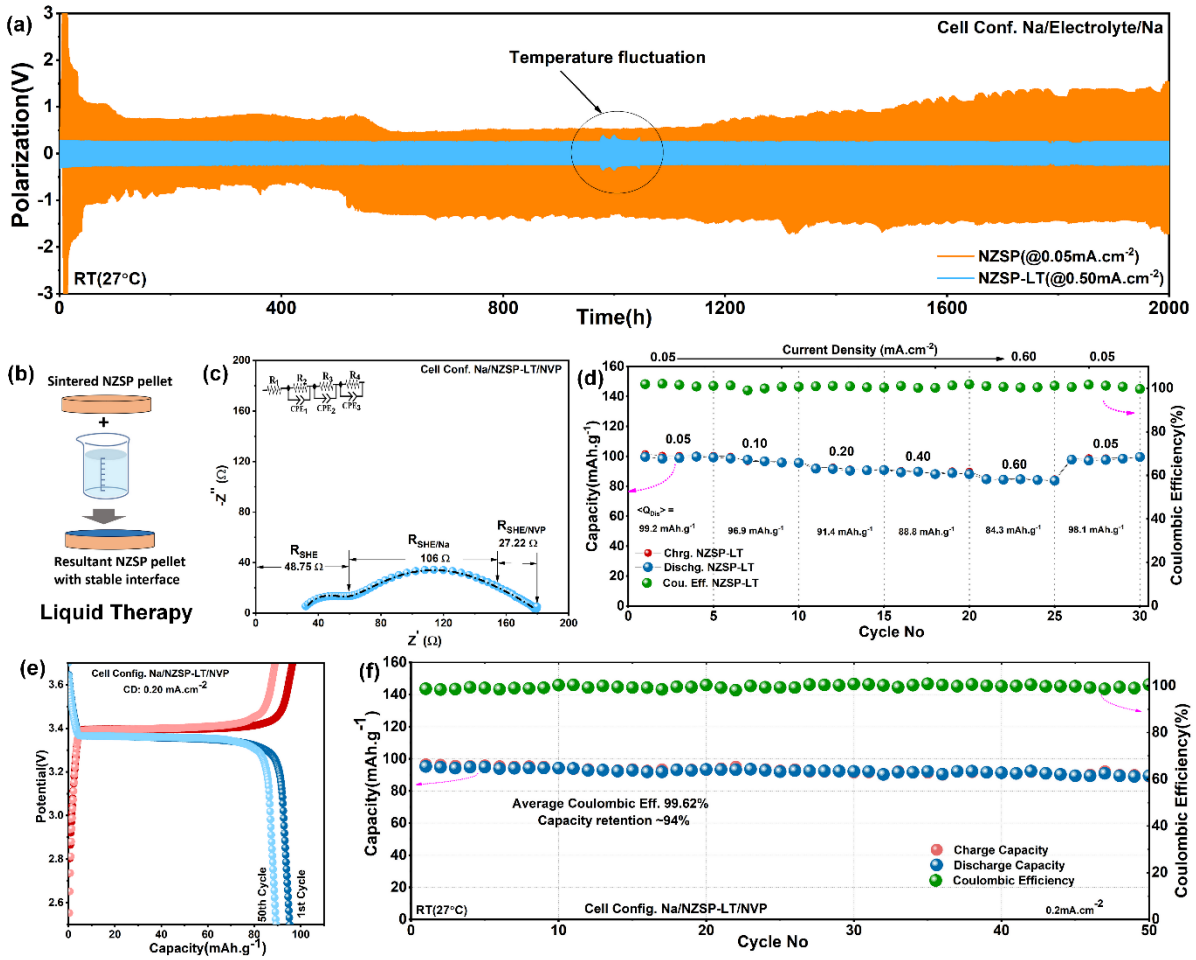

Figure 8.6 *(a) Na plating/striping stability test over 2000h for NZSP and NZSP-LT electrolyte, (b) Schematic of liquid therapy process. (c) EIS spectrum of NZSP-LT electrolyte in Na/NZSP-LT/NVP full cell. (d) Rate performance of Na/NZSP-LT/NVP full cell at various current densities. (e) Typical Charge-discharge profiles at 0.2 mA·cm^{-2}. (f) Long-term cycling stability of Na/NZSP-LT/NVP full cell.*

The electrochemical performance of NZSP and NZSP-LT electrolyte was measured in symmetric Na/Na and full Na/NZSP/NVP cells presented in ***Figure 8.6***. Studying the Na plating/stripping behaviour over an extended period of time was essential for understanding the compatibility of any solid electrolyte with the Na metal in solid-state sodium metal batteries (SSSMBs). ***Figure 8.6(a)*** compares the long-term cycling behavior of Na/NZSP/Na and Na/NZSP-LT/Na symmetric cells. Pristine NZSP showed very large and unstable polarization, with sharp voltage fluctuations at a very low current density of 0.05 mA.cm^{-2}. The large voltage polarization and irregular voltage response suggest the poor interfacial wettability of Na metal

foil on NZSP solid electrolyte. It is likely to form some resistive interphase at the metal/electrolyte boundary. In comparison, NZSP-LT solid hybrid electrolyte delivers stable plating/stripping behavior throughout the long cycling process over 2000h at a high current density of 0.50 $mA.cm^{-2}$. This suggests that the liquid therapy is effective in mitigating the interface instability in metal batteries. It also helps in the wettability of Na metal on NZSP while maintaining uniform contact. The liquid therapy in NZSP solid electrolyte is further summarized and illustrated in ***Figure 8.6(b)***. The improvement is most likely due to the formation of a stable SEI structure, which may be generated from the decomposition product of PF_6^- anion during cycling.

Both the electrolyte was further tested using NVP commercial cathode and Na metal anode. However, the cell with NZSP solid electrolyte was not operated due to the large resistance at the metal/electrolyte and cathode/electrolyte interface. So, further, only the performance of NZSP-LT was measured and presented. In ***Figure 8.6(c)***, the EIS spectrum of the Na/NZSP-LT/NVP full cell revealed that the cell shows a very low electrolyte bulk resistance of 48.75 Ω, a metal/electrolyte interfacial resistance of 106 Ω, and a cathode interface resistance of only 27.22 Ω. This further suggests that the liquid therapy also stabilizes the cathode interfacial resistance in metal batteries.The electrochemical full cell performance of NZSP-LT electrolyte is presented ***in Figure 8.6(d),*** which reveals good capacity retention under variable current densities. The cell delivered an average discharge capacity of 99.2, 96.9, 91.4, 88.8, and 84.3 $mAh.g^{-1}$ at current densities of 0.05, 0.10, 0.20, 0.40, and 0.60 $mA \cdot cm^{-2}$, respectively. It also maintained excellent coulombic efficiency of >99%. The cell shows very low capacity degradation even at higher current densities. During the step up to the initial current densities, the cell shows good reversibility. Long-term cycling performance in Na/NVP cells was also measured and presented in ***Figure 8.6(f)***. The cells retain almost 94% capacity even after 50 cycles with an excellent coulombic efficiency of >98%. Typical charge-discharge at the 1st and 50th cycles are also presented in ***Figure 8.6(e)***, reveals well-defined voltage plateaus corresponding to the Na^+ insertion/extraction in the NVP cathode with minimal polarization growth during long-term cycling. Thus, the overall electrochemical results highlight that the liquid therapy stabilizes various interfaces and delivers excellent performance even at high current densities.

8.2.2.5 Post Electrochemical Studies

Post-mortem studies of cycled electrolytes were carried out to investigate the interfacial changes in both symmetric cells and full cells. ***Figure 8.7*** describes the FTIR spectra taken

before and after the symmetric cell performance for both the electrolytes. P-O stretching (1016-1030 cm^{-1} and 926 cm^{-1}), -P-O bending (599 and 557 cm^{-1}), and Zr-O vibrations (417 cm^{-1}) were intact for both the electrolytes, which suggests that the NASICON framework was retained even after long cycling. For pristine NZSP in ***Figure 8.7(a)***, the most noticeable changes were observed at 1441 cm^{-1}, corresponding to carbonate species (CO_3^{2-}). This suggests that the accumulation of Na_2CO_3-type interphase may be due to the air exposure and interfacial reaction with Na metal during cycling. Such carbonate formation is detrimental in nature and can promote dendrite growth during cycling. In comparison, NZSP-LT in ***Figure 8.7(b)*** shows a more complex vibrational spectrum after cycling. In addition to the earlier vibration associated with the NZSP structure, various bands at 2916 cm^{-1} (C-H stretching) and multiple features in the 1200-1500 cm^{-1} region (1456, 1357, 1248 cm^{-1}) appear. These bands mainly originate from the $NaPF_6$/tetraglyme liquid phase and its partial decomposition. Thus, the liquid therapy in NZSP solid electrolyte might form a mixed organic–carbonate interphase and help in stabilizing the Na/NZSP interface.

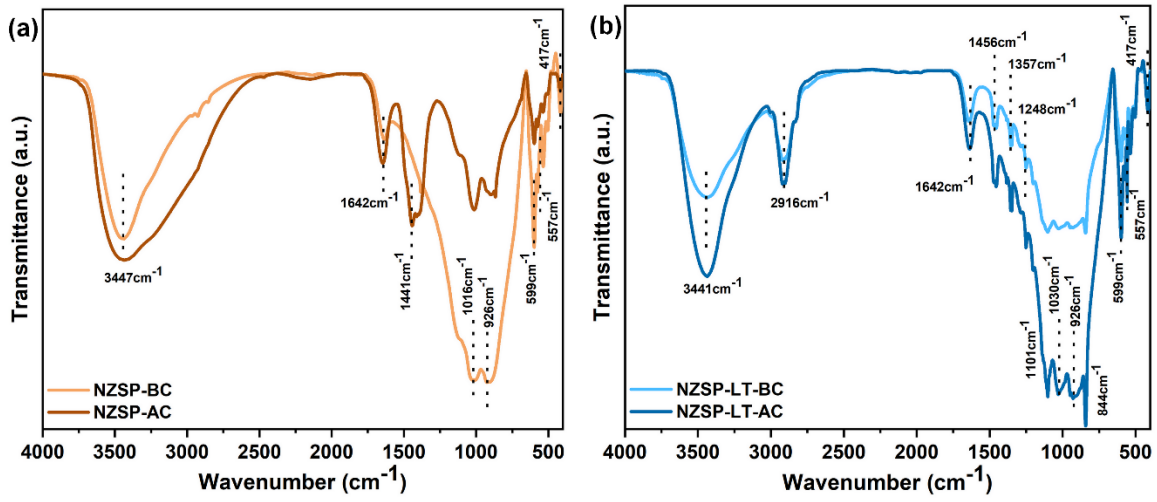

Figure 8.7 *FTIR spectra of (a) NZSP solid electrolyte before and after cycling, and (b) NZSP-LT solid hybrid electrolyte before and after cycling.*

FESEM was also carried out for both the symmetric cell and the full cell, as shown in ***Figure 8.8***. For the Na/Na symmetric cell, the surface morphology of cycled pellets, as shown in ***Figure 8.8(a)-(d)***, revealed that the pristine NZSP interface was rough and non-uniform, and with clear evidence of dendrite growth (***Figure 8.8 (a)*** and ***(b)***). Needle-like and mossy deposits are likely unstable due to the Na plating/stripping behaviour, which is consistent with earlier observations. In comparison, the NZSP-LT interface, as shown in ***Figure 8.8(c)-(d)***, shows a relatively dense and compact morphology, with no dendritic formation. The smoother surface

texture suggests that the liquid phase successfully infiltrates and provides a more homogeneous and uniform Na-ion flux. It also suppressed the dendrite propagation, which is consistent with the earlier observation.

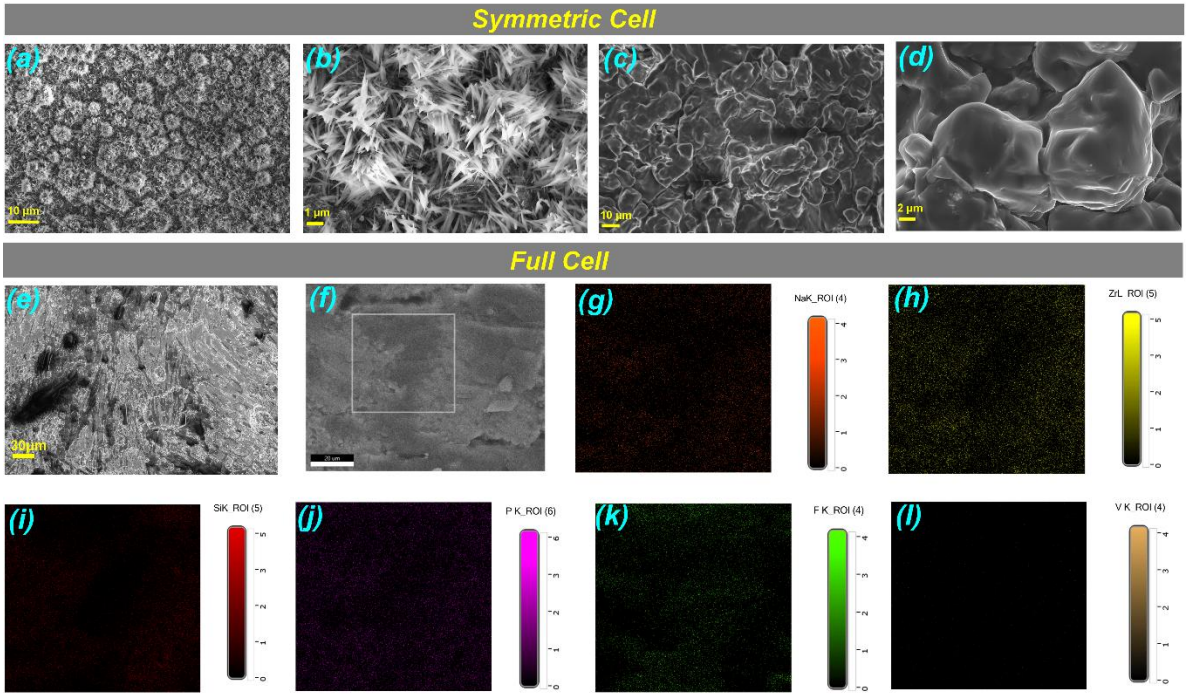

Figure 8.8 *Post-cycling FESEM and elemental mapping of NZSP and NZSP-LT electrolyte material. Symmetric Na/Na cells interfacial morphology of pristine NZSP (a, b) and NZSP-LT (c, d) at two different scales. (e, f) FESEM of a full Na/NZSP-LT/NVP cell. (g-l) EDX elemental mapping of Na, Zr, Si, P, F, and V at the cathode-side NZSP-LT surface.*

The cathode-side interface of the Na/NZSP-LT/NVP full cell was further examined by FESEM and elemental mapping as shown in ***Figure 8.8(e)-(l)***. The FESEM micrograph, as presented in ***Figure 8.7(e)*** and ***(f)***, shows a smoother and more uniform surface compared to the symmetric cell. No deep cracks or dendritic growth was visible. Elemental mapping of Na, Zr, Si, and P confirmed the retention of the NZSP structure. Importantly, the elemental mapping of F, as shown in ***Figure 8.8(k)***, was distributed across the whole interface, suggesting the formation of an F-rich interphase. The V signal, as shown in ***Figure 8.8(l)***, was negligible and indicates the minimal cathode element migration into the electrolyte. Thus, the liquid therapy reduces interfacial resistance and helps to restrict the growth of dendrites in metal batteries. In symmetric cells, dendritic instability was mitigated to some extent, and in full cells, interfacial degradation was suppressed. Thus, optimization of the liquid therapy chemistry to minimize

such decomposition with enhanced interfacial stabilization will be a key step toward practical sodium solid-state batteries.

8.3 Introduction of S in Al doped LLZO material

8.3.1 Experimental

Al-doped LLZO ($Li_{6.25}La_3Al_{0.25}Zr_2O_{12}$) was synthesized via an alanine-assisted auto-combustion route as described earlier **Chapter 2**, ***Section 2.3.1***. $Al(NO_3)_3$ was introduced as a dopant precursor. For S-modified LLZO ($Li_{6.25}La_3Al_{0.25}Zr_2O_{12-x}S_x$ with x = 0.01 to 0.1), Li_2S was used as the sulfur precursor, and the same synthesis protocol was used in the same section. The detailed characterization is already discussed in the same chapter in ***Section 2.7***. The composition and theor corresponding nomenclature are discussed in ***Table 8.1***.

Table 8.1 *Compositions and corresponding nomenclature of Al-doped and S-substituted LLZO samples synthesized in this work.*

Composition	Nomenclature
$Li_7La_3Zr_2O_{12}$	L00
$Li_{6.25}La_3Al_{0.25}Zr_2O_{12}$	S00
$Li_{6.25}La_3Al_{0.25}Zr_2O_{11.99}S_{0.01}$	S01
$Li_{6.25}La_3Al_{0.25}Zr_2O_{11.98}S_{0.02}$	S02
$Li_{6.25}La_3Al_{0.25}Zr_2O_{11.97}S_{0.03}$	S03/A25S03
$Li_{6.25}La_3Al_{0.25}Zr_2O_{11.95}S_{0.05}$	S05
$Li_{6.25}La_3Al_{0.25}Zr_2O_{11.93}S_{0.07}$	S07
$Li_{6.25}La_3Al_{0.25}Zr_2O_{11.9}S_{0.10}$	S1
$Li_{6.1}La_3Al_{0.30}Zr_2O_{11.97}S_{0.03}$	A30S03
$Li_{6.4}La_3Al_{0.20}Zr_2O_{11.97}S_{0.03}$	A20S03
$Li_{6.55}La_3Al_{0.15}Zr_2O_{11.97}S_{0.03}$	A15S03

8.3.2 Results and Discussion

8.3.2.1 Thermal and Structural Studies

To study the thermal decomposition behaviour and to find out the calcination temperature, Thermogravimetric analysis (TGA) coupled with differential thermal analysis (DTA) was carried out for the S-incorporated LLZO powders (S02, S03, S05, and S07) and presented in

Figure 8.9. It is a multi step weight loss profile similar to the pristine LLZO material described in the ***Chapter 3***, ***Figure 3.5***. The weight-loss profiles can be divided into distinct regions. The initial weight loss below ~200 °C (Region I-II) mainly corresponds to the removal of residual water. A second stage of gradual weight loss between ~200 to 450°C (Region III) is mainly attributed to the decomposition of surface carbonates, mainly formed during the combustion synthesis process. The broad weight loss between ~450 to 750°C (Region IV) is may be associated with the gradual decomposition of residual carbonate species. After this region, no significant weight loss is observed. An endothermic peak around 600°C appeared, attributed to the formation of the LLZO material. Also, DTA peak near ~1010°C (Region V), corresponding to the phase crystallization/densification of the garnet lattice.

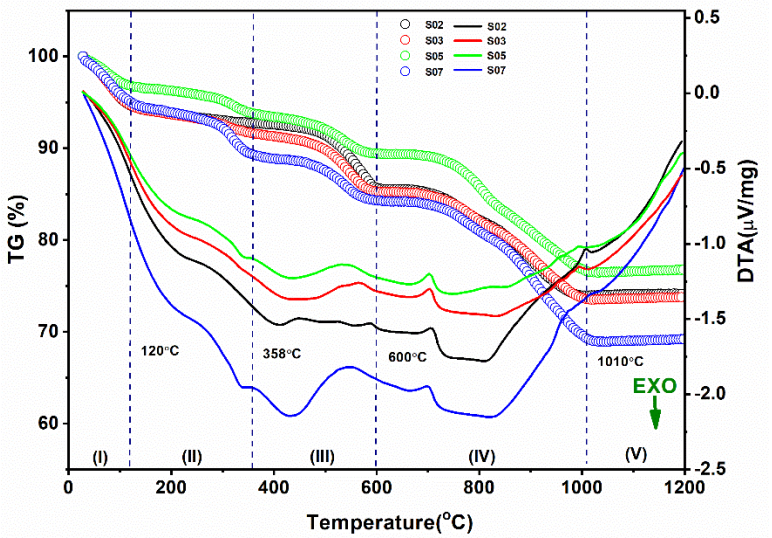

Figure 8.9 *TGA/DTA profiles of S-incorporated LLZO powders (S02, S03, S05, and S07) heated up to 1200 °C in air.*

X-ray diffraction (XRD) was used to check the crystal structure and phases present in all the developed samples. To understand the role of S in the Al-doped LLZO matrix, S was systematically varied. The XRD pattern of S incorporated material is stacked in ***Figure 8.10(a)***. The pattern for the S01-900 and S1-900 samples shows several minor additional peaks along with the c-LLZO phase. At a nominal sulfur incorporation, between S02 and S07 samples, these impurity peaks drastically reduced, and some of them are entirely missing. This suggests that the sulfur co-doping can restrict the formation of secondary phases and promote the formation of cubic LLZO. In ***Figure 8.10(b)***, the XRD patterns of pristine, Al-doped and probable Al-S co-doped materials are shown. As discussed earlier, S incorporation helps in stabilizing the cubic garnet phase and reducing any secondary impurity phases. Whereas, Al doped alone can

stabilise the cubic garnet, which is consistent with the literature. However, Various secondary phases appear in the undoped LLZO system.

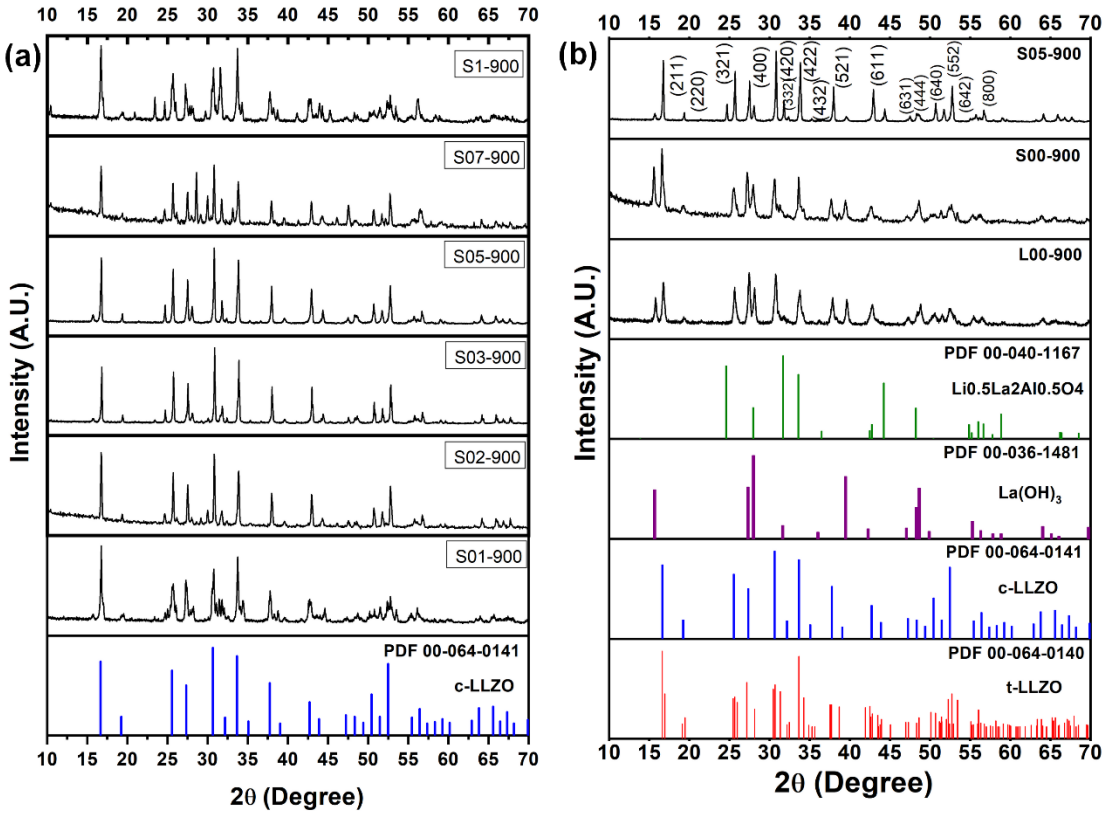

Figure 8.10 (a) *XRD patterns of S incorporated samples in Al-doped LLZO after calcined at 900°C compared with standard JCPDS reference of cubic LLZO, (b) XRD patterns of L00, S00, and S05 compared with reference cards for cubic LLZO (PDF 00-064-0141), tetragonal LLZO (PDF 00-064-0140), $La(OH)_3$ (PDF 00-036-1481), and K_2NiF_4 type phase (PDF 00-040-1167).*

To understand the effect of the concentration of Al in Al-S co-doped material, various samples were prepared and calcined under the same conditions. The XRD pattern of co-doped sample with varation in Al is presented in ***Figure 8.11(a)***. All compositions (A15S03, A20S03, A25S03, and A30S03) calcined at 900 °C for 10h display diffraction peaks that match well with cubic LLZO (PDF 00-064-0141). The absence of strong peak splitting around 30-35° confirms that the cubic phase is dominant. However, with the increasing content of Al, the peak intensity of secondary phases, particularly with Al content impurity phases such as $Li_{0.5}La_2Al_{0.5}O_4$, $LaAlO_3$ etc.) is enhanced.

Whereas ***Figure 8.11(b)*** shows the effect of sintering dwell time on the co-doped (Al25S03 or S03) matrix calcined at 900 °C. At the short durations (2-5 h), weak additional peaks

corresponding to $La_2Zr_2O_7$ are detected which indicates that the incomplete reaction or secondary phase formation. With the increasing in dwelling time, these peaks diminish, and the cubic LLZO phase becomes dominant. This demonstrates that the longer dwelling time improves the phase purity and suppresses the pyrochlore-type $La_2Zr_2O_7$ impurities. Overall, the results confirm that both Al content and sintering duration play key roles in phase stability.

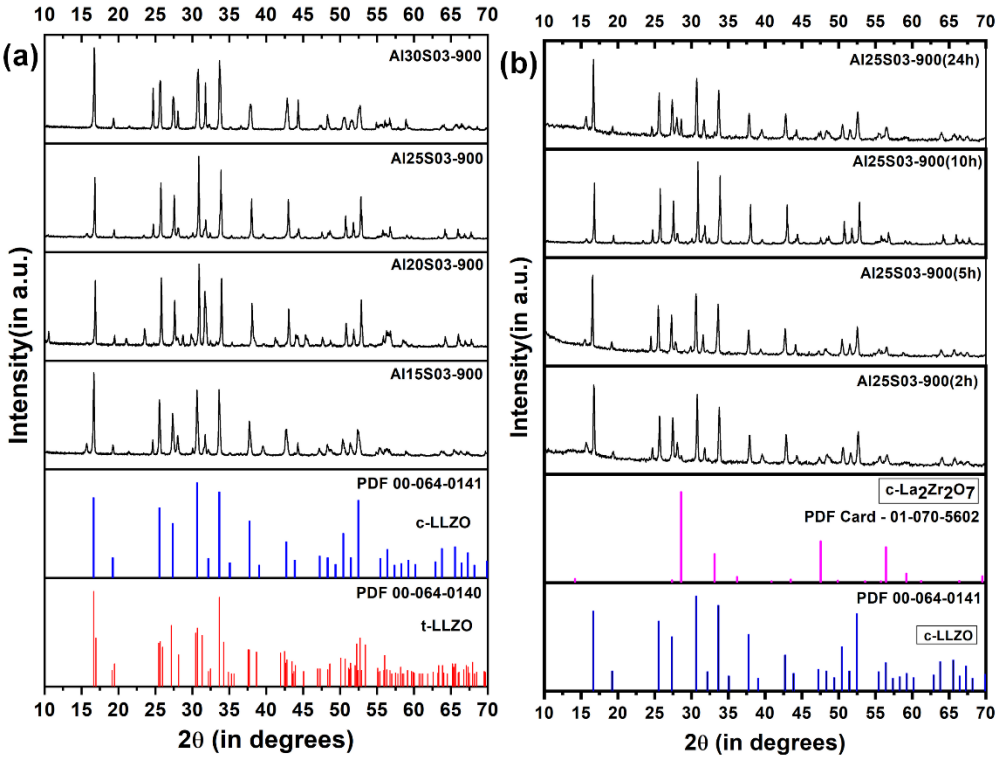

Figure 8.11 *XRD patterns of Al/S co-doped LLZO powders sintered at 900 °C. (a) Samples with varying Al content (b) With various calcination holding times (2-24 h).*

To check whether the co-doping has any effect on lowering the cubic phase stabilisation, Al/S doped sample was also calcined at 800°C for 10h and its X-ray diffraction pattern is collected and shown in ***Figure 8.12***. The XRD pattern of the co-doped sample clearly shows reflections that match well with the cubic garnet phase (PDF 00-064-0141). This is a significant observation, as the cubic polymorph of LLZO is typically stabilized only at higher temperatures (>1000 °C). At lower calcination temperatures, they generally remain in the tetragonal phase or form secondary impurity phases. Achieving cubic stabilization at 800°C is therefore noteworthy because it reduces the lithium loss due to evaporation, and suppresses the formation of unwanted secondary phases such as Li_2ZrO_3 or $La_2Zr_2O_7$. Moreover, the ability to obtain the cubic phase at such a low temperature can help preserve stoichiometry, improve phase purity,

and limit abnormal grain growth, which are all critical for optimizing the ionic conductivity and facilitating scale-up.

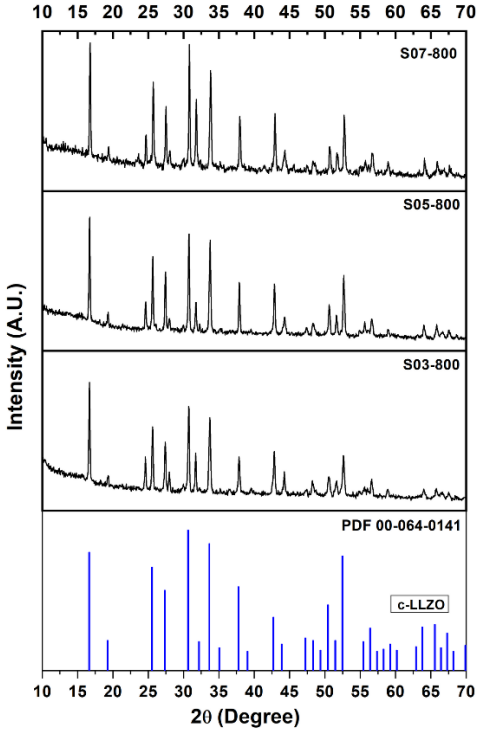

Figure 8.12 XRD patterns of S03, S05, and S07 samples sintered at 800 °C for 10h.

In the FTIR spectra of pristine, Al-doped, and Al/S co-doped LLZO samples sintered at 900 °C are shown in ***Figure 8.13***. In all the samples, the characteristic vibrational bands of garnet-type LLZO are observed. The peaks near 594 cm^{-1} and 499 cm^{-1} correspond to Zr-O stretching in ZrO_6 octahedra. However, the weak band at 418 cm^{-1} is related to lattice bending vibrations. A sharp absorption near 866 cm^{-1}, together with features at 1427 cm^{-1} and 1639-1699 cm^{-1}, arises from CO_3^{2-} vibrations due to surface Li_2CO_3/$La_2(CO_3)_3$ species formed by absorbing atmospheric CO_2 as discussed in ***Chapter 1***. This is very common in garnet electrolytes and often increase the grain boundary resistance.

Interestingly, an additional absorption band at near 721 cm^{-1} is clearly observed in the S-containing samples (S02-S07), but is absent in pristine (L00) and Al-doped (S00) LLZO. This new band suggests the lattice perturbation caused by sulfur incorporation and may indicate the presence of S-related vibrational modes or defect-activated phonons. A broadening of the band around 639 cm^{-1} is also noted in S-doped samples which is consistent with increased structural disorder. Together, the thermal and structural features suggest that the garnet lattice framework remains intact when sulfur is incorporated in the Al-doped matrix. The suppression of

secondary phases, the stabilization of the cubic phase at reduced temperatures, and the appearance of distinct vibrational signatures all indicate that sulfur plays a beneficial role in enhancing phase purity and structural stability.

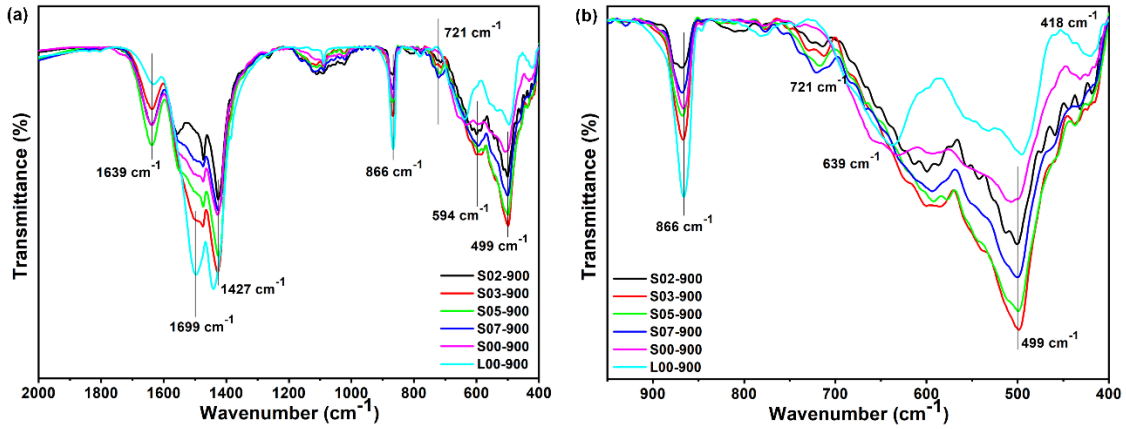

Figure 8.13 FTIR spectra of pristine (L00), Al-doped (S00), and Al/S co-doped LLZO calcined at 900°C.

8.3.2.2 Microstructural Studies

The microstructural features of the Al/S co-doped LLZO samples (S02, S03, S05, and S07) are shown in ***Figure 8.14***. The S02 sample, as presented in Figure 8.14(a), shows fine, nearly spherical nanoparticles (<200 nm) with strong agglomeration, which suggests that the incomplete grain growth occurs at this stage. The S03 sample in ***Figure 8.14(b)*** shows slightly larger particles forming porous agglomerates, where surface roughness indicates the ongoing crystallization. With further increasing in sulfur content, the S05 sample in ***Figure 8.14(c)*** develops irregular micron-sized grains, with several faceted surfaces becoming visible, consistent with the stabilization of the cubic phase. At higher sulfur content S07 as presented in Figure 8.14(d), well-developed plate-like grains with sharp edges are observed. This confirms the formation of a dense and crystalline garnet structure.

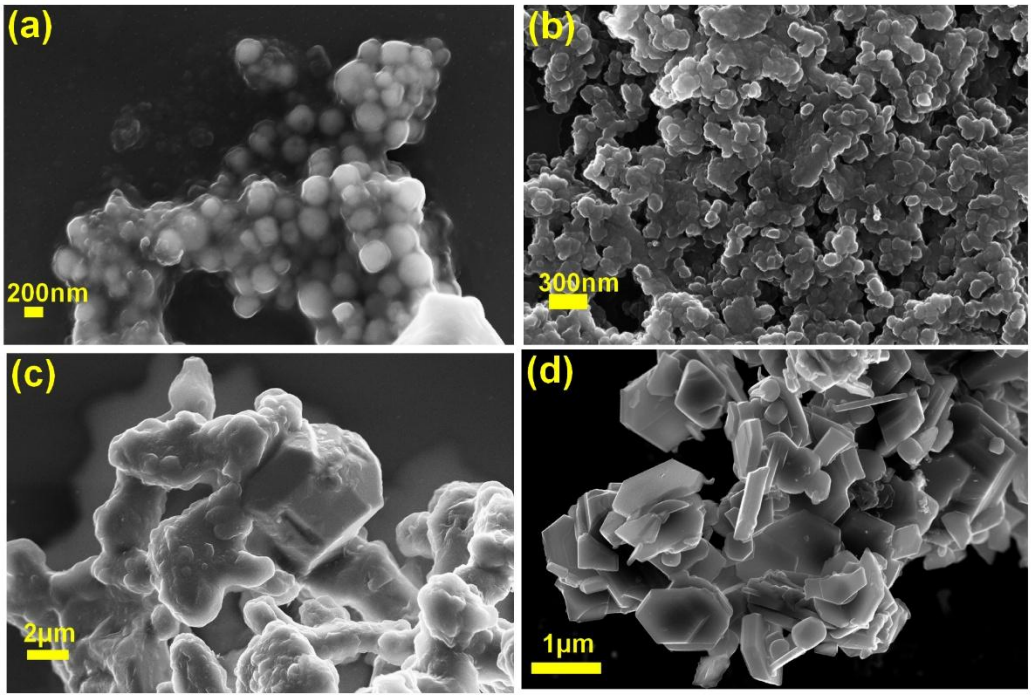

Figure 8.14 *FESEM images of Al/S co-doped LLZO samples: (a) S02, (b) S03, (c) S05, and (d) S07 sintered powders.*

Thus, the evolution from nanoscale particles in S02 to faceted grains in S07 demonstrates the role of sulfur incorporation in enhancing grain growth and crystallinity during calcination.

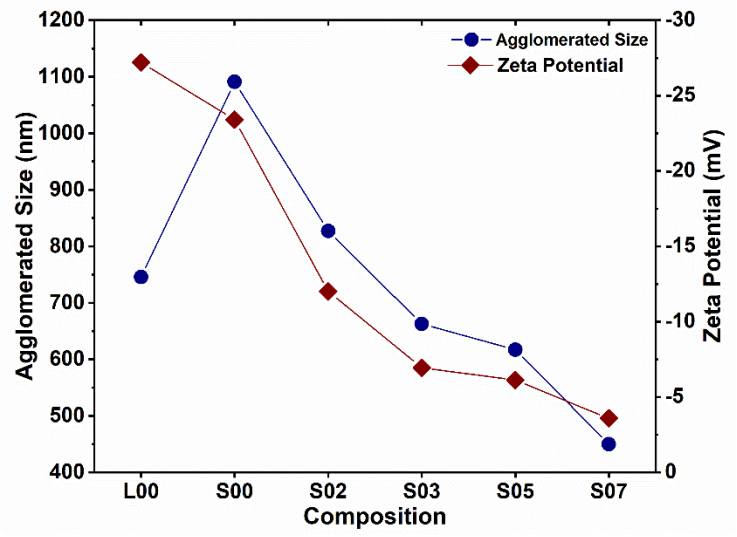

Figure 8.15 *Variation of agglomerated particle size and zeta potential for L00, S00, and Al/S co-doped LLZO samples (S02-S07).*

The correlation between agglomerated size and zeta potential for the L00-S07 series is shown in ***Figure 8.15***. The undoped sample (L00) exhibits a moderate agglomerate size (745.5 nm) with a relatively negative zeta potential (-27.2 mV), suggesting reasonable surface stability. This is consistent with the literature. Upon Al doping (S00), the zeta potential becomes less negative (-23.4 mV) which resulted in poor surface stabilization and a sharp increase in agglomerated size (1091 nm). Interestingly, with the sulfur incorporation (S02-S07), the agglomerated size decreases systematically to 450.1 nm for S07. The zeta potential also moves towards a positive value. This indicates that sulfur modifies the surface charge environment and the nucleation and growth behaviour of the particles, resulting in suppressing the large-scale agglomeration. The results are consistent with earlier FESEM observations, where sulfur-containing samples show finer, faceted grains. Thus, sulfur incorporation appears to modify the structural and morphological changes and reduce the agglomeration and improve phase stability.

8.3.2.3 Electrical Studies

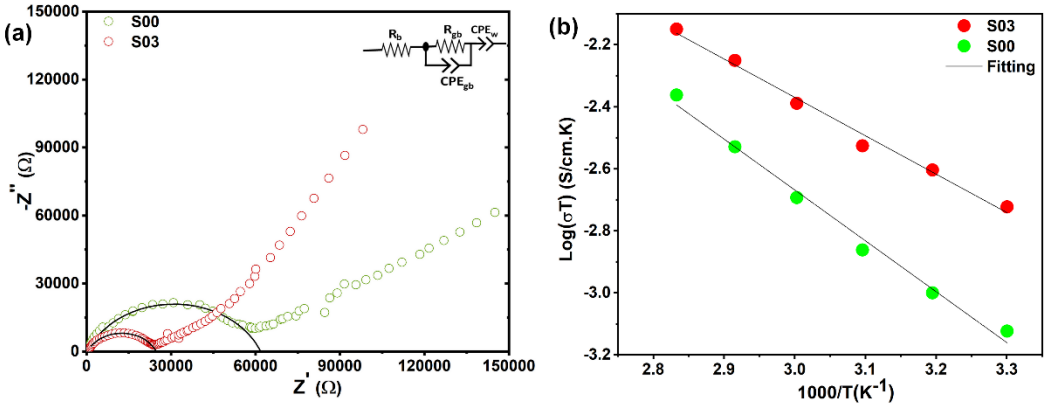

Figure 8.16 (a) Nyquist plots of Al-doped (S00) and Al/S co-doped (S03) LLZO samples fitted with the equivalent circuit model. (b) Arrhenius plots from the conductivity values measured from 30°C-80°C.

The ionic conductivity of the Al-doped (S00) and Al/S co-doped (S03) LLZO materials was measured by EIS in a ZIVE potentiostat. The results are presented in ***Figure 8.16***. The Nyquist

plots in ***Figure 8.16(a)***, showing one semicircular arcs that were fitted using an equivalent circuit model using ZView software. The Al/S co-doped sample (S03) exhibits a lower overall resistance compared to S00 which indicates the improved Li-ion transportation.

The Arrhenius plots are also presented in Figure 8.16(b) reveal a thermally activated behavior consistent with the hopping mechanism of Li^+ ions in the garnet framework. The calculated room-temperature ionic conductivity of S00 is 2.48×10^{-6} S cm^{-1} with an activation energy of 0.33 eV, whereas S03 achieves a higher conductivity of 6.25×10^{-6} S cm^{-1} with a reduced activation energy of 0.25 eV. The enhanced performance of S03 can be attributed to the synergistic effect of sulfur incorporation with Al stabilization, which reduces the energy barrier for Li^+ migration and facilitates higher ionic conductivity.

In summary, Sulfur incorporation successfully modified the structural and electrochemical behaviour of Al-doped LLZO, as seen from the newer bond appearance FTIR, enhanced phase purity, and lower activation energy. Although EDX did not detect sulfur, likely due to its low concentration or dispersed state, the observed improvements confirm its positive influence on cubic stability and Li-ion transport.

8.4 Conclusion

This chapter presented two exploratory studies in parallel, one is related to the interface stabilization and the second one is unconventional lattice engineering in garnet-based electrolyte.

First, liquid therapy was successfully applied to NZSP solid electrolyte, where even a low amount liquid uptake improved the Na metal wettability, reduced interfacial resistance, and delivered long-term stable plating/stripping and full-cell cycling. This demonstrated the versatility of liquid-assisted interfacial stabilization.

Second, Al/S co-doping in LLZO was investigated to explore the effect of co-doping. However, sulfur was not detected by EDX but FTIR and TGA revealed distinct changes, whereas XRD confirmed suppression of secondary phases and cubic stabilization at lower temperatures. Also, impedance studies demonstrated improved conductivity and reduced activation energy. Together, these results highlight that liquid therapy can be generalized to other solid electrolytes and that cation-anion co-doping represents a promising, though challenging, pathway for tailoring the garnet electrolytes.

8.5 References

1 J. B. Goodenough, H. Y.-P. Hong and J. A. Kafalas, *Mater Res Bull*, 1976, 11, 203–220.

2 H. Y.-P. Hong, *Mater Res Bull*, 1976, 11, 173–182.

3 J. Schuett, F. Pescher and S. Neitzel-Grieshammer, *Physical Chemistry Chemical Physics*, 2022, 24, 22154–22167.

4 L. Liu, J. Su, X. Zhou, D. Liang, Y. Liu, R. Tang, Y. Xu, Y. Jiang and Z. Wei, *Mater Today Chem*, 2023, 30, 101495.

5 N. J. Williams, E. Quérel, I. D. Seymour, S. Skinner and A. Aguadero, 2022, preprint, DOI: 10.26434/chemrxiv-2022-hd73j.

6 R. Sampathkumar, M. Echeverría, Y. Zhang, M. Armand and M. Galceran, *Batteries*, 2022, 9, 8.

7 K. Cao, Y. Xia, H. Li, H. Huang, S. Iqbal, M. Yousaf, B. Bin Xu, W. Sun, M. Yan, H. Pan and Y. Jiang, *Sci Bull (Beijing)*, 2024, 69, 49–58.

8 T. Li, B. Chen, T. Wang, C. Liu, W. Yin, Q. Mao, D. Zhou, Y. Hao and X. Liu, *Nat Commun*, 2025, 16, 5668.

9 L. Xiang, X. Li, J. Xiao, L. Zhu and X. Zhan, *Advanced Powder Materials*, 2024, 3, 100181.

10 R. Wagner, G. J. Redhammer, D. Rettenwander, A. Senyshyn, W. Schmidt, M. Wilkening and G. Amthauer, *Chemistry of Materials*, 2016, 28, 1861–1871.

11 N. Bernstein, M. D. Johannes and K. Hoang, *Phys Rev Lett*, 2012, 109, 205702.

12 Y. He, W. Chen, Y. Zhao, Y. Li, C. Lv, H. Li, J. Yang, Z. Gao and J. Luo, *Energy Storage Mater*, 2022, 49, 19–57.

13 Y. Yang and H. Zhu, *ACS Appl Energy Mater*, 2022, 5, 15086–15092.

14 B. Dong, A. R. Haworth, S. R. Yeandel, M. P. Stockham, M. S. James, J. Xiu, D. Wang, P. Goddard, K. E. Johnston and P. R. Slater, *J Mater Chem A Mater*, 2022, 10, 11172–11185.

15 A. Kızılaslan, M. Kırkbınar, T. Cetinkaya and H. Akbulut, *Physical Chemistry Chemical Physics*, 2020, 22, 17221–17228.

CHAPTER 9

Conclusion and Future Perspective

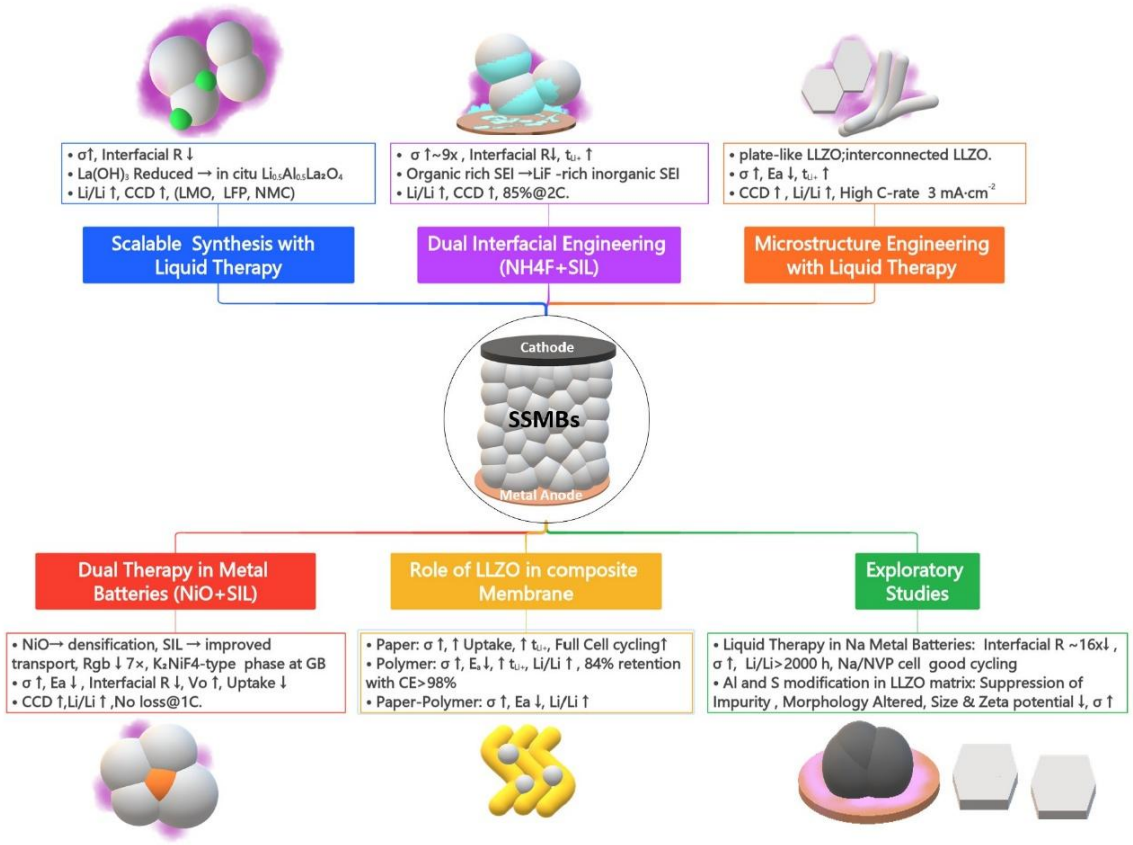

Figure 9.1 *Summary of the key strategies developed in this work for advancing solid-state metal batteries, highlighting improvements in conductivity, interfacial stability, and cycling performance through LLZO-based interfacial and structural engineering.*

9.1 Research Summary

The main aim of this thesis was to address the various challenges associated with the garnet-type solid electrolytes in SSLMBs via a progressive and multi-scale engineering approach. In this thesis, each chapter has some distinct aims and objectives, but together form a coherent roadmap from synthesis optimization to interfacial stabilization, microstructural design, dual therapy, and composite integration, with extensions to exploratory chemistries.

➢ Established Optimized Synthesis and Liquid Therapy

In *Chapter 3*, a facile one-step aqueous combustion synthesis process was optimized using alanine as fuel to synthesize pristine cubic LLZO solid electrolyte. The optimization resulted in a unique neck-fused microstructure with high yield due to control of exothermicity. Structural and spectroscopic characterization (XRD, FESEM, FTIR, ^{1}H NMR, Raman) confirmed the phase stabilization at low temperature. The presence of impurity at the grain boundaries severely impacts the ionic transport and sinterability. However, the solvated ionic liquid (SIL) infusion in engineered LLZO delivers significantly improved electrochemical performance.

- Stable plating/stripping for >200 hours at 0.05 mA.cm^{-2} with no short-circuit was observed with a critical current density reached to 0.45 mA.cm^{-2}.
- A unique in situ lithiated intergranular phase ($Li_{0.5}Al_{0.5}La_2O_4$) was detected post-cycling. Interestingly, the amount of $La(OH)_3$ impurities in c-LLZO is also reduced during cycling.
- This solid hybrid electrolyte delivered excellent cycling performance (up to 360 cycles), high coulombic efficiency (>99%), and robust rate capability (0.05-1.2 mA.cm^{-2}) in Li/$LiMn_2O_4$ configuration.
- Visualization of dendritic penetration at high current density restricts high C-rate operation.

Overall, the combination of morphologically tailored LLZO and SIL infusion delivers high ionic conduction, long-term cycling, and multi-cathode compatibility. Thus, this way a baseline was created using a hybrid configuration for further development in the subsequent chapter.

➢ Breakthrough in Dual Interfacial Engineering

Building on the concept of liquid therapy, the thesis then advanced into a dual interfacial engineering strategy combining chemical surface treatment and liquid infusion in *Chapter 4*. A dual-interfacial engineering strategy was introduced by combining rapid NH_4F surface fluorination with solvated ionic liquid (SIL) infusion in garnet-type LLZO electrolytes. This synergistic approach stabilized the various interfaces, suppressing any parasitic reactions and avoiding any uneven Li deposition. The modification markedly improved the ionic transport, interfacial stability, and electrochemical performance.

- Ionic conductivity enhanced ninefold (7.43×10^{-4} S cm^{-1}) with an electronic conductivity was suppressed to 8.88×10^{-8} S cm^{-1}.
- Li^+ transference number increased from 0.47 to 0.78, and interfacial resistance reduced from ~200 to 36 $\Omega.cm^2$ at room temperature.
- Critical current density reached to 1.45 $mA.cm^{-2}$ compared to 0.45 $mA.cm^{-2}$ for untreated LLZO-SIL.
- Stable Li plating/stripping sustained for >1200 hours at 0.2 $mA.cm^{-2}$ with low overpotential (65 mV vs. 290 mV for untreated).
- DRT analysis suggests the long-term stabilization of various interfacial and charge-transfer resistances.
- Post-cycling XPS further validates the presence of an organic-inorganic hybrid interphase with LiF rich SEI.
- Full-cell tests (Li/SHEs/LMO) delivered 122.2 mAh g^{-1} at 0.1 $mA.cm^{-2}$, with 85% capacity retention after 200 cycles at 2C.

Overall, this strategy provided robust interfacial stabilization with higher conductivity, superior CCD, long-term cycling stability, and LiF rich SEI. Thus, this chapter establishes a scalable pathway to overcome interfacial limitations in SSLMBs.

➢ Proven Microstructural Engineering via Bio-Templating

While interfacial stabilization is a key challenge in metal batteries, the grain and grain boundary transport are also critical for improved performance. To address this in *Chapter 5*, bio-templating strategies were used to engineer the microstructure of Ga-doped LLZO electrolytes using waste biomass (Water Hyacinth) and cellulose as exo-templates. This approach demonstrated a cost-effective and sustainable pathway to fabricate solid electrolytes with improved ion-transport properties and less prone to dendrite growth.

- A novel water hyacinth exo-templating method produced plate-like Ga-LLZO (LLZOWH) mimicking the intercellular structure of the aquatic plant.
- LLZOWH delivers a bulk conductivity of 3.94×10^{-5} S $cm^{-1}$and stable Li plating/stripping cycling up to 295 hours without short circuit in hybrid mode.
- A cellulose exo-templating route (LLZOCET) shows a unique 3D interconnected microstructure of Ga doped LLZO.
- It reduced the grain boundary resistance by half compared to conventional gel-combustion LLZO (LLZOGC).
- The activation energy for ion transport decreased from 0.59 eV (LLZOGC) to 0.37 eV (LLZOCET).
- SIL enhanced wetting and ionic transport in LLZOCET with an impressive ionic conductivity of 0.215 $mS.cm^{-1}$ with very low electronic conductivity (7.59×10^{-8} $S.cm^{-1}$) at room temperature.
- Symmetric cells with LLZOCET-SIL showed stable plating/stripping for >1350 hours without dendrite penetration, with a CCD of 0.7 $mA \cdot cm^{-2}$ compared to 0.4 $mA \cdot cm^{-2}$ for conventional LLZO.
- Full-cell tests with $LiMn_2O_4$ cathodes demonstrated >500 stable cycles across 0.1–3.0 $mA.cm^{-2}$, retaining 94% capacity at 1C with coulombic efficiency >98%.
- Post-cycling analysis confirmed phase stability and microstructural integrity.

Overall, microstructural engineering via natural bio-templates significantly improved ionic transport, grain connectivity, and dendrite suppression. Thus, it establishes the critical role of mesoscale morphology in advancing garnet electrolytes for SSLMBs.

➢ Effective Dual Therapy with NiO and SIL

In *Chapter 6*, a dual-therapy strategy was introduced by combining solid therapy (NiO as sintering aid) with liquid therapy (SIL infusion) to address interfacial incompatibility and dendrite growth in SSLMBs. This combined approach improved both grain boundary transport and Li wettability, leading to enhanced performance in symmetric and full cells.

- NiO addition (0.5 wt%) to Ga-doped LLZO (GN050) helps in densification (~90%) with a formation of a new conductive K_2NiF_4-type lithiated phase and reduced grain boundary resistance by ~7times.

- With SIL infusion (GN050-SIL) in liquid therapy, room-temperature ionic conductivity reached to a maximum of 0.252 $mS.cm^{-1}$ and Li/LLZO interfacial resistance decreased to 87.4 Ω, and the electrochemical stability window broadened to >5.5 V.
- GN050-SIL also showed stable plating/stripping for >1000 hours with a CCD of 0.55 $mA.cm^{-2}$, outperforming pristine Ga-LLZO (GN000-SIL).
- Full cells (Li/GN050-SIL/LMO) delivered superior charge/discharge performance across 0.1-1.4 $mA.cm^{-2}$, maintaining >99% coulombic efficiency and no capacity loss at 1C for 100 cycles, while GN000–SIL cells failed rapidly.
- DRT analysis before, during, and after cycling confirmed stabilization of interphases and improved charge-transfer kinetics across electrode-electrolyte interfaces.

Overall, the dual-therapy approach effectively coupled grain boundary engineering with interfacial stabilization, reducing reliance on excess SIL and moving garnet-based systems closer to practical, scalable SSLMB designs.

➢ LLZO-Based Composite Membranes for Flexi-Batteries

Beyond ceramic pellets, the thesis addressed the critical issue of scalability and mechanical integration by developing composite membranes. In *Chapter 7*, the role of LLZO-based fillers was explored across paper, polymer, and hybrid systems to enhance conductivity, stability, and flexibility in next-generation solid-state batteries. These approaches aimed to overcome the limitations of conventional separators and polymer electrolytes by combining structural reinforcement with active ion-transport pathways.

- Paper-based membranes: Ga-LLZO was impregnated into cellulose paper using a scalable dip-coating method. The resulting separators exhibited improved electrolyte uptake, Li^+ transference number (0.73), and enhanced performance in Li-ion cells compared to Al_2O_3-coated or pristine paper. However, their limited mechanical strength restricted application in Li-metal systems.
- Composite solid polymer electrolytes (CSPEs): Dual-polymer (PVDF-HFP/PEO) matrices loaded with LLZO fillers reduced polymer crystallinity, increased ionic conductivity to ~10^{-4} $S \cdot cm^{-1}$, and delivered wide electrochemical stability (5.23 V). Li/CSPE/Li cells showed >900 hours of stable cycling, while full Li/LFP cells demonstrated ~84% capacity retention with >98% coulombic efficiency.
- Hybrid paper–polymer composites: By integrating cellulose scaffolds with dual-polymer/LLZO matrices, hybrid membranes achieved mechanical reinforcement,

flexibility, and stable ionic conduction. These composites provided improved interfacial stability, reduced polarization, and excellent cycling performance, offering a practical pathway to flexible SSLMBs.

Overall, this chapter demonstrated that LLZO fillers play an active role in enhancing ionic transport and mechanical stability across diverse membrane designs, paving a versatile and scalable route toward flexible and high-performance solid-state lithium batteries.

- **Strategic Extensions**

Finally, the scope of this thesis was extended to alternative chemistries and unconventional doping strategies. In NASICON-type NZSP, SIL infusion reduced interfacial resistance and enabled stable Na plating/stripping, demonstrating that liquid-assisted stabilization is transferable across oxide electrolyte families.

In parallel, Al-S co-doping in LLZO was explored as an unconventional lattice-engineering strategy. Although sulfur incorporation could not be conclusively confirmed, preliminary impedance studies indicated subtle conductivity improvements compared to Al-only systems. These findings underscore both the challenges and opportunities of anion doping in garnets, pointing toward new directions in lattice design.

9.2 Key Insights

A central feature of the current thesis is the multi-scale approach adopted for engineering garnet electrolytes. While each chapter targeted a specific bottleneck- synthesis, interface, microstructure, or scalability. However, when the results are viewed collectively, several common goals coexist. These insights provide a solid framework for the reader and the upcoming researcher in the field of solid-state batteries.

- **Interface Chemistry: The Decisive Frontier**

Across the thesis, strategies that addressed the Li/LLZO interface showed the most significant improvement in performance. From the initial SIL infusion in Chapter 3 to the dual interfacial modification in Chapter 4, it was evident that stabilizing the interphase was the most effective way to lower down the interfacial resistance, suppressing the dendritic growth, and enable long-term cycling. XPS and DRT analyses provided direct mechanistic evidence, showing inorganic LiF-rich SEI and stabilization of relaxation processes. This highlights that interface chemistry

is more crucial than any bulk conductivity. It often restricts the successful operation of practical cell performance in SSLMBs.

- **Synergistic Dual Strategies: The Way Forward**

Another important insight is the superiority of the dual strategy. In both Chapter 4 (NH_4F + SIL) and Chapter 6 (NiO + SIL), dual strategies produced results that were not only quantitatively better but also qualitatively more stable over long-term operation. The dual therapy concept demonstrated that combining solid-phase modifications (densification, phase formation, low uptake) with liquid-phase engineering (wettability, ion solvation, low polarisation) leads to outcomes that neither approach could achieve alone. This insight suggests that future garnet research should prioritize hybrid solutions rather than single-point fixes.

- **Microstructural Engineering: The Overlooked Advantage**

The bio-templating results in Chapter 5 illustrate the often-underestimated role of mesoscale morphology. However, the interfacial treatments improve the contact at the electrode/electrolyte boundary in a better way. But the bulk transport efficiency is equally dependent on grain connectivity and the distribution of grain boundaries. The cellulose-derived LLZO frameworks achieved some of the highest performance metrics because they minimized tortuosity and reduced grain boundary resistance. This confirms that microstructural engineering is a critical, and sometimes overlooked, design dimension in garnet electrolytes.

- **Composites: The Bridge to Scalability**

Chapter 7 demonstrated that dense ceramics are scientifically compelling and can have more potential to deliver higher energy and power density, but they are mechanically brittle and difficult to integrate at scale. On the other hand, composite membranes combining LLZO fillers with polymer or paper matrices offered a pathway to flexibility and processability without sacrificing the ionic performance.

- **Beyond Garnets: Transferability Across Chemistries**

The exploratory studies in Chapter 8 further suggest that the concepts developed for LLZO are not just confined to a single electrolyte system or lithium-based batteries. The success of SIL infusion in reducing the interfacial resistance in NASICON-type NZSP indicates that liquid-assisted stabilization is a generalizable strategy across oxide families. Similarly, even the preliminary Al-S doping studies suggest that unconventional compositional modifications can

provide meaningful changes in conductivity. These outcomes broaden the overall impact of this work and show that the principles developed here can be easily deployed towards other battery chemistries or any related fields.

9.3 Limitations of the Present Research Work

Despite the encouraging results, several limitations are still there. Such as, the interpretations regarding the interfacial stabilization and the role of secondary phases (e.g., K_2NiF_4-type during the solid therapy via NiO sintering aid in LLZO) were largely based on XRD, FESEM, Impedance, DRT, cycling performance. Thus, more direct operando characterizations such as in situ XPS, neutron depth profiling, or bias-dependent electron microscopy are necessary to validate the interphase evolution, Li-ion transport pathways, and dendrite suppression. Similarly, the exploration of unconventional dopants such as S in Al-S co-modified LLZO was preliminary, with incorporation not conclusively confirmed, and no theoretical or AI/ML-based modelling has been conducted so far. Thus, to predict the dopant site preference, stability, or transport mechanisms the theoretical validation is necessary. At the device level, testing was foucsed only via coin cells, which provided mechanistic insights but do not capture the realistic constraints of pouch cells (e.g., stack pressure, electrode loading, thermal gradients). Thus, the performance cannot be directly extrapolated to industrial scales. Scalability challenges also remain a major factor mainly during aqueous combustion and bio-templating process. Also, several performance in Li/Li symmetric cell have conducted with a stability beyond 1000 h but for commercial viability the cell has to run few multi-thousand-hour operation under high-rate conditions, which was beyond the scope of the present work.

9.4 Future Perspective

In this direction, several research directions can be built, particularly on the grounds of the present research work. Advanced interfacial engineering remains a priority, where multifunctional interphases (e.g., Li_3PO_4, Li_3N, LiF-Li_2O bilayers) or ultrathin coatings applied by ALD/MLD could provide conformal, stable, and conductive interfaces. The interface engineering can be done via polymer-assisted methods. At the materials level, systematic doping and lattice engineering including controlled anion substitution, co-doping, and defect engineering should be pursued with the help of theoretical modeling and AI/ML-guided screening. Parallel to this, operando characterisation (e.g., XPS, NDP, in situ TEM, synchrotron tomography) will be vital to directly visualise the interfacial evolution, Li-ion transport, and

dendrite suppression mechanisms under realistic cycling conditions. This provides the mechanistic clarity missing from post-mortem analyses in the current study. On the device engineering aspect, the scale-up of composite and hybrid electrolytes through methods like tape casting, screen printing, or roll-to-roll lamination will be very crucial to reduce the thickness of the solid electrolyte for the successful application. The mechanical and electrochemical benchmarking will be very crucial in this design. Future work should also extend to device-level demonstrations, with pouch cell fabrication tested under realistic stack pressures, high cathode loadings, and fast-charging conditions, targeting lifetimes beyond 2000 cycles. Finally, the principles developed here could be extended across chemistries, including Na-ion, multivalent (Mg, Zn, Al), and halide-based solid electrolytes, where interfacial instability and dendrite suppression remain bottlenecks.

9.4 Commercial Outlook

The strategies developed in this work demonstrate that the LLZO-based solid electrolytes can achieve practical levels of ionic conductivity, interfacial stability, and cycling performance, bringing them closer to industrial benchmarks as outlined in ***Table 9.1***. Scalable synthesis routes (combustion-assisted methods, liquid therapy, and composite membranes) provide a pathway for cost-effective processing. However, challenges such as high sintering costs, moisture sensitivity, and reliable electrode-electrolyte integration must still be addressed. With further optimization toward thin-film electrolytes and pouch-cell demonstrations, LLZO-based systems hold strong potential for next-generation solid-state batteries in electric vehicles.

Table 9.1 *The optimized LLZO-based systems demonstrated competitive electrolyte properties, stable electrode integration, and promising full-cell performance, underscoring their potential for next-generation solid-state batteries.*

S.No	PARAMETER		ACHIEVED VALUE
ELECTROLYTE			
1.	Ionic Conductivity		~10^{-4} S.cm^{-1} (LLZO-SIL)
2.	Electronic Conductivity		10^{-6}-10^{-9} S/cm
3.	Electrochemical Window		~ 5-6V
4.	Thickness of the Electrolyte pellet		600-800 µm
5.	Diameter/dimension of the Electrolyte pellet		19 mm
6.	Particle Size		100-250 nm (as-synthesized) 2-5 µm (after granulation)
7.	Aerial Loading		Weight of the pellet ~0.6-0.7 g ~276 mg/cm² equivalent to 400-600 µm thickness
8.	Sintering Temperature		1000ºC
9.	Electrolyte Synthesis Technique		Soft Chemical Method, Aqueous
ANODE (Li Metal)			
1.	Aerial Loading		Equivalent thickness 18-20 µm
2.	Thickness		50 µm
3.	Columbic Capacity		>95%
CATHODE (Commercial)			
1.	Aerial Loading		Equivalent to 150-200 µm thickness
2.	Thickness		150-200 µm
3.	Columbic Capacity		>95%
CELL			
1.	Dimension / Diameter of Cell		2032 coin cell/ 20 mm dia, 3.2 mm thickness
2.	Operating Pressure		Ambient
3.	Current Density		0.05-3.0 mA.cm^{-2}
4.	Critical Current Density		1450 µA.cm^{-2}
5.	Capacity	Ambient	0.98-1.0 mAh (depending on cathode)
6.	Operating C-rates	Ambient	Up to 3C (pulse 18C)
7.	Open Circuit Voltage		2.8-3.5V (depending on the cathode used)
8.	Operating Cell Voltage Range		2.5-3.8V/2.5-4.2V/3.0-4.5V (for LFP/NMC/LMO)
9.	No. of Cycles	Ambient	500 cycles (lab level)
10.	Columbic Efficiency		>98%

Appendix I

List of Publications/Conference Papers/Awards

Research Publications

1. **Kuntal Ghosh,** Mir Wasim Raja, *Ga-Doped LLZO Solid-State Electrolyte with Unique "Plate-like" Morphology Derived from Water Hyacinth (Eichhornia crassipes) Aquatic Weed: Waste to Wealth Conversion*, ACS Omega 2022, 7, 37, 33385–33396.

2. **Kuntal Ghosh**, Mir Wasim Raja, *Engineered $Li_7La_3Zr_2O_{12}$ (LLZO) for Pseudo-Solid-State Lithium Metal Batteries (SSLMBs): Tailor-Made Synthesis, Evolution of the Microstructure, Suppression of Dendritic Growth, and Enhanced Electrochemical Performance*, ACS Applied Energy Materials 2023, 6,7, 4035–4052.

3. **Kuntal Ghosh**, Mir Wasim Raja, *Facile Li-ion transport in microstructurally engineered hybrid LLZO electrolyte for application in pseudo-Solid State Lithium Metal Batteries*, Chemical Engineering Journal 2024, 480, 148200.

4. Mononita Das**, Kuntal Ghosh**, Mir Wasim Raja, *Flexible ceramic based 'paper separator' with enhanced safety for high performance lithium-ion batteries: Probing the effect of ceramics impregnation on electrochemical performances,* J*ournal of Power Sources 2024, 606, 234573.*

5. **Kuntal Ghosh**[1], Mononita Das[1], Mir Wasim Raja, *Role of LLZO active filler in PVDF-modified cellulosic paper matrix: A sustainable, thermally durable and high-performance separator for next generation lithium batteries,* Journal of Power Sources, 2025,654, 237838. ([1]Contribute Equally)

6. Mononita Das, **Kuntal Ghosh**, Vijaya, Mir Wasim Raja, *The critical role of Al2O3, BaTiO3 and ZrO2 nanoceramic fillers in PVDF-HFP based composite polymer electrolytes for high performance lithium-metal batteries,* Solid State Ionics, 430, 2025, 117008

7. **Kuntal Ghosh**[1], Mononita Das[1], Mir Wasim Raja, *LLZO incorporated Dual Polymer-based Composite Electrolyte for Enhanced Conductivity and Long-Term Stability for Solid-State Lithium-Metal Batteries,* Journal of Solid State Electrochemistry (In Press). ([1]Contribute Equally)

8. **Kuntal Ghosh**, Mononita Das, Alok Kumar Chaudhary, Mir Wasim Raja, *High-Performance Quasi-Solid-State Lithium Metal Batteries: Interface Engineering Using Solid-Liquid Dual Therapy by Solvated Ionic Liquid and NiO,* ACS Applied Materials & Interfaces (Under Review).

9. **Kuntal Ghosh**, Mononita Das, Mir Wasim Raja, LiF-Rich Dual Interface Engineering in LLZO Electrolytes via NH_4F Treatment and Solvated Ionic Liquid Infusion for Solid-State Lithium Metal Batteries. (In Submission)

10. **Kuntal Ghosh**, Mononita Das, Mir Wasim Raja, Mitigating Solid-Solid Interfacial Challenges in NZSP Solid Electrolytes Using Ether-Based Liquid Therapy for High-Performance Quasi-Solid-State Sodium Metal Batteries. (In Submission)

11. Mononita Das, **Kuntal Ghosh**, Koushik Dana, Mir Wasim Raja, Paper-Clay Separator: Montmorillonite clay impregnated paper-based sustainable advanced separator for Lithium-ion Battery application. (In Preparation)

12. Mononita Das, **Kuntal Ghosh**, Srikrishna Manna, Mir Wasim Raja, Inclusion of Zr-based Organo-Inorgano hybrid materials in paper matrix: The next generation sustainable Paper Separator' for lithium-ion batteries with improved electrochemical performance and safety. (In Preparation)

Conferences Attended

1. Kuntal Ghosh, Sudip Kumar Ghosh, and Mir Wasim Raja
Aqueous-Based Synthesis of $Li_7La_3Zr_2O_{12}$ Garnet Electrolyte for All-Ceramic Monolithic Lithium Batteries (ACMLBs)
5th National Symposium on Shaping the Energy Future: Challenges and Opportunities (SEFCO-2021)
Organized by CSIR–IIP, Dehradun, Uttarakhand, India, August 27, 2021

POSTER

2. Kuntal Ghosh, Sudip Kumar Ghosh, and Mir Wasim Raja
Engineered Microstructure of $Li_7La_3Zr_2O_{12}$ Garnet Electrolyte Derived from Water Hyacinth for All-Ceramic Monolithic Lithium Batteries
International Virtual Conference on Advances in Ceramics & Cement Technologies: Materials & Manufacturing (ICACT-2021)
Organized by Indian Ceramic Society, PDA College of Engineering, Kalaburagi, Karnataka, India, December 13–14, 2021

FLASH TALK PRESENTATION

3. Kuntal Ghosh and Mir Wasim Raja
Towards "Safer & Better Batteries": Engineered Solid-State Electrolyte Derived from Biowaste for Next-Generation Solid-State Lithium Batteries
161st Birth Anniversary Celebration of Acharya P.C. Ray & International Seminar on Recent Advances in Chemistry and Material Science (RACMS 2022)
Jointly organized by Ramakrishna Mission Institute of Culture, Golpark, and Jadavpur University, Kolkata, India, July 30 – August 3, 2022

ORAL PRESENTATION

4. Kuntal Ghosh and Mir Wasim Raja
Next-Generation Solid-State Lithium Metal Batteries (SSLMBs) with Engineered $Li_7La_3Zr_2O_{12}$ Garnet Electrolyte: Tailor-made Synthesis, Unique Microstructure, and Enhanced Cell Performance
International Conference on Global Trends in Traditional to Space Ceramics (GT-TSC'22)
Organized by IIT BHU, Varanasi, India, December 8–9, 2022

POSTER

5. Kuntal Ghosh and Mir Wasim Raja
Introducing Li–LLZO–LMO Advanced Solid-State Lithium Batteries: No Capacity Fading, Fast Charging & Long-Life Cycle
Young Scientist Colloquium 2022
Organized by MRSI (Kolkata Chapter), CSIR–CGCRI, Kolkata, India, December 16, 2022

POSTER

6. Kuntal Ghosh and Mir Wasim Raja
Engineered Solid Electrolyte with Interfacial Liquid Therapy: A Synergistic Strategy for Facile Li-ion Transportation in Metal Batteries
Young Scientist Colloquium 2023
Organized by MRSI (Kolkata Chapter), Jadavpur University, Kolkata, India, December 1, 2023

POSTER

7. Kuntal Ghosh and Mir Wasim Raja
LiF-Enriched SEI: Stabilizing $Li_7La_3Zr_2O_{12}$–Li Metal Interface in High-Performance Pseudo-Solid-State Lithium Metal Batteries (SSLMBs)
International Meeting on Energy Storage Devices (IMESD 2023)
Organized by IIT Roorkee, Uttarakhand, India, December 7–10, 2023

POSTER

8. **Kuntal Ghosh** and Mir Wasim Raja
Solid-State Electrolyte with Unique Plate-like Morphology Derived from Water Hyacinth for Inhibiting Lithium Dendrite Penetration in Metal Batteries
38th National Science Day Celebration & National Seminar on Accelerating Photobiology Research towards Achieving the Sustainable Development Goals
Organized by the Indian Photobiology Society, Kolkata, India, March 1–2, 2024

ORAL PRESENTATION

9. Kuntal Ghosh, Mononita Das, and Mir Wasim Raja
LiF-Enriched SEI: Enhancing Stability at $Li_7La_3Zr_2O_{12}$–Li Interface in High-Performance Pseudo-Solid-State Metal Batteries
International Conference on Advanced Energy Materials and Interfaces (AEMI 2024)
Jointly organized by IISER Pune, TCG CREST, and Wiley, IISER Pune, Maharashtra, India, December 9–11, 2024

POSTER

10. Kuntal Ghosh, Mononita Das, and Mir Wasim Raja
LLZO-Incorporated Duo-polymer based Composite Electrolyte: Boosting Critical Current Density and Long-Term Stability for Solid-State Metal Batteries
International Conference on Advances in Sustainable Solutions for Energy Transitions (ASSET 2025)
Organized by IIT Guwahati, Assam, India, January 2–4, 2025

ORAL PRESENTATION

11. Kuntal Ghosh, Mononita Das, Alok Kumar Chaudhary, and Mir Wasim Raja
NiO-Assisted Sintering of LLZO-Based Hybrid Electrolytes for Metal Batteries: An Innovative Approach Towards Semi-Solid to Almost Solid-State Systems
International Conference on Energy Conversion and Storage (IECS-2025)

IIT Madras, Chennai, Tamil Nadu, India, January 27–29, 2025

POSTER

12. Kuntal Ghosh, Mononita Das, and Mir Wasim Raja
Plate-like LLZO Derived from Biowaste Eichhornia Crassipes: An Effective Strategy for Dendrite-Inhibited Metal Batteries
International Conference on Sustainable Batteries (ICSB 2025)
Organized by TCG CREST, Biswa Bangla Convention Center, Kolkata, West Bengal, India, February 24–27, 2025

POSTER

13. Kuntal Ghosh, Mononita Das, and Mir Wasim Raja
"Plate-like" LLZO Exo-templated from Eichhornia Crassipes: An Effective Strategy for Dendrite-Inhibited Solid State Metal Batteries
Glamics Fiesta-2025, Research Scholars' Day- 2025
Organized by CSIR – CGCRI, Kolkata, West Bengal, India, June 19-20, 2025

ORAL

Awards

1. **Kuntal Ghosh** and Mir Wasim Raja "*Solid State Electrolyte with Unique Plate-like Morphology Derived from Water Hyacinth for Inhibiting Lithium Dendrite Penetration in Metal Batteries*", 38th National Science Day Celebration & National Seminar on -Accelerating Photobiology Research towards Achieving the Sustainable Development Goals 1st –02nd March, 2024 Organized By Indian Photobiology Society, Kolkata, India.

- ***Young Scientist Award 2024 (Research Scholar/ RA Category)***

2. **Kuntal Ghosh**, Mononita Das, and Mir Wasim Raja, "*Plate-like LLZO Derived from Biowaste Eichhornia Crassipes: An Effective Strategy for Dendrite-Inhibited Metal Batteries*" International Conference on Sustainable Batteries (ICSB), Organized by TCG CREST, 24- 27 February 2025, Biswas Bangla Convention Center, Kolkata, West Bengal.

- ***Poster Prize Award 2024 (Sustainable Energy and Fuels, RSC)***

Reprint of the Published Works

ACS OMEGA

http://pubs.acs.org/journal/acsodf

Article

Ga-Doped LLZO Solid-State Electrolyte with Unique "Plate-like" Morphology Derived from Water Hyacinth (*Eichhornia crassipes*) Aquatic Weed: Waste to Wealth Conversion

Kuntal Ghosh and Mir Wasim Raja*

Cite This: *ACS Omega* 2022, 7, 33385−33396

Read Online

ACCESS | Metrics & More | Article Recommendations | Supporting Information

ABSTRACT: An attempt has been made for the first time to convert waste biomass such as water hyacinth (WH) to a functional energy material in a cost-effective way. The present research describes a novel exo-templating methodology to develop engineered microstructure of Ga-doped $Li_7La_3Zr_2O_{12}$ ($Li_{6.25}La_3Ga_{0.25}Zr_2O_{12}$, referred as WH-Ga-LLZO) solid-state electrolyte for its use in all solid-state lithium batteries (ASSLBs) by mimicking the intercellular structure of water hyacinth (*Eichhornia crassipes*), an invasive and noxious aquatic plant. The developed exo-templated methodology offers a low calcination temperature of 1000 °C in air where all the major peaks could be indexed as cubic garnet, as confirmed by XRD. The FESEM micrographs revealed a unique "plate-like" morphology that mimicked the intercellular structure of water hyacinth fiber. The bulk lithium-ion conductivity in the WH-Ga-LLZO electrolyte was found to be 3.94×10^{-5} S/cm. Li/WH-Ga-LLZO/Li cells were galvanostatically cycled for a continuous 295 h with increasing step current densities from 28 $\mu A/cm^2$ without a short circuit. The highest current density as measured for maximum polarization in a symmetric cell was found to be 452 $\mu A/cm^2$. The WH exo-templated methodology was thus developed and optimized and can be extended for synthesizing any application-specific multifunctional materials.

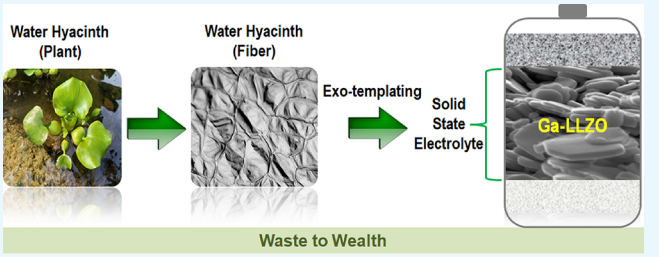

INTRODUCTION

It is always fascinating to design application-specific materials with self-assembling architectures, controlled morphology, and a high degree of crystallinity by using templates of geometrically complex biostructures available in nature. In the last two decades, varieties of biotemplates, such as bacteria,[1,2] eggshell membranes,[3] paper,[4] insect wings,[5] cotton,[6−8] algae,[9] fruits,[10] etc., have been used to synthesize metals, alloys, metal oxides, semiconductors, ceramics, and composite materials. These templates or bioscaffolds offer plenty of room to engineer material structures same as the template's morphology. Depending on their nature of synthesis, Ozin et al.[11] proposed that biotemplating methods may be classified in three broad categories, that is, the negative template method, positive template method, and surface step edge template method. Among them, exo-templating offers an easy synthesis option where the bioscaffold is used as a sacrificial template and is removed at the end of the synthesis process, resulting in an exo-pattern of the template used. Several researchers worldwide reported hierarchically ordered structures using biotemplates of different natures and types. Chen et al. reported the synthesis of $SrCrO_4$ nanostructures with excellent optical properties by mimicking an inner squama layer of onion.[12] In 2014, Song et al.[7] successfully synthesized $LaFeO_3$ hollow fibers from cotton with enhanced gas-sensing properties. TiO_2 crystals derived from the eggshell membrane by Kale et al.[4] showed a unique morphology and interesting properties when tested in dye-sensitized solar cells. Zhang et al.[10] successfully used grapefruit exocarp as a template for the synthesis of porous hierarchical biomorphic SnO_2 crystalline materials with an average particle size of ∼10 nm. Wang et al.[13] used butterfly wings to synthesize quasi-periodic structures of Titania photoanodes. In the recent past, we also successfully synthesized a $BaBi_{0.2}Co_{0.35}Fe_{0.45}O_{3-\delta}$ (BBCF) perovskite-type oxygen separation membrane with a "nanorod" microstructure using water hyacinth (*Eichhornia crassipes*; *E. crassipes*) as an exo-template and obtained a twofold increase in electronic conductivity compared to the conventionally prepared BBCF materials.[14]

In the present work, an attempt has been made for the first time to develop a unique "plate-like" microstructure by mimicking the intercellular structure of WH fibers. Here, we particularly emphasizes a facile synthesis process of preparing a

Received: June 27, 2022
Accepted: August 31, 2022
Published: September 9, 2022

ACS APPLIED ENERGY MATERIALS

www.acsaem.org Article

Engineered $Li_7La_3Zr_2O_{12}$ (LLZO) for Pseudo-Solid-State Lithium Metal Batteries (SSLMBs): Tailor-Made Synthesis, Evolution of the Microstructure, Suppression of Dendritic Growth, and Enhanced Electrochemical Performance

Kuntal Ghosh and Mir Wasim Raja*

Cite This: *ACS Appl. Energy Mater.* 2023, 6, 4035−4052 Read Online

ACCESS | Metrics & More | Article Recommendations | Supporting Information

ABSTRACT: Morphologically engineered $Li_7La_3Zr_2O_{12}$ (LLZO) impregnated with a common solvated ionic liquid (SIL) can greatly influence the cycling performance (360 cycles), coulombic efficiency (>99%), and high rate capability (0.05−1.2 mA·cm^{-2}) of pseudo-solid-state lithium metal batteries (SSLMBs). In this report, to obtain a unique microstructure of cubic-LLZO, a fine-tuned combustion synthesis process was first designed; synthetic parameters were duly optimized, and powders were characterized by X-ray diffraction (XRD), field emission scanning electron microscopy (FESEM), Fourier transform infrared spectroscopy (FTIR), ^{1}H NMR, and Raman spectroscopy. An in-depth analysis of powder properties and electrochemical behavior of the fabricated SSLM cells revealed that impurities present in LLZO significantly facilitated electrochemical cell performances. Such a combination of the engineered LLZO impregnated with the SIL enabled the plating and stripping cycles in Li symmetric cells with up to 200 h of operation at a constant current density of 0.05 mA·cm^{-2} avoiding short circuit. The critical current density (CCD) was found to be 450 μA cm^{-2}, which is significantly higher than the other reported CCD values for pristine LLZO. The post-electrochemical study revealed that transgranular lithium dendritic growth, a genuine problem in SSLMBs, was impeded to a significant extent by the engineered LLZO and an in situ formed phase, $Li_{0.5}Al_{0.5}La_2O_4$, at grain boundaries during cycling. The multicathode compatibility tests as performed (Li/LLZO-SIL/LMO, Li/LLZO-SIL/LFP, and Li/LLZO-SIL/NMC111) exhibited that morphologically altered LLZO with the SIL interface is compatible with most of the commercial cathodes. The study thus envisaged that the engineered LLZO solid electrolyte impregnated with the SIL can exert a synergistic effect to enhance faster Li-ion conduction as well as resistance to Li dendritic growth, providing a path for developing high-performance SSLMBs.

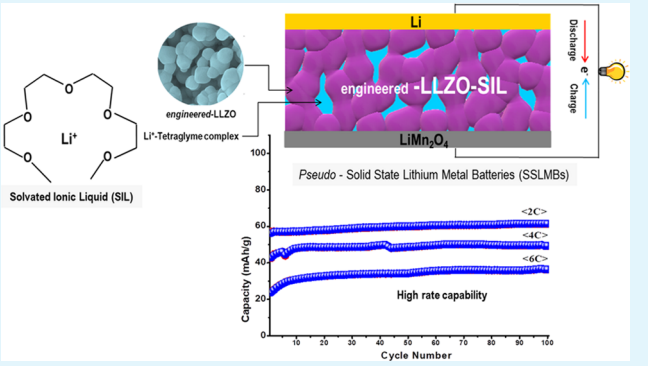

KEYWORDS: *solid-state lithium metal batteries, solid electrolyte, combustion synthesis, engineered microstructure, solvated ionic liquid, critical current density, rate capability, charge−discharge cycle*

1. INTRODUCTION

In the post-"rocking-chair" era of the lithium-ion battery technology, a new configuration of solid-state lithium metal batteries (SSLMBs) has now emerged with promise to deliver high-energy and high-power density batteries. Such a configuration relies on the use of the Li-metal anode (3860 mAh g^{-1}) instead of the conventional low-capacity graphite (372 mAh g^{-1}) and fast Li-ion conducting ceramic electrolytes instead of the organic liquid electrolyte.[1,2] It is envisaged that the solid electrolyte can (i) eliminate safety issues, which are major concerns of flammable liquid electrolytes, (ii) impede lithium dendritic growth, creating an opportunity to use the lithium metal anode, and (iii) control parasitic side reactions, resulting in a longer cycle life of the batteries.[1−3] Despite several advantages, producing all-solid-state lithium batteries (ASSLBs) using ceramic electrolytes still faces serious scientific and engineering challenges related to establishing stable solid electrolyte−electrode interfaces.[4] One of the possible solutions is to build an electrolyte that can deliver the benefits of both solid-state and liquid electrolytes.[5] Here, the concept of a "hybrid electrolyte" comprising a solid inorganic fast ion-conducting robust ceramic matrix impregnated with a solvated ionic liquid (SIL) shows real promise to deliver the desired

Received: February 3, 2023
Accepted: March 10, 2023
Published: March 21, 2023

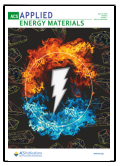

https://doi.org/10.1021/acsaem.3c00291
ACS Appl. Energy Mater. 2023, 6, 4035−4052

Chemical Engineering Journal 480 (2024) 148200

Contents lists available at ScienceDirect

Chemical Engineering Journal

journal homepage: www.elsevier.com/locate/cej

Facile Li-ion transport in microstructurally engineered hybrid LLZO electrolyte for application in pseudo-solid state lithium metal batteries

Kuntal Ghosh, Mir Wasim Raja *

Energy Materials and Devices Division, CSIR-Central Glass and Ceramic Research Institute, Kolkata 700032, India

ARTICLE INFO

Keywords:
LLZO garnet
Microstructure
Solvated ionic liquid
Solid state lithium metal batteries
Electrochemical performance
Hybrid solid electrolytes

ABSTRACT

The present study probes the effects of microstructurally engineered Ga-LLZO ($Li_{6.25}La_3Ga_{0.25}Zr_2O_{12}$) infused with solvated ionic liquid (SIL) as an advanced solid-state hybrid electrolyte (SHE) for application in pseudo-solid state lithium metal batteries (SSLMBs). To obtain unique microstructure, gel impregnated based cellulose *exo*-templating process (LLZOCET) designed and the product powder was duly characterized by XRD, RAMAN, FTIR, FESEM and TEM. The electrical properties of engineered Ga-LLZO demonstrated a two-fold reduction in grain boundary resistance and improved lithium-ion transport at RT with lower activation energy (E_a = 0.37 eV) compared to conventionally prepared Ga-LLZO (E_a = 0.59 eV) by gel combustion method (LLZOGC). SHE was prepared using sintered Ga-LLZO pellets infused with solvated ionic liquid (SIL). The presence of SIL was found to enhance lithium metal wettability at the electrolyte-anode interface facilitating Li-ion transport. The impedance spectroscopy (EIS) revealed 3D interconnected morphology in LLZOCET electrolyte which offered lowered impedance, higher lithium ionic conductivity (0.215 mS/cm) and lowered electronic conductivity (7.59×10^{-8} S/cm) at RT compared to LLZOGC. The developed SHE showed stable lithium platting/stripping behaviour for >1350 h without dendritic penetration with critical current density (CCD) of 700 μA/cm^{2}which was higher than conventional prepared Ga-LLZO (400 μA/cm^2). The electrochemical performance was tested in full cells using $LiMn_2O_4$ cathode and Li metal as anode and cycled (>500 cycles) at different current densities (0.1–3.0 mA/cm^2). At 1C, engineered LLZO demonstrated 94% capacity retention with >98% columbic efficiency. The post-electrochemical analysis revealed no change in cubic phase or morphological degradation even after prolonged cycling. The compiled data thus clearly established that engineering at the microstructural level might be one of the critical steps for the realization of workable SSLMBs.

1. Introduction

The next generation lithium batteries (LIBs) demand electrolytes either in the form of solid glass or ceramic, but not as liquid or polymer. Although existing LIB technology achieved tremendous commercial success relying upon liquid or polymer electrolytes, but in the expense of reduced energy density, power density, and safety. The underlying reason is that the liquid or polymer battery does not permit the use of Li metal as anode (with the highest theoretical capacity of 3860 mAhg^{-1}) due to several problems, particularly the formation of uncontrolled dendritic growth leading to short circuit and solid electrolyte interphase (SEI) which continuously consumes Li metal and dry up the electrolyte, resulting in an increase in internal cell resistance and, subsequently, reduction in coulombic efficiency.[1–3] The focus is thus to develop solid inorganic electrolytes which offer opportunity to use Li metal as an anode. Furthermore, they can mitigate the above-mentioned-problems; they can mechanically suppress dendritic growth, and eliminate SEI formation.[4,5] In the last two decades, several solid electrolyte materials (SSEs) were explored e.g., $Li_7La_3Zr_2O_{12}$ (LLZO), $Li_{1+x}Al_xTi_{2-x}(PO_4)_3$ (LATP), $Li_{3.3}La_{0.56}TiO_3$(LLTO), Li_2S-P_2S_5, $Li_{1.5}Al_{0.5}Ge_{1.5}(PO_4)_3$ (LAGP), $Li_{10}GeP_2S_{12}$ (LGPS) with fast li-ion conducting properties at room temperature.[5,6] Nevertheless, the realization of workable all solid-state lithium metal batteries (ASSLMBs) is still far away than it was thought. Two major bottlenecks are mainly reported: (i) instability of the interface between SSEs and the electrode, causing unwanted chemical reactions with the generation of large interfacial impedance and finally loss of anodic contact and (ii) transgranular lithium dendritic migration across the grain boundaries of solid electrolyte, posing threat to short circuit.[4–9].

Several strategies are now being considered to address the

* Corresponding author.
E-mail address: mwraja@cgcri.res.in (M. Wasim Raja).

https://doi.org/10.1016/j.cej.2023.148200
Received 15 September 2023; Received in revised form 14 December 2023; Accepted 18 December 2023
Available online 20 December 2023

Journal of Power Sources 606 (2024) 234573

Contents lists available at ScienceDirect

Journal of Power Sources

journal homepage: www.elsevier.com/locate/jpowsour

Flexible ceramic based 'paper separator' with enhanced safety for high performance lithium-ion batteries: Probing the effect of ceramics impregnation on electrochemical performances

Mononita Das, Kuntal Ghosh, Mir Wasim Raja *

Energy Materials & Devices Division, CSIR-Central Glass & Ceramic Research Institute, Kolkata, West Bengal, 700032, India

HIGHLIGHTS

- Sustainable, flexible and high safety ceramic based paper separators for LIBs.
- Separators were developed using easy to scale up wet-coating process.
- Ceramic impregnation affects physical and electrochemical properties of the separators.
- Paper separators show superior electrolyte wettability and high thermal stability.
- Better electrochemical performances and flame safety are other important advantages.

GRAPHICAL ABSTRACT

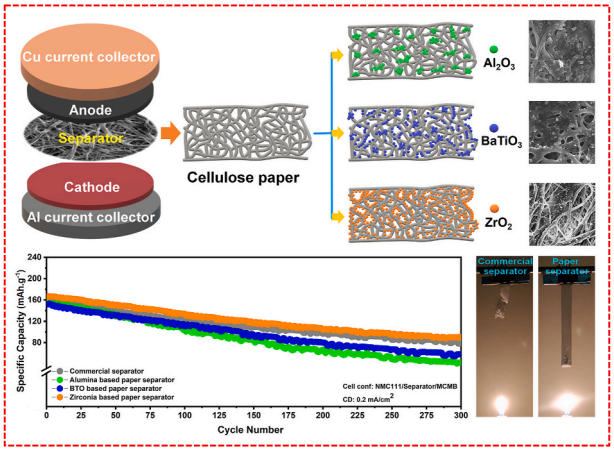

ARTICLE INFO

Keywords:
Cellulose
Ceramics
Paper separator
Lithium-ion battery
Flame resistance

ABSTRACT

Cellulose is now considered as an appealing environment friendly material for the development of sustainable separators for rechargeable batteries. This study thus aims to develop high performance paper based ceramic separators with superior electrolyte wettability (>170 %), high thermal stability (>200 °C) and excellent flame safety. While developing paper based ceramic separator, extensive studies are carried out to understand the-nature and functionality of different nano-structured ceramic materials (Al_2O_3, $BaTiO_3$ and ZrO_2) impregnated in paper matrix. Nano-ZrO_2 facilitates an effective pathway for Li^+-ion transport ($t_{Li}^+ = 0.51$), whereas $BaTiO_3$ and Al_2O_3 ceramics show moderate Li^+-ion transport properties (t_{Li+} of 0.29 and 0.30 respectively). Electrochemical Impedance Spectroscopy (EIS) measurement clearly reveals that ZrO_2 exhibits more interfacial compatibility with the electrodes (MCMB and $LiNi_{1/3}Mn_{1/3}Co_{1/3}O_2$) compared to the other two ceramic separators during full cell operation. The developed paper separators show excellent electrochemical properties in terms of cycling (tested 300 cycles), multi-electrode compatibility and rate capabilities at different current densities of 0.1–1.2 $mAcm^{-2}$. The pre- and post-electrochemical EIS data reveal that ZrO_2 based impregnation offers significantly

* Corresponding author.
E-mail addresses: das.mononita17@gmail.com (M. Das), kuntalghosh1004@gmail.com (K. Ghosh), mwraja@cgcri.res.in (M.W. Raja).

https://doi.org/10.1016/j.jpowsour.2024.234573
Received 5 February 2024; Received in revised form 4 April 2024; Accepted 16 April 2024

Journal of Power Sources 654 (2025) 237838

Contents lists available at ScienceDirect

Journal of Power Sources

journal homepage: www.elsevier.com/locate/jpowsour

Role of LLZO active filler in PVDF-modified cellulosic paper matrix: A sustainable, thermally durable and high-performance separator for next generation lithium batteries

Kuntal Ghosh [1], Mononita Das [1], Mir Wasim Raja [*]

Energy Materials & Devices Division, CSIR-Central Glass & Ceramic Research Institute, Kolkata, 700032, India

HIGHLIGHTS

- Sustainable, flexible paper separator impregnated with LLZO for high performance LIBs.
- An industry-friendly wet-coating process optimized for 'roll-to-roll' fabrication.
- Paper separator with LLZO shows better Li-ion transport than Al_2O_3 loaded separator.
- Improved flame resistance and multi-electrode compatibility for LLZO-coated separator.
- Better electrochemical performance of LLZO coated separator after thermal shock.

GRAPHICAL ABSTRACT

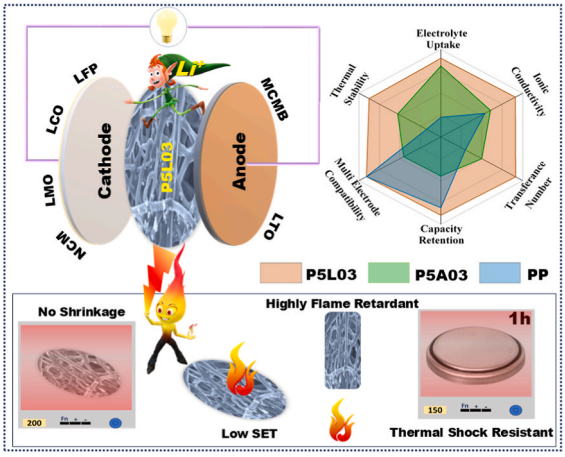

ARTICLE INFO

Keywords:
Paper separator
LLZO electrolyte
Flame retardant
High-rate capability
Multielectrode compatibility

ABSTRACT

The present study highlights the effect of active (LLZO) and inactive (Al_2O_3) ceramic impregnation in paper-based cellulosic separators developed using an industry-friendly dip-coating process. The fabricated separator with 30 wt% LLZO (P5L03) exhibits superior ionic conductivity (1.23 mS cm^{-1}), higher Li-ion transport properties (t_{Li}^{+} = 0.64), wider electrochemical window (>5.5V) as compared to Al_2O_3 (30 wt%) based (P5A03) and commercial PP based separators. The enhancement in electrical properties is likely due to the intrinsic Li-ion conductivity of LLZO and the structural modification of PVDF chain induced by the Lewis basic environment of LLZO. P5L03 shows better capacity retention after long cycling and excellent compatibility against different cathodic (LFP, LMO, LCO, NMC) and anodic (LTO, MCMB) configurations. The developed P5L03 separator exhibits excellent flame retardancy and better self-extinguishing properties with lowest self-extinguishing time of 5.55s, as compared to P5A03 (8.76s) and PP (11.10s). It also shows outstanding electrochemical performance even after self-extinguishing test and thermal shock treatment at 120 °C and 150 °C for 1 h. In summary, paper

* Corresponding author.
E-mail addresses: kuntalghosh1004@gmail.com (K. Ghosh), das.mononita17@gmail.com (M. Das), mwraja@cgcri.res.in (M.W. Raja).
[1] These two authors contributed equally to this work.

https://doi.org/10.1016/j.jpowsour.2025.237838
Received 9 January 2025; Received in revised form 24 June 2025; Accepted 4 July 2025
Available online 11 July 2025

Solid State Ionics 430 (2025) 117008

Contents lists available at ScienceDirect

Solid State Ionics

journal homepage: www.elsevier.com/locate/ssi

The critical role of Al_2O_3, $BaTiO_3$ and ZrO_2 nanoceramic fillers in PVDF-HFP based composite polymer electrolytes for high performance lithium-metal batteries

Mononita Das [a], Kuntal Ghosh [a], Vijaya [b], Mir Wasim Raja [a,*]

[a] Energy Materials & Devices Division, CSIR-Central Glass & Ceramic Research Institute, India
[b] School of Energy Science and Engineering, Indian Institute of Technology Guwahati, India

ARTICLE INFO

Keywords:
Composite solid polymer electrolytes
Lithium-metal batteries
Inorganic fillers
Li dendritic growth
Ionic conductivity

ABSTRACT

Lithium metal batteries (LMBs) can be the ultimate choice for future battery technologies since they use Lithium metal as anode, which offers high theoretical capacity (3860 $mAh.g^{-1}$) and lowest electrochemical potential (−3.04 V vs. SHE). However, their commercialization is limited by dendritic growth, interfacial instability, and safety risks associated with liquid electrolytes. In this work, composite solid polymer electrolytes (CSPEs) are developed by incorporating various (Al_2O_3, $BaTiO_3$, and ZrO_2) ceramic fillers into a PVDF-HFP/LiTFSI matrix via a scalable solution casting method. Among these, optimized 10 wt% ZrO_2-based CSPE (PLZ) delivers the highest room-temperature ionic conductivity (9.26×10^{-5} S cm^{-1}), excellent Li^+ transference number (0.55), superior tensile strength (3.23 MPa), wide potential window (5.33 V), and good flame retardancy. Li/Li symmetric cells using PLZ showed stable lithium plating/stripping for more than 480 h at 0.10 $mA.cm^{-2}$ with a low overpotential of ~7 mV. Electrochemical impedance spectroscopy and equivalent circuit fitting confirmed the lowest increase in interfacial resistance after cycling. Time-resolved distribution of relaxation time (DRT) and 2D contour analysis revealed that PLZ maintained stable SEI and charge-transfer resistances, while bare CSPEs showed growing interfacial instability during cycling. These improvements are attributed to Lewis acid-base interactions and surface charge effects that reduce crystallinity and promote Li^+ mobility. Full-cell evaluations with $LiFePO_4$ and NMC111 cathodes demonstrated high discharge capacities and good cycling stability. Thus, this study offers a promising pathway for developing robust and safe CSPEs for next-generation solid-state LMBs.

1. Introduction

In the ongoing digital era, Lithium-ion batteries (LIBs) are an integral part of daily life. They are essential in powering almost every needful device, ranging from household to sustainable transportation and e-mobility, due to their high theoretical capacity and impressive energy and power density. Conventional LIBs consist of Graphite-based anodes and Nickel or Cobalt-rich cathodes, along with carbonate-based liquid electrolytes containing $LiPF_6$ and polyolefin-based separator membranes [1]. While the carbonate-based liquid electrolytes are efficient to use due to their high ionic conductivity (~10^{-3} S.cm^{-1}), they impose several challenges like leakage, flammability, narrow electrochemical stability window, and untimely decomposition inside the battery [2,3]. Additionally, the plastic-based separators are also prone to dimensional instability and combustion at high temperatures [4,5]. Together, these components can cause serious safety concerns, which mandates the exploration of more efficient, sustainable, thermally stable, and flame-retardant alternatives with similar or better performance.

Here, solid electrolytes could be an effective alternative as they do not present any risk of leakage and flammability, and can additionally provide a wider electrochemical stability window, high performance, and good compatibility with Lithium metal anodes [6]. In view of this, the replacement of both liquid electrolyte and polymeric separator with solid electrolyte can be a promising approach to overcome the challenges of short-circuit and thermal runaway [7]. Solid electrolytes can be of three major types: (a) inorganic solid electrolytes (ISEs), (b) solid polymer electrolytes (SPEs), and (c) composite solid polymer electrolytes (CSPEs) [8,9]. The inorganic solid electrolytes like oxides (LLZO,

* Corresponding author.
E-mail addresses: das.mononita17@gmail.com (M. Das), kuntalghosh1004@gmail.com (K. Ghosh), vijaya19@iitg.ac.in (Vijaya), mwraja@cgcri.res.in, mwraja.cgcri@csir.res.in (M.W. Raja).

https://doi.org/10.1016/j.ssi.2025.117008
Received 20 June 2025; Received in revised form 14 August 2025; Accepted 24 August 2025